ENERGY DEPENDENCE OF THE EFFECTIVE INTERACTION FOR NUCLEON-NUCLEUS SCATTERING

by

Helmut Seifert

Dissertation submitted to the Faculty of the Graduate School
of The University of Maryland in partial fulfillment
of the requirements for the degree of
Doctor of Philosophy
1990

Advisory Committee:

Dr. James J. Kelly, Advisor
Dr. Chia-cheh Chang
Dr. Nicholas S. Chant
Dr. Stephen J. Wallace
Dr. Timothy M. Heckman

Abstract

Title of Dissertation: Energy Dependence of the Effective Interaction for Nucleon-Nucleus Scattering

Helmut Seifert, Doctor of Philosophy, 1990

Dissertation directed by: James J. Kelly, Associate Professor
Department of Physics and Astronomy

We have measured cross sections and analyzing powers for ^{40,42,44,48}Ca and ^{16}O at IUCF using the new high-resolution K600 spectrometer for 100 and 200 MeV protons. Measurements at 318 MeV for ^{40,42,44,48}Ca and ^{32,34}S were done at LAMPF using the HRS spectrometer.

In this work, we obtain empirical effective interactions by fitting inelastic scattering data for many low-lying normal-parity isoscalar excitations of the self-conjugate nuclei ^{16}O and ^{40}Ca, assuming a local $t\rho$ folding model. One-nucleon transition densities are from (e, e'). The fitted interactions are iterated to generate optical potentials self-consistently. We find that the fitted parameters are essentially target independent, which supports the validity of the local density hypothesis. Elastic scattering is predicted by extracting the rearrangement factor $(1 + \rho d/d\rho)$ from the fitted inelastic interactions. Below 300 MeV the strength of the empirical interaction is reduced at zero density and the general density dependence is weaker compared to the theoretical interaction. Above 300 MeV we find the density dependence is stronger than expected. The empirical interactions provide better descrip-

tions of elastic and inelastic data than IA calculations or LDA calculations using theoretical G-matrices, and can be used for nuclear structure studies of other nuclei. Fitted optical potentials above 300 MeV are comparable to equivalent Schrödinger potentials from the relativistic IA2 model.

Dedication

To all the ones I love:
my family, my friends
and
Tuleen Parveen

Acknowledgements

I first would like to thank my advisor, James J. Kelly, for guiding me through all these years of exciting research, and for suggesting this interesting dissertation topic. I also want to thank him for helping me through the for me as a foreign student sometimes difficult time at the beginning of my graduate career.

I would like to thank the Experimental Nuclear Physics group as a whole—faculty, staff, and all my collegues—for providing a very pleasant work atmosphere which I will always fondly remember. To my family goes, of course, my deepest gratitude for their neverending support.

During my time here in Maryland I have also met some very special people who have become very good friends of mine, and whom I want to mention here. First, there are Raul and Steve, and especially Grace, who have shared all the good times and bad times with me, and who were always there for me. John and Sabrina, George and Liz I want to thank for having invited me so many times to spend the holidays together with their wonderful family. Finally, last but certainly not least, there is Tuleen Parveen who will always be in my heart.

Contents

List of Tables

List of Figures

1 Introduction

Studies of the projectile-nucleon effective interaction in the nuclear medium and of the internal structure of nuclei are among the dominant themes of intermediate energy nuclear physics. Electron scattering for a long time has been an extremely popular tool for nuclear structure studies. The electroexcitation of discrete nuclear transitions can be described as a direct reaction which is driven by a local two-body interaction. We believe that both the reaction mechanism and the effective interaction are understood accurately. Together with the fact that nuclei are essentially transparent to high energy electrons, this permits us to extract the relevant aspects of the structure of the nucleus with very high precision. Since electromagnetic probes are sensitive to several one-body target densities, including charge, spin, current, and spin-current degrees of freedoms, a wealth of important structural information on nuclei can be obtained [Pet 81].

In spite of all these advantages, the versatility of the electron as a nuclear probe is limited. Electrons are largely insensitive to the bulk neutron distribution and view neutrons almost exclusively through the magnetic moment of a single unpaired valence neutron. Hadronic projectiles, on the other hand, are about equally sensitive to neutrons and to protons. They also sample transition densities which are not accessible to electron scattering at all. Direct $0^+ \rightarrow 0^-$ transitions are examples of a type of transition which is forbidden in first order for electron scattering [DeF 66], which are however readily excited by proton scattering through the longitudinal spin

response [Lov 83]. Therefore, a truly comprehensive investigation of all the one-body aspects of nuclear structure requires the inclusion of a complementary analysis of hadron scattering. To make hadrons a quantitative probe for nuclear structure, however, we must understand or at least calibrate the relevant aspects of the reaction mechanism and of the projectile-nucleus effective interaction.

Of the hadronic interactions, the nucleon-nucleon interaction is the one which has the most sound theoretical foundation. Furthermore, there is a roughly 300 MeV wide "window of visibility" within which the interior sensitivity for nucleons becomes quite comparable to that of electrons. The good interior sensitivity is primarily due to the fact that the isoscalar part of the dominant matter interaction, which drives distortion effects, passes through a broad minimum between about 200 and 500 MeV [Car 85]. Also, at these energies the wavelength of the probe is short which provides for excellent radial resolution. Finally, in this region multistep processes are at a minimum which allows us to assume that direct, one-step excitations are the dominant reaction mechanism. The sensitivity of protons to the nuclear interior and the energy dependence of this sensitivity has been studied for the lowest lying monopole transition in ^{40}Ca for energies between 60 and 800 MeV with pseudodata [Kel 88]. The results of the pseudodata analysis are shown in Figure 1.1. Even though absorption increases steadily throughout this energy range the interior sensitivity improves dramatically between 60 and about 200 MeV. The improving sensitivity is due to the decreasing importance of Pauli blocking in the nuclear interior. This causes the con-

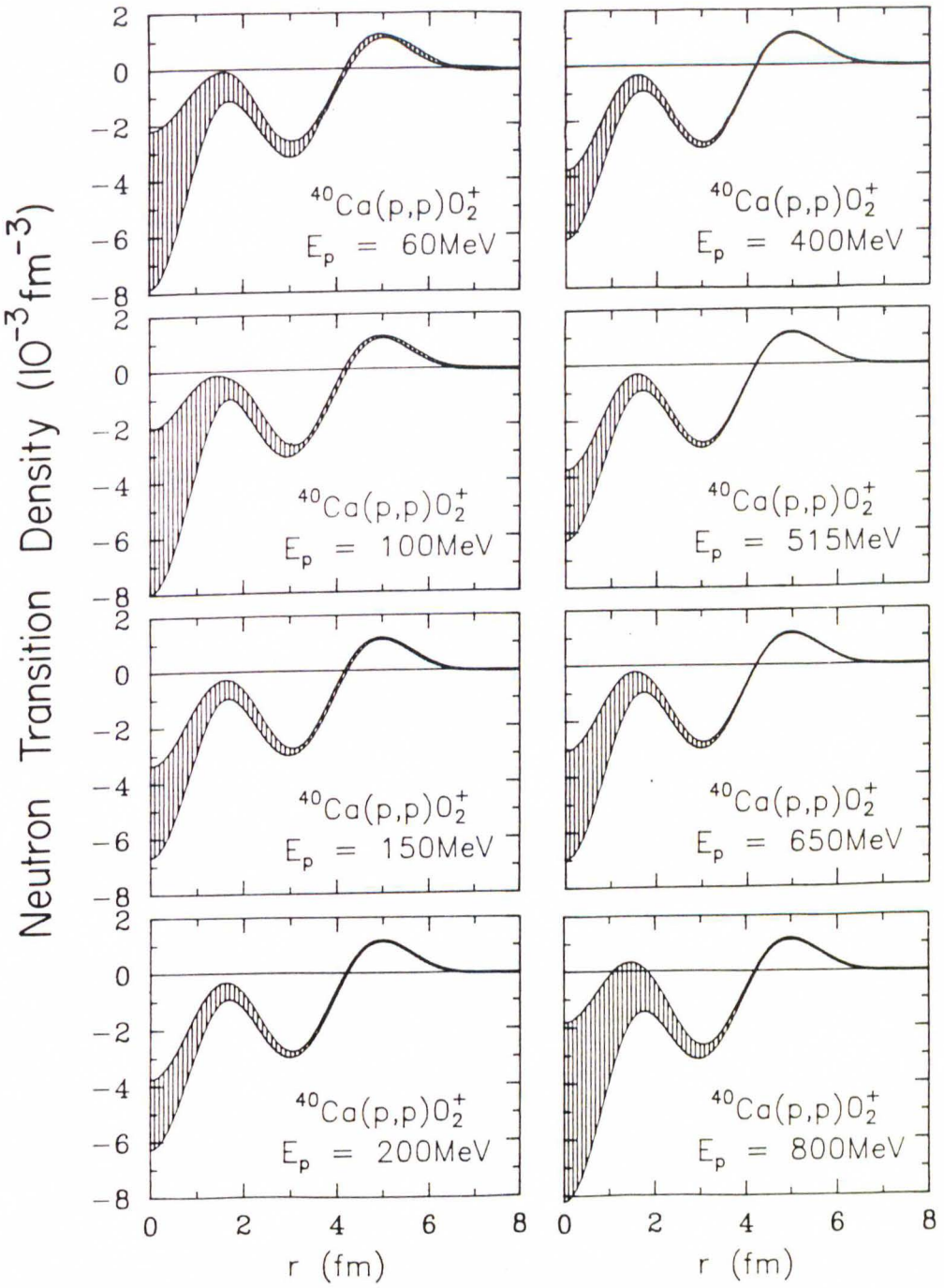

Figure 1.1: Energy dependence of the interior sensitivity of nucleon inelastic scattering; the window of maximum transparency is between about 200 and 500 MeV. The figure shows the results of a pseudodata analysis for the 0_2^+ state of ^{40}Ca [Kel 88].

tribution of the interior to increase relative to that of the surface, thereby improving the interior sensitivity. The sensitivity is optimal between about 200 and 500 MeV since in this energy region declining density dependence and increasing absorption balance. At higher energies absorption becomes dominant and because of the decreasing penetrability, the interior sensitvity deteriorates.

Direct, one-step reactions can be conveniently treated within the single-scattering framework by means of a local "$t\rho$" folding model, where the scattering amplitude is constructed from the effective nucleon-nucleon interaction weighted by the nucleon distribution inside the target nucleus. Within this model, knowledge of either the interaction factor t or the stucture factor ρ permits the systematic evaluation of the unknown factor. In practice, the complete amplitude for a certain transition contains not only an implied sum over charge indices, but may additionally involve a whole variety of different densities and interaction components. The first problem can be ignored for the case of self-conjugate nuclei where transitions are purely isoscalar or isovector in character. Furthermore, for a few special classes of transitions the number of relevant $t\rho$ terms can effectively be reduced. The most important class of transitions is comprised of natural parity transitions ($\Delta\pi = (-)^{\Delta J}$ with $\Delta\pi = \pi_i\pi_f$) to low-lying collective states in the target nucleus. Not only is the matter density for this type of transition much larger than either spin, current, or spin-current densities, in addition the matter interaction also dominates over the other interaction components [Car 85]. In proton scattering, the excitation of natural parity states is driven exclusively by

the spin-independent central and spin-orbit components of the interaction. For natural parity transitions, therefore, we will be able to study these two components of the nucleon-nucleus interaction, since both the reaction mechanism is reasonably well known and all the relevant nuclear structure aspects can be reliably determined by independent means such as electron scattering.

The self-conjugate nuclei ^{16}O and ^{40}Ca are the ideal laboratory for effective interaction studies. Both nuclei have doubly closed shells (see Figure 1.2) and their spectra contain many strong well separated low-lying collective states for which also comprehensive electron scattering data are available [But 86, Mis83, Har 84]. Some of these states are surface excitations, such as the 3_1^- states, and are sensitive to the low-density apects of the effective interaction. Other states, such as the inelastic monopole transitions or the 1_1^- state of ^{16}O, peak in the interior and thus probe the high-density properties of the effective interaction. Intermediate cases like the 3_2^- state of ^{40}Ca, which has strong lobes of the transition density both in the interior and at the surface, will provide interesting challenges for any effective interaction. Finally, we find in these targets states which give insights into different reaction mechanisms, such as the 2_2^+ state of ^{16}O which is a good candidate for a two-step excitation. For some states, such as the 0_3^+ state in ^{16}O, densities other the matter density might become important for certain energies and momentum transfers [Pet 85].

The quality of theoretical interactions and their usefulness in quantitative studies of nuclear structure can be easily tested on the isoscalar natural parity states of these targets. Unsuccessful nonrelativistic impulse ap-

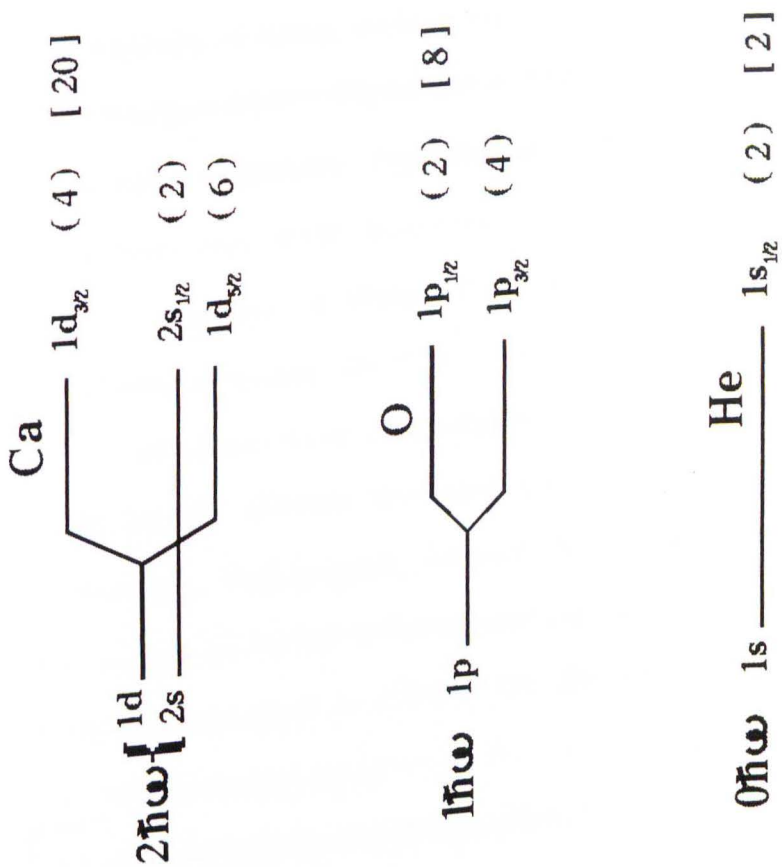

Figure 1.2: Shell structure of the doubly magic self-conjugate nuclei ^{16}O and ^{40}Ca for protons (or neutrons). On the left are the harmonic oscillator levels, to the right the actual levels including the spin-orbit splitting. The numbers in parentheses are the occupation numbers for the level, the numbers in brackets the sum of all particles up to and including the level.

proximation calculations, especially for interior-peaked states (e.g. [Kel 82]), suggested the necessity of strong medium modifications to the effective interaction. The strongest density dependence is exhibited by the central spin-independent isoscalar component. Pauli blocking manifests itself as damping of the imaginary part, while short-range correlations modify the real part of the central component by adding a short-range repulsive contribution which is proportional to density. All of the available theoretical models produce medium modifications which are qualitatively similar [Ger 79, Ger 83, Rik 84, Nak 88, Ray 90]. However, their predictions of scattering data differ significantly [Kel 89a]. Unfortunately, however, the various models do not only use different nucleon-nucleon potentials but also use different numerical procedures and approximations to calculate the effective interactions. Additionally, all the interactions are given in the form of enormous tables of amplitudes or tables of Yukawa expansion coefficients in different representations which do not allow much insight into the physics of the respective model. A comparison of one model to others based on these interaction tables is therefore extremely difficult, if not altogether impossible.

The interactions presently available have been found not to be sufficiently accurate for detailed nuclear structure applications [Kel 86c], raising the question whether this problem is due to deficiencies of the interaction or due to the local density prescription [Jeu 74, Jeu 76] which is used to apply the effective interaction to nucleon-nucleus scattering. The prescription assumes that the knowledge of only the local density of the medium in which the particular reaction takes place is sufficient to evaluate projectile-nucleus

scattering. Within this framework it should not matter whether the interaction takes place in the interior or at the surface of the nucleus; it should also not matter whether the reaction occurs in a small or a large nucleus. Although physically plausible, this prescription has never been established as an actual approximation to a more accurate theory whose corrections can, even in principle, be evaluated. Presently, the local density prescription is more of a convenient ansatz than an actual approximation.

In an alternate approach, we use a physically motivated phenomenology which can serve both as a means to compare theoretical models to each other, as well as a means to describe data [Kel 85a]. The effective interaction which emerges from such a fit to data can then be considered a measured interaction for a finite nuclear system. A comparison to parameters which were obtained from a fit to theory will help assess differences and/or deficiencies of the theoretical model. Finally, we will have a means to assess the validity of the local density hypothesis in a consistent and more or less model independent fashion by systematically studying the dependence of the interaction on the local density, the target, and the energy. These studies, therefore, are the major goal of the present work, in which we will systematically address all the major premises of the local density prescription.

* * *

In Chapter 2 an attempt is made to review more or less carefully and completely all the theoretical background which is relevant for this work, including the relativistic impulse approximation and the more recent full-folding calculations. We present in this chapter various IA and LDA calcula-

tions, as well as IA2 calculations, and compare them with our new ^{16}O and ^{40}Ca data at 100, 200 and 318 MeV. Also, in this chapter we introduce the tools which will be used for our phenomenological analysis.

Chapter 3 deals primarily with the experimental setup, including the accelerator, the beam line optics, the apertures and targets used, the spectrometer and focal plane detectors, and the electronics and data acquisition. Chapter 4 explains the necessary calibrations for our experiment. Some of these calibrations were done on-line during the experiment, such as vertical scans and the matching of the spatial and angular dispersion; others were done during data analysis based on measurements taken during the experiment. This includes the determination of the beam polarization, the true scattering angle, and various tests addressing the stability of the cross sections with respect to parameters like acceptance and event rate. Chapter 5 is dedicated to our drift chamber detectors. Here we discuss the observed event types and the methods used to accurately determine particle trajectories. We also will identify all the global corrections to the cross section which are required due to the efficiency of the chambers, as well as to certain background modified events which are not processed in the analyzer. Finally, we will mention some of the diagnostics that are available for finding problems in the chamber performance.

Chapter 6 deals with the data reduction. This includes a discussion of the data replay and the cuts used, as well as a brief discussion of the line-shape fitting part of the analysis. Also covered in this chapter are the computation of the unpolarized cross section, the analyzing power, and their

errors, as well as the kinematic formulae which were used to express our results in c.m. quantities. Furthermore, the various normalizations that have to be applied to the data are explained. At the end of this chapter we present and discuss our experimental results. In Chapter 7 we show and discuss the results of our effective interaction analysis. We will compare the ability of our empirical interaction to accurately predict scattering data with that of the available theories, including some relativistic models. To test the validity of the local density prescription, we will study the dependence of the effective interaction on both the mass number A and the energy E. Finally, in Chapter 8 we will give a brief summary of our conclusions.

2 Theoretical Background

2.1 The Transition Matrix as an Effective Interaction

To motivate the concept of an effective interaction let us consider an example from elementary scattering theory. The Schrödinger equation for the scattering of a particle of mass μ and energy E by a potential $v(\boldsymbol{r})$ can be written

$$(E - K)\chi(\boldsymbol{r}) = v(\boldsymbol{r})\chi(\boldsymbol{r}), \tag{2.1}$$

where $K = -\nabla^2/2\mu$ is the kinetic energy operator[1]. A solution of Eq. (2.1) can be obtained succinctly by dividing both sides by $(E - K)$

$$\chi = \frac{1}{E - K} v\chi. \tag{2.2}$$

Proper treatment of the singularity by insertion of an infinitesimal $+i\varepsilon$ in the denominator and addition of any solution of the homogeneous equation

$$(E - K)\phi(\boldsymbol{r}) = 0 \tag{2.3}$$

to satisfy the required boundary conditions, incoming plane waves and outgoing spherical waves, yields the formal solution of the Schrödinger equation

$$\chi^{(+)} = \phi + \frac{1}{E^+ - K} v\chi^{(+)} \equiv \phi + G_0^+(E)v\chi^{(+)}, \tag{2.4}$$

with $E^+ = E + i\varepsilon$. This is known as *Lippmann-Schwinger* equation, where $G_0^+(E)$ is the free-particle Green function with outgoing boundary conditions.

[1] Alternatively, this problem can also be thought of as the scattering of two nucleons where μ is the reduced mass and v is the nucleon-nucleon *(NN)* potential.

The transition amplitude for elastic scattering from an incident momentum $\boldsymbol{k}$ to a final momentum $\boldsymbol{k}'$ is

$$T(\boldsymbol{k}', \boldsymbol{k}) = \langle \phi(\boldsymbol{k}') | v | \chi^{(+)}(\boldsymbol{k}) \rangle. \tag{2.5}$$

If one assumes that the effect of the scattering potential on the incident wave is small, one can replace in the matrix element $\chi^{(+)}$ by ϕ and write the transition amplitude in the *first Born approximation* as

$$T(\boldsymbol{k}', \boldsymbol{k}) \approx \langle \phi(\boldsymbol{k}') | v | \phi(\boldsymbol{k}) \rangle. \tag{2.6}$$

It is now useful to introduce the *transition matrix* t by

$$t\phi = v\chi^{(+)}. \tag{2.7}$$

Eq. (2.4) then gives a Lippmann-Schwinger equation for t

$$t = v + vG_0^+ t \tag{2.8}$$

and the transition amplitude, Eq. (2.5), can be written as the plane wave matrix element

$$T(\boldsymbol{k}', \boldsymbol{k}) = \langle \phi(\boldsymbol{k}') | t | \phi(\boldsymbol{k}) \rangle. \tag{2.9}$$

Thus, the significance of the transition matrix here is that it acts as an effective interaction for which the Born approximation is exact, provided an appropriate t can be found [Sat 83, Kel 85]. This feature will be applied later, when we treat the Born approximation as an exact model for scattering to extract an effective interaction.

2.2 Elastic Nucleon-Nucleus Scattering—The Optical Model

Since its introduction by Feshbach, Porter and Weisskopf [Fes 54] in the 1950s, the nuclear *optical model* has been a simple and yet powerful tool for describing the complex problem of elastic nucleon-nucleus scattering. The name "optical model" comes from the many similarities between nuclear elastic scattering and optical refraction and absorption of light. The wave describing the incident particle experiences within the range of the nuclear potential refraction, very much like a light wave entering a medium with different index of refraction[2]. If the potential is not constant but has, for instance, a Woods-Saxon shape, the scattering process is comparable to a light wave incident on a crystal ball with a radially variable index of refraction. The occurence of nuclear reactions due to interactions of the projectile with the target nucleons leads to absorption from the elastic channel. Here the optical analog is the absorption of a light wave in a "clouded" crystal ball [Fes 54]. Absorption increases with increasing incident energy since the probability for interaction with the nucleons in the target becomes larger; in the presence of very strong absorption one, therefore, observes cross section angular distributions that are similar to those for diffraction of electromagnetic waves by an absorptive "black disk".

To account for both its refractive and absorptive feature the optical

[2] For example, the index of refraction n for a spuare-well potential of depth $-V_0$ and an incident particle with energy E is simply $n = \sqrt{1 + V_0/E}$.

potential has to be complex

$$U(r) = V(r) + iW(r), \tag{2.10}$$

where the imaginary part W of the potential must be negative to allow for particle absorption. Furthermore, the optical potential is composed of a *central* part (U^C) and a term (U^{LS}) which accounts for the *spin-orbit* coupling[3] between target and projectile. We thus have the form

$$U(r) = U^Z(r) + U^C(r) + U^{LS}(r)\boldsymbol{L}\cdot\boldsymbol{\sigma}, \tag{2.11}$$

where U^Z describes Coulomb scattering.

Macroscopically, the real central part of $V(r)$ usually is assumed to have the Woods-Saxon shape $V(r) = -V_0 f(r)$, where the radial function $f(r) = [1 + e^{(r-R_{1/2})/a}]^{-1}$ reflects the density distribution of the nucleons[4]. For the spin-orbit part one assumes that a particle in the inner, flat part of the potential moves in a homogeneous medium without a center with respect to which an angular momentum could be defined. Therefore, only the nuclear surface should contribute to the real part of the spin-orbit interaction. This radial dependence is phenomenologically often described by a *Thomas*-form, $h(r) \sim r^{-1}\partial f(r)/\partial r$. It is less straightforward to define a phenomenological form for the imaginary part W of the optical potential. For energies below

[3] It is found experimentally that unpolarized particles are polarized by the scattering potential; for polarized particles, one finds a left-right asymmetry in the angular distribution of the cross section.

[4] For $r = R_{1/2}$, the density decreases by one half; within the surface thickness t, related to the surface diffuseness a by $t = 4.4a$, the density decreases from 90% to 10%.

about 20 MeV a potential which features predominantly surface absorption has been found adequate, while for higher energies (above 80 MeV) a potential with volume absorption appears to be more appropriate. Cross section angular distributions, however, have been shown to be not very sensitive to the exact details of the shape of the imaginary potential [May 84].

An important extension to the optical model are *coupled channels* calculations, where certain reaction channels are treated explicitly, rather than being represented by simple absorption. The total wave function is expanded with respect to wave functions of the elastic and the prominent inelastic channels and only the remaining reaction channels are treated by simple absorption. The resulting system of coupled differential equations can be solved for certain simple cases, e.g. for collective excitations.

On a microscopic level, construction of the optical potential is a more difficult problem due to the complexities of the interplay between target ground-state properties, the effective nucleon-nucleon interaction, and medium modifications. The traditional nonrelativistic approaches to the optical potential in nucleon-nucleus scattering are the multiple scattering formalisms of Watson [Wat 53], and of Kerman, McManus and Thaler (KMT) [Ker 59] and the nuclear matter self-energy formalism developed by Hüfner and Mahaux [Hüf 72]. More recently, a relativistic approach was initiated by McNeil, Shepard and Wallace [McN 83]. In the next sections these different approaches will be reviewed.

2.3 Multiple Scattering Approach

2.3.1 Introduction

In the multiple scattering approach the optical potential is the sum of interactions in which the incident projectile excites the target nucleus out of the ground state and does not de-excite it back until the last step. The first order term of the potential, the so-called single-scattering term, is a coherent sum of terms representing the scattering of the incident projectile by each individual target nucleon. The second order term, called the double-scattering term, involves a sum in which the incident projectile scatters sequentially from any pair of nucleons. Nucleon-nucleon correlations in the nuclear wave function are, therefore, represented by this term. At intermediate energies the single-scattering term of the optical potential dominates: the excitation of a single nucleon in a two-body collision with the incident projectile is the most likely reaction process due to the short range of the interaction and the high velocity (and associated short transit time through the target nucleus) of the projectile [Wal 87].

The Watson multiple scattering series [Wat 53] for the optical potential operator appropriate to the elastic scattering of a projectile (0) from a bound state of A particles is

$$U = \sum_{i=1}^{A} \tau_{0i} + \sum_{j \neq i}^{A} \tau_{0i} Q G^{+} \tau_{0j} + \cdots . \tag{2.12}$$

Here Q is the $(A+1)$-particle projection operator onto the complete, anti-

symmetric space of the target nucleons with exception of the ground state[5] and G^+ is the propagator with outgoing boundary conditions. $\mathcal{H}_{QQ}$ is the asymptotic Hamiltonian projected off the ground state and contains the sum of the projectile kinetic energy operator K_0 and the target Hamiltonian H_A

$$G^+ = \frac{1}{E^+ - \mathcal{H}_{QQ}}. \tag{2.13}$$

The scattering operator τ_{0i} is a solution of

$$\tau_{0i} = v_{0i} + v_{0i} Q G^+ \tau_{0i}, \tag{2.14}$$

where v_{0i} is the bare internucleon potential between the incident projectile and the ith target nucleon.

In the *single-scattering approximation*, the first term of the scattering series, Eq. (2.12), yields the momentum-space optical potential matrix element

$$U(\boldsymbol{k}', \boldsymbol{k}) \approx \sum_{i=1}^{A} \langle \boldsymbol{k}'; \Phi_0 | \tau_{0i} | \boldsymbol{k}; \Phi_0 \rangle_{\mathcal{A}}. \tag{2.15}$$

The scattering operator τ can be related to the t-matrix, the solution of the scattering of two nucleons (see Section 2.1), by

$$\tau_{0i} = t_{0i} - t_{0i} P G^+ \tau_{0i}, \tag{2.16}$$

where

$$t_{0i} = v_{0i} + v_{0i} \mathcal{A} G^+ t_{0i}. \tag{2.17}$$

[5] Related operators are P which projects *onto* the ground state Φ_0, and $\mathcal{A} = P + Q$ which projects onto the complete, antisymmetric space including the ground state.

The essence of the *impulse approximation* (NRIA) is now to approximate t in Eq. (2.16) by the free two-nucleon t-matrix and to calculate the optical potential from Eq. (2.15), without any further approximations[6].

There is an asymmetry between the propagation of the incident projectile and the bound target nucleon which is characteristic of the multiple scattering approach: the projectile propagates freely in intermediate states, while the target nucleon moves in the nuclear mean field. In the nuclear matter many-body approach (see below) the symmetry is restored by including the self-energy of the incoming projectile. One of the shortcomings of the multiple scattering approach is the potentially very slow convergence rate of the scattering series at low energies.

2.3.2 The Full Folding Potential and its Approximations

For simplicity, in the following expressions we will neglect the fact that the optical potential is actually an operator in the spin and isospin spaces of the projectile and adopt a somewhat schematic, not always rigorous, notation. We will also omit the boost from the NN c.m. to the NA c.m. frame (e.g. via the Møller factor [Møl 45]).

If the target ground state is taken to be a Slater determinant of single-particle states $\{\varphi_\alpha\}$, the optical potental, Eq. (2.15), can be compactly writ-

[6] The KMT optical potential differs by a scale factor of $\frac{A-1}{A}$ from the Watson optical potential. The difference arises from a different organization of the multiple scattering series and becomes relevant only for higher order terms. In the single-scattering approximation, we do not make a mistake if we simply omit the KMT factor.

ten as (we follow the notation of [Are 90a])

$$U(\boldsymbol{k}', \boldsymbol{k}; E) = \int d\boldsymbol{P} \sum_{\epsilon_\alpha < \epsilon_F} \varphi_\alpha^\dagger(\boldsymbol{p}') \hat{t}(\boldsymbol{q}, \boldsymbol{Q}; z_\alpha) \varphi_\alpha(\boldsymbol{p}), \tag{2.18}$$

where the initial and final momenta of the incident projectile (bound nucleon) are denoted by $\boldsymbol{k}$ and $\boldsymbol{k}'$ ($\boldsymbol{p}$ and $\boldsymbol{p}'$) and the initial and final relative momenta of the interacting pair by $\boldsymbol{\kappa} = \frac{1}{2}(\boldsymbol{k} - \boldsymbol{p})$ and $\boldsymbol{\kappa}' = \frac{1}{2}(\boldsymbol{k}' - \boldsymbol{p}')$, respectively. The momentum transfer is defined as $\boldsymbol{q} = \boldsymbol{k} - \boldsymbol{k}'$ or $\boldsymbol{\kappa} - \boldsymbol{\kappa}'$, and the exchange momentum transfer as $\boldsymbol{Q} = \boldsymbol{K} - \boldsymbol{P}$ or $\boldsymbol{\kappa} + \boldsymbol{\kappa}'$. The vectors $\boldsymbol{K} = \frac{1}{2}(\boldsymbol{k} + \boldsymbol{k}')$ and $\boldsymbol{P} = \frac{1}{2}(\boldsymbol{p} + \boldsymbol{p}')$ are averages of the initial and final projectile and target nucleon momenta. The total energy available in the NN center-of-mass system is

$$z_\alpha = E + \epsilon_\alpha - \frac{(\boldsymbol{P} + \boldsymbol{K})^2}{2M}, \tag{2.19}$$

where M is the total mass of the interacting pair and ϵ_α the energy of the single-particle states.

The reduced one-body t-matrix

$$\hat{t}(\boldsymbol{q}, \boldsymbol{Q}; z_\alpha) = \langle \boldsymbol{\kappa}' | \hat{t}(z_\alpha) | \boldsymbol{\kappa} \rangle_{\mathcal{A}} \tag{2.20}$$

is an antisymmetrized matrix element between states of initial ($\boldsymbol{\kappa}$) and final ($\boldsymbol{\kappa}'$) relative momenta of the interacting pair. This t-matrix satisfies a Lippmann-Schwinger equation of the form

$$\hat{t}(z) = v + v G_0^+(z) \hat{t}(z). \tag{2.21}$$

In calculating the optical potential from Eq. (2.18), the required antisymmetric structure is conserved by limiting the t-matrix to NN states which are

allowed by the Pauli principle. The knock-on exchange term for NN scattering is accounted for naturally with this prescription and it is not necessary to separate the interaction into direct and exchange components. At higher projectile energies the variation of the single-particle energy becomes relatively unimportant and above about 100 MeV it is possible to replace ϵ_α by its weighted average $\langle\epsilon\rangle$ in z. With the definition

$$\tilde{\rho}(\boldsymbol{q},\boldsymbol{P}) = \sum_\alpha \varphi_\alpha^\dagger(\boldsymbol{p}')\varphi_\alpha(\boldsymbol{p}), \tag{2.22}$$

for the mixed target density, the optical potential can then be written in the so-called *full-folding* form

$$U^{full}(\boldsymbol{q},\boldsymbol{Q}) = \int d\boldsymbol{P}\, \hat{t}(\boldsymbol{q},\boldsymbol{Q};z)\tilde{\rho}(\boldsymbol{q},\boldsymbol{P}), \tag{2.23}$$

a convenient starting point for several further approximations. Nonlocality enters into the full-folding optical potential through the interplay between off-shell degrees of freedom of the interaction and the nonlocality of the ground-state mixed density. In the subsequent approximations more or less off-shell and nonlocality information in the ingredients of the optical potential will be sacrificed for expediency.

If one assumes that the nucleon-nucleon amplitude varies only slowly as a function of its arguments compared to the nuclear density (or equivalently, that the range of the nuclear force is small compared to the nuclear size), one can expand $\hat{t}$ in a Taylor series in $\boldsymbol{P}$ about a fixed value $\boldsymbol{P}_0$. The reference momentum $\boldsymbol{P}_0$ is determined from the requirement that the contribution of the first derivative term be minimized. In the *optimum factorization approx-*

imation for elastic scattering, $\boldsymbol{P}_0$ is chosen to be zero[7]. After integration over the mixed density matrix one obtains the optimum factorized optical potential U^{fac} in terms of the diagonal one-body density

$$U^{fac}(\boldsymbol{q}, \boldsymbol{Q}) = \hat{t}(\boldsymbol{q}, \boldsymbol{Q}; z)\tilde{\rho}(\boldsymbol{q}). \tag{2.24}$$

Since $\boldsymbol{q}$ and $\boldsymbol{K}$ and z are completely arbitrary and independent of each other, this is also known as "off-shell $t\rho$" approximation [Pic 84, Els 90]. Although the off-shell t-matrix enters (albeit over a restricted range of momentum), information about the nonlocal structure of the mixed density is lost in this approximation [Are 90b].

If for any $\boldsymbol{Q}$ the two-body t-matrix $\hat{t}(\boldsymbol{q}, \boldsymbol{Q}; z)$ in Eq. (2.24) is equal to its on-shell value $\hat{t}^{on}(\boldsymbol{q}; z)$, one has the "local $t\rho$" approximation. Here the exchange momentum transfer $\boldsymbol{Q}$ is completely determined by the argument $\boldsymbol{q}$ at a given energy z, via $\boldsymbol{q} \cdot \boldsymbol{Q} = 0$ and $\boldsymbol{q}^2 + \boldsymbol{Q}^2 = 4\boldsymbol{\kappa}^2 = 4\boldsymbol{\kappa}'^2 = 4mz$. The potential is independent of the variable $\boldsymbol{Q}$ and, therefore, local. Explicitly we have

$$U^{on}(\boldsymbol{q}) = \hat{t}(\boldsymbol{q}; z)\tilde{\rho}(\boldsymbol{q}). \tag{2.25}$$

This latter form has been rather popular due to its computational simplicity and due to the fact that a local NRIA optical potential is conveniently constructed from an on-shell NN t-matrix which can be derived from experimental scattering amplitudes and the nuclear point density, also directly

[7] For elastic scattering this corresponds to *Breit frame* kinematics as defined in [McN 83]; the reason that this factorization may be optimal lies in the time-reversal property of the nuclear groud state [Pic 84].

accessible experimentally[8]. However, in a recent paper Redish and Stricker-Bauer [Red 87] pointed out the possible importance of retaining the nonlocality in the optical potential. In a later section we will mention some of the studies where the full off-shell characteristics of the *NN* interaction and the effects of full folding were explicitly treated.

2.3.3 Expressions for the Mixed Target Density

The mixed target density in momentum-space $\tilde{\rho}(\boldsymbol{q}, \boldsymbol{P})$, Eq. (2.22), can be Fourier transformed to its coordinate-space representation, and it is found that $\rho(\boldsymbol{r}, \boldsymbol{r}')$ can be adequately described by the Slater expansion

$$\rho(\boldsymbol{r}, \boldsymbol{r}') = \rho(\boldsymbol{R}) C(\hat{k}, s), \tag{2.26}$$

where the separation $\boldsymbol{s}$ between a projectile at $\boldsymbol{r}$ and a bound nucleon at $\boldsymbol{r}'$ is defined as $\boldsymbol{r} - \boldsymbol{r}'$, and their midpoint $\boldsymbol{R}$ as $\frac{1}{2}(\boldsymbol{r} + \boldsymbol{r}')$. The nuclear point density $\rho(\boldsymbol{R})$ is given by the diagonal terms of the general mixed density, while the correlation function C measures the degree of nonlocality of the mixed density [Are 90b].

A simple choice for the correlation function is the Slater form. For elastic scattering it is obtained from a Fermi gas model [Sla 51], while for inelastic scattering an approximate form appropriate for excitations near the

[8] Ground state charge densities can be obtained experimentally from elastic scattering, transition charge densities from inelastic scattering. The nuclear point densities for folding calculations can be obtained from the charge densities by unfolding the nucleon form factor (see Appendix A).

Fermi surface is used [Lov 78]. We get the functions

$$C(\hat{k}, s) = \begin{cases} 3\frac{j_1(\hat{k}s)}{\hat{k}s} & \text{elastic} \\ j_0(\hat{k}s) & \text{inelastic} \end{cases} \tag{2.27}$$

where $\hat{k}$ is a function of $\boldsymbol{R}$ and

$$\hat{k}(\boldsymbol{R}) = k_F(\boldsymbol{R}) = \frac{3\pi^2}{2}\rho(\boldsymbol{R}). \tag{2.28}$$

Refinements to this model account for the nonuniformity of the density in a finite system. Curvature corrections which consider the slope of the density in the tail region have been studied by Negele and Vautherin [Neg 72] and by Campi and Bouyssy [Cam 78]. While Negele and Vautherin performed a Taylor expansion of $\rho(\boldsymbol{r}, \boldsymbol{r}')$ around the Slater expansion, Campi and Bouyssy suggested a form which maintains the functional form of the Slater expansion, but with

$$\hat{k}(\boldsymbol{R}) = \sqrt{\frac{5}{3\rho(\boldsymbol{R})}\{\tau(\boldsymbol{R}) - \frac{1}{4}\nabla^2\rho(\boldsymbol{R})\}}, \tag{2.29}$$

where

$$\tau(\boldsymbol{R}) = \sum_{\alpha} |\nabla\varphi_\alpha(\boldsymbol{R})|^2. \tag{2.30}$$

The mixed density constructed with one of these correlation functions can be transformed into momentum-space and used in the full-folding integral given above [Are 90b], and has also been used in the local density approximation for the exchange part of the optical potential (see Sections 2.4.3 and 2.4.4) [Bri77/8].

2.3.4 A Local Pseudopotential

Before we discuss general off-shell t-matrices from realistic NN potentials or from inverse scattering, we first want to examine the local t-matrix by Love and Franey (FL) which has been extensively used in NRIA calculations of nucleon-nucleus scattering at energies up to 800 MeV [Lov 81, Fra 85]. This interaction has some appealing features. Its on-shell values are realistic since they are fitted to NN data[9], and its off-shell extension is well defined with its assumed functional form.

The Love and Franey (FL) t-matrix is constructed by fitting the on-shell NN amplitude with the form

$$\tilde{t}_{NN}(q,Q) = \tilde{t}^D(q) \pm \tilde{t}^X(Q_{on}), \tag{2.31}$$

which enforces exchange symmetry off the energy shell by having the proper symmetry in each two-body state (Q_{on} denotes the on-shell value of Q); the resulting function is then used for all values of q and Q. Since both the *direct* and the *exchange* term in Eq. (2.31) are intrinsically local functions, in this model off-shell and nonlocal effects only enter into t_{NN} through the interplay of the two terms [Pic 84, Red 87]. A local *pseudopotential* with central, spin-orbit and tensor components can be represented as [Lov 81, Kel 89a]

$$V = \sum_{ST} V_{ST}^C(r) P_S P_T + \sum_T V_T^{LS}(r) \boldsymbol{L}\cdot\boldsymbol{S} P_T + \sum_T V_T^T(r) S_{12}(\hat{\boldsymbol{r}}) P_T, \tag{2.32}$$

[9] In the NN c.m. system, the on-shell t-matrix is related to the NN amplitude via $t_{NN} = \eta M_{NN}$, where $\eta = -4\pi(\hbar c)^2/E_{NN}$. With the nucleon mass m and the c.m. wave number k of either particle, $E_{NN}^2 = m^2c^4 + (\hbar ck)^2$ [Lov 81].

where P_S and P_T are spin and isospin projection operators (S and T are the total spin and isospin of the nucleon-nucleon system)

$$\begin{aligned} P^{S=0} &= \tfrac{1}{4}(1 - \boldsymbol{\sigma}_1 \cdot \boldsymbol{\sigma}_2), \quad P^{S=1} = \tfrac{1}{4}(3 + \boldsymbol{\sigma}_1 \cdot \boldsymbol{\sigma}_2) \\ P^{T=0} &= \tfrac{1}{4}(1 - \boldsymbol{\tau}_1 \cdot \boldsymbol{\tau}_2), \quad P^{T=1} = \tfrac{1}{4}(3 + \boldsymbol{\tau}_1 \cdot \boldsymbol{\tau}_2), \end{aligned} \tag{2.33}$$

and where

$$\begin{aligned} \boldsymbol{L} &= \tfrac{1}{2}(\boldsymbol{r}_1 - \boldsymbol{r}_2) \times (\boldsymbol{p}_1 - \boldsymbol{p}_2) \\ \boldsymbol{S} &= \tfrac{1}{2}(\boldsymbol{\sigma}_1 + \boldsymbol{\sigma}_2) \\ S_{12}(\hat{\boldsymbol{r}}) &= 3\boldsymbol{\sigma}_1 \cdot \hat{\boldsymbol{r}} \boldsymbol{\sigma}_2 \cdot \hat{\boldsymbol{r}} - \boldsymbol{\sigma}_1 \cdot \boldsymbol{\sigma}_2. \end{aligned} \tag{2.34}$$

The antisymmetrized matrix elements of the pseudopotential are required to reproduce the on-shell t-matrix

$$\tilde{t}_{NN}(\boldsymbol{k}', \boldsymbol{k}) = \langle \boldsymbol{k}' | V(1 - X) | \boldsymbol{k} \rangle, \tag{2.35}$$

where the exchange operator $X = X^r X^S X^T$ is the product of the space-exchange operator

$$X^r |\boldsymbol{r}\rangle = |-\boldsymbol{r}\rangle, \tag{2.36}$$

the spin-exchange operator

$$X^S |SM_S\rangle = (-)^{1+S} |SM_S\rangle \tag{2.37}$$

and the isospin-exchange operator

$$X^T |TM_T\rangle = (-)^{1+T} |TM_T\rangle. \tag{2.38}$$

For computational convenience, and to simulate to some extent the exchange of various mesons, the radial parts of the central and spin-orbit components of V are expressed as sums of Yukawas; the tensor term includes an additional

factor r^2. With the Yukawa function $Y_i(r) = e^{-\mu_i r}/r$ we have

$$\begin{aligned} V^C(r) &= \textstyle\sum_i V_i^C Y_i(r) \\ V^{LS}(r) &= \textstyle\sum_i V_i^{LS} Y_i(r) \\ V^T(r) &= \textstyle\sum_i V_i^T r^2 Y_i(r), \end{aligned} \tag{2.39}$$

where the V_i are complex strengths. Several masses μ_i were chosen to represent in some fashion the meson carriers of the interaction (the smallest mass is that of the pion, responsible for the long-range part of the interaction).

Inserting V from Eq. (2.32) into Eq. (2.35), we can express $\tilde{t}_{NN}$ in terms of the momentum transfer $\boldsymbol{q} = \boldsymbol{k}' - \boldsymbol{k}$, the exchange momentum transfer $\boldsymbol{Q} = \boldsymbol{k}' + \boldsymbol{k}$, and $\hat{\boldsymbol{n}} = \hat{\boldsymbol{q}} \times \hat{\boldsymbol{Q}}$, as

$$\begin{aligned} \tilde{t}_{NN}(q,Q) &= \sum_{ST} \tilde{t}_{ST}^C P_S P_T + i \sum_T \tilde{t}_T^{LS} (\boldsymbol{\sigma}_1 + \boldsymbol{\sigma}_2) \cdot \hat{\boldsymbol{n}} P_T \\ &\quad - \sum_T [\tilde{V}_T^T(q) S_{12}(\hat{\boldsymbol{q}}) - (-)^{1+T} \tilde{V}_T^T(Q) S_{12}(\hat{\boldsymbol{Q}})] P_T. \end{aligned} \tag{2.40}$$

The quantities $\tilde{t}_{ST}^C$ and $\tilde{t}_T^{LS}$ are given by

$$\begin{aligned} \tilde{t}_{ST}^C &= \tilde{V}_{ST}^C(q) - (-)^{S+T} \tilde{V}_{ST}^C(Q), \\ \tilde{t}_T^{LS} &= \tfrac{1}{4} qQ [\tilde{V}_T^{LS}(q) + (-)^{1+T} \tilde{V}_T^{LS}(Q)]. \end{aligned} \tag{2.41}$$

It is also convenient to introduce the auxiliary quantity $\tilde{\tau}^{LS}$, such that

$$\tilde{t}^{LS} = -qQ\tilde{\tau}^{LS}/2 = -(k^2 \sin\theta)\tilde{\tau}^{LS}. \tag{2.42}$$

Finally, the Bessel transforms $\tilde{V}^C$, $\tilde{V}^{LS}$ and $\tilde{V}^T$ are defined as

$$\begin{aligned} \tilde{V}^C(q) &= 4\pi \textstyle\int dr\, r^2 j_0(qr) V^C(r) \\ \tilde{V}^{LS}(q) &= 4\pi \textstyle\int dr\, r^4 \frac{j_1(qr)}{qr} V^{LS}(r) \\ \tilde{V}^T(q) &= 4\pi \textstyle\int dr\, r^2 j_2(qr) V^T(r), \end{aligned} \tag{2.43}$$

with analogous expressions for the transforms that are functions of Q.

To apply the above results to nucleon-nucleus scattering, one evaluates the knock-on exchange contributions to the NA amplitudes in a short-range approximation(e.g. [Pet 69]), which is well established and thought to be accurate for most natural-parity transitions at intermediate energies [Kel 89]. In its simplest form, the *zero-range approximation* (ZREA), the exchange part of the interaction is reduced to a zero-range form by replacing Q in the exchange terms by k_A, the projectile wave number in the nucleon-nucleus system[10]. That is, to a good approximation the momentum transfer required for the exchange term in the nucleon-nucleus system is just that associated with stopping the incident nucleon [Lov 81]. Additionally, a transformation of the interaction from the NN to the NA system is necessary via the above mentioned Møller factor [Møl 45]. More specifically,

$$\tilde{t}_{NA}(q) = \frac{\epsilon_0^2}{\epsilon_p \epsilon_t} \tilde{t}_{NN}(q, k_A), \tag{2.44}$$

where ϵ_p (ϵ_t) is the total energy of the incident (target) nucleon in the NA system and ϵ_0 the total energy of the projectile in the NN system [Lov 81].

For the isoscalar natural-parity inelastic transitions ($\Delta\pi = (-)^{\Delta J}$ with $\Delta\pi = \pi_i\pi_f$) which we consider in this work, the effective interaction for a

[10] This is based on a Born approximation argument for NN scattering, treated using NA kinematics where the motion of the struck nucleon is negligible and Q is almost angle independent. Thus, the momentum transfer for exchange scattering is sharply peaked at a value approximately equal to k_A, justifying an expansion about that point and retaining only its first term [Pet 69, Kel 81].

projectile with spin $\boldsymbol{\sigma}$ reduces to

$$t(q) = t^C(q) + it^{LS}(q)\boldsymbol{\sigma} \cdot \hat{\boldsymbol{n}}, \tag{2.45}$$

provided that all target spin and current densities may be neglected [Kel 89a]. Because $\sigma(q) \propto |T_{fi}(q)|^2$, in the plane wave limit the differential cross section for inelastic scattering of an unpolarized incident beam is

$$\sigma(q) = \frac{\mu\mu'}{(2\pi)^2}\frac{k'}{k}\frac{1}{2J+1}|\Delta\rho|^2\{|t^C(q)|^2 + |t^{LS}(q)|^2\}, \tag{2.46}$$

where μ (μ') and k (k') are the reduced energies and projectile wave numbers in the initial (final) channel, and J is the target spin[11]. The plane wave analyzing power is

$$A_y = \frac{2\mathrm{Im}[t^C(q)t^{LS^*}(q)]}{|t^C(q)|^2 + |t^{LS}(q)|^2}. \tag{2.47}$$

2.3.5 Off-Shell T-Matrices

It has been criticized [Lov 81, Red 87] that the form Eq. (2.31) involves a certain ambiguity in that $\tilde{t}^D(q)$ may differ for two fits of equivalent quality, with $\tilde{t}^X(Q)$ compensating for the difference, to yield essentially the same on-shell NN amplitude. In the NA system, however, where $\tilde{t}^D(q)$ stays the same for a given q, $\tilde{t}^X(k_A)$ obtained from different on-shell fits may well lead to different values for $\tilde{t}_{NA}$. The uncertainty in this off-shell extension prescription is a serious problem for realistic NA scattering calculations since an on-shell NN t-matrix exists only over a range of momentum transfer which

[11] The factor $\sigma_{00} \equiv |t_m(q)|^2 = |t^C(q)|^2 + |t^{LS}(q)|^2$ in Eq. (2.46) is called *matter interaction*.

is significantly less than the one accessible in NA scattering. With the NN energy fixed at the value determined from the beam energy, the on-shell NN momentum k is approximately half of the on-shell NA momentum k_A for a heavy target. Therefore, beyond a nucleon-nucleus scattering angle of about 60°, which corresponds to a NN scattering angle of 180°, the interaction t must be extrapolated off the energy shell.

Because of the aforementioned problems and their importance for both full-folding and factorized calculations, there has been renewed interest in fully off-shell t-matrices and their properties. Starting with realistic potentials from meson exchange theory like the Paris [Lac 80] or Bonn [Mac 87] potentials, or, more recently, from *inverse scattering* [Kir 89], fully off-shell t-matrices have been constructed, with various methods for the solution of the Lippmann-Schwinger equation, and their properties have been investigated in detail [Red 87, Amo 88, Ger 90].

Motivated by the paper of Redish and Stricker-Bauer [Red 87], one of the most important questions then posed was, to what degree the off-shell behaviour of the resulting t-matrices would depend on the different input NN potentials. All of the potentials listed above reproduce the on-shell NN observables, usually in the form of phase shifts, with comparable quality. However, while the Paris and Bonn potentials include explicit momentum and energy dependencies, potentials from inverse scattering are constructed to be local and energy independent in all channels. Because of the way they were generated, the inversion potentials yield exact on-shell NN t-matrices. On the other hand, one might think that the strong energy and momentum

dependencies of the meson exchange theory would produce unique off-shell behaviour which a local and energy independent inversion potential could not reproduce [Ger 90].

Amos et.al. [Amo 88] compared off-shell interactions based on the Reid [Rei 68] and Paris potentials with a new phenomenological potential, while von Geramb and Amos [Ger 90] compared half-off-shell interactions based on the Paris, the Bonn, and the inversion potential from experimental phase shifts [Arn 87]. Both groups came to the same conclusion: off-shell interactions are very similar over any physically significant region of momenta whenever they give essentially the same phase shifts at all energies, i.e. if they are *phase equivalent*. Any differences *off* the energy shell can be traced to differences *on* the energy shell. This result allows, therefore, comparison of full-folding calculations utilizing different potentials, provided the same approximations (e.g. treatment of the energy in the interaction matrix element and the mixed particle density) are being used.

2.3.6 NRIA Calculation Results

In Figures 2.1–2.3 we compare the PH and NL interactions (see Section 2.4.2) at zero density with the FL t-matrix at 100, 200, and 318 MeV. To illustrate some of the effects which the various free t-matrices will have on NRIA predictions for natural-parity transitions, we also display the matter interactions σ_{00} (or $|t_m|^2$) and analyzing powers A_y in the plane wave approximation (see Section 2.7.1). As can be seen, the differences between the interactions become progressively bigger with increasing energy.

At 100 MeV all the $\mathrm{Re}t_{00}^{C}$ components are very nearly equal for $q <$ 2 fm^{-1}, but then separate at larger momentum transfer. The $\mathrm{Im}t_{00}^{C}$ and $\mathrm{Re}t_{0}^{LS}$ components of the PH and NL interactions are essentially equal over the whole momentum transfer range of 3 fm^{-1}, but the FL t-matrix starts to differ already at small momentum transfers for the $\mathrm{Im}t_{00}^{C}$ component and it begins to differ for the $\mathrm{Re}t_{0}^{LS}$ component for $q >$ 1.5 fm^{-1}. The $\mathrm{Im}t_{0}^{LS}$ component of the PH interaction resembles very much that of the NL interaction at momentum transfers below 0.5 fm^{-1}. Above about 1.5 fm^{-1}, on the other hand, the NL interaction much more resembles the FL interaction. The matter interactions begin to differ beyond about 2 fm^{-1}, and the analyzing powers beyond about 1.2 fm^{-1}.

At 200 MeV the $\mathrm{Re}t_{00}^{C}$ component of the PH interaction is about 20% stronger[12] than the FL interaction and about 30% stronger than the NL interaction at $q = 0$. At 3 fm^{-1} it is twice as strong as the FL interaction and about 50% stronger than the NL interaction. Also, because of a more rapid q dependence it changes sign first. Although at $q = 0$ the $\mathrm{Im}t_{00}^{C}$ component for PH is about 20% stronger than for NL, the NL component is about 88% stronger than PH at 3 fm^{-1}. FL is intermediate between PH and NL. The resulting matter interaction for PH is 25% (35%) stronger than FL (NL) at $q = 0$ and about 35% (15%) stronger than FL (NL) at $q = 3$ fm^{-1}. For the $\mathrm{Re}t_{0}^{LS}$ component the NL and FL interactions are very similar for $q <$ 1 fm^{-1}, for $\mathrm{Im}t_{0}^{LS}$ they are very similar both below 0.5 fm^{-1} and again

[12] The relative strengths which are quoted here are defined as $100(t - t')/t'$.

above 2 fm^{-1}. For Ret_0^{LS} PH is somewhat stronger than the other interactions below 1.5 fm^{-1}, but it becomes weaker at large momentum transfers. For the Imt_0^{LS} component PH is stronger than the other interactions over the whole momentum transfer region. As for 100 MeV, the FL analyzing power begins to differ from around 1.2 fm^{-1}, while PH and NL analyzing powers remain almost equal up to 1.7 fm^{-1}. At $q = 3$ fm^{-1} the FL and NL analyzing powers become again almost equal, but both are more than twice as large as the PH analyzing power.

At 318 MeV the Ret_{00}^{C} component of the PH interaction at $q = 0$ is about twice as strong as the NL interaction, but only about 10% stronger than FL. Again, the q dependence of PH is much stronger and at 3 fm^{-1} PH is now about 65% stronger than NL and about twice as strong as FL. At $q = 0$ the PH matter interaction is about 70% (25%) stronger than NL (FL), at 3 fm^{-1} about 65% (50%) stronger than NL (FL). For the spin-orbit components the situation is very similar to 200 MeV, albeit amplified. The main difference is that all the analyzing powers converge again at 3 fm^{-1}.

In the Figures 2.4–2.11 we show NRIA calculations at 100, 200, and 318 MeV for elastic and inelastic scattering data from ^{16}O and ^{40}Ca. Elastic cross sections are presented as ratios to the point-charge Rutherford cross section σ_R to enhance detail. The bands represent the range of variation due to the different free interactions. For both targets, the 3_1^- states are transitions with surface-peaked transition densities. The 1_1^- state in ^{16}O peaks in the high-density interior and has only a small lobe in the low-density region, while the 3_2^- state in ^{40}Ca has a lobe in the high-density interior which

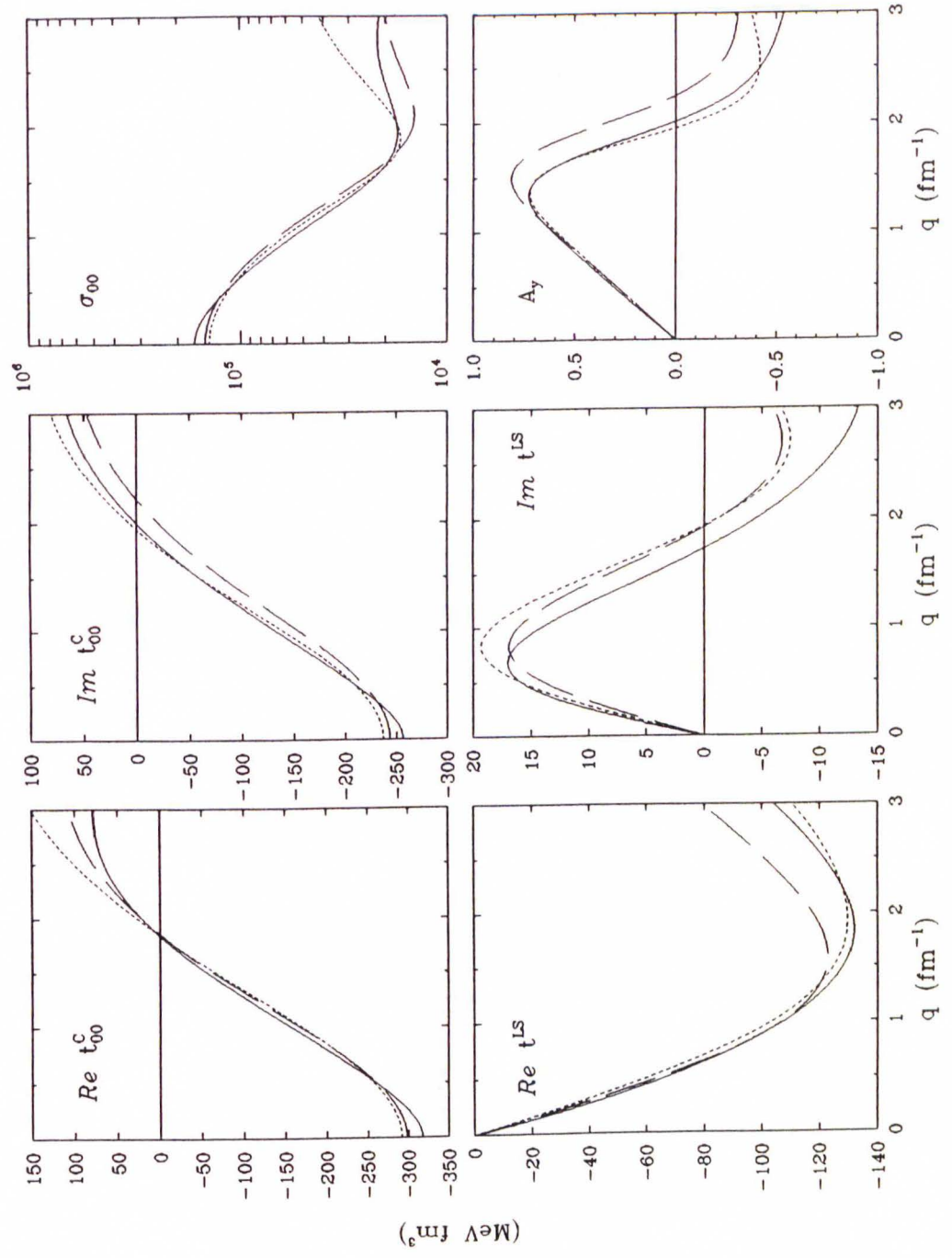

Figure 2.1: Comparison of the free t-matrices for the PH (solid line), NL (short dashes), and FL (long dashes) interactions at 100 MeV, including knock-on exchange.

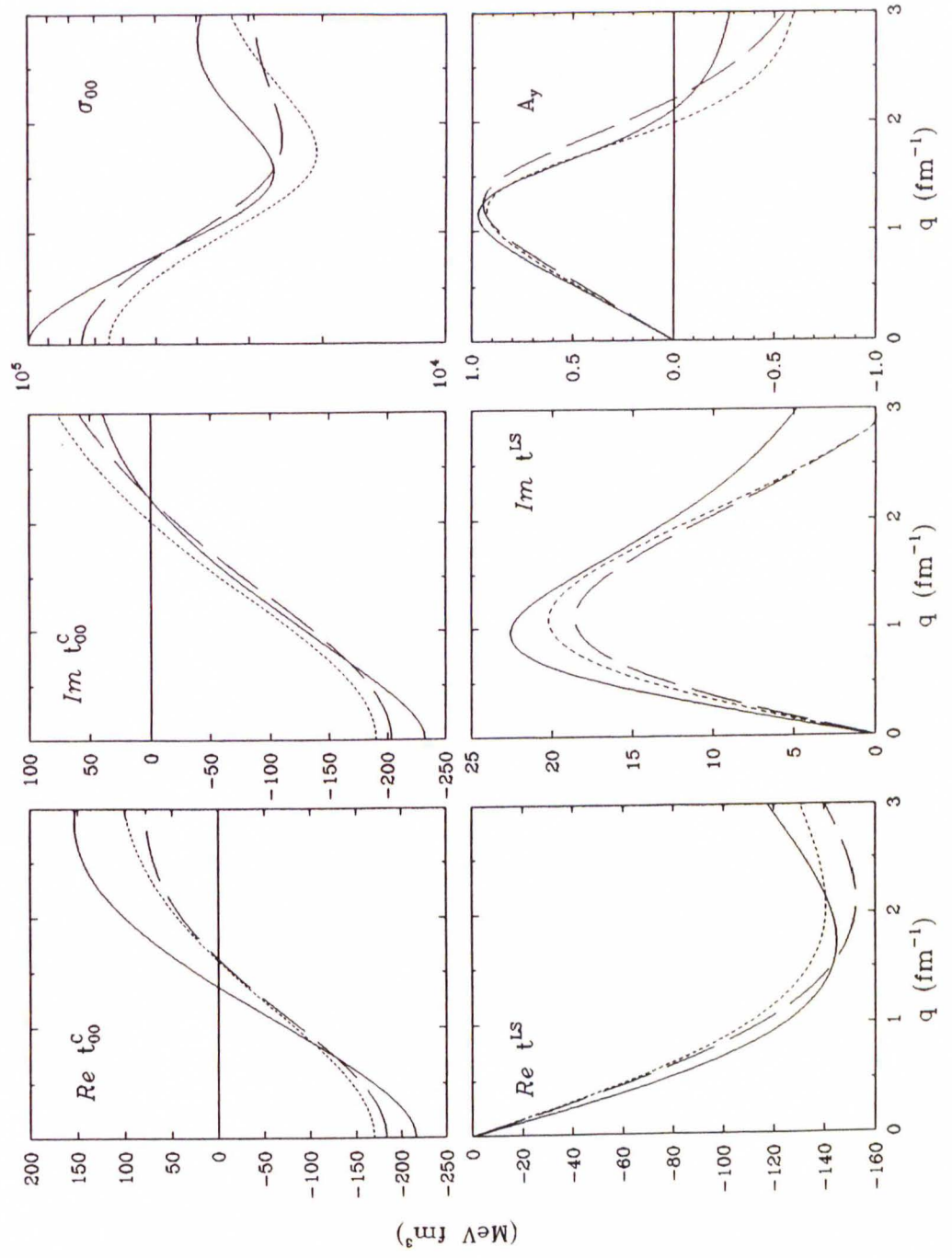

Figure 2.2: Comparison of the free t-matrices for the PH (solid line), NL (short dashes), and FL (long dashes) interactions at 200 MeV, including knock-on exchange.

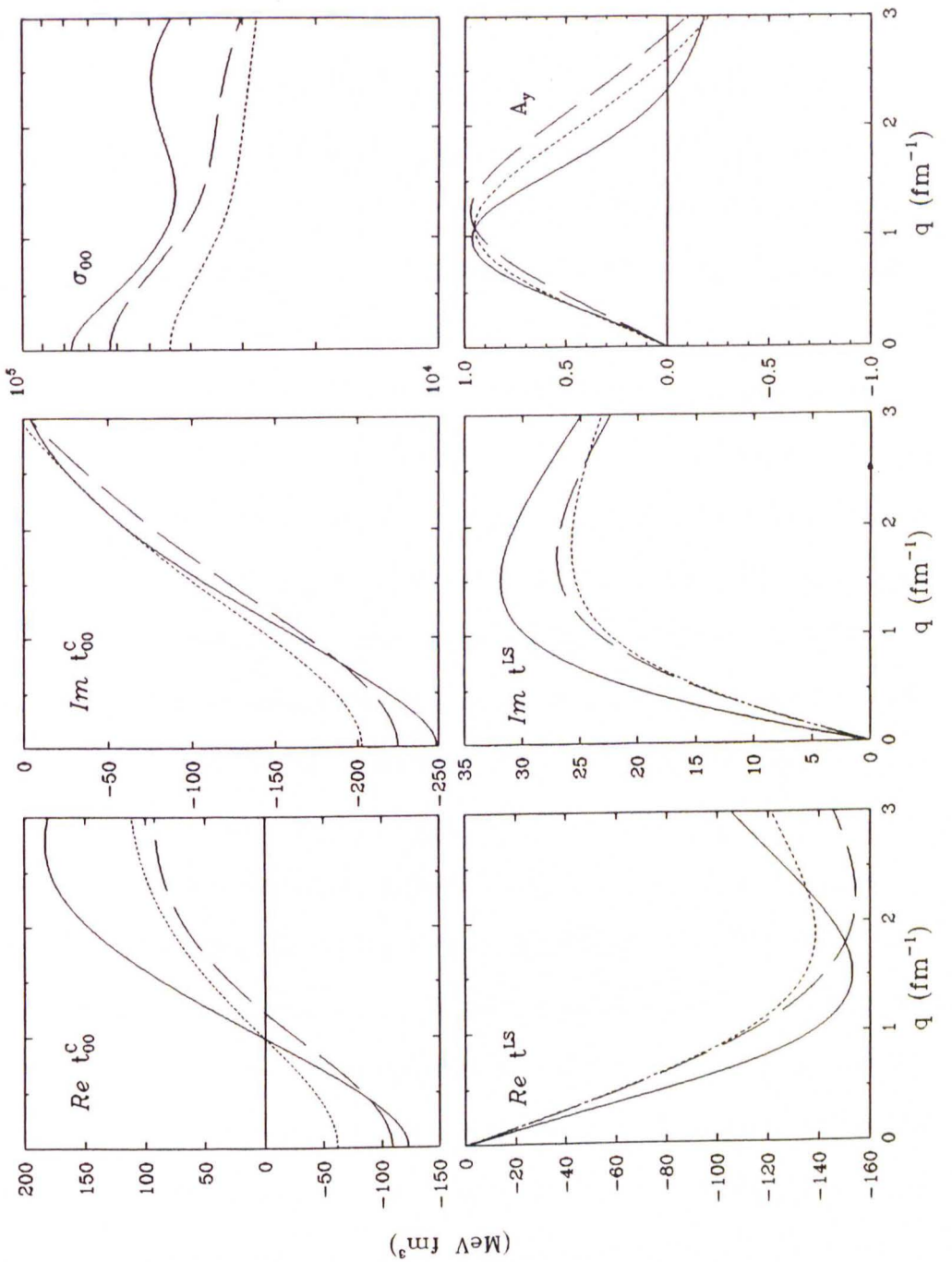

Figure 2.3: Comparison of the free t-matrices for the PH (solid line), NL (short dashes), and FL (long dashes) interactions at 318 MeV, including knock-on exchange.

is twice as strong as the exterior lobe in the low-density surface region (see Appendix A). The 100 and 200 MeV cross sections and analyzing powers for ^{16}O and for ^{40}Ca are from this work (see Chapter 6 and Appendix F). The 318 MeV cross sections and analyzing powers for ^{40}Ca are taken from [Fel 90], those for ^{16}O from [Kel 90b]; the 318 MeV data for the spin rotation function are from [Ble 88]. The 200 MeV spin rotation function data for both ^{16}O and ^{40}Ca are taken from [Ste 85] and P. Schwandt (private communication).

Although all the elastic scattering calculations used optical potentials based on the free interactions, for the inelastic states we generated distorted waves with a density dependent interaction. We used the PH g-matrix to calculate distorted waves for NRIA calculations based upon the PH and FL interaction, but we chose to use the NL g-matrix for distortion of the NRIA calculations using the NL interaction. The inelastic transitions are driven by the respective free interaction. It was pointed out in [Kel 89a] that the use of the NRIA potential for inelastic scattering, although more consistent, would be misleading since in the absence of Pauli blocking we would have an unrealistically strong absorption. This absorption would both overly suppress inelastic cross sections and at the same time distort the analyzing powers.

The first observation is that for all the energies NRIA calculations based on the various free interactions are reasonably consistent with each other. At 100 MeV the predicted analyzing powers are much too positive and display a structure which does not resemble that of the data at all. Elastic cross sections for both targets are reasonable well described for $q < 1$ fm^{-1} and for ^{16}O also again above 2 fm^{-1}. The cross sections of both the 3_1^- surface states

are slightly overestimated at forward angles, the cross section for the interior 1_1^- state of ^{16}O is overestimated by up to a factor of 10. The forward cross section of the 3_2^- in ^{40}Ca, on the other hand, looks reasonable. A prediction of the cross section that is too large at forward angles is due to the omission of Pauli blocking and the effect is especially grave for a state that is almost entirely peaked in the interior, such as the 1_1^- state. For states that peak predominantly at the surface the omission of Pauli blocking appears to have less impact. The 3_2^- is an interesting case in the sense that, because of the two strong lobes in both the high- and low-density of the nucleus, a cancellation of various density dependent effects seems to take place, making the forward angle cross section prediction correct. At large momentum transfers the predicted cross section for the 3_1^- state of ^{40}Ca is slightly too high. The cross sections for the 3_1^- and 1_1^- states in ^{16}O and for the 3_2^- state of ^{40}Ca, on the other hand, fall well below the data, indicating a need for a short-range repulsive correction to the free interaction.

At 200 MeV the analyzing powers for all the states improve somewhat, becoming more negative, and the ones for the 3_1^- states of ^{16}O and ^{40}Ca look quite reasonable. The overestimation of the cross section at small momentum transfers due to the omission of Pauli blocking, and the underestimation at large momentum transfers due to the absence of short-range repulsion is evident clearly for all the states, including the 3_2^- state of ^{40}Ca at this energy. Also, the predicted cross sections appear to be shifted slightly towards smaller momentum transfers for all the inelastic states. The addition of short-range repulsion would cause a shift towards larger momentum trans-

fers and alleviate this problem. The spin rotation functions Q at this energy look not unreasonable for momentum transfers beyond about 1.2 fm^{-1} for ^{16}O and about 1.0 fm^{-1} for ^{40}Ca, although they should become slightly more negative to describe all the data points. At small momentum transfers, the NRIA predictions fall well below the data.

At 318 MeV the overall description of the data for the two targets, both elastic and inelastic, has improved dramatically over the lower energies, although again better agreement could be attained by a slight shift of the patterns towards a larger momentum transfer. At small momentum transfers the cross section calculations now appear to fall below the data, a fact that has also been noted by Kelly *et al.* [Kel 90b]. It seems that while Pauli blocking so far has suppressed the absorptive potential in the interior, we now find an enhancement. At 500 MeV this effect has been reported to be even larger [Fla 90]. With exception of the 3_2^- state of ^{40}Ca, the predicted analyzing powers at forward angles are substantially larger than the measured data. Since for small momentum transfers the Imt_{00}^C component of the interaction is much larger than the Ret_0^{LS} component, Eq. (2.47) in Section 2.7.1 suggests that a suppression of these analyzing powers could be achieved either by an enhancement of Imt_{00}^C or by suppression of Ret_0^{LS} [Kel 90b]. The ^{40}Ca spin rotation function falls well below the data for momentum transfers in the range between 0.5 fm^{-1} and 1.0 fm^{-1}; the oscillation between 1.0 fm^{-1} and 1.5 fm^{-1} is not reproduced adequately and above 1.5 fm^{-1} the pattern is shifted too much towards smaller momentum transfers.

At 500 MeV the trends observed for the 318 MeV data become more

pronounced. For states peaking in the high-density interior, the forward angle NRIA predictions fall even more below the data, and the low-q analyzing powers are still systematically too large. The oscillatory structure of the analyzing powers is both too strong and too rapid to describe the data adequately. For a more thorough discussion of the 500 MeV data and interactions we refer to the paper by Flanders *et al.* [Fla 90]. At even higher energies ($\geq$800 MeV), inclusion of second-order terms of the optical potential which account for target nucleon correlations, and electromagnetic spin-orbit (EMSO) corrections appear to improve the NRIA [Ray 85]. For 650 and 800 MeV, the beneficial impact of the EMSO potential on the forward angle spin observables for nonrelativistic calculations has been reported by Coker and Ray [Cok 90].

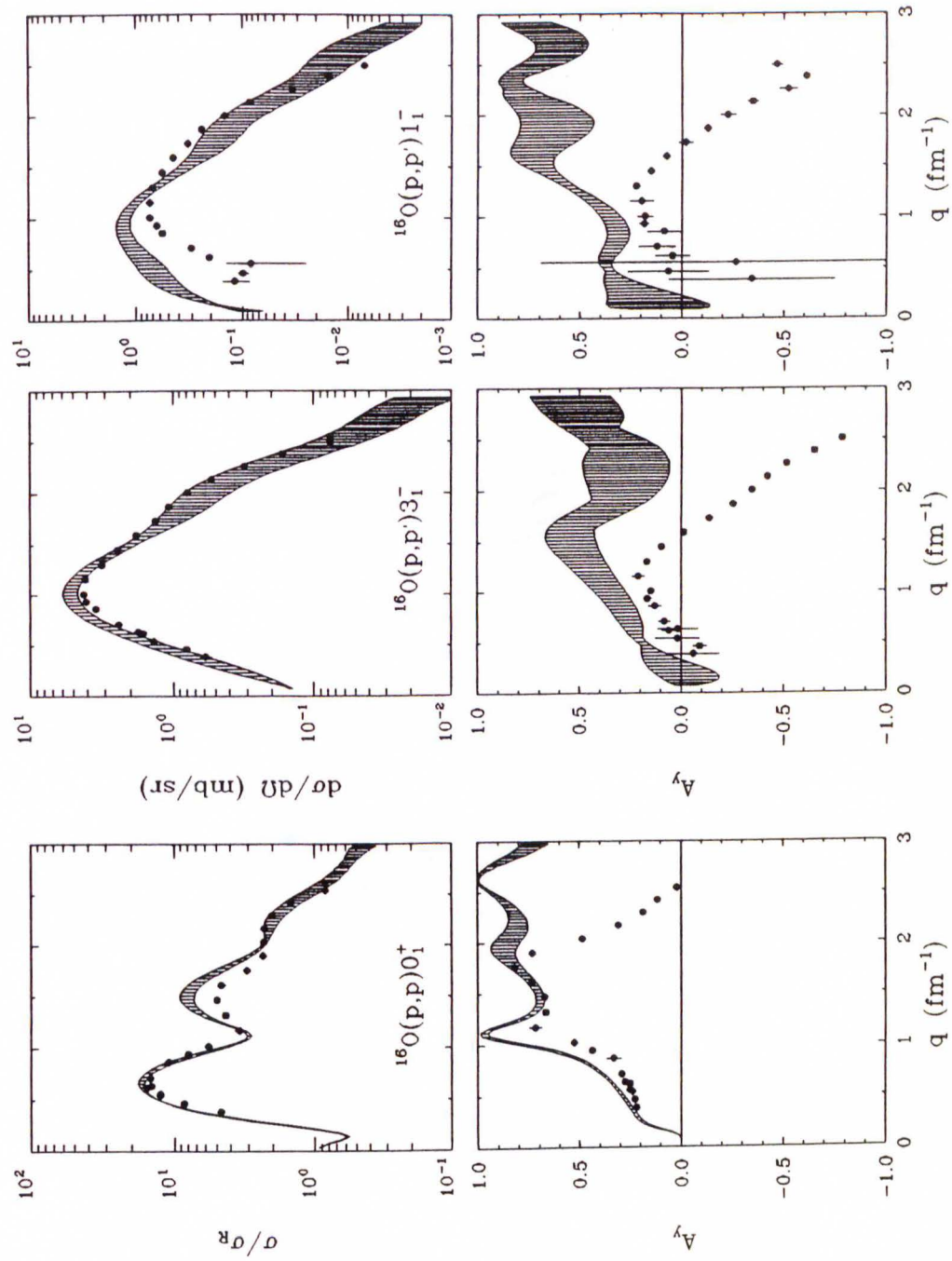

Figure 2.4: NRIA calculations of $\sigma(q)$ and A_y for selected states of ^{16}O at 100 MeV; the elastic cross section is presented as ratio to the point-charge Rutherford cross section (σ_R) to enhance detail. The bands represent the range of variation of the calculation due to the different free interactions. The data are from this work.

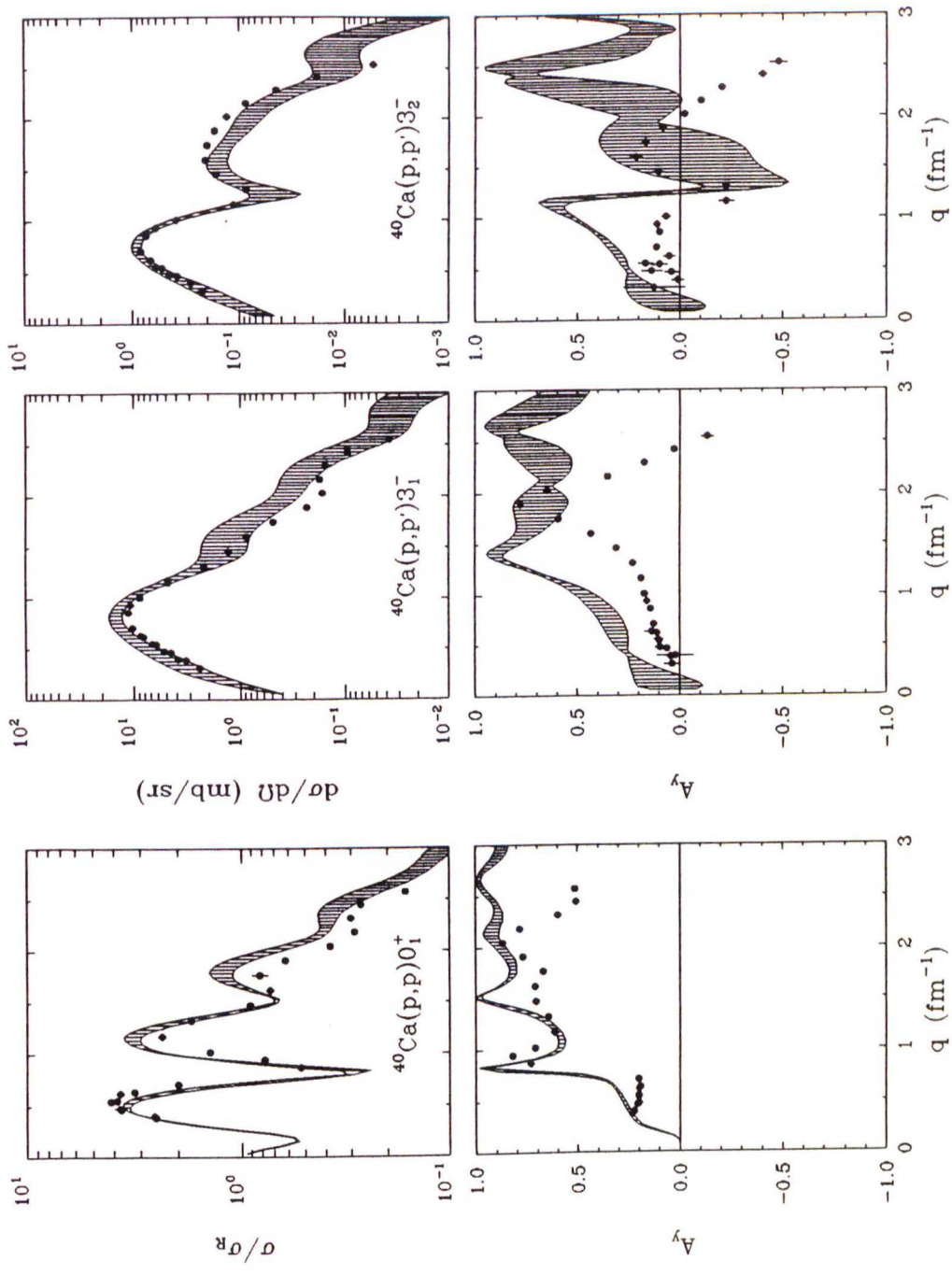

Figure 2.5: NRIA calculations of $\sigma(q)$ and A_y for selected states of ^{40}Ca at 100 MeV; the elastic cross section is presented as ratio to the point-charge Rutherford cross section (σ_R) to enhance detail. The bands represent the range of variation of the calculation due to the different free interactions. The data are from this work.

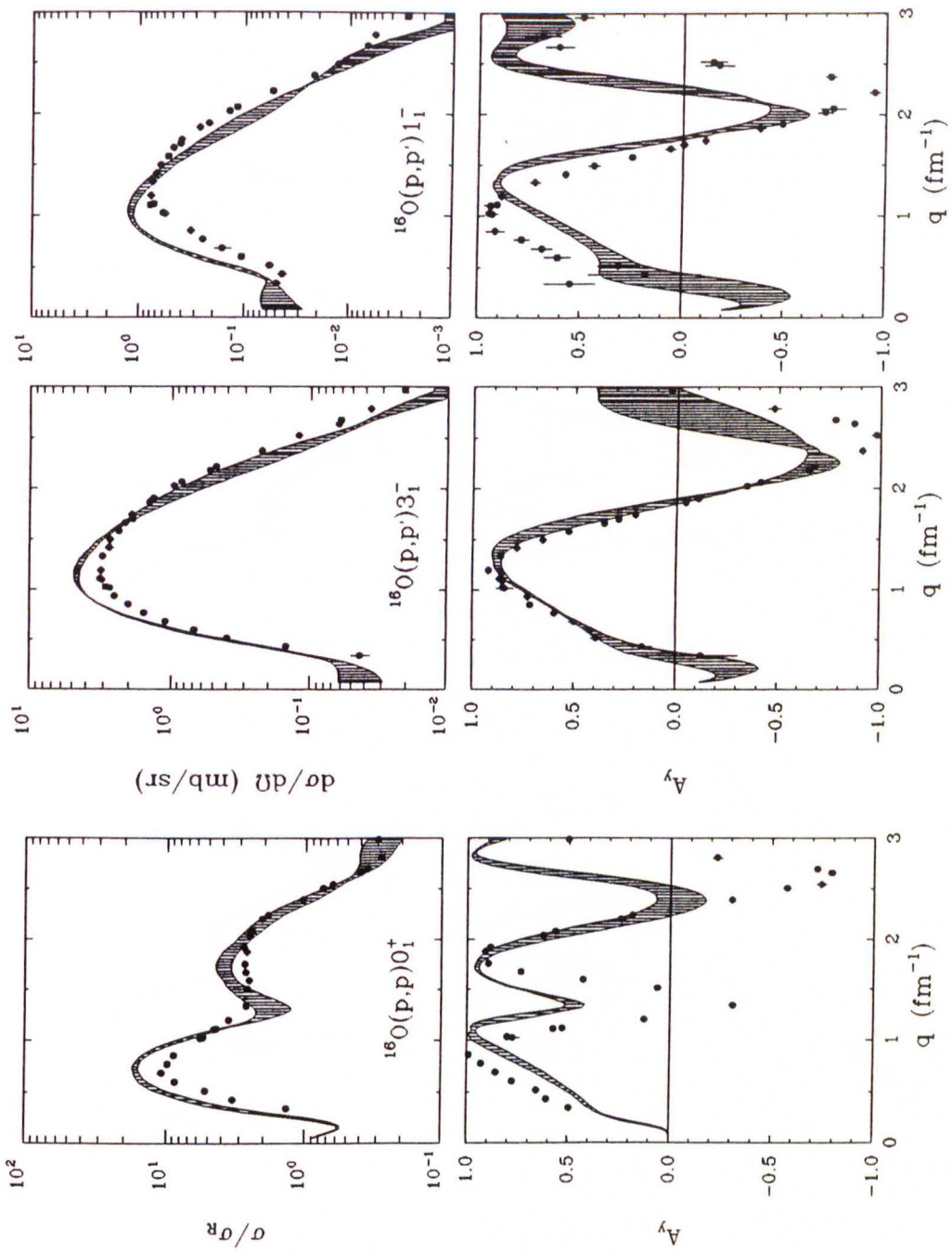

Figure 2.6: NRIA calculations of $\sigma(q)$ and A_y for selected states of ^{16}O at 200 MeV; the elastic cross section is presented as ratio to the point-charge Rutherford cross section (σ_R) to enhance detail. The bands represent the range of variation of the calculation due to the different free interactions. The data are from this work.

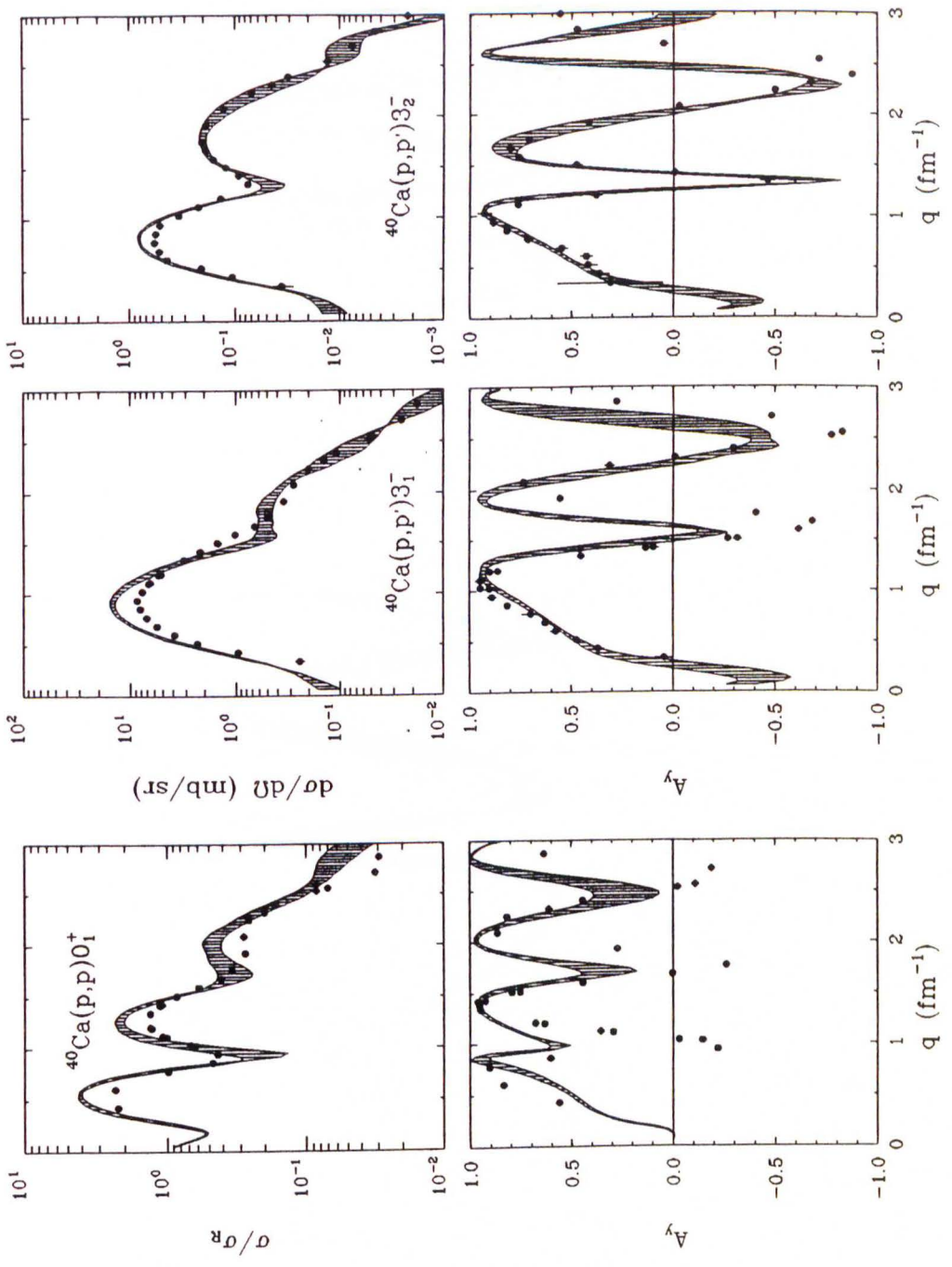

Figure 2.7: NRIA calculations of $\sigma(q)$ and A_y for selected states of ^{40}Ca at 200 MeV; the elastic cross section is presented as ratio to the point-charge Rutherford cross section (σ_R) to enhance detail. The bands represent the range of variation of the calculation due to the different free interactions. The data are from this work.

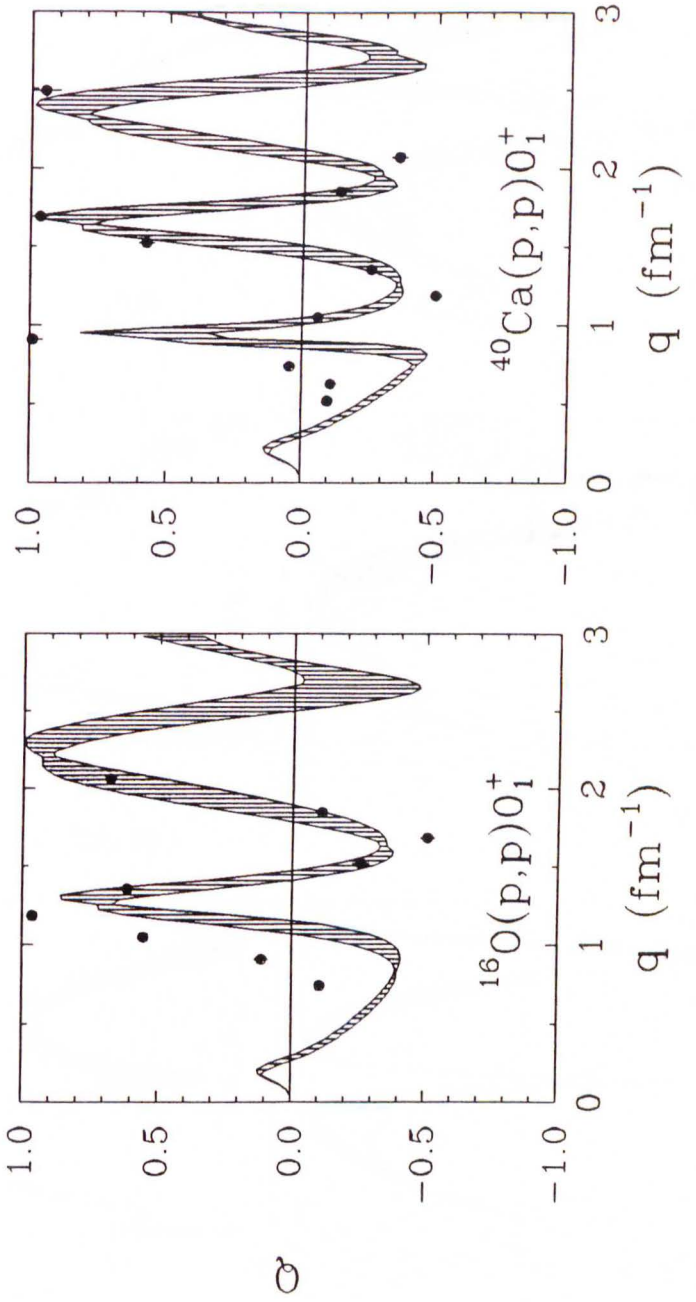

Figure 2.8: NRIA calculations of Q for elastic scattering of ^{16}O and ^{40}Ca at 200 MeV. The bands represent the range of variation of the calculation due to the different free interactions. The data are from [Ste 85] and P. Schwandt, private communication.

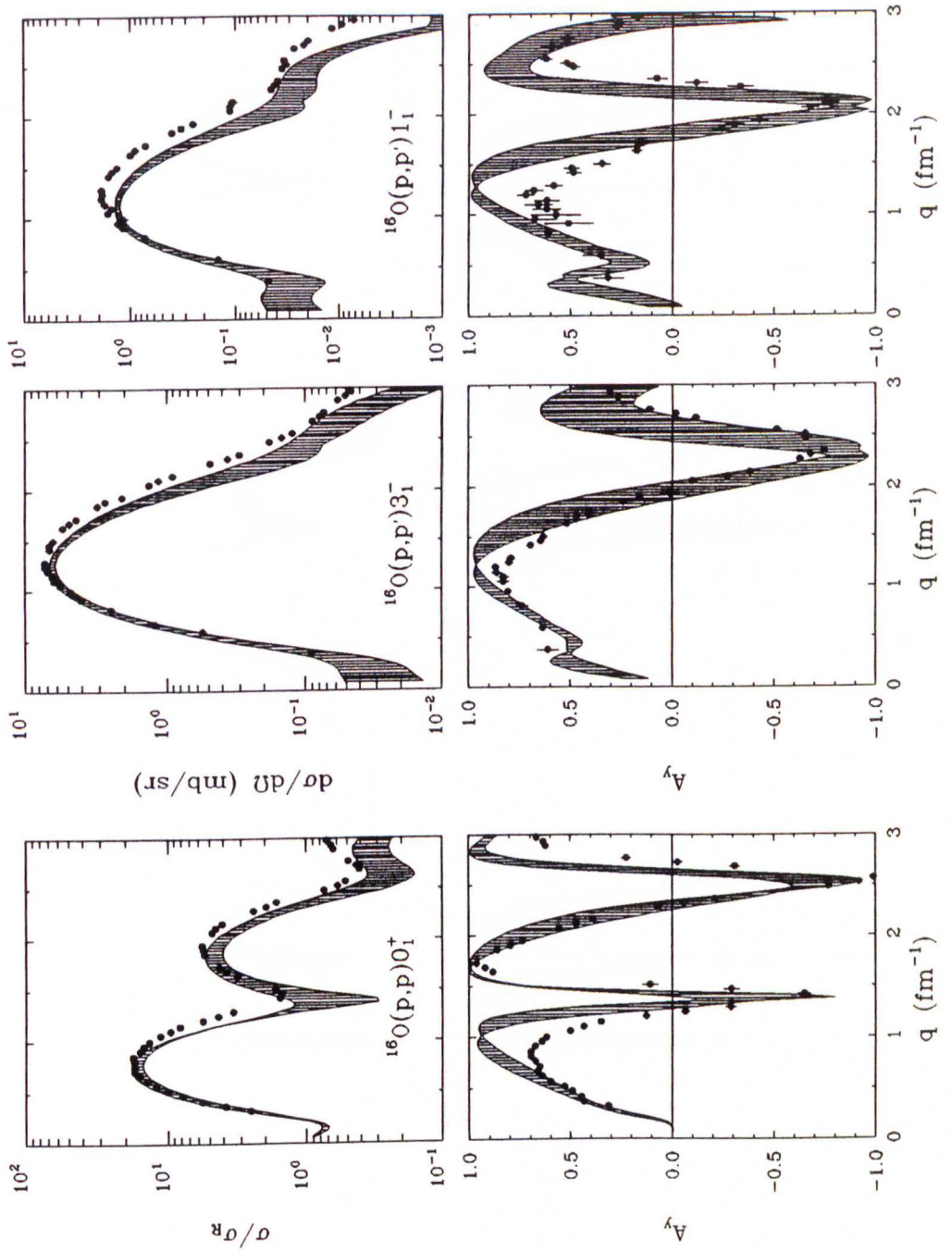

Figure 2.9: NRIA calculations of $\sigma(q)$ and A_y for selected states of ^{16}O at 318 MeV; the elastic cross section is presented as ratio to the point-charge Rutherford cross section (σ_R) to enhance detail. The bands represent the range of variation of the calculation due to the different free interactions. The data are from [Kel 90b].

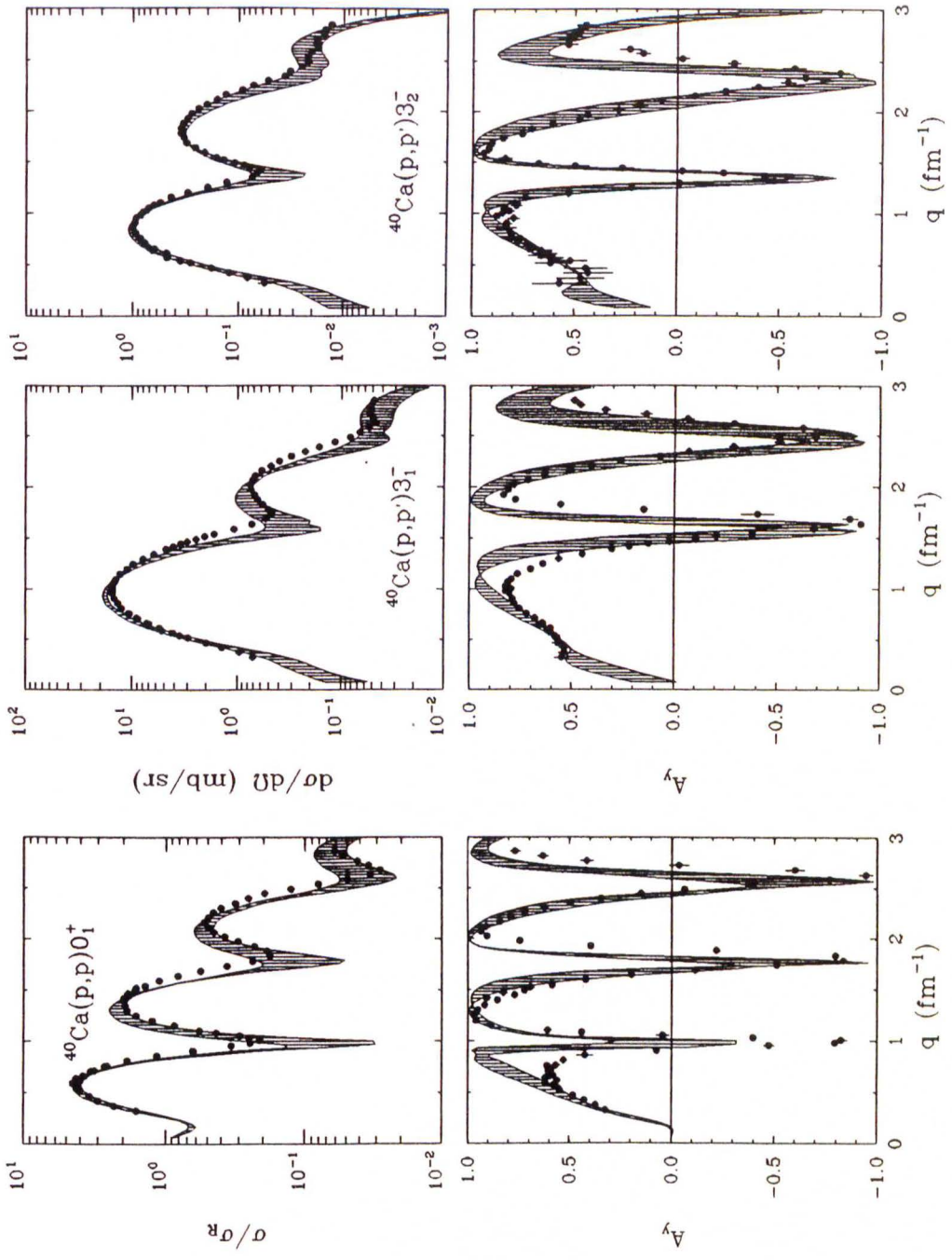

Figure 2.10: NRIA calculations of $\sigma(q)$ and A_y for selected states of ^{40}Ca at 318 MeV; the elastic cross section is presented as ratio to the point-charge Rutherford cross section (σ_R) to enhance detail. The bands represent the range of variation of the calculation due to the different free interactions. The data are from [Fel 90].

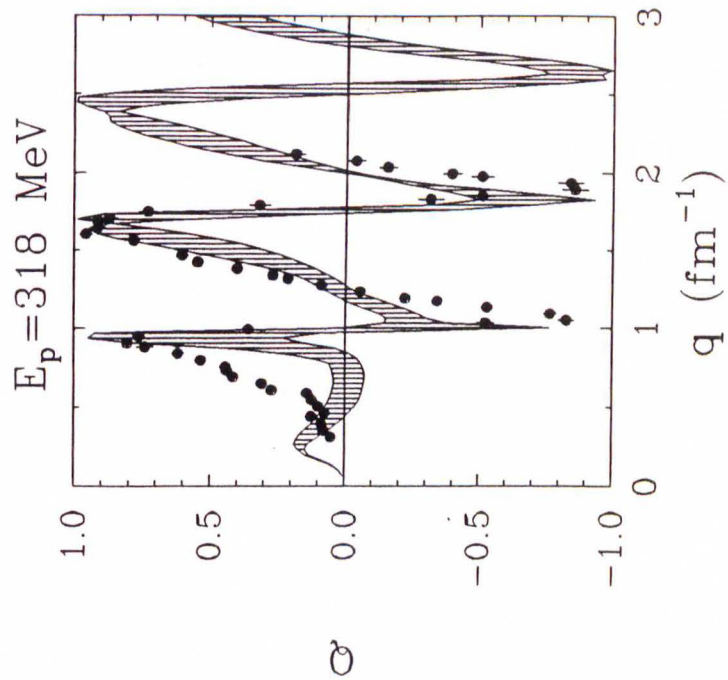

Figure 2.11: NRIA calculations of Q for elastic scattering of ^{40}Ca at 318 MeV. The bands represent the range of variation of the calculation due to the different free interactions. The data are from [Ble 88]).

2.4 Nuclear Matter Approach

2.4.1 Introduction

At low and intermediate energies the nuclear matter approach [Hüf 72] has proven to be an alternative and very fruitful approach to nucleon-nucleus scattering. The optical model in infinite nuclear matter is identified with the lowest order term in the hole-line expansion of the self-energy or mass operator of the projectile nucleon propagating through the target medium. Density dependence enters into the model through the effective interaction, the so-called reaction or g-matrix. This interaction satisfies the analog of the Lippmann-Schwinger equation, the *Bethe-Goldstone* equation, and includes medium effects via Pauli blocking and energy shifts in the intermediate projectile–target-nucleon scattering states. Further density dependence enters through the the various averaging procedures which are used to reduce the energy and momentum dependent interactions to simple local forms.

For a nucleon with energy E and momentum $\boldsymbol{k}$ moving in infinite nuclear matter of density[13] (i.e. Fermi momentum) k_F one can write down, following Hüfner and Mahaux, the average complex potential felt by the incident projectile as the diagonal, plane wave, antisymmetrized two-body Brueckner reaction matrix element

$$U(\boldsymbol{k}, E; k_F) = \sum_{|\boldsymbol{p}|<k_F} \langle \boldsymbol{pk}|g(\omega)|\boldsymbol{pk}\rangle_{\mathcal{A}}, \tag{2.48}$$

[13] The Fermi momentum k_F and the nuclear matter density ρ_{NM} of an isotropic, symmetric and noninteracting Fermi gas are related by $\rho_{NM} = \frac{2}{3\pi^2}k_F^3$.

Where $|\boldsymbol{pk}\rangle_{\mathcal{A}} = |\phi(\boldsymbol{p})\phi(\boldsymbol{k})\rangle - |\phi(\boldsymbol{k})\phi(\boldsymbol{p})\rangle$ is the antisymmetrized two-body plane wave function, and $\boldsymbol{p}$ is again the momentum of the bound nucleon[14]. To account for off-shell effects (e.g. the effects of short-range correlations), the *starting energy* $\omega = E + \epsilon(p)$ is defined self-consistently for all particles above and below the Fermi level. This is done by chosing the single-particle energy $\epsilon(p)$ as

$$\epsilon(p) \approx p^2/2m + \mathrm{Re}[U(p, \epsilon(p); k_F)], \tag{2.49}$$

with the nucleon mass m and the (self-consistent) optical potential U; in this equation we have also approximated the full potential[15] by its real part [Bri77/8].

The reaction matrix satisfies the Bethe-Goldstone equation

$$g(\omega) = v + vQ_P G^+(\omega) g(\omega) \tag{2.50}$$

[14] It is a fundamental result of many-body theory that in the cluster expansion of the total energy all self-energy terms to all orders cancel against the terms involving the single-particle potential U, provided the above form for U, also known as *Brueckner-Hartree-Fock* condition, is satisfied (for finite nuclei additional conditions for the off-diagonal matrix elements between hole states exist). Also, it is easy to see that U indeed represents the average effect of all particles in the medium on the particle in a state $\boldsymbol{k}$. With g being the effective interaction between particles in the medium, the potential energy for a particle in state $\boldsymbol{k}$ is just the interaction energy of a pair of particles in states $\boldsymbol{k}$ and $\boldsymbol{p}$, summed over all occupied states $\boldsymbol{p}$ [Pre 75].

[15] Nakayama and Love [Nak 88] discuss to some extent the sensitivity of their g-matrix to the choice of the single-particle energy. Specifically, they set the potential at large momenta, where the real part of the fully self-consistent potential becomes repulsive, to zero. They find, however, only small sensitivity even for the strong spin-independent isoscalar central component which should be particularly sensitive to the effects of short-range correlations.

where v is the internucleon potential, and the Green function

$$G^+(\omega) = \frac{1}{\omega^+ - \epsilon(q_1) - \epsilon(q_2)} \tag{2.51}$$

includes outgoing boundary conditions and medium effects through the influence of the average potential on the single-particle states[16]. In this equation, q_1 and q_2 are the momenta of nucleons in intermediate states. The projection operator Q from Section 2.3.1 becomes for nuclear matter the *Pauli operator* Q_P with the properties

$$Q_P(\boldsymbol{q}_1, \boldsymbol{q}_2)|\boldsymbol{q}_1\boldsymbol{q}_2\rangle = \begin{cases} |\boldsymbol{q}_1\boldsymbol{q}_2\rangle & \text{if } q_1 \text{ and } q_2 > k_F \\ 0 & \text{otherwise.} \end{cases} \tag{2.52}$$

This operator, therefore, restricts intermediate scattering states to outside the Fermi sphere.

To calculate the reaction matrix g, one can define the correlated two-nucleon wave function ψ by

$$g\phi = v\psi, \tag{2.53}$$

where $\phi(\boldsymbol{\kappa})$ is a plane wave with the relative momentum of the interacting pair[17]. From Eqs. (2.50) and (2.50) follows a Bethe-Goldstone integral

[16] In comparison, the single-particle energies in the energy denominator of the Lippmann-Schwinger equation for two free nucleons contain only the kinetic energy.

[17] In this form the nature of g as an effective interaction becomes plain: we replace the actual potential v by a quantity g, so that g acting on the model (uncorrelated) two-body wave function ϕ is the same as v applied to the actual (correlated) wave function. This supposition, the *independent pair model*, is justified if the *healing distance* for the correlated wave function is small, which is to a good approximation the case for low density [Pre 75].

equation for the correlated wave function

$$\psi = \phi + Q_P G^+(\omega) v \psi. \tag{2.54}$$

These developments are very similar to those in Section 2.1 for the free NN scattering case and the t-matrix.

2.4.2 Density Dependent Interactions

Starting from realistic NN potentials, several complex, energy and density dependent interactions have been constructed for nuclear matter for medium energies below about 400 MeV. Brieva, Rook and von Geramb [Ger 79] constructed an interaction (BRG) based on the Hamada-Johnston potential [Ham 62], the Hamburg group under von Geramb [Ger 83, Rik 84] an interaction (PH) based on the Paris potential [Lac 80], and another interaction (NL) based on the Bonn potential [Mac 87] was constructed by Nakayama and Love [Nak 88]. More recently, Ray [Ray 90] evaluated medium modifications to the Watson optical model for energies above the pion threshold. The resulting interaction is based on a nucleon-isobar coupled channels potential model [Ray 87] which explicitly includes NN inelasticities in the form of NN, $N\Delta(1232)$ and $NN^*(1440)$ channels. In the following we want to outline briefly, how the PH [Ger 83, Rik 84] NL [Nak 88] and LR [Ray 90] interactions were generated and then discuss some of their important properties.

* * *

The Bethe-Goldstone equations, Eqs. (2.50) or (2.51), are the starting points from which all of the abovementioned effective interactions are computed. The first step in these calculations is a *partial wave decomposition* of the respective integral equation to be solved. For an operator $F(\boldsymbol{k}', \boldsymbol{k})$ we can write for each isospin channel

$$\langle S'|F(\boldsymbol{k}', \boldsymbol{k})|S\rangle = 4\pi \sum_{LL'JM} i^{L-L'} \mathcal{Y}^{M}_{L'S'J}(\hat{\boldsymbol{k}'}) F^{JSS'T}_{LL'}(k', k) \mathcal{Y}^{M\dagger}_{LSJ}(\hat{\boldsymbol{k}}) P_T, \quad (2.55)$$

where

$$F^{JSS'T}_{LL'}(k', k) P_T = \frac{1}{4\pi} \int d\hat{\boldsymbol{k}'}\, d\hat{\boldsymbol{k}}\, \mathcal{Y}^{M\dagger}_{L'S'J}(\hat{\boldsymbol{k}'}) F(\boldsymbol{k}', \boldsymbol{k}) \mathcal{Y}^{M}_{LSJ}(\hat{\boldsymbol{k}}) P_T, \quad (2.56)$$

and the spin-spherical harmonics are defined as

$$\mathcal{Y}^{M}_{LSJ}(\hat{\boldsymbol{k}}) = \sum_{M_L, M_S} \langle LM_L; SM_S|JM\rangle Y^{M_L}_{L}(\hat{\boldsymbol{k}}) \chi^{M_S}_{S}. \quad (2.57)$$

It will also be convenient to define $F^{JSST}_{LL'} \equiv F^{JST}_{LL'}$.

Solving the full Bethe-Goldstone equation for the scattering problem in nuclear matter is a very complex and numerically difficult problem and one employs, therefore, certain approximations to simplify the propagator. The first approximation, spherical angle averaging of the Pauli blocking operator Q_P, is a standard procedure which has been shown to be a reasonable and quite accurate approximation in nuclear matter[18]. If we define $\boldsymbol{K} = \boldsymbol{k} + \boldsymbol{p}$ to be the total momentum of the interacting nucleon pair, $\boldsymbol{\kappa} = \frac{1}{2}(\boldsymbol{k} - \boldsymbol{p})$ to be

[18] Nakayama and Love discuss in their paper [Nak 88] the uncertainty in the interaction due to the use of an angle averaged Pauli operator $\overline{Q}_P$ and find for the largest interaction component, the isoscalar, spin-independent central component, that a 20% change in $\overline{Q}_P$ corresponds roughly to a 10% change in the modulus of the interaction.

their relative momentum, and $\boldsymbol{q} = \frac{1}{2}(\boldsymbol{q}_1 - \boldsymbol{q}_2)$ to be the relative momentum of the intermediate states (momentum conservation also yields $\boldsymbol{Q} = \boldsymbol{q}_1 + \boldsymbol{q}_2 = \boldsymbol{K}$ for the intermediate scattering states), Eq. (2.52) and angle averaging combined give the nonrelativistic *Pauli function* [Bri77/8]

$$\overline{Q}_P(K, q; k_F) = \frac{1}{4\pi} \int d\hat{\boldsymbol{q}}\, Q_P(\boldsymbol{K}, \boldsymbol{q}; k_F) = \begin{cases} 0, & a < 0 \\ a, & 0 \le a \le 1 \\ 0, & a > 1, \end{cases} \tag{2.58}$$

where $a = (\frac{1}{4}K^2 + q^2 - k_F^2)/Kq$. Here, and in all the following integrations over the angle between two vectors, we always choose one of the vectors to be oriented along the z-axis. Ray evaluates for his interaction an angle averaged Pauli blocking operator for each of the three channels NN, $N\Delta$ and NN^* using relativistic kinematics to relate two-body c.m. and laboratory frames [Ray 90].

The energy denominator in the propagator can be averaged in several ways. First we observe that the single-particle energies $\epsilon(q)$ in Eq. (2.51) contain implicitly the angle between the total momentum $\boldsymbol{K}$ and the relative momenta $\boldsymbol{\kappa}$ and $\boldsymbol{q}$. The NL [Nak 88] interaction is constructed using the method proposed by Brueckner and Gammel [Bru 58] which treats the angle averaging procedure in an approximate way. The method consists of writing a polynomial expansion of $\epsilon(q_1) + \epsilon(q_2)$ and expressing $\boldsymbol{q}_1$ and $\boldsymbol{q}_2$ as $\frac{1}{2}\boldsymbol{K} \pm \boldsymbol{q}$, respectively. Then, in the quartic term, $(\boldsymbol{K} \cdot \boldsymbol{q})^2$ is replaced by its spherical average

$$\frac{1}{4\pi} \int d\hat{\boldsymbol{q}}\, (\boldsymbol{K} \cdot \boldsymbol{q})^2 Q_P(\boldsymbol{K}, \boldsymbol{q}; k_F). \tag{2.59}$$

To fourth order in the energy expansion, this is equivalent to replacing in the single-particle energies $q_{1,2} \rightarrow q_{\pm} = \frac{1}{4}K^2 + q^2 \pm \sqrt{\frac{1}{3}} \cdot \overline{Q}_P(K, q; k_F)Kq$. The same procedure is applied to the starting energy ω, when expressed as $\epsilon(\boldsymbol{k}) + \epsilon(\boldsymbol{p})$; one only has to replace q by κ [Bri77/8].

The PH [Rik 84] interaction uses a slightly different approximation scheme. First, the kinetic energy terms are collected in terms of the relative momenta κ and q, then angle averaging is performed on the individual potentials, which bear the full angular dependence, without any approximations. Thus, for instance, for the projectile with momentum $\boldsymbol{k}$ we have

$$\frac{\int d\hat{\kappa}\, U(|\frac{1}{2}\boldsymbol{K} + \boldsymbol{\kappa}|)Q_P(\boldsymbol{K}, \boldsymbol{\kappa}; k_F)}{\int d\hat{\kappa}\, Q_P(\boldsymbol{K}, \boldsymbol{\kappa}; k_F)}, \tag{2.60}$$

and similar terms for the nucleons with momenta $\boldsymbol{p}$, $\boldsymbol{q}_1$ and $\boldsymbol{q}_2$.

The LR interaction which is based on Watson multiple scattering ignores the self-energy of the incoming projectile and applies binding energy corrections to the target nucleons only. Here, a quadratic expression of the form $U(\kappa^2) = A + B\kappa^2$ is being used. For the NN channel, with exception of the A parameter of the initial state, the parameters are chosen to reproduce the well depths of fitted Schrödinger equivalent real, central optical potentials from Dirac phenomenology. The binding potentials for $N\Delta$ and NN^* were assumed to be 60% that of the NN channel. Instead of the above averaging schemes Ray makes an effective mass approximation in combining the kinetic energy terms with the velocity dependent B terms. He thus arrives at a simple form for the energy denominator which includes the reduced effective mass of the target nucleon and its effective momentum in the entrance

channel. For the calculation of this momentum, the correct c.m. relativistic value was used and finally, for nucleon-isobar channels, also the energy dependent isobar widths Γ were included [Ray 90].

In the following, we want to briefly discuss the *generalized reference spectrum method* [Bri77/8] as one representative example of how the Bethe-Goldstone of the scattering problem in nuclear matter can be solved. This technique transforms the integral equation for the correlated wave function ψ into a system of two coupled differential equations, which are then readily solved by numerical quadrature and partial wave decomposition. Let us adopt a simplified notation and write $Q_P G^+$ in Eq. (2.54) as G_P^+. The generalized reference spectrum method is effectively an interpolation between the two limiting cases of

- free NN scattering: here G_P^+ becomes the free propagator G_0^+ and Eq. (2.54) reduces to the Lippmann-Schwinger equation. The pole in the Green function introduces a phase shift in the asymptotic wave function.

- the bound state problem: $\omega < 2\epsilon(k_F)$ and the kernel of G_P^+ is always non-singular and positive due to the Pauli principle. Asymptotically, no phase shifts occur and the correlated wave function ψ (which is purely real) heals towards the uncorrelated plane wave ϕ.

To achieve this interpolation Brieva and Rook separated the Green function G_P^+ into two parts

$$G_P^+ \approx G_R + G_F^+, \tag{2.61}$$

where the two components have the form

$$G_R = m\frac{c_R}{q^2+\gamma^2}$$
$$G_F^+ = m\frac{c_F}{Q_0^2+q^2+i\varepsilon}. \tag{2.62}$$

Here q is again the relative momentum in the intermediate states, Q_0 is the pole position in G_P^+, and the other parameters are optimized to satisfy Eq. (2.61) as closely as possible. That this is indeed a good approximation has been shown in the paper by Brieva and Rook [Bri77/8].

Now the integral equation for ψ, Eq. (2.54), can be written as a system of two coupled differential equations

$$\Lambda = \phi - G_R v\psi$$
$$\psi = \Lambda - G_F^+ v\psi \tag{2.63}$$

where ψ should be a good approximation to the true wave function. The quantity Λ is an auxiliary wave function. This system of differential equations can be also written as

$$(\nabla^2 - \gamma^2)[\Lambda - \phi] = mc_R v\psi$$
$$(\nabla^2 + Q_0^2)[\psi - \Lambda] = mc_F v\psi, \tag{2.64}$$

which can be solved numerically by means of partial wave expansions. However, one can easily recognize the following limiting cases

- for free NN scattering with the free propagator G_0^+ one has $c_R = 0$, $c_F = 1$ and $\Lambda \equiv \phi$. One is left with the Schrödinger equation for free NN scattering

$$(\nabla^2 + Q_0^2)\psi = mv\psi, \tag{2.65}$$

where Q_0 is the asymptotic relative momentum.

- for the bound state problem one has $c_F = 0$ because of the non-singular kernel. Hence, one is left with the traditional reference spectrum method equation where $\Lambda \equiv \psi$, i.e.

$$(\nabla^2 - \gamma^2)[\psi - \phi] = mc_R v\psi. \tag{2.66}$$

* * *

Although the generalized reference spectrum method was used by von Geramb, Brieva and Rook for the BRG interaction [Ger 79]), another procedure was chosen for the PH interaction. With the above approximations for the numerator and the denominator of the propagator, Eqs. (2.58) and (2.60), the integral equation for the correlated wave function in coordinate-space, $u_{LL'}^{JST}(r,\alpha)$, was solved in each partial wave $J \leq 10$ with standard matrix techniques for Fredholm integral equations of the second kind (α represents the dependence of the wave function on E, $\boldsymbol{k}$, $\boldsymbol{p}$ and k_F). The self-consistency process was initiated with the choice $U = 0$ and was iterated once [Ger 83, Rik 84].

The prescription of Siemens [Sie 70] was then used to construct a local energy and density dependent effective interaction in coordinate-space. The method simulates, in an average way, all the properties of the correlated wave functions, including the behaviour at small r. In this way, important off-shell amplitudes which arise from short-range, repulsive anticorrelation effects which tend to keep identical nucleons apart are retained at least on the average [Kel 89a]. The basic idea is that with the correlated wave function ψ the plane wave matrix element of g can be deduced from $\langle\phi|g|\phi\rangle = \frac{\langle\phi|v|\psi\rangle}{\langle\phi|\phi\rangle}$.

Explicitly, one has

$$g_{LL'}^{JST}(\boldsymbol{k}, E; k_F) = \frac{\sum_{L''} \int_{|\boldsymbol{p}|\leq k_F} d\boldsymbol{p}\, j_L(\kappa r) v_{LL''}^{JST}(r) u_{LL''}^{JST}(r,\alpha)}{\int_{|\boldsymbol{p}|\leq k_F} d\boldsymbol{p}\, j_L(\kappa r) j_{L'}(\kappa r)}, \tag{2.67}$$

where the $v_{LL''}^{JST}(r)$ are the two-body NN potential radial form factors of the Paris potential in the channel $(JST; LL'')$ [Rik 84]. The angular momentum indices are such that the unprimed L refers to the entrance channel, while the primed ones refer to subsidiary channels.

An interaction in the form of a local pseudopotential, Eq. (2.32), can be obtained if one expresses $g(r)$ as a scalar product of the rank k tensor operators $R_k(r)$, acting only in coordinate-space, and S_k, acting only in spin and isospin space

$$g(r) = \sum_{k=0}^{2} R_k(r) \cdot S_k. \tag{2.68}$$

Using partial wave analysis and Racah algebra, one can isolate the tensor amplitudes which are related to the g-matrix elements of Eq. (2.67). One finds for instance for the central component ($k = 0$) that $S_0 = P_S P_T$ and

$$R_0 = R_0^{(LL,ST)} = \frac{\sum_J \hat{J} \cdot g_{LL}^{JST}}{\hat{S}\hat{L}}. \tag{2.69}$$

In the here adopted notation we have $\hat{x} = 2x + 1$. The remaining L dependence in the R_k can be eliminated by performing a weighted average over the Fermi sphere. The appropriate weighting factor for the central interaction is the statistical factor $\hat{L}$ times the probability that the relative angular momentum of projectile and target nucleon is L [Kel 81], i.e.

$$w_L = \int_{|\boldsymbol{p}|\leq k_F} d\boldsymbol{p}\, |j_L(\kappa r)|^2. \tag{2.70}$$

With this result we get for the central interaction

$$g^C_{ST} = \frac{\sum_L \varepsilon w_L \hat{L} R_0^{(LL,ST)}}{\sum_L \varepsilon w_L \hat{L}}, \tag{2.71}$$

where the factors ε restrict the sum to allowed antisymmetrized states. Analogous expressions for the spin-orbit ($k = 1$) and tensor ($k = 2$) components are given in [Ger 79, Ger 83, Rik 84].

Finally, following the procedure in Section 2.3.4, a parametrization in terms of Yukawas is done. The final interaction is available for densities between 0.5 and 1.4 fm^{-1}. However, for $k_F \to 0$, the PH interaction is only required to reduce to the free NN t matrix for the two momentum transfers $q = 0$ and $q = k$, which might explain the large differences that have been found, particularly at intermediate momentum transfers, for the low-density PH tensor interaction and the tensor components of the FL t-matrix [Kel 89a].

* * *

The NL interaction is calculated in momentum-space on the energy shell by solving the operator equation, Eq. (2.50), directly for the $g^{JST}_{LL'}(K, \kappa, \kappa)$ in each Pauli allowed partial wave channel ($J \leq 10, 15, 18$ for $T_L(\text{MeV}) \leq 100$, $100 < T_L(\text{MeV}) \leq 270$ and $270 < T_L(\text{MeV}) \leq 425$, respectively) via matrix-inversion[19] [Nak 88]. The calculation is fully self-consistent. Apart from the approximations for the propagator described above, a simple Fermi average

[19] The method which is generally used, is the one described by Haftel and Tabakin [Haf 70].

for the magnitude of the initial momentum of the struck nucleon was chosen, namely $\langle|\boldsymbol{p}|\rangle = \frac{3}{4}k_F$. Subsequently, for simplicity, the magnitudes of the total momentum $\boldsymbol{K}$ and the initial relative momentum κ were determined from k and p by an unweighted average over the direction of $\boldsymbol{p}$ with respect to the local momentum $\boldsymbol{k}$ of the incident projectile

$$\langle\kappa\rangle = \langle\frac{K}{2}\rangle = \frac{k_>}{2} + \frac{1}{6}\frac{k_<^2}{k_>}, \tag{2.72}$$

where $k_>$ ($k_<$) is the larger (smaller) of k and $\frac{3}{4}k_F$. The advantage of this simple averaging procedure is that nonrelativistically one recovers the free NN t matrix in the limit $k_F \to 0$, independent of momentum transfer [Nak 88]. Simply substituting the $g_{LL'}^{JST}(K,\kappa,\kappa)$ back into the partial wave expansion for the g-matrix, gives a local and angular momentum independent interaction for a particular projectile energy, without further averaging. Finally, the interaction is cast in the operator form, Eq. (2.40), using certain relationships between the g-matrix and the coefficients $\tilde{g}_{ST}^C$, $\tilde{g}_T^{LS}$ and $\tilde{g}_T^T$ [Nak 88, Nak 84]. Subsequently, the interaction components are fitted for several energies and densities to sums of antisymmetrized momentum-space Yukawa forms, similar to Section 2.3.4, using only on-shell momenta $q < 2k$.

Nakayama and Love have studied, to a certain extent, the off-shell and nonlocal behaviour of the $\tilde{g}_{00}^C$ component of their interaction. The authors justify the on-shell prescription which was used to construct their local interaction by observing that at moderate excitation energies the on-shell or near on-shell matrix elements will be the dominant ones due to the limited spread in relative collision momenta allowed by the momentum distributions of the

initial and final target state wave functions. To show the off-shell effect, Nakayama and Love compare at $k_F = 0$ the parametrized (i.e. local) form of the g-matrix with the exact g-matrix, evaluated under special kinematic conditions: while they vary the magnitude of the final relative momentum κ', both $\boldsymbol{\kappa}$ and $\boldsymbol{\kappa}'$ are taken to be parallel (i.e. the on-shell point is at $\kappa' = \kappa$, where $qQ = 0$). They observe that large differences between the exact and local interactions only exist for such significantly different relative momenta which are unphysical and not allowed by the nuclear wave functions.

To study nonlocality, they make use of the fact that in momentum-space a purely local interaction depends solely on the momentum transfer $\boldsymbol{q}$ but not on the exchange momentum transfer $\boldsymbol{Q}$. Thus, examining the $\boldsymbol{Q}$ dependence at a fixed value of $\boldsymbol{q}$ samples the overall nonlocality of an interaction. Considering Eq. (2.50), they observe that for a purely real NN input potential v the nonlocality of the imaginary part of the interaction will be entirely due to the correlation term $G_P^+ g$. A comparison with the Q dependence of the bare NN potential, in this case the Bonn potential [Mac 87] which itself is strongly nonlocal due to the exchange of σ and ω mesons, seems to indicate that the nonlocality contributions from the potential greatly outweigh those due to correlations.

* * *

For the LR interaction, the evaluation of the Watson t-matrix was achieved by introducing a correlated wave function, $u^{JST}_{\beta LL'}(r, \alpha)$, in coordinate-space and solving equation Eq. (2.54) in each partial wave and for each nucleon-isobar channel β with matrix techniques. The treatment of

the propagator has been discussed earlier. With the correlated wave functions, medium modified *NN* amplitudes f are generated on the energy shell with $f = \langle\phi|v|\psi\rangle$ for specific initial and final two-nucleon spin projections [Ray 90]. Following the notation of [Ray 85], these amplitudes are then transformed into *Wolfenstein amplitudes* for *(pp)* and *(pn)* channels

$$f(q) = A(q) + B(q)\sigma_{1n}\sigma_{2n} + C(q)(\sigma_{1n} + \sigma_{2n}) + D(q)\sigma_{1q}\sigma_{2q} + E(q)\sigma_{1Q}\sigma_{2Q}, \tag{2.73}$$

where $\sigma_{ix} \equiv \boldsymbol{\sigma}_i \cdot \hat{\boldsymbol{x}}$, and $\boldsymbol{q}$, $\boldsymbol{Q}$ and $\hat{\boldsymbol{n}}$ are defined as before in Section 2.3.4. From this equation, a medium corrected t-matrix in the *NN* system can be directly obtained by multiplying the scattering amplitudes by the factor η which was also given in Section 2.3.4.

2.4.3 The Local Density Approximation

Effective interactions are conveniently applied to nucleon-nucleus scattering using the *local density approximation* (LDA), in which the effective interaction between an incident projectile and a target nucleon bound in a finite system is assumed to be the essentially the same as that appropriate for infinite nuclear matter with the same local density [Jeu 74, Jeu 76, Bri77/8]. For natural-parity isoscalar transitions, the scattering potential can be expressed as

$$U(\boldsymbol{r}) = U^Z(\boldsymbol{r}) + U^C(\boldsymbol{r}) + \nabla F^{LS}(\boldsymbol{r}) \times \frac{1}{i}\nabla \cdot \boldsymbol{\sigma}, \tag{2.74}$$

where U^Z is the potential obtained from folding the Coulomb interaction with either the ground-state or the transition charge density. The elastic

optical potential has the form Eq. (2.11), where

$$U^{LS}(r) = \frac{1}{r}\frac{\partial F^{LS}}{\partial r} \tag{2.75}$$

The central and spin-orbit potentials U^C and F^{LS} are expanded in terms of their multipoles as

$$\begin{aligned} U^C(\boldsymbol{r}) &= \textstyle\sum_J U_J^C(r) \cdot Y_J(\hat{\boldsymbol{r}}) \\ F^{LS}(\boldsymbol{r}) &= \textstyle\sum_J F_J^{LS}(r) \cdot Y_J(\hat{\boldsymbol{r}}). \end{aligned} \tag{2.76}$$

The multipoles are obtained by folding the matter transition density $\tilde{\rho}_J$ with central and spin-orbit components of the effective interaction $\tilde{t}^C$ and $\tilde{\tau}^{LS}$ according to[20]

$$\begin{aligned} U_J^C(r) &= \tfrac{2}{\pi} \textstyle\int dq\, q^2 j_J(qr) \tilde{t}^C(q) \tilde{\rho}_J(q), \\ F_J^{LS}(r) &= \tfrac{2}{\pi} \textstyle\int dq\, q^2 j_J(qr) \tilde{\tau}^{LS}(q) \tilde{\rho}_J(q), \end{aligned} \tag{2.77}$$

where the point transition densities $\tilde{\rho}_J(q)$ will be taken directly from (e, e') inelastic scattering. The essence of the local density approximation is that the interaction is assumed to be the one calculated in infinite nuclear matter. The density dependence of the effective interaction is evaluated at the projectile position r, i.e. $\tilde{t}(q) \rightarrow \tilde{t}(q, \rho_g(r))$, where $\rho_g(r)$ is the local ground-state density [Kel 89a].

This approach to the LDA is the numerically most simple one, but is not unique. Other forms can be employed in the coordinate-space representation of the optical potential described, for example, by Brieva and Rook [Bri77/8]. For instance, the central potential in coordinate-space reads

$$U^C(\boldsymbol{r}) = \int d\boldsymbol{r}' \, [t^D(s, \rho_g)\rho(\boldsymbol{r}') + j_0(ks) t^X(s, \rho_g)\rho(\boldsymbol{r}, \boldsymbol{r}')], \tag{2.78}$$

[20] From now on, $\tilde{t}^C$ and $\tilde{\tau}^{LS}$ can also denote components of the density dependent interaction.

where the mixed transition density and the relative coordinate s are defined as in Section 2.3.3 and where k is the local wave number. Again, both the direct (t^D) and the exchange (t^X) interactions are approximated by the corresponding effective interactions in nuclear matter with the appropriate density. However, in the coordinate-space form the ground state density, and thus the interaction, can now be evaluated at either r, r', or the midpoint $R = \frac{1}{2}|\boldsymbol{r} + \boldsymbol{r}'|$.

2.4.4 Treatment of the Exchange Interaction

Eq. (2.78) is derived from a more general formulation of the *NA* optical potential which is nonlocal in coordinate-space and energy dependent [Bri77/8]. This potential can be approximated by the sum of a local direct term and a nonlocal exchange term. For the exchange term it is convenient to define a local equivalent potential via

$$U^X(\boldsymbol{r})\psi(\boldsymbol{r}) = \int d\boldsymbol{r}'\, U^X(\boldsymbol{r},\boldsymbol{r}')\psi(\boldsymbol{r}'), \tag{2.79}$$

where ψ is the scattering wave function of the incident projectile nucleon. If the potential is small compared to the total energy of the projectile and if furthermore its spatial variation is small compared to the projectile wavelength, it is reasonable to approximate the momentum in the vicinity of $\boldsymbol{r}$ by its (self-consistent) local value $k(r) = \sqrt{2m[E_P - \mathrm{Re}U(r)]}$. The wave function $\psi(\boldsymbol{r}')$ can then be written, using the translation operator from elementary quantum mechanics, as

$$\psi(\boldsymbol{r}') = \psi(\boldsymbol{r} - \boldsymbol{s}) = e^{i\boldsymbol{k}(\boldsymbol{r})\cdot\boldsymbol{s}}\psi(\boldsymbol{r}), \tag{2.80}$$

where $\boldsymbol{s} = \boldsymbol{r} - \boldsymbol{r}'$ was used. This leads to

$$U^X(\boldsymbol{r}) = \int d\boldsymbol{r}' \, e^{i\boldsymbol{k}(\boldsymbol{r})\cdot\boldsymbol{s}} U^X(\boldsymbol{r}, \boldsymbol{r}'). \tag{2.81}$$

If $U^X(\boldsymbol{r}, \boldsymbol{r}')$ is sufficiently short-ranged so that all non-spherical contributions can be neglected, integration over the angle between $\boldsymbol{k}(\boldsymbol{r})$ and $\boldsymbol{s}$ yields with $j_0(x) = \frac{\sin x}{x}$

$$U^X(\boldsymbol{r}) = \int d\boldsymbol{r}' \, j_0(ks) U^X(\boldsymbol{r}, \boldsymbol{r}'), \tag{2.82}$$

where a factor of 4π was put back into the volume element [Kel 81]. If $U^X(\boldsymbol{r}, \boldsymbol{r}')$ is expressed in the folding model approach as $t^X(ks)\rho(\boldsymbol{r}, \boldsymbol{r}')$, we get the above expression, Eq. (2.78).

* * *

At this point several further approximations to the exchange term can be discussed. For this we recall the expression for the mixed density, Eq. (2.29), as product of a point density and a correlation function, here $\rho(\boldsymbol{r}, \boldsymbol{r}') = \rho(\boldsymbol{r}')C(\hat{k}, s)$.

- ZREA *(zero-range exchange approximation)*: since $s \approx 0$, both j_0 and $C(\hat{k}, s)$ go to unity (see also Section 2.3.4).

- FREA *(finite-range exchange approximation)*: j_0 is retained, while the correlation function goes to unity.

- SEA *(Slater exchange approximation)*: both the spherical Bessel function and the correlation function are retained. The correlation function is assumed to have the Slater form.

- AEA *(Asymptotic energy approximation)*: the local wave number k is calculated with the asymptotic energy E_P, i.e. $k = \sqrt{2mE_P}$, rather than with the fully self-consistent local energy (LEA) which was used in the previous paragraph. Although the choice of the local energy can also affect the direct part through the intrinsic energy dependence of the g-matrix, this contribution is usually much less important. However, Kelly *et al.* find for 135 MeV that AEA and LEA scattering calculations using the PH interaction are almost indistinguishable, and that the largest effect is a 6% reduction in the real central part of the optical potential [Kel 89a].

2.4.5 LDA Calculation Results

Optical potentials for elastic scattering of 100, 200, and 318 MeV protons from ^{16}O and ^{40}Ca are shown in Figures 2.12–2.17. In these figures we compare the optical potentials for the PH (solid line), NL (short dashes), LR (dashes), and FL (long dashes) interactions. For 100 MeV only the PH and NL interactions are available. In the following calculations the LDA was evaluated at the projectile position and exchange was treated using ZREA and AEA. As anticipated, all the LDA potentials approach the NRIA in the low-density surface region. While all the central potentials are subject to strong medium modifications, the effects on the real part of the spin-orbit interaction are only modest. The medium modifications of the imaginary spin-orbit potential are quite significant, but have no large impact on the

calculations because this potential is very small[21].

Relative to the NRIA, represented by the FL potential, all the LDA imaginary central potentials are smoothly damped in the interior due to Pauli blocking. The PH potential remains for all energies the most absorptive. By contrast, the NL interaction produces the weakest absorption. The potential generated with the LR interaction is intermediate between the two others. The PH potential is always about 50% more absorptive than the NL potential, the LR potential always between about 5 and 10% more absorptive than the NL potential.

The real central potentials are generally more repulsive than the NRIA potential and for 100 and 200 MeV show more radial structure. The PH potential is more repulsive and has more structure than either the NL or LR potentials. At 100 MeV the NL potential is very similar to the FL potential and only slightly more repulsive in the center. For 200 MeV the LR potential has the same strength in the center as the PH potential, but becomes virtually identical with the NL potential for $r > 1.5$fm. For 318 MeV even the NL and LR interactions produce potentials with significant radial structure.

[21] The "wiggles" in the small ImU^{LS} potentials are due to the fact that for these LDA calculations, we evaluate the density dependence of the interaction using q-folding at each projectile position and by interpolating expansion coefficients of a given Yukawa table. The density dependence of the interaction which is represented by such a table is not entirely smooth. Evaluating the interaction in coordinate-space instead, comprises effectively a smoothing process because the potentials are first calculated on a radial mesh and then interpolated by a smooth polynomial. On the other hand, reparametrized theoretical interactions, as well as the empirical interactions in Chapter 7, do have smooth density dependence and, hence, produce smooth potentials. In either case, the wiggles are too small to affect the observables.

The very characteristic radial shape of the LDA potentials, commonly called "wine-bottle" shape, is due to the delicate competition between short-range repulsion and attraction in the interaction. The details of the balance depend upon the difference between the gradient of the density and the gradient of the repulsive component [Kel 89a]. The energy dependence of the shape is due to the different energy dependencies of the direct and exchange parts of the folding potential, the exchange part having a slightly sharper energy dependence than the direct part. As we will see later the wine-bottle shape also arises from our empirical interaction, the IA2 [Ott 88], and Dirac phenomenology [Ham 90]. Finally, the equivalent local potentials which will be discussed in Section 2.7.2 also show this shape.

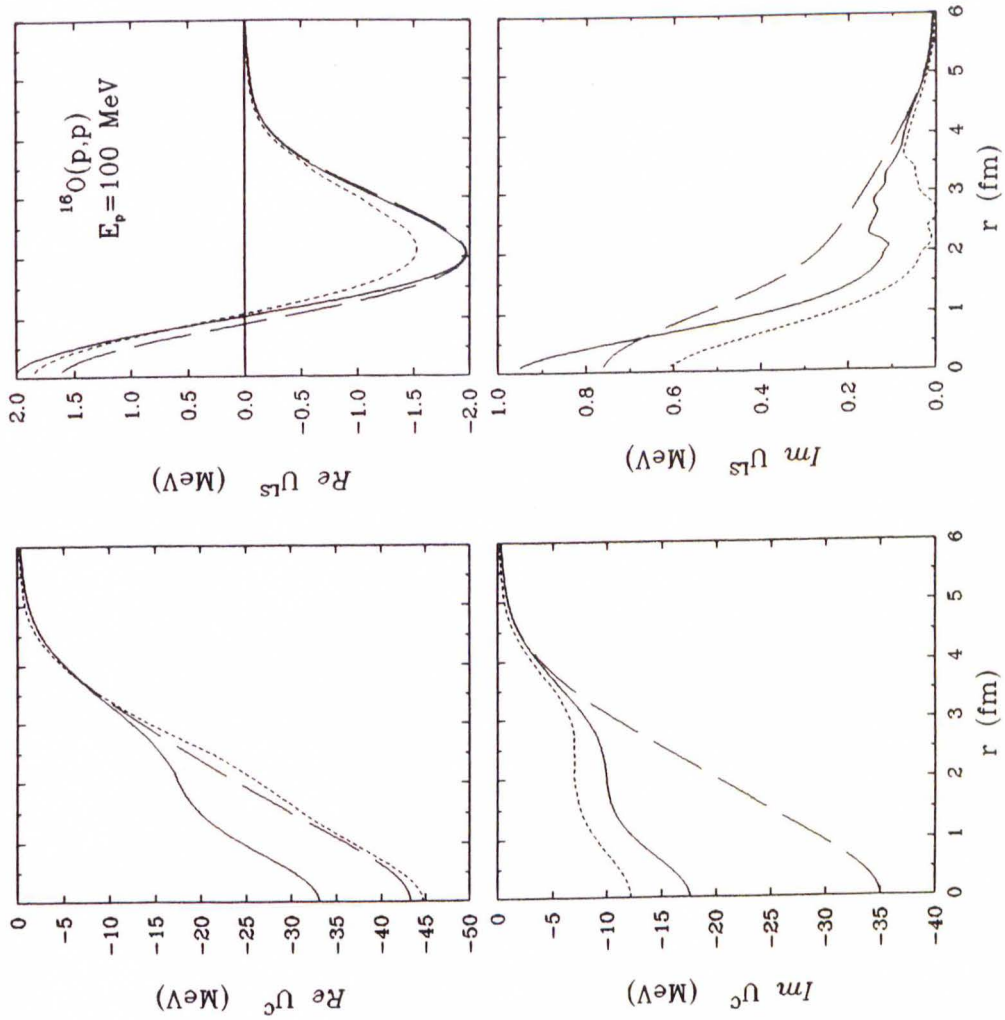

Figure 2.12: Optical potentials for elastic scattering of 100 MeV protons by ^{16}O for the PH (solid line), NL (short dashes), and FL (long dashes) interactions.

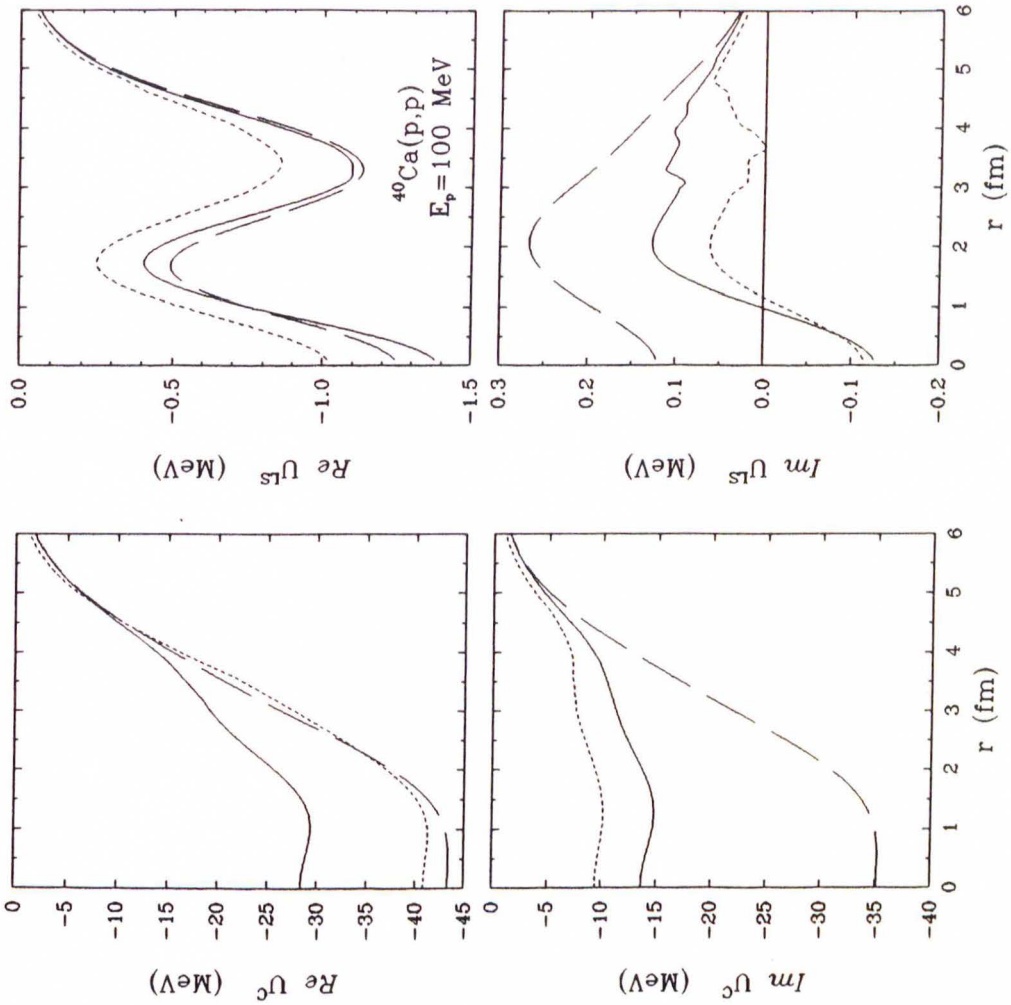

Figure 2.13: Optical potentials for elastic scattering of 100 MeV protons by ^{40}Ca for the PH (solid line), NL (short dashes), and FL (long dashes) interactions.

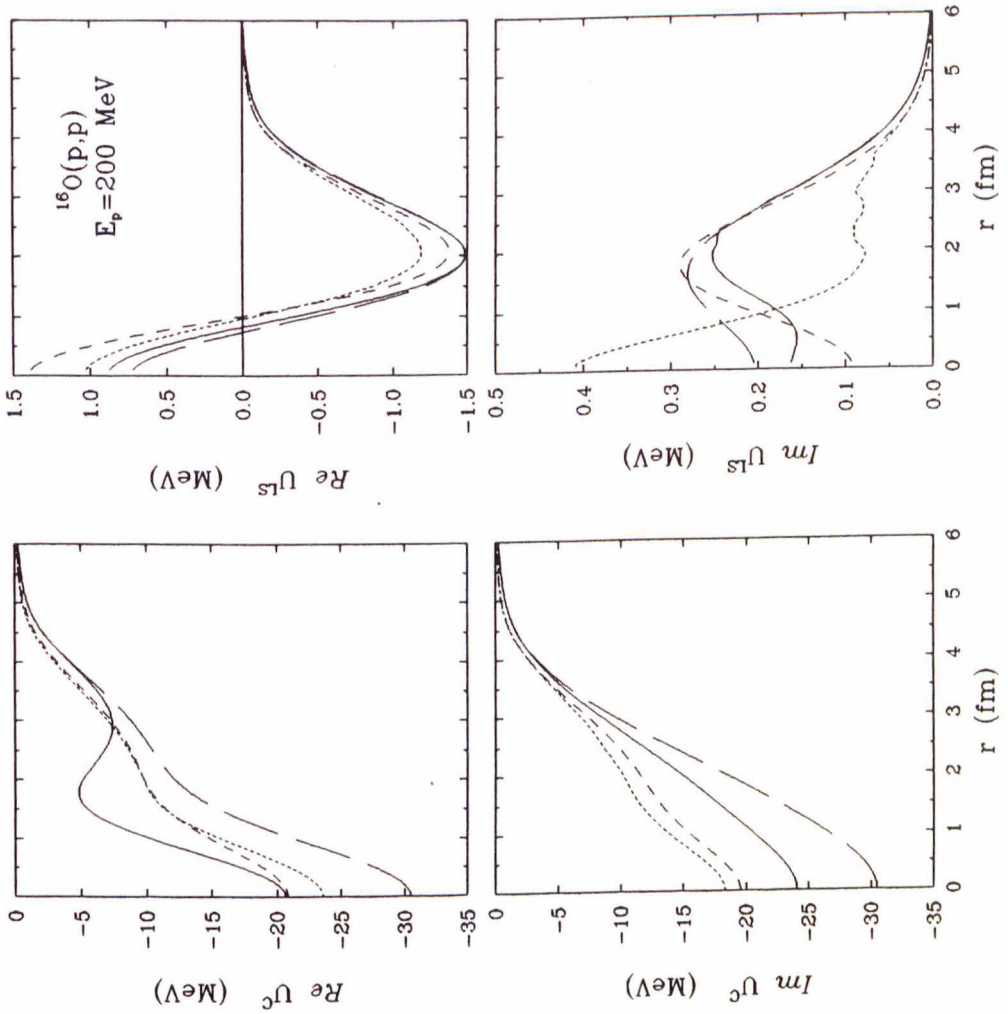

Figure 2.14: Optical potentials for elastic scattering of 200 MeV protons by ^{16}O for the PH (solid line), NL (short dashes), LR (dashes), and FL (long dashes) interactions.

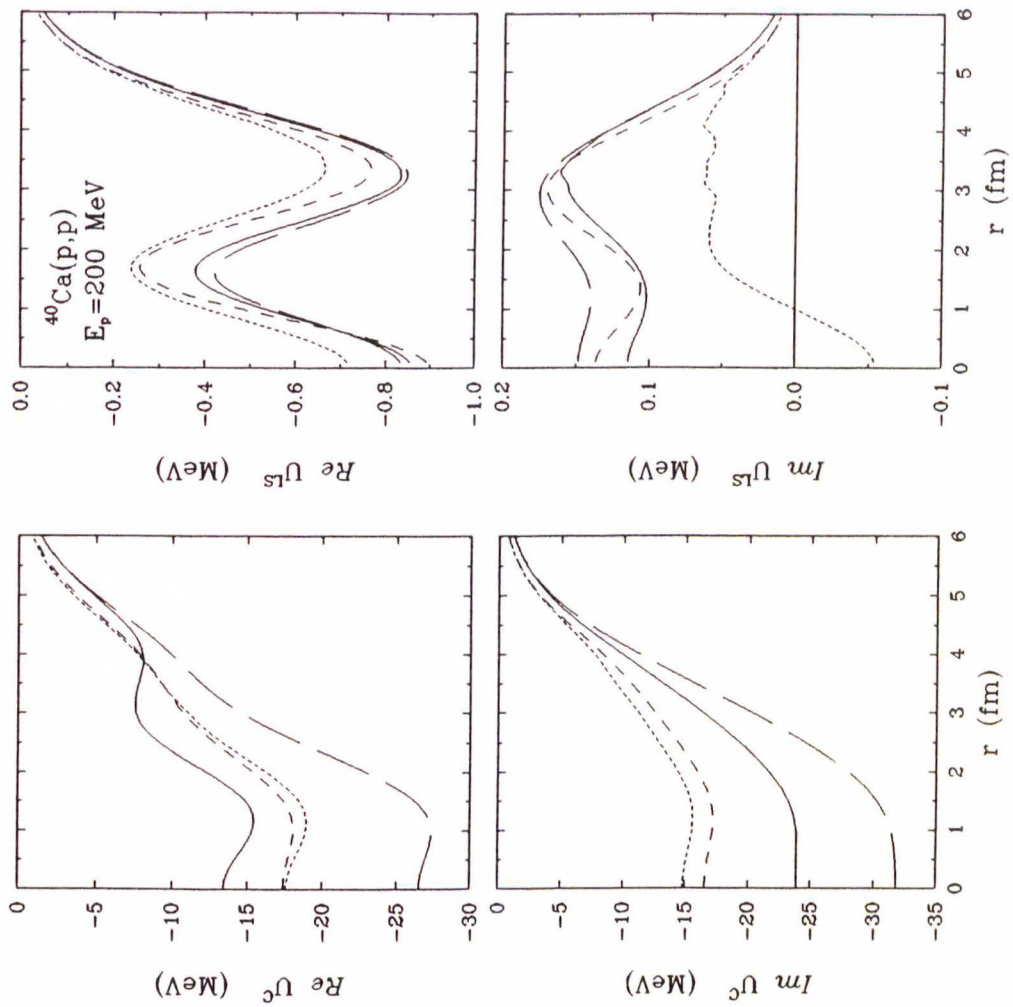

Figure 2.15: Optical potentials for elastic scattering of 200 MeV protons by ^{40}O for the PH (solid line), NL (short dashes), LR (dashes), and FL (long dashes) interactions.

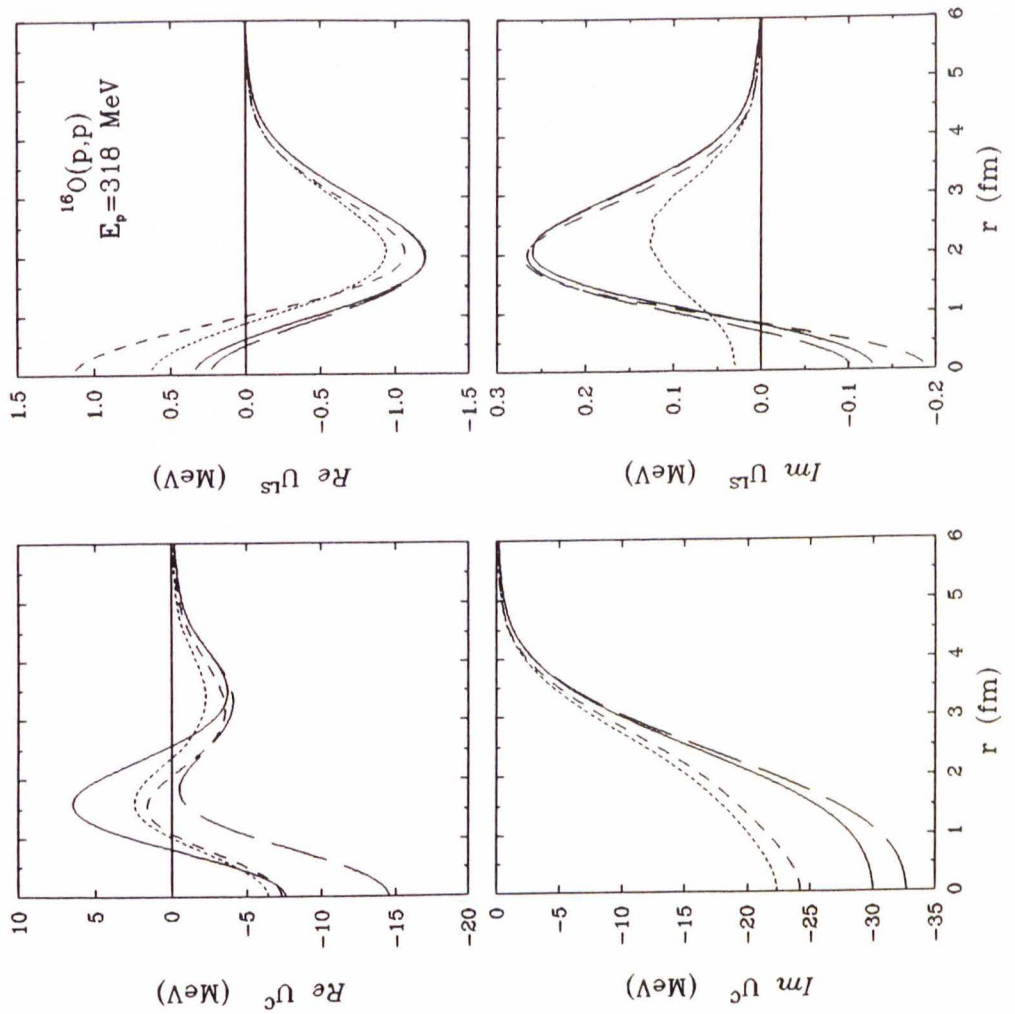

Figure 2.16: Optical potentials for elastic scattering of 318 MeV protons by ^{16}O for the PH (solid line), NL (short dashes), LR (dashes), and FL (long dashes) interactions.

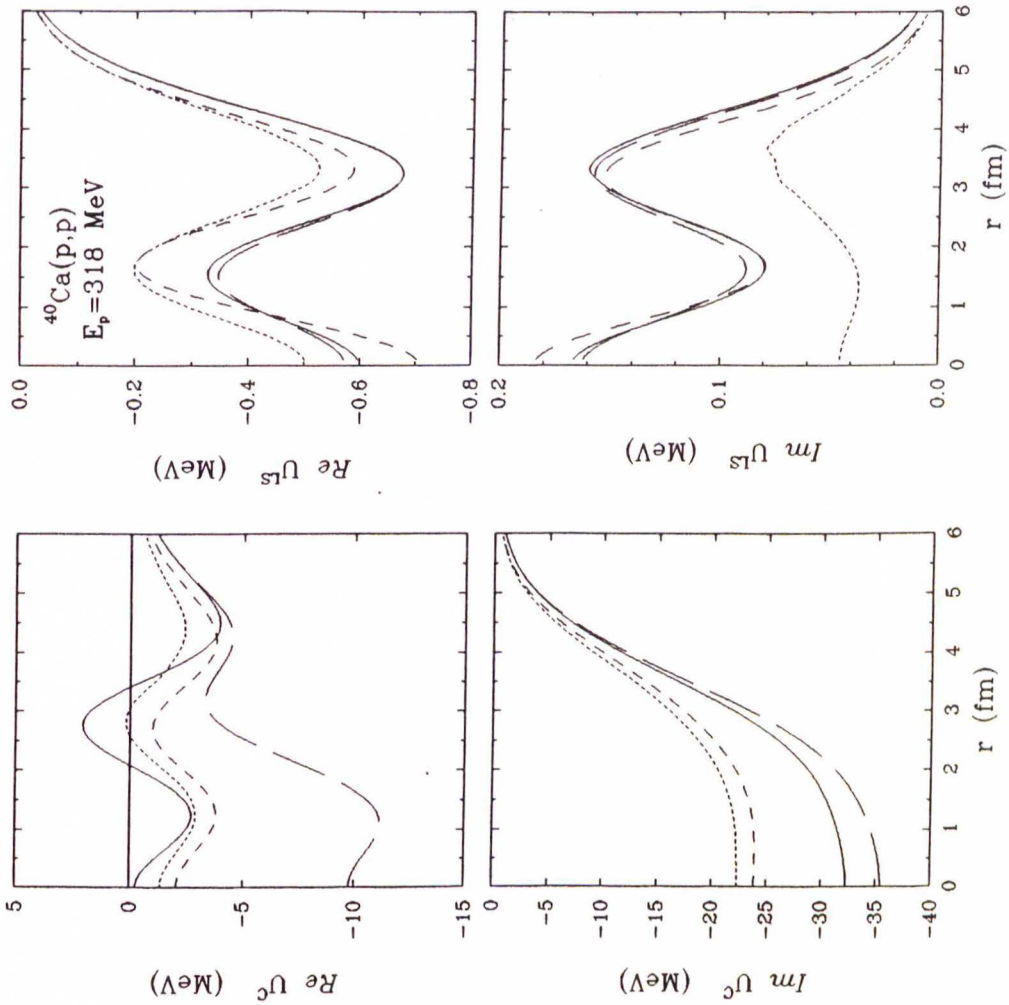

Figure 2.17: Optical potentials for elastic scattering of 318 MeV protons by ^{40}Ca for the PH (solid line), NL (short dashes), LR (dashes), and FL (long dashes) interactions.

In Figures 2.18–2.25 we show LDA calculations for the same data and in the same format as in Section 2.3.6. The line code is the same as in the previous figures for the optical potentials: PH (solid), NL (short dashes), and LR (dashes). All of the calculations employ self-consistent distorted waves and transition densities from electron scattering (see Appendix A).

While the cross section calculations based on the PH interaction look reasonable for elastic scattering and the 3_1^- states at 100 MeV, neither the 1_1^- state of ^{16}O, nor the 3_2^- state of ^{40}Ca are particularly well described. The NL forward cross sections are generally too high, a consequence of the weak absorption of the NL potential. The PH interaction provides an overall better description of the analyzing powers than the NL interaction which gives much too positive analyzing powers at large momentum transfers, and which for ^{40}Ca produces rapid oscillations in the analyzing power which are not present in the data. Nevertheless, neither interaction describes the data particularly well.

At 200 MeV, although both the NL and the LR interaction describe the elastic cross sections slightly better than the PH interaction, their predictions for the forward angle elastic analyzing powers and spin rotation functions fall well below the data. The PH interaction, on the other hand, describes these data quite well. Inclusion of Pauli blocking and short-range anticorrelations lower the inelastic forward cross sections and fill in strength at large momentum transfers. The analyzing powers become more negative and are closer to the data. On the other hand, if we compare the LDA calculations for the 3_2^- state of ^{40}Ca with the corresponding NRIA calculations in Figure 2.7 we

do not see much improvement: on the contrary, the second maximum in the cross section appears to be slightly to high. The reason for this behaviour might be the special shape of the transition density which has a strong lobe both in the high-density interior and the low-density surface region. It is also striking that all the LDA models overestimate the forward cross sections of the surface-peaked 3_1^- peaks. This suggests that the effective interaction is modified even for low densities. The spin rotation functions are clearly improved over the NRIA in Figure 2.8, especially at forward angles. Finally, the LDA calculation follows more closely the large amplitude of the oscillatory pattern which is described by the analyzing power data. While the PH interaction is clearly superior at small momentum transfers, it appears that the NL and LR interactions become slightly superior at larger momentum transfers. Overall, the PH interaction provides the best description of all the data. While the cross section predictions for the LR interaction are very similar to those for the NL interaction, the LR analyzing powers are clearly superior to those of the NL interaction. Analyzing powers for energies at or below 135 MeV are especially poor with the NL interaction.

At 318 MeV the PH interaction provides a clearly superior description of the ^{16}O cross section data, while the NL and LR predictions fall well below the data. The PH analyzing powers, on the other hand, appear to be shifted a little bit too much towards lower momentum transfers while the two other interactions follow the data more closely. For ^{40}Ca the NL and LR interactions perform better on the cross sections and approach the PH predictions. Their predictions of the analyzing powers and the spin rotation

function at larger momentum transfers are still slightly superior to the PH predictions. It is significant, however, that even the LDA is not able to suppress enough the forward angle analyzing powers at this energy.

Kelly *et al.* attribute the superior performance of the PH interaction over the NL interaction for isoscalar natural-parity transitions to the special procedures used in reducing the g-matrices to a local form. As discussed above, the PH interaction is believed to reproduce more realistically the short-range correlations of the interaction, thus giving rise to off-shell behaviour that may be more realistic. Since the on-shell behaviour of the two interactions, as judged from the the Pauli suppression of the forward scattering cross section, appears to be comparable, the off-shell performance of an interaction seems to be indeed important. In spite of the careful justifications for their on-shell and momentum averaging prescriptions leading to a local pseudopotential form, the off-shell behaviour of the NL interaction by Nakayama and Love might be inadequate. On the other hand, it has also been observed that the NL interaction, in some respects is more sound than the PH interaction, especially with regard to self-consistency and the low density limit. And indeed, the NL tensor interaction, being in better agreement with the FL t-matrix, gives a better description of the excitation of stretched states than does the PH interaction [Kel 89a]. A comparison of the PH and NL interactions to the LR interaction is less straightforward and we defer it to a later section.

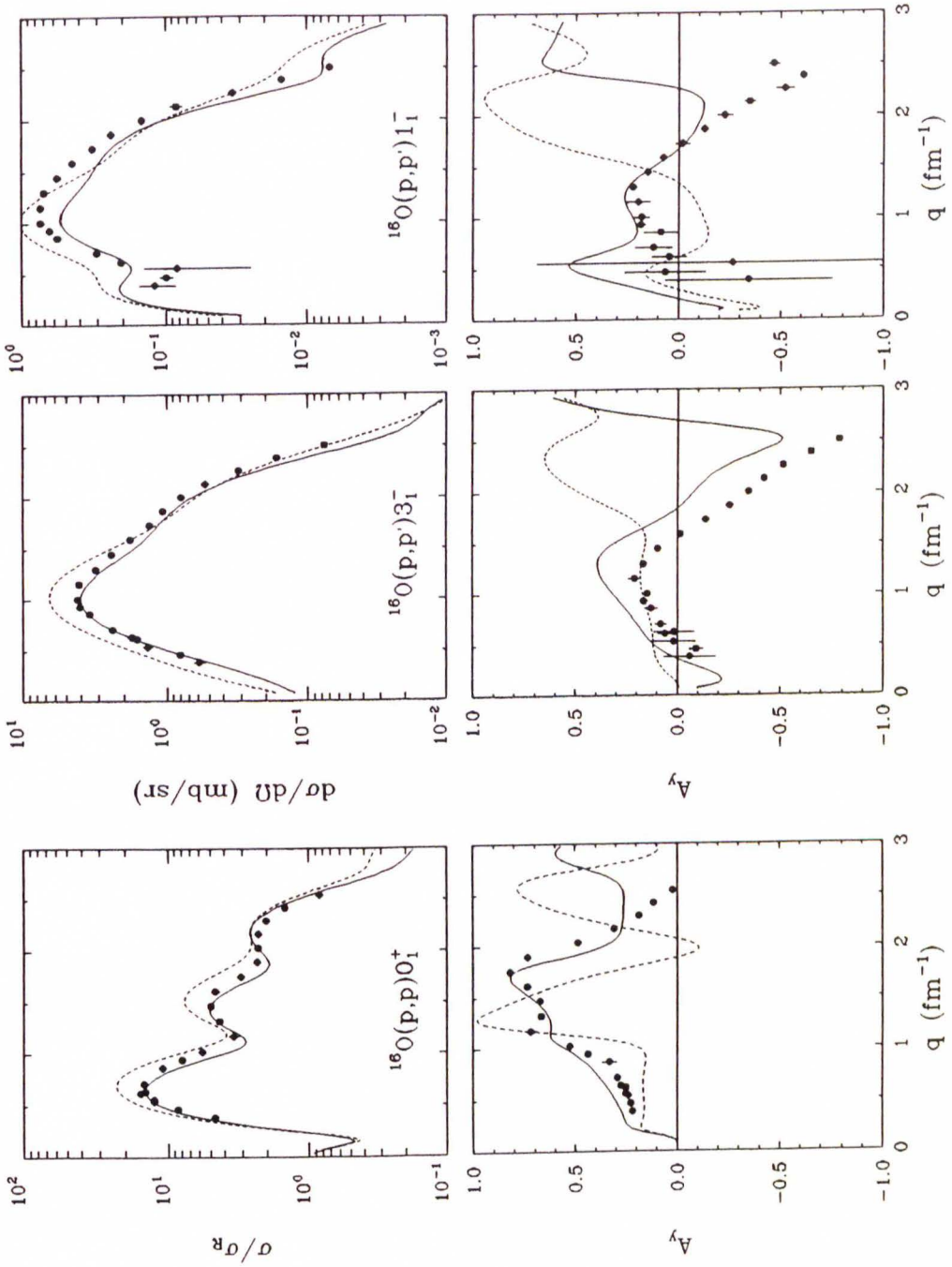

Figure 2.18: LDA calculations of $\sigma(q)$ and A_y for selected states of ^{16}O at 100 MeV; the elastic cross section is presented as ratio to the point-charge Rutherford cross section (σ_R) to enhance detail. Line code: PH (solid), NL (short dashes). The data are from this work.

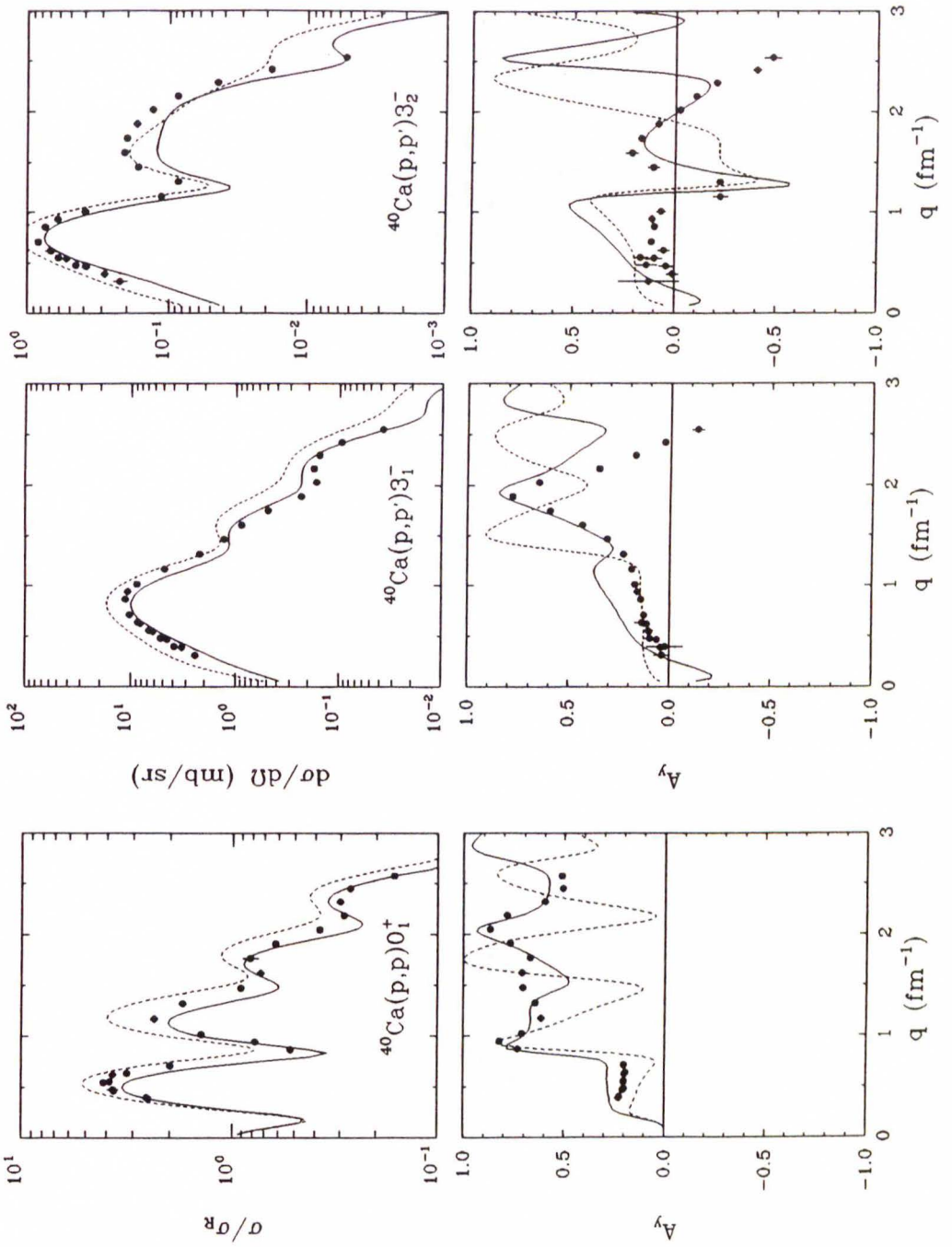

Figure 2.19: LDA calculations of $\sigma(q)$ and A_y for selected states of ^{40}Ca at 100 MeV; the elastic cross section is presented as ratio to the point-charge Rutherford cross section (σ_R) to enhance detail. Line code: PH (solid), NL (short dashes). The data are from this work.

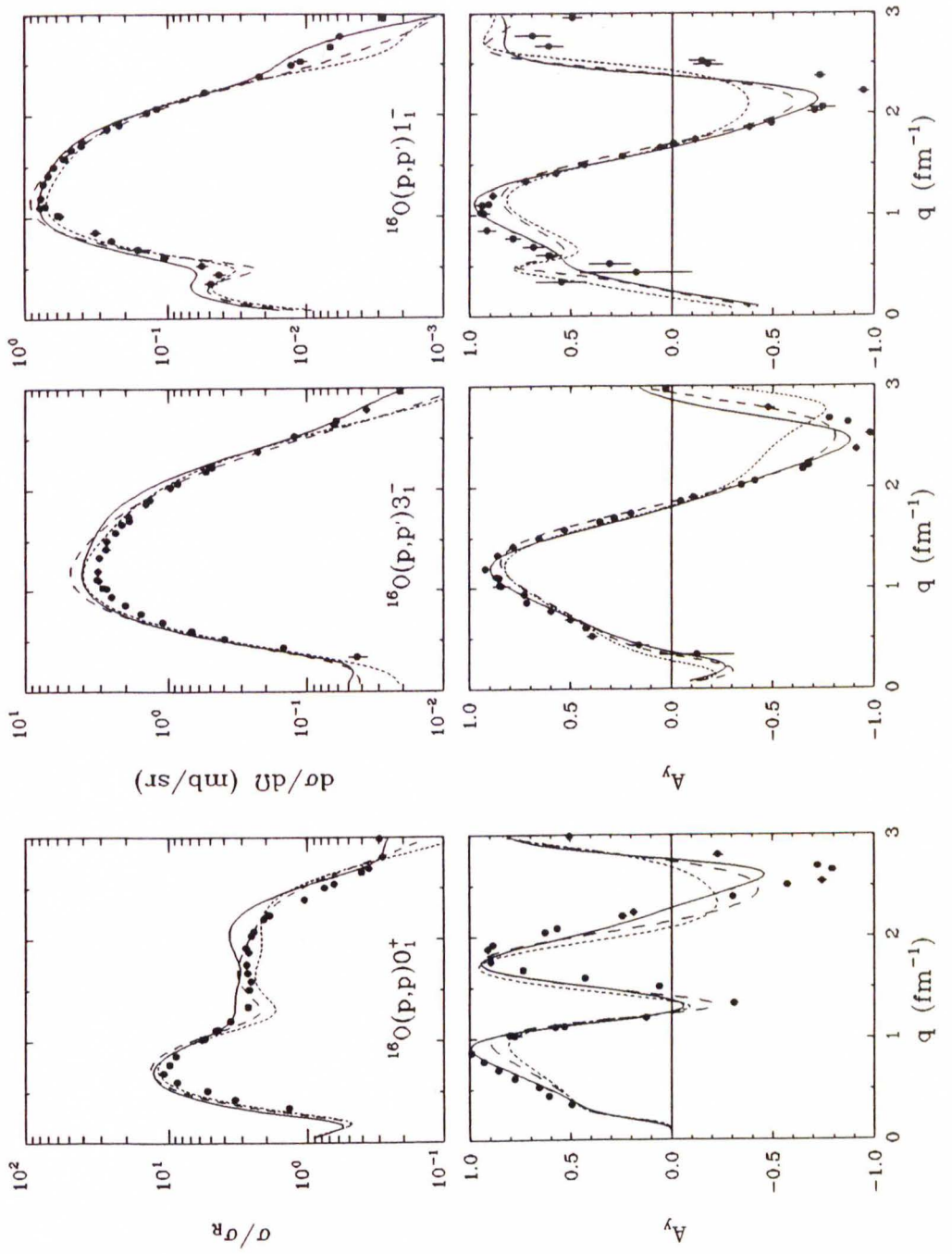

Figure 2.20: LDA calculations of $\sigma(q)$ and A_y for selected states of ^{16}O at 200 MeV; the elastic cross section is presented as ratio to the point-charge Rutherford cross section (σ_R) to enhance detail. Line code: PH (solid), NL (short dashes), LR (dashes). The data are from this work.

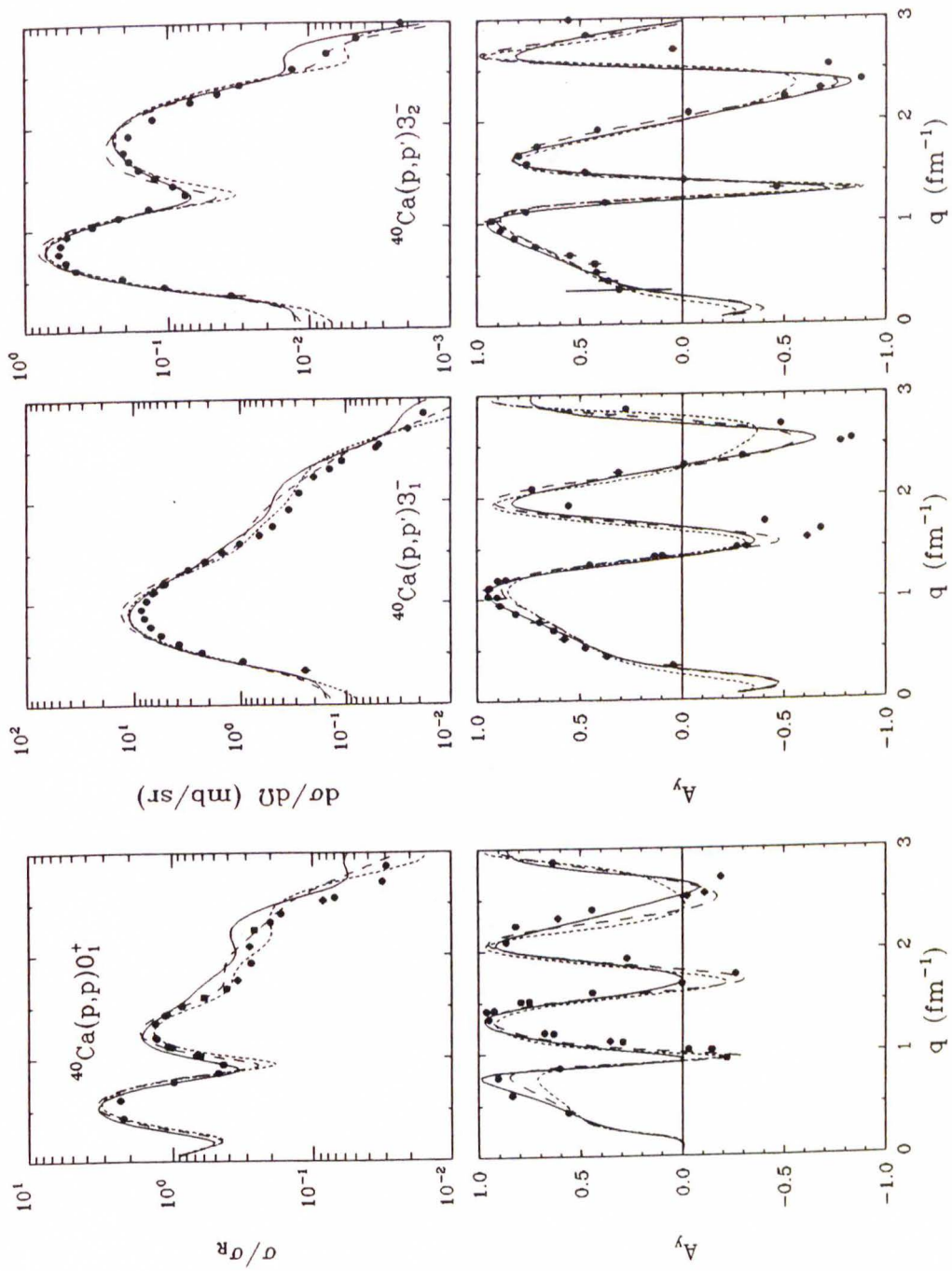

Figure 2.21: LDA calculations of $\sigma(q)$ and A_y for selected states of ^{40}Ca at 200 MeV; the elastic cross section is presented as ratio to the point-charge Rutherford cross section (σ_R) to enhance detail. Line code: PH (solid), NL (short dashes), LR (dashes). The data are from this work.

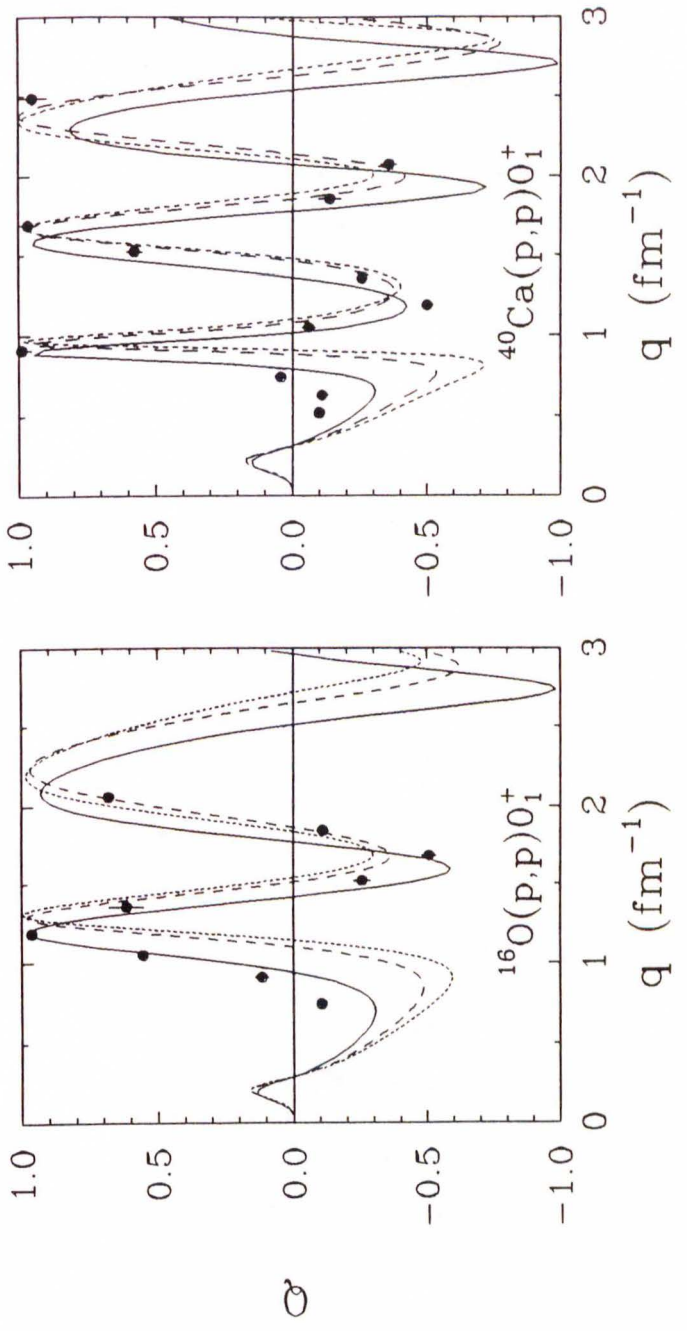

Figure 2.22: LDA calculations of Q for elastic scattering of ^{16}O and ^{40}Ca at 200 MeV. Line code: PH (solid), NL (short dashes), LR (dashes). The data are from [Ste 85] and P. Schwandt, private communication.

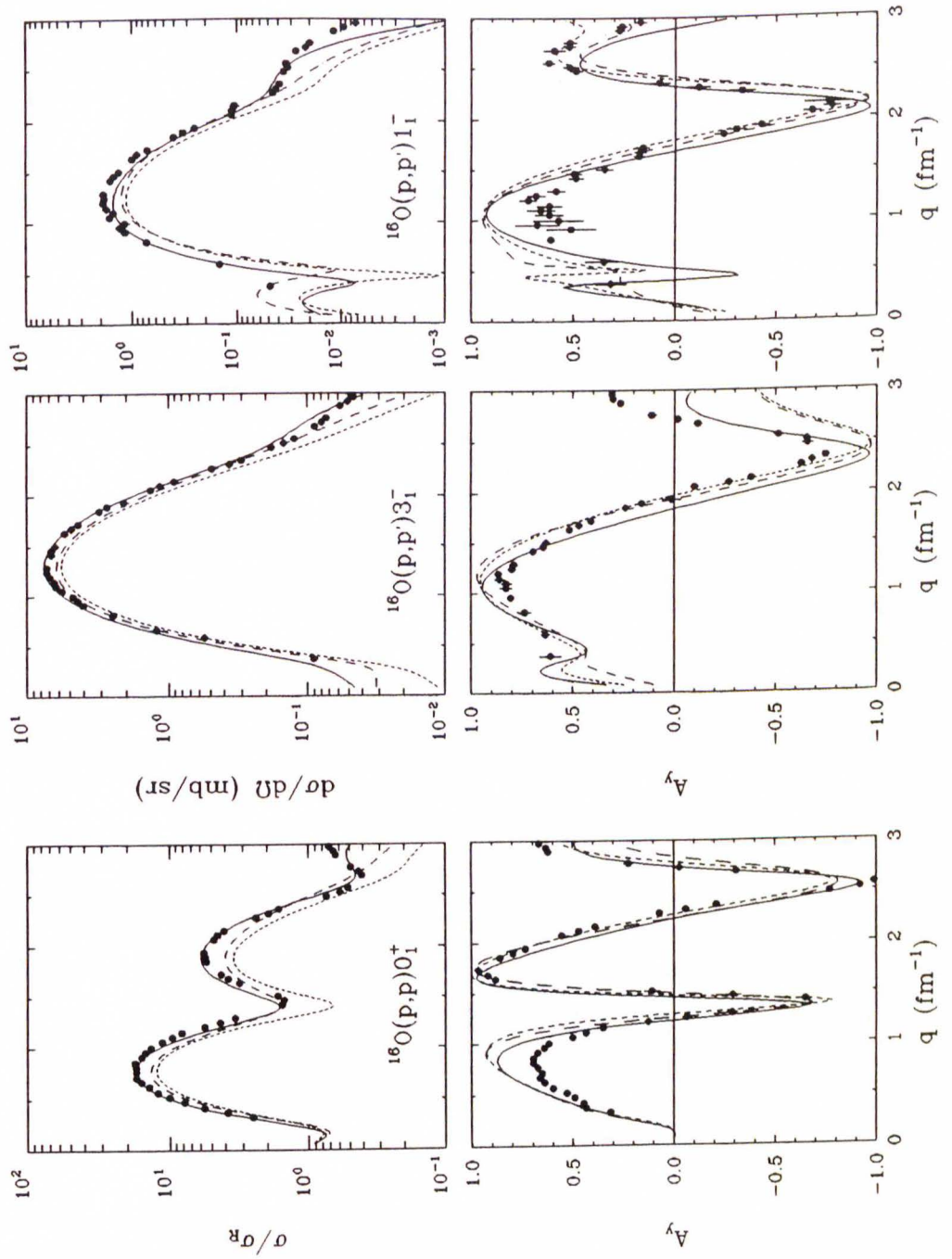

Figure 2.23: LDA calculations of $\sigma(q)$ and A_y for selected states of ^{16}O at 318 MeV; the elastic cross section is presented as ratio to the point-charge Rutherford cross section (σ_R) to enhance detail. Line code: PH (solid), NL (short dashes), LR (dashes). The data are from [Kel 90b].

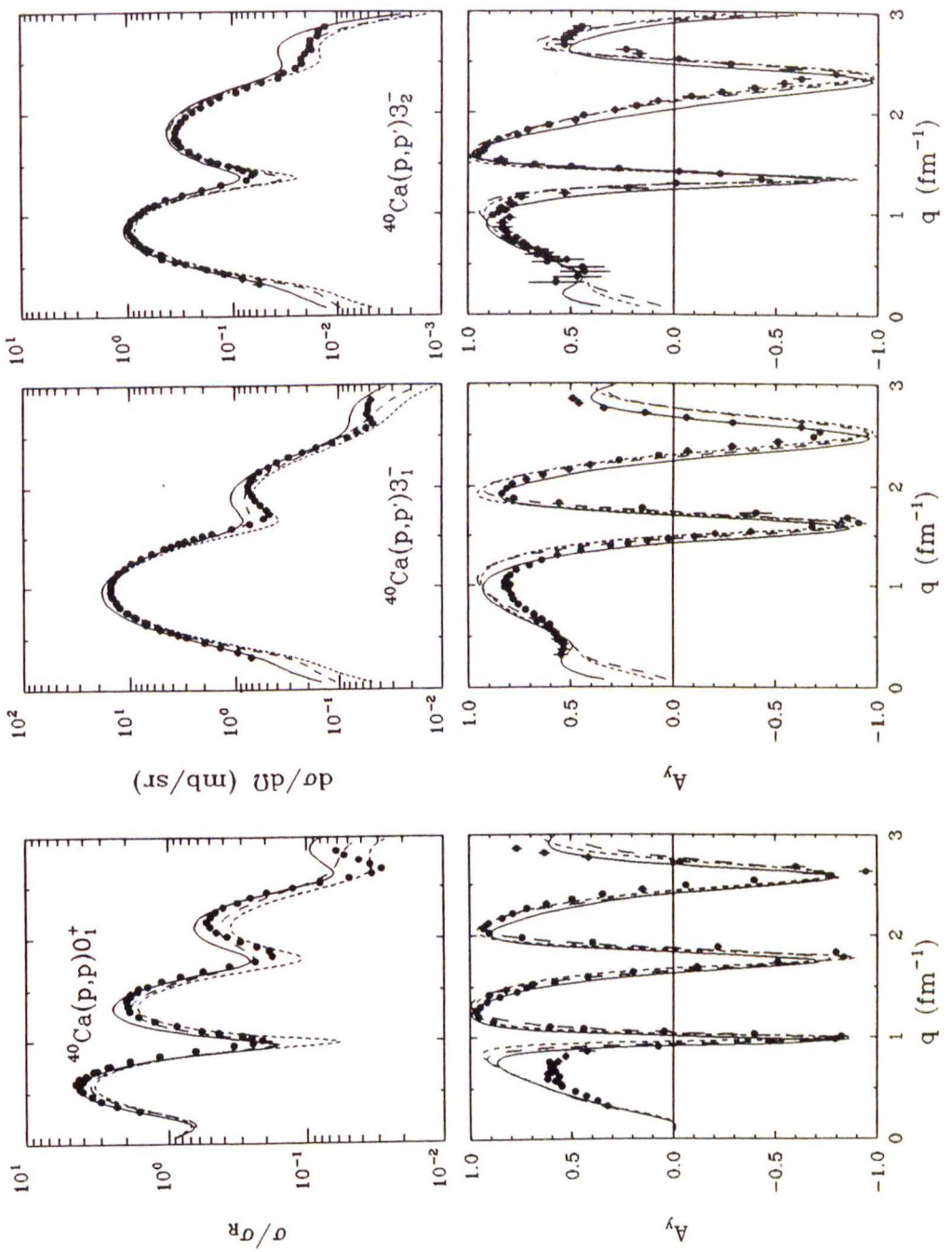

Figure 2.24: LDA calculations of $\sigma(q)$ and A_y for selected states of ^{40}Ca at 318 MeV; the elastic cross section is presented as ratio to the point-charge Rutherford cross section (σ_R) to enhance detail. Line code: PH (solid), NL (short dashes), LR (dashes). The data are from [Fel 90].

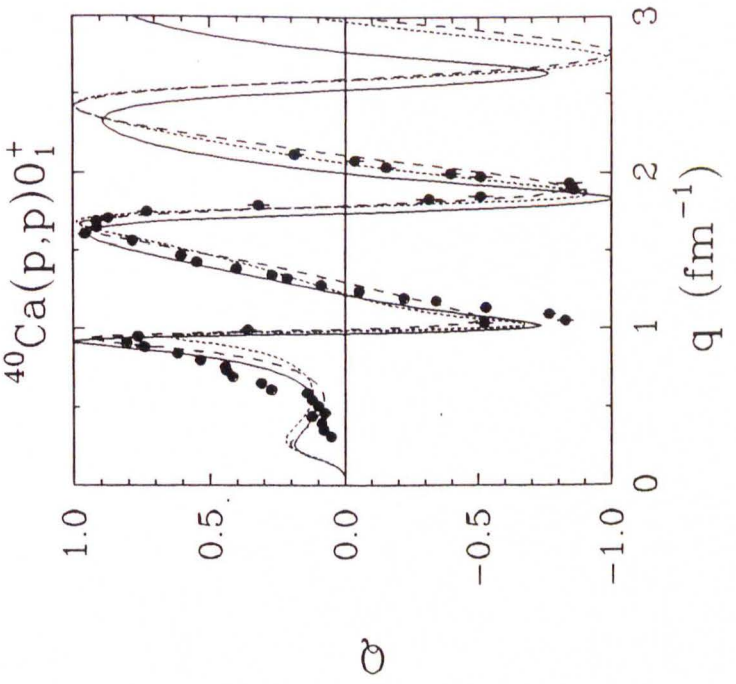

Figure 2.25: LDA calculations of Q for elastic scattering of ^{40}Ca at 318 MeV. Line code: PH (solid), NL (short dashes), LR (dashes). The data are from [Ble 88].

2.5 Relativistic Impulse Approximation

2.5.1 Introduction

The failure of nonrelativistic calculations to reproduce elastic scattering data at 500 MeV, especially the forward angle spin observables, and the problems of the NRIA even at higher energies lead to the question whether the underlying theory of nuclei is in fact relativistic. Clark *et al.* showed a phenomenological fit to the 500 MeV $\sigma(q)$ and A_y data which was obtained with the Dirac equation using large scalar ($S \sim -300$ MeV) and vector ($V \sim +250$ MeV) potentials [Cla 83]. They showed that without further variations of the fitted parameters the third observable for elastic scattering, the spin rotation function Q, was predicted correctly.

Spin observable measurements in intermediate energy proton scattering provide information about the spin-orbit interaction which, at a fundamental level, is due to the strong spin dependence of the NN interaction. Spin phenomena are difficult to understand within a nonrelativistic framework. They arise however very naturally within the relativistic Dirac theory. The fact that Dirac phenomenology appeared to be so successful in linking the spin observables provided a major incentive to develop a rigorous relativistic theory for proton-nucleus scattering. In 1983, therefore, a relativistic version of the impulse approximation was developed by McNeil, Shepard and Wallace [McN 83]. The success of these relativistic calculations, especially of the recent IA2 [Ott 88], in describing all the elastic scattering observables above 300 MeV is remarkable. The essential difference between the Schrödinger and

the Dirac approach has been identified as the implicit inclusion of virtual $N\overline{N}$ pair effects.

Some of the other topics in relativistic nuclear physics, which are beyond the scope of this work, include the bound state problem of nuclear matter. Here, the combination of attractive scalar and repulsive vector potentials provides a simple mechanism for nuclear saturation. A field of research which, in analogy to quantum electrodynamics (QED), is called "quantum hadrodynamics" or QHD, provides a complete and consistent theoretical treatment of nuclei and includes a complete description of all the baryonic and mesonic degrees of freedom in the nuclear system [Ser 86]. Finally, relativistic theories also allow to unify the theoretical descriptions of nucleon-nucleus scattering with that of NN scattering and, to a certain extent, with that of meson exchange currents.

In the following we will give a brief outline of the relativistic IA2 model and its interpretation, and define the Schrödinger equivalent potentials which will be compared in Chapter 7 to potentials formed from our empirical non-relativistic model. Most of the presented material is taken from the following sources, and references therein: [Che 86, Wal 87a, Wal 87b, Ott 88, Ott 90].

2.5.2 The IA2 Model

In the relativistic theory, wave propagation of a nucleon with mass m, momentum $\boldsymbol{p}$ and energy $E = \sqrt{\boldsymbol{p}^2 + m^2}$ is described by the Dirac equation

$$[E\gamma^0 - \boldsymbol{\gamma} \cdot \boldsymbol{p} - m - \hat{U}]\psi(\boldsymbol{r}) = 0, \tag{2.83}$$

where the optical potential $\hat{U}$ contains apart from the attractive scalar potential and the repulsive vector potential, which were used in the phenomenology, a small tensor potential and two even smaller scalar and vector spin-orbit potentials

$$\hat{U}(r) = S(r) + \gamma^0 V(r) - i\boldsymbol{\alpha} \cdot \hat{\boldsymbol{r}} T(r) - [S_{LS}(r) + \gamma^0 V_{LS}(r)]\boldsymbol{\sigma} \cdot \boldsymbol{L}. \quad (2.84)$$

This form of the optical potential is derived from a optimum factorized $t\rho$ approximation in momentum-space, very similar to the nonrelativistic case, Eq. (2.24), when t is replaced by the Feynman amplitude $\hat{M}$ and the nonrelativistic form factor by a relativistic one, $\hat{\rho}(\boldsymbol{q})$. More specifically, one can write

$$\hat{U}(\boldsymbol{p}, \boldsymbol{q}) = -\frac{1}{4}\mathrm{Tr}_2[\hat{M}(\boldsymbol{p}, \boldsymbol{q})\hat{\rho}(\boldsymbol{q})]. \quad (2.85)$$

In this expression, the trace is over the Dirac indices of particle 2, conventionally designated to be the target nucleon. The nuclear form factor, when based on the Dirac-Hartree model of nuclear shell structure, is comprised of three distinct form factors: scalar, vector and tensor. These form factors are determined in the IA2 from the wave functions of Horowitz and Serot which were obtained by solving the Dirac equation with large scalar and vector potentials from meson exchange models.

The correct construction of the Feynman amplitude $\hat{M}$ is critical for the quality of the optical potential and has been shown to explain the superior description of data by the present IA2 model, as compared to previous versions of the relativistic impulse approximation. In simple terms, the NN amplitude in the full Dirac space of two nucleons can be expanded in terms

of a complete set of Lorentz invariant amplitudes times kinematical covariants formed out of Dirac matrices and the four-momenta which characterize initial and final scattering states. The kinematical covariants must properly take into account parity invariance, time-reversal invariance, charge symmetry and the generalized Pauli principle. They must be linearly independent and the associated amplitudes must be free of kinematical singularities.

For on-shell kinematics, 44 independent amplitudes are needed in each isospin channel. Of these, only the five Fermi amplitudes which are part of the positive-energy sector of Dirac space are determined directly from phase shift analysis of NN scattering data. Their contribution to the full Feynman amplitude is

$$\hat{M}(\boldsymbol{p},\boldsymbol{q}) = -\eta \sum_{i=1}^{5} F_i K_i, \tag{2.86}$$

where η is a kinematical factor, and the Fermi covariants are $K_1 = 1$ (scalar), $K_2 = \gamma_1\gamma_2$ (vector), $K_3 = \sigma_1^{\mu\nu}\sigma_{2\mu\nu}$ (tensor), $K_4 = \gamma_1^5\gamma_2^5$ (pseudoscalar) and $K_5 = \gamma_1^5\gamma_2^5\gamma_1\gamma_2$ (axial vector); the F_i are the corresponding amplitudes. The remaining 39 amplitudes have vanishing matrix elements in the positive-energy states and must be predicted from an adequate model which allows an unambiguous extension to all sectors of the Dirac space. The method adopted by the IA2 as a dynamical basis for this task is a relativistic meson exchange model with appropriate vertex cutoffs. Inelasticity in the NN channel is included via couplings between NN, $N\Delta$ and $\Delta\Delta$ states. The cou-

pled channel integral equations are solved in a Bethe-Salpeter framework[22] with pseudovector πN coupling (important for maintaining reasonable behaviour at low energies and large momenta) and are easily extended to include negative-energy intermediate states.

In order to treat nucleon exchange contributions to the optical potential, each of the 44 amplitudes is fitted by a direct and exchange part, very similar to Eq. (2.31), and thus each amplitude is explicitly symmetric or antisymmetric with respect to particle exchange. The exchange terms are then localized, as was done for the nonrelativistic optical potential in Section 2.4.4, to yield a local optical potential suitable for coordinate-space analysis.

2.5.3 The Virtual Pair Interpretation

The basic new ingredient of the Dirac approach is the implicit coupling to virtual nucleon-antinucleon states through the Dirac optical potential $\hat{U}$. This contribution introduces the additional density dependence which appears to be necessary to describe data above 300 MeV.

In the relativistic theory the central scalar and vector potentials are of considerable strength and therefore can allow the projectile nucleon to scatter

[22] The *Bethe-Salpeter* equation is the four-dimensional covariant version of the Lippmann-Schwinger equation, the *NN* amplitude here being the sum of all distinct Feynman diagrams from field theory in which the two particles are interacting through the exchange of field bosons.

to a virtual negative-energy state[23] at time, say, t_2. In this state the nucleon propagates backward in time until an earlier time $t_1 < t_2$ when it is scattered back into a positive-energy state which then propagates forward in time. The backward going negative-energy state is equivalent to a positive antiparticle state propagating forward in time. Therefore, in the time interval between t_1 and t_2 in addition to the incident nucleon a virtual nucleon-antinucleon pair is present. Figure 2.26 shows the time-ordered process [Wal 85].

In the following, we will try to quantify the differences between the nonrelativistic and the relativistic approaches to the optical potential. For this purpose it is very instructive to find an *equivalent Schrödinger potential* which yields the same scattering as the Dirac potential. This can be accomplished by writing the Dirac equation as coupled equations for the upper- and lower-component wave functions, Φ and χ (for simplicity, we consider here only the scalar and vector potential fields)

$$\begin{aligned} (E - m - S - V)\Phi - \boldsymbol{\sigma} \cdot \boldsymbol{p}\,\chi &= 0 \\ \boldsymbol{\sigma} \cdot \boldsymbol{p}\,\Phi - (E + m + S - V)\chi &= 0. \end{aligned} \tag{2.87}$$

The second equation yields for the lower component

$$\chi = \frac{\boldsymbol{\sigma} \cdot \boldsymbol{p}}{E + m + S - V}\Phi. \tag{2.88}$$

Substituting back into the equation for the upper component, one gets

$$(E - m - S - V - \boldsymbol{\sigma} \cdot \boldsymbol{p}\frac{1}{E + m + S - V}\boldsymbol{\sigma} \cdot \boldsymbol{p})\Phi = 0. \tag{2.89}$$

[23] The amplitudes for these negative-energy states vanish when the scattering nucleon is far away from the nucleus; they are virtually present, however, in the interaction region where the optical potential is strong, i.e. in the immediate vicinity of the nucleus.

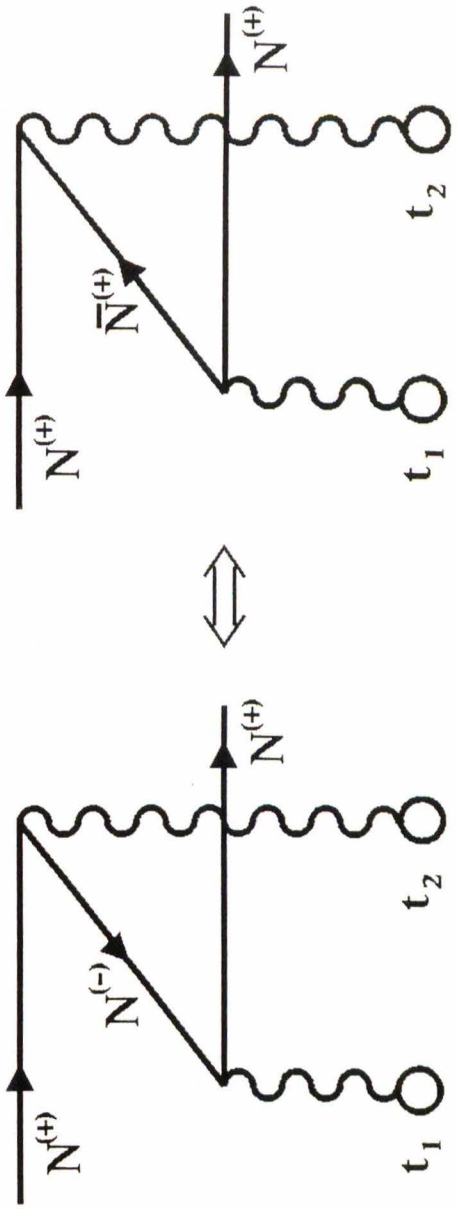

Figure 2.26: Z-graph for a Dirac particle scattering from an external potential at times t_1 and t_2, where $t_1 < t_2$.

Assuming the potentials S and V are almost constant with respect to r, allows us to neglect the spin-orbit and Darwin terms. Rescaling the wavefunction by the substitution $\psi = \frac{1}{E+m+S-V}\Phi$ leads with $k^2 = E^2 - m^2$ to an equation in the form of a Schrödinger equation for the central potential with relativistic kinematics:

$$(p^2 - k^2 + 2EU_{NR})\psi = 0, \tag{2.90}$$

where the equivalent Schrödinger potential is

$$U_{NR} = (\frac{m}{E}S + V) + \frac{1}{2E}(S^2 - V^2). \tag{2.91}$$

If one assumes a local $t\rho$ model for the optical potential, one can set $S = s\rho$ and $V = v\rho$ and write Eq. (2.91) as

$$U_{NR} = t_{NR}\rho = (\frac{m}{E}s + v)\rho + \frac{1}{2E}(s^2 - v^2)\rho^2. \tag{2.92}$$

Since only the first term of t_{NR} remains in the limit $\rho \to 0$ limit, the first term of the potential U_{NR} comprises the nonrelativistic impulse approximation. The second term represents the relativistic, density dependent correction due to virtual nucleon-antinucleon pairs. Since in actual nuclei the absolute value of s is larger than that of v, the relativistic correction manifests itself as a short-range repulsion which becomes stronger in the nuclear high-density interior region.

Other forms for the two terms in Eq. (2.92) can be found by expanding the Dirac wave function in terms of positive and negative-energy states $\psi^{\pm} = \Lambda^{\pm}\psi$ of the potential-free Dirac equation[24]. Elimination of negative-energy

[24] The projection operators are defined as $\Lambda^{\pm} = \frac{\pm\not{p}+m}{2m}$, where $\not{p} = \gamma^0 E_P - \boldsymbol{\gamma}\cdot\boldsymbol{p}$.

components from the Dirac equation then yields an equation for the positive-energy component. At the level of approximations that has been used before, one gets

$$[p^2 - k^2 + 2E(\hat{U}^{++} + \hat{U}_{pair})]\psi^+ = 0, \tag{2.93}$$

where $\hat{U}^{\pm\pm} = \Lambda^{\pm}\hat{U}\Lambda^{\pm}$ and where the *pair potential* is

$$\hat{U}_{pair} = \hat{U}^{+-}\left[E + \sqrt{p^2 + m^2} - \hat{U}^{--}\right]^{-1}\hat{U}^{-+}. \tag{2.94}$$

The potentials $\hat{U}^{+-}$ and $\hat{U}^{-+}$ are responsible for the scattering into and out of the negative energy states. In Figure 2.26 these potentials are represented by the little bubbles at end of the wavy lines. Thus, the equivalent Schrödinger central optical potential is essentially the combination of a part $\hat{U}^{++}$, which is the sum of strong scalar (~ -400 MeV) and vector ($\sim +300$ MeV) potentials, and a pair term which includes coupling to the other energy sectors of the Dirac space. Nonrelativistivcally, the $\frac{1}{2E}(S^2 - V^2)$ term is linked to the spin-orbit force.

If one includes additionally medium effects like Pauli blocking etc., a density and energy dependent interaction for elastic scattering at intermediate energies is well described by [Che 86]

$$t(\rho) = t_{free} + \delta t_{MC}(\rho) + \delta t_{RC}(\rho), \tag{2.95}$$

or, with the Brueckner g-matrix by

$$t(\rho) \approx g(\rho) + \delta t_{RC}(\rho), \tag{2.96}$$

where

$$\delta t_{RC}(\rho) = \frac{1}{2E}(s^2 - v^2)\rho. \tag{2.97}$$

The $1/2E$ factor in the relativistic correction term suggests that in the high energy region the Dirac and Schrödinger approaches might converge.

2.5.4 IA2 Calculation Results

In Figures 2.27–2.30 we compare the full IA2 optical potential (solid) for elastic scattering of 200, and 318 MeV protons from ^{16}O and ^{40}Ca with a nonrelativistic LDA potential based on the PH interaction (long dashes). In the "no-pair" analysis of the IA2, all couplings to negative-energy states are eliminated and all the relativistic nuclear densities are taken to be equal to the measured nonrelativistic matter density. The Schrödinger potential equivalent to the Dirac potential from the "no-pair" analysis is called the NP potential (dashes). Finally, for comparison we also display an NRIA potential based on the PH t-matrix. Comparisons of the IA2 with our empirical model and a recent, very successful Dirac phenomenology by Hama *et al.* [Ham 90] will be made in Chapter 7.

At 200 MeV the real central IA2 potential is, although on the whole still attractive, much more repulsive in the nuclear center than any of the other potentials, including the LDA potential which is about intermediate between the IA2 and the NP and NRIA potentials. Like the LDA potential, the IA2 potential has a "wine-bottle" shape. The NP potential is slightly more repulsive in the center than the NRIA potential but, like the NRIA potential, does not have the surface depression of the LDA or IA2 potential. For the imaginary central component, the IA2 potential is virtually identical to the NP and NRIA potentials, being only slightly less absorptive for ^{40}Ca. This

fact is due to the absence of Pauli blocking. The real spin-orbit potentials are essentially all the same for ^{16}O; for ^{40}Ca the IA2 potential resembles somewhat the LDA potential. The imaginary spin-orbit potentials differ significantly, but are again too small to affect calculations significantly.

At 318 MeV both the IA2 and the LDA potentials become repulsive in the nuclear interior, while the NP and NRIA potentials stay attractive. The IA2 potential stays repulsive even at the center where the LDA potential is again attractive. The strong repulsion in the real part is due to the virtual $N\overline{N}$ pairs. In the imaginary central part of the optical potential for ^{16}O we see an interesting effect whose discussion we will pick up again in Chapter 7 in context with our empirical effective interaction: the IA2 imaginary central potential at this energy becomes more absorptive relative to the NRIA potential. This effect, which becomes very pronounced for 500 MeV, is in this work often called "anti-Pauli" blocking.

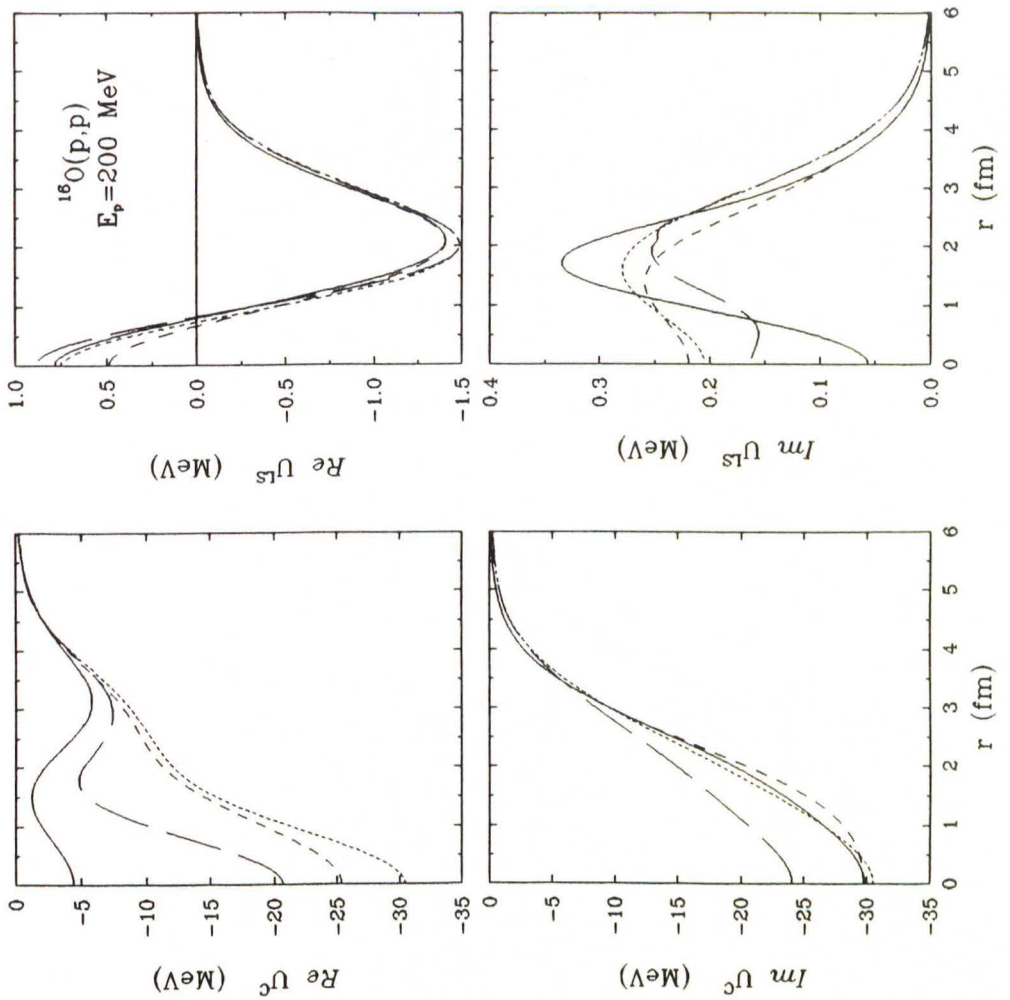

Figure 2.27: Comparison of the full IA2 (solid), LDA (long dashes), NP (dashes), and NRIA (short dashes) optical potentials for 200 MeV elastic scattering by ^{16}O. Both LDA and NRIA are based on the PH interaction.

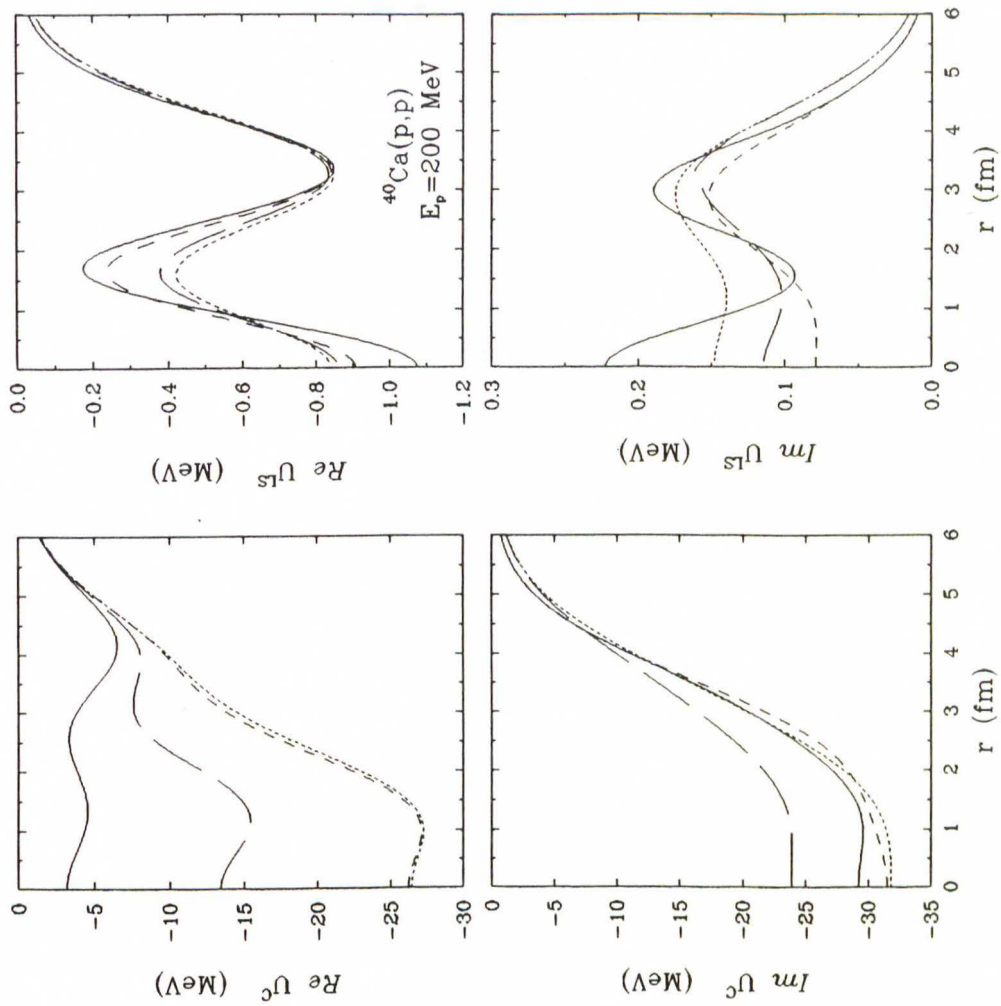

Figure 2.28: Comparison of the full IA2 (solid), LDA (long dashes), NP (dashes), and NRIA (short dashes) optical potentials for 200 MeV elastic scattering by ^{40}Ca. Both LDA and NRIA are based on the PH interaction.

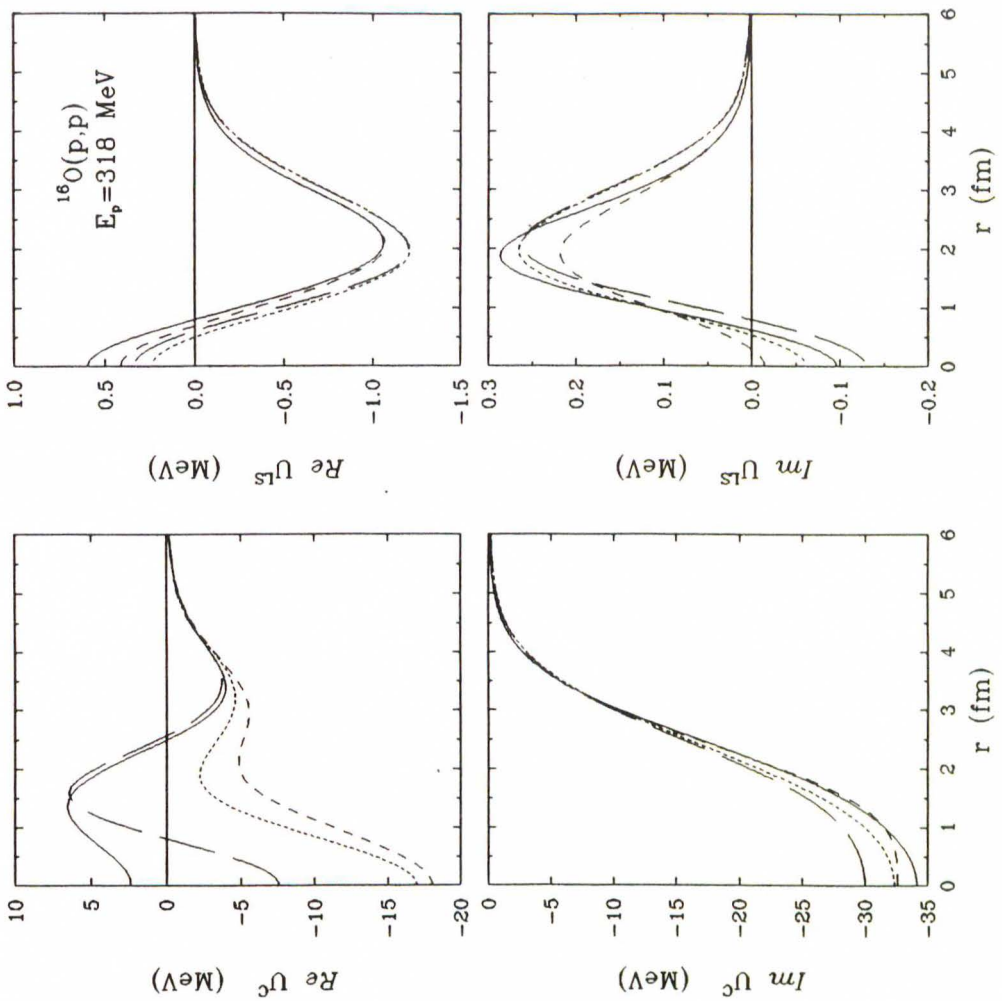

Figure 2.29: Comparison of the full IA2 (solid), LDA (long dashes), NP (dashes), and NRIA (short dashes) optical potentials for 318 MeV elastic scattering by ^{16}O. Both LDA and NRIA are based on the PH interaction.

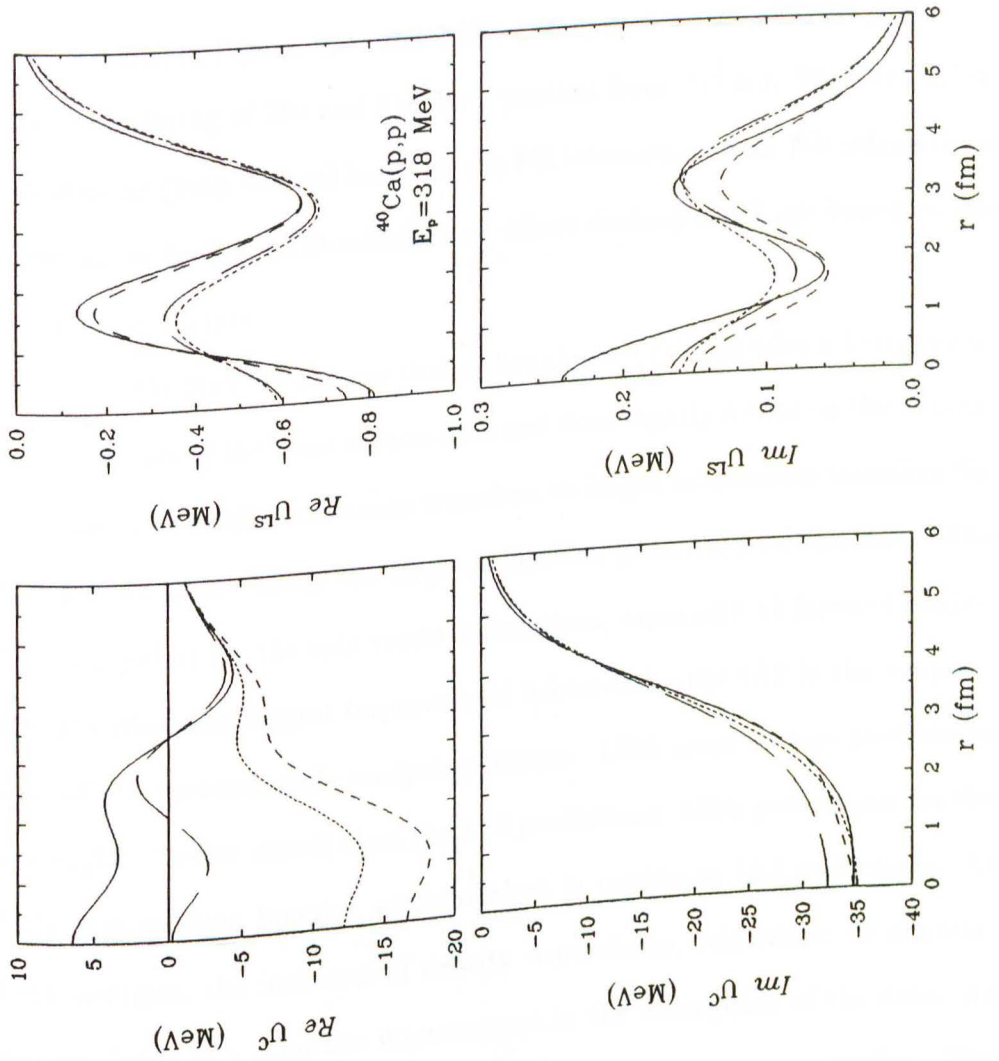

Figure 2.30: Comparison of the full IA2 (solid), LDA (long dashes), NP (dashes), and NRIA (short dashes) optical potentials for 318 MeV elastic scattering by ^{40}Ca. Both LDA and NRIA are based on the PH interaction.

Finally, in Figures 2.31 and 2.32 we compare IA2 calculations (solid) for elastic scattering of 200 and 318 MeV protons from ^{16}O and ^{40}Ca with LDA calculations (long dashes) based on the PH interaction, with NP calculations (dashes), and with NRIA calculations (short dashes) which are based on the free PH interaction.

For 200 MeV we observe that although the LDA provides a better overall description of the cross section data and does slightly better on the analyzing powers at small momentum transfers, at larger momentum transfers the IA2 follows more closely the large oscillations prescribed by the data. The IA2 is superior for the spin rotation functions, especially at forward angles. For 318 MeV the biggest improvement achieved by the IA2 is the suppression of the forward angle analyzing powers. LDA cross section predictions are slightly better overall than the IA2 predictions. LDA predictions for the ^{40}Ca spin rotation function are equivalent in quality to IA2 predictions. At both energies, the inclusion of density dependence, relativistic or nonrelativistic, leads to a dramatic improvement in the description of the data. As the figures show, the NP and the NRIA predictions are very similar. The slight differences are due to the fact that the NP potentials were constructed with Dirac-Hartree wave functions and phase shifts, while the NRIA was constructed from measured (e, e') charge densities and the PH t-matrix.

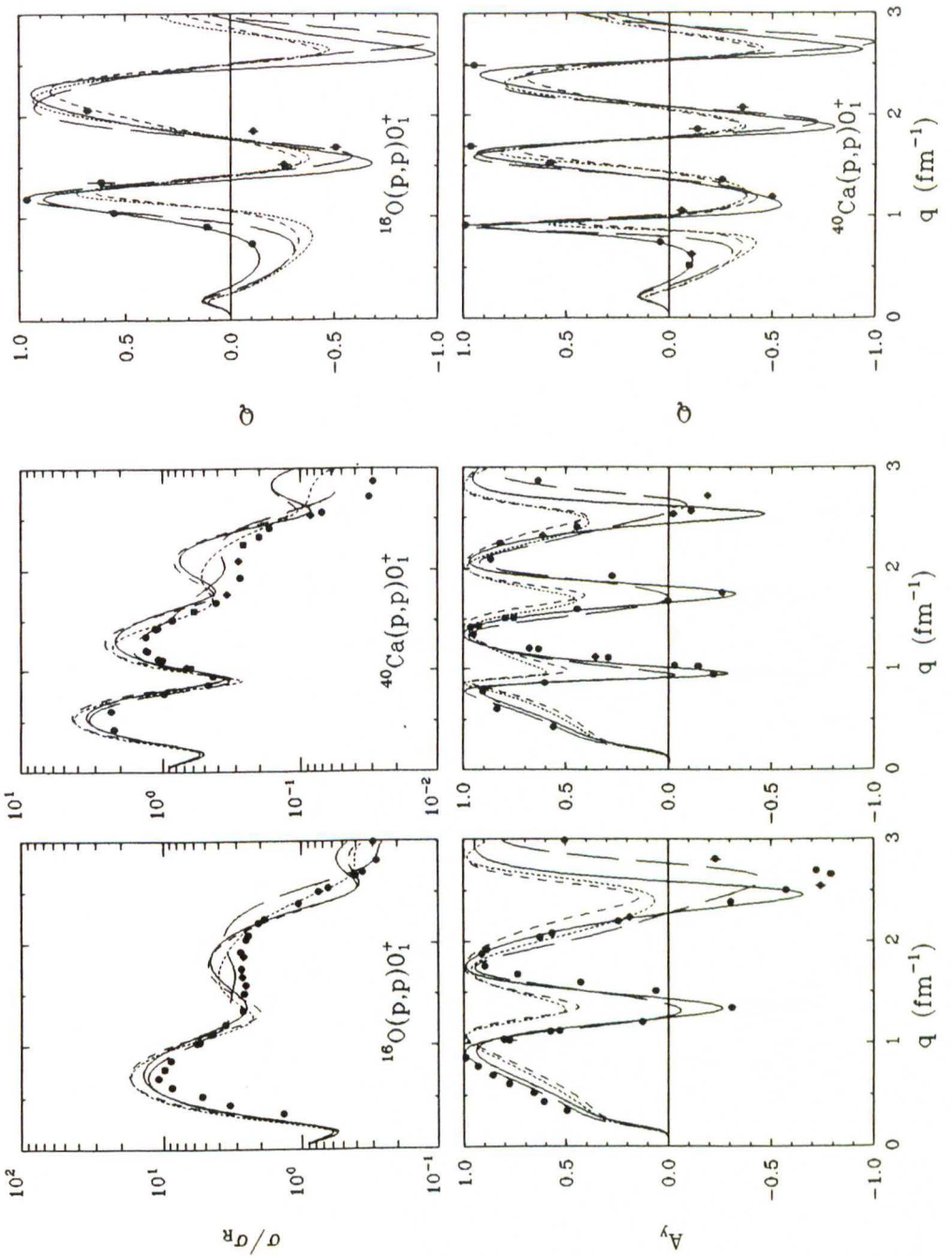

Figure 2.31: Comparison of IA2 (solid), LDA (long dashes), NP (dashes), and NRIA (short dashes) calculations for elastic scattering at 200 MeV. Elastic cross sections are presented as ratios to the point-charge Rutherford cross section (σ_R) to enhance detail. Both LDA and NRIA are based on the PH interaction (data for σ and A_y from this work, data for Q from [Ste 85] and P. Schwandt, private communication).

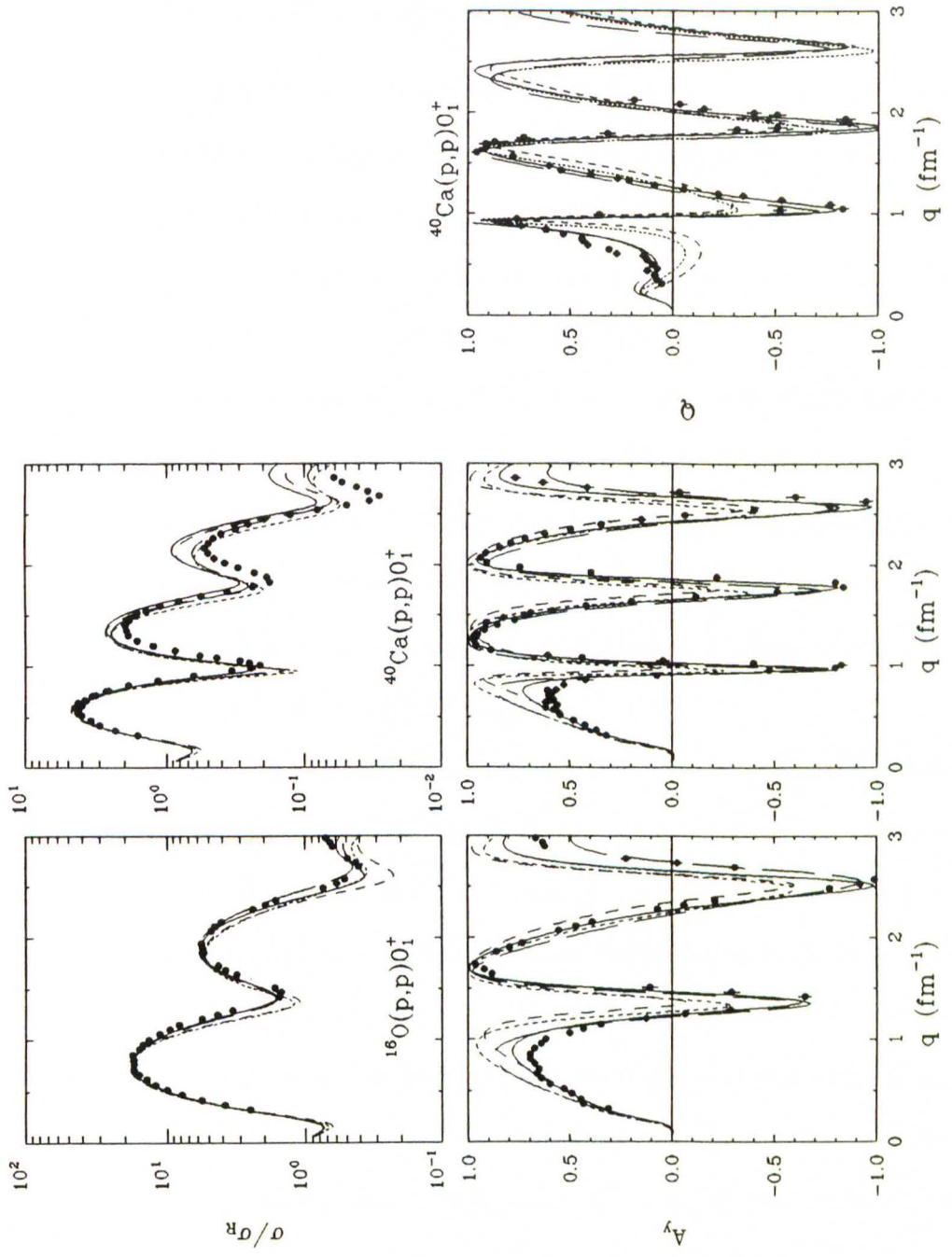

Figure 2.32: Comparison of IA2 (solid), LDA (long dashes), NP (dashes), and NRIA (short dashes) calculations for elastic scattering at 318 MeV. Elastic cross sections are presented as ratios to the point-charge Rutherford cross section (σ_R) to enhance detail. Both LDA and NRIA are based on the PH interaction (data for σ and A_y from [Fel 90, Kel 90b], data for Q from [Ble 88]).

2.6 Off-Shell Effects and Full-Folding

The optical potentials introduced in the last two sections, the ones based on nonrelativistic density-dependent interactions as well as the ones based on a relativisic impulse approximation model (RIA), give very good descriptions of nucleon-nucleus scattering data at intermediate energies. In contrast, the NRIA seems to have failed in this task.

It was noted, however, by Redish and Stricker-Bauer [Red 87] that the g-matrix and RIA approaches are local models which disregard the effect of the full off-shell interaction. It was found that an optical model which retains this nonlocality can reproduce some of the characteristics of elastic spin observables which have been generally attributed to medium effects such as Pauli blocking and/or relativistic effects.

In an earlier study, Pickelsimer *et al.* [Pic 84] tried to estimate the role of nonlocality, off-shell, and relativistic effects using the free NN t-matrix of Love and Franey [Lov 81, Fra 85]. In particular, they compared various factorizations with the optimum factorized potential. It was found that nonlocality only plays a role at relatively large angles above about 60° and/or energies lower than about 150 MeV. At 500 MeV nonlocal and off-shell effects were found to be unsufficient, by themselves, to explain the data; the relativistic description was generally superior. However, as was explained in Section 2.3.4, the method used to extrapolate the on-shell t-matrix off the energy shell probably has serious ambiguities and problems and, hence, the resulting off-shell behaviour is probably not realistic.

Cheon [Che 87], on the other hand, suggested in his paper that a non-

relativistic theory with a realistic off-shell t-matrix and proper treatment of the nonlocality can indeed successfully describe intermediate energy nucleon-nucleus scattering. Subsequently, other authors studied off-shell and full-folding effects using interactions based on the Bonn potential [Els 89, Els 90] and on the Paris potential [Are 89, Are 90a].

Elster and Tandy [Els 89] compare optimum factorized off-shell and on-shell $t\rho$ calculations and find substantial effects for the spin observables, in particular an improvement in A_y, of ^{40}Ca at 200 MeV. At 500 MeV they also find a strong off-shell effect on the spin observables; the cross section, however, is only being moderately affected in its diffraction minima. Improvement with the off-shell potential is only found for the spin rotation function Q, but an impairment is seen for the analyzing power A_y.

It was suggested by Pickelsimer *et al.* [Pic 84] that uncertainties are being introduced in the optical potential by uncertainties in the NN t-matrix, as well as by the nuclear density and the applied factorization method; the uncertainties being largest for very light nuclei and back angles. It was argued, therefore, that these cases require a complete folding calculation involving a realistic off-shell t-matrix.

Taking up this point, full-folding studies were done by Elster *et al.* [Els 90] and by Arellano *et al.* [Are 89, Are 90]. The former paper compares local on-shell, optimum factorized off-shell, and full-folding calculations for ^{16}O. It is found that the optimum factorized off-shell potential is a very good approximation to the full-folding potential for energies as low as 100 MeV. The main source of nonlocality in the optical potential was identified to be

the off-shell structure of the t-matrix. In this calculation, the energy variation of the interaction was ignored and the energy z in Eq. (2.18) was fixed at the two-body c.m. energy corresponding to free NN scattering at the beam energy.

In the calculations by Arellano *et al.* the full energy-dependence of the t-matrix is included. They find, in contrast to Elster *et al.*, significant differences between calculations using full-folding potentials and even the off-shell optimum factorized potential. The full-folding provides a superior description of the data at both 200 MeV and 300 MeV. These latter calculations might be consistent with the former ones by Elster *et al.* if the energy variation of the interaction indeed plays an important role in the full-folding.

The studies which we have just described have caused new interest in the nonrelativistic impulse approximation and they have certainly motivated a critical review of density-dependent interactions and/or relativistic models. However, it has been observed recently by Ottenstein [Ott 90] that a correct treatment of the Coulomb interaction, as well as a correct treatment of the boost from the NN c.m. frame of the t-matrix to the frame in which the optical potential is evaluated, is very crucial for a meaningful interpretation of the results and a judgement of the size and importance of off-shell effects. All of the nonrelativistic off-shell and full-folding studies mentioned above use a nonrelativistic Galilean boost (the Møller factor) instead of the correct relativistic boost which includes Wigner rotation effects [Ott 90]. Furthermore, the above calculations used various nonequivalent methods for treating the Coulomb interaction. Ottenstein *et al.* conclude that the observed off-shell

effects in [Els 89] are probably too large.

2.7 Inelastic Nucleon-Nucleus Scattering

2.7.1 Distorted Wave Approximation

Since it is the main purpose of the present work to extract an effective interaction from inelastic scattering observables, in the following we will give a brief and more or less schematic summary of inelastic scattering. For our calculations we will assume that the transition potential is sufficiently weak so that its effect can be calculated in perturbation theory and we will further assume that we are dealing with direct[25], one-step excitations which can be described accurately in the *distorted wave approximation* (DWA) when using an effective interaction.

In the DWA the total scattering potential U is decomposed into a dominant term which is responsible for elastic scattering (the optical potential U_{opt}) and a perturbation which induces inelastic transitions (the transition potential ΔU)

$$U = U_{opt} + \Delta U. \tag{2.98}$$

The optical for elastic scattering was discussed earlier. Because of the refractive and absorptive features of the optical potential, the solutions χ to the Schrödinger equation

$$(E - K)\chi^{(+)} = U_{opt}\chi^{(+)} \tag{2.99}$$

[25] A very thorough treatment of direct reactions can be found in the book of Satchler [Sat 83].

are not plane waves, but so-called *distorted waves*. Asymptotically, they have the form of an incident plane wave plus outgoing scattered spherical waves, hence the (+) superscript[26].

The transition amplitude for inelastic scattering in the DWA is the matrix element of the transition potential, evaluated between the distorted waves of the initial and final channels

$$T_{fi}(\boldsymbol{k}', \boldsymbol{k}) = \langle \chi_f^{(-)}(\boldsymbol{k}')\phi_f | \Delta U | \chi_i^{(+)}(\boldsymbol{k})\phi_i \rangle. \tag{2.100}$$

Analogously to elastic scattering, the transition potential can be described by an effective interaction, a t- or g-matrix, folded with the transition density $\Delta\rho$ which carries all the nuclear structure information, i.e. $\Delta U(q) = t(q)\Delta\rho(q)$.

In the plane wave limit, the differential cross section and analyzing power for natural-parity transitions are simply given by Eqs. (2.46) and (2.47) from Section 2.3.4. For the general case of distorted waves, one constructs instead the quadratic forms

$$X_{\alpha\beta}(q) = \mathrm{Tr}[T(q)\sigma_\alpha T^\dagger(q)\sigma_\beta] \tag{2.101}$$

which are traces over the spin projections of both the projectile and the target [Kel 89b]. One can identify

$$I_0(q)D_{\alpha\beta} = \frac{1}{2}X_{\alpha\beta}. \tag{2.102}$$

Here, $D_{00} = 1$ and the analyzing power $A_y = D_{y0}$ are simply elements of the depolarization matrix $D_{\alpha\beta}$. The cross section can now be compactly written

[26] The distorted wave $\chi^{(-)}(\boldsymbol{k}, \boldsymbol{r}) = \chi^{(+)^*}(-\boldsymbol{k}, \boldsymbol{r})$ has incoming spherical waves [Sat 83].

as

$$\sigma(q) = \frac{\mu\mu'}{(2\pi)^2}\frac{k'}{k}\frac{I_0(q)}{2J+1}. \tag{2.103}$$

* * *

There are certain corrections which have been proposed to be important specifically for inelastic scattering: first, the effect of nonlocality in the optical potential on the interior wave function and, second, the effect of certain diagrams in the hole-line expansion of the effective interaction t which are not present for the elastic interaction.

2.7.2 The Perey Effect

Elastic scattering is more or less insensitive to the interior of the nucleus and the fine details of the optical potential, only measuring the aymptotic properties of the scattering wave function. On the other hand, inelastic scattering, transfer, and knockout reactions require in the DWA treatment the elastic nucleon-nucleus wave function in the nuclear interior. Thus, although potentials with different nonlocal structure may produce equivalent elastic scattering observables results, they still may yield different interior wave functions.

Nonlocal optical potentials were first studied in the *effective mass approximation* [Fra 57, Wya 60, Lem 60]. The Schrödinger equation with a nonlocal kernel

$$(E-K)\chi(\boldsymbol{r}) = \int d\boldsymbol{r}'\, v(\boldsymbol{r},\boldsymbol{r}')\chi(\boldsymbol{r}'), \tag{2.104}$$

was reduced to the usual form, Eq. (2.1), but with $K = -\nabla^2/2\mu$ replaced

by $K = -\frac{1}{4}\{\nabla^2 \frac{1}{2\mu^*} + \nabla \frac{2}{2\mu^*} \nabla + \frac{1}{2\mu^*} \nabla^2\}$. Here μ^* denotes a spatially variable *effective mass* which is defined as

$$\mu^*(\boldsymbol{r}) = \frac{\mu}{1 - \frac{\beta^2 \mu}{2} v(\boldsymbol{r})}. \tag{2.105}$$

In this expression, the parameter β is of the order of 1 fm and characterizes the range of nonlocality in the potential. It is defined such that $\beta = 0$ corresponds to the local case. In the literature, the ratio $P(\boldsymbol{r}) = \mu^*(\boldsymbol{r})/\mu$ is often called the *Perey factor*.

The effective mass approximation is based on the assumption that $k\beta \ll 1$, where k is the wave number of the nucleon. Since β has been found empirically to be of the order 1 fm, however, $k\beta$ is expected to be small only for very low energies. Perey and Buck [Per 62, Per 63], therefore, chose a different approach. They found that over a wide range of energy the results predicted by a nonlocal model could always be reproduced by using an equivalent local optical potential. For a given nonlocal potential depth U_N, they find that at a given energy E the corresponding local potential depth U_L should be chosen such that

$$U_N = U_L \exp\left[\frac{\beta^2 \mu}{2}(E - U_L)\right]. \tag{2.106}$$

This implies that for a fixed nonlocal potential depth the equivalent local one decreases with energy [Per 62]. For very small energies $E \ll U_L$, an expansion of the exponential function yields to first order an expression which includes the Perey factor from the effective mass approximation

$$U_N \approx [1 - \frac{\beta^2 \mu}{2} U_L] U_L \Leftrightarrow U_L = P \cdot U_N. \tag{2.107}$$

More general treatments of the nonlocality which were applied to energies up to 500 MeV can be found in [Che 87, Els 90].

The equivalent local potential by dint of its construction gives the same asymptotic wave function as the nonlocal one. However, Perey [Per 63] finds that the wave functions differ in the region of the potential. More specifically, he finds a reduction of the wave function in the nuclear interior by a factor of $\sqrt{P(\boldsymbol{r})}$ due to the nonlocality of the original potential. While for surface excitations the effect of this reduction should be small, only moving the interaction to a slightly larger radius, he generally expects, however, the nonlocality to reduce the contributions of interior wave functions to transition matrix elements for DWBA calculations.

Several authors find the Perey factor in the nuclear center, $P(0)$, to be approximately 0.8 for medium energies (e.g. [Els 90]). With this the radial dependence of the Perey factor can be parametrized by

$$P(r) \approx A + B\rho(r)/\rho_0, \tag{2.108}$$

where $A = 1$, $B \approx -0.2$, and the saturation density is $\rho_0 = 0.16$ fm^{-3}.

2.7.3 The Rearrangement Effect

In the past it had been observed that the BRG interaction with its stronger density dependence described inelastic scattering better than the PH interaction. The PH interaction, on the other hand, was superior to the BRG interaction in the description of elastic scattering data. A consistent description of both elastic and inelastic scattering with the PH interaction

(and also the disqualification of the BRG interaction) was reached in the mid 1980s. It was recognized that an important rearrangement contribution in the diagrammatic expansion of the inelastic interaction, not present in the elastic interaction, had been overlooked [Che 85].

The effect is most easily explained in the collective model and with the $t\rho$ folding approach to the optical potential, i.e. $U = t(\rho)\rho$; here, $t(\rho)$ is the Brueckner g-matrix and ρ is the ground state density. In the simple case that an inelastic transition can be considered as the excitation of a spin- and isospin independent collective mode of the target nucleus, the transition density $\Delta\rho$ can be described as a variation of the ground state density ρ with respect to the collective variable implicitly included in ρ. With this interpretation one can express the transition potential ΔU as the functional derivative

$$\Delta U = \frac{\delta U}{\delta \rho}\Delta\rho. \tag{2.109}$$

With the folding prescription, the consistent microscopic transition potential becomes

$$\Delta U = \left\{ t(\rho) + \rho\frac{\delta t(\rho)}{\delta\rho} \right\} \Delta\rho \equiv \left\{ \left[1 + \rho\frac{\partial}{\partial\rho} \right] t(\rho) \right\} \Delta\rho, \tag{2.110}$$

a result which also holds for transition potentials that include relativistic corrections [Che 86]. The density derivative of the g-matrix introduces terms of second order in the number of g-matrices. The diagrams associated with these derivatives are, therefore, intimately related to the Brueckner rearrangement term in the two-hole line contribution to the self-energy [Hüf 72].

The $(1 + \rho\partial/\partial\rho)$ factor causes an elastic medium modification which

is proportional to k_F^n to be enhanced for inelastic scattering by a factor of $(1+n/3)$. As we will see later, this leads to medium modifications for inelastic scattering which are about twice as strong as those for elastic scattering.

2.8 An Empirical Effective Interaction

2.8.1 Description of Theoretical Interactions

The effective interactions which were discussed in Section 2.4.1 include medium effects due to phase space blocking and binding energy corrections of intermediate scattering states, as well as due to the various averaging procedures which were used to construct convenient local forms. However, although the general features of the medium modifications are common to all the interactions, we saw in Section 2.4.5 that their quantitative predictions for nucleon-nucleus scattering may differ, the differences arising from both the different input NN potentials and the different approximations schemes used in the construction of the local form of the interaction. In order to compare the various effective interactions more easily, it is convenient to search for an empirical parametrization which is guided by nuclear matter theory. Another useful feature of such a parametrization is that parameters from fits to data can easily be compared to those obtained from theoretical models.

To gain some insight into the nature of the medium modifications to the effective interaction, we want to consider the dominant isoscalar spin-inde-

pendent central component[27], t_{00}^{C}. Qualitatively, the medium modifications can be interpreted with help of the correlated pair wave function ψ in nuclear matter. Relative to the uncorrelated wave pair function ϕ, the correlated pair wave function ψ in a low-density environment is reduced in amplitude, possesses a wound[28] in the repulsive core region, and is shifted inwards by the overall attraction of the interaction. In a high-density environment, on the other hand, Pauli blocking inhibits scattering and absorption, enhances the amplitude relative to the unblocked wave function and also enhances the wound as it keeps the nucleons apart. Finally, the overall attractiveness of the interaction is reduced, shifting the wave function to a phase intermediate between the noninteracting and the unblocked interacting case [Kel 82].

These effects can be clarified by examining separately the imaginary absorptive, and real part of t_{00}^{C} (see for instance Figure 2.34). It appears that the density dependence of the absorptive part is best described by a multiplicative damping factor which suppresses the total cross section. A simple phase space estimate of this blocking factor, due to Clementel and Villi [Cle 55], evaluates the effective laboratory cross section $\langle\sigma\rangle$ for scattering of a nucleon with kinetic energy E_0 from a Fermi gas with Fermi momentum k_F

[27] Density dependence is less important for the spin-orbit interaction because relative s-states are absent [Kel 89a].

[28] The *defect wave function* is defined as $\zeta = \phi - \psi$ and goes to zero for large values of separation s as the wave function heals. The integral $w = \int dr dr' \, |\zeta|^2$ is often called the *wound* in the wave function and is the probability of finding the actual system excited out of the noninteracting Fermi sea, relative to the probability of finding it in the ground state [Pre 75].

under the simplifying assumption that the free two-nucleon cross section σ_0 is independent of energy and isotropic in the center of mass [Kel 82]. With dimensionless quantities which will be convenient later, $\kappa_F = k_F/k_{F_0}$ and $\epsilon = E_0/\varepsilon_{F_0}$ (at saturation density $k_{F_0} \approx 1.33$ fm^{-1} and $\varepsilon_{F_0} \approx 37$ MeV), the Pauli blocking factor can be written as

$$\frac{\langle\sigma\rangle}{\sigma_0} = \begin{cases} 1 - \frac{7}{5}\frac{\kappa_F^2}{\epsilon} & \text{if } \epsilon \geq 2\kappa_F^2 \\ 1 - \frac{7}{5}\frac{\kappa_F^2}{\epsilon} + \frac{2}{5}\frac{\kappa_F^2}{\epsilon}(2 - \frac{\epsilon}{\kappa_F^2})^{5/2} & \text{if } \epsilon \leq 2\kappa_F^2. \end{cases} \tag{2.111}$$

Invoking the optical theorem, which connects the total cross section with the imaginary part of the interaction at forward angles, we expect $\mathrm{Im}t_{00}^C$ for $E_0 > 2\varepsilon_{F_0}$ to be damped by a factor $(1 - d\kappa_F^2)$, where d decreases with energy as E_0^{-1}. The damping factor is shown as a function of the (dimensionless) energy ϵ and Fermi momentum κ_F in Figure 2.33.

The density dependence of the real part of the central interaction, $\mathrm{Re}t_{00}^C$, is best described by the addition of a short-ranged repulsive core whose amplitude is proportional to density, i.e. κ_F^3. The repulsive core is due to the anticorrelation between identical nucleons and its effect is to enhance the differential cross section for large momentum transfer. As can be seen for example in Figure 2.34 where the different symbols and curves represent different densities, with increasing density the curves are displaced upwards by an amount proportional to density and almost independent of momentum transfer. The curves are not quite parallel because the finite range of the repulsive core reduces its effectiveness and thereby causes the curves to draw together for large momentum transfers [Kel 89a].

With these results, a parametrized form for the various components

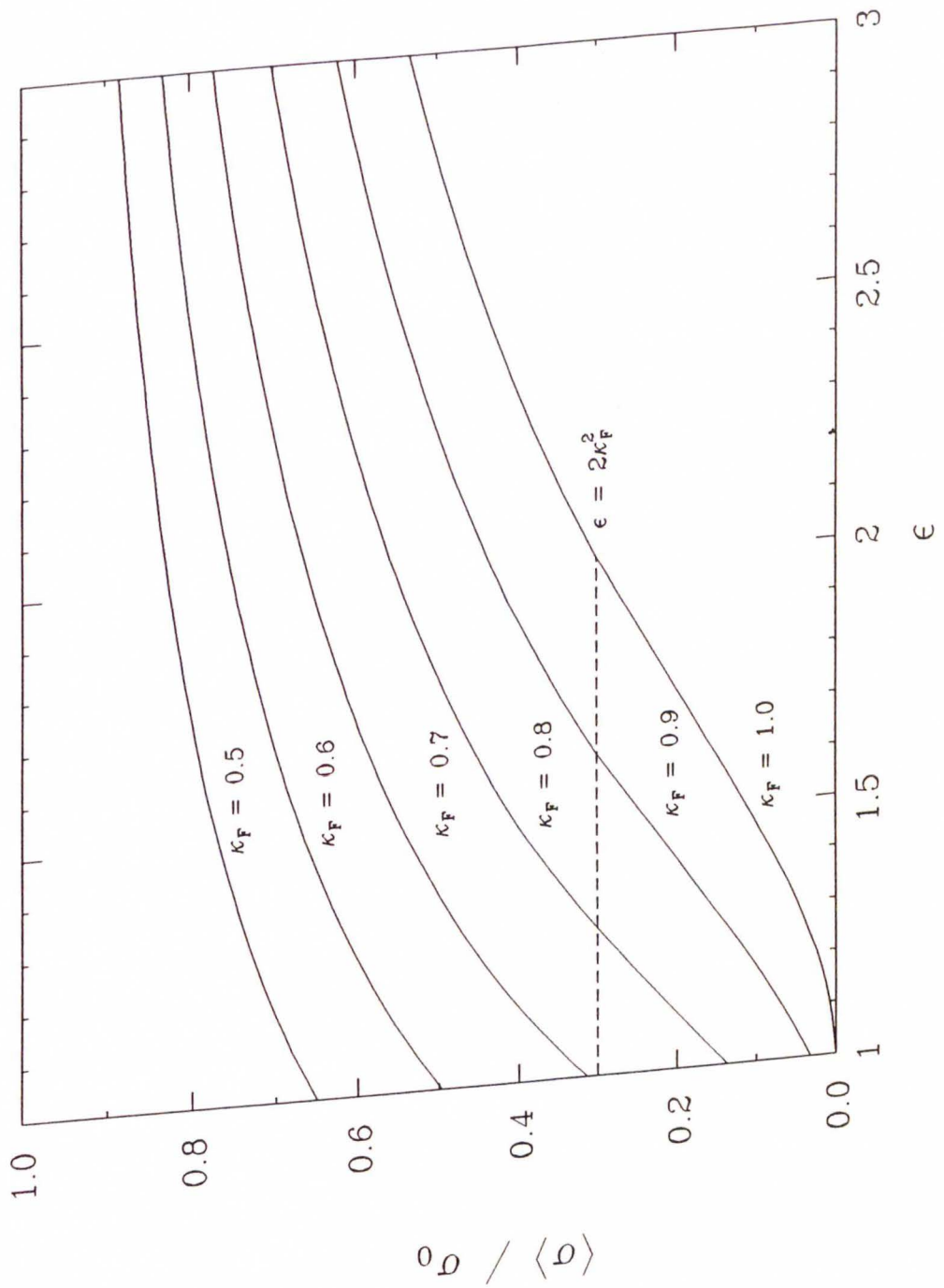

Figure 2.33: Clementel and Villi estimate of the Pauli blocking factor.

of the isoscalar effective interaction can be developed. Following the (new) notation of Kelly *et al.* [Kel 90b], all the central and spin-orbit components of the interaction can be parametrized by separate functions of the generic form

$$t_i(q,\kappa_F) = (S_i - d_i\kappa_F^{\alpha_i})\, t_i^{(f)}(q) + \kappa_F^{\gamma_i} q^{\delta_i} \sum_{n=1}^{N} a_{in} y^{\beta_i}(q/\mu_{in}). \qquad (2.112)$$

Here, $t^{(f)}(q)$ is a free interaction, $y(x) = (1+x^2)^{-1}$ is a Yukawa function, and the μ_n are various mass parameters which were chosen to optimize the fit. If the individual components of the interaction are considered to be appropriate Fourier transforms of Yukawa expansions, one finds that the natural exponents β are 1 for central, 2 for spin-orbit, and 3 for tensor interactions. Similarly, for the tensor interaction $\delta = 2$ is used and $\delta = 0$ otherwise. As we have already discussed, the Clementel and Villi model predicts for the imaginary part of the central interaction $\alpha = 2$ and $d \propto E_0^{-1}$. In order to recover the free interaction at zero density, the scale factors S are required to be unity for theoretical effective interactions. This restriction can and, as we will see, must be relaxed for the phenomenological analysis of data.

We performed empirical interaction fits for the PH, NL and LR effective interactions for energies between 100 MeV and 500 MeV. We used the free PH t-matrix for the PH fits and the FL t-matrix for the LR fits; the NL interaction contains the t-matrix as the $k_F \to 0$ limit. The PH interaction was fitted in the ranges $0 \le q \le 3$ fm^{-1} and $0.6 \le k_F \le 1.4$ fm^{-1} with a step size of 0.1 fm^{-1} for the momentum transfer and a step size of 0.2 fm^{-1} for the Fermi momentum. The NL interaction was fitted in the same momentum

transfer range, and with the same step size for q, for Fermi momenta in the range $0.6 \leq k_F \leq 1.4$ fm^{-1} (step size 0.2 fm^{-1}), except for 100 MeV where only $k_F = 0.0$ and 1.36 fm^{-1} were used because the density dependence is not monotonic at that energy. The LR interaction was fitted for $k_F = 0.0$, 0.7, and 1.4 fm^{-1}; the momentum transfer ranges were $0 \leq q \leq 2.5$ fm^{-1} (200 MeV), and $0 \leq q \leq 3$ fm^{-1} (318 MeV and 500 MeV). The c.m. wave number was evaluated for ^{16}O.

The fitted parameters are listed in Tables 2.1–2.3, and both the theoretical interactions and the empirical fits are shown in Figures 2.34–2.42 (the PH and NL parameters for 135 MeV are from [Kel 89b], the PH parameters for 180 MeV from [Kel 90a]). Considering that only two parameters are being used for each component, the fits are remarkable over the whole energy range. Also, apart from 100 MeV and 318 MeV where some modifications to the mass parameters and exponents are necessary, it appears that one functional form is able to accommodate all the interactions: PH, NL, and LR.

		$\mathrm{Re}t_{00}^{C}$		$\mathrm{Im}t_{00}^{C}$		$\mathrm{Re}\tau_{0}^{LS}$		$\mathrm{Im}\tau_{0}^{LS}$	
T_L	P	a_{11}	a_{12}	d_2	a_{21}	a_{31}	a_{32}	d_4	a_{41}
100	c	-123.67	201.13	0.561	-2.29	-20.09	15.73	0.603	-4.61
	μ	0	3.0	-	0	3.0	6.0	-	3.0
	e	[3310]		[2210]		[3320]		[3220]	
135	c	-94.71	181.29	0.443	-6.36	-13.80	10.71	0.571	-5.26
	μ	0	3.0	-	0	3.0	6.0	-	3.0
	e	[3310]		[2210]		[3320]		[2220]	
180	c	-74.33	157.32	0.326	-10.27	- 8.73	7.21	0.586	-5.64
	μ	0	3.0	-	0	3.0	6.0	-	3.0
	e	[3310]		[2210]		[3320]		[2220]	
200	c	-64.15	141.31	0.287	-10.49	-7.39	6.40	0.384	-3.36
	μ	0	3.0	-	0	3.0	6.0	-	4.0
	e	[3310]		[2210]		[3320]		[3220]	
318	c	-45.90	123.23	0.173	-24.17	-4.61	3.69	0.324	-2.78
	μ	0	3.0	-	0	3.0	6.0	-	7.0
	e	[2210]		[2210]		[3320]		[1140]	

Table 2.1: Reparametrization of the PH interaction. Units: T_L (MeV), d (1), a (MeV fm^3) for central and (MeV fm^5) for spin-orbit components, μ (fm^{-1}); an entry of 0 for μ is to be interpreted as a delta function with $\mu^{-1} = 0$. The exponents for each component are given in the form $[\alpha\gamma\beta\delta]$.

T_L	P	$\mathrm{Re}t_{00}^C$		$\mathrm{Im}t_{00}^C$		$\mathrm{Re}\tau_0^{LS}$		$\mathrm{Im}\tau_0^{LS}$	
		a_{11}	a_{12}	d_2	a_{21}	a_{31}	a_{32}	d_4	a_{41}
100	c	-186.80	200.54	0.700	-4.06	-24.56	14.20	0.705	-0.69
	μ	0	3.0	-	0	3.0	6.0	-	3.0
	e	[3310]		[2210]		[3320]		[2220]	
135	c	-62.78	85.15	0.671	-6.64	-18.89	12.00	0.728	-1.30
	μ	0	3.0	-	0	3.0	6.0	-	3.0
	e	[3310]		[2210]		[3320]		[2220]	
180	c	0.34	24.93	0.568	-4.96	-14.14	9.18	0.663	-1.30
	μ	0	3.0	-	0	3.0	6.0	-	3.0
	e	[3310]		[2210]		[3320]		[2220]	
200	c	15.00	9.63	0.458	-5.34	-10.72	7.13	0.610	-1.61
	μ	0	3.0	-	0	3.0	6.0	-	3.0
	e	[3310]		[2210]		[3320]		[2220]	
318	c	9.73	18.53	0.280	-9.46	-5.00	3.45	0.052	1.64
	μ	0	3.0	-	0	3.0	6.0	-	3.0
	e	[3310]		[2210]		[3320]		[2240]	

Table 2.2: Reparametrization of the NL interaction. Units: T_L (MeV), d (1), a (MeV fm^3) for central and (MeV fm^5) for spin-orbit components, μ (fm^{-1}); an entry of 0 for μ is to be interpreted as a delta function with $\mu^{-1} = 0$. The exponents for each component are given in the form $[\alpha\gamma\beta\delta]$.

T_L	P	$\mathrm{Re}t_{00}^C$		$\mathrm{Im}t_{00}^C$		$\mathrm{Re}\tau_0^{LS}$		$\mathrm{Im}\tau_0^{LS}$	
		a_{11}	a_{12}	d_2	a_{21}	a_{31}	a_{32}	d_4	a_{41}
200	c	-67.84	108.10	0.443	-5.46	-8.93	7.54	-0.027	-1.17
	μ	0	3.0	-	0	3.0	6.0	-	4.0
	e	[3310]		[2210]		[3320]		[3220]	
318	c	-38.89	100.03	0.263	0.83	-3.31	3.76	-0.020	-1.53
	μ	0	3.0	.-	0	3.0	6.0	-	2.0
	e	[3310]		[2210]		[3320]		[3220]	
500	c	-35.08	108.28	0.174	-4.65	-1.03	1.92	-0.007	-1.44
	μ	0	3.0	-	0	3.0	6.0	-	2.0
	e	[3310]		[2210]		[3320]		[3220]	

Table 2.3: Reparametrization of the LR interaction. Units: T_L (MeV), d (1), a (MeV fm^3) for central and (MeV fm^5) for spin-orbit components, μ (fm^{-1}); an entry of 0 for μ is to be interpreted as a delta function with $\mu^{-1} = 0$. The exponents for each component are given in the form $[\alpha\gamma\beta\delta]$.

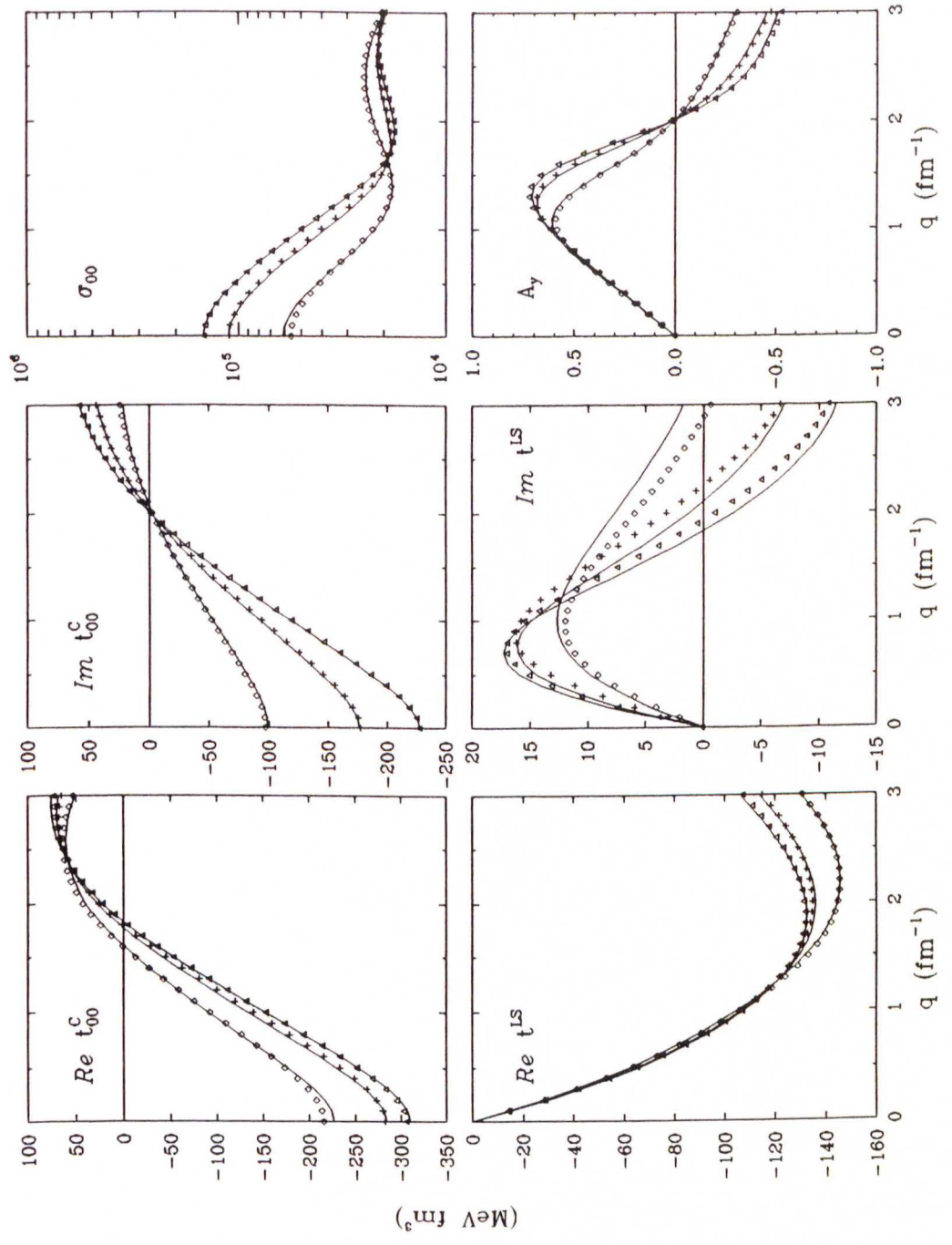

Figure 2.34: Reparametrization of the PH interaction (100 MeV). The symbols show the original interaction for $k_F = 0.6$ fm^{-1} (triangles), $k_F = 1.0$ fm^{-1} (crosses), and $k_F = 1.4$ fm^{-1} (diamonds). The curves show two-parameter fits.

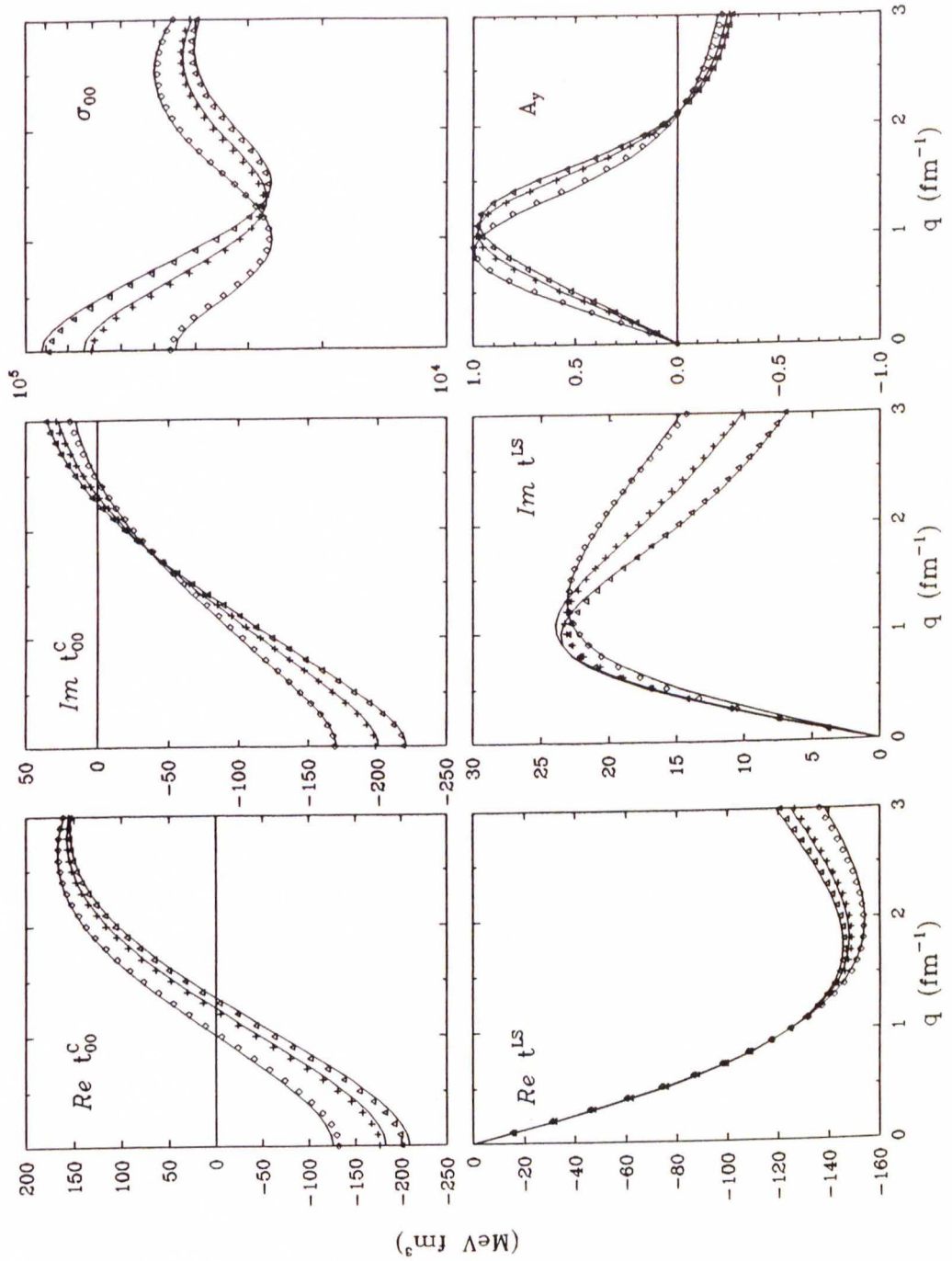

Figure 2.35: Reparametrization of the PH interaction (200 MeV). The symbols show the original interaction for $k_F = 0.6$ fm^{-1} (triangles), $k_F = 1.0$ fm^{-1} (crosses), and $k_F = 1.4$ fm^{-1} (diamonds). The curves show two-parameter fits.

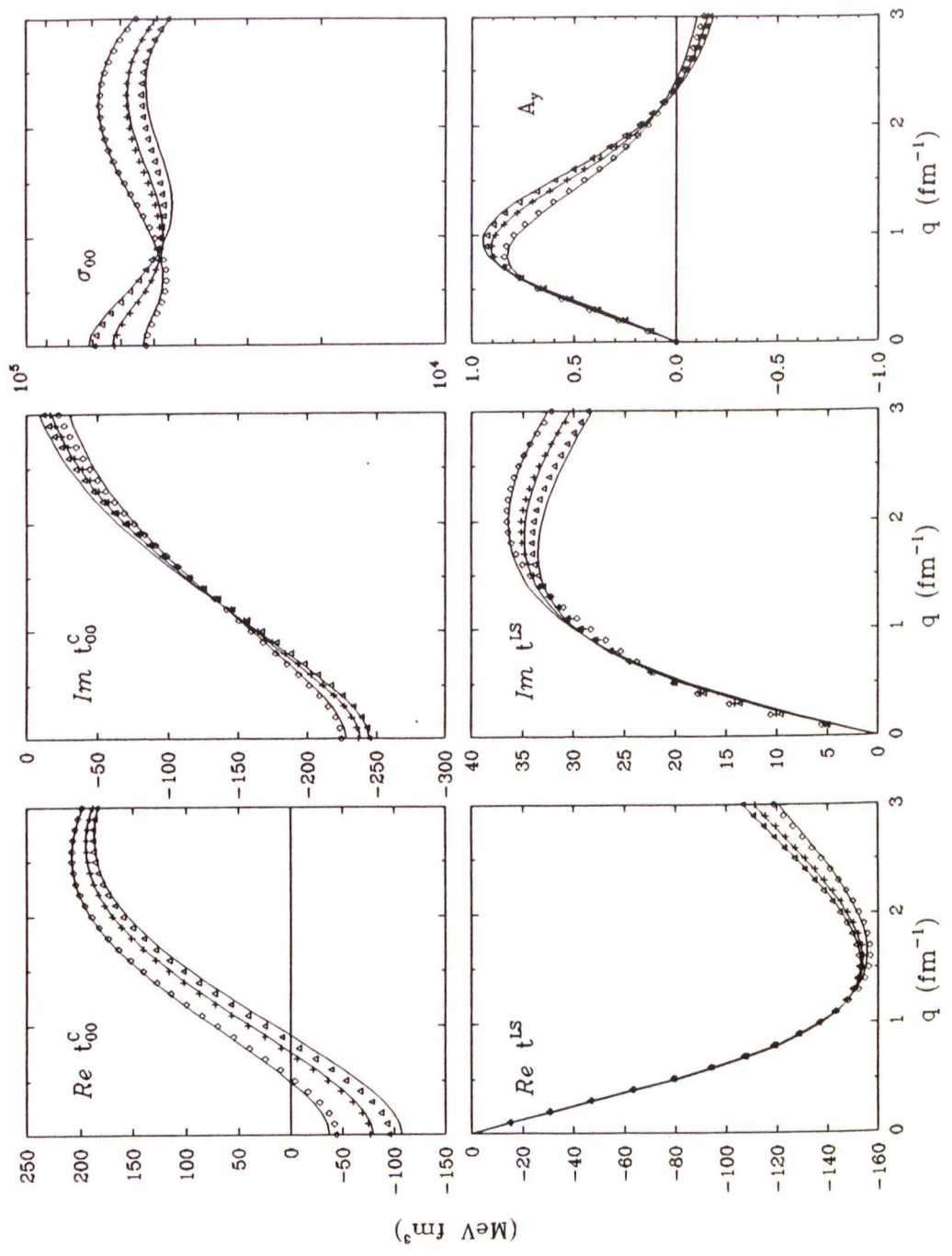

Figure 2.36: Reparametrization of the PH interaction (318 MeV). The symbols show the original interaction for $k_F = 0.6$ fm^{-1} (triangles), $k_F = 1.0$ fm^{-1} (crosses), and $k_F = 1.4$ fm^{-1} (diamonds). The curves show two-parameter fits.

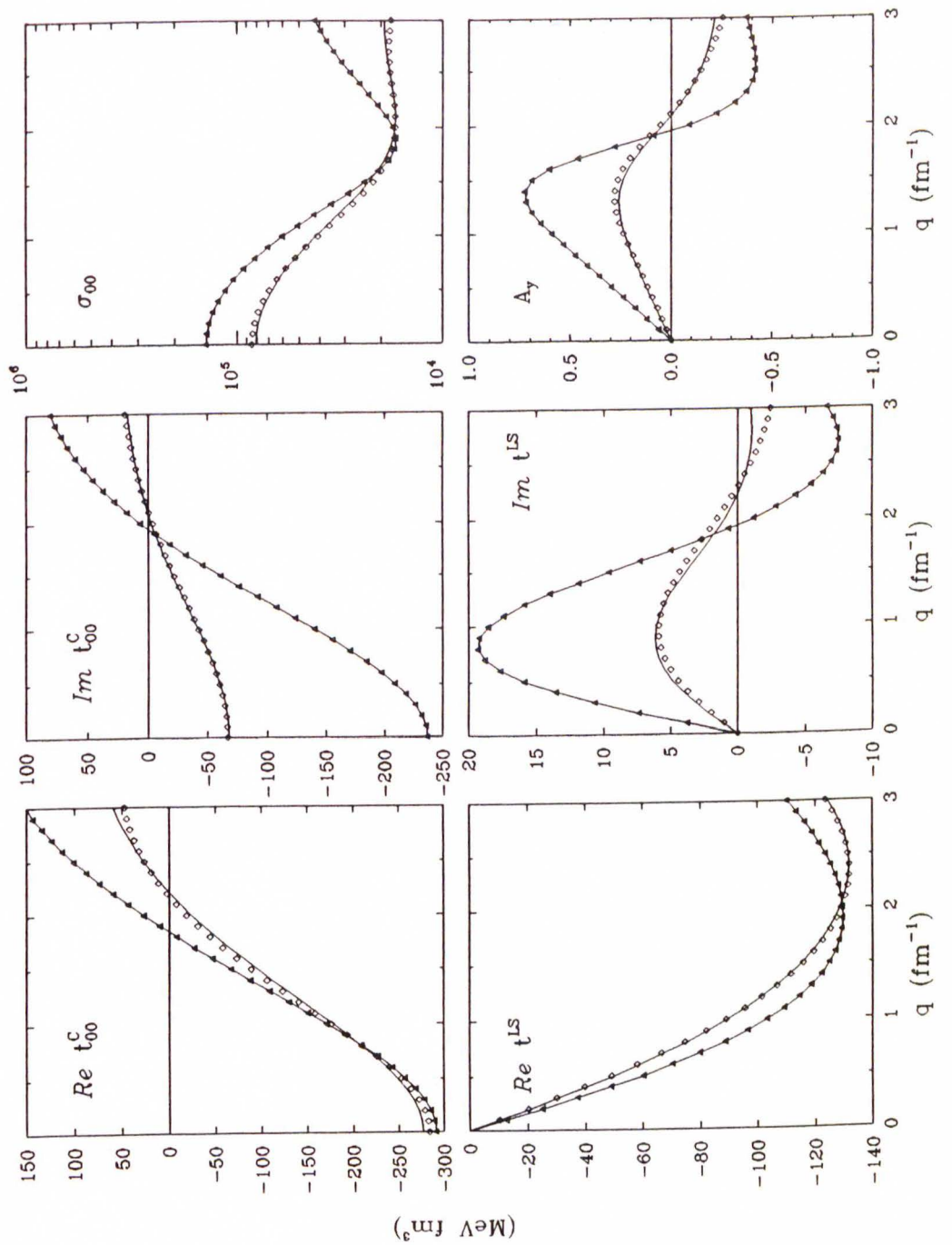

Figure 2.37: Reparametrization of the NL interaction (100 MeV). The symbols show the original interaction for $k_F = 0.0$ fm^{-1} (triangles), and $k_F = 1.36$ fm^{-1} (diamonds). The curves show two-parameter fits.

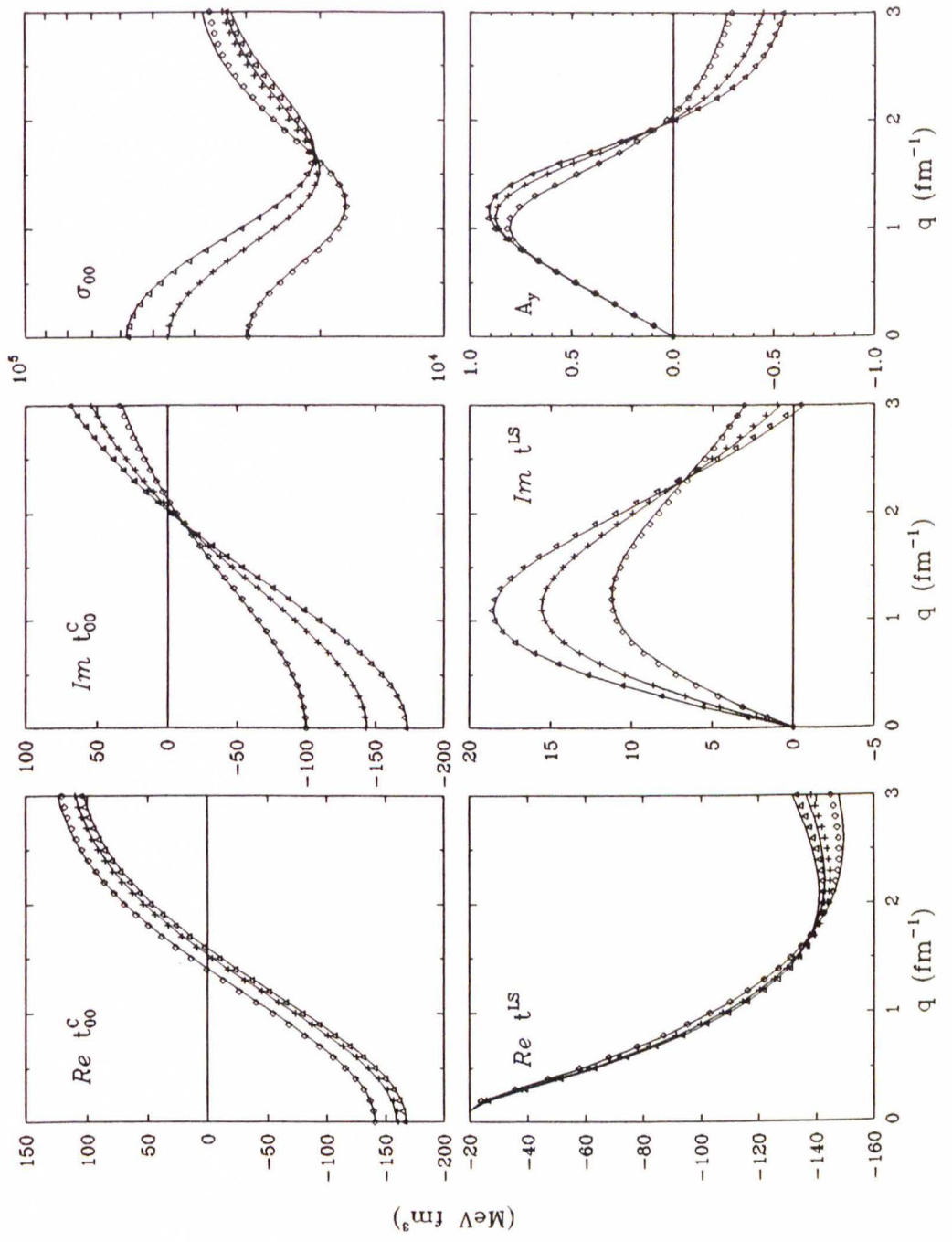

Figure 2.38: Reparametrization of the NL interaction (200 MeV). The symbols show the original interaction for $k_F = 0.6$ fm^{-1} (triangles), $k_F = 1.0$ fm^{-1} (crosses), and $k_F = 1.4$ fm^{-1} (diamonds). The curves show two-parameter fits.

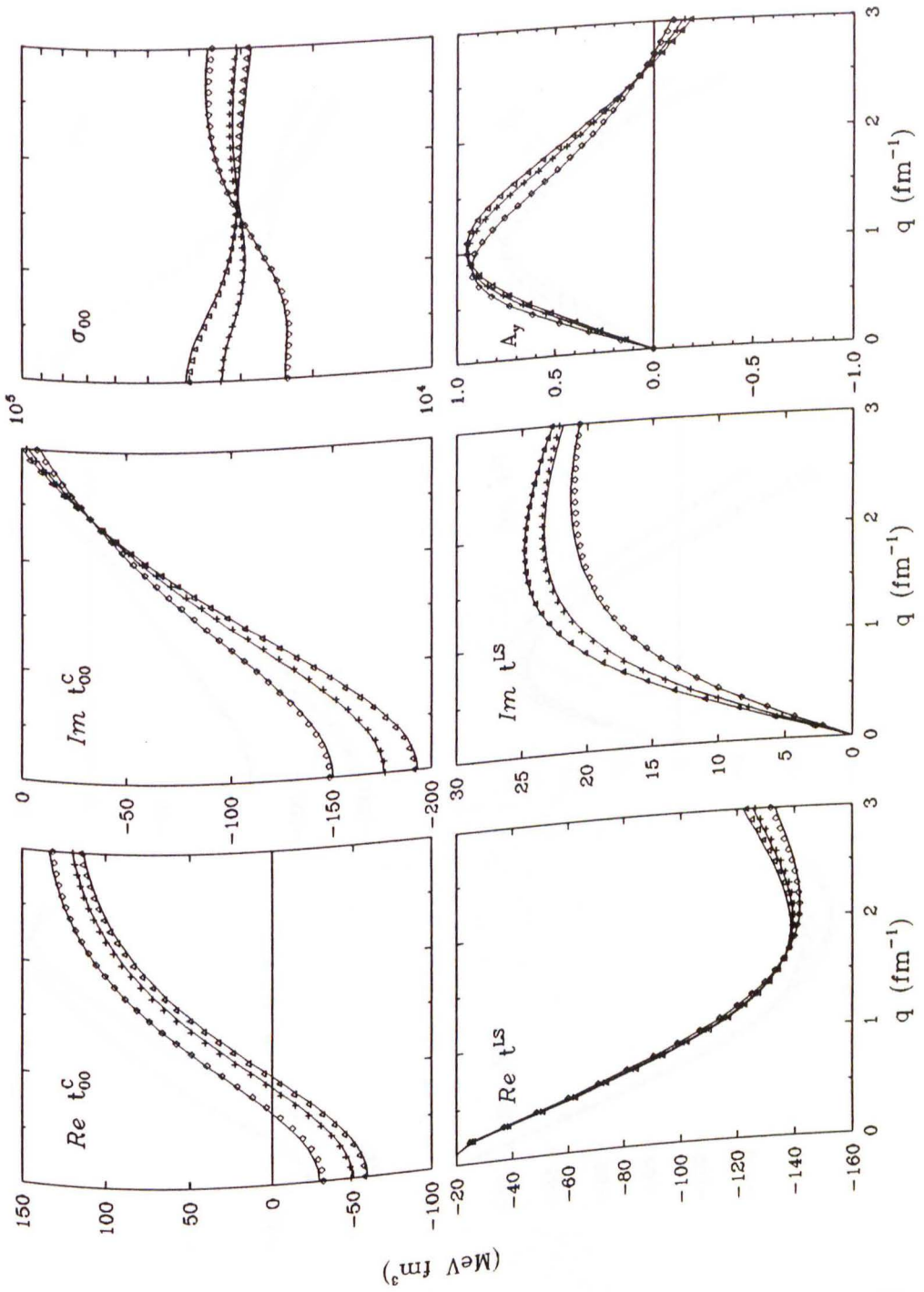

Figure 2.39: Reparametrization of the NL interaction (318 MeV). The symbols show the original interaction for $k_F = 0.6$ fm^{-1} (triangles), $k_F = 1.0$ fm^{-1} (crosses), and $k_F = 1.4$ fm^{-1} (diamonds). The curves show two-parameter fits.

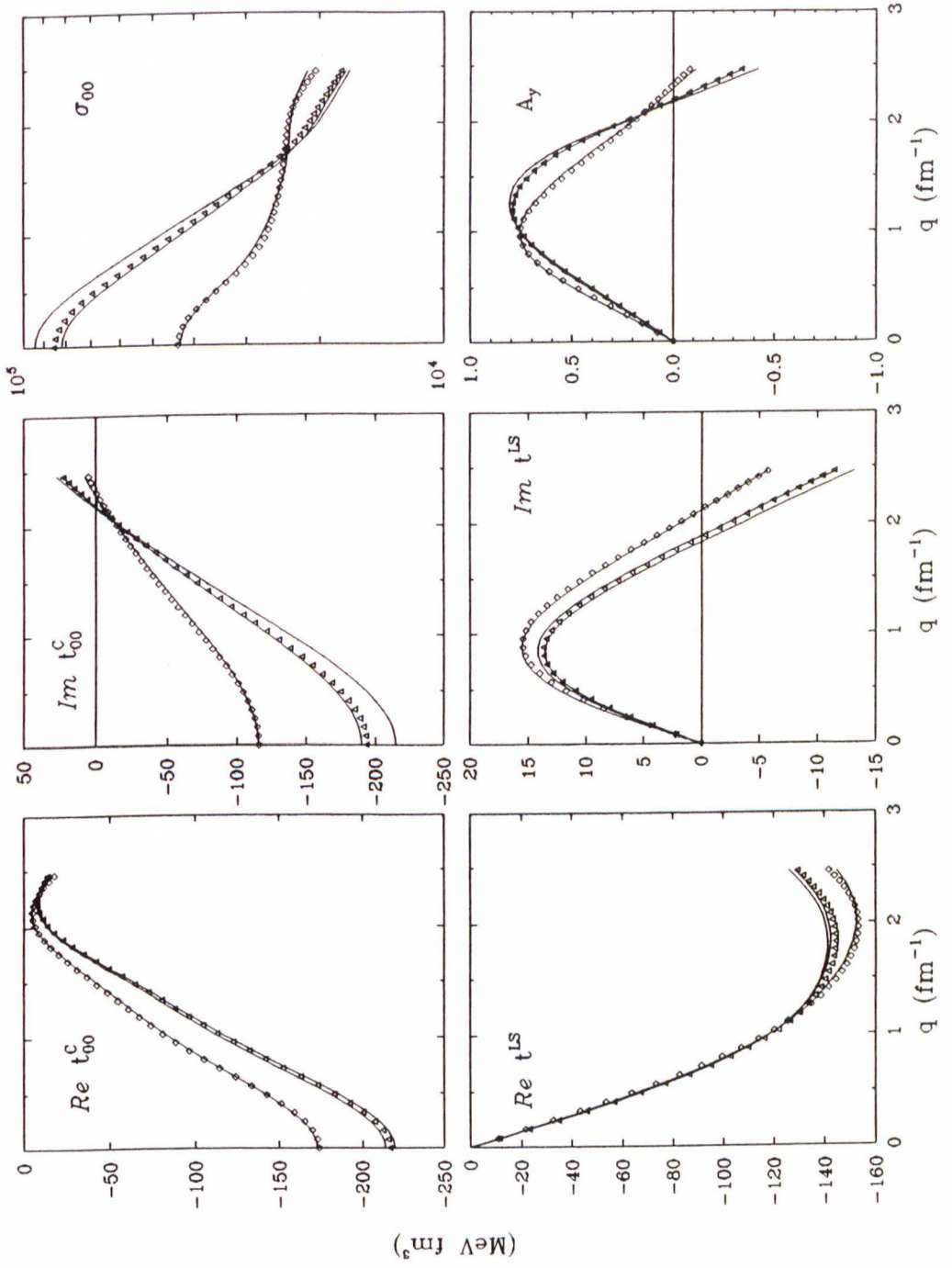

Figure 2.40: Reparametrization of the LR interaction (200 MeV). The symbols show the original interaction for $k_F = 0.0$ fm^{-1} (dots), $k_F = 0.7$ fm^{-1} (triangles), and $k_F = 1.4$ fm^{-1} (diamonds). The curves show two-parameter fits.

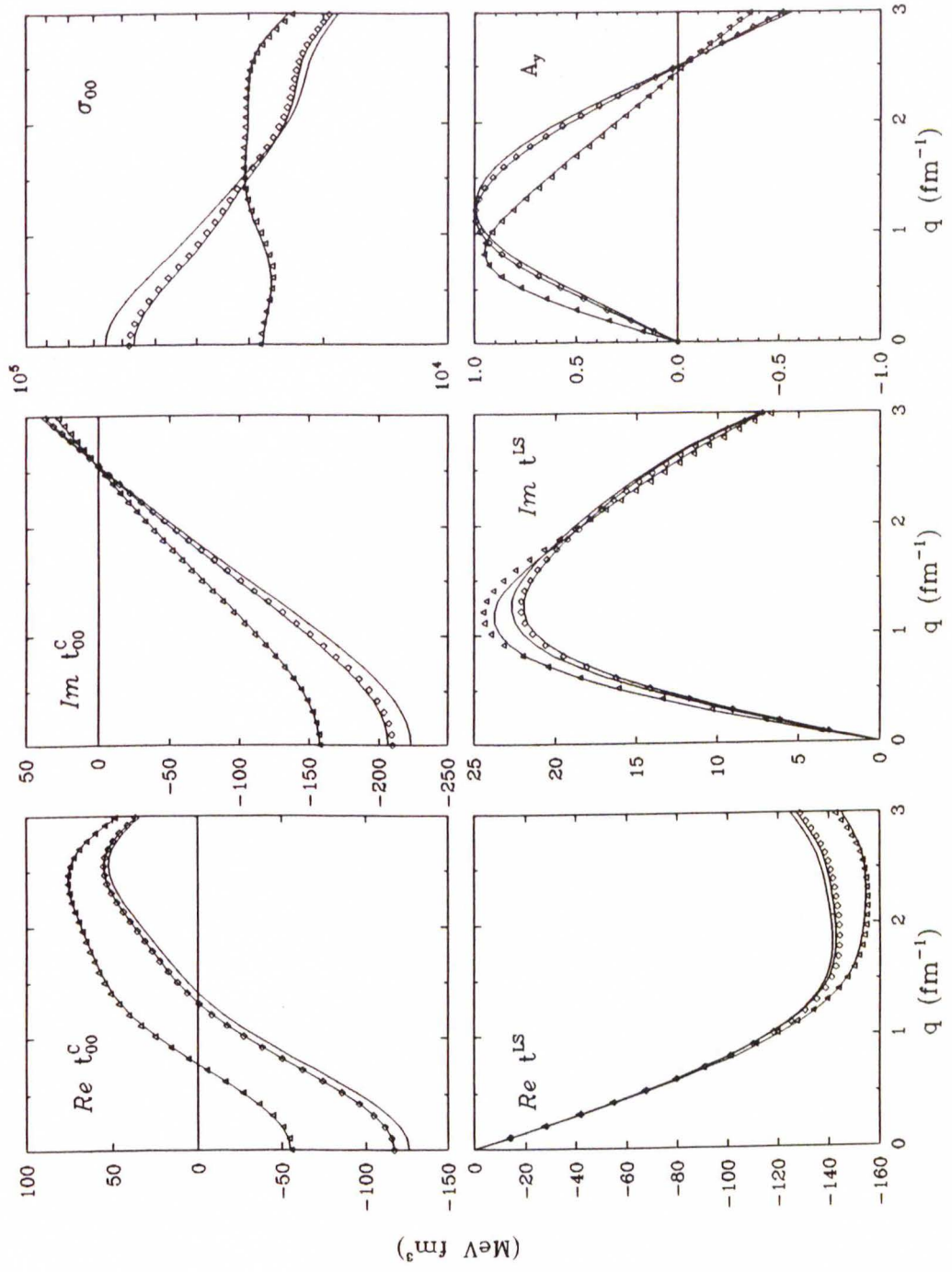

Figure 2.41: Reparametrization of the LR interaction (318 MeV). The symbols show the original interaction for $k_F = 0.0$ fm^{-1} (dots), $k_F = 0.7$ fm^{-1} (triangles), and $k_F = 1.4$ fm^{-1} (diamonds). The curves show two-parameter fits.

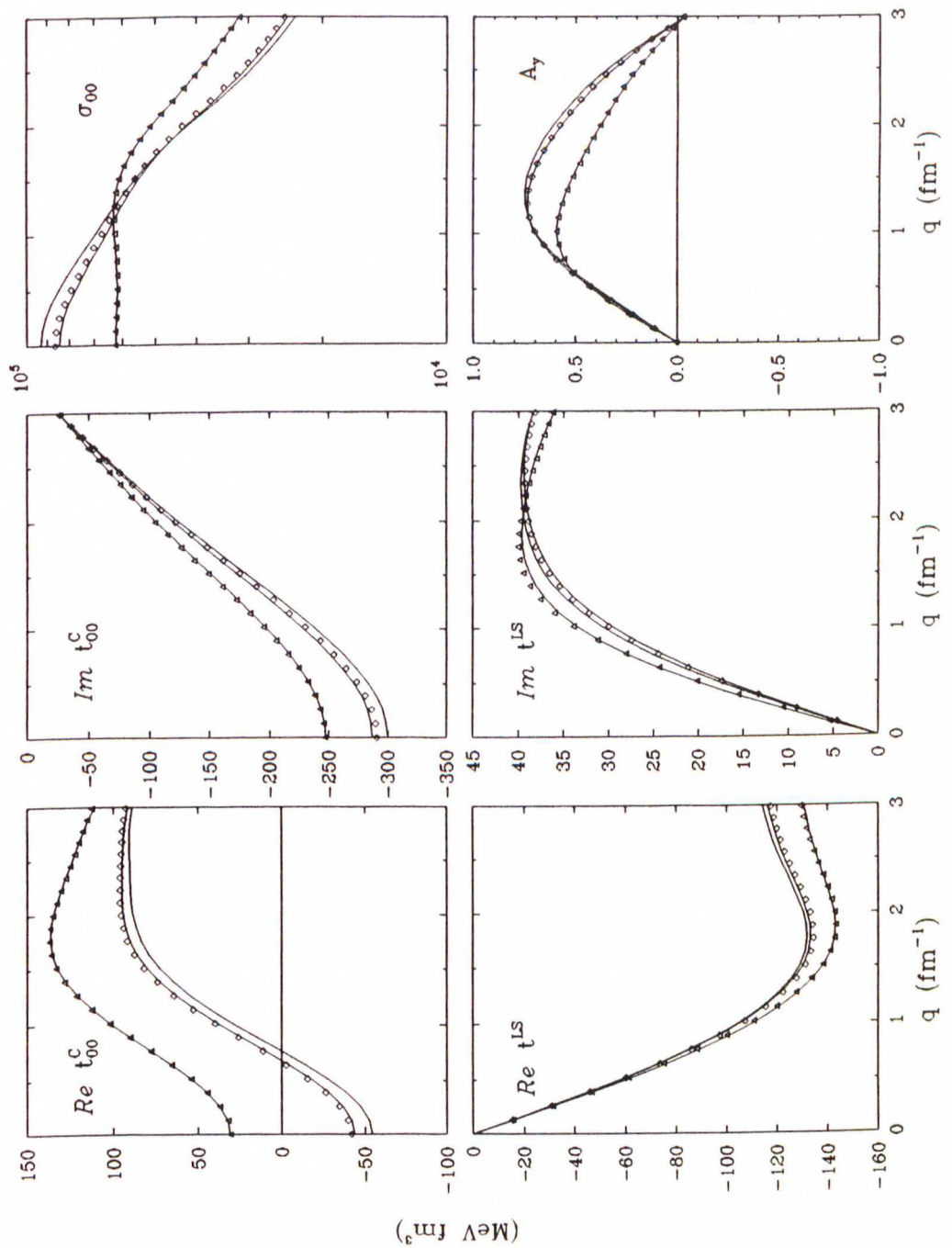

Figure 2.42: Reparametrization of the LR interaction (500 MeV). The symbols show the original interaction for $k_F = 0.0$ fm^{-1} (dots), $k_F = 0.7$ fm^{-1} (triangles), and $k_F = 1.4$ fm^{-1} (diamonds). The curves show two-parameter fits.

The strength V_R and the range R of the repulsive core of $\mathrm{Re}t_{00}^C$ can be identified from the above parametrization more easily in the low-q expansion

$$\mathrm{Re}t_{00}^C(q,\kappa_F) \approx \mathrm{Re}t_{00}^C(q,0) + \kappa_F^3 V_R \left[1 - \frac{q^2R^2}{6}\right], \qquad (2.113)$$

where $V_R = a_1 + a_2$ and $R^2 = \frac{6a_2}{\mu_1^2 V_R}$. Table 2.4 lists these two quantities for the three interactions. For the PH interaction V_R increases between 100 and 135 MeV and then decreases until about 200 MeV where it goes through a minimum. Above 200 MeV, the repulsive core becomes again slightly stronger with increasing energy. For the NL interaction V_R increases until about 180 MeV, decreases slightly and also goes through a minimum around 200 MeV. Above this energy the strength of the repulsive core increases rapidly with energy. The strength V_R of the LR real central interaction (which is only available for energies above 200 MeV) increases monotonically with energy. For all the interactions the range R of the repulsive core decreases monotonically with increasing energy. The table also shows that V_R for the NL interaction is much weaker than for the PH interaction. The shorter range of the NL repulsive core above 180 MeV makes the density dependence of the real central component almost independent of momentum transfer (see also Figures 2.38 and 2.39). The strength of the LR repulsive core is intermediate between the ones for the PH and NL interactions, its range however is slightly larger than for the PH interaction.

2.8.2 Description of Data

It has been previously established that an empirical effective interaction provides an excellent description of both elastic and inelastic scattering data

T_L	PH		NL		LR	
(MeV)	V_R	R	V_R	R	V_R	R
100	77.5	1.32	13.7	3.12	-	-
135	86.6	1.18	22.4	1.59	-	-
180	83.0	1.12	25.3	0.81	-	-
200	77.2	1.11	24.6	0.51	40.3	1.34
318	79.2	1.03	28.3	0.66	61.1	1.04
500	-	-	-	-	73.2	0.99

Table 2.4: Low-q form of Ret_{00}^{C}: strength of the repulsive core V_R (MeV fm^3), and range R (fm).

that is superior to any prediction based on a theoretical model. Examples can be found in [Kel 89b, Kel 90a, Kel 90b, Fla 90]. The resulting parameters represent the effective interaction in a finite nuclear system, and a comparison with parameters obtained from theory allows us to critically review the various models and approximation schemes for the nucleon-nucleus scattering problem. The parametrization itself provides greater insight into the physics of the effective interaction than do theoretical interactions presented in the form of voluminous tables of Yukawa amplitudes.

Apart from its use in the study of the nuclear effective interaction proper, another equally important use for the effective interaction is its application to phenomenological nuclear structure studies. The extraction of neutron transition densities from proton scattering data requires a rather accurate description of the two-nucleon effective interaction and its density dependence. Kelly demonstrated that nucleon inelastic scattering for energies

between roughly 200 and 500 possesses very good intrinsic radial sensitivity and permits neutron densities to be determined even in the nuclear interior, particularly for targets with moderate A [Kel 88]. However, residual errors in the effective interaction can induce artificial distortion of the fitted densities and thereby limit the accuracy which can be achieved in practice [Kel 89b]. While the accuracy of presently available theoretical effective interactions is not sufficient for this task, empirical interactions have already been successfully applied [Kel 86b, Kha 89, Kel 90a, Fel 90].

If we want to use the empirical interaction, Eq. (2.112), to fit data we can not use exactly the same form which was used in the previous section to fit theoretical interactions. First, it appears that data for states with surface-peaked transition densities cannot be fitted unless one allows for a scaling of the free interaction. The interpretation of this is that the interaction does not heal to the free interaction at low densities. Second, the strong correlations among terms with various range parameters μ complicate the analysis of scattering data and it is difficult to obtain stable fits with more than two free parameters per interaction component. Kelly, therefore, proposed simpler parametrizations to interpret scattering data involving only a scale factor and one more free parameter for each component [Kel 89b]. In this work we found it convenient to use for the real central part of the interaction

$$\mathrm{Re}t_{00}^{C}(q,\kappa_F) = S_1 \mathrm{Re}t_{00}^{C(f)}(q) + \kappa_F^3 b_1 y(q/\mu_1), \tag{2.114}$$

for the imaginary central part

$$\mathrm{Im}t_{00}^{C}(q,\kappa_F) = [S_2 - d_2\kappa_F^2]\mathrm{Im}t_{00}^{C(f)}(q), \tag{2.115}$$

	PH			LR		
T_L	b_1	d_2	b_3	b_1	d_2	b_3
100	72.74	0.551	3.70	-	-	-
135	89.99	0.415	2.57	-	-	-
180	89.38	0.272	2.11	-	-	-
200	83.99	0.229	2.10	38.10	0.410	1.83
318	80.52[a]	0.035	1.03	61.19[a]	0.267	1.90
500	-	-	-	76.02[a]	0.153	1.34

Table 2.5: Simple reparametrization of the PH and LR interactions (100 MeV–500 MeV) with the same units as above.
[a] $\mu_1 = 2.0$ fm^{-1}.

and for the real spin-orbit part

$$\mathrm{Re}\tau_0^{LS}(q,\kappa_F) = S_3 \mathrm{Re}\tau_0^{LS(f)}(q) + \kappa_F^3 b_3 y^2(q/\mu_3). \tag{2.116}$$

Usually, the imaginary part of the spin-orbit interaction is too weak to be fitted and is fixed to its nuclear matter value from the previous section. Here, b_1 plays the role of V_R in the low-q expansion of $\mathrm{Re}t_{00}^C$ and μ_1 provides a finite range comparable to R (in the low-q approximation $\mu_1 \approx \sqrt{6}/R$). The parameters b_1, d_2, and b_3 resulting from a fit of this simpler form to the PH and LR theoretical interactions are listed in Table 2.5. The scale factors for this fit are of course all unity. The ranges for q and k_F, the calculation of the wave number, and the free interactions used, are the same as in the previous section. The masses used were $\mu_1 = 1.5$ fm^{-1} for all the energies up to 200 MeV; above 200 MeV we used $\mu_1 = 2.0$ fm^{-1}. The value $\mu_3 = 6.0$ fm^{-1} proved to be acceptable for all energies. We found that

these fits for the PH and, especially, for the LR interactions are almost as good as the two-parameter fits in the previous section. The NL interaction is not as easily parametrized in terms of the simple form. However, we will later compare the parameters from the fit to data only to the PH and LR parameters, since those two theoretical interactions describe the data best. The PH interaction is available for energies up to 400 MeV and gives superior results over all the other interactions at 100, 200, and 318 MeV (see Section 2.4.5). For higher energies, the LR interaction is the only available nonrelativistic effective interaction with medium modifications.

2.8.3 Linear Expansion Analysis and Fitting Procedure

An empirical interaction can be obtained from a fit to the scattering observables of isoscalar natural-parity transition in a self-conjugate nucleus. One assumes that, in the absence of significant transverse form factors, all densities with the exception of the matter density are negligible (e.g. spin and current densities) and that this density is accurately determined from electroexcitation data. Charge symmetry ensures that the neutron and proton transition densities are approximately equal. Thus, all the nuclear structure information required to interpret proton scattering data within the $t\rho$ folding model for the scattering potential is specified through electron scattering measurements. This enables us to isolate the effective interaction with little residual ambiguity due to nuclear structure.

In the following we want to outline very briefly the *linear expansion analysis* (LEA) method. A more complete and thorough discussion of the

method can be found in the paper by Carr *et al.* [Car 85], in the papers by Kelly [Kel 85a, Kel 86a, Kel 86c, Kel 87], and in the paper by Kelly *et al.* [Kel 86b].

* * *

In the linear expansion analysis, the transition amplitude T is expanded as a linear series

$$T(q) = \sum_n a_n T_n(q), \tag{2.117}$$

where the basis amplitudes $T_n(q)$ are expressed in the folding model as the convolution of the effective interaction with the transition density. With Eq. (2.100) we get the overlap integrals

$$T_n(q) = \langle \chi_f^{(-)}(\boldsymbol{k}')\phi_f | \Delta U_n | \chi_i^{(+)}(\boldsymbol{k})\phi_i \rangle, \tag{2.118}$$

where $\Delta U_n = t_n \Delta\rho$ is a component of the transition potential, and t_n the corresponding component of the interaction t which is expanded as $t = \sum_n a_n t_n$. For example, in our simple parametrization the total interaction has six components whose parameters a_n can be adjusted, plus the components of the imaginary spin-orbit interaction which are generally kept fixed. With the basis amplitudes $T_n(q)$ one then constructs the quadratic forms $X_{\alpha\beta}^{nn'}(q)$, analogous to Eq. (2.101). Evaluating contractions of these quadratic forms leads to

$$I_0(q) D_{\alpha\beta} = \frac{1}{2} \sum_{nn'} a_n X_{\alpha\beta}^{nn'}(q) a_{n'}^{*} \tag{2.119}$$

in place of Eq. (2.102). The connection with the scattering observables was discussed in Section 2.7.1. Fitting of the expansion coefficients a_n to data is

done using a relatively simple but efficient search procedure: in the first step, the distorted waves χ are generated with a good approximation to the optical potential, such as provided by the PH interaction or a previous empirical interaction. Then for each term t_n in the linear expansion of the effective interaction the overlap integrals T_n are computed. Subsequently, the quadratic forms X are constructed and stored for the entire data set. Since both the overlap integrals and the quadratic forms are independent of the expansion coefficients a_n, it is then straightforward to optimize the coefficients with a very simple search algorithm. To achieve consistency between elastic and inelastic scattering, the fitted interaction is iterated and the optical potential in each step is computed self-consistently after the $(1 + \rho\partial/\partial\rho)$ contibution has been removed from the interaction. Removing the rearrangement contribution is crucial for self-consistency, and self-consistency cannot achieved without it.

As a recent development, we have now also the option to include elastic scattering in the fit. This provides an independent means to check both self-consistency and the $(1 + \rho\partial/\partial\rho)$ prescription. In order to treat elastic scattering within the same perturbative framework as inelastic scattering, we decompose the optical potential U_{opt} into a dominant reference potential U_{ref} and a small perturbation δU which serves as a "correction"

$$U_{opt} = U_{ref} + \delta U, \tag{2.120}$$

where $U_{ref} = t\rho_g$ and $\delta U = \delta t\rho_g$. The correction to the elastic scattering

amplitude, therefore, is

$$\delta T(q) = \langle \chi_f^{(-)}(\boldsymbol{k}')\phi_f | \delta U | \chi_i^{(+)}(\boldsymbol{k})\phi_i \rangle. \tag{2.121}$$

The correction to the interaction, δt, is expanded as $\delta t = \sum_n \delta a_n t_n$. Hence, for a reference interaction t which may be a theoretical interaction or an interaction from inelastic scattering, the elastic fit finds the *corrections* to the interaction parameters rather than the interaction parameters proper. The new interaction parameters a'_n are then $a'_n = a_n + \delta a_n$.

Finally, we want to make some further remarks to the data selection for the empirical interaction fits. It is the fundamental premise of the local density approximation that the medium modifications depend solely upon the local density in which the interaction occurs, but not upon the specific structure of each target. The interaction should not depend upon the final state of the nucleus. If this concept is sound, therefore, as a minimum requirement the empirical interaction has to reproduce the data for all the states of a single target. For this analysis it is important to include both surface-peaked states which are sensitive to the low-density properties of the effective interaction, as well as interior-peaked states which sample the medium modifications at high density. For a finite nucleus, the low-density properties of the effective interaction need not necessarily be the same as those of the free interaction. Finally, intermediate cases will determine the rate at which the medium effects depend upon density. Another, more stringent test of the local density hypothesis, is to test whether the interaction is independent of target. In this work, therefore, we will extract and compare interactions

from single-target fits to ^{16}O and ^{40}Ca, as well as from combined fits to ^{16}O and ^{40}Ca. Since many data between 100 MeV and 500 MeV are available, the smooth dependence of the parameters upon the projectile energy can be tested as well.

3 Experiment

3.1 Introduction

Experiment 268 was conducted at the IUCF cyclotron facility in four run periods between January 1987 and March 1988 and it was the first experiment to utilize the new K600 spectrometer. The objective was to measure cross sections and analyzing powers of the low-lying states of the Ca isotopes ^{40}Ca, ^{42}Ca, ^{44}Ca and ^{48}Ca at the two energies 100 MeV and 200 MeV. A BeO target was used to get scattering angle information from differential recoil. We obtained excellent measurements of some of the lower ^{9}Be states, as well as of all the important ^{16}O states up to about 14 MeV excitation energy.

In January 1987 we collected data at 100 MeV for BeO and all the Ca isotopes, with exception of ^{44}Ca which was destroyed early in the run. 200 MeV large angle measurements for the same targets were done in April 1987. In January 1988 we completed the forward angle measurements at 200 MeV and also took data for the new ^{44}Ca target over the whole angular range. In March 1988 we concentrated on 100 MeV measurements for ^{44}Ca and ^{48}Ca. Finally, in all our run periods a lot of diagnostic and development work was done. In parallel to the experiment at IUCF, we took 318 MeV data for all Ca isotopes (EXP 919) and for ^{32}S and ^{34}S (EXP 956) at LAMPF, using the HRS spectrometer.

This chapter describes the IUCF experiment in detail; main references are the IUCF K600 Lectures [K600 L] and several IUCF Scientific and Technical Reports ([Ber 86, Ber 88, Ber 89]). A brief comparison of the HRS

and K600 spectrometers can be found in this chapter; a more detailed and comprehensive discussion of the LAMPF experiments is presented in [Fel 90].

3.2 Accelerator and Beam

A floor plan of the IUCF cyclotron laboratory is shown in Figure 3.1. [IUCF 86]. Beam from the polarized ion source first passes three preprocessing units: a chopper, a buncher and a pulse selector. Acceleration to the final energy is achieved in two isochronous cyclotrons. The smaller injector cyclotron accelerates the 0.5 MeV protons from the source up to 15.2 MeV, the field limit. Before entering the bigger mainstage cyclotron the beam is guided through a short beam line section which contains a polarimeter. The polarization was generally about 75 percent. More about the polarization measurements and their analysis will be reported in Chapter 4. Beam splitting and momentum analysis is done after extraction from the mainstage in beam line 3 (BL 3).

The average energy of the beam delivered by the dual cyclotron was determined from several readings of the BL 3 bending magnet NMR. In January 1987 the average proton energy varied between 100.5 MeV and 100.7 MeV. In April 1987 the average beam energy was 201.53 MeV and in January 1988 it varied between 201.24 MeV and 201.4 MeV. In March 1988 the average proton energy was found to be 100.5 MeV. This is summarized in Table 3.1.

Beam line 8 (BL 8) is the section between the bending magnet at the end of BL 6 and the beam dump in the K600 experimental area. It con-

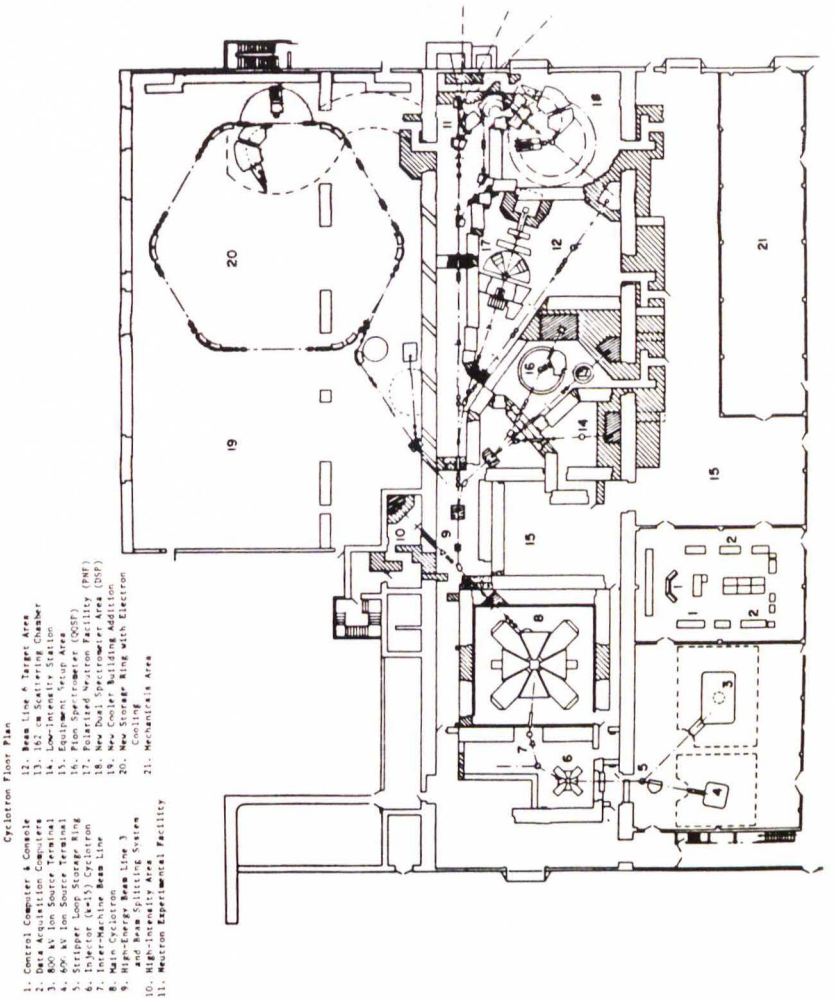

Figure 3.1: IUCF Cyclotron Floor Plan

Beam Energy (nominal)	*Run Period*	*Beam Energy (measured)*	*Runs*
100 MeV	January 1987	100.5 MeV	1–145
		100.7 MeV	146–416
	March 1988	100.5 MeV	2221–2353
200 MeV	April 1987	201.53 MeV	501–651
	January 1988	201.24 MeV	761–979
		201.4 Mev	982–1023

Table 3.1: Beam Energies for Experiment 268.

tains among other beam optical components the old QDDM spectrometer as a bending magnet and momentum analyzer. The size of the horizontal object slit upstream of the QDDM determines the *resolving power* of the system ($R = \delta^{-1} = p/dp = D_x/\Delta x_0 M_x$) and the *energy dispersion* on the target ($dT/T = (2 - T/m_p)/R$). With $D_x = 10.3\ m$ and $M_x = 0.9$ for the QDDM one gets for the 1.1 mm slit (transmission generally better than 90%) a resolving power of 10,404 which corresponds to about 18 keV at 100 MeV and about 35 keV at 200 MeV. These values also correspond roughly to the width of the image in the K600 focal plane, and thus provide a lower bound to the focal plane resolution. An available 0.55 mm slit improves the resolution by a factor of two, however at the price of lower intensity since only about 60% of the beam can be focussed through this slit. The thickness of the brass object slit is chosen to degrade the beam in the slit jaws by about 1% in δ, corresponding to a deviation of about 3 inches in the QDDM focal plane. The

degraded beam is stopped in a flange ahead of the first of four quadrupoles between the QDDM and the scattering chamber while the main beam continues to the target. The four quadrupoles after the QDDM serve to adjust the momentum dispersion on the target and to provide a monochromatic focus on the target (or slightly beyond it for reactions with a large kinematic factor), as well as the correct angular dispersion so that the scattering angle remains constant across the target.

The bottom of the scattering chamber holds a rotating platter with a three-hole hodoscope used for dispersion matching. An internal Faraday cup necessary for forward angle measurements can also be mounted on this platter. There are two beam exits at the scattering chamber. One connects with the K600 spectrometer and contains a cassette holding several apertures of different geometrical shapes (circular and rectangular) and different horizontal and vertical acceptances (c.f. Table 3.2)[1]. The other leads to the beam dump with the external Faraday cup. Measurements down to 18 deg were possible with the external cup and the old dump pipe. In March 1988 a small pipe was available, making measurements with the external cup possible down to about 15 deg.

[1] The acceptances were calculated with $d\Omega = A/R^2$ where A is the aperture area and R the distance from the target (the rounded corners were taken into consideration). An exact formula for circular apertures (radius a) is $d\Omega = 2\pi(1 - \sqrt{1-(a/R)^2})$. For rectangular apertures with half-height a and half-width b the exact expression is $d\Omega = 4\arctan(\frac{ab}{Rd})$ where $d = \sqrt{a^2 + b^2 + R^2}$ [Cra 53].

Aperture	*Ap.#*	*Dimensions (h × v; r)*	*Acceptance*
1/2 in diam.	A1	1.27 cm	0.2500 msr
1.6 in × 1.6 in	A7	4.06 cm × 4.06 cm; 1/8 in	3.2345 msr
3/8 in diam.	B1	0.95 cm	1.4000 msr
1/2 in × 1 in	B2	1.27 cm × 2.54 cm; 1/4 in	0.5681 msr
1/2 in × 2 in	B3	1.27 cm × 5.08 cm; 1/8 in	1.2556 msr
2 in × 1 in	B4	5.08 cm × 2.54 cm; 1/8 in	2.5282 msr
1.6 in × 1.6 in	B5	4.06 cm × 4.06 cm; 1/4 in	3.1834 msr
.56 in × 1.48 in	B7	1.43 cm × 3.74 cm; 9/32 in	0.9875 msr

Table 3.2: Apertures used for Experiment 268: the *A* apertures are machined from 1/2 inch thick brass, the *B* apertures are 3/4 inch thick. Horizontal *(h)* and vertical *(v)* acceptances can be calculated from the corresponding dimensions and the distance from the target (71.2 cm). For the rectangular apertures the radius of curvature *(r)* of the corners is given in inches.

Tgt	^{40}Ca	^{40}Ca	^{42}Ca	^{44}Ca,old	^{44}Ca,new	^{48}Ca
t	15.2(4)	5.2(2)	9.6(2)	28.5(1.0)	9.85(50)	15.2(2)
^{40}Ca	99.965(10)		5.08	1.25(2)		2.20(5)
^{42}Ca	0.009(3)		93.71	0.04(1)		0.03(1)
^{43}Ca	0.002(1)		0.334	0.02(1)		<0.01
^{44}Ca	0.022(3)		0.869	98.68(2)		0.07(1)
^{46}Ca	<0.001		<0.003	<0.005		<0.005
^{48}Ca	0.002(1)		0.014	0.008		97.69(5)

Table 3.3: Targets for Experiment 268. Thicknesses *(t)* are given in mg/cm^2, abundances in %.

3.3 Targets

Table 3.3 lists the thicknesses (in mg/cm^2) and compositions of the Ca targets (abundances in %) as determined by Oak Ridge National Lab. Uncertainties are given where available. The old ^{44}Ca (28.5 mg/cm^2) and BeO (21.58 mg/cm^2) targets were destroyed early in the January 1987 run period. The thicknesses of the new ^{44}Ca and BeO targets were determined at IUCF. The ^{44}Ca thickness was measured with a micrometer; the BeO thickness (22.26(7) mg/cm^2) was calculated from the target mass and the known areal density of BeO (the error is likely to be greater than the above quoted one but probably less than 5 percent).

A previous measurement of the BeO thickness with a micrometer had yielded 21.99 mg/cm^2 and all the ^{9}Be and ^{16}O cross sections were calculated with this value. An overall normalization factor of 0.988 was therefore applied

to the final data to reflect the new measurement.

3.4 Spectrometer

3.4.1 The K600 Spectrometer

A schematic drawing of the K600 spectrometer is shown in Figure 3.2. The spectrometer is of the QDD type and operates in HHH (**H**orizontal Dispersion, **H**orizontal Scattering, **H**orizontal Analysis) momentum-loss configuration. The main components of the spectrometer are an entrance quadrupole (Q) and two dipoles (D). The K600 entrance quad provides most of the vertical focusing of the spectrometer. It should be adjusted such that the cross-over of the vertical and horizontal focal planes (which are inclined steeply relative to each other) occurs near the central momentum ray. This ensures that the vertical image size at the extreme ends of the focal plane is within the vertical acceptance of the detectors. In the absence of any y-information, for the duration of our experiment the quad current was set according to ion-optics calculations based on measured quad properties. A triangular shaped poleface winding within the second dipole, the K-coil, acts effectively as a combination of a dipole and quadrupole lens. It modifies the $(x \mid \theta)$ transport coefficient and thereby corrects kinematic image broadening by keeping the image plane location fixed (for $k = p^{-1}dp/d\theta > 0$ the image plane moves downstream and for $k < 0$ upstream by a distance $l_k = -\frac{M_x D_x k}{1+(\theta|\delta)M_x k}$). The H-coil is another poleface winding which is located in the first dipole. It is of elliptical shape and provides a combination of dipole

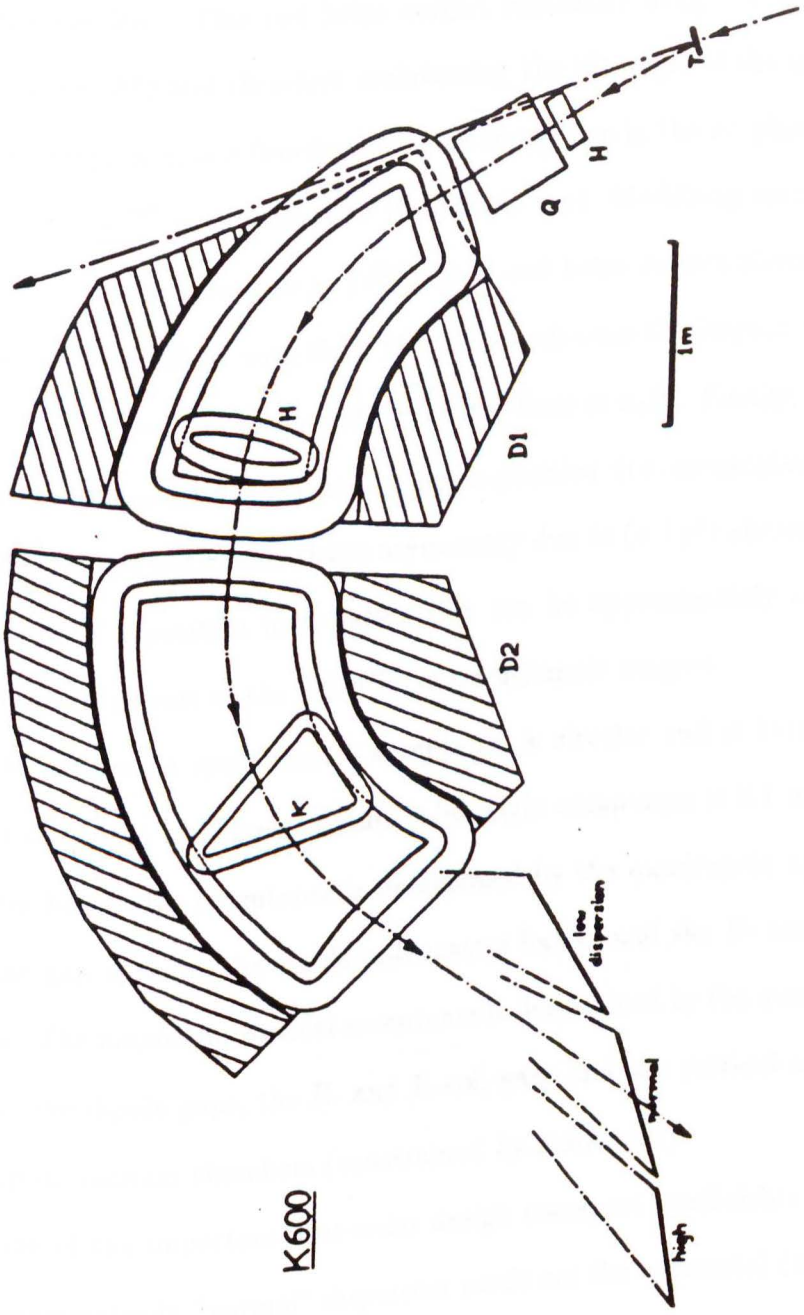

Figure 3.2: K600 Spectrometer

and hexapole lens. This coil helps correct kinematic image broadening by modifying $(x \mid \theta\delta)$ and therefore maintaining the tilt angle of the image line (since the dispersion is a function of k, the image line in the xz plane rotates by $\tan\psi = -\frac{(x|\theta\delta)}{M_\theta D_x}$ with respect to the central ray). Modifying second-order transport coefficients such as $(x \mid \theta^2)$, the H-coil helps correct aberrations—in Appendix C we show with RAYTRACE simulations the impact of the H- and K-coils on the focal plane and on nuclear lines in $x_f\theta_f$. Finally, for large vertical acceptances, a sharp line in the x-position (i.e. momentum) spectrum may exhibit noticeable shape asymmetry due to $(x \mid y^2)$ aberration. In the absence of y-position information this can be approximately corrected on-line by adjustment of the K600 entrance hexapole magnet.

The maximum spectrometer acceptance is circular and is horizontally and vertically ± 44 mr; the maximum solid angle acceptance is 6.1 msr. The maximum horizontal acceptance is determined by the quadrupole aperture, the dipole-gap spacers, the dipole anti-scatter baffles and the H- and K-coil supports. The maximum vertical acceptance is determined by the quadrupole aperture, the dipole gaps, the H- and K-coil gaps and the vertical openings of the dipole vacuum chambers (constrained by main coils).

Some of the important first-order design transport coefficients for the K600 spectrometer in "normal" dispersion mode are the horizontal (vertical) linear magnification $M_x = (x \mid x) = -0.53$ ($M_y = (y \mid y) = -5.7$), the horizontal (vertical) angular magnification $M_\theta = (\theta \mid \theta) = -1.90 \approx M_x^{-1}$ ($M_\phi = (\phi \mid \phi) = -0.17 \approx M_y^{-1}$), and the spatial dispersion $D_x = (x \mid \delta) =$ 8.4 m. An astigmatic double focus implies that to first order both $(x \mid \theta)$

	HRS	*K600*
Maximum Proton Energy	800 MeV	493 MeV
Bend Radius	3.5 m	2.1 m
Solid Angle Acceptance	3.6 msr	6.1 msr
Resolving Power ($R = p/dp$)	10^4	$\approx 3.5 \times 10^4$
Angular Resolution	0.8 mrad	$\approx$3 mrad
Dispersion	18.2 m	8.4 m

Table 3.4: Comparison of HRS and K600 specifications. The HRS resolving power is given for a 20 MeV bite.

and $(y \mid \phi)$ must vanish.

3.4.2 The HRS Spectrometer

The HRS spectrometer, as the K600 spectrometer, is of the QDD type and utilizes the momentum-loss principle. The mode of operation is VHV (**V**ertical Dispersion, **H**orizontal Scattering, **V**ertical Analysis), a configuration which effectively decouples scattering angle and energy. Table 3.4 compares some of the important design specifications of HRS with those of the K600 (normal dispersion mode) [Zei 71, K600 P, K600 L].

3.5 Detectors

We used two types of detectors in the focal plane: plastic scintillators and multi-wire vertical drift chambers (VDCs) which served as horizontal (x, θ) detectors. At the time of our experiment the proposed horizontal drift chambers (HDCs) which would have provided vertical (y, ϕ) information were

not yet available.

3.5.1 Scintillators

Two plastic scintillators paddles with photomultiplier (PM) tubes on either ends were used in all our run periods (the two scintillation detectors used in January 1987 were originally designed for pion detection with the QDDM and covered only slightly more than half of the available focal plane). Both paddles were mounted behind the wire chambers. While the front scintillator (S1) had a thickness of 1/4 in, the rear scintillator (S2) had a thickness of 1/2 in. During the 100 MeV runs a 1/16 inch aluminum absorber sheet was inserted between S1 and S2. For the 200 MeV run periods a combination of two 1/16 inch and one 0.09 inch aluminum sheets was used. To find the correct operating voltages for the photomultiplier tubes the standard *plateau method* was used. This involves measuring the count rate as a function of the applied PM voltage and then fixing the voltage in the middle of the plateau. The scintillator stack has several functions. S1·S2 coincidence provides an *event trigger* and also a position-independent *start signal* for the VDC drift time measurement. Plotting ΔE_1 versus ΔE_2 allows *particle identification* and *background rejection*.

3.5.2 Wire Chambers

The front VDC plane (X1) is positioned along the focal plane. The rear plane (X2) is parallel to X1 and is mounted at a distance of 103.2 mm from X1. The horizontal offset between the chambers is 79.2 mm, i.e. channel 0

of X1 coincides with channel 792 of X2 (10 channels $\equiv$ 1 mm). Each chamber consists of 160 gold-plated 20 μm tungsten *sense wires* with a spacing of 6 mm. Located between each pair of sense wires are two 50 μm *guard wires* (Be-Cu) such that the overall wire spacing is 2 mm. All the wires are held at ground potential. The active detector area is approximately 100 cm horizontally and 7 cm vertically. Two stretched 1 mil graphite-coated aluminum mylars constitute the cathode planes (cathode-to-cathode spacing: 12.7 mm, operating voltage: ≈ -4.5 kV) and serve at the same time as gas barriers. The filling gas is a mixture of 50% argon gas and 50% isobutane quencher gas. This gas mixture is bubbled through refrigerated n-propanol, an antipolymerizing agent. During the experiment a steady gas flow was maintained. At the operating voltage the electron drift velocity saturates to 46.1 mm/μs. As in the case of the scintillators, the correct operating voltages were found by a plateau measurement in which for a given threshold the efficiency is plotted as a function of the applied chamber voltage. For this measurement all the wires should be illuminated uniformly by the beam. The definition of the efficiency usually includes the requirement of good hit patterns in the chamber.

3.6 Electronics

3.6.1 Scintillator Electronics

Signals from the four scintillator photomultiplier tubes (the high-momentum side tubes are denoted by P, the low-momentum side tubes by N)

are divided by linear fans (PS 744) into signals going to charge sensitive analog-digital converting units (LRS 2249 QDCs) for pulse-height analysis and into signals going to constant-fraction discriminators (EG&G 934 CFDs) (c.f. Figure 3.3). CFD output signals are fed into time-digital converters (LRS 2228A TDCs) and each pair of P and N signals is also collected in a mean-timer unit (LRS 624) to generate a position-independent timing signal for each of the two scintillators.

The rear scintillator timing signal is the signal we want to use to define a START for the wire TDCs. Due to its thickness, the energy loss in S2 is larger than in S1 and, hence, the signals are stronger. Also, the front scintillator and the aluminum plate(s) eliminate most of the noise[2]. Therefore, the S1 mean-timer signal should be delayed with respect to the corresponding S2 signal. Pulse shaping and delay of the S1 signal are done with a computer programmable delay (IUCF), the S2 mean-timer pulse is shaped in a discriminator unit (LRS 821). Figure 3.3 schematically shows the pulse shapes and their relative timing. Finally, the S1 and S2 signals are collected in a PS 755 module with coincidence level two. The coincidence unit is vetoed by the run gate and the CAMAC read from the output register (JORWAY 41).

3.6.2 VDC Readout Electronics

For each VDC there are ten printed boards (LRS 2735B) with four amplifier chips per board. Each board thus amplifies and discriminates signals

[2] The fast circuit in March 1988 used S1 as a basis for timing.

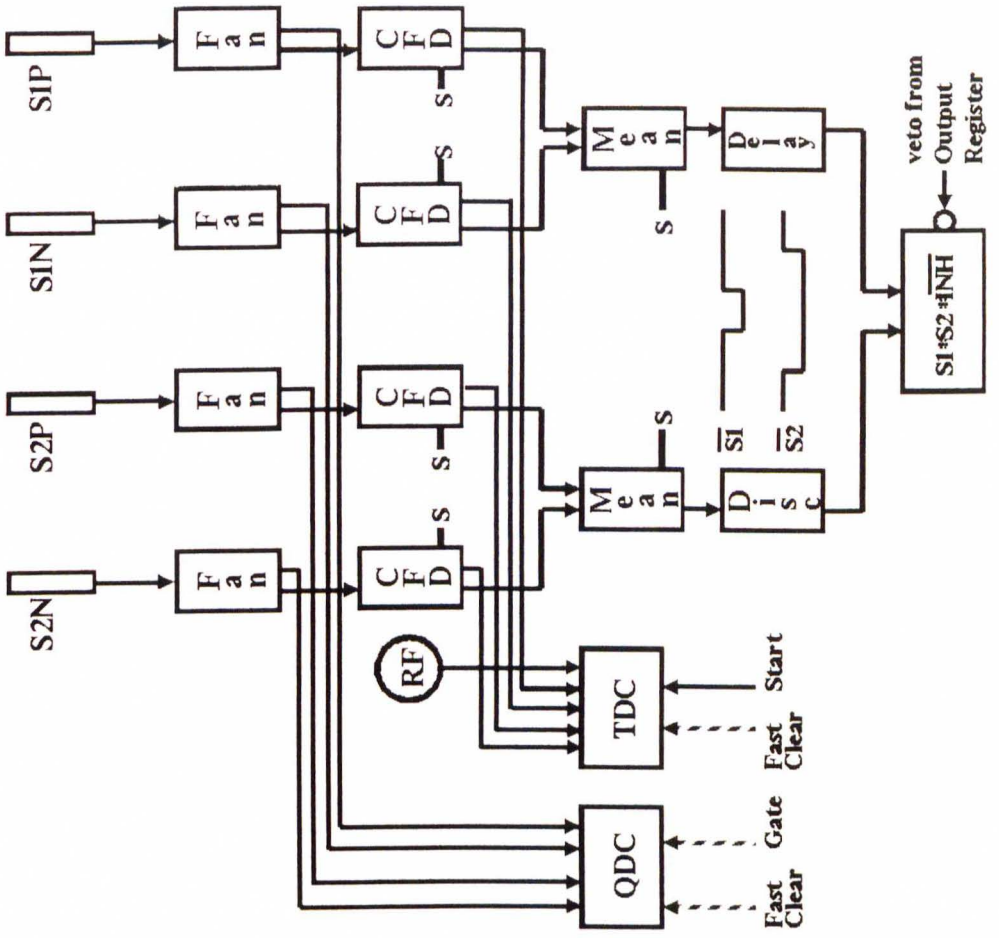

Figure 3.3: Scintillator Electronics

of sixteen consecutive wires. This is schematically shown in Figure 3.4. At some stage of the experiment we were concerned about cross talk between wires within a chip. IUCF technicians ascertained that either the first wire or the fourth wire of each chip picked up noise from the other three wires, i.e. either wires 1, 5, 9 and 13 or wires 4, 8, 12 and 16 on each card showed most cross talk. It was also determined that the cross talk signal followed the original signal by about 25 ns. In the March 1988 run period we were able to control the cross talk problem by setting the threshold[3] values of each card individually.

Signals from consecutive wires are fed to five consecutive multiplexers (IUCF MUX) via a sixteen-line ribbon cable (total delay $\approx$ 210 ns), such that every fifth wire is connected to the same MUX. The IUCF Multiplexer is a single width CAMAC module which accepts 32 ECL-level differential inputs from two LRS 2735B wire chamber preamplifier cards or their equivalents, and a gate input (NIM). During a gate, a fast OR output is generated and latched for the first event (available at a front panel connector). Events are also written into registers for CAMAC readout. Two of the three registers, A and B, are simple 16 bit registers, corresponding to the upper and lower 34-pin connectors on the module, respectively. Into these, events are latched directly during a gate. The third register, register E, provides encoded information about single or multiple events (bit 16), module address (bits 6–11) and the address of the highest number wire being hit (bits 1–5). If no valid

[3] Another indicator for insufficiently high thresholds is an increase in the observed number of so-called multiple hits, see Chapter 5.

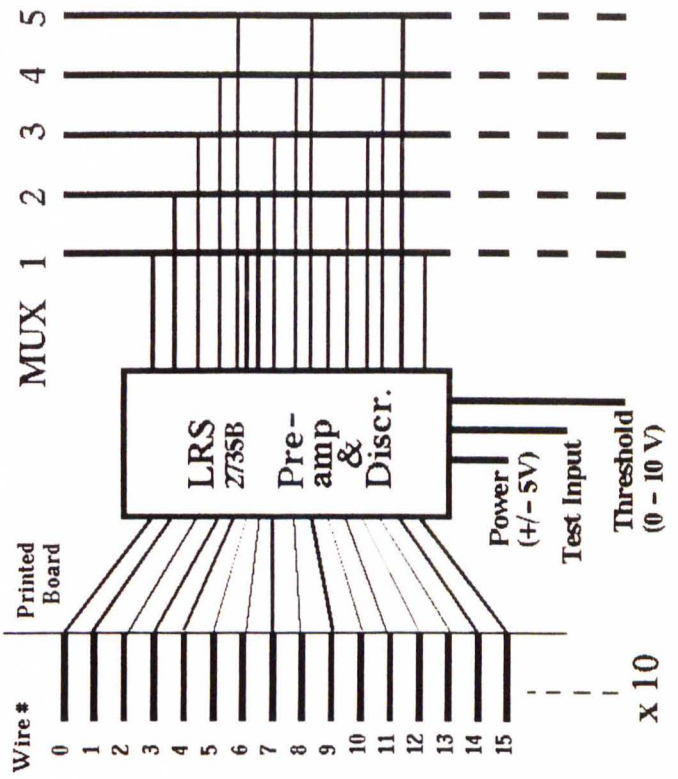

Figure 3.4: Wiring of LRS 2735b Printed Board

events have occured, all the bits are set to zero. To limit multiple events, the gate is internally shortened to a maximum of 33 ns following the first event. The module is capable to operate both in a normal or a fast 400 ns CAMAC cycle.

All MUXs are gated by a S1·S2·$\overline{\text{BUSY}}$ coincidence which is distributed by a 16-fold fan (Figure 3.5). The fan also provides a common START signal for the ten wire TDCs (LRS 4210). An OR output from a MUX is discriminated (LRS 821) and serves as a STOP for its TDC. In March 1988 a sum of the five front (and rear VDC discriminators, respectively) was used to form a coincidence (see next section).

3.6.3 Coincidence Electronics

The coincidence circuit is shown in Figure 3.6. There are several inputs to the coincidence circuit. One is the scintillator coincidence which has already been discussed. The output register has two outputs: bit 1 is the run gate and bit 2 is set while the CAMAC is being read. When the run gate is off or the CAMAC is being read or the spin valid bit is not set (i.e. during spin flip) or in the case of a B-Hive alarm, an inhibit (INH) is generated in a logic fan (LRS 429A) which inhibits all the scalers (Event 10), and via the scintillator coincidence all of the further regular event (Event 4) processing (e.g. gates on the MUXs and STARTs on the wire TDCs). Also, a scintillator coincidence via a gate and delay generator (EG&G GG8000) generates a BUSY signal and vetoes accepting any new events until processing of the old events has been completed. A BUSY signal can also be generated via

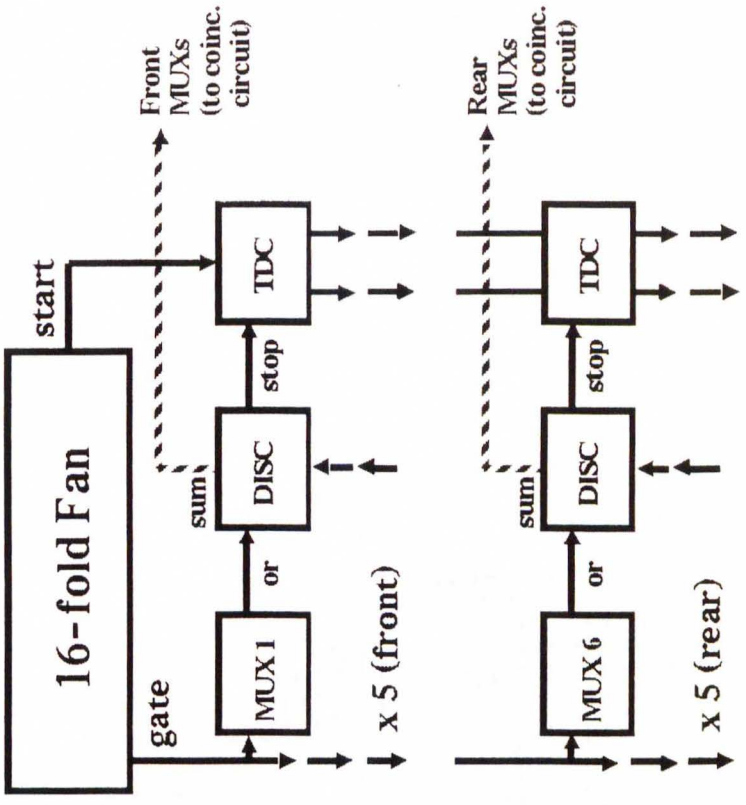

Figure 3.5: VDC Logic Circuit

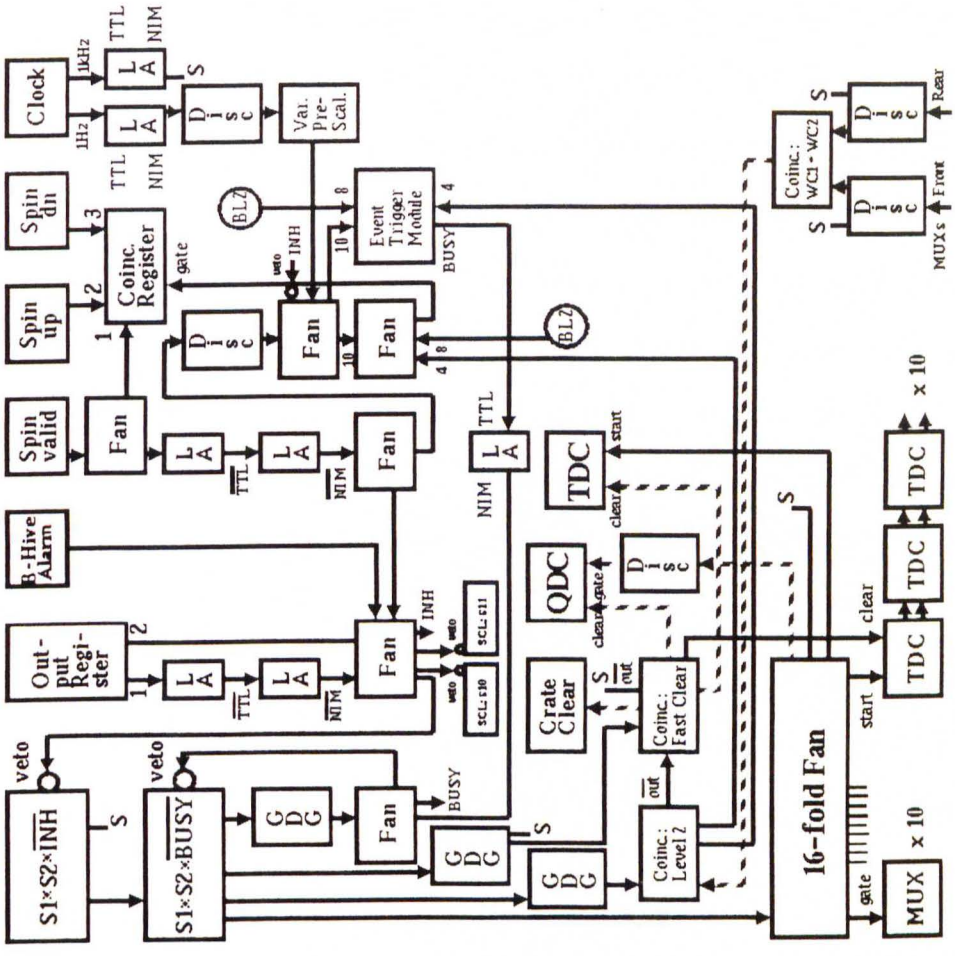

Figure 3.6: Coincidence Circuit

the LAMPF Event Trigger Module by a scaler event or a beam line 2 (BL 2) event (Event 8). The spin bits (valid, up, down) are collected in the coincidence register (LRS 2341) which is gated by either an INH, a spin not valid, an Event 8 or Event 10. The B-Hive alarm was temporarily disabled during some of the run periods. The connection between the clock and the coincindence circuit was disabled early in the experiment since we decided to read scalers during the spin flip. In March 1988, a fast coincidence between S1 and S2 triggered the STARTs for the TDCs and opened the MUX and QDC gates; a second coincidence tested for hits in both chambers (PS 755). A fast CLEAR halted focal plane processing and issued a crate CLEAR in the case of one-chamber-only hits; also, the event trigger to the CAMAC crate was suppressed. When the level 2 coincidence is set to 1-fold (all the events from S1·S2·$\overline{\text{BUSY}}$ pass) and the fast clear coincidence to 3-fold, the fast CLEAR is effectively disabled and the circuit identical to the previously used one.

3.6.4 Electronics for Integrators and BL 2

Signals from the left and right integrators are passed through gate and delay generators and are discriminated before they are fed into coincidence units and scalers (c.f. Figure 3.7). A BUSY vetoes updating of the corresponding scalers (INH also inhibits all scalers). Both BUSY and INH gate through a logic fan and a 2-fold coincidence with the BL 2 strobe any BL 2 signal processing in the LRS 3511 ADCs.

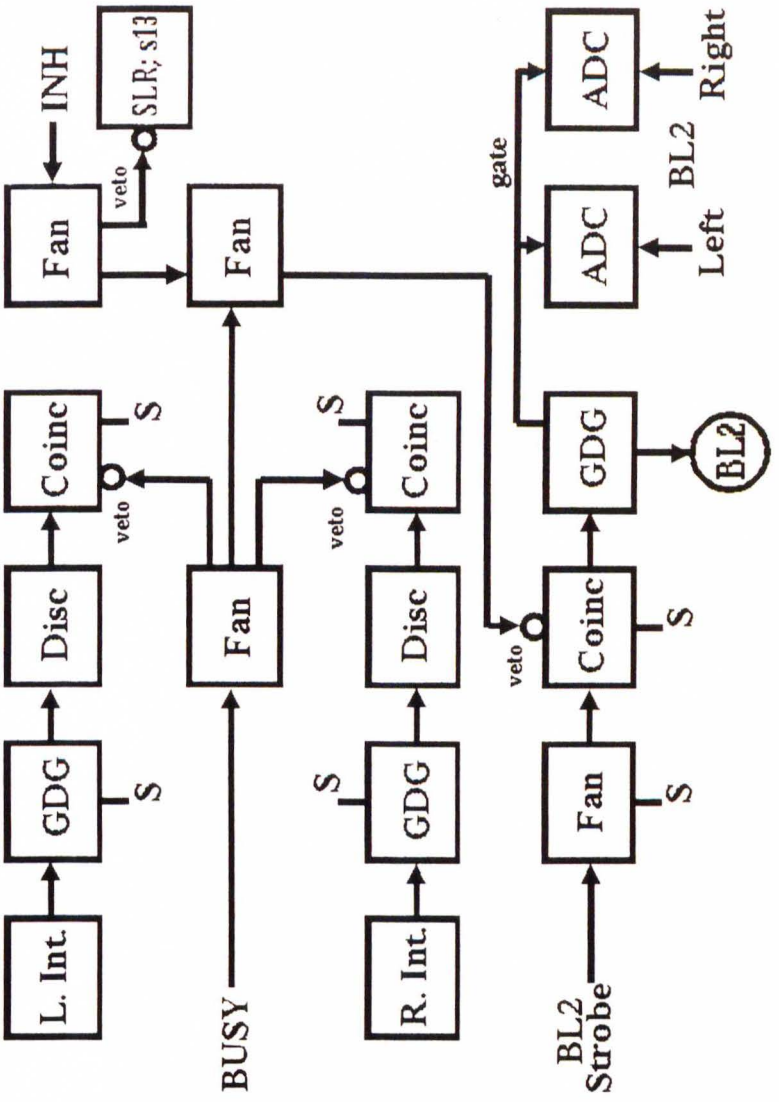

Figure 3.7: Electronics for Integrators and BL 2

3.6.5 Data Acquisition

With exception of the integrator and BL 2 circuit components which could be found in CAMAC crate 1 (data acquisition area) all the other electronics was gathered in crates 2 and 3 in the K600 cave. Data from these crates reached crate 1 and the MBD through a Branch Highway. A UNIBUS fed data to a VAX 11/750.

4 Calibrations

4.1 Matching Between Beam Line and Spectrometer

In principle, the energy spread of the beam determines the available energy resolution for an experiment. As a result, in order to achieve a highly monochromatic beam for high resolution, the greater part of the primary beam from the accelerator has to be discarded after the energy analysis on energy defining slits. Of course, this severely limits the available beam intensity. In contrast, dispersion-matching systems are able to make use of essentially all the beam, at the price that the beam has to be dispersed spatially across the target. In this way, at each point on the target a highly monochromatic beam can be provided. In the case of energy-loss spectroscopy the desired information gained from a measurement is the scattering angle and the state of the residual nucleus. If, as in the case of our experiment, the cross section varies very slowly with energy, e.g. there are no sharp resonances, only the momentum difference between incident and outgoing particles need to be determined. This may be accomplished by properly matching the beam to the spectrometer. It is then not necessary, or even possible, to determine the point on the target from which an event originated. In energy-loss configuration the accelerator, beam transport, and spectrometer form an achromatic system that images the beam onto the spectrometer focal plane. Each monochromatic component is focussed on the target (or slightly beyond the target), but the beam is dispersed spatially across the target to match the spectrometer [Ber 79, Zei 71].

On the way from the cyclotron extraction to the detector plane the coordinates of a particle undergo several transformations. If we denote the (horizontal) coordinates at the entrance slit of the beam line system by $(x_0, \theta_0, \delta_0)$ and the ones in the detector plane with (x, θ, δ) the transformation in the bending plane can be described as

$$\begin{pmatrix} x \\ \theta \\ \delta \end{pmatrix} = \mathbf{S} \cdot \mathbf{T} \cdot \mathbf{B} \cdot \begin{pmatrix} x_0 \\ \theta_0 \\ \delta_0 \end{pmatrix}, \tag{4.1}$$

where $\mathbf{S}$ is the transport matrix representing the spectrometer, $\mathbf{T} = T \cdot \mathbf{1}$ is the target transformation which takes care of the scattering angle α and the target angle Φ, and $\mathbf{B}$ is the beam line transport matrix. In terms of the target transformation $T = \cos(\alpha - \Phi)/\cos\Phi$, the kinematic broadening factor $K = \frac{1}{p}\frac{\partial p}{\partial \alpha}$ governing the variation of momentum with scattering angle[1], and the dispersion matching factor $C = \frac{p_0}{p}\frac{\partial p}{\partial p_0}$, the transformation Eq. (4.1) can be written more explicitly as

$$\begin{aligned} x \;=\; & x_0(s_{11}b_{11}T - s_{16}b_{21}K) \\ & + \theta_0(s_{11}b_{12}T - s_{16}b_{22}K) \\ & + \delta_0(s_{11}b_{16}T - s_{16}b_{26}K + s_{16}C) \\ & + \theta_2(s_{12} + s_{16}K). \end{aligned} \tag{4.2}$$

In this equation the s_{ij} and b_{ij} are elements of the transport matrices $\mathbf{S}$ and $\mathbf{B}$, respectively. The ij transport matrix elements are associated with the matrix

[1] K is identical to the k factor from Section 3.4.1.

elements of Section 3.4.1 as follows: $11 \rightarrow (x \mid x) \equiv M_x$ (magnification), $22 \rightarrow (\theta \mid \theta) \equiv M_\theta$ (angular magnification), $12 \rightarrow (x \mid \theta)$ (point-to-point focus), $21 \rightarrow (\theta \mid x)$ (parallel-to-parallel focus), $16 \rightarrow (x \mid \delta) \equiv D_x$ (spatial dispersion), and $26 \rightarrow (\theta \mid \delta) \equiv D_\theta$ (angular dispersion). The angle θ_2 is defined by the angular acceptance of the spectrometer. When properly matched, the coefficients of θ_0, δ_0 and θ_2 vanish. The (momentum) resolving power of the matched system is then

$$R = \frac{p}{dp} = \frac{1}{x_0} \frac{s_{16}}{M_{\text{ov}}}, \tag{4.3}$$

where the *overall magnification* is given as $M_{\text{ov}} = s_{11} b_{11} T - s_{16} b_{21} K$. Therefore, the resolution of the total system is a function of K and will usually become worse for large values of K. Tuning the spectrometer such that the coefficient of θ_2 vanishes is done in the K600 with the K-coil; this so-called *kinematic displacement* of the focal plane has been described earlier in Section 3.4.1. Tuning the beam to eliminate the influence of the momentum spread in the beam on the image width restricts the dispersion of the beam line. From Eq. (4.2) we see that the coefficient of δ_0 vanishes if

$$b_{16} = -\frac{s_{16}}{s_{11}} \left(\frac{C}{T} - b_{26} \frac{K}{T} \right). \tag{4.4}$$

For $K = 0$, i.e. light particles on heavy targets, one recovers the well known *dispersion matching condition*

$$D_{\text{beam}} = -\left(\frac{D_x}{M_x} \right)_{\text{spec}} \frac{C}{T}. \tag{4.5}$$

Because C and T are always close to unity[2], this implies that the dispersion

[2] In transmission configuration where $\Phi = \alpha/2$, the target transformation T is exactly unity.

of the beam has to be equalized by the resolution s_{16}/s_{11} of the spectrometer. Finally, for a finite K value the beam line tune has to fulfill the condition

$$\frac{b_{12}}{b_{22}} = \frac{s_{16}}{s_{11}}\frac{K}{T} \equiv L, \tag{4.6}$$

called the *kinematic defocusing* of the beam at the target. The quantity L represents the defocusing distance. This step eliminates kinematic broadening due to the angular spread of the incident beam by forming a correlation at the target between position and incident angle (see Figure 4.1) [Mar 83, K600 L]. A prerequisite for kinematic defocusing to work is a convergent beam. Convergence or divergence of the beam, and also the beam angle and its temporal fluctuations, can be monitored to a certain extent with the left-right integrator asymmetry.

Quadrupoles Q8, Q9 and Q10 in BL 8 between the QDDM and the target are used to control both kinematic defocusing and dispersion matching. Also, the vertical spot size can be varied with Q9. For 120 MeV and 200 MeV beam energies extensive grid searches covering the space of relative changes $\delta Q_i = \Delta Q_i/Q_i$ (i = 8, 9, 10) in the quadrupole strengths were performed. The result of these investigations was that in this space there is a more or less well defined "valley" where the beam is correctly (de)focussed. Subsequently, one moves along this valley until the dispersion is matched. For this task we used a full target (usually either a Au or Ca target) and the three-hole hodoscope which was mentioned in Chapter 3. First, the correct K- and H-coil settings were verified by inspecting the slope and the curvature of the elastic line in an $x_f\theta_f$ histogram without the hodoscope. Then,

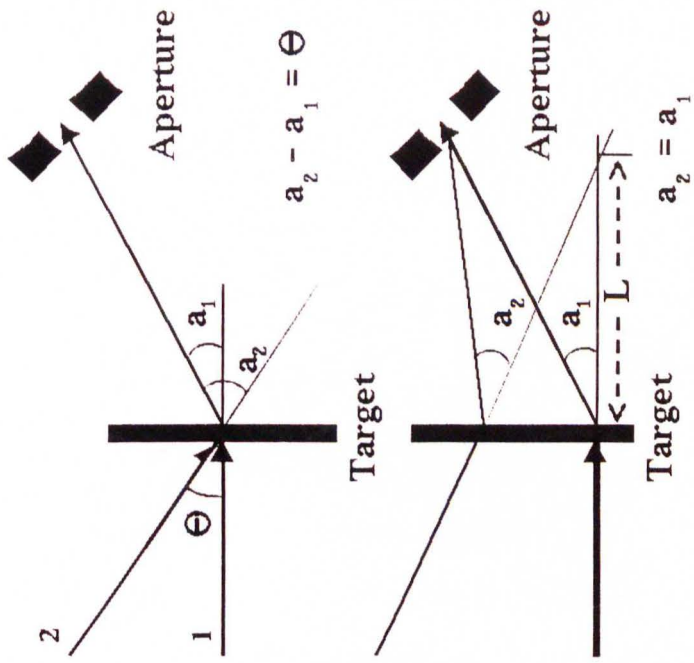

Figure 4.1: Kinematic defocusing; if a convergent beam (the extreme rays of the beam define a cone with opening angle Θ) is defocused by the correct distance L, the scattering angle a becomes independent from the position on the target.

the center hole of the hodoscope was positioned such that a section of the elastic line with $\Delta\theta_f \approx 50$ mrad appeared in $x_f\theta_f$ between approximately 550 and 650 mrad (i.e. in the good region of the focal plane). Subsequently, we subdivided this section by two or three software windows which defined different positions on the target and gated 1-d x_f histograms on these windows. With the help of the 1-d histograms we determined both (de)focusing and dispersion matching: the former was tested by examining the FWHM line widths, the latter was evaluated from the difference of the centroid positions found in the histograms gated on the low-θ_f and high-θ_f windows, respectively. Figure 4.2, taken from the March 1988 run book, shows sample histograms. The procedure is to first find the focus valley by varying Q8 and then adjusting Q9 and Q10 according to

$$\begin{aligned} \delta Q_{10} &= \frac{1}{a}\delta Q_8 \\ \delta Q_9 &= \frac{1}{6}(\delta Q_8 + \delta Q_{10}), \end{aligned} \tag{4.7}$$

where $a = 4.23$ (3.24) for 120 MeV (200 MeV); this ensures that we approach the focus valley perpendicularly. The beam is correctly (de)focussed when the FWHM line widths are minimized. Then, for dispersion matching we vary Q10 and adjust Q8 and Q9 according to

$$\begin{aligned} \delta Q_8 &= -\frac{1}{a}\delta Q_{10} \\ \delta Q_9 &= \frac{1}{6}(\delta Q_8 + \delta Q_{10}). \end{aligned} \tag{4.8}$$

This ensures that we now go parallel to the bottom of the focus valley and thus maintain the correct focus. The dispersion is matched when the low-θ_f

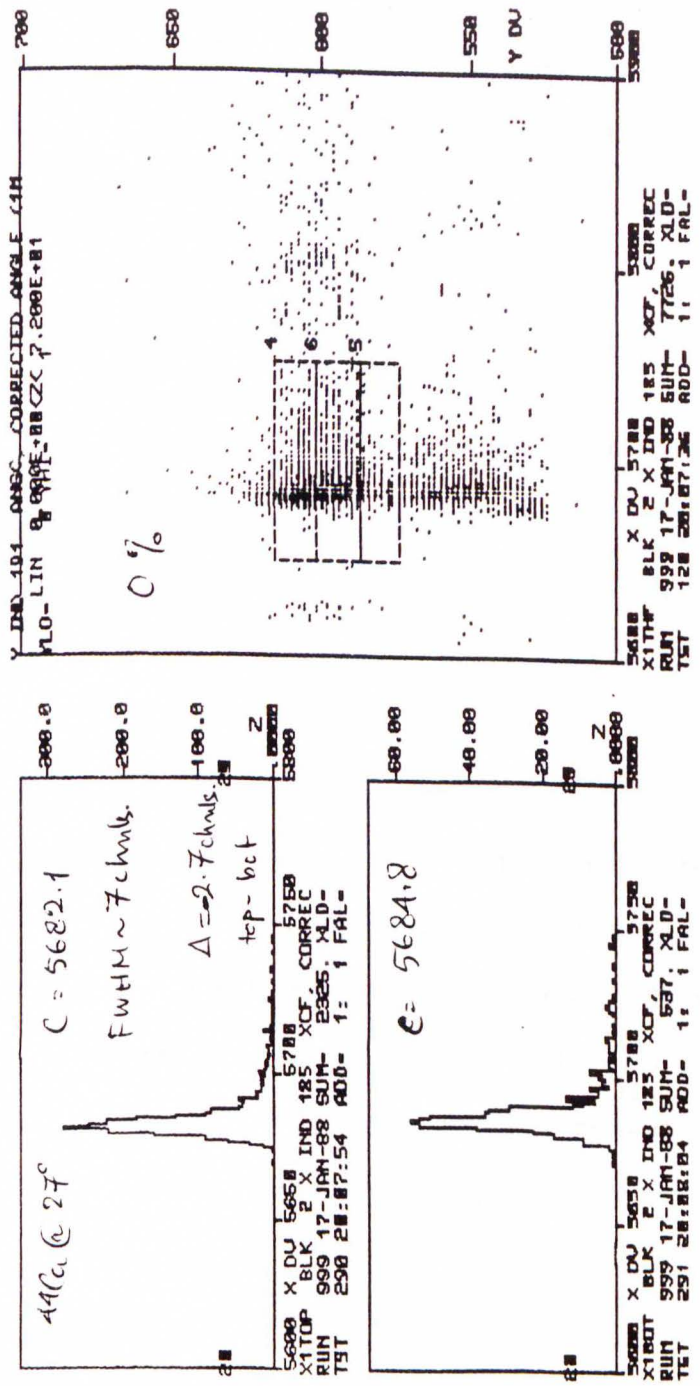

Figure 4.2: Kinematic defocusing and dispersion matching. The beam is correctly (de)focussed when the FWHMs are minimum; when the dispersion is matched correctly, additionally the centroid positions are the same.

and high-θ_f centroid positions are equal. Finally, in order to maintain dispersion matching once it was achieved for a particular k for different kinematic values, the K-coil and the quadrupoles were corrected with $d\mathrm{K}/dk = +1586$, $dQ_8/dk = -2138$, $dQ_9/dk \approx 0$, and $dQ_{10}/dk = +1466$ (K600 Development Logbook #9, page 123). With this prescription, ^{16}O peak widths of $\sim$120 keV (dispersion matched for a gold target) could be reduced to $\sim$60 keV.

Expanding the angle θ in the fashion of Eq. (4.2) for x, reveals the dependence of the scattering angle on the incident momentum. Therefore, the sometimes large spread of the dispersed beam on target could lead to significant uncertainties in the scattering angle, especially if the illumination of the target varies with different beam tunes, unless the *angular dispersion* of the beam is properly adjusted. Correct angular dispersion will also ensure that the cross section will be stable against small fluctuations in the cyclotron beam energy. The goal, therefore, is to tune the beam such that, for different beam rays across the target (for a dispersion matched beam these different rays correspond to different beam momenta), the incident angle changes in a way that leaves the scattering angle the same. In other words, if R is the distance from slit 2 in BL 8 to the target and T is the target transformation, one has to adjust the angular dispersion b_{26} of the beam such that $b_{26} = b_{16}T/R$.

To test whether the angular dispersion is correctly matched one can shift the beam across the target with the QDDM bending magnet and record the cross sections for each beam position. Usually, this test is performed with a BeO target because the beam creates a clearly visible luminescent

spot on the target, thus allowing an accurate position determination. The spectrometer angle is chosen to be in a steep region of the cross section angular distribution to optimize the sensitivity to changes in the scattering angle (for example, at 22° the slope of the 100 MeV ^{16}O elastic cross section is about 25%/deg). A $(\theta \mid \delta)$ correlation for a dispersion matched beam will translate scattering angle dependence of the cross section into a position dependence.

This position dependence can be removed if the angular dispersion is properly matched. As described in [Ber 89], the spatial and angular dispersions on the target can be decoupled by shifting the focus of the QDDM analyzing system into the middle of quadrupole Q7 of BL 8. It was demonstrated that with appropriate settings of the kinematic coils within the QDDM the angular dispersion can then be varied using Q7 until the scattering angle into the spectrometer is nearly independent of the beam ray on target. The spatial dispersion on target, the dispersion matching, and resolution are not affected by this procedure. This procedure was not available, however, at the time of our experiment. Therefore, we are not sure whether our beam was indeed properly angular dispersion matched, although the aforementioned "slope" test was performed and at the time seemed to indicate so.

4.2 Scattering Angle

During the experiment the spectrometer angle was set with help of an electronic encoder. The calibration which related the encoder reading to the

spectrometer angle was

$$\Theta_{\mathrm{spec}} = \Theta_{\mathrm{enc}} - 0.115(8). \tag{4.9}$$

For each scattered event an angle θ_f in the focal plane is determined. This angle is related with the angle at the target (Θ_{tgt}) and with the scattering angle[3] (Θ_{scatt}) according to

$$\Theta_{\mathrm{scatt}} = \Theta_{\mathrm{spec}} - \Theta_{\mathrm{tgt}} + \Delta\Theta, \tag{4.10}$$

where $\Delta\Theta$ is the *scattering angle offset*. The ability to reconstruct the scattering angles from the focal plane quantities is especially important when the acceptance is to be divided into smaller bins[4]. Although we only analyzed unbinned position spectra and employed the angle at the target almost exclusively only for background rejection, we want to outline in the following our calibration of Θ_{tgt}. For the calibration we used a multislit aperture which was mounted on a 1/2 inch thick brass frame. The width of the slits was $\pm$1.2 mrad, with exception of the center slit which had a width of $\pm$2.3 mrad. The centers of the seven slits defined angles of -41.587, -27.681, -13.925, 0.792 (center slit), 15.555, and 29.296 mrad at the target. For the calibration we

[3] While the scattering angle is counted positive to the *left* of the beam (counterclockwise), the angle at the target is counted positive to the *right* of the beam (clockwise).

[4] Binned spectra are x_f spectra gated on Θ_{tgt}; the observed Θ_{tgt} spectrum shape $y(x)$ for an angular acceptance $2a$ results from the convolution of the cross section angular distribution $D(x)$, an acceptance function $A(x)$ which is unity for $|x| \leq a$ and zero otherwise, and a (Gaussian) resolution function $R(x - x') = \frac{1}{\sigma\sqrt{2\pi}} e^{-\frac{1}{2}\left(\frac{x-x'}{\sigma}\right)^2}$: $y(x) = D(x) \otimes A(x) \otimes R(x)$. For the simplest case where $D(x) \approx D$, a short calculation yields $y(x) = \frac{D}{2}\left\{\mathrm{erf}\left(\frac{x+a}{\sigma\sqrt{2}}\right) - \mathrm{erf}\left(\frac{x-a}{\sigma\sqrt{2}}\right)\right\}$, where *erf* is the error function; the quantities σ and, if unknown, D can be obtained from fitting a Θ_{tgt} spectrum by $y(x)$.

used a BeO target (18°, 100 MeV, $k = p^{-1}dp/d\theta = 0.022$) and a ^{197}Au target (24°, 100 MeV, $k = 0.002$). The slits generate for each nuclear line distinct "splotches" in a $x_f\theta_f$ histogram. Gating on these splotches allows to associate unambiguously the x_f and θ_f coordinates of each event with its Θ_{tgt} value. The three values x_f, θ_f and Θ_{tgt} for each event were stored in a file as "rays". The angle at the target, Θ_{tgt}, was then fitted as a polynomial in terms of the focal plane quantities, x_f and θ_f. Using the form

$$\Theta_{tgt} = a + bx_f + c\theta_f + dx_f\theta_f + e\theta_f^2 \tag{4.11}$$

for the BeO target, we found the following values for the coefficients and their relative uncertainties:

Coefficient	*Value*	$\pm\Delta$ (%)
a	−3.01048E+02	0.7
b	−2.27857E−02	7.0
c	+5.78602E−01	1.3
d	−6.23202E−05	4.3
e	−3.24431E−05	22.6

The uncertainties in this table were estimated from the error matrix. In order to achieve uniform weighting, the same number of rays for each Θ_{tgt} were used in the fit. For BeO, the centroid angles of the slits could be reproduced with this polynomial to better than 0.27 mrad, corresponding to about 0.015°. For gold, with its ten times smaller k-factor, we found that the reproducibility became correspondingly worse by a factor of ten. The reason for this worse reproducibility are, as we will show in Appendix C, the different kinematical coil settings for targets with different k.

In our experiment, the k-factor varied between about 0.002 (forward angles, heavy targets) and 0.065 (large angles, light targets), corresponding to uncertainty contributions to the calculated scattering angle of about 0.15° and 0.05°, respectively. The k-factor is plotted for ^{16}O and ^{40}Ca at both 100 and 200 MeV in Figure 4.3. We see that for ^{40}Ca at 100 MeV we should get reasonably small scattering angle uncertainty contributions which are less than 0.05° for lab angles above about 14° (for ^{48}Ca above about 17°). A more accurate Θ_{tgt} calibration would find the coefficients in Eq. (4.11) for a variety of k values. Each coefficient will then be a function of k and the value of the coefficient appropriate for a specific reaction can be gained by interpolation.

For the angle calibration to succeed, it is important that the H- and K-coils be set correctly (i.e. all the lines are straight and not tilted in $x_f\theta_f$) for both the experiment and the calibration. This is crucial since, as the RAYTRACE calculations in Appendix C demonstrate, the dipole contributions and the associated shifts in both x_f and θ_f produced by the kinematic coils are quite significant. In Appendix C we show the results for a Θ_{tgt} and a δ or *missing mass* calibration with the H- and K-coil to dipole ratios as explicit variables in the calibration polynomial. The simulation was done with rays which were generated by the code RAYTRACE. The rays were then transformed from the so-called D-coordinate system of RAYTRACE into the x_f, θ_f coordinate system of our front drift chamber wire plane. The fairly complicated polynomials which emerge describe the input rays with an accuracy of about 0.17 mrad (or about 0.01°) for Θ_{tgt} and about 0.03% for

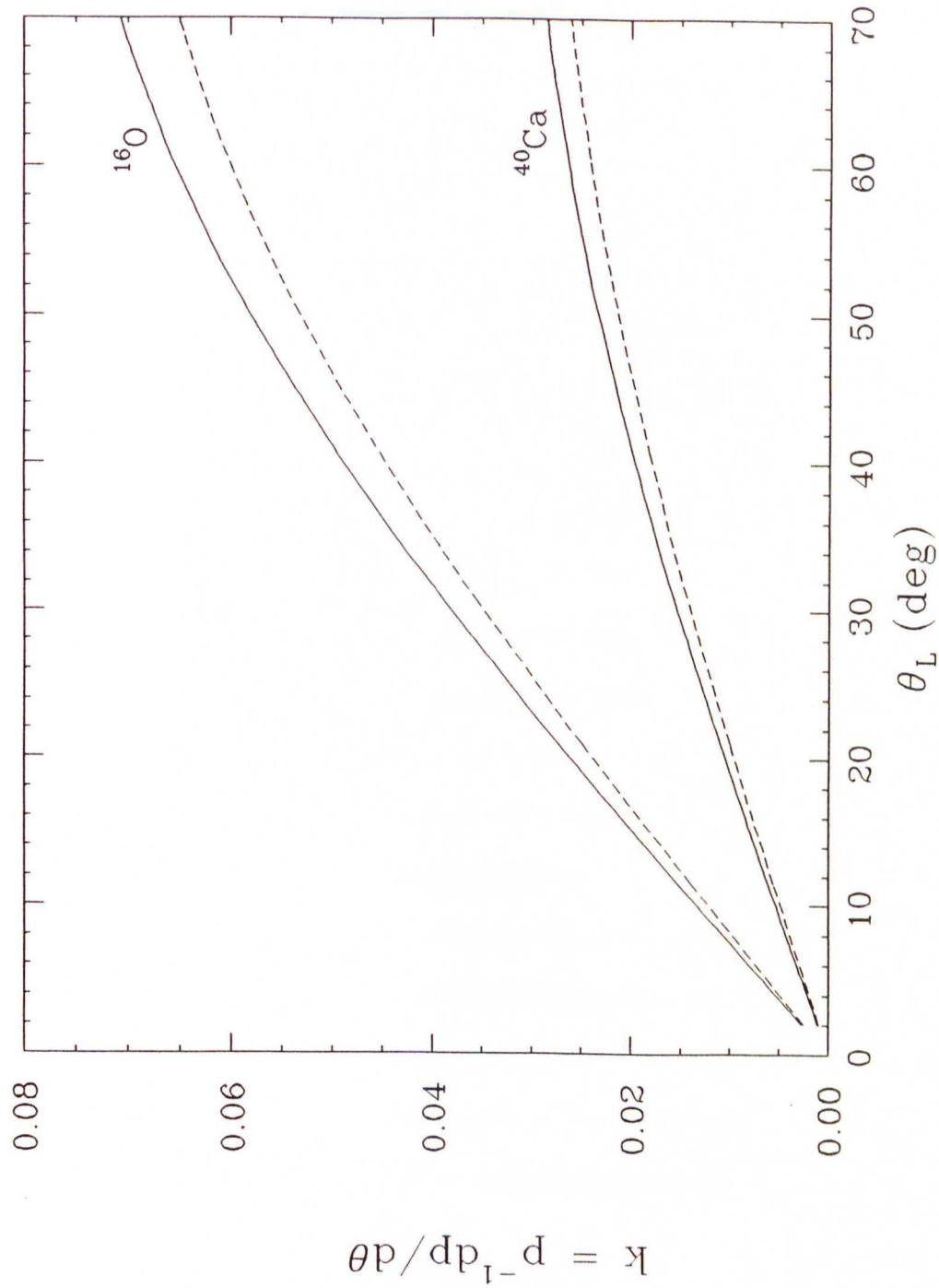

Figure 4.3: Kinematic factor $k = p^{-1}dp/d\theta$ for ^{16}O and ^{40}Ca; dashed lines are for 100 MeV, solid lines for 200 MeV protons.

δ.

The scattering angle offset was determined, where possible, with two methods. First, elastic cross sections were measured at several angles on either side of the beam. Second, the differentail recoil of ^9Be with respect to ^{16}O was used. The first method was only used for redundancy and as a check for the 100 MeV runs from January 1987. The April 1987 runs were at large angles, and a problem with the integrator scale in January 1988 rendered many of the elastic forward angle runs useless. An analysis of March 1988 data is underway. Elastic measurements for the first method were performed in 2° steps between 10° and 16° and -10° and -16°, respectively. The simplest way to graphically extract the scattering angle offset is to plot the unpolarized cross sections for these measurements, as shown in Figure 4.4, symmetrically about the midpoint at $\pm 13^\circ$ and find the intersection point, where the cross sections are the same. The distance of the intersection point to the midpoint is the scattering angle offset; if there were no offset the cross plot would be perfectly symmetric about the midpoint. In our sign convention the scattering angle offset is *positive* if the intersection point is to the left of the midpoint and is *negative* if it is to the right of the midpoint. Instead of doing the plot by hand, we fitted the data points with a quadratic function which takes into account the cross plot geometry. With

$$x = \begin{cases} \Theta_{\text{spec}} + \Delta\Theta - 13, & \text{for } \Theta > 0 \\ \Theta_{\text{spec}} + \Delta\Theta + 13, & \text{for } \Theta < 0 \end{cases} \qquad (4.12)$$

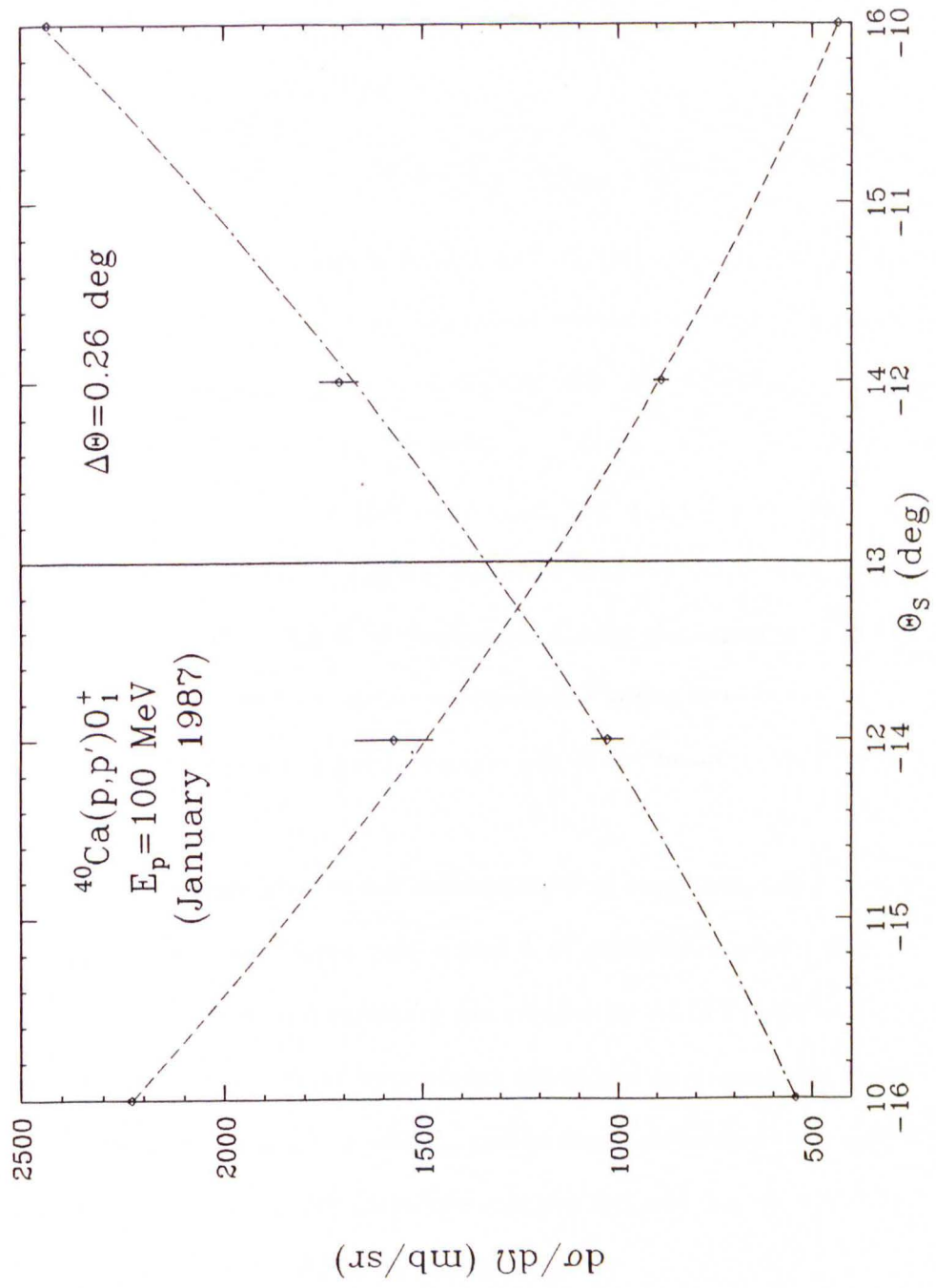

Figure 4.4: Determination of the scattering angle with the cross plot method; Θ_s is the spectrometer angle. The dashed (positive angles) and dot-dashed (negative angles) lines are fits to the data points using the same fitting function.

it can be demonstrated that the fitting function for both positive and negative angles can be accomodated by

$$y = a + b(|\Theta_{\mathrm{spec}} + \Delta\Theta| - 13) + c(|\Theta_{\mathrm{spec}} + \Delta\Theta| - 13)^2. \qquad (4.13)$$

The fitting parameters are a, b, $\Delta\Theta$ and c. Imposing the same shape for positive and negative angles makes the fit robust even with only a few data points. A simple grid search program (GRIDLS, [Bev 69]) is used to optimize the parameters. The fit to ^{40}Ca yields a scattering angle offset of 0.26°. A fit to ^{16}O elastic data, on the other hand, yields a value of 0.40° which is probably too large. It is possible, however, that the asymmetry in angle of the data set used in this fit is responsible for the discrepancy. The forward angle measurements for negative spectrometer angles were between -10 and $-16°$, while those on the positive angle side of the beam were between $+14°$ and $+18°$.

For the differential recoil method we first read the peak positions p_{xa} and p_{xb} of any convenient pair a and b of calibration peaks (e.g. ^{16}O 0_1^+ and ^{9}Be $3/2_1^-$) from the summary file created by ALLFIT [Kel ALL]. Since the peak positions for our experiment are stored as momentum losses, the experimental differential recoil Δ_{exp} can be easily calculated. It is simply the difference of the outgoing projectile energies E_{3a} and E_{3b} or, with the mass m and momentum p_1 of the incoming projectile,

$$\Delta_{\mathrm{exp}} = E_{3a} - E_{3b} = \sqrt{(p_1 - p_{xa})^2 + m^2} - \sqrt{(p_1 - p_{xb})^2 + m^2}. \qquad (4.14)$$

Using the kinematical formulae in Appendix B, a computer code calculates differential recoils $\Delta(\theta)$ as a function of the scattering angle and then mini-

mizes $|\Delta_{exp} - \Delta(\theta)|$ using a grid search. The method was used for many runs and a wide range of spectrometer angles. Subsequently, the scattering angle offset was determined as weighted average of the individual measurements. We found 0.14(7)° for the 100 MeV run in January 1987, and for the 200 MeV runs scattering angle offsets of 0.19(7)° (April 1987) and 0.06(9)° (January 1988), respectively. Thus, it appears that the scattering angle offset for January 1987 found with the differential recoil method is smaller than the one found with the cross plot method. The reason for this is as follows: since the spectrometer magnetic fields are set for ^{16}O kinematics and due to the finite horizontal angular acceptance, the Be lines appear slanted in $x_f\theta_f$ (the slope is a function of scattering angle and can be estimated from Figure B.2 in Appendix B). The projection of a Be-peak onto x_f is weighted by its cross section angular distribution within the acceptance and, therefore, yields a systematically smaller peak position. Hence, the differential recoil method systematically underestimates the scattering angle.

Over a wide range of angles the ^{9}Be $3/2_1^-$ cross section angular distribution can be approximately described by an exponential $\sigma(q) = ce^{-aq}$. For 100 MeV one finds $a = 4.26$ and $c = 1480.3$, whereas for 200 MeV the corresponding parameters are $a = 3.88$ and $c = 735.1$. To estimate the necessary correction to the scattering angle from differential recoil we evaluate the weighted average

$$\langle q \rangle = \frac{\int q\sigma(q)dq}{\int \sigma(q)dq} \tag{4.15}$$

over the acceptance $q_0 \pm \Delta$, where $2\Delta \equiv \Delta q$ is the angular acceptance expressed in terms of momentum transfer and q_0 is the central momentum

transfer. With the approximations

$$\sinh a\Delta \approx a\Delta + \tfrac{1}{6}(a\Delta)^3$$
$$e^{\pm a\Delta} \approx 1 \pm a\Delta + \tfrac{1}{2}(a\Delta)^2$$
$$(1+x)^{-1} \approx 1 - x,$$

Eq. (4.15) becomes

$$\langle q \rangle \approx q_0(1 - \frac{1}{6}a^2\Delta^2) - \frac{1}{2}a\Delta^2 + \frac{1}{12}a^3\Delta^4. \tag{4.16}$$

Evaluating this expression for the parameters quoted above, we find

$$\langle q \rangle \approx \begin{cases} q_0(1 - 0.7562\Delta q^2) - 0.5325\Delta q^2 + 0.4026\Delta q^4, & (100 \text{ MeV}) \\ q_0(1 - 0.6273\Delta q^2) - 0.4850\Delta q^2 + 0.3042\Delta q^4, & (200 \text{ MeV}). \end{cases} \tag{4.17}$$

The momentum transfer is a function of the scattering angle and one can approximate this function for 100 MeV by $q \approx 0.05 \cdot \theta^{0.94}$ and for 200 MeV by $q \approx 0.06 \cdot \theta^{0.97}$. The quantity Δq in Eq. (4.17) can then be approximated by

$$\Delta q = \left.\frac{\partial q}{\partial \theta}\right|_{\theta_0} \Delta\theta \approx \begin{cases} 0.0021 q_0^{-0.0672}\Delta\theta, & (100 \text{ MeV}) \\ 0.0031 q_0^{-0.0267}\Delta\theta, & (200 \text{ MeV}), \end{cases} \tag{4.18}$$

where $\Delta\theta$ is in units of mrad. For $q_0 = 1.5\text{fm}^{-1}$ and an aperture with a width of 1/2 inch, corresponding to a 17.84 mrad horizontal angular acceptance, we get from Eq. (4.17) $\langle q \rangle = 1.4978\text{fm}^{-1}$ for 100 MeV ($\langle q \rangle = 1.4957\text{fm}^{-1}$ for 200 MeV). Thus, the average correction to the scattering angle from differential recoil should be 0.06° for 100 MeV and 0.08° for 200 MeV, respectively. With the correction we obtain therefore from differential recoil a scattering angle offset of $\Delta\Theta = 0.20(7)°$ for the 100 MeV run in January 1987, which is consistent with the cross plot value of 0.26 from ^{40}Ca. For the 200 MeV

runs we obtain angle offsets of 0.27(7)° (April 1987) and 0.14(9)° (January 1988).

It was pointed out (G. P. Berg, IUCF, private communication) that 3.2 mm steering in the last quadrupole before the target, Q10, causes an angle change at the target of 0.1° ($\text{distance}_{\text{Q10-target}} = 183.88$ cm). The scattering angle offset is characteristic for a particular beam tune and should not vary in time. However, steering in the quadrupoles could make the offset time dependent. To investigate a possible time dependence we plotted the original individual angle offsets (which were measured at different times) versus their integrator left-right asymmetries (which are a measure of the beam angle on the Faraday cup). This is shown in Figures 4.5 and 4.6 for the 100 MeV run in January 1987 and the 200 MeV run in April 1987. The figures show that in January 1987 the beam was fairly evenly distributed over the left and right half of the split cup, implying a small beam angle at the target, while in April 1987 the beam was centered more on the right half (looking upstream), implying a larger beam angle at the target. This is consistent with the larger angle offset observed in April 1987. However, there appears to be no obvious correlation between the scattering offset and the integrator asymmetry, and no time dependence of the angle offset. We believe, therefore, that it is justified to use an averaged offset.

* * *

At the end of the 100 MeV run in January 1988 (runs 946–991) the encoder had an electronics problem causing a systematic offset of 3.4°. Until the encoder problem was fixed, the spectrometer angle was set with help of

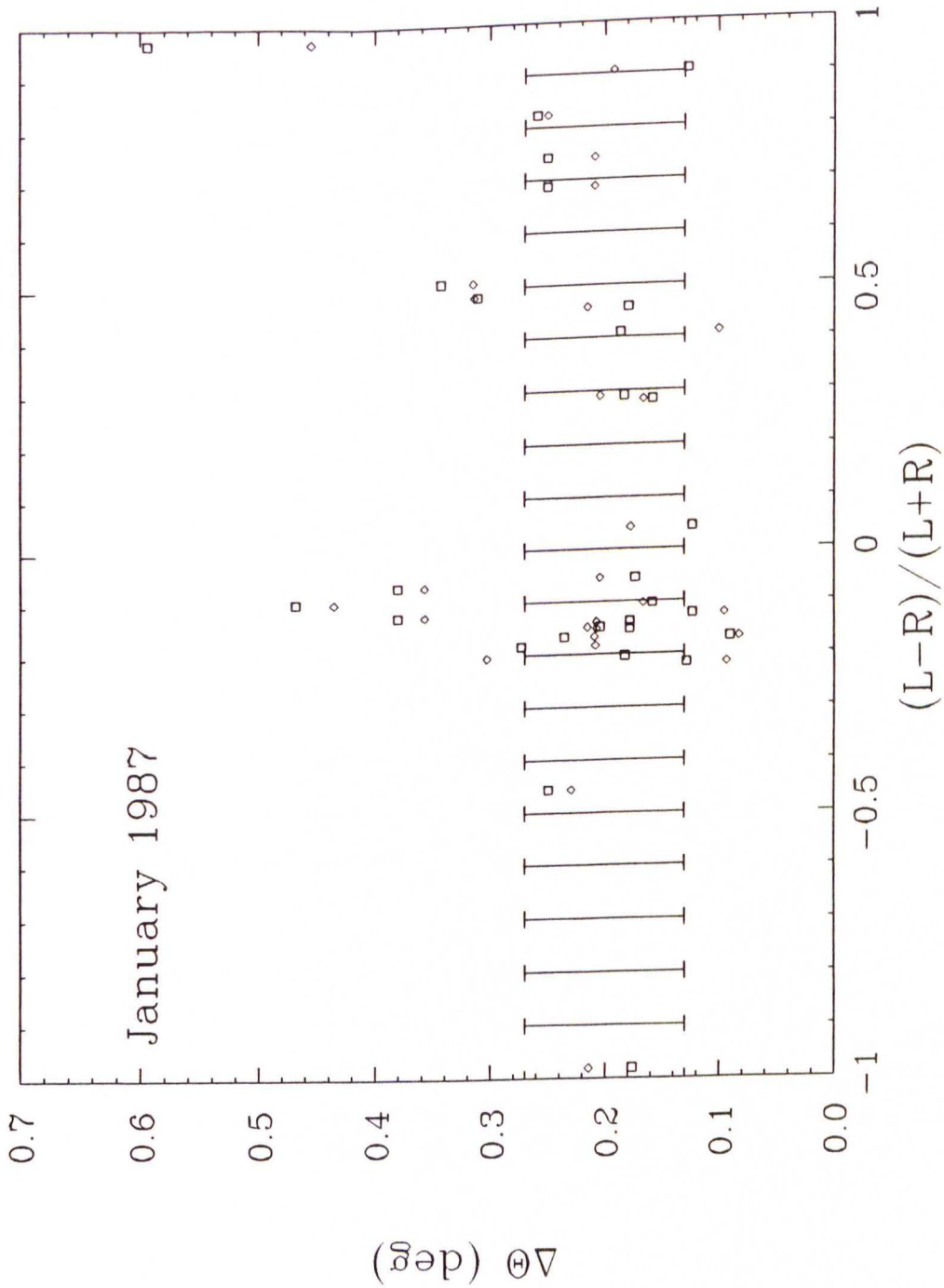

Figure 4.5: Correlation betweeen the scattering angle offset and the integrator left-right asymmetry (January 1987). The diamonds denote angle offsets from spectra with spin-up, the squares angle offsets extracted from spectra with spin-down.

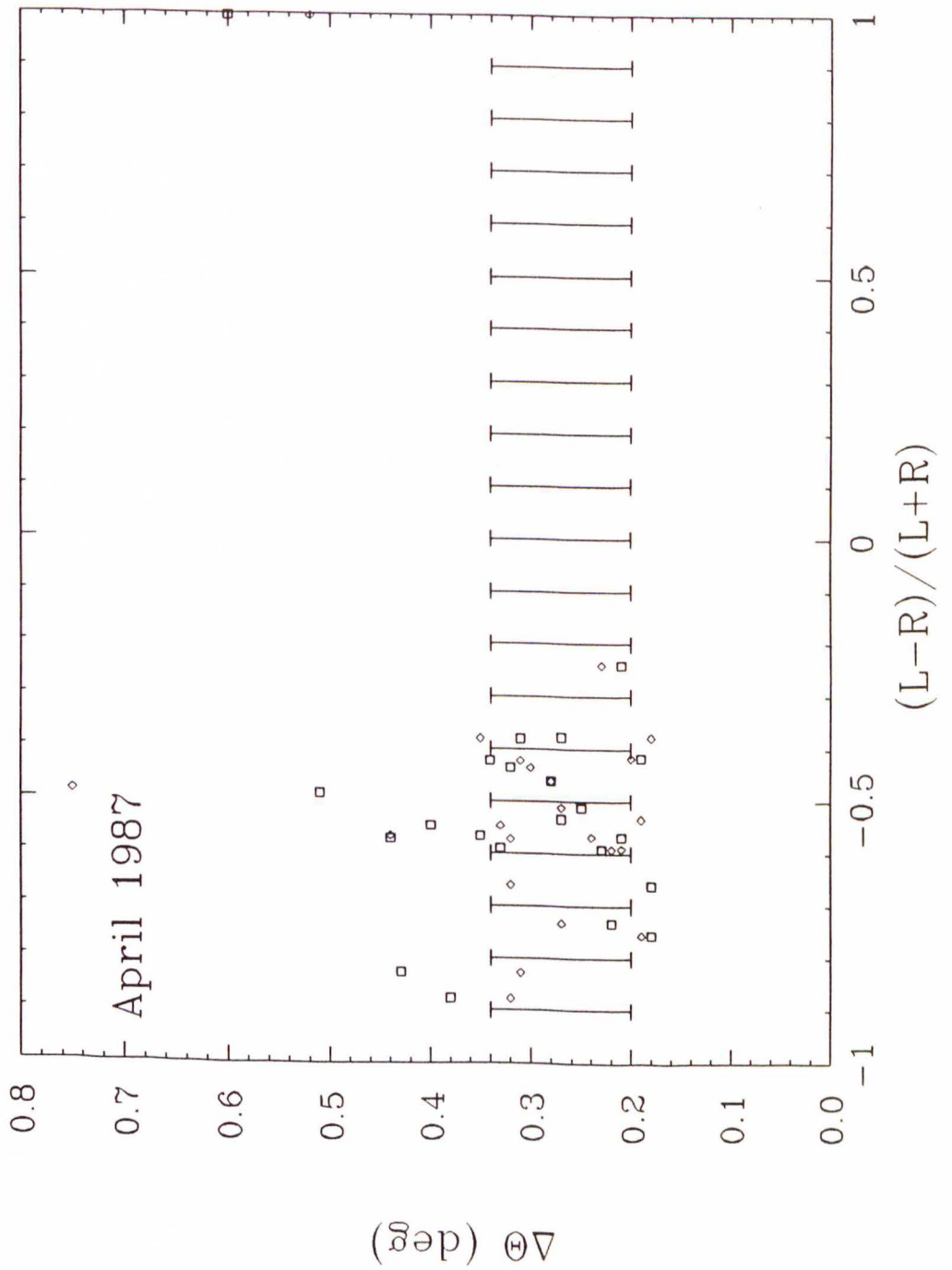

Figure 4.6: Correlation betweeen the scattering angle offset and the integrator left-right asymmetry (April 1987). The diamonds denote angle offsets from spectra with spin-up, the squares angle offsets extracted from spectra with spin-down.

the mechanical scale on the K600 rail and a tape measure. The angles of runs with the encoder problem were corrected by the appropriate amount (in the list of runs, Appendix E, runs with encoder problem are marked with an asterix).

4.3 Beam Polarization

The polarization of the beam was determined in the same way as has been described in ref. [Kel 89a]. In absence of a continuous on-line polarimeter, the beam polarization was measured every few hours using a ^{4}He cell which was lowered into the beam line segment connecting the injector and main-stage cyclotrons (BL 2). Surface barrier detectors placed symmetrically on either side of the beam line at scattering angles $\pm 122^\circ$ were used to measure the left-right asymmetry for both beam orientations. The intrinsic detector asymmetry, due to differences in detector geometry or efficiency, was measured on two occasions (January 1987 and March 1988) with an unpolarized beam obtained from the outgassing of the walls of the source when the atomic beam valve was closed; both times it differed from unity by about 2%. The transfer line energy is 8.6 MeV for 100 MeV protons and around 15 MeV (field limit) for 200 MeV protons. Over this energy range, the ^{4}He analyzing power is known to be essentially unity at the chosen scattering angle [Dod 76, Dod 77]. More specifically, we are using $A_y = 0.985$ for 100 MeV protons and $A_y = 0.991$ for 200 MeV protons (H. Petri, IUCF, private communication).

To eliminate the effect of detector efficiencies, the left and right yields $Y_{l,r}$ for each beam orientation were normalized with respect to corresponding

pulser signals $N_{l,r}$. In terms of the ratios $R_{l,r} = Y_{l,r}/N_{l,r}$ for each beam orientation, we obtain for spin-up and spin-down polarizations

$$P_{u,d} = \frac{1}{A_y} \frac{\alpha R_{lu,d} - R_{ru,d}}{\alpha R_{lu,d} + R_{ru,d}}, \tag{4.19}$$

where $\alpha = R_{r0}/R_{l0}$ is the intrinsic detector asymmetry; the subscript "0" denotes quantities for unpolarized beam. Using Poisson statistics, the (statistical) uncertainties of spin-up and spin-down polarizations are given as

$$\Delta P_{u,d} = P_{u,d}\sqrt{(N_{lu,d} + N_{ru,d})\,[(N_{lu,d} - N_{ru,d})^{-2} + (N_{lu,d} + N_{ru,d})^{-2}]}. \tag{4.20}$$

The beam polarization for each orientation was measured to a statistical precision of generally about 1% or better.

The measured and interpolated beam polarizations for all the run periods are shown in Figures 4.7 and 4.8. The appropriate beam polarizations for individual runs were determined by interpolation of the measured polarizations. We assign errors of up to 2% to the interpolated polarizations in the January 1987 and January 1988 "dip regions" of the polarization. The interpolated beam polarization values and their uncertainties for each run are stored in a file which is read by a computer sort code that calculates unpolarized cross sections and analyzing powers from ALLFIT summary files [Kel ALL].

In January 1987 (100 MeV) the spin-up polarization varied between 71 and 75.5%, while the spin-down polarization varied between 73 and 77.5%. We can not explain the observed wide dip in the polarizations, with exception of the very deep excursion at about 250 hours when the filament of the ion source burned out. In April 1987 (200 MeV) the beam polarizations

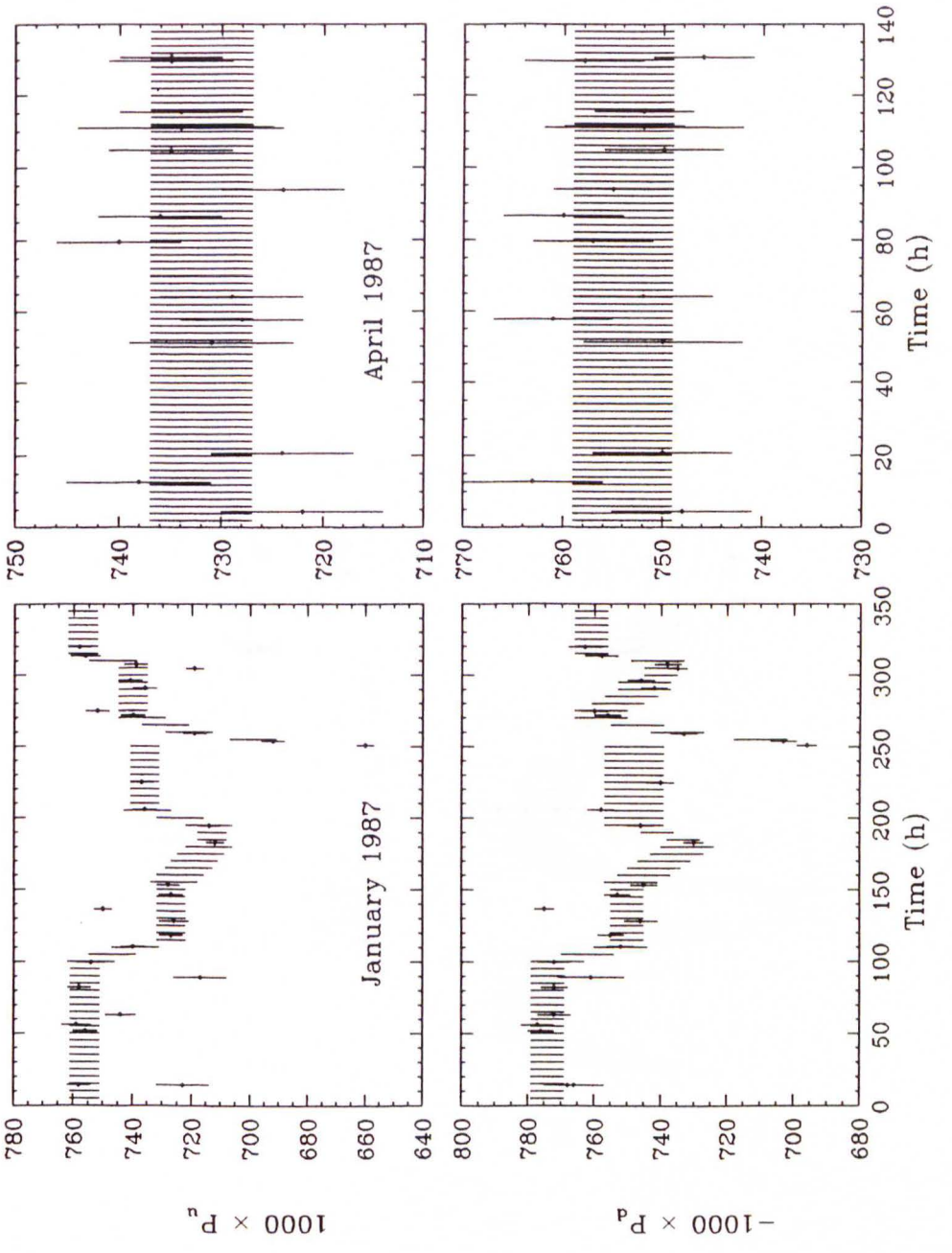

Figure 4.7: Beam polarizations in January 1987 (100 MeV) and April 1987 (200 MeV).

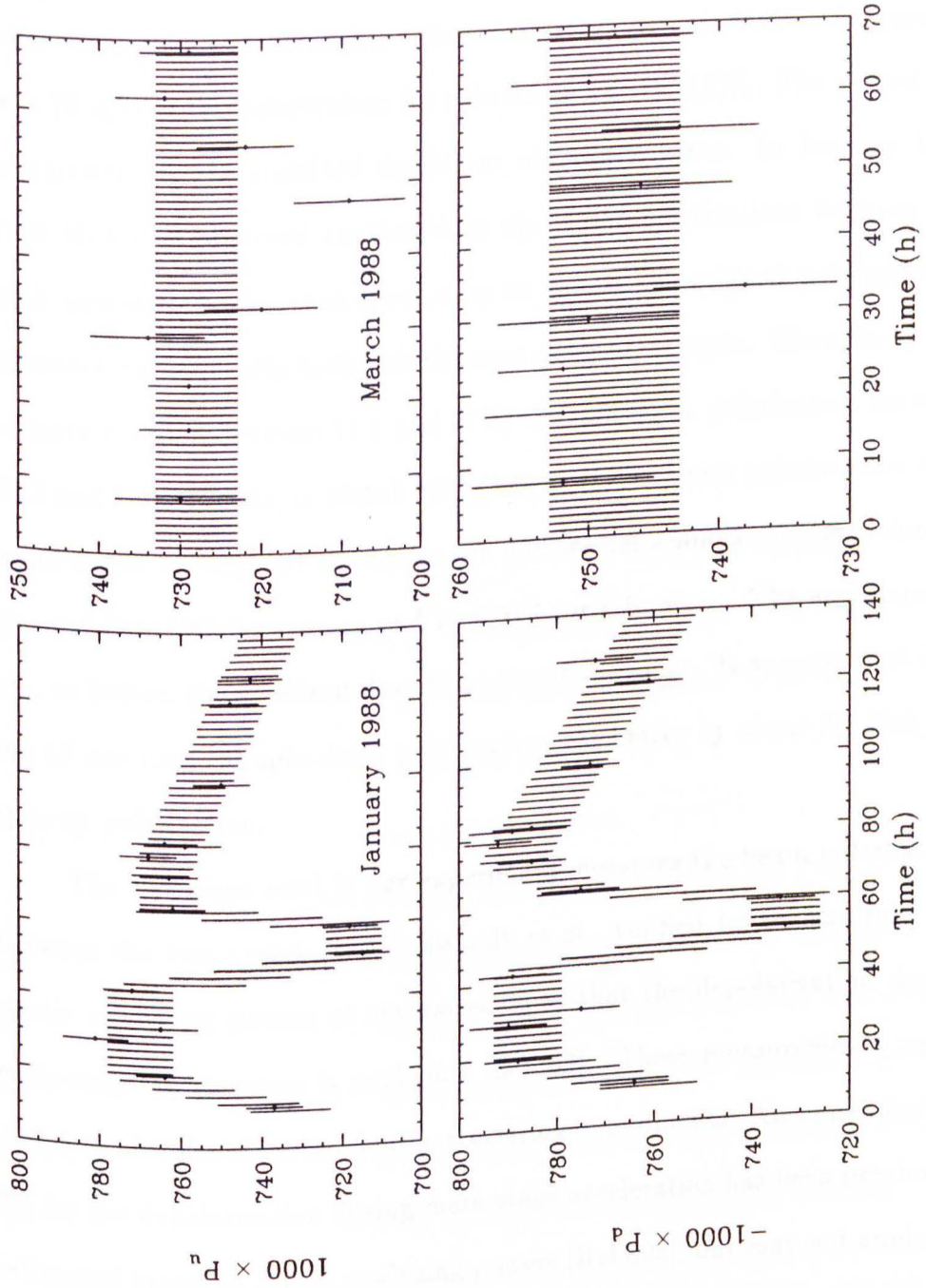

Figure 4.8: Beam polarizations in January 1988 (200 MeV) and March 1988 (100 MeV).

were fairly constant throughout the whole run: the polarization for spin-up was 73.2(5)%, the polarization for spin-down was 75.4(5)%. The quoted uncertainties are the standard deviations about the mean. In January 1988 (200 MeV) we observed another deep dip in the polarizations between the 50th and 60th hours, then a recovery to almost the original polarizations. However, subsequently both polarizations deteriorate again. The spin-up polarization varied between 71.5 and 77%, the spin-down polarization between 73.5 and 79%. Finally, in March 1988 (100 MeV) the beam polarizations were again stable throughout the entire run and we determined average polarizations of 72.8(5)% for spin-up and 74.8(5)% for spin-down. The uncertainties are, as before, the standard deviations about the mean. It appears that during all our runs the spin-down polarization was better by about 2% that the spin-up polarization.

The technique used in our experiment measures the beam polarization between the two cyclotrons. Schwandt *et al.* verified by remeasuring ^{12}C elastic analyzing powers at several energies that the depolarization during main-stage acceleration is negligible [Sch 82]. These measurements reproduced the results of earlier double-scattering experiments. An upper limit of 3% for the depolarization during main-stage acceleration has been previously estimated based on elastic analyzing powers [Kel 89a], but may not apply for 200 MeV because of a depolarizing resonance near 180 MeV (J. J. Kelly, private communication).

4.4 Other Calibrations and Tests

Because of the large vertical magnification of the K600 spectrometer (of the order 6 in "normal" dispersion mode, see Chapter 3), correct vertical centering of the beam on target is critical for proper vertical centering of the image in the focal plane[5]. This is especially important at the extreme ends of the focal plane because of the potentially large vertical image size for a large ϕ-acceptance. In the absence of a y-position chamber, vertical centering of the image in the focal plane was first checked by means of a pair of small, thin "top" and "bottom" diagnostic scintillators which overlapped vertically by about ± 5 mm centered about the K600 median plane. Measurements of the scintillator coincidence yield versus vertical position of beam on target (determined by the current of vertical steerer VT 5 in BL 8) for a small entrance aperture were used as an indicator for correct vertical centering[6]. In the course of these measurements, however, it became apparent that the optical alignment of the wire chambers and the scintillators relative to the median plane was off by about 1 cm and that the center of the magnet acceptance did not coincide with the center defined by the detectors. For subsequent vertical scans, therefore, it was decided to use a different method where the cross section of the $^{12}C\ 2_1^+$ state was measured as a function of the

[5] Proper vertical centering on the target is also important for accurate charge measurements in the Faraday cups since, like the spectrometer magnets, the dump pipe defines a vertical acceptance.

[6] Result of these measurements is a trapezoidal shape; the correct VT 5 current is then defined by the middle of the plateau.

VT 5 current. For these measurements the spectrometer angle was chosen to be 22°, an angle where the 2_1^+ cross section is known to be flat.

* * *

With help of a CH_2 target we checked the stability of the ^{12}C 2_1^+ cross section with respect to

- acceptance,
- computer live time,
- beam current (i.e. accuracy of charge integration), and
- elastic/inelastic run (i.e. position on focal plane *and* rate dependence).

While the sensitivity of cross sections to the acceptance was tested in dedicated runs for both 100 and 200 MeV, dedicated rate and charge integration studies were done only at 100 MeV. At 100 MeV, the 1/2 inch diameter aperture (A1, 0.25 msr) was the smallest aperture used for the acceptance test and a 2 inch diameter aperture (4.0 msr, not listed in Table 3.2) was the largest. At 200 MeV the smallest aperture used for the test was the 1/2 inch diameter aperture (A1) and the largest was the 1.6 inch×1.6 inch aperture (B5, 3.18 msr). We found at both energies that cross sections measured with various acceptances were consistent within 2%. Therefore, no special acceptance corrections to our cross section results are necessary provided that proper vertical centering has been achieved.

First, we found that ^{12}C 2_1^+ cross sections from a sample of elastic and inelastic spectra agreed within 3%. The elastic spectrum was taken with a

1 nA beam, the two inelastic spectra with an 11 nA beam. Furthermore, one inelastic spectrum contained the elastic peak (high rate) while in the other the elastic peak was shifted behind a copper block (low rate, different focal plane position). Second, we studied the cross section dependence of the 2_1^+ state as a function of both computer live time and beam current. For this test we used inelastic spectra. In one sample of runs the live time varied between 21 and 96%, while the beam current[7] for these same runs varied between 2.5 and 16.3 nA. Here we observed a total spread of 1.8% in the cross section. In the other sample the live time varied between 51 and 76%, while the beam current varied between 2.8 and 29.4 nA. For this sample, a smaller total spread of 1.1% in the cross section was observed. It appears from these results that the accuracy of the live time correction might be slightly more important for the correct cross section than the beam current. Charge integration seems to be fairly accurate for a wide range of beam currents. Off-line analysis of the 100 and 200 MeV production runs confirmed these findings.

Although the data rate for the production runs was usually lower than about 300 Hz, our group studied for a few cases the effect of the fast clears (run period in March 1988) on the dead time for runs with high data rates (B. S. Flanders, American University, private communication). It was found that the live time seems to be independent of the fast clear rate for rates up to 1 kHz. In this region the live time correction which is aplied to the

[7] Average beam currents are calculated from the sum of the left and right integrator scalers.

cross section should be therefore reasonably accurate. However, fast clears do appear to reduce the live time for rates in excess of 1 kHz. Based on some test cases, for 3–3.5 kHz the dead time increases between 1 and 5%, for 3–4 kHz by about 5%, for 4–5 kHz between 7 and 10%, and for 8–10 kHz the dead time increases between 16 and 19%.

5 Drift Chamber Detectors

5.1 Introduction

The K600 drift chambers detectors allow the accurate determination of an ncident particle trajectory by measuring the drift times of ionization electr ns with the help of appropriate electronics (see Section 3.6.2). As an energe ic incident particle ionizes the chamber gas along its track, it generates positive ions which travel to the cathode planes and electrons which drift to the anode wires in the mid-plane of the chamber. The electrons which are collected at the anode create a signal which is used as a STOP for the TDC associated with the wire (we remember that the START signal is provided by a scintillator coincidence). Figure 5.1 shows a typical drift time spectrum for one of the multiplexers. On the software level, drift times are first converted into drift distances. Then, after the character of the chamber event has been identified, an appropriate algorithm computes the exact position and angle of the trajectory in the focal plane (which coincides fairly well with the wire plane of the front VDC). Finally, since certain classes of events (e.g. multiple hits), while not being analyzed, may contain good events, appropriate corrections of the final cross sections are necessary.

The configuration of the (guard and sense) wires and the cathode planes is such that each sense wire defines a drift cell of 2.0 mm width and 12.7 mm length. Consecutive sense wires are separated by 6 mm. The electric field is very uniform across the whole drift cell and only in the immediate vicinity of the anode wires and very close to the cathode plane do we find nonlinearities.

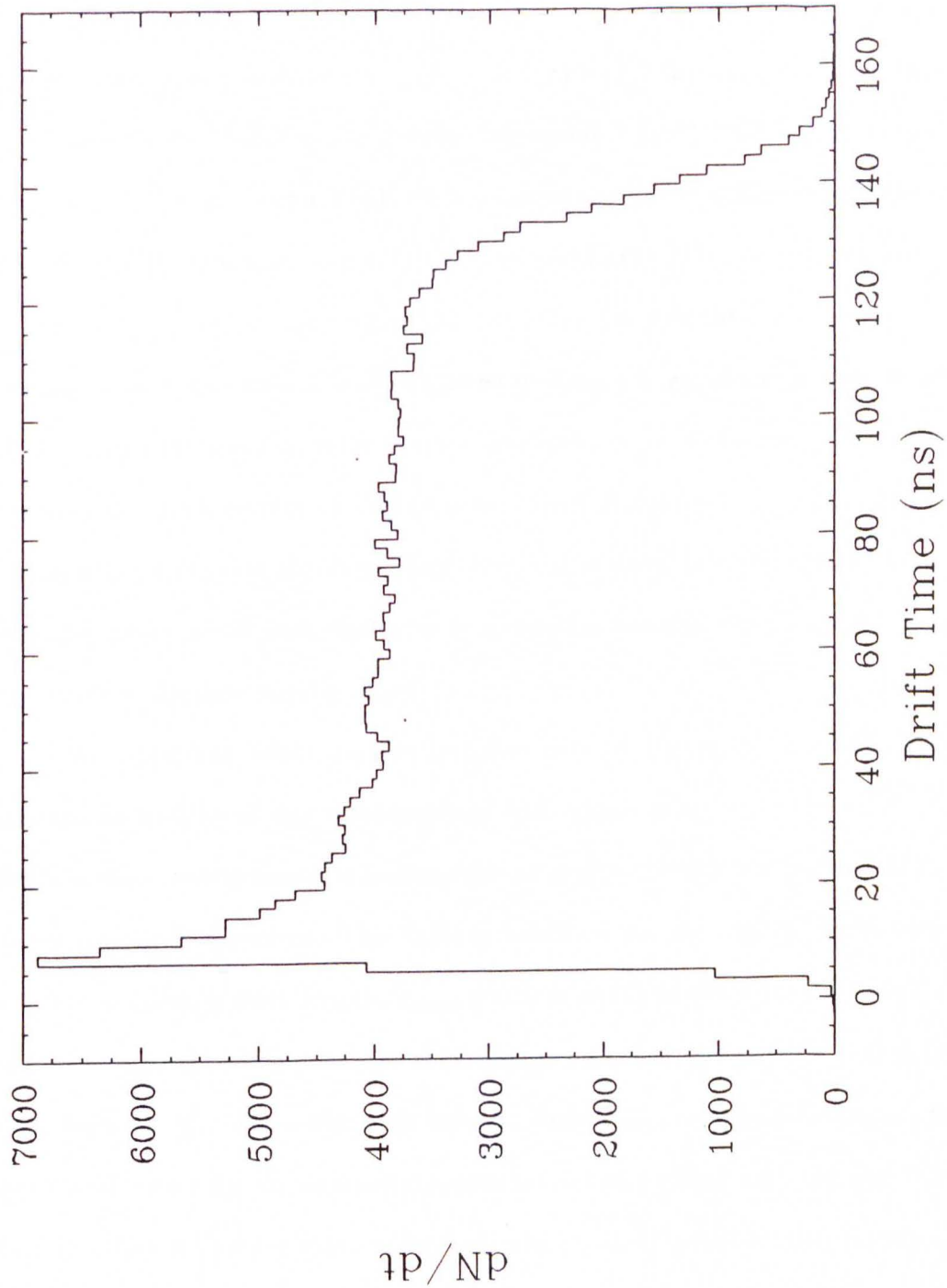

Figure 5.1: Typical drift time spectrum; each multiplexer is associated with one such spectrum. The spectrum shown was taken by illuminating the whole drift chamber uniformly.

If the electric field were exactly the same everywhere, we could just form the product of the drift velocity (46.1 mm/μs) and the measured drift time (1 channel in the drift time spectrum corresponds to 0.317 ns) to get the drift distance. However, because of the nonlinear behaviour at both very short and very long drift distances, this method may lead to errors in the determination of the correct particle trajectory. Also, although for each chamber the relative timing of the drift times is easily adjusted by simply aligning the leading edges of the drift time spectra, there remains an unknown overall timing offset. For algorithms which involve the differences of drift distances (e.g. three or more consecutive hits) this absolute offset does not matter, but algorithms which include the sums of drift distances (e.g. two-hit events) will be sensitive to the correct absolute timing offset.

An approach which implicitly takes care of the problem of absolute timing, as well as of any nonlinearities and inhomogenities in the chamber fields is the construction of a *lookup-table* or *drift table* which transforms drift times into drift distances. This table is based on the knowledge of the measurable maximum drift length, $s_{\max}$, which is equal to the distance between the wire and cathode planes, the total charge collected, Q, and the drift time distribution, $\frac{dN}{dt}$. After the drift time to drift distance transformation has been performed for an internally consistent set of multiplexers, an absolute timing offset no longer matters because the shortest possible drift length is zero and the longest possible drift length is the distance from the cathode plane to the wire. The details of the drift time spectrum incorporate all the non-linearities and inhomogenities of the chamber fields. For example, the

strong field in the immediate vicinity of a wire accelerates a drift electron until it creates by ionization secondary electrons which in turn may create more electrons. This avalanche effect and the associated increase in particles collected at the wire is responsible for the spike at the leading edge of the drift time spectrum. The flat region of the spectrum represents the linear region of the drift cell. Finally, the trailing edge is not abrupt but is smeared out, in part because electrons with long drift distances may be lost (e.g. due to recombination, etc.) and not be collected at the anode wire.

If we assume that the ionization occurs uniformly along the track, the vertical axis of the drift time spectrum, Figure 5.1, represents a (time dependent) velocity $\frac{dN}{dt} = \frac{dN}{ds}\frac{ds}{dt} = cv(t)$. Thus, integration of the drift time spectrum up to a time t will yield the corresponding drift distance $s(t)$ according to

$$s(t) = c\int_0^t \frac{dN}{dt'}dt'. \tag{5.1}$$

The constant c in this equation is $c = s_{\max}/N_{\rm tot}$, where $s_{\max} = 12.7$ mm, and where $N_{\rm tot} = Q/e$ is the total number of counts in the drift time spectrum. In Figure 5.2 we display graphically a drift table, in this case for the front chamber in January 1987. Experimentally, the drift time spectra which are the input for a drift table are generated by illuminating the entire chamber uniformly using the high excitation energy continuum of some target.

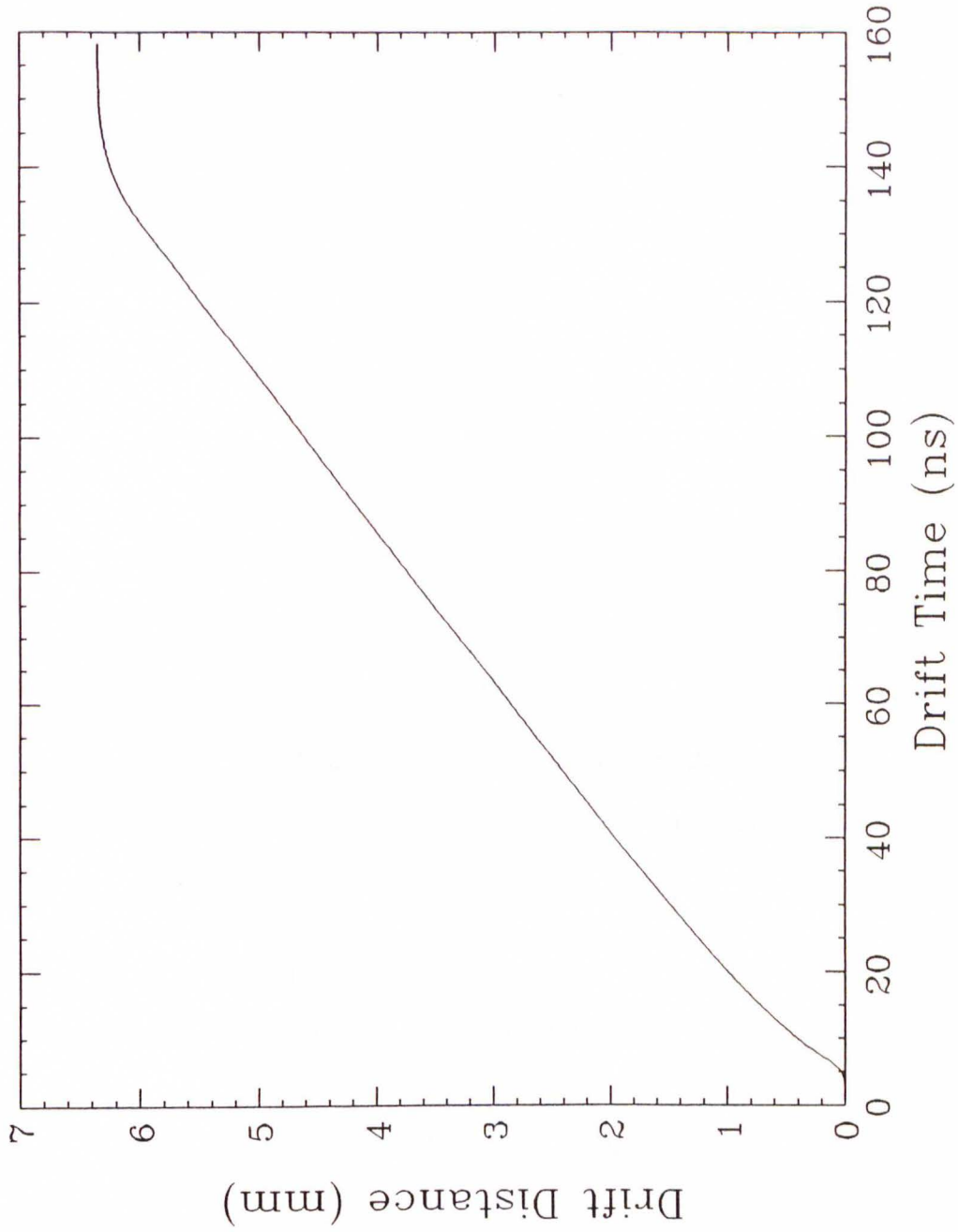

Figure 5.2: Graphical Representation of a drift table; note the deviation of the drift distance $s(t)$ from linearity for drift times t below about 40 ns and above about 130 ns.

5.2 Classification of Events

Before we can calculate the position and angle of a particle track in the focal plane we need to characterize the chamber event. Then the appropriate algorithm can be applied to calculate the desired information. To this end, one examines the MUX register E data words. As stated in Section 3.6.2, information is encoded as follows:

- the data word is zero if the MUX did not fire;
- the data word is negative, i.e. bit 15 is set, if the MUX fired at least twice;
- the data word is positive if the MUX fired exactly once; then the first five bits (bits 0–4) contain the encoded wire number, the next five bits (bits 5–9) the encoded MUX number, and the remaining bits (bits 10–15) are all zero.

If any MUX register E data word is negative the event is classified as a multiple hit and rejected. Otherwise, the MUX (and associated wire) with the shortest drift distance is determined, and a hit pattern is established by examining the adjacent MUXs on either side. We usually denote the MUX with the shortest wire by "0", the two MUXs on the left by "M1" and "M2", and the two MUXs on the right by "P1" and "P2". If n of the five MUX register E data words are nonzero, the event is called an n-hit event. The number of hits a ray can make, i.e. the number of drift cells traversed by the ray, is a function of angle. As we can see in Figure 5.3, n decreases

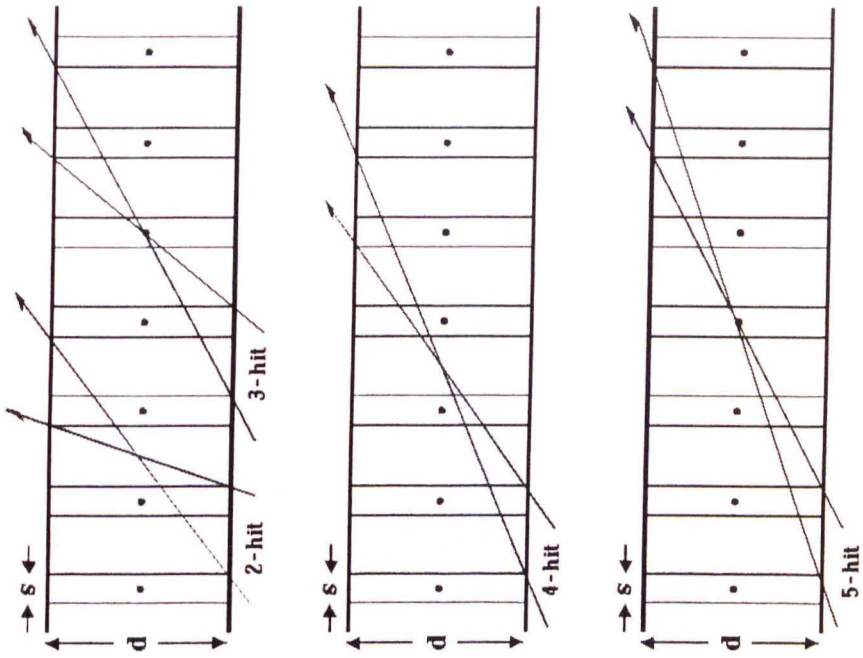

Figure 5.3: Extremum rays for n-hit events; $d = 12.7$ mm is the spacing between the cathode planes, $s = 2.0$ mm is the width of a single drift cell. Both the minimum and maximum angles increase with decreasing n.

with increasing angle. With the cathode spacing, $d = 12.7$ mm, and the width of a single drift cell, $s = 2.0$ mm, the minimum and maximum angles for an n-hit trajectory with the wire plane are $\theta_{\rm min}^{(n)} = \arctan\frac{d}{(3n+2)s}$ and $\theta_{\rm max}^{(n)} = \arctan\frac{d}{(3n-4)s}$, respectively. This is also summarized in the following table [K600 L].

n	2	3	4	5
$\theta_{\rm min}$	38.4°	30.0°	24.4°	20.5°
$\theta_{\rm max}$	72.5°	51.8°	32.4°	30.0°

Our calibration for $\Theta_{\rm tgt}$ gives an angular magnification of about 1.7 (see Section 4.2), and RAYTRACE calculations (see Appendix C) yield for central (in $\Theta_{\rm tgt}$) rays with various δ's the first order relationship

$$\theta_f(x_f) \approx 561.7 + 0.12x_f, \tag{5.2}$$

where x_f is in units of mm, and θ_f is in units of mrad. Because of the slope in $\theta_f(x_f)$, apertures with 0.5, 1.0, 1.6, and 2.0 inch width, corresponding to horizontal angular acceptances of 17.8, 35.7, 60.0, and 71.4 mrad, define slanted windows in an $x_f\theta_f$ histogram of 30.2, 60.7, 102.0, and 121.4 mrad width in θ_f, respectively. If we look at the focal plane region of 200 mm $< x_f <$ 800 mm, where most of our data are taken, we find that the various acceptances cover the following angles:

Aperture	0.5 in	1.0 in	1.6 in	2.0 in
$\theta_{\rm min}$	32.7°	31.8°	30.6°	30.1°
$\theta_{\rm max}$	38.5°	39.4°	40.6°	41.2°

From this table it follows that while 5-hits should be relatively unimportant, 2-hit events will become increasingly important for large x_f, i.e. high excitation energies, and large scattering angles. Events that make only a scintillator coincidence (0-hits) or one hit in either chamber (1-hits) are most likely due to background and are not analyzed. Indeed, in March 1988 0-hits were eliminated altogether on the hardware level by the fast clear coincidence circuit which was described in Section 3.6.3.

The particles which traverse a drift chamber at an angle to the anode plane usually produce a cluster of firings as they cross over several wires. The low-energetic drift electrons involved are produced in "grazing" atomic collisions (primary ionization). Additionally, high-energy electrons, so-called δ-rays, can be formed in "knock-on" atomic collisions. These high-energy electrons traverse the chamber and can produce fresh electrons and ions as well (secondary ionization). Those events cause multiple firings elsewhere in the chamber and have to be distinguished from the original cluster which carries the real position and angle information for the incident track[1]. In hardware, additional multiple firings can be limited to a certain extent by choosing the gate width of the MUXs appropriately. As mentioned in Section 3.6.2, for this we internally shortened the gate width to a maximum of

[1] The probability for another valid event to occur simultaneously to the first event is small: with the usual cyclotron pulse period of 33 ns and with a typical event rate of 300 Hz we find a probability of 9×10^{-6} for one event per pulse. The probability for two real events to occur in one pulse is thus 8.1×10^{-11}, corresponding to a rate of 2.7×10^{-3} Hz. The rate of true simultaneous events is five orders of magnitude smaller and therefore negligible.

33 ns following the first event. Other, less important mechanisms to generate firings of chamber wires, which are unrelated to those from the primary ionization, are pick-up of noise by wires (e.g. discriminator threshold too low) and, to some extent, ionization or pair production by background photons. For a regular event which causes only one cluster of wires to fire, all the wire numbers in the cluster should be consistent with that of the shortest wire. Additional wire firings due to δ-rays, pick-up, or photons that occur somewhere else in the chamber but at the same time, can cause a MUX to fire twice. This kind of event is called a *multiple hit* and bit 15 in MUX register E is set; we don't process these events further and only correct the final cross section by a factor which represents the probable fraction of good events among the multiples. Since the probability for multiple hits is proportional to the amount of background present, we call this correction a *clutter* correction. In the case of an accidental coincidence where no MUX is firing more than once, the wire numbers of the extra cluster are inconsistent with the ones of the good cluster. We call these events *extra hits* and we do calculate position and angle for most of them, assuming that the shortest wire is part of the good cluster. This assumption is good for the majority of the extra hits[2].

In the analyzer code the character of an event is represented by a *hit pattern*. The hit pattern is a ten bit word (bits 0–9), where bit 2 always

[2] Most extra hits are caused by δ-rays. Since the extra cluster is due to electrons from the secondary ionization, it occurs later in time than the good cluster which is due to electrons from the primary ionization.

represents the shortest wire and is unity, and where bit 7 is always zero. While bits 0–4 are reserved for MUXs which have "consistent" wire numbers, i.e. wire numbers which are within ± 2 of the shortest wire, bits 5–9 are reserved for MUXs with "inconsistent" wire numbers. As an example, let us consider a 3-hit event for which MUX n (and wire m) is the MUX with the shortest shortest drift distance, and where the adjacent multiplexers MUX $(n-1)$ and MUX $(n+1)$ fired also. Further, let us assume that the encoded wire number of MUX $(n+1)$ is $m+1$ and thus consistent, and that the encoded wire number of MUX $(n-1)$ is $l = m - 5k - 1$ ($k \geq 1$ and integer, $l \geq 0$) and thus inconsistent. The hit pattern for such an event would then be

9	8	7	6	5	4	3	2	1	0
0	1	0	0	0	0	0	1	1	0
M2	M1		P1	P2	M2	M1	0	P1	P2
accidental hits					regular hits				

This very comprehensive pattern word was, however, used only for diagnostic purposes. The streamlined analyzer code which was employed for production data replay utilized a simpler pattern word in which only the M1 and P1 wires and the lower five bits of the pattern were used, and no bit was set for inconsistent wires. The resulting pattern word was thus always of the form **0x1x0**, where $x = 1, 0$. The above example would be represented by the pattern **00110**, which means that this 3-hit event with an inconsistent wire would be treated like a regular consecutive 2-hit event.

With a diagnostic analyzer and test package we examined several runs from the various run periods. We found that the great majority of events (usually about 95%) were always events that made 3 hits or more. However,

we also found that generally over 80% of all the 5-hits were comprised of a 4-hit and an accidental coincidence with an inconsistent wire. The number of 0-hits and 1-hits was observed to increase with background. But, while the fraction of 0-hits in some cases could be up to about 70% of all scintillator coincidences (one of the reasons for developing the fast clear), the fraction of 1-hits stayed always below about 1.5%. The fraction of non-consecutive hits (e.g. patterns **10101**, **01101**, **00101**, etc.) was found to be generally less than 0.5%. Between 1 and 2% of all events were 2-hit events, becoming more important at large x_f and θ_f. This was found by a grid in $x_f\theta_f$ (see Table 5.1). Omission of the 2-hit events (Figure 5.4c) leaves "holes" in the x_f spectrum (see Figure 5.4b). Because of the periodicity of the holes, a global correction of the efficiency is not possible. We also found that the probability of losing a wire, thus making a 2-hit out of a 3-hit or a 1-hit out of a 2-hit event, is very small. Therefore, 2-hits are real events with a steep angle and should be included in the efficiency. On the other hand, since 1-hit events are not generated by 2-hit events, they are true background events (e.g. due to the beam or the Faraday cup) and should not be included in the efficiency. The fraction of multiple events generally stayed below 1.5%, while the fraction of extra hits was often between 2 and 3%. This is a somewhat surprising result since most of the hits are 3-hits or more. The probability for an accidental coincidence to fire the same MUX twice, and therefore make a multiple hit rather than an extra hit, should be more than 60% for these types of events. As mentioned before, extra n-hit events usually have only one inconsistent wire and therefore can be treated like an $(n-1)$-hit.

Thetaf/xf	2000 - 3500	3500 - 5000	5000 - 6500	6500 - 8000	8000 - 9500	channels
665 - 725			96.47 +- 7.19	97.86 +- 1.86	98.44 +- 0.84	
605 - 665		98.24 +- 2.17	97.90 +- 1.11	97.35 +- 0.81	97.30 +- 0.61	efficiency
545 - 605		98.28 +- 1.69	98.31 +- 1.12	97.86 +- 1.10	97.78 +- 1.17	(%)
485 - 545		97.54 +- 5.29	97.98 +- 4.04	96.30 +- 8.84		
665 - 725			1.09 +- 0.61	0.45 +- 0.09	0.33 +- 0.03	
605 - 665		0.12 +- 0.06	0.29 +- 0.04	0.32 +- 0.03	0.36 +- 0.03	bent hits
545 - 605		0.04 +- 0.03	0.12 +- 0.03	0.17 +- 0.03	0.23 +- 0.04	(%)
485 - 545		0.14 +- 0.21				
665 - 725			13.32 +- 2.04	13.07 +- 0.51	17.19 +- 0.27	
605 - 665		1.84 +- 0.21	1.67 +- 0.10	2.95 +- 0.10	3.39 +- 0.08	2-hits
545 - 605		1.81 +- 0.17	0.55 +- 0.06	0.94 +- 0.08	1.01 +- 0.09	(%)
485 - 545		1.01 +- 0.41	0.17 +- 0.15			
665 - 725			82.34 +- 6.40	84.83 +- 1.67	80.98 +- 0.73	
605 - 665		93.01 +- 2.08	86.33 +- 1.01	83.86 +- 0.73	83.52 +- 0.55	3-hits
545 - 605		78.46 +- 1.44	58.97 +- 0.78	55.92 +- 0.74	56.58 +- 0.79	(%)
485 - 545		44.49 +- 3.06	27.97 +- 1.74	25.93 +- 3.69		
665 - 725			2.72 +- 0.91	1.60 +- 0.17	1.43 +- 0.07	
605 - 665		4.64 +- 0.34	11.50 +- 0.29	12.67 +- 0.22	12.57 +- 0.17	4-hits
545 - 605		19.05 +- 0.58	39.60 +- 0.60	42.23 +- 0.61	41.43 +- 0.64	(%)
485 - 545		52.90 +- 3.43	70.18 +- 3.17	72.84 +- 7.22		
Thetaf/xf	2000 - 3500	3500 - 5000	5000 - 6500	6500 - 8000	8000 - 9500	channels

Table 5.1: Grid in $x_f\theta_f$ for run 556 (^{40}Ca, 200 MeV, $\theta = 49°$): efficiency, "bent" hits (see Section 5.4), 2-, 3-, and 4-hits. The number of 2-hits increases with increasing x_f and θ_f, the number of 3-hits and 4-hits decreases. The number of bents tracks with the number of 2-hits.

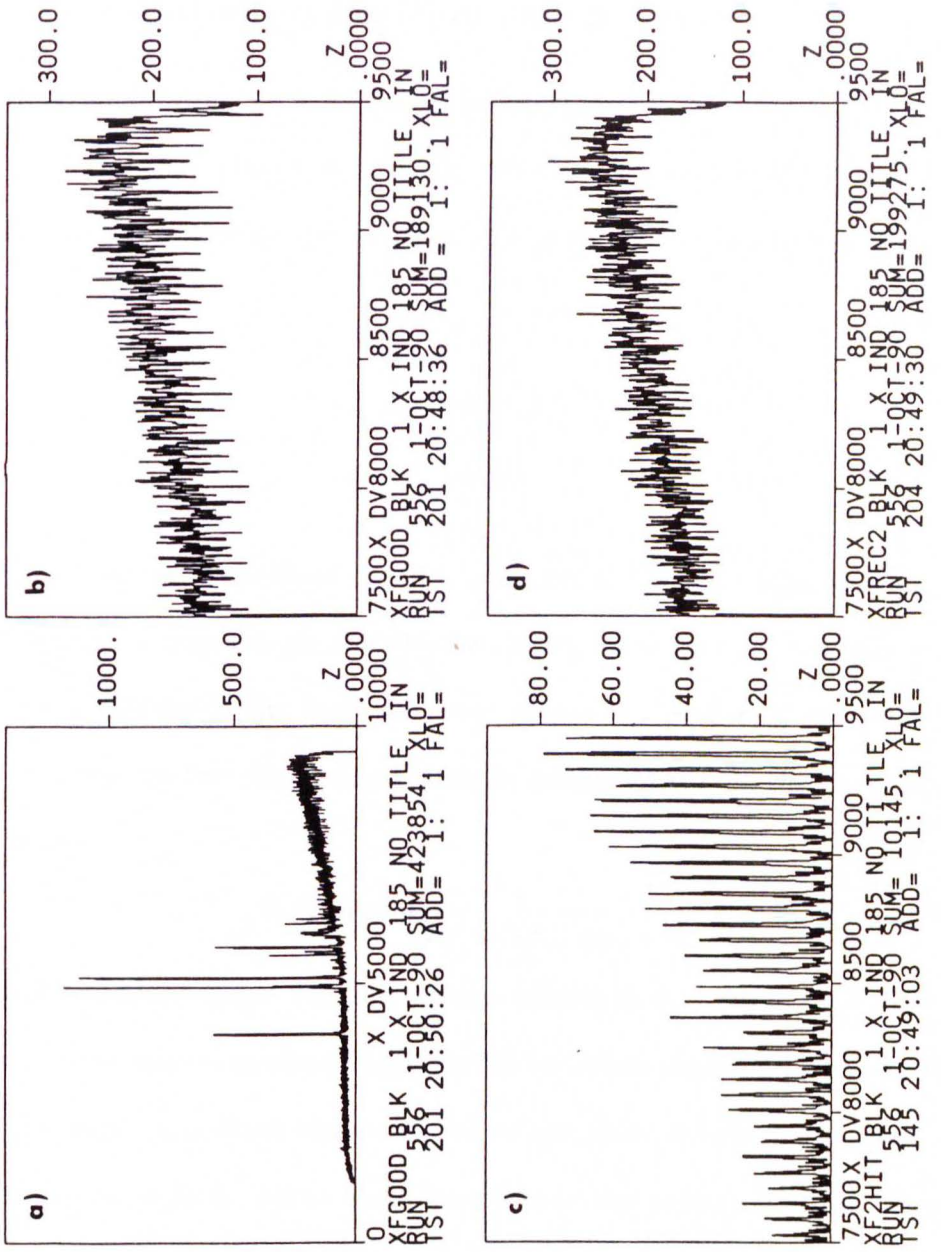

Figure 5.4: For run 556 we display in a) and b) the x_f spectrum for 3 or more consecutive hits. In c) we display the same spectrum for 2-hits only. In d) we show the spectrum for 2 or more consecutive hits.

5.3 Calculation of Position and Angle

In the following, we will denote the interpolated fractional wire spacing by f and the (one-plane) slope by a. With the wire spacing s, and the shortest wire number n, the position and angle in the focal plane can be expressed as

$$\begin{aligned} x &= s(n+f) \\ \theta &= \arctan a. \end{aligned} \tag{5.3}$$

The track position in the front chamber is always the position which we quote as x_f. The focal plane angle can also be calculated as two-plane angle from the track positions in the front and rear planes (x_F and x_R), the relative offset between the two planes (Δx), and the distance between the two planes (z). We get

$$\theta_f = \arctan \frac{z}{x_F + \Delta x - x_R}. \tag{5.4}$$

It is this two-plane angle which is always quoted as θ_f. For a good event, however, we require consistency between the two-plane and one-plane angles.

The most important classes of events are those which make three of more consecutive hits. All of these events have the pattern **x111x**, where $x = 1, 0$. The calculation of position and one-plane angle for such a track is based on the drift distances d_{M1}, d_0 and d_{P1}. As Figure 5.5a shows, the trajectory can pass either between the M1 and the 0 (**x1.11x**), or between the 0 and the P1 wire (**x11.1x**). We find for the **x1.11x** case

$$f = -\frac{1}{2}\frac{d_{\mathrm{P1}} - d_{\mathrm{M1}}}{d_{\mathrm{P1}} - d_0}, \qquad a = \frac{d_{\mathrm{P1}} - d_0}{s}, \tag{5.5}$$

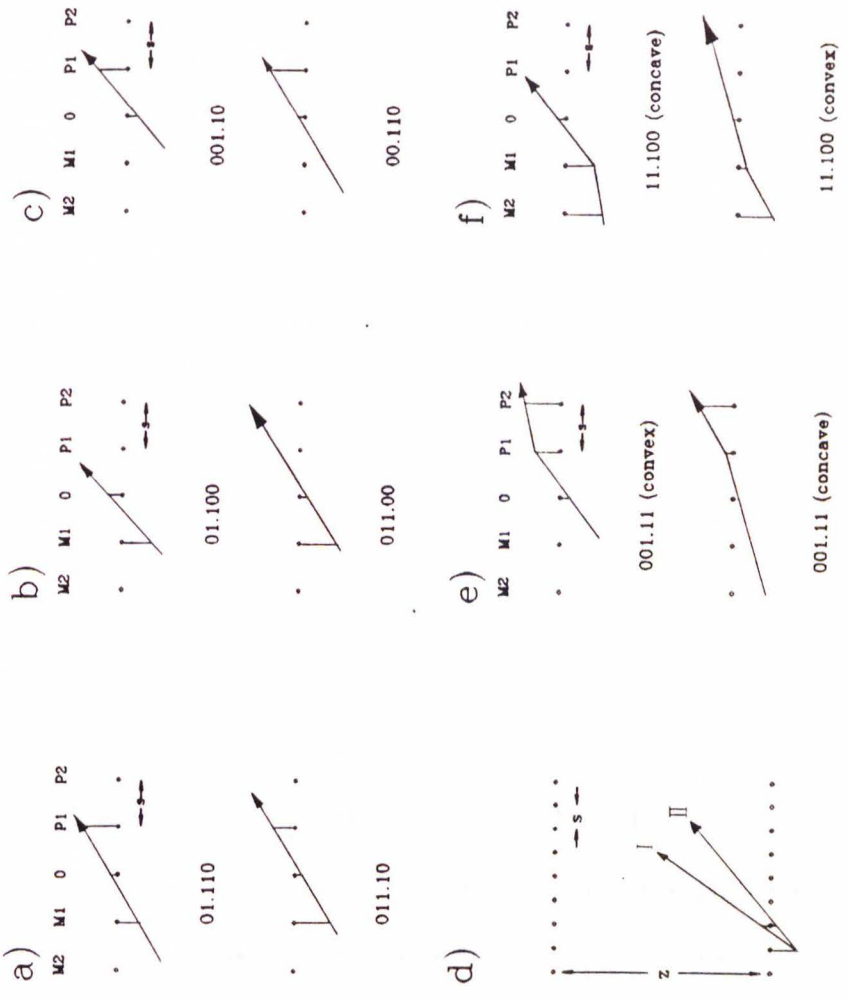

Figure 5.5: Event types: a) consecutive 3-hit events; b,c) consecutive 2-hit events; d) recovery of 2-hit events via two-plane consistency; e,f) asymmetric 3-hit events (bent rays).

and for the **x11.1x** case

$$f = -\frac{1}{2}\frac{d_{P1}-d_{M1}}{d_{M1}-d_0}, \qquad a = \frac{d_{M1}-d_0}{s}. \tag{5.6}$$

Another very important class of events are consecutive 2-hits (patterns **00110** and **01100**) which have to be included to ensure a flat efficiency in $x_f\theta_f$. As before, for each case we have the two possibilities that the track passes left or right of the shortest wire (see Figures 5.5b and 5.5c). In contrast to 3-hits, however, the positive identification of the left- or right-case is less straightforward since two driftlengths are insufficient for unambiguously determining their relative sign. Intuitively, it is obvious that most consecutive 2-hits will be of the type **001.10** or **01.100**, rather than of type **00.110** or **011.00** because of the steep angle required for a true 2-hit. Events for which the track passes outside the cluster feature smaller angles and should have been 3-hit rather than 2-hit events. Indeed, it was found that the majority of 2-hits are are of the interior type. We believe that the 2-hits of the exterior type are probably due to the loss of either the M1 or P1 wire of a potential consecutive 3-hit event. We calculate position and angle for consecutive 2-hits as follows: for the **001.10** case we use

$$f = \frac{d_0}{d_{P1}+d_0}, \qquad a = \frac{d_{P1}+d_0}{s}, \tag{5.7}$$

and for the **00.110** case

$$f = \frac{d_0}{d_{P1}-d_0}, \qquad a = \frac{d_{P1}-d_0}{s}. \tag{5.8}$$

For the **01.100** case we use

$$f = \frac{d_0}{d_{M1}+d_0}, \qquad a = \frac{d_{M1}+d_0}{s}, \tag{5.9}$$

and for the **011.00** case

$$f = \frac{d_0}{d_{M1} - d_0}, \qquad a = \frac{d_{M1} - d_0}{s}. \tag{5.10}$$

We can identify the appropriate 2-hit case in two ways: the first way uses two-plane consistency while the second method employs the one-plane slope. In the first method one calculates the projected position in the other plane for both the left and the right case of a given 2-hit pattern (rays **I** and **II** in Figure 5.5d). The correct ray will minimize the difference between the crude position (i.e. the shortest wire) and the projected position in the other plane. For example, let us consider the **01100** pattern from Figure 5.5d. If we assume typical values for the d_{M1} and d_0 drift distances of 6 mm and 2 mm, respectively, we find for ray **I**

$$\frac{ms}{d_{M1} + z} = \frac{s}{d_{M1} + d_0}, \qquad \text{i.e.} \quad m = \frac{d_{M1} + z}{d_{M1} + d_0} \approx 13, \tag{5.11}$$

and for ray **II**

$$\frac{ms}{d_{M1} + z} = \frac{s}{d_{M1} - d_0}, \qquad \text{i.e.} \quad m = \frac{d_{M1} + z}{d_{M1} - d_0} \approx 26, \tag{5.12}$$

i.e. the two projected positions differ by 13 wire spacings. The correct ray can therefore be easily identified, even if only the crude position in the other plane is available for comparison.

The other method for identifying whether the track passes left or right of the shortest wire makes use of the fact that if, for example, a **00.110** type event is treated like a **001.10** event, the calculated one-plane slope will increase. That this is indeed the case can be seen if one compares the slope in Eq. (5.8), which involves the difference of d_{P1} and d_0, with the one in

Eq. (5.7), which involves the sum of the same drift distances. Assuming again 2 mm for a typical d_0 drift length, the difference of the two slopes, Eqs. (5.7) and (5.8), is $\frac{2d_0}{s} \approx 0.67$ which corresponds to 588 mrad or 33.7°. Figure 5.6 shows the one-plane slope (times a factor 1000) calculated from Eq. (5.7). The **001.10** events comprise the large peak. The **00.110** events which are treated like **001.10** events are responsible for the long tail on the large-slope side of the peak (beyond about channel 875). It is evident that here the interior type constitutes the majority of all **00110** events. The same can be shown for the **01100** case: for most of the 2-hit events the track lies between the two firing wires. The same conclusion can be drawn from the next figure, Figure 5.7, where we compare the calculated drift length d_{M1} for **00110** events with the corresponding measured drift length for consecutive 3-hit events. Most of the calculated drift lengths are very large, which is consistent with the steep angle of the **001.10** case. The **00.110** case which features a smaller slope would require small d_{M1} drift lengths.

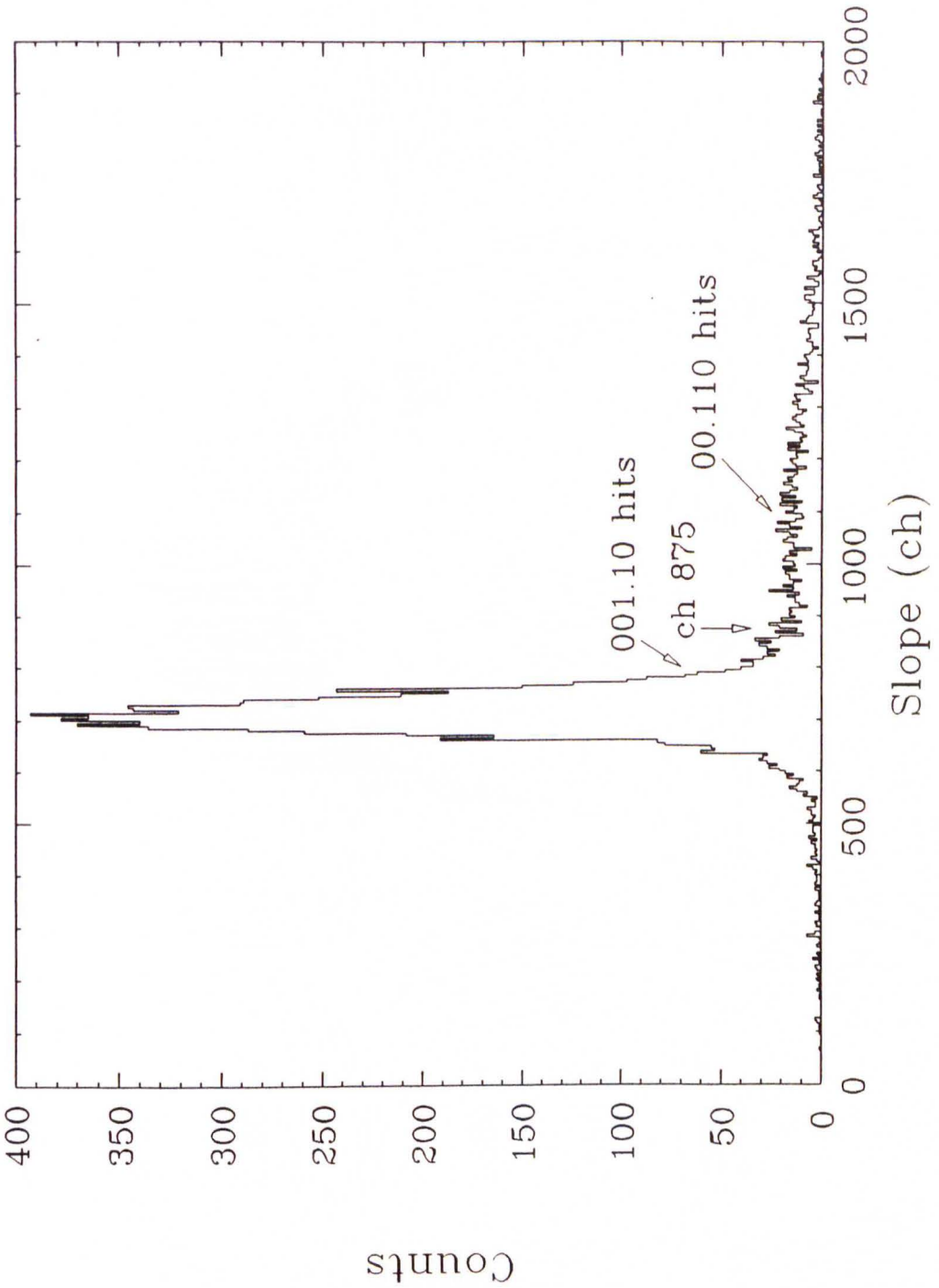

Figure 5.6: 2-Hit recovery by examination of the one-plane slope; if a **00.110** event is treated like **001.10** the slope increases by a significant amount. The slope shown in this histogram is the slope from Eq. (5.7), multiplied by a factor 1000.

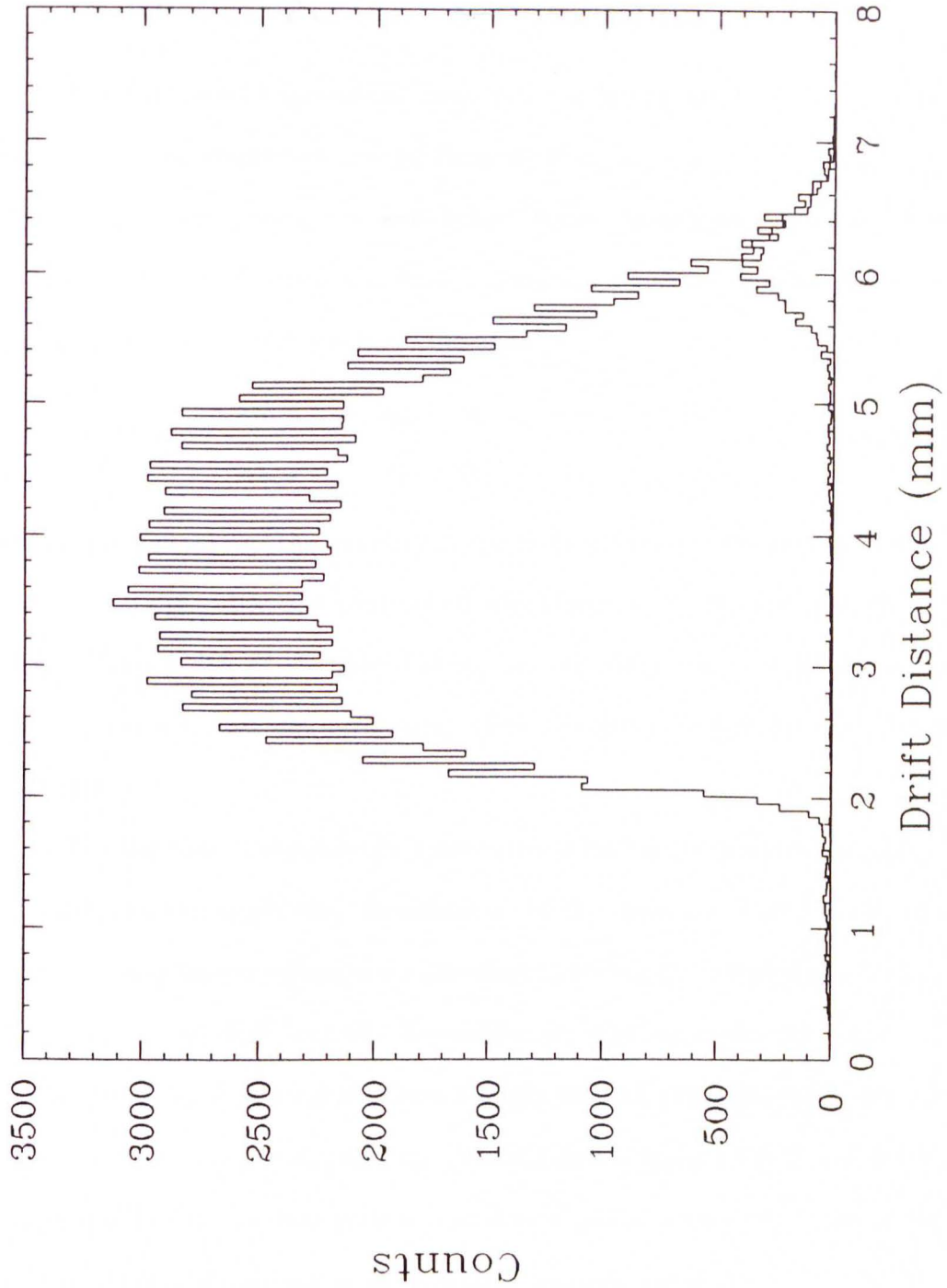

Figure 5.7: Comparison of the calculated d_{M1} drift length for a **00110** event with the corresponding measured drift length for consecutive 3-hits. Most of the reconstructed 2-hit drift lengths are very large, indicative of the steep angle which is characteristic for the **001.10** case.

5.4 Drift Cell Resolution—Straightness of Tracks

For the case of symmetric consecutive 3-hit events (see Figure 5.5a) two interesting quantities can be derived: first, as mentioned before, if no drift table is being used the knowledge of the absolute timing offset Δ is important for any position and angle calculation which involves sums, rather than differences of drift times t. One finds

$$\begin{aligned} 2\Delta &= t_{\mathrm{P1}} - t_{\mathrm{M1}} - 2t_0, \qquad (01.110) \\ 2\Delta &= t_{\mathrm{M1}} - t_{\mathrm{P1}} - 2t_0, \qquad (011.10). \end{aligned} \tag{5.13}$$

When one histograms the quantity Δ one finds a Gaussian-shape distribution with a certain width, the centroid of which represents the absolute timing offset. The width of the distribution, on the other hand, is proportional to the intrinsic drift cell resolution. This resolution is found to be about 0.25 mm.

For the case of asymmetric consecutive 3-hit events (pattern **001.11** or **11.100**) one can study the "straightness" of the track (see Figures 5.5e and 5.5f). Testing the straightness is equivalent to testing the internal consistency of the measured drift lengths. Especially, we want to study the reliability of the very long drift lengths. For a straight **001.11** (**11.100**) track, typical values for d_{P2}, d_{P1}, and d_0 (d_{M2}, d_{M1}, and d_0) drift lengths are 6, 2, and 2 mm, respectively. These values yield a typical focal plane angle of $\theta_f = 588$ mrad. The working assumptions in the following analysis are that

- the drift length d_0 associated with the shortest wire is correct;
- the particle track crosses the wire plane *within* the cluster, i.e. we have

the cases **001.11** or **11.100**;

- together with the shortest wire a *consistent* wire reproduces the "bench mark" angle of 588 mrad, while an *inconsistent* wire does not.

For the case of a straight **001.11** track the quantity $\delta = d_{P2} - 2d_{P1} - d_0$ vanishes. If $\delta < 0$ the track is *bent* and *convex*, while for $\delta > 0$ it is bent and *concave* (see Figure 5.5e). The convex case arises if either d_{P2} is too short or if d_{P1} is too large. The concave case, on the other hand, occurs if either d_{P2} is too large or if d_{P1} is too short. In order to identify the inconsistent wire we have to form, as we have indicated above, separately the one-plane angles of d_{P2} with d_0, and of d_{P1} with d_0. We do this by evaluating the quantities $\alpha = |8 - d_{P2} - d_0|$ and $\beta = |4 - d_{P1} - d_0|$. In the case that $\alpha > \beta$ we can identify d_{P2} to be the inconsistent drift distance; from $\alpha < \beta$ it would follow that d_{P1} is the inconsistent drift length.

Analogously, for the case of a straight **11.100** track the quantity $\delta = d_{M2} - 2d_{M1} - d_0$ must vanish. For negative δ the track is bent and concave, for positive δ it is bent and convex (see Figure 5.5f). The concave case arises for either a d_{M2} that is too short or for a d_{M1} which is too large. The convex case occurs if either d_{M2} is too large or if d_{M1} is too short. Here we form the quantities $\alpha = |8 - d_{M2} - d_0|$ and $\beta = |4 - d_{M1} - d_0|$. For $\alpha > \beta$ the drift length d_{M2} is inconsistent, while for $\alpha < \beta$ it follows that d_{M1} is inconsistent.

We histogramed the quantity δ for asymmetric 3-hit events and found it to be predominantly positive for both **001.11** (i.e. concave) and **11.100** (i.e. convex) events. Additionally, for these cases it was found that generally

the outer wires P2 and M2 were the inconsistent wires and that their drift lengths were longer than they were supposed to be. It was also observed that the frequency of occurence for bent rays increased with x_f and that it showed a certain periodicity which suggests that there is a possible connection with 2-hit events. If, for example, the P2 or M2 signal were due to pickup, the associated drift length will be inconsistent with the ones that are caused by the incident particle track. A similar analysis for symmetric consecutive 3-hit events demonstrated that the P1 and M1 drift lengths produce reasonably straight tracks.

5.5 Summary and Conclusions

We can summarize the major results of this chapter as follows:

- it is sufficient to consider only consecutive hits.
- the long drift lengths associated with the M2 and P2 wires are often inconsistent and, therefore, should not be used for position and angle calculations. The M1 and P1 drift lengths, on the other hand, yield reasonably straight tracks.
- if δ-rays are the predominant mechanism for accidental coincidences with an inconsistent wire, we can assume that the shortest wire is part of the good cluster. We can then treat the n-hit event with the inconsistent wire just like an $(n-1)$-hit event where all wires are consistent.
- we correct the final cross section for multiple events by a global factor $(1 + f^{multi})$, where f^{multi} is the fraction of multiple events. Since the

number of multiple events seems to track with the overall background we call this correction a "clutter" correction to distinguish it from the intrinsic efficiency of the chamber.

- a similar global correction for 2-hit events is not possible because of the x_f and θ_f dependence. Without the (significant number of) 2-hit events the efficiency surface in $x_f\theta_f$ is not flat and has holes. We have means to resolve the left-right problem which is characteristic for 2-hit events and are, therefore, able to include them in the efficiency explicitly.

- we require from a good event that it

  1. passes the particle identification test;
  2. is not a multiple event or background event (usually 0-hit or 1-hit);
  3. is not an event due to beam halo or slit scattering which can be discerned by examining the angle at the target (see next chapter);
  4. allows the accurate reconstruction of the focal plane angle. Here we require that the two one-plane angles as well as the two-plane angle are all internally consistent.

- We define our efficiency ε to be the fraction of good events that have additionally a good hit pattern, i.e. events which make at least two consecutive hits. The contribution to the efficiency of events which are not included in this definition, e.g. certain classes of non-consecutive or extra hits, is negligible. With this definition, the efficiency was generally between 95 and 100%.

5.6 Some Diagnostics

We developed some useful diagnostics to identify problems with the discriminator thresholds on the preamp cards (see Section 3.6.2):

- if all the discriminator thresholds are zero, every chamber hit becomes a multiple hit (example in March 1988).

- during the development run in September 1988 the threshold of one single preamp card was too low, producing what was long believed to be a "hot" wire. Certain wires of the card were picking up noise and appeared, therefore, for most events as the shortest wire. Additionally, however, the adjacent wires were misidentified. When the chamber is illuminated uniformly, this feature can be seen in a plot of the the shortest wire versus the M2, M1, P1, and P2 (extra) wires (see Figure 5.8). Normally, shortest and extra wires are distributed uniformly among all the wires, yielding the diagonal lines in the figure. The fact that certain wires fire more often than others, together with their adjacent wires being misidentified, explains the off-diagonal "hot spot".

- cross talk between wires (example March 1988) manifests itself, depending on the individual thresholds, on all the cards. This leads to a more or less pronounced periodic structure which can be observed in any spectrum for inconsistent wires (see Figure 5.9). The cross talk can be removed by adjusting the individual thresholds of the preamp cards appropriately.

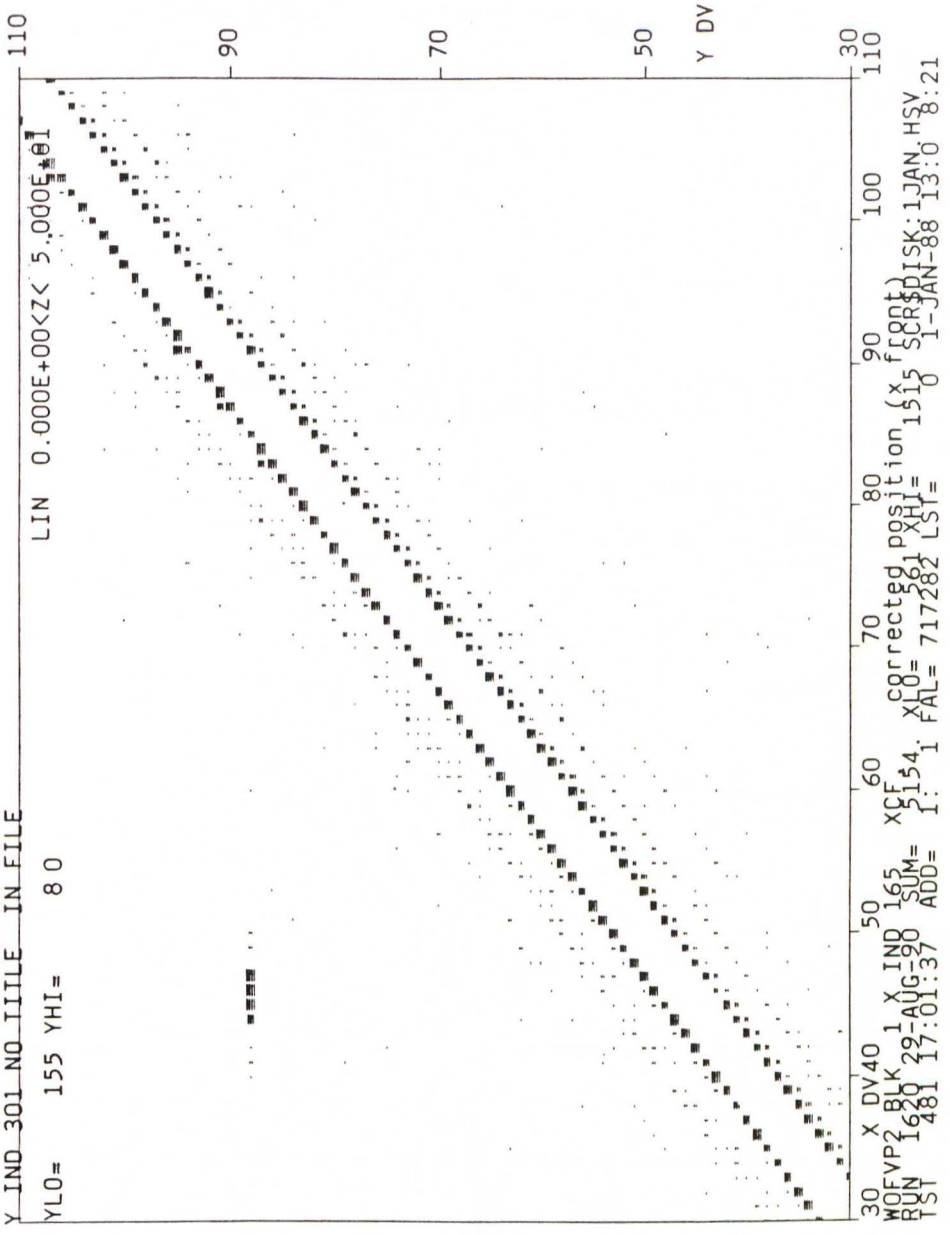

Figure 5.8: Diagnostics for a "hot wire" which is caused by the corresponding preamp threshold being set too low. The figure displays the shortest wire versus its (extra) adjacent wires. Since the adjacent wires of the shortest wires with the noise problem are misidentified, they appear off-diagonally.

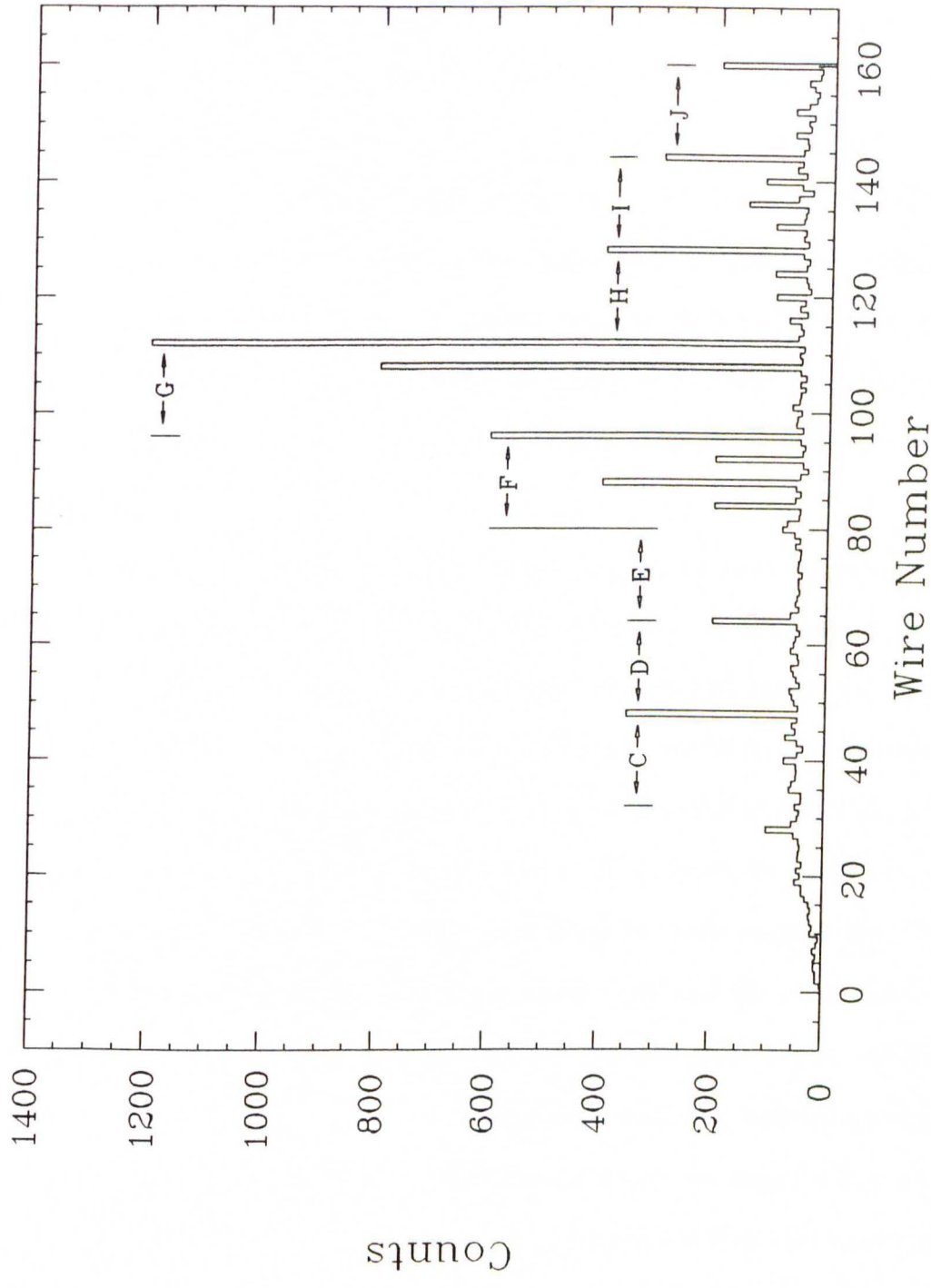

Figure 5.9: Diagnostics for cross talk; the wire spectrum of any (extra) wire will display a periodicity due to the individual preamp cards (A–J).

6 Data Reduction

6.1 Replay

Our data were replayed under the Q-system. The analyzer, as well as the test- and histogram-setup files were streamlined for speed and incorporated many of the results from the previous chapter. Several important cuts were applied to the data during replay. The particle identification (PID) cut and tests for multiple, zero- and one-hits in each VDC plane were hardwired in the analyzer.

The PID cut is made on a two-dimensional histogram of the geometric mean pulse heights $\sqrt{\mathrm{S1N} \cdot \mathrm{S1P}}$ and $\sqrt{\mathrm{S2N} \cdot \mathrm{S2P}}$ and we eliminate with it deuterons, reaction tail from the scintillators, and general backgound. The analyzer also examines the MUX register E data words for multiple hits (bit 16 set, i.e. the data word has a negative value) and for zero-hits (all bits zero, i.e. the data word has a value of zero). If an event does not have a good PID or if it is a multiple hit or if it does not make at least two hits in either of the two planes, further processing halts and the next event is processed. The cut on the difference of the two one-plane angles ensures consistency and correctness of the position and angle calculations for each chamber. Finally, a cut on the reconstructed angle at the target[1], Θ_{tgt}, was necessary to remove from position spectra backgound due to slit scattering (mainly for elastic spectra) and to beam-halo (mainly for inelastic spectra at

[1] In the convention used here $\Theta_{\mathrm{tgt}} = -\Theta_{\mathrm{scatt}}$.

forward angles).

During the early 1987 runs, the long low-momentum tail of the beam extended out to the beam pipe walls and caused there a halo which, because of the special geometric configuration at forward angles, reached the spectrometer acceptance and appeared as significant background in the spectra (c.f. Figure 6.1). Due to the large distance from the beam pipe port to the spectrometer entrance, halo events generally make very small angles with the beam axis and, therefore, always appear under a smaller (less negative) scattering angle than real events from the target at positive (negative) spectrometer angles[2]. Halo events can be seen as a very distinct feature (c.f. Figure 6.2) in the Θ_{tgt} spectrum, and can easily be separated from good events. At positive (negative) spectrometer angles they will have, with our sign convention, negative (positive) Θ_{tgt} values. Slit scattering can often also be easily recognized (c.f. Figure 6.2). Assuming the cross sectional angular distribution of the aperture material (brass) falls very steeply over the angular range of the aperture at forward angles, the intensity of slit scattered rays coming from the right (left) edge of the aperture will be much higher than of rays scattered from the left (right) edge for positive (negative) spectrometer angles (c.f. Figure 6.3). Scattering changes the direction of the rays towards larger (more negative) scattering angles for positive (negative) spectrometer angles. Hence, they appear as a pedestal or tail on the negative (positive)

[2] A simple geometric argument shows that the halo angle would always be exactly half of the spectrometer angle if the halo originated on the beam-axis at the entrance to the scattering chamber.

side of the center peak, the good events, in Θ_{tgt}.

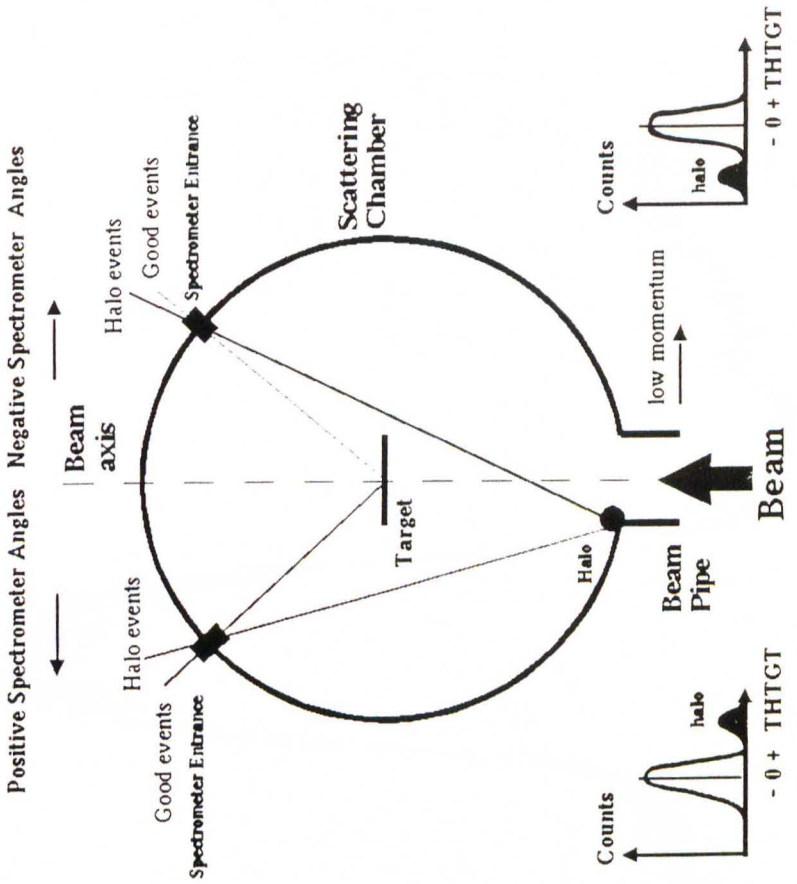

Figure 6.1: Background due to beam halo.

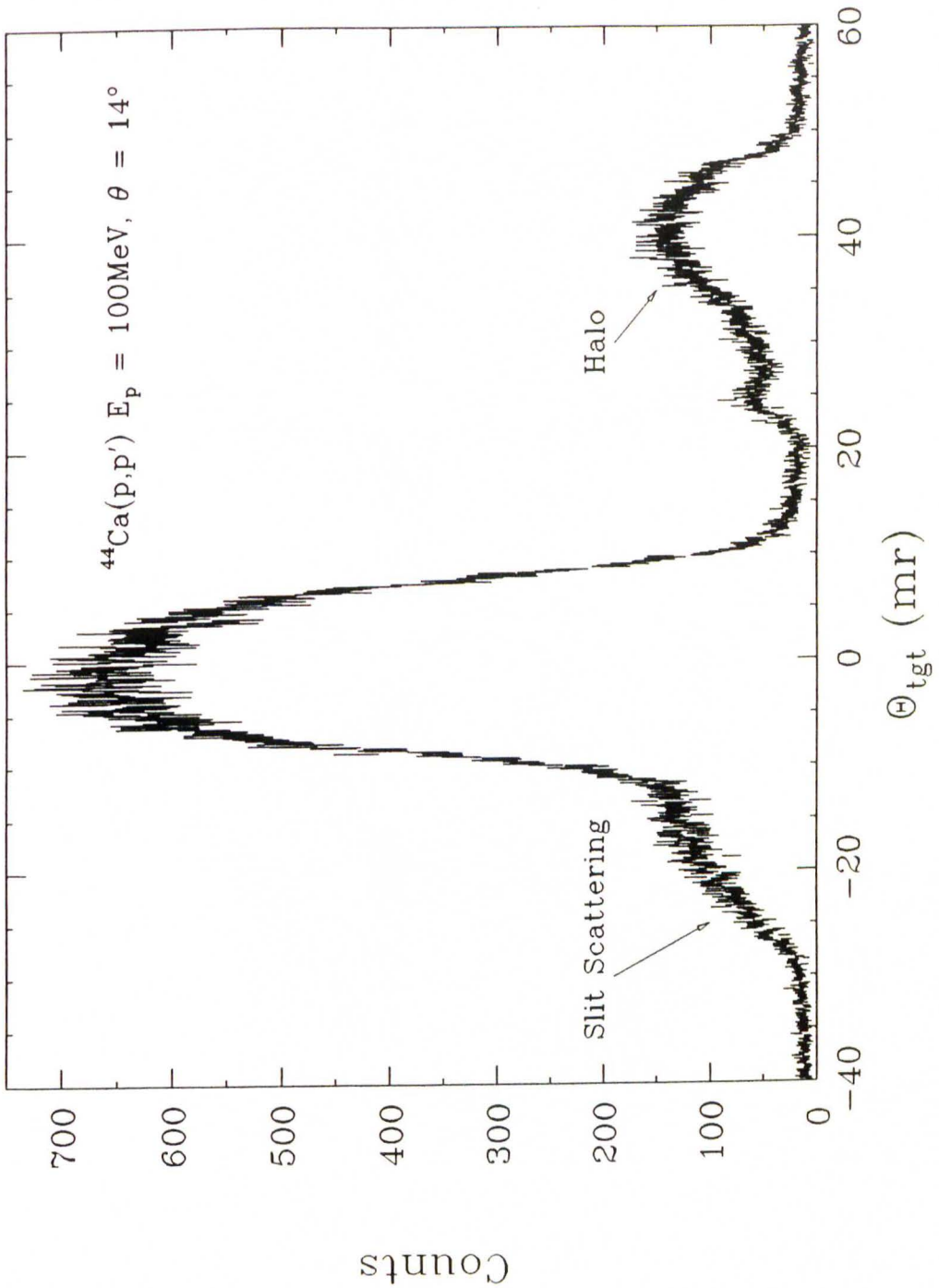

Figure 6.2: Θ_{tgt}-Spectrum for Run with Beam Halo and Slit Scattering

Figure 6.3: Background due to Slit Scattering

6.2 Line-shape Fitting

Fitting of the replayed spectra was performed with the line-shape fitting code ALLFIT [Kel AL]. The search code employs a Poisson (Ξ^2) rather than a Gaussian (χ^2) goodness-of-fit criterion and thus avoids the under-fitting of low-statistics data, which is a problem with the standard Gaussian criterion [Kel 81, Hyn 81]. The spectrum is descibed by a model function which is constructed from a background and a sum of individual peaks

$$y(x) = B(x) + \sum_{i=1}^{N} y_i(x). \tag{6.1}$$

Each peak can be described as the convolution of an intrinsic line-shape $I(x)$ and a resolution function $R(x)$ which empirically considers spectrometer aberrations, target thickness effects, kinematic broadening (dependent on target mass and scattering angle) and beam properties

$$y_i(x) = I_i(x) \otimes R_i(x). \tag{6.2}$$

Peaks, whose natural width is negligible are described by just the resolution function.

The most often employed resolution function shape is an asymmetric hyper-Gaussian in the central region[3] with left (L) and right (R) exponential

[3] The widths of the left and right central regions might differ and the exponent of the argument of the Gaussian need not be 2; exponents less (greater) than 2 produce pointed (flat) tops).

tails

$$R(x) = \begin{cases} f_L H e^{-\lambda_L (p - m_L - x)/w_L} & x \le p - m_L \\ H e^{-\left|\frac{x-p}{\kappa_\gamma w_L}\right|^\gamma} & p - m_L \le x \le p \\ H e^{-\left|\frac{x-p}{\kappa_\gamma w_R}\right|^\gamma} & p \le x \le p + m_R \\ f_R H e^{-[\lambda_R (x - p - m_R)/w_R]^\mu} & x \ge p + m_R. \end{cases} \tag{6.3}$$

H and p are the height and the position of the peak, $\lambda_{L,R}$ the left and right slopes of the exponential tails, and $w_{L,R} = w(1 \mp \alpha)$ the left and right widths; herein, w and α are the total width and the asymmetry of the peak, respectively. The exponent of the Gaussian is γ, $\kappa_\gamma = 0.5(\ln 2)^{-1/\gamma}$, and the left and right match points, $m_{L,R} = \kappa_\gamma w_{L,R}(-\ln f_{L,R})^{1/\gamma}$, include the left and right match fractions, f_L and f_R. Finally, μ represents the curvature of the right tail.

The standard shape for the ^{9}Be and ^{16}O peaks which have intrinsic width is a Lorentzian with height H, position p, width Γ and threshold x_t

$$I(x) = \begin{cases} \frac{H(x-x_t)^2\Gamma^2}{[(x-x_t)^2+(p-x_t)^2]+(x-x_t)^2\Gamma^2} & x \le x_t \\ 0 & x > x_t, \end{cases} \tag{6.4}$$

appropriate when the resonance position is within a few widths of the reaction threshold (here all the positions are to be interpreted as *Q-values*). The threshold for all of the low-lying ^{9}Be peaks is at 1.665 MeV (^{9}Be $\rightarrow$ ^{8}Be + n). 7.162 MeV, corresponding to the decay ^{16}O $\rightarrow$ ^{12}C + α, is appropriate for most of the ^{16}O peaks; for the 0_2^- state a threshold of 12.128 MeV, corresponding to (^{16}O $\rightarrow$ ^{15}N + p), is assumed to apply. Excitation energy, width and threshold of each state in the fit are stored in a "levels" file which is read by ALLFIT. These data are taken from [Ajz86/8, Dix 86] for ^{9}Be, from

J_n^π	E_x (MeV)	$\Gamma_{c.m.}$ (MeV)	Decay	t (MeV)	Comments
$3/2_1^-$	0		stable		
$1/2_1^+$	1.680	0.217	n	1.665	
$5/2_1^-$	2.429				
$1/2_1^-$	2.78	1.08	n	1.665	
$5/2_1^+$	3.049	0.282	n	1.665	
$3/2_1^+$	4.704	0.743	n	1.665	
Lor	6.5	1.25	n	1.665	$7/2_1^-$ and $9/2_1^+$

Table 6.1: Energy Levels of ^{9}Be; data from [Ajz86/8, Dix 86].

[Ajz86/8] for ^{16}O; the data for ^{40}Ca are from [End 78]. Tables 6.1–6.4 are a summary (comments to some of the states appearing in these tables are made in Section 6.6.1).

J_n^π	E_x (MeV)	$\Gamma_{c.m.}$ (MeV)	Decay	t (MeV)	Comments
0_1^+	0		stable		
0_2^+	6.0494				
3_1^-	6.12989				
2_1^+	6.9171				
1_1^-	7.11685				
2_1^-	8.8719				
1_2^-	9.585	0.420	α	7.162	
2_2^+	9.8445				
4_1^+	10.356	0.026	α	7.162	
0_1^-	10.957				
3_1^+	11.080				unresolved
4_2^+	11.0967				
2_3^+	11.520	0.069	α	7.162	

Table 6.2: Energy Levels of ^{16}O; data from [Ajz86/8].

J_n^π	E_x (MeV)	$\Gamma_{c.m.}$ (MeV)	Decay	t (MeV)	Comments
0_3^+	12.049				
1_3^-	12.440	0.091	α	7.162	
2_2^-	12.530				
0_2^-	12.796	0.040	p	12.128	
2_3^-	12.969				
13.08	13.08	0.13	α	7.162	2^+ and 1^-
3_4^-	13.259	0.021	α	7.162	
1_1^+	13.664	0.064	α	7.162	
4_3^+	13.869	0.089	α	7.162	
2_5^-	13.98	0.02	α	7.162	
0_4^+	14.032	0.185	α	7.162	
4_1^-	14.302				
5_1^+	14.399				

Table 6.3: Energy Levels of ^{16}O;(cont.) data from [Ajz86/8].

J_n^π	0_1^+	0_2^+	3_1^-	2_1^+	5_1^-	0_3^+	2_2^+
E_x	0	3.3521	3.7364	3.9041	4.4915	5.213	5.249
J_n^π	4_1^+	4_1^-	2_3^+	1_1^-	6.028	3_2^-	4_2^+
E_x	5.279	5.6143	5.6301	5.9033	6.028	6.2858	6.5084
					2^- and 3^+		
J_n^π	4_3^+	3_3^-	2_2^-	6.909	6.931	1_2^-	7.11
E_x	6.5436	6.5833	6.7509	6.909	6.931	6.951	7.11
				2^+	triplet		1^- and 4^-

Table 6.4: Energy Levels of ^{40}Ca; all states have negligible intrinsic width (data from [End 78]).

Figure 6.4 shows a representative fitted spectrum for BeO. The abrupt rise in the backgound is due to the aforementioned decay threshold for ^{9}Be. Noticeable are the strong asymmetry of the $1/2_1^+$ state, which is only 15 keV above the threshold, and the broad Lorentzian peak[4] which is prominent in the continuum region. The 2_3^+ state (11.52 MeV) of ^{16}O with $\Gamma = 69$ keV is a good example of a strong state with non-negligible intrinsic width. A fit to this state with the resolution function alone would be too narrow and underestimate the true cross section.

Small peaks or unresolved peaks in multiplets can be extracted by locking their positions and shapes together or to those of a strong peak nearby. Examples are the 0_2^+ of ^{16}O which was always locked to its strong neighbour, the 3_1^- peak, and the doublet and triplet states in ^{40}Ca (e.g. 0_3^+, 2_2^+, 4_1^+ or 4_1^-, 2_3^+). Figure 6.5 shows a representative spectrum for this target. The pedestals visible to the left and right of the strong 3_1^-, 2_1^+ and 5_1^- states cannot be attributed to $(x \mid \theta^2)$- or $(x \mid \theta^3)$-type aberrations (which would be visible in an $x_f\theta_f$ plot). We believe they are either due to correlations with the vertical coordinates (y, ϕ) via matrix elements like $(x \mid \phi)$ or $(x \mid y)$ or to the beam itself (tails, split beam, etc.)[5].

There was some small ^{12}C contamination in the BeO target, and the

[4] A combination of the $7/2_1^-$ state at 6.384(59) MeV ($\Gamma = 1.207(231)$ MeV) and the $9/2_1^+$ state at 6.76(6) MeV ($\Gamma = 1.332(90)$ MeV) in ^{9}Be [Dix 86, Gli 89].

[5] We examined the effect of the pedestals on the measurement of the 0_2^+ state. Comparing the ratios of 3_1^- and 0_2^+ heights with a typical peak-pedestal ratio shows that the pedestal is generally much smaller than the 0_2^+ state.

ground state and 2_1^+ state of carbon are clearly visible in many of the spectra. The ^{40}Ca target had traces of ^{12}C, ^{16}O and ^{27}Al. The elastic peaks of these contaminants are present in most of the elastic spectra. For some of the inelastic spectra the 2_1^+ state of ^{12}C and the 3_1^- state of ^{16}O also have to be included. Some of the other background and structure might be attributed to some of the excited states of ^{27}Al, but a clear identification is impossible.

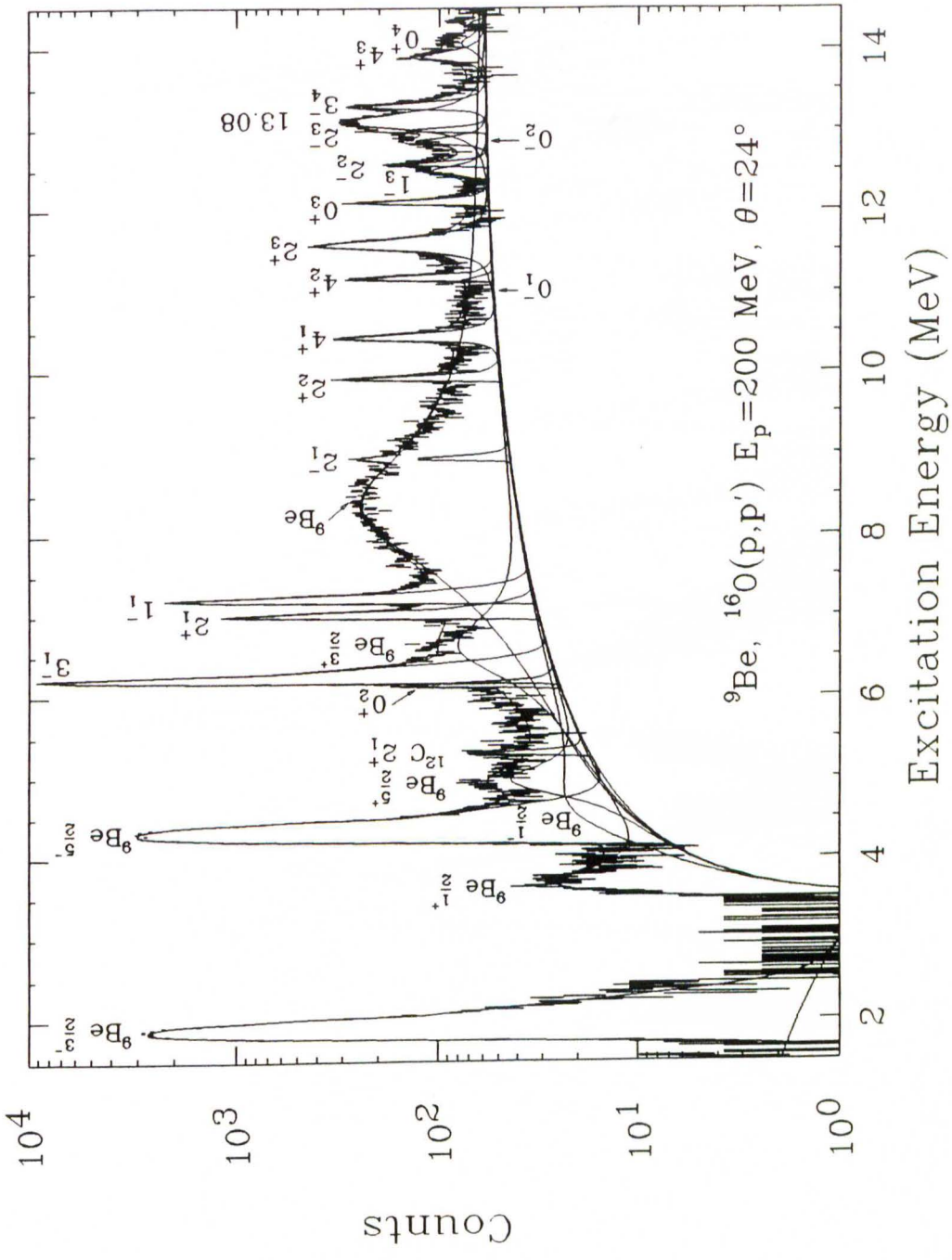

Figure 6.4: Fitted BeO Spectrum

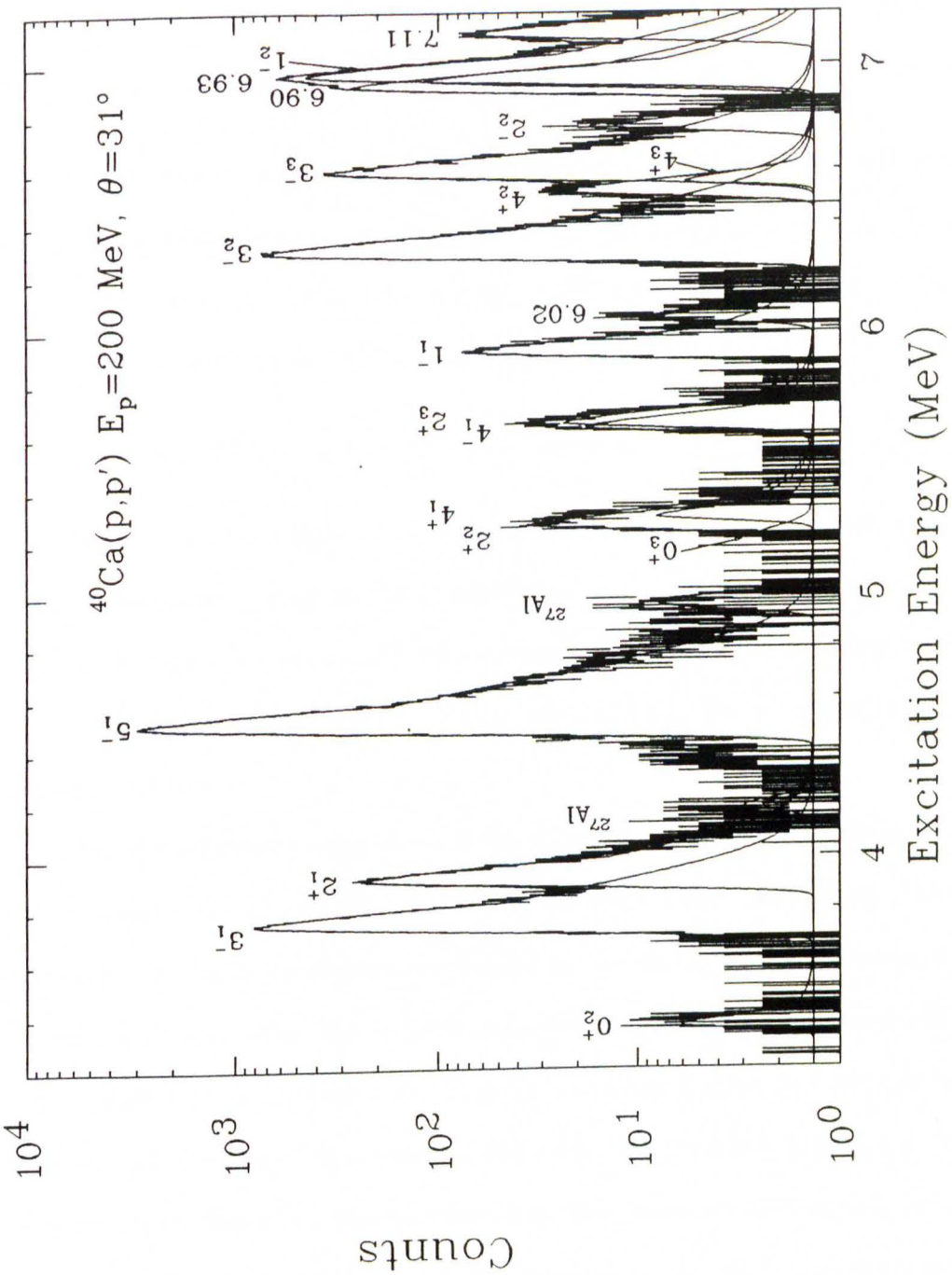

Figure 6.5: Fitted ^{40}Ca Spectrum

6.3 Formulae For Cross Sections and Analyzing Powers

In the following we denote the *differential cross sections* for up- and down-beam orientations as $\sigma_u(\theta) = (d\sigma/d\Omega)_u$ and $\sigma_d(\theta) = (d\sigma/d\Omega)_d$. The unpolarized cross section is, analogously, denoted by $\sigma_0(\theta) = (d\sigma/d\Omega)_0$. For each beam orientation the differential cross section is given as

$$\sigma_{u,d}(\theta) = N_{u,d}(1 + f_{u,d}^{multi})/(LT_{u,d} \cdot \varepsilon_{u,d} \cdot d\Omega \cdot t \cdot n_{u,d}), \qquad (6.5)$$

where $\sigma_{u,d}(\theta)$ are the differential cross sections (in mb/sr), $N_{u,d}$ the peak sums of the state of interest, $LT_{u,d}$ the scintillator (or computer) live times, $\varepsilon_{u,d}$ the chamber efficiencies, $d\Omega$ the acceptance solid angle (in sr), t the areal number thickness of the target (in nuclei/mb), and $n_{u,d}$ the total numbers of incident protons.

The scintillator or computer live times can be calculated from the ratios of the scalers S1 · S2 · $\overline{\text{BUSY}}$ and S1 · S2 for each beam orientation. The efficiencies for each orientation are defined as the ratio of events that make at least two consecutive hits in both chambers and satisfy an extended PID test (includes particle identification, good one-plane angles and the cut in Θ_{tgt}) and *all* the events that pass the extended PID (multiple hits and 0- or 1-hit events in either chamber are automatically excluded by the analyzer). Finally, the "clutter" factor $(1 + f_{u,d}^{multi})$, applied to the final cross sections, accounts globally for those events which fire a single MUX twice (multiple hits) and which are not processed by the analyzer. The total number of incoming protons can be calculated from the ratio of the total charge and

the elementary charge (1.602×10^{-19}C). The total charge is the product of the sum of the left and right integrators, the integrator full scale and a device characteristic scale factor

$$n_{u,d} = Q_{u,d}/e = [(INT(L) + INT(R)) \times FS/1000]/e. \tag{6.6}$$

For a composite target with n components of atomic masses A_i (in g) the areal number thickness of the relevant species (i) is the number of scattering centers for the beam and is given with the above units for charge and acceptance as

$$t_i = N_A \times \frac{f_i}{\sum_{i=1}^{n} f_i A_i} \times \frac{d}{\cos\theta_t}, \tag{6.7}$$

where N_A is Avogadro's number ($6.022 \times 10^{23}\text{mol}^{-1}$), f_i the stoichometric fraction of species (i), d the target areal density in g/mb and θ_t the target angle (angle of the normal on the target with the beam axis).

The target orientation was chosen to be in transmission geometry and the target angle usually to be half of the scattering angle. In this geometry the path length for the projectile in the target is independent of the position of the scattering center. Losses in resolution due to straggling are thus minimized. However, the cross sections may reflect nonuniformities in target composition and thickness, since the position where the beam strikes the target depends on the scattering angle.

The spin-up and spin-down cross sections are given with the unpolarized cross section, $\sigma_0(\theta)$, the beam polarizations $P_{u,d}$, and the analyzing power of the target A_y as

$$\sigma_{u,d}(\theta) = \sigma_0(\theta)[1 \pm P_{u,d} \cdot A_y]. \tag{6.8}$$

Conversely, both the unpolarized cross section and the analyzing power can be obtained from the spin-up and spin-down cross sections

$$\sigma_0(\theta) = \frac{P_d\sigma_u(\theta) + P_u\sigma_d(\theta)}{P_u + P_d} \tag{6.9}$$

and

$$A_y(\theta) = \frac{\sigma_u(\theta) - \sigma_d(\theta)}{P_d\sigma_u(\theta) + P_u\sigma_d(\theta)}. \tag{6.10}$$

If we assume that all the errors are uncorrelated, we can write the uncertainties of cross sections and analyzing powers as

$$\Delta\sigma_0 = \frac{\sqrt{(P_d\Delta\sigma_u)^2 + (P_u\Delta\sigma_d)^2 + [(P_d\Delta P_u)^2 + (P_u\Delta P_d)^2](\sigma_0 A_y)^2}}{P_u + P_d} \tag{6.11}$$

and

$$\begin{aligned} \Delta A_y \;=\; & \{[(\sigma_d\Delta\sigma_u)^2 + (\sigma_u\Delta\sigma_d)^2](P_u + P_d)^2 \\ & + [(\sigma_d\Delta P_u)^2 + (\sigma_u\Delta P_d)^2](\sigma_d - \sigma_u)^2\}^{1/2} \\ & \times(P_d\sigma_u + P_u\sigma_d)^{-2}. \end{aligned} \tag{6.12}$$

* * *

For a number of runs there was a problem with either the spin-up or the spin-down integrator scalers. Assuming the same current for both beam orientations, the correct integrator scaler value was reconstructed from the clock scaler and the calculated current from the other beam orientation. The corresponding spin-up or spin-down cross section was then multiplied with an appropriate correction factor. The multiplication code generated a new ALLFIT summary file with the corrected polarized cross section. The runs with a scaler problem are marked in the list of runs, Appendix E, and the applied scale factor for the polarized cross section is given.

6.4 Kinematic Formulae

The final data will be expressed in the center-of-mass system. In the following, all the lab quantities are unprimed and the center-of-mass quantities primed. The notation is the same as in the code ALLFIT [Kel AL]. In the binary reaction $m_1 + m_2 \rightarrow m_3 + m_4$ we choose m_1 to be the incoming projectile and m_2 to be the target. The (detected) outgoing projectile particle is m_3 and the (undetected) outgoing target particle m_4. The target may be excited and, hence, $m_4 = m_3 - Q$ where Q is the Q-value of the reaction. Utilizing conservation of four-momenta, the lab-energy and momentum of the outgoing particle can be expressed as

$$\varepsilon_3 = \frac{A + u\cos\theta\sqrt{A^2 - m_3^2(1 - u^2\cos\theta)}}{1 - u^2\cos^2\theta} \tag{6.13}$$

$$p_3 = \sqrt{\varepsilon_3^2 - m_3^2}. \tag{6.14}$$

In these equations, with $\varepsilon_t = \varepsilon_1 + m_2$ (the total energy of the system), the velocity of the center-of-mass is $u = p_1/\varepsilon_t$, and the auxiliary quantity A is $A = (\varepsilon_t^2 - p_1^2 + m_3^2 - m_4^2)/2\varepsilon_t$. Transformation of the incoming (p_1) and outgoing (p_3) projectile momenta is achieved by the Lorentz boosts

$$\begin{aligned} p_1' &= \gamma(p_1 - u\varepsilon_1) \\ p_{3\perp}' &= p_{3\perp} = p_3\sin\theta \\ p_{3||}' &= \gamma(p_{3||} - u\varepsilon_3) = \gamma(p_3\cos\theta - u\varepsilon_3) \\ p_3' &= \gamma\sqrt{p_3^2 - u^2p_3^2\sin^2\theta - 2u\varepsilon_3 p_3\cos\theta + u^2\varepsilon^2}, \end{aligned} \tag{6.15}$$

where $\gamma = 1/\sqrt{1-u^2}$. With $\tan\theta' = p'_{3\perp}/p'_{3\parallel}$ and the geometrical identity $1 + \tan^2\theta' = 1/\cos^2\theta'$ we find ($r = u\varepsilon_3/p_3$)

$$\cos\theta' = \frac{\cos\theta - r}{\sqrt{1 - u^2\sin^2\theta + r^2 - 2r\cos\theta}}. \tag{6.16}$$

The momentum transfer $\mathbf{q}'$ in the center-of-mass is defined as $\mathbf{q}' = \mathbf{p}'_1 - \mathbf{p}'_3$, and its magnitude is

$$q' = \sqrt{p_1'^2 + p_3'^2 - 2p'_1 p'_3\cos\theta'}. \tag{6.17}$$

For the calculation of the Jacobian $\frac{d\cos\theta}{d\cos\theta'}$ we replace in the equation for $\cos\theta'$ all unprimed quantities by primed ones and observe that $r \to -r'$. With $\varepsilon' = m_3^2 + p_3'^2$ and $r' = u\varepsilon'_3/p'_3$ we can write

$$\cos\theta = \frac{\cos\theta' + r'}{\sqrt{1 - u^2\sin^2\theta' + r'^2 + 2r'\cos\theta'}}. \tag{6.18}$$

The Jacobian is then easily evaluated to be

$$\frac{d\cos\theta}{d\cos\theta'} = \frac{(1-u^2)(1 + r'\cos\theta')}{(1 - u^2\sin^2\theta' + r'^2 + 2r'\cos\theta')^{3/2}}. \tag{6.19}$$

Finally, to enhance detail, we will display for elastic scattering always the ratio of the differential cross section and the point-charge Rutherford cross section σ_R which is

$$\sigma_R(q') = (2Z_1 Z_2 e^2\mu)^2 \cdot \frac{1}{q'^4}. \tag{6.20}$$

Here μ is the reduced energy in the center-of-mass, $\mu = \frac{\varepsilon'_1\varepsilon'_2}{\varepsilon'_1+\varepsilon'_2}$, where $\varepsilon'_1 = \sqrt{p_1'^2 + m_1^2}$ and $\varepsilon'_2 = \gamma m_2$.

6.5 Normalizations

Depending on the spectrometer angle, during our experiment various Faraday cups had to be used. As mentioned before in Chapter 3, the external

cup was used at angles above 18 deg (March 1988, above 15 deg) together with a dump pipe. At smaller angles, various internal cups which were mounted on the rotating platter in the scattering chamber were used. We believe the external cup to be accurate to about 1 percent and to be more accurate than the internal cups which have energy-dependent normalization problems [Nad 77]. All data are, therefore, normalized to the external cup standard.

6.5.1 100 MeV Cups

For the normalization of the 100 MeV January 1987 *long internal* cup we had overlapping measurements with the external cup at 18 deg for ^{40}Ca and at 18 deg and 22 deg for ^{16}O. Cross section ratios for the 0_1^+, 3_1^-, 2_1^+ and 1_1^- states in ^{16}O and for the 0_1^+, 3_1^-, 2_1^+ and 5_1^- states in ^{40}Ca were computed and weighted averages calculated. For the ^{40}Ca states we get $\left\langle \frac{E87}{I87} \right\rangle_{wgt} = 1.008(55)$ and for the ^{16}O states $\left\langle \frac{E87}{I87} \right\rangle_{wgt} = 1.004(21)$. The overall normalization is thus $\left\langle \frac{E87}{I87} \right\rangle_{wgt} = 1.005(20)$.

For the normalization of the *short internal* cup in January 1987 we had overlap points at -10 deg for ^{40}Ca and at -10 deg and -12 deg for ^{16}O. For ^{40}Ca we have only data for the 0_1^+ state. For ^{16}O again the four lowest states were available at -10 deg and the three lowest states at -12 deg. We find for ^{40}Ca $\left\langle \frac{E87}{S87} \right\rangle_{wgt} = 0.999(55)$ and for the ^{16}O states $\left\langle \frac{E87}{S87} \right\rangle_{wgt} = 1.022(23)$. This gives an overall normalization factor of $\left\langle \frac{E87}{S87} \right\rangle_{wgt} = 1.019(21)$.

6.5.2 200 MeV Cups

For the cup normalizations at 200 MeV it was necessary to compare cross sections of different run periods. In April 1987 we used exclusively the external cup; in January 1988 both the internal and the external cup were used. Because of the different scattering angle offsets in different run periods cross sections at the same spectrometer angles are not immediately comparable. We found comparable cross sections by first- or, where necessary, by second-order interpolation of the data points in the vicinity of the overlap.

Overlap points with the *internal* cup for ^{40}Ca and ^{16}O were at 18 deg and at 19.5 deg. Cross section ratios were computed for the same four states as in the 100 MeV case. For the ^{16}O states the weighted average for the normalization factor is $\left\langle \frac{\text{E87}}{\text{I88}} \right\rangle_{\text{wgt}} = 0.873(22)$; for the ^{40}Ca states we find $\left\langle \frac{\text{E87}}{\text{I88}} \right\rangle_{\text{wgt}} = 0.900(32)$. The overall normalization is $\left\langle \frac{\text{E87}}{\text{I88}} \right\rangle_{\text{wgt}} = 0.884(29)$. There was also a difference in normalization between the *external* cup runs in January 1988 (after the encoder problem was fixed) and April 1987. Based on interpolated cross sections from external cup measurements in 1988 at 18 deg, 19.5 deg, 21 deg and 25 deg for the four ^{40}Ca states 0_1^+, 3_1^-, 2_1^+ and 5_1^- we find a normalization factor of $\left\langle \frac{\text{E87}}{\text{E88}} \right\rangle_{\text{wgt}} = 0.931(27)$. It appears that the runs *with* the encoder problem do not differ in normalization from the external cup runs in April 1987.

6.5.3 Normalizations between Targets

For the normalization between the old (BeO I) and the new BeO (BeO II) targets in January 1987 we had cross sections for both targets at

Energy	*Item*	*Normalization*	*Normalization Factor*
100 MeV	Cups	E87 / I87	1.005(20)
		E87 / S87	1.019(21)
	BeO Targets	BeO II / BeO I	1.105(41)
		new / old meas.	0.988
	Ca Targets	thick / thin	0.959(15)
200 MeV	Cups	E87 / I88	0.884(29)
		E87 / E88	0.931(27)

Table 6.5: Overall Normalization Factors for Experiment 268.

angles between 18 deg and 70 deg (all of these runs used the external cup). The weighted average for the cross section ratios is $\left\langle \frac{\text{BeO II}}{\text{BeO I}} \right\rangle_{\text{wgt}} = 1.105(41)$.

All the BeO cross sections were calculated assuming a target thickness of 21.99 mg/cm^2. Recently, a new measurement of the target thickness at IUCF yielded a value of 22.26 mg/cm^2 (see Chapter 3). Therefore, all BeO cross sections were additionally multiplied by a factor of 0.988.

In January 1987 we tried to obtain better computer live times for forward angle measurements by using a *thin* ^{40}Ca target. Normalization points for the 0_1^+, 3_1^- and 2_1^+ states were at angles between -16 deg and $+18$ deg. The weighted average for the 0_1^+ normalization is $\left\langle \frac{\text{Thick}}{\text{Thin}} \right\rangle_{\text{wgt}} = 0.976(29)$, for the 3_1^- normalization $\left\langle \frac{\text{Thick}}{\text{Thin}} \right\rangle_{\text{wgt}} = 0.952(19)$ and for the 2_1^+ normalization $\left\langle \frac{\text{Thick}}{\text{Thin}} \right\rangle_{\text{wgt}} = 0.956(48)$. The overall normalization factor is then $\left\langle \frac{\text{Thick}}{\text{Thin}} \right\rangle_{\text{wgt}} = 0.959(15)$. All the overall normalization factors are summarized in Table 6.5.

6.6 Cross Section and Analyzing Power Results

6.6.1 Fitted Data

We fitted ^{40}Ca states below about 7 MeV in excitation energy. In this excitation energy range the peaks are in a good region of the focal plane and are still relatively well separated. Also, all the states of interest with available complementary electron excitation data are in this range. Some of the states were named in our own notation as follows: the state at 6.028 MeV is comprised of a 2^- (6.026 MeV) and a 3^+ (6.029 MeV) state [End 78]; the 6.909 MeV state is in the same reference quoted to be a 2^+ state. The 6.931 MeV state is a triplet: a state at 6.927 MeV, at 6.930 MeV (6^+), and at 6.938 MeV. Finally, the 7.11 MeV state is a combination of a 1^- (7.113 MeV) and a 4^- (7.114 MeV) state.

100 MeV spectra for ^{9}Be and ^{16}O were fitted, whenever possible, up to the ^{16}O 3^- state at 13.259 MeV. Higher excitation energies were not accessible mainly because of the smaller effective focal plane in January 1987, when the short scintillators were used. The 200 MeV spectra we tried to fit, only partially successfully though, up to the ^{16}O 5^- state at 14.399 MeV. The problems that occur for many of the high-lying small states, especially reflected in their analyzing powers, come from the fact that they appear above a large background, due to the beryllium continuum and resonances, which has a very significant analyzing power of its own. As was mentioned on page 233, the broad ^{9}Be Lorentzian peak is the combination of a $7/2^-_1$ and $9/2^+_1$ state ([Dix 86, Gli 89]). The ^{16}O state at 13.08 MeV is the combination

of a 2^+ (13.02 MeV) and 1^- (13.09 MeV) state. Finally, we did not succeed in isolating the nearby ($\approx$ 10 keV) 3^+ state from the 4_2^+ of ^{16}O. Since the analyzing powers for abnormal-parity transitions are generally small, one would expect the cross section of the doublet to be enhanced and the analyzing power to be somewhat diluted [Kel 89a]. The quality of our measurement of this doublet at both energies was so poor, however, that we can not see this effect.

Several fitted data points had to be excluded from the final data tables and figures—the list of runs in Appendix E makes a note of every state that was omitted for a particular run. There are various reasons which can warrant an exclusion. Generally, when a state was excluded, there was sufficient redundancy available, however.

- Problems in added spectra: during the experiment prospective extremely long runs, typically inelastic runs where good statistics for the small states was required, were often broken down into several shorter runs with identical magnet settings, etc. Off-line, the spectra were added to improve both the statistics of the small states and to facilitate the fitting of problematic line shape parameters (tails, etc.). Due to small drifts of the magnetic fields in the spectrometer or, in the case of non-consecutive runs, due to imperfect reproducibility of the fields, slight variations in the already highly non-linear energy-position calibration occured. Affected by this are often, but not exclusively only, the unresolved ^{40}Ca doublets and triplets in which a random redistribution of strength among the constituents can be observed. The results are

then totally incompatible with other measurements at the same angle or with the overall angular distribution. In hindsight, spectra should probably not be added.

- Peaks at the edge of the effective focal plane: although we found no evidence for a position-dependent efficiency beyond the one which was resolved by the recovery of the 2-hit events, for some January 1987 runs with the short scintillators we find a more or less abrupt loss of strength in peaks at the edge of the effective area. Because of redundancy we did not try to recover these particular states which, in the first place, were often only put in the fit to constrain the background as in the case of some high-lying ^{16}O states on top of the beryllium continuum.

- Obstructed peaks: because of differential recoil the beryllium states move with respect to the oxygen states as one goes to larger angles. Some of the ^{9}Be states are very strong and narrow such as the $5/2_1^-$, others are moderately strong but with a large intrinsic width such as the Lorentzian ($\Gamma \approx 1.25$ MeV). These peaks cross at certain angles over some of the ^{16}O states, making a reliable measurement either difficult or even impossible. In Appendix B we provide recoil diagrams appropriate for 100 and 200 MeV kinematics where this situation is displayed graphically.

- Normalization with respect to current: during some of the runs we noticed that the cup or the associated electronics seemed to leak current to some small extent, thereby introducing some uncertainty in the

normalization. Evidence for a systematic dependence of this effect on the beam current or the integrator full scale was not found, however. Runs in January 1988 with the 2 nA integrator scale had a very serious charge integration problem of this kind and had to be discarded. Apart from leakage, correctly zeroing the integrators during the run sometimes posed a problem. This may also have contributed to errors in the absolute normalization of certain runs which were found to have many of their states inconsistent.

- Non-reproducibility of the scattering angle: although we found generally good reproducibility for our measurements (2–3% for the 200 MeV measurements), we find some cases (most notably among the ^{16}O measurements at 100 MeV) which differ systematically from earlier measurements by about 10–20%. A different scattering angle is one explanation for the observed systematics (the uncertainty in the laboratory scattering angle may be up to 0.2° depending on the beam tune), although normalization problems due to charge integration are also possible.

- Background at forward angles: certain elastic measurements at forward angles were only done at positive spectrometer angles or at negative angles but with a useless intgrator scale (example: ^{40}Ca elastic measurements with the 2 nA scale in January 1988). In the off-line analysis, the very strong background due to the internal Faraday cup, which is present in spectra at positive angles, proved to be unmanageable and

the respective runs had to be discarded.

6.6.2 Some General Observations

In Figure 6.6 the fitted widths for ^{9}Be, ^{16}O and ^{40}Ca are summarized. The states used to generate the histograms did not have any intrinsic width. Hence, the fitted widths can be regarded as a measure of the spatial resolution that was achieved in our experiment. Because resolution depends critically on all the beam and spectrometer parameters, and since all these parameters were set for either ^{16}O or ^{40}Ca kinematics, we are not surprised to find large widths for ^{9}Be. However, as the histograms for ^{16}O and ^{40}Ca also show, for most of our ^{40}Ca runs the resolution was between about 30 and 50 keV, while for ^{16}O we find resolutions between about 50 and 80 keV. The reason for this better ^{40}Ca resolution is the smaller target thickness.

As a cross-check for the accuracy of the overall normalization of our 200 MeV data, we compare in Figure 6.7 elastic cross sections and analyzing powers for ^{16}O and ^{40}Ca with previous data taken at IUCF ([Glo 85]) and TRIUMF ([Ste 85] and P. Schwandt, private communication), respectively. We find consistency, with the exception of the ^{16}O cross sections at momentum transfers between about 0.7 and 1.7 fm^{-1} where we believe our data to be better than the previous measurements. In this momentum transfer range the ^{16}O analyzing powers of the previous measurement agree with ours, while the corresponding cross sections appear to be too high. This possibly points to a normalization problem in the IUCF data.

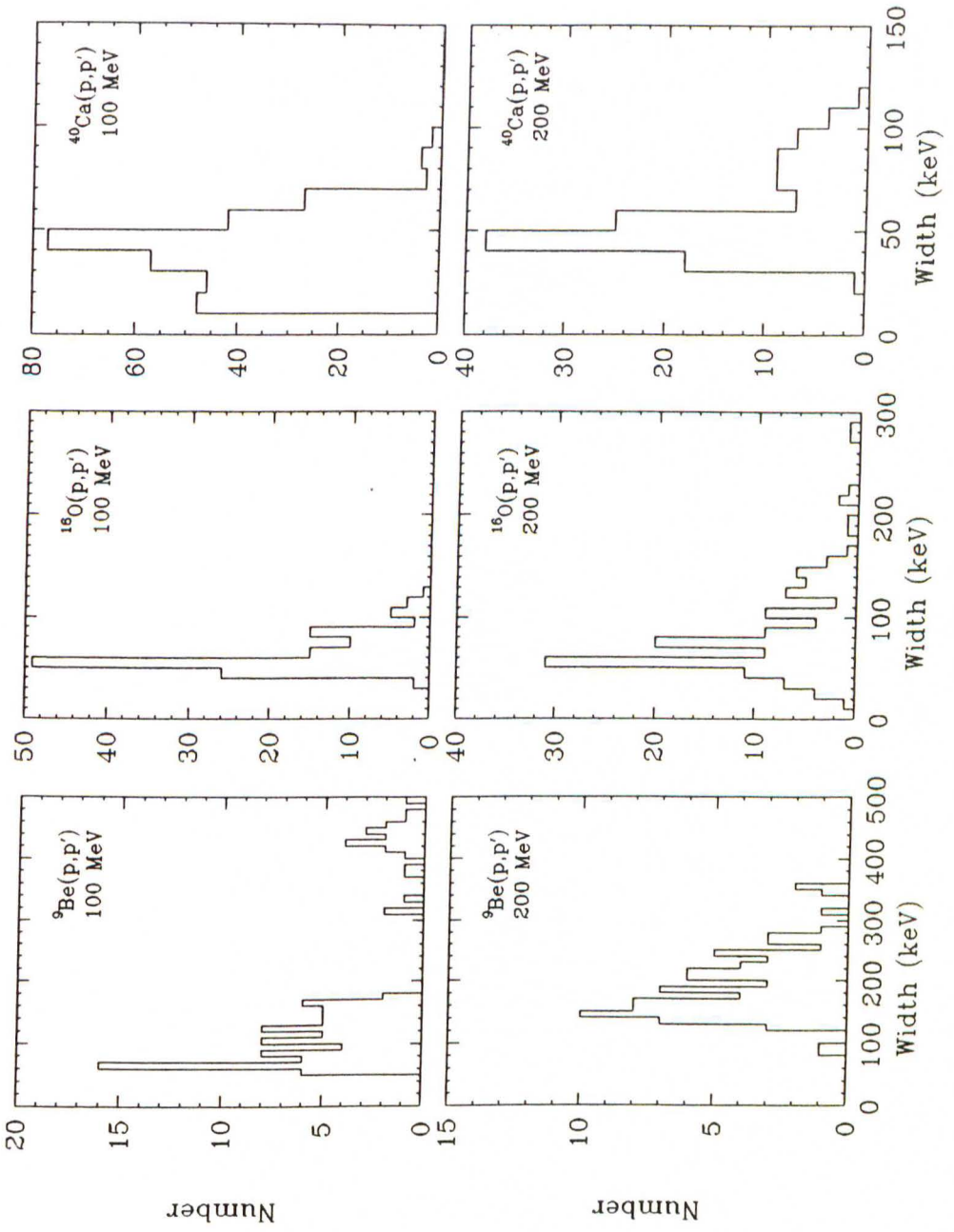

Figure 6.6: Histograms of Fitted Peak Widths.

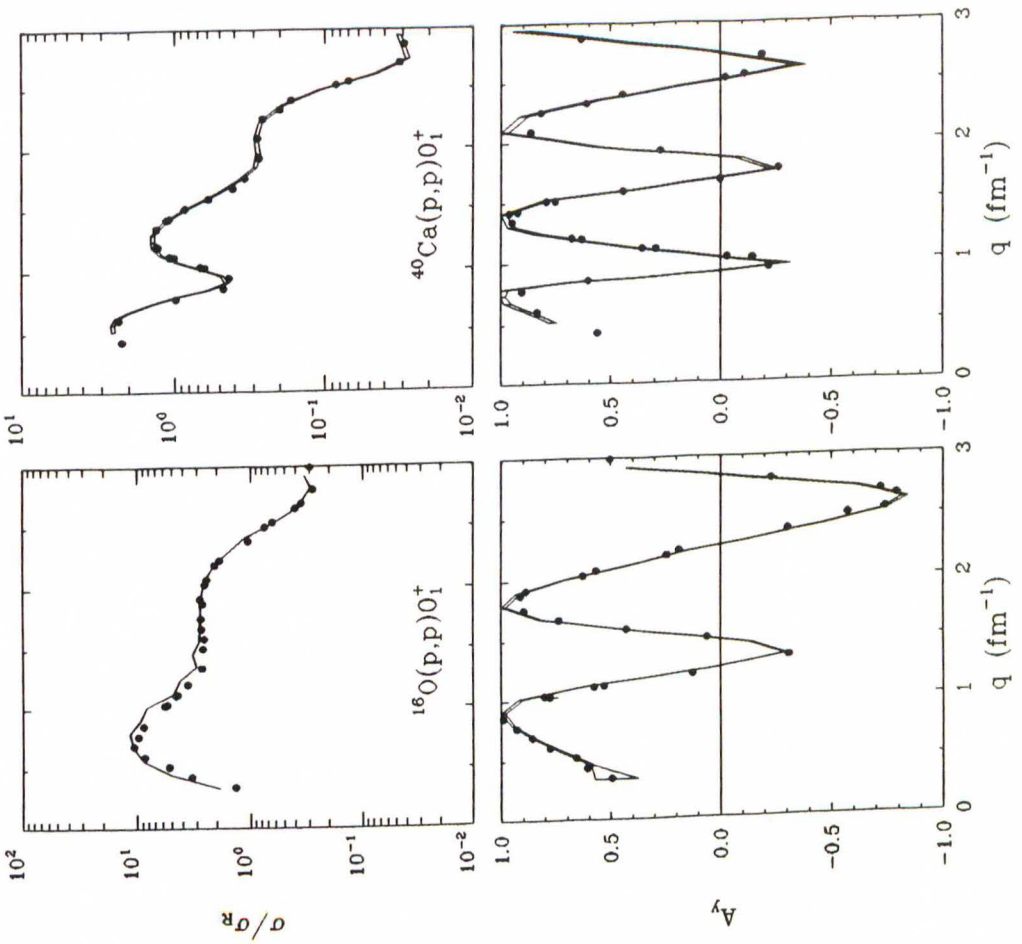

Figure 6.7: Comparison with Previous 200 MeV Elastic Measurements. E268 data are displayed as symbols, ^{16}O IUCF data ([Glo 85]) and ^{40}Ca TRIUMF data ([Ste 85] and P. Schwandt, private communication) as bands.

6.7 Results and Treatment of Errors

The data for all the ^{9}Be, ^{16}O and ^{40}Ca states at 100 and 200 MeV are plotted in Figures 6.8–6.43 of this chapter, and are also tabulated in Appendix F. The quoted values and associated uncertainties for cross sections and analyzing powers have been obtained as follows: for *single* measurements they are simply calculated from Eqs. (6.9)–(6.12). Input for these equations are the fitted spin-up and spin-down cross sections $\sigma_{u,d}$, their uncertainties $\Delta\sigma_{u,d}$, the spin-up and spin-down beam polarizations $P_{u,d}$, and their uncertainties $\Delta P_{u,d}$. The quantities $\Delta\sigma_{u,d}$ are the larger of the estimated fitting error or the statistical error. The values for $P_{u,d}$ and $\Delta P_{u,d}$ were estimated in Chapter 4. Although the presented data contain all the cup and target normalizations listed in Table 6.5, the normalization uncertainties were not included. Finally, in the case of *repeated* measurements a weighted average is quoted; the associated uncertainty is the larger of the uncertainty of the mean or the standard deviation about the mean [Bev 69].

For 200 MeV we did a detailed study on the case of the three lowest strong states of both ^{16}O and ^{40}Ca. We found that with the exception of some odd points the reproducibility of both our cross section and analyzing power measurements was between 2 and 3% (which is consistent with the earlier findings described in Chapter 4). The fluctuations in the cross sections are mainly due to normalization uncertainties from variations in uniformity of the target and from variations in the charge integration, dead time correction, efficiency, etc. Uncertainties in the polarization should not have much impact on the cross section if the difference of the spin-up and spin-down

beam polarizations is small—for our experiment this difference was about 0.02. It is striking, however, that for the aforementioned January 1987 runs which were inconsistent by 10–20% with previous runs, the beam polarization was also consistently very low. Uncertainties and fluctuations in the beam polarization have a bigger impact on the analyzing powers; the effect of large backgrounds with analyzing power on the analyzing powers of small states has been discussed above. The uncertainty in overall normalization is estimated to be about 5%.

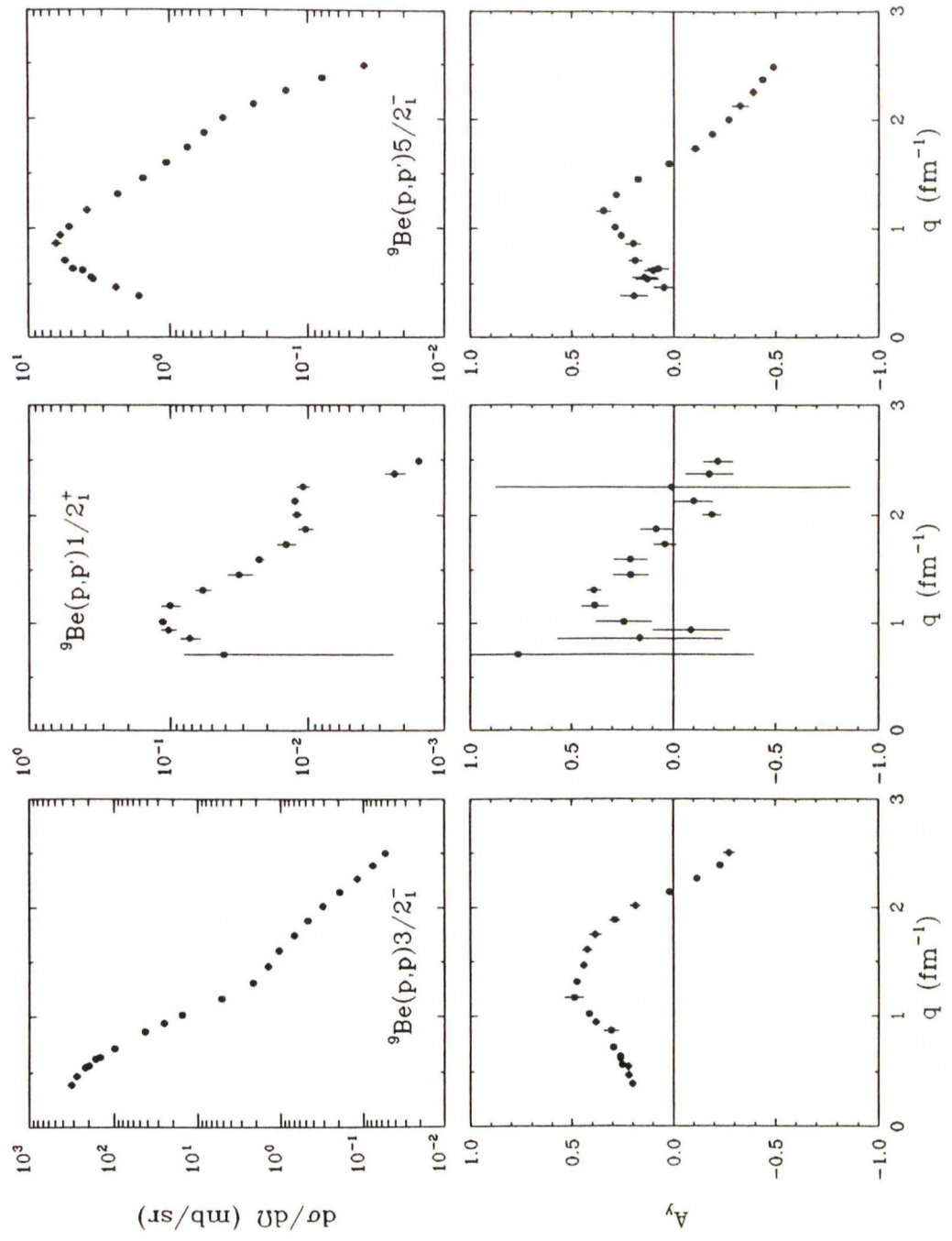

Figure 6.8: ^{9}Be$(\vec{p}, p')$ at E_P = 100 MeV: $3/2_1^-$, $1/2_1^+$ (1.680 MeV), and $5/2_1^-$ (2.429 MeV).

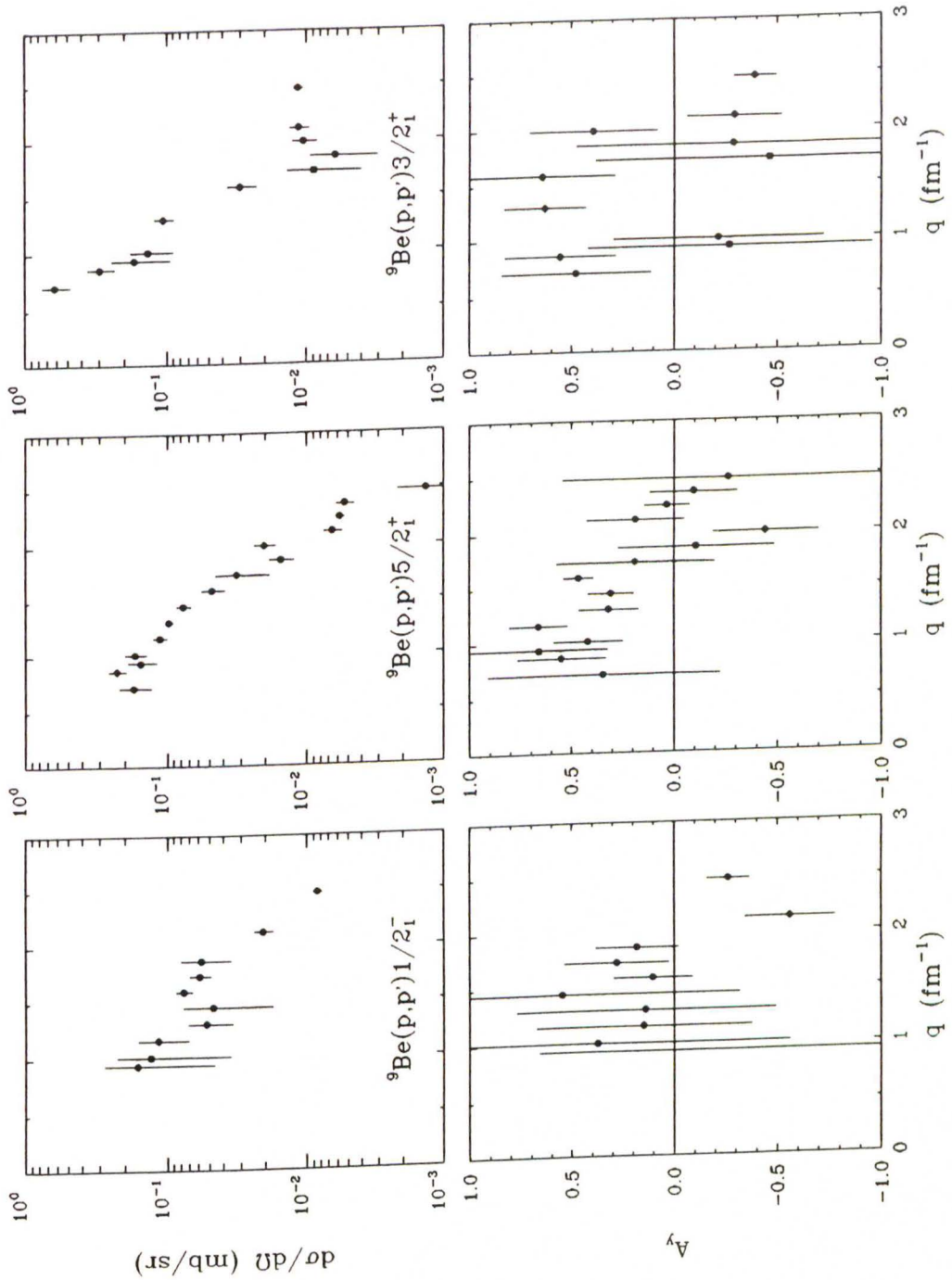

Figure 6.9: ^{9}Be$(\vec{p},p')$ at E_P = 100 MeV: $1/2^-_1$ (2.78 MeV), $5/2^+_1$ (3.049 MeV) and $3/2^+_1$ (4.704 MeV).

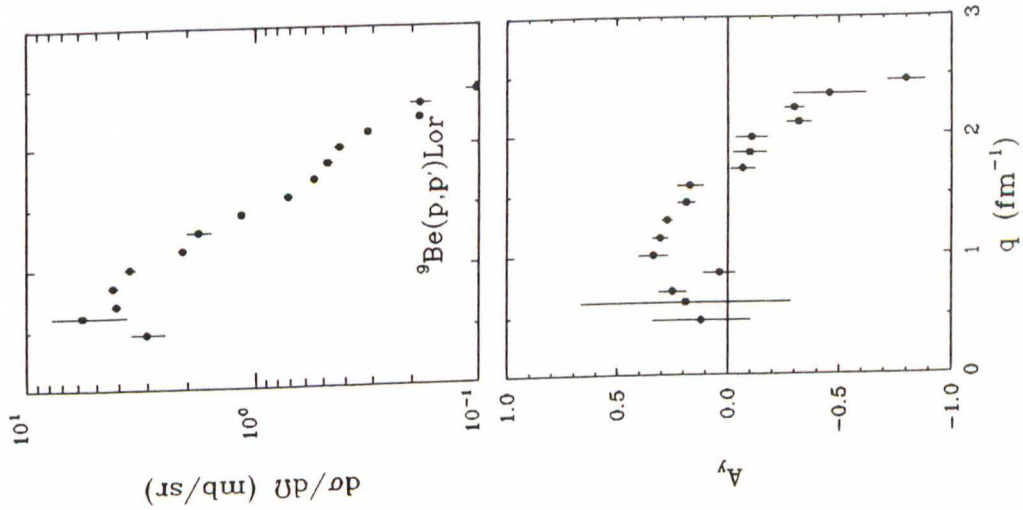

Figure 6.10: ^{9}Be$(\vec{p},p')$ at E_P = 100 MeV: Lor (6.5 MeV)

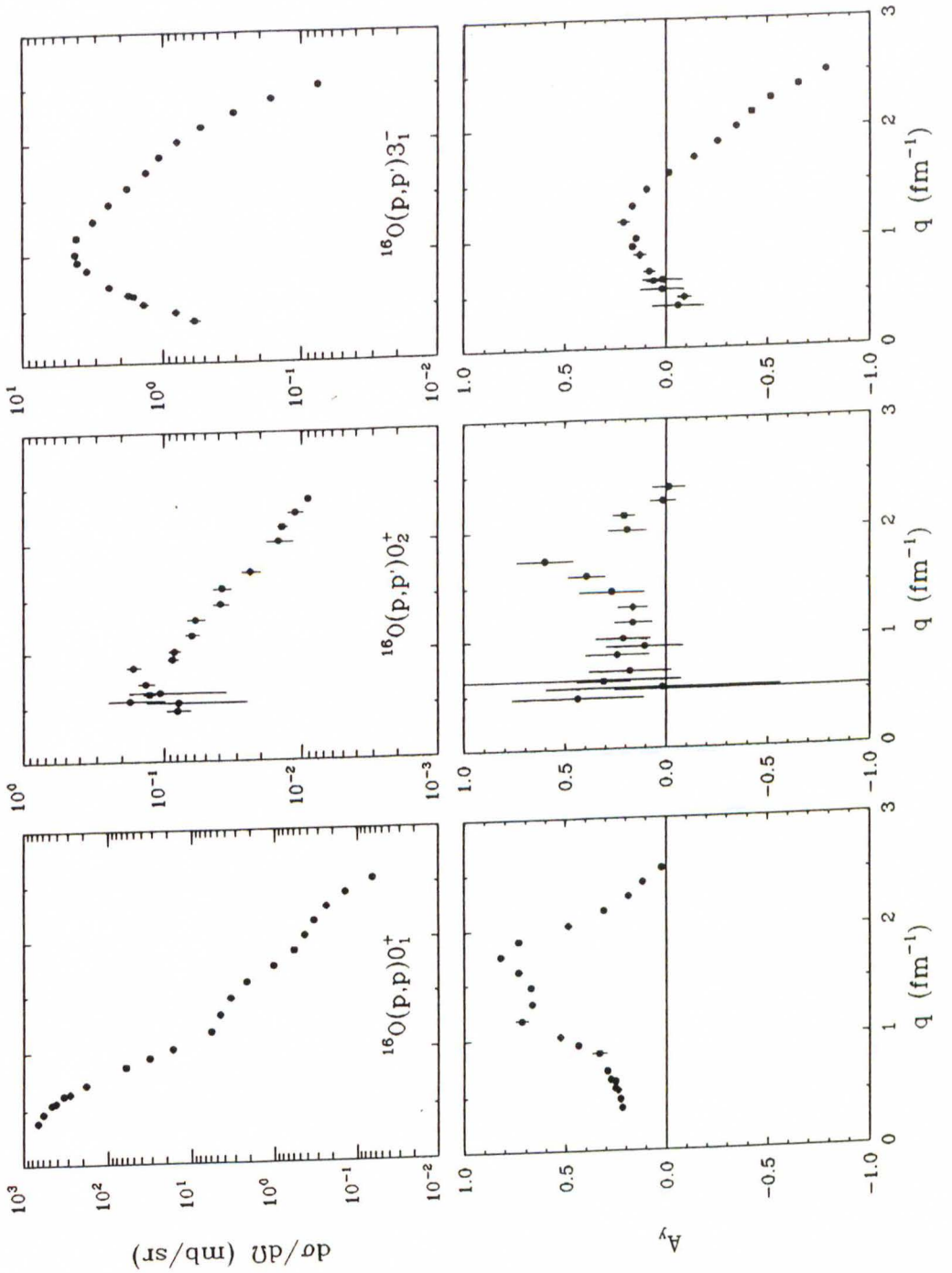

Figure 6.11: $^{16}O(\vec{p},p')$ at E_P = 100 MeV: 0_1^+, 0_2^+ (6.0494 MeV), and 3_1^- (6.1299 MeV).

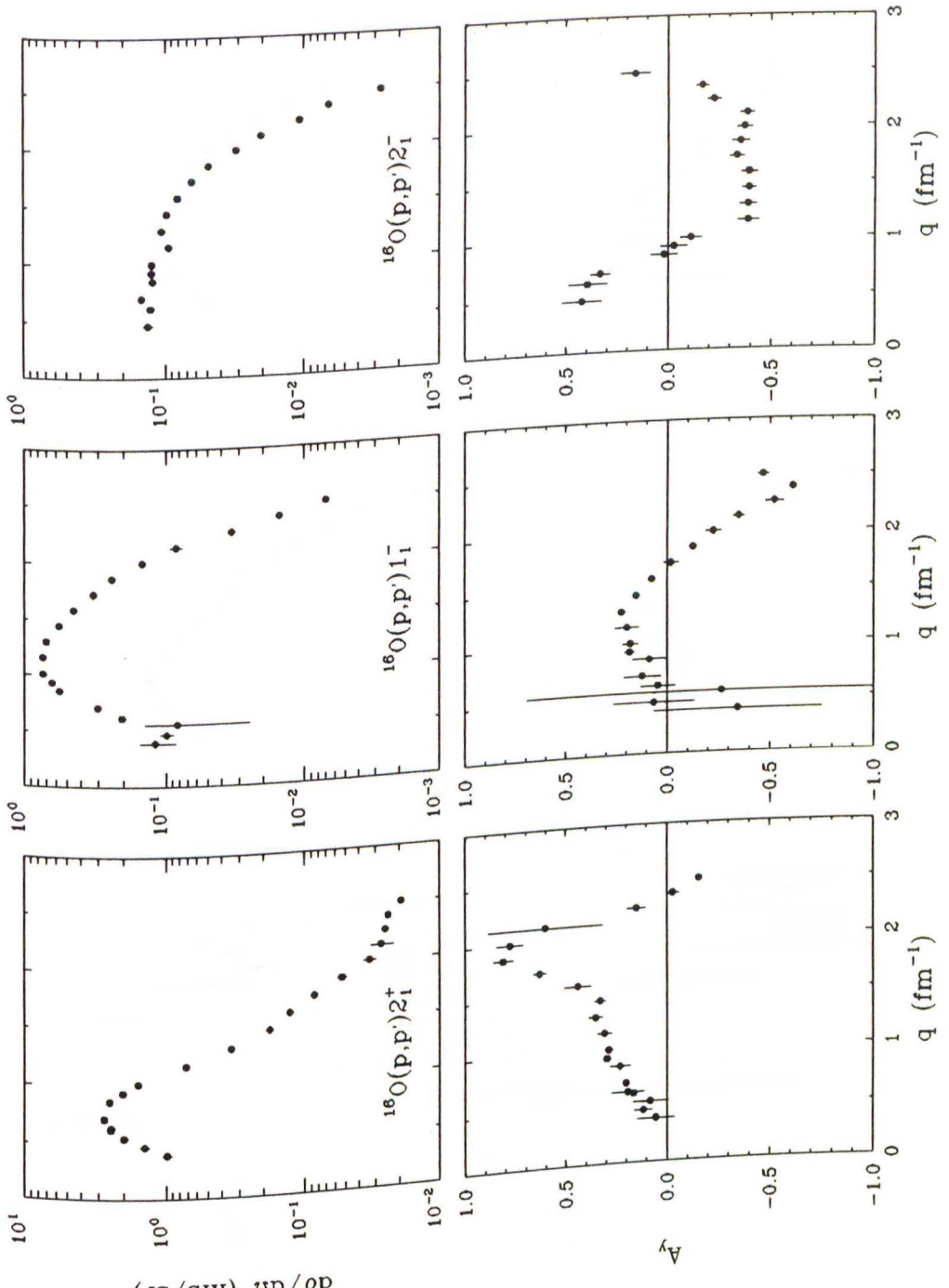

Figure 6.12: $^{16}O(\vec{p},p')$ at E_P = 100 MeV: 2_1^+ (6.9171 MeV), 1_1^- (7.1169 MeV), and 2_1^- (8.8719 MeV).

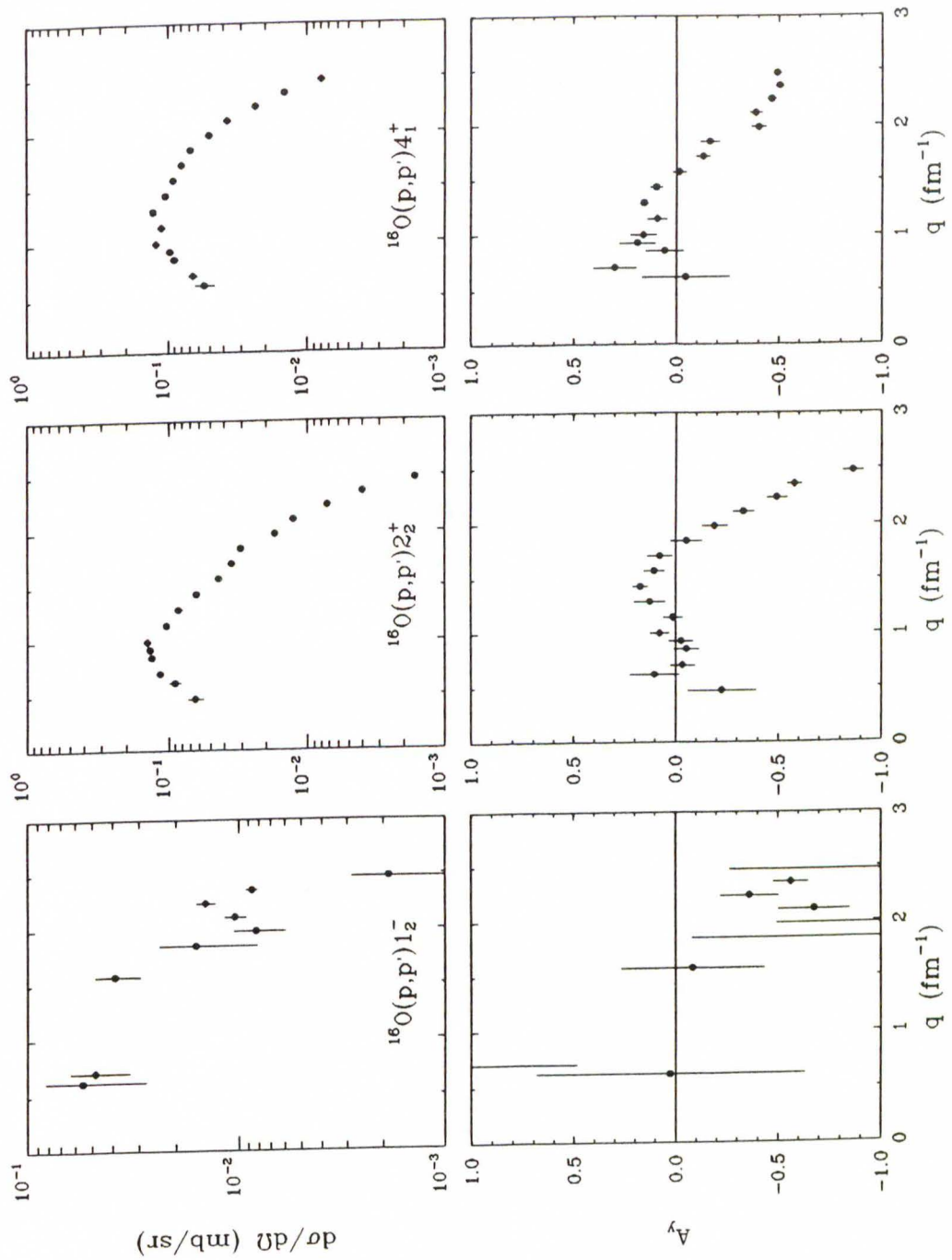

Figure 6.13: $^{16}O(\vec{p},p')$ at E_P = 100 MeV: 1^-_2 (9.585 MeV), 2^+_2 (9.8445 MeV), and 4^+_1 (10.356 MeV).

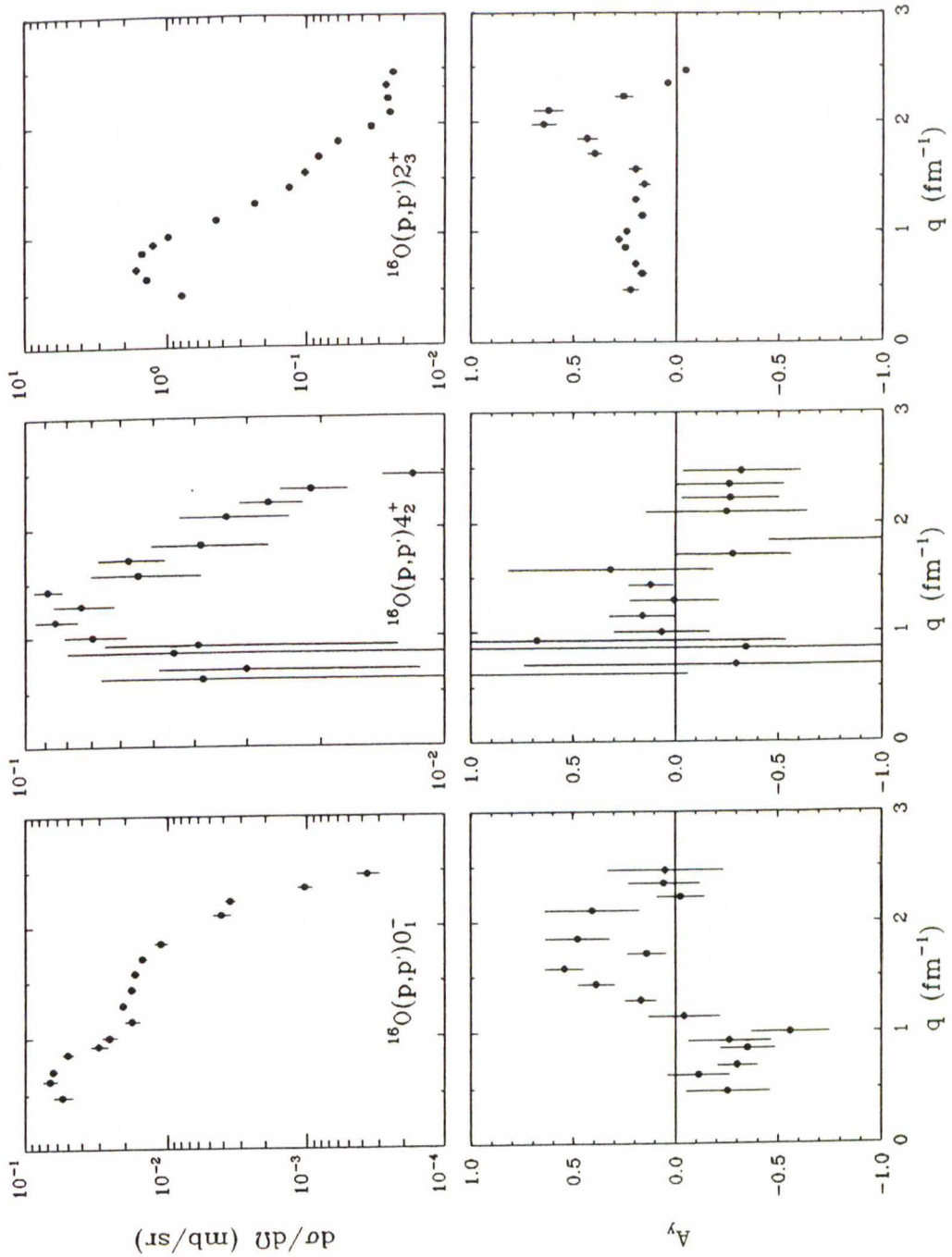

Figure 6.14: $^{16}O(\vec{p},p')$ at E_P = 100 MeV: 0^-_1 (10.957 MeV), 4^+_2 (11.097 MeV), and 2^+_3 (11.520 MeV).

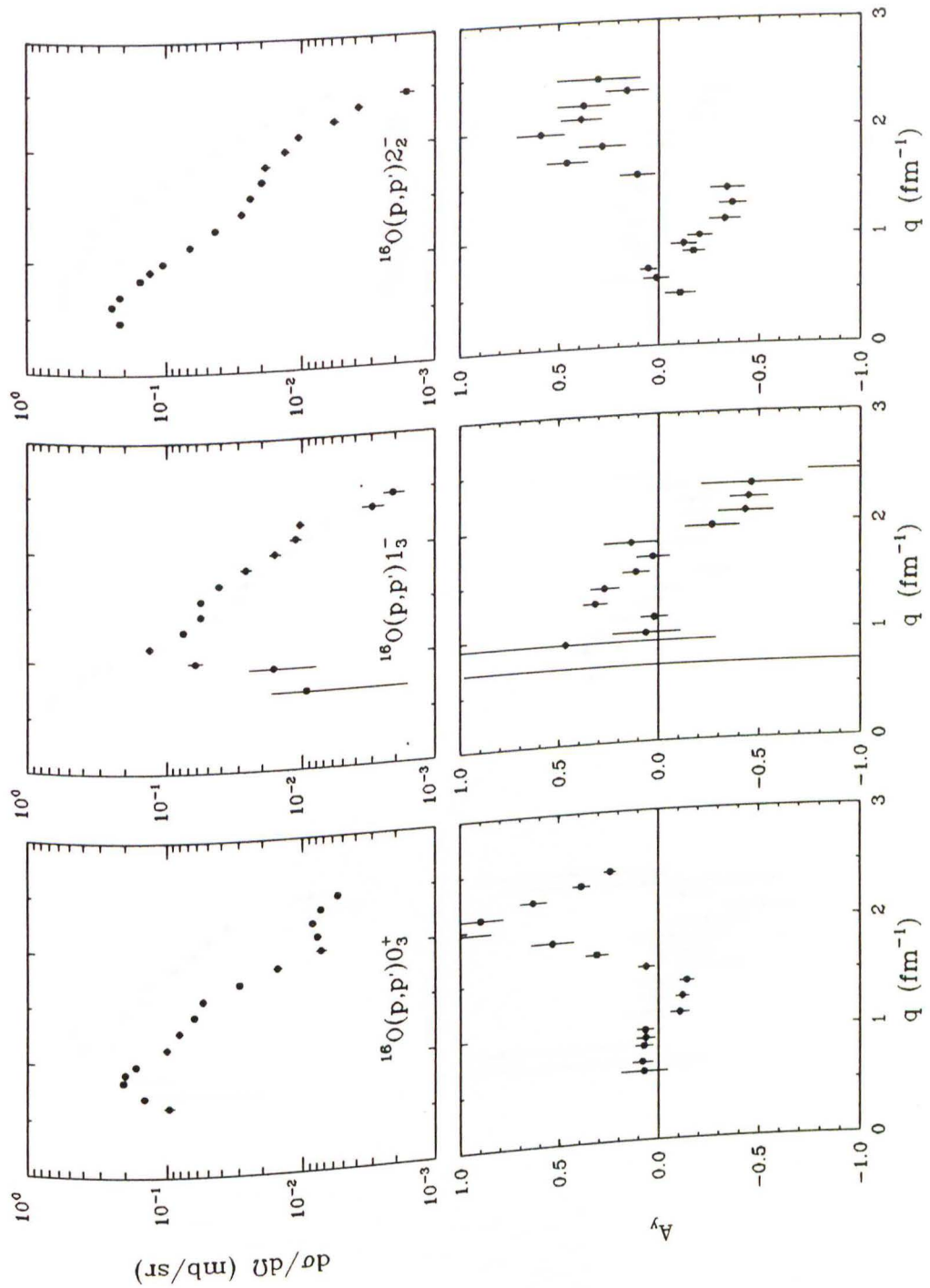

Figure 6.15: $^{16}O(\vec{p},p')$ at E_P = 100 MeV: 0^+_3 (12.049 MeV), 1^-_3 (12.440 MeV), and 2^-_2 (12.530 MeV).

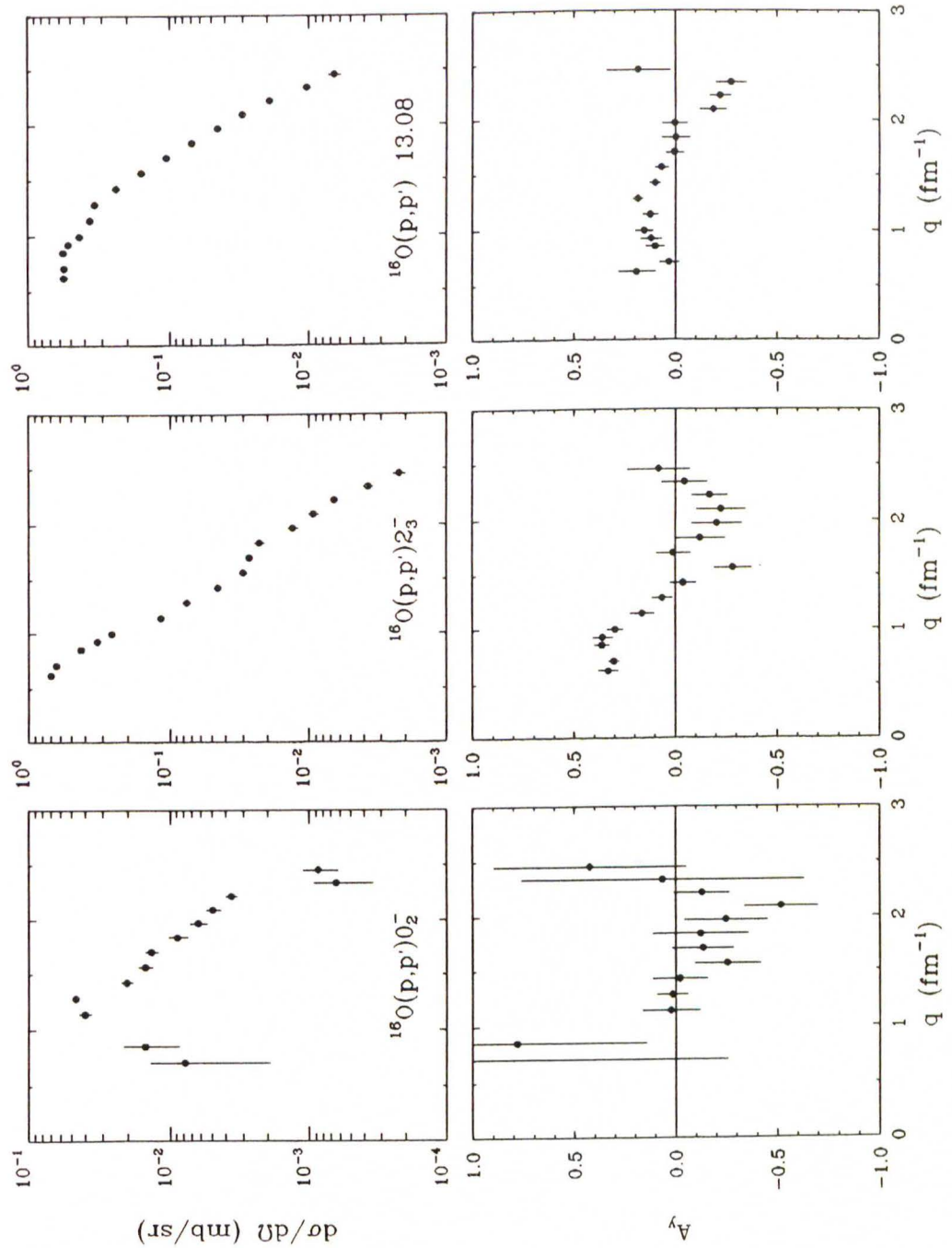

Figure 6.16: $^{16}O(\vec{p},p')$ at E_P = 100 MeV: 0_2^- (12.796 MeV), 2_3^- (12.969 MeV), and 13.08 (13.08 MeV).

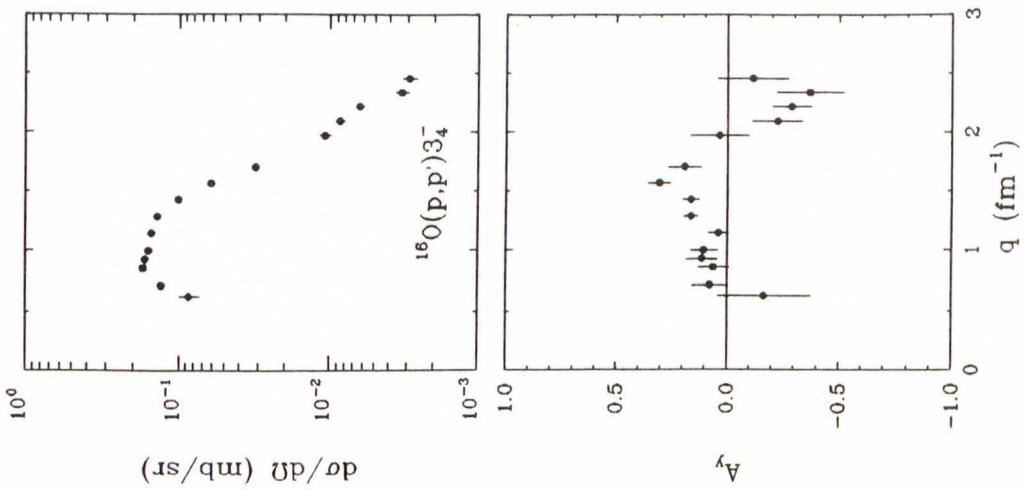

Figure 6.17: $^{16}O(\vec{p},p')$ at E_P = 100 MeV: 3^-_4 (13.259 MeV).

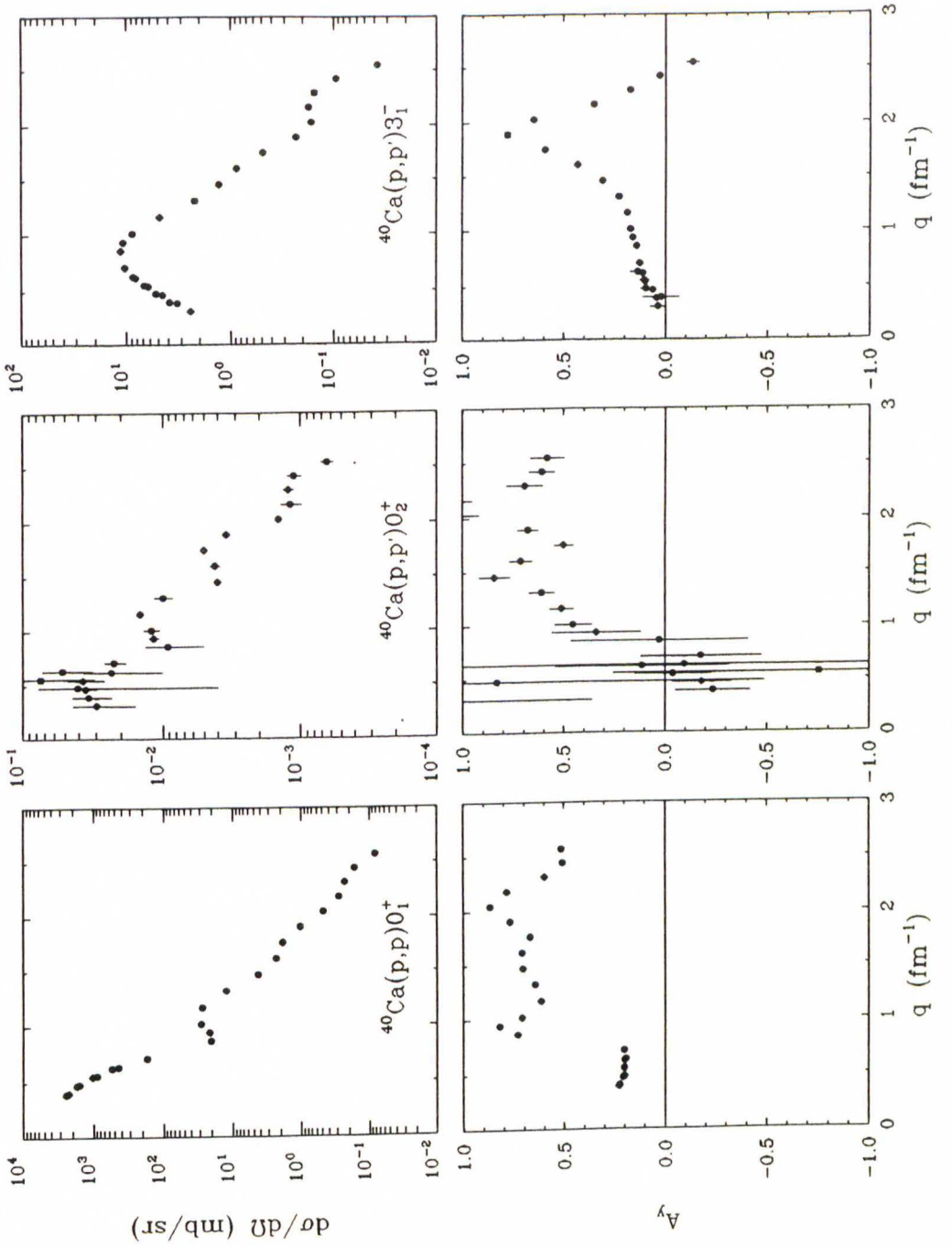

Figure 6.18: $^{40}\mathrm{Ca}(\vec{p},p')$ at E_P = 100 MeV: 0^+_1, 0^+_2 (3.3521 MeV), and 3^-_1 (3.7364 MeV).

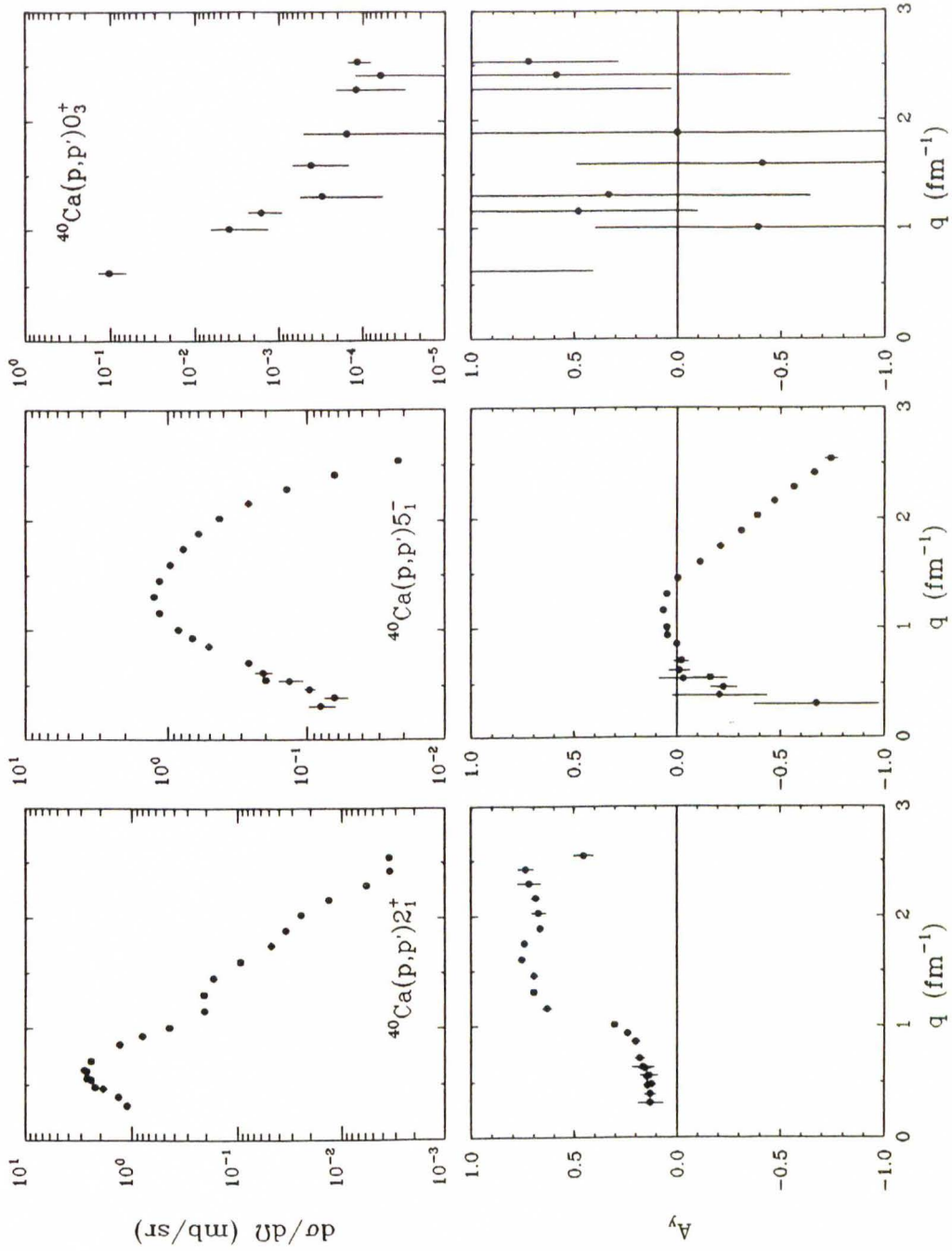

Figure 6.19: ^{40}Ca$(\vec{p},p')$ at E_P = 100 MeV: 2_1^+ (3.9041 MeV), 5_1^- (4.4915 MeV), and 0_3^+ (5.213 MeV).

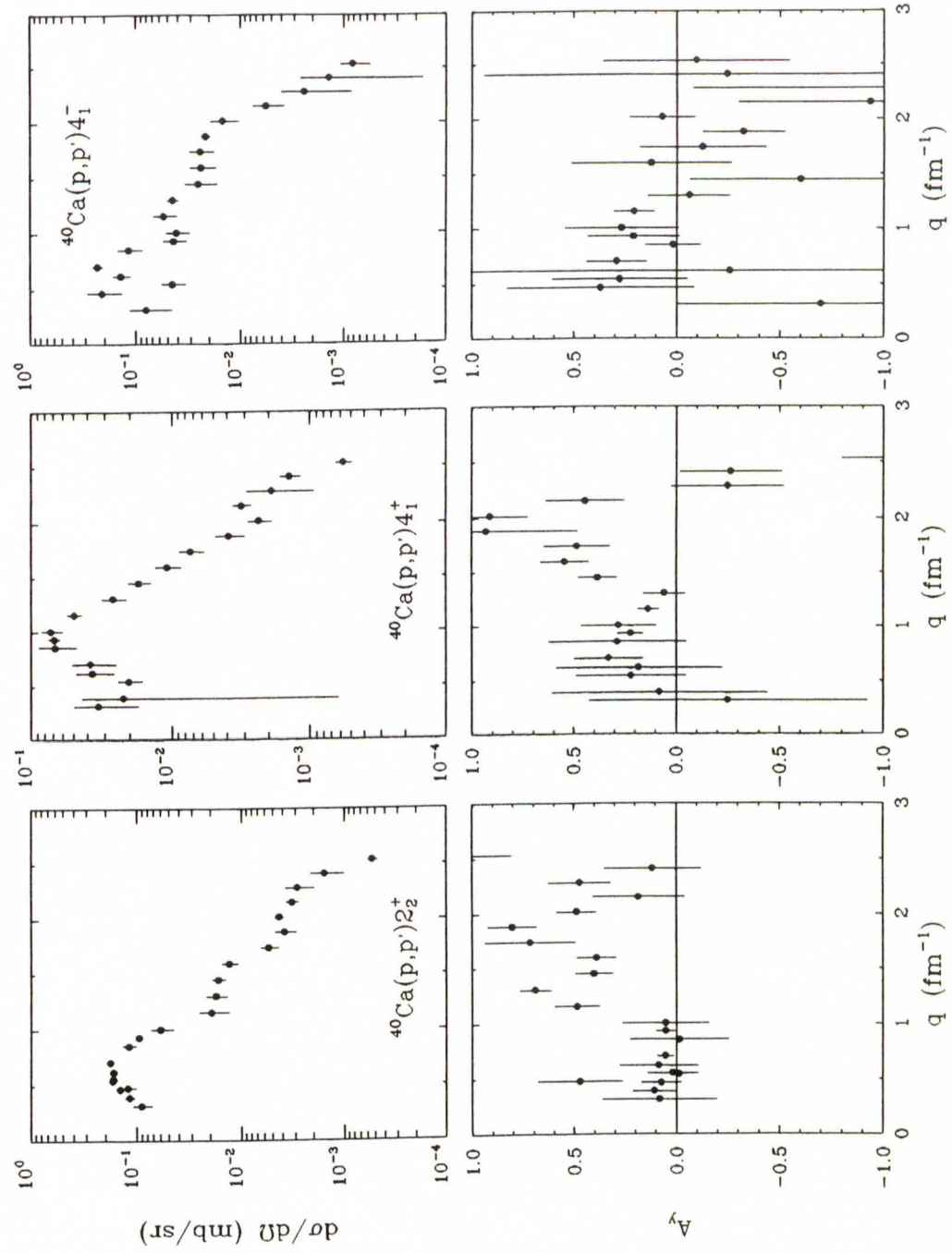

Figure 6.20: ^{40}Ca$(\vec{p},p')$ at E_P = 100 MeV: 2_2^+ (5.249 MeV), 4_1^+ (5.279 MeV), and 4_1^- (5.6143 MeV).

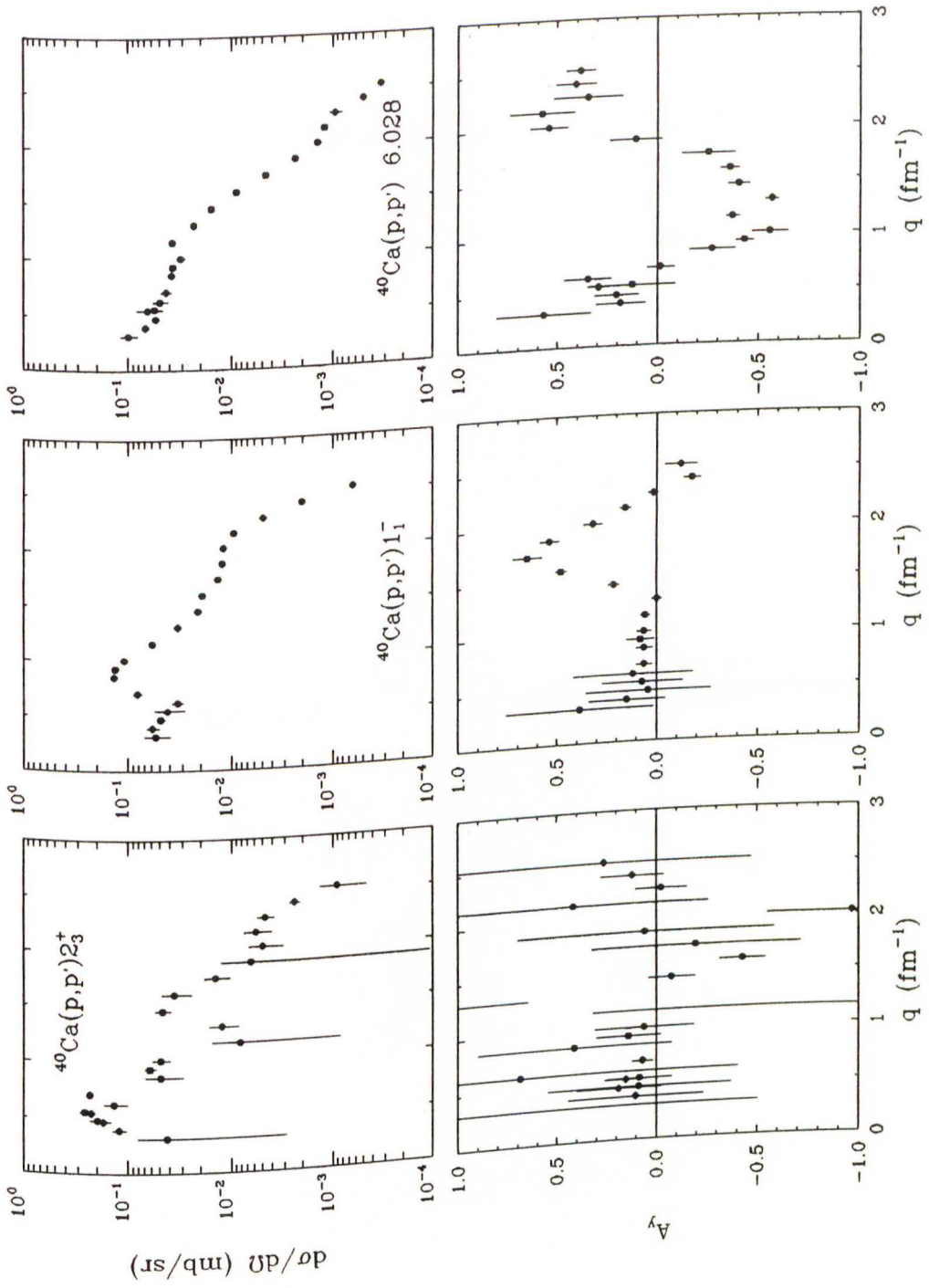

Figure 6.21: $^{40}Ca(\vec{p},p')$ at E_P = 100 MeV: 2_3^+ (5.6301 MeV), 1_1^- (5.9033 MeV), and 6.028 (6.028 MeV).

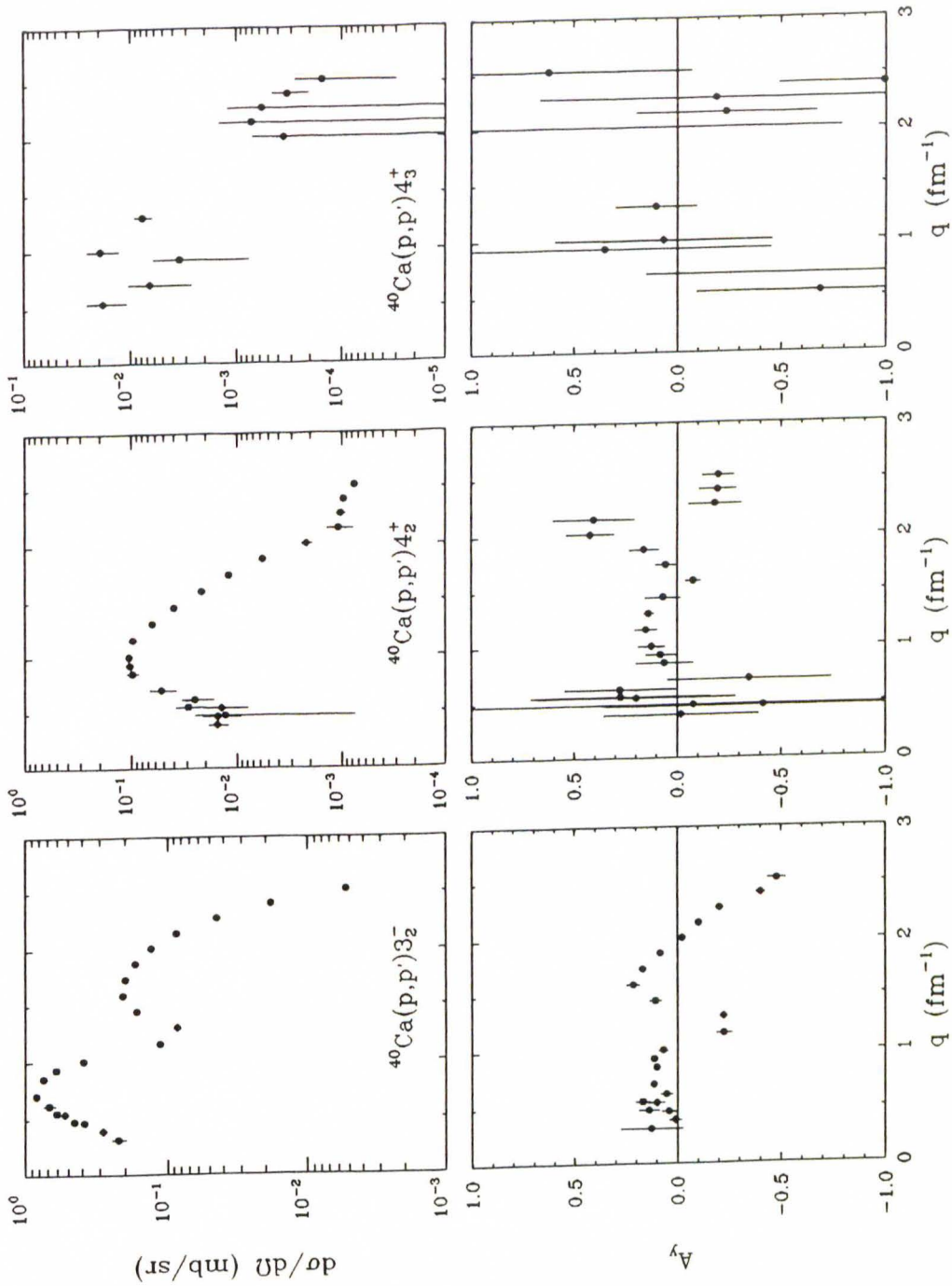

Figure 6.22: ^{40}Ca$(\vec{p}, p')$ at E_P = 100 MeV: 3^-_2 (6.2858 MeV), 4^+_2 (6.5084 MeV), and 4^+_3 (6.5436 MeV).

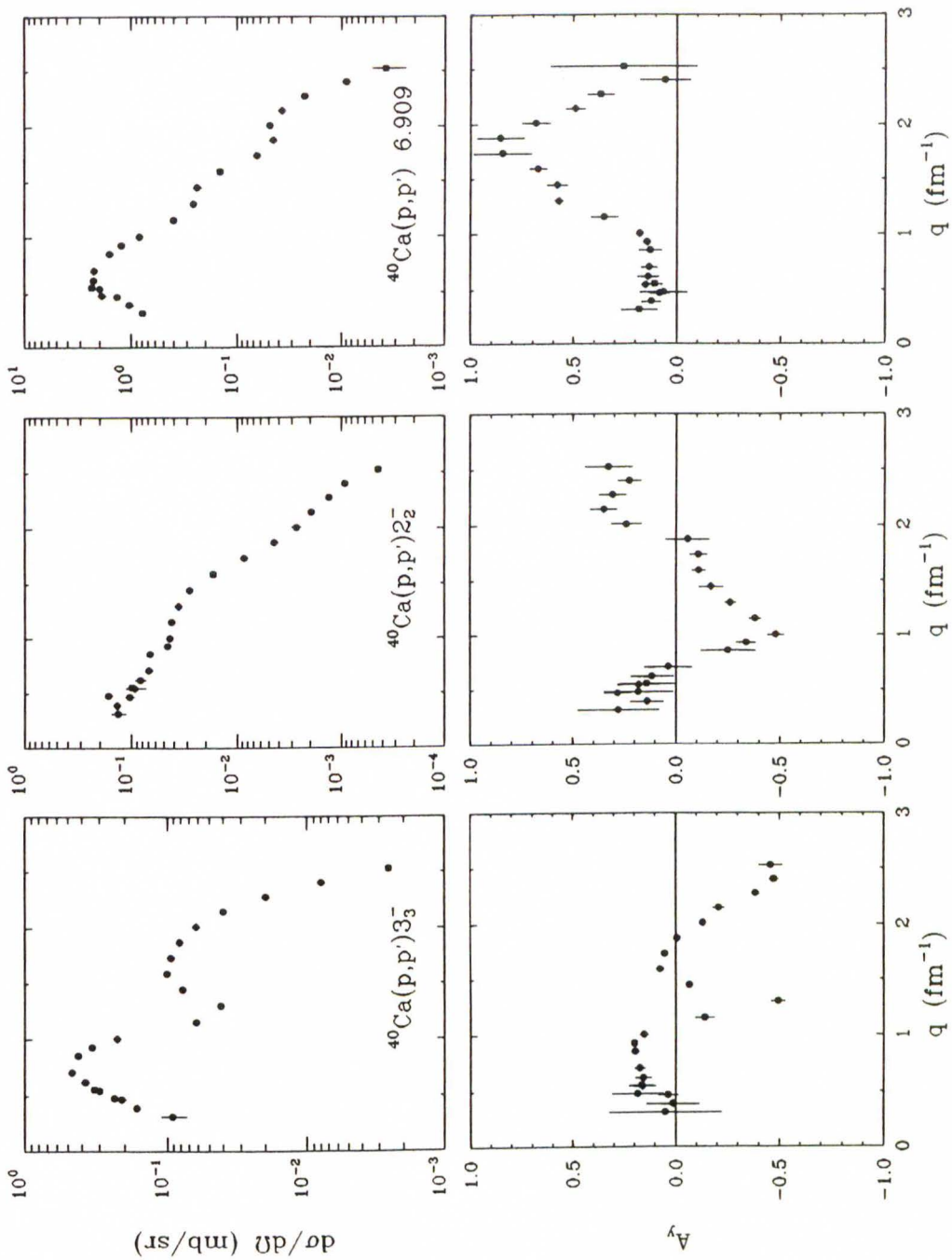

Figure 6.23: ^{40}Ca$(\vec{p}, p')$ at E_P = 100 MeV: 3_3^- (6.5833 MeV), 2_2^- (6.7509 MeV), and 6.909 (6.909 MeV).

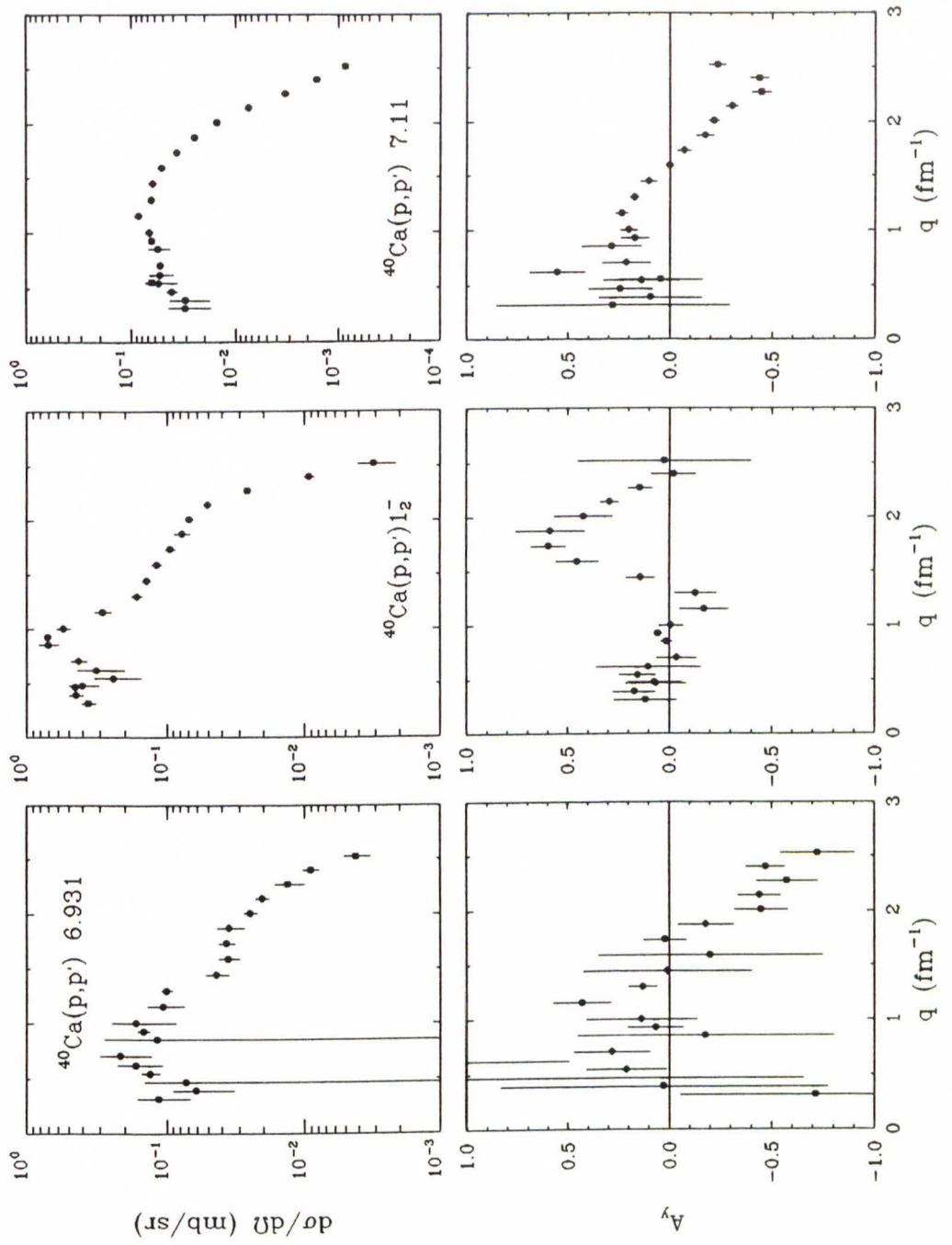

Figure 6.24: ^{40}Ca$(\vec{p}, p')$ at E_P = 100 MeV: 6.931 (6.931 MeV), 1_2^- (6.951 MeV), and 7.11 (7.11 MeV).

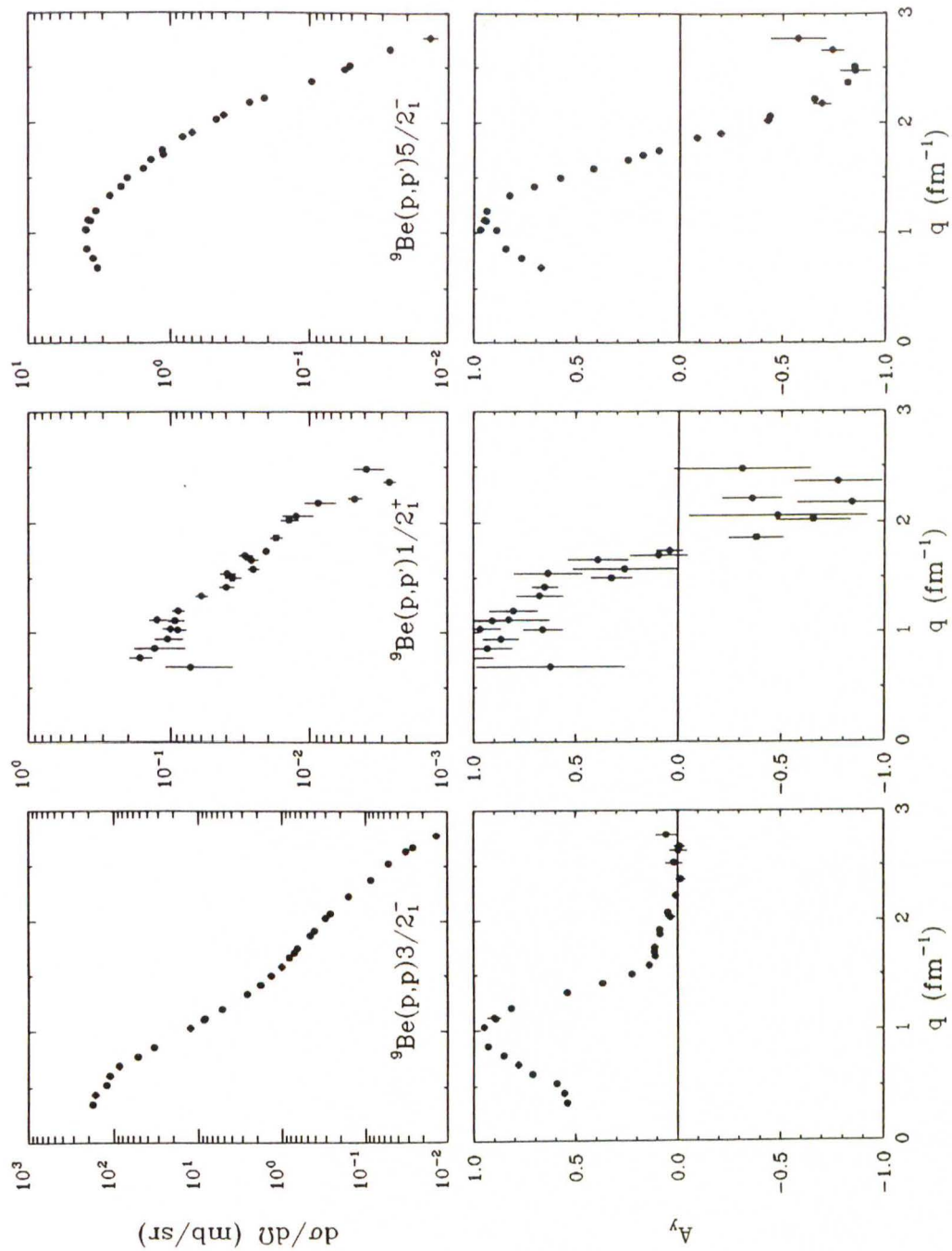

Figure 6.25: ^{9}Be$(\vec{p},p')$ at E_P = 200 MeV: $3/2_1^-$, $1/2_1^+$ (1.680 MeV), and $5/2_1^-$ (2.429 MeV).

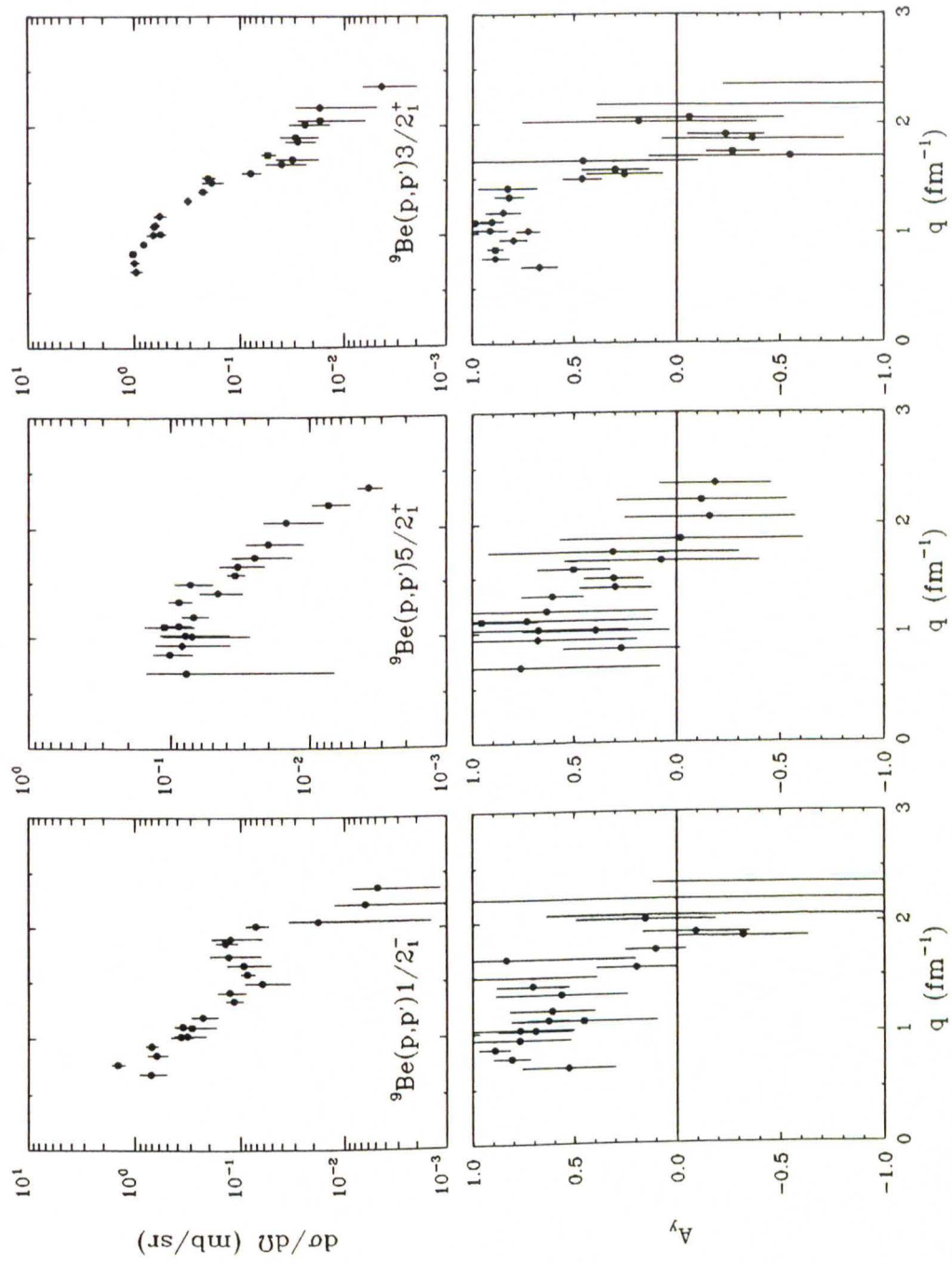

Figure 6.26: ^{9}Be$(\vec{p}, p')$ at E_P = 200 MeV: $1/2^-_1$ (2.78 MeV), $5/2^+_1$ (3.049 MeV) and $3/2^+_1$ (4.704 MeV).

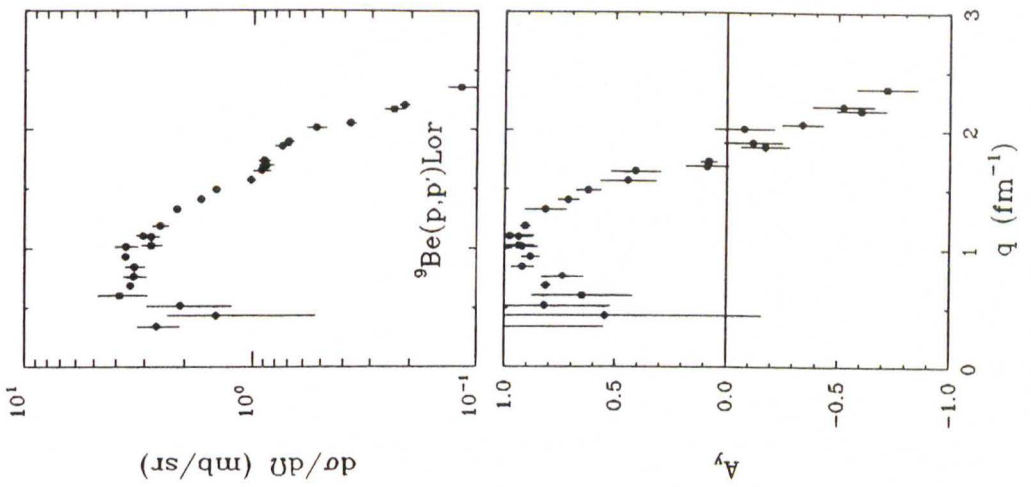

Figure 6.27: $^9\mathrm{Be}(\vec{p},p')$ at E_P = 200 MeV: Lor (6.5 MeV)

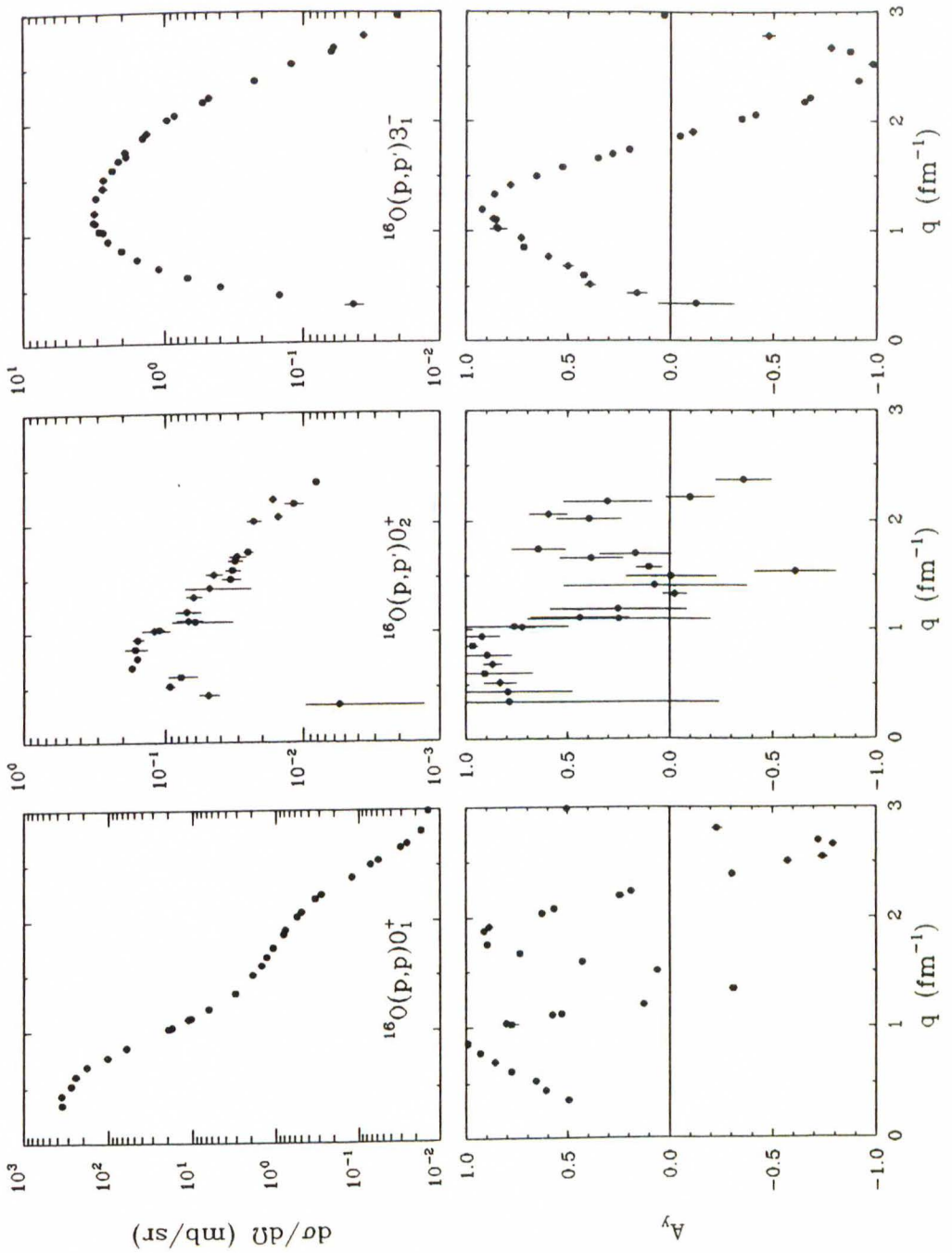

Figure 6.28: $^{16}O(\vec{p},p')$ at E_P = 200 MeV: 0^+_1, 0^+_2 (6.0494 MeV), and 3^-_1 (6.1299 MeV).

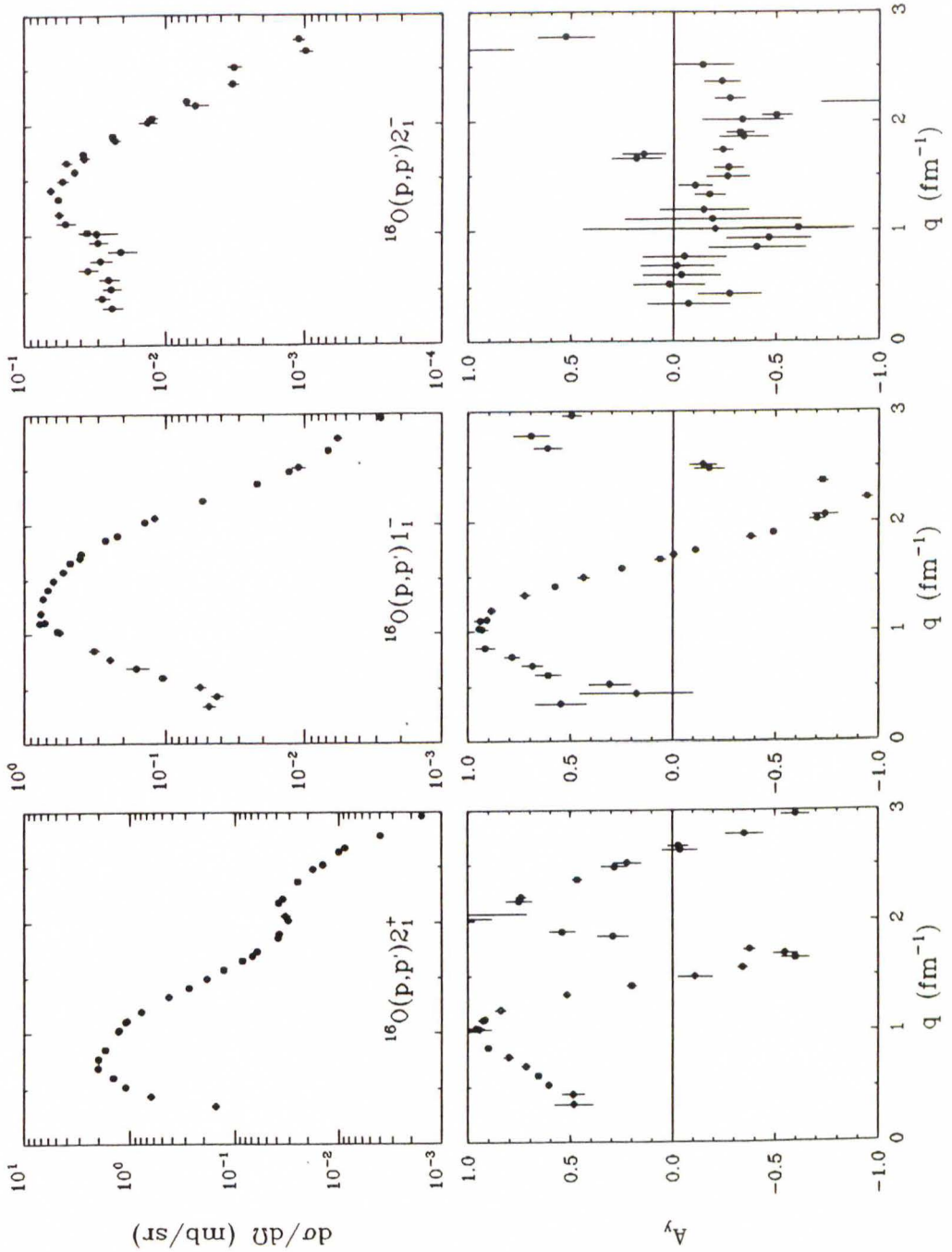

Figure 6.29: $^{16}O(\vec{p},p')$ at E_P = 200 MeV: 2^+_1 (6.9171 MeV), 1^-_1 (7.1169 MeV), and 2^-_1 (8.8719 MeV).

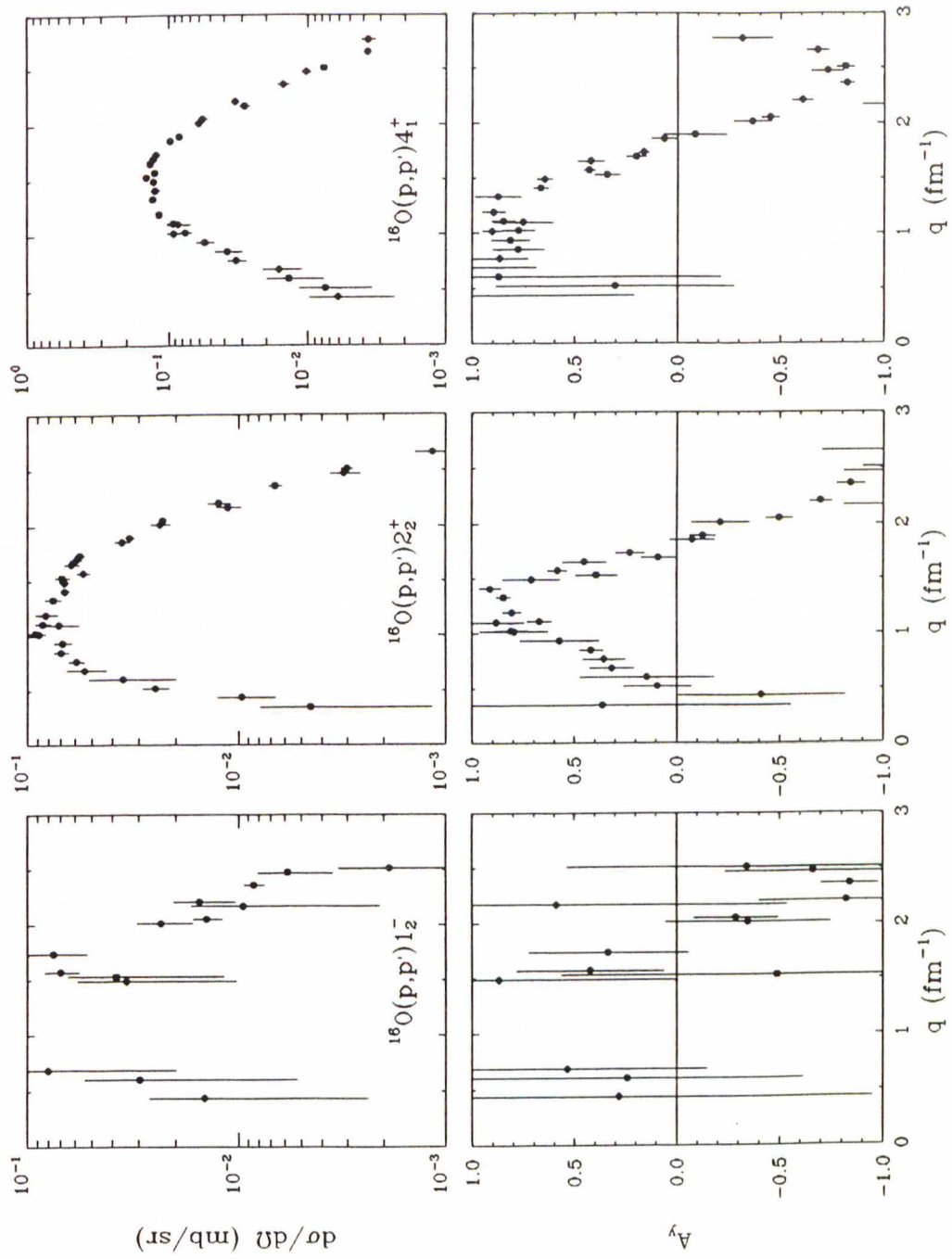

Figure 6.30: $^{16}O(\vec{p},p')$ at E_P = 200 MeV: 1^-_2 (9.585 MeV), 2^+_2 (9.8445 MeV), and 4^+_1 (10.356 MeV).

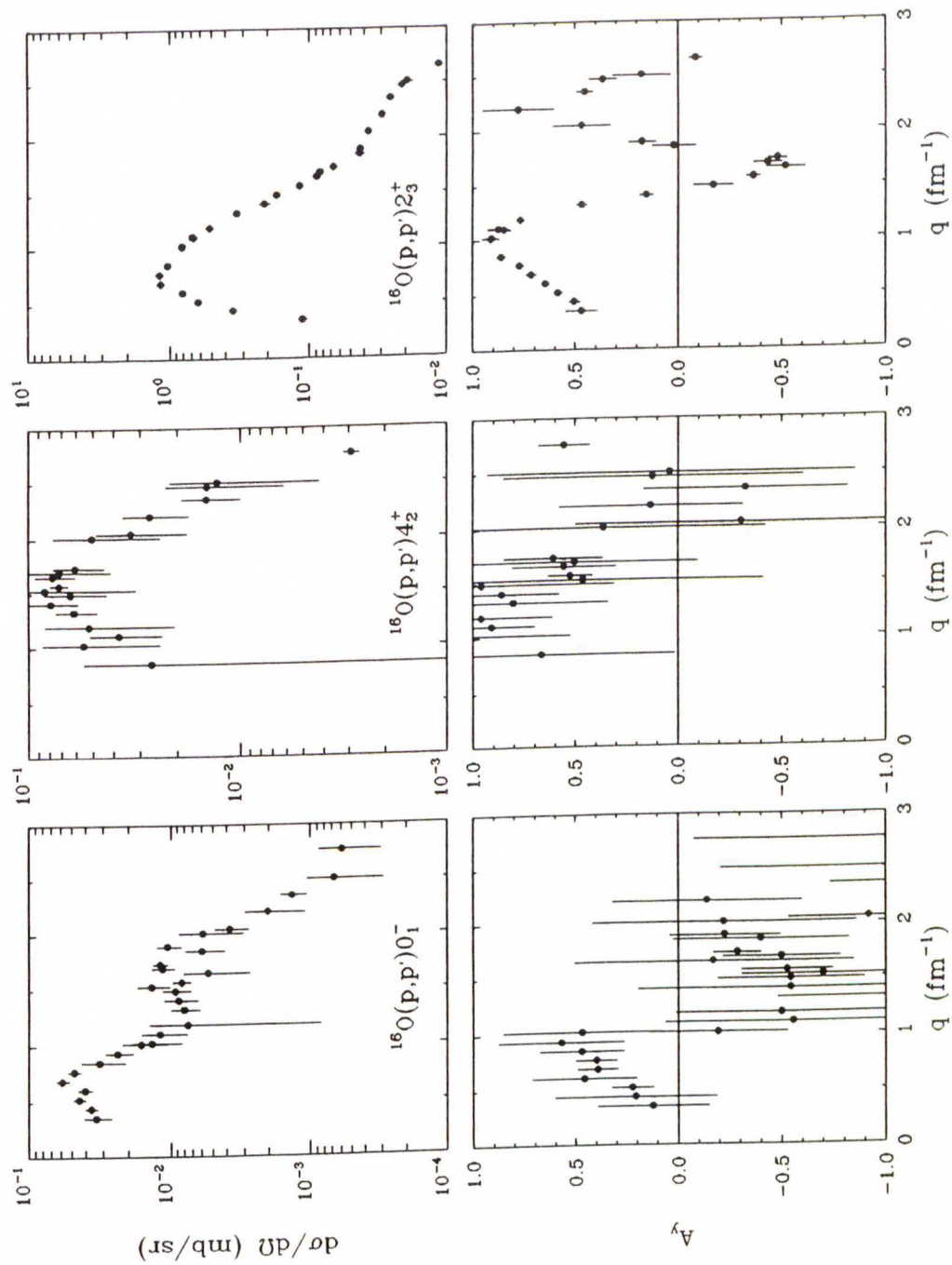

Figure 6.31: $^{16}O(\vec{p},p')$ at E_P = 200 MeV: 0_1^- (10.957 MeV), 4_2^+ (11.097 MeV), and 2_3^+ (11.520 MeV).

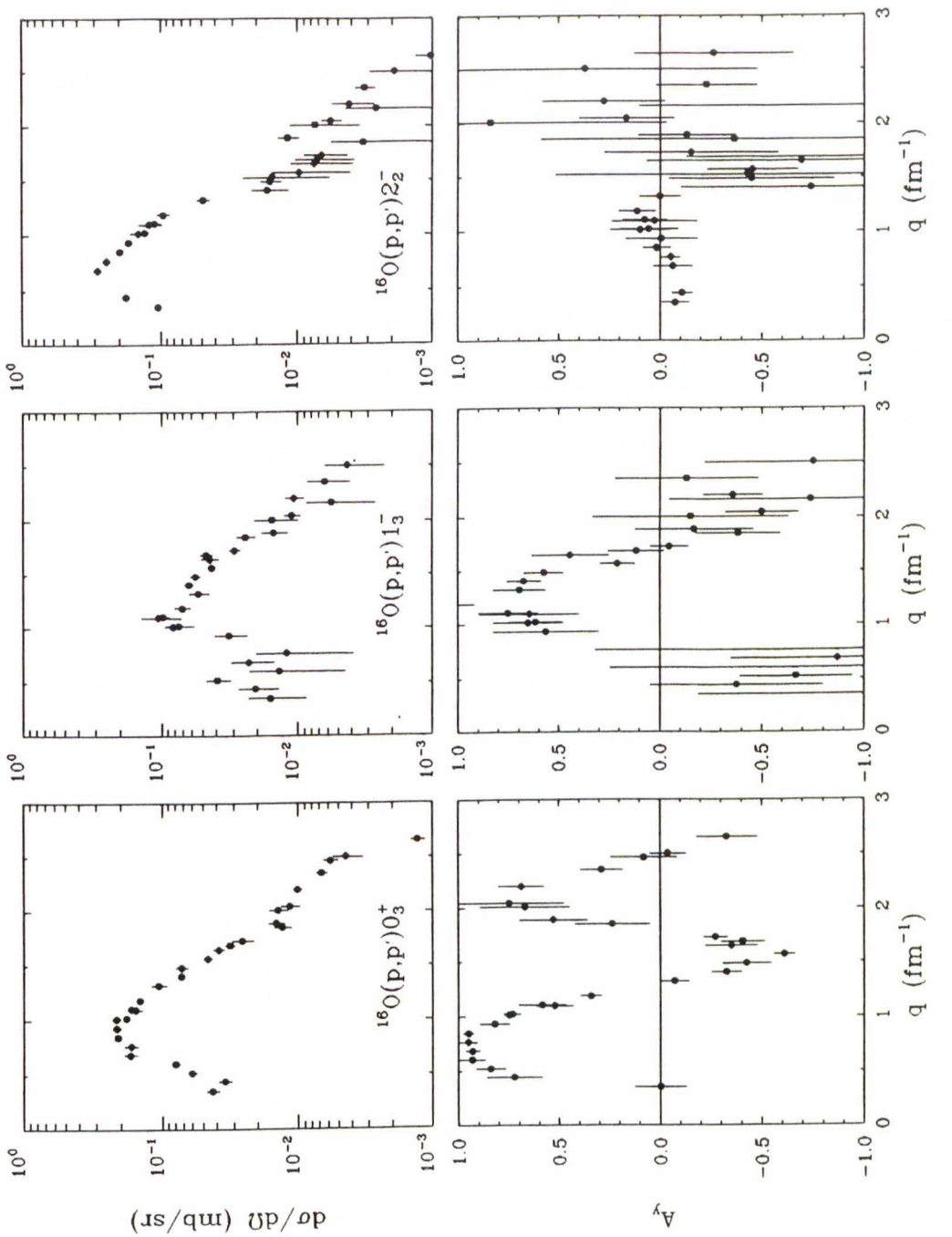

Figure 6.32: $^{16}O(\vec{p},p')$ at E_P = 200 MeV: 0^+_3 (12.049 MeV), 1^-_3 (12.440 MeV), and 2^-_2 (12.530 MeV).

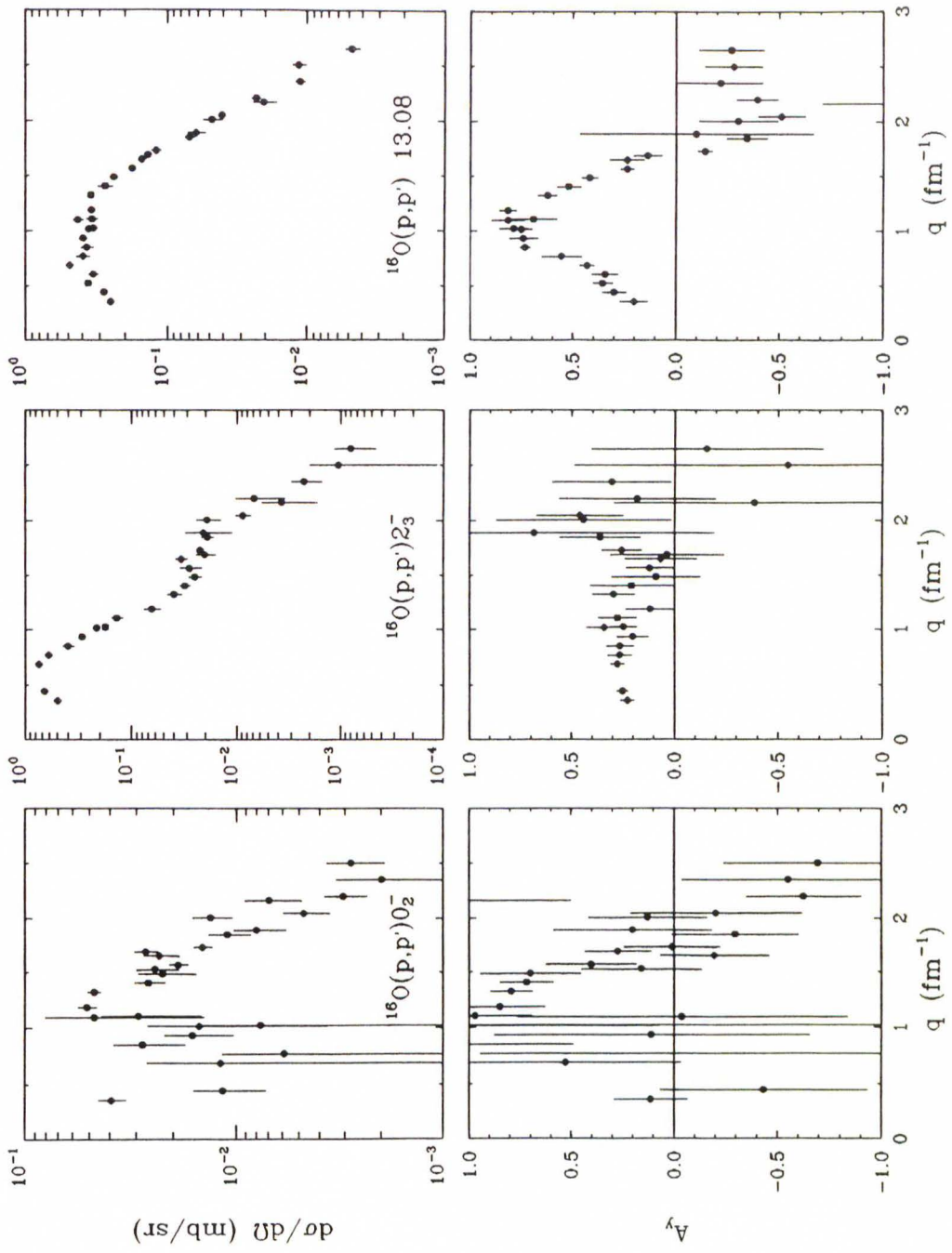

Figure 6.33: $^{16}O(\vec{p},p')$ at E_P = 200 MeV: 0_2^- (12.796 MeV), 2_3^- (12.969 MeV), and 13.08 (13.08 MeV).

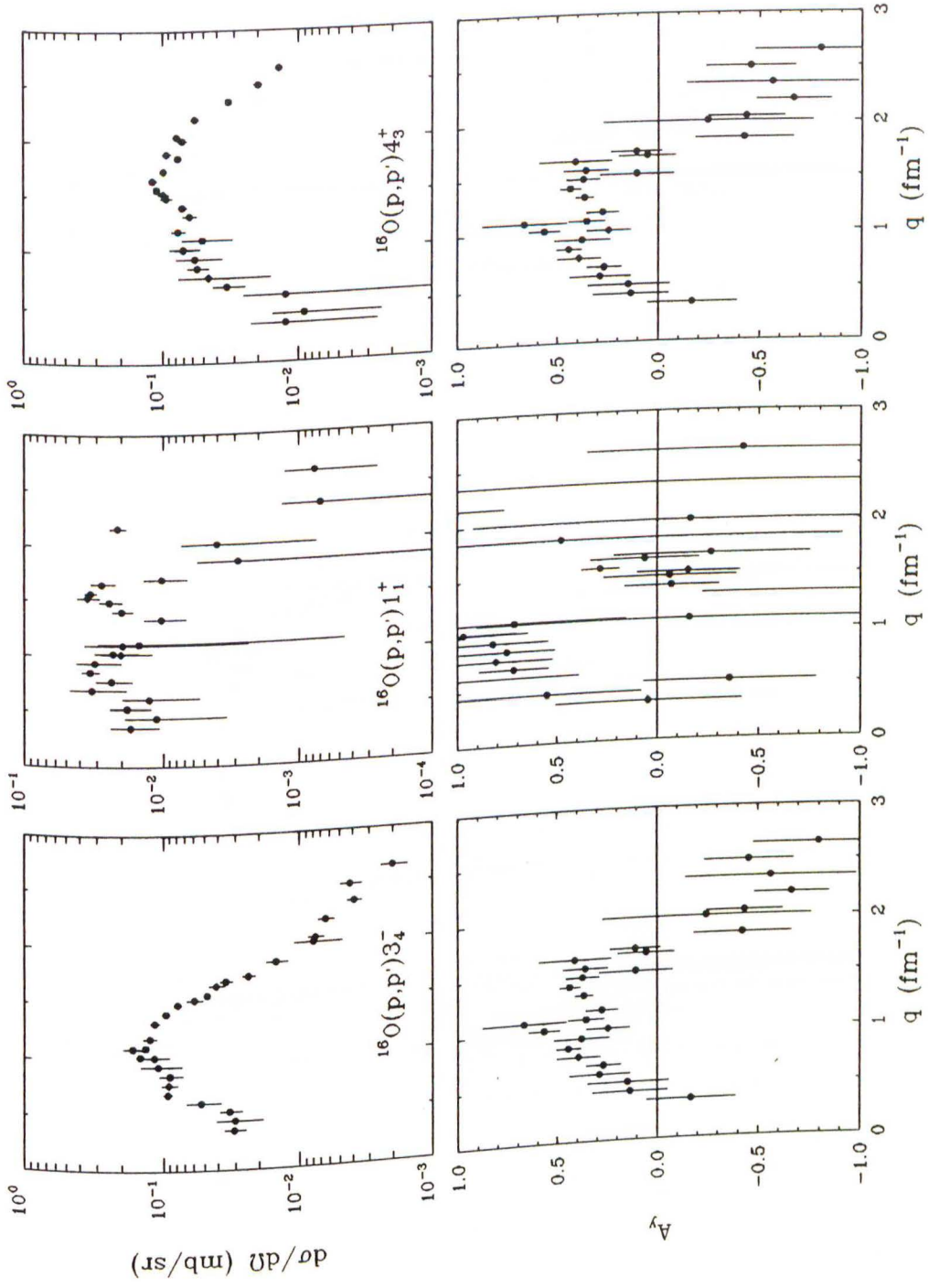

Figure 6.34: $^{16}O(\vec{p},p')$ at E_P = 200 MeV: 3^-_4 (13.259 MeV), 1^+_1 (13.664 MeV), and 4^+_3 (13.869 MeV).

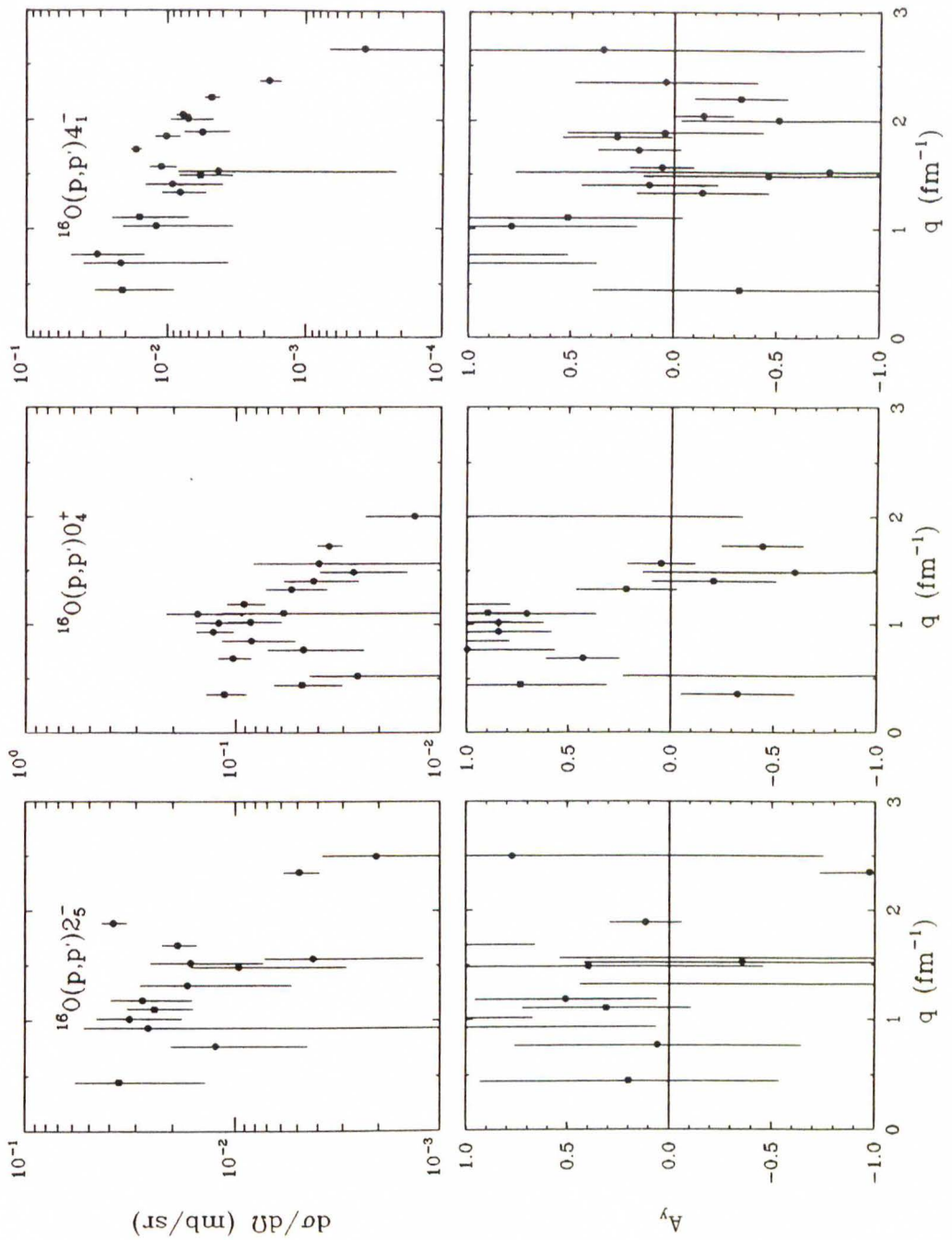

Figure 6.35: $^{16}O(\vec{p},p')$ at E_P = 200 MeV: 2^-_5 (13.98 MeV), 0^+_4 (14.032 MeV), and 4^-_1 (14.302 MeV).

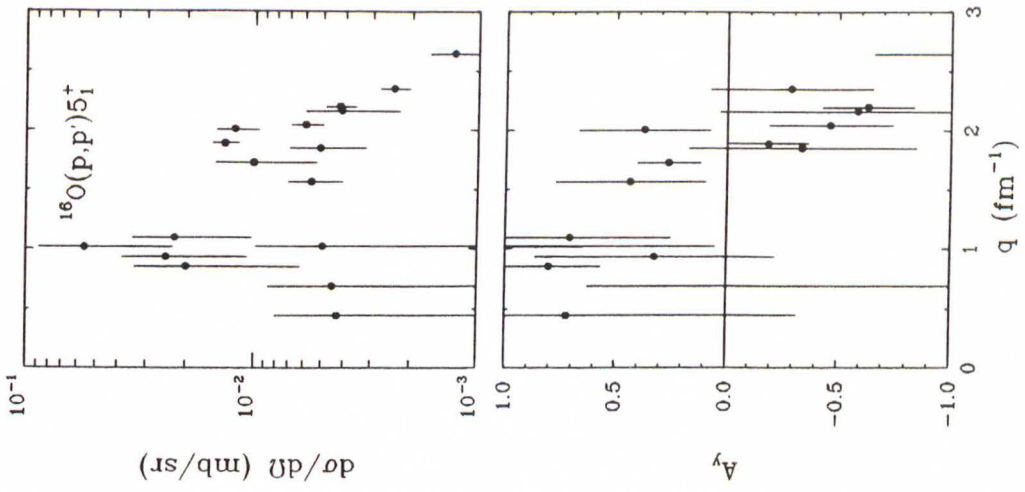

Figure 6.36: $^{16}O(\vec{p},p')$ at E_P = 200 MeV: and 5_1^+ (14.399 MeV).

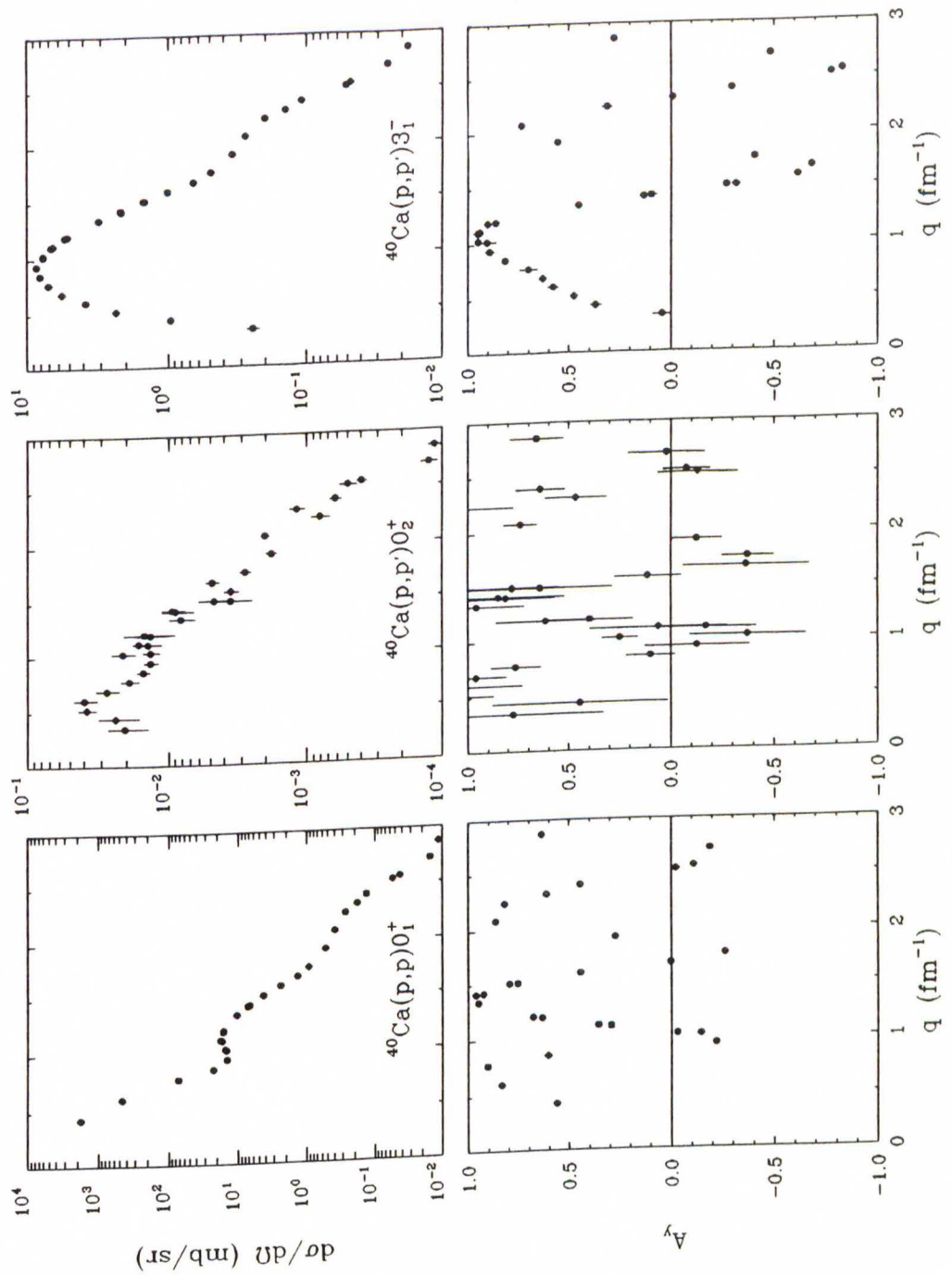

Figure 6.37: ^{40}Ca$(\vec{p},p')$ at E_P = 200 MeV: 0^+_1, 0^+_2 (3.3521 MeV), and 3^-_1 (3.7364 MeV).

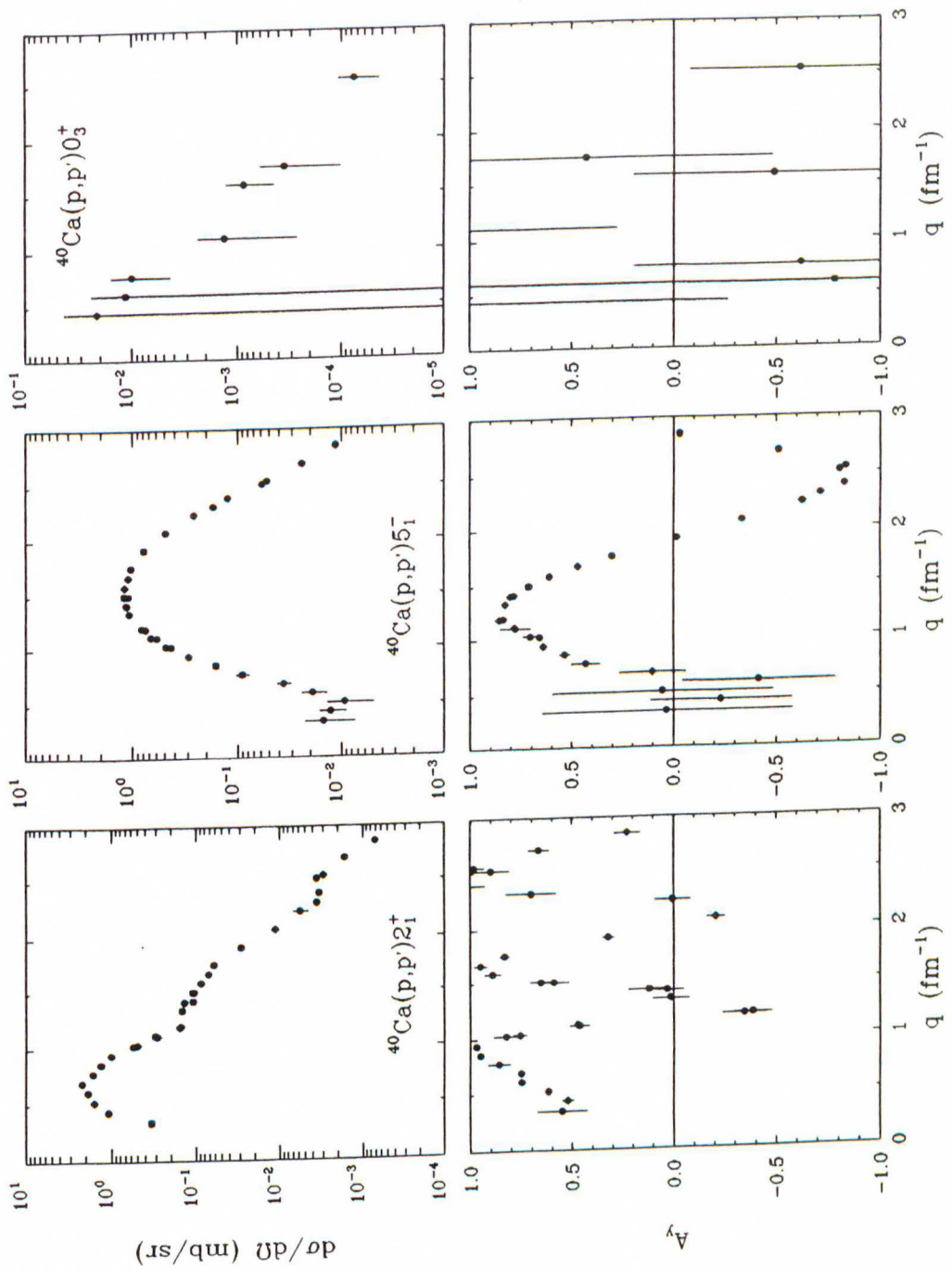

Figure 6.38: $^{40}Ca(\vec{p}, p')$ at E_P = 200 MeV: 2_1^+ (3.9041 MeV), 5_1^- (4.4915 MeV), and 0_3^+ (5.213 MeV).

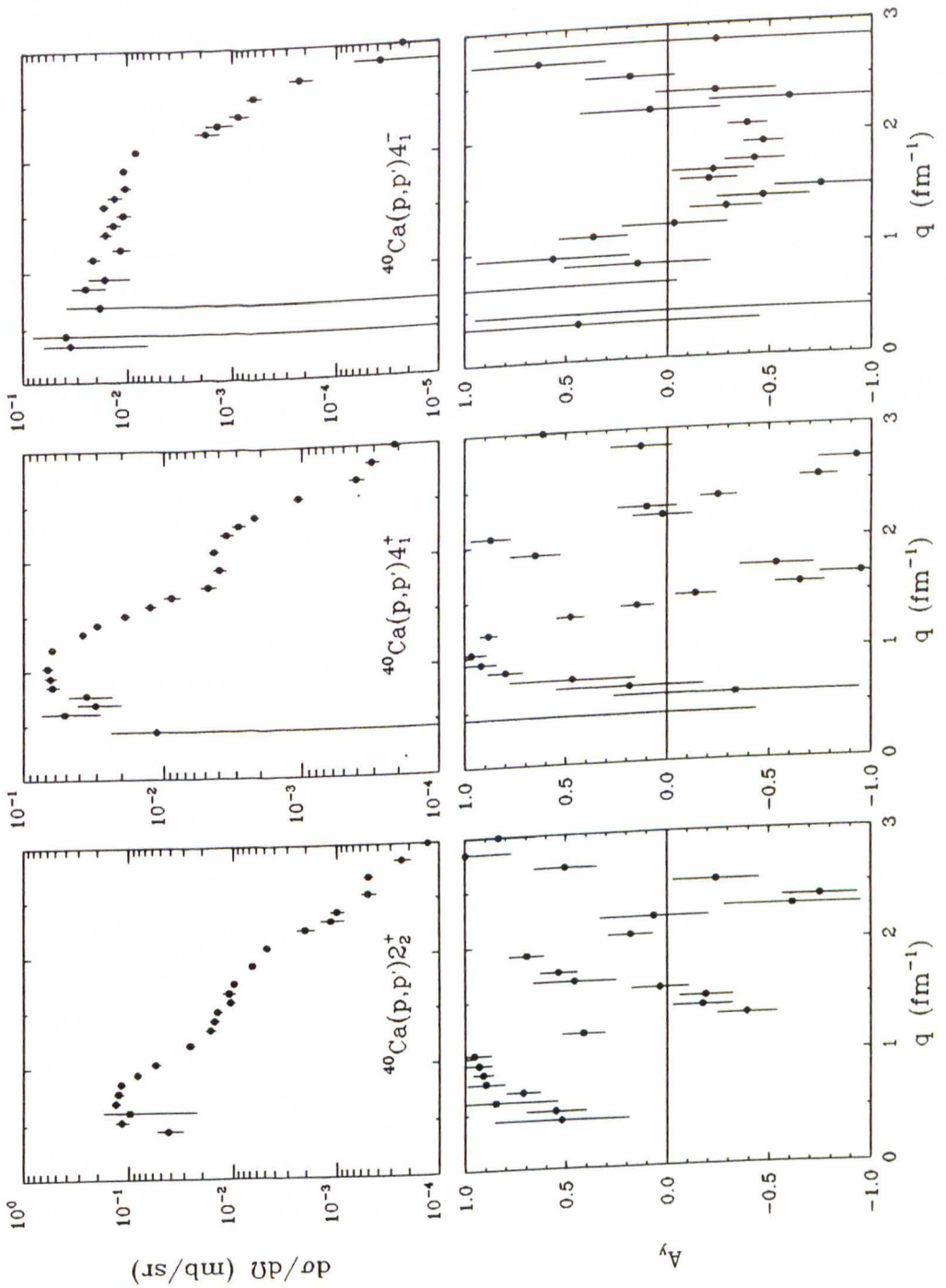

Figure 6.39: ^{40}Ca$(\vec{p},p')$ at E_P = 200 MeV: 2_2^+ (5.249 MeV), 4_1^+ (5.279 MeV), and 4_1^- (5.6143 MeV).

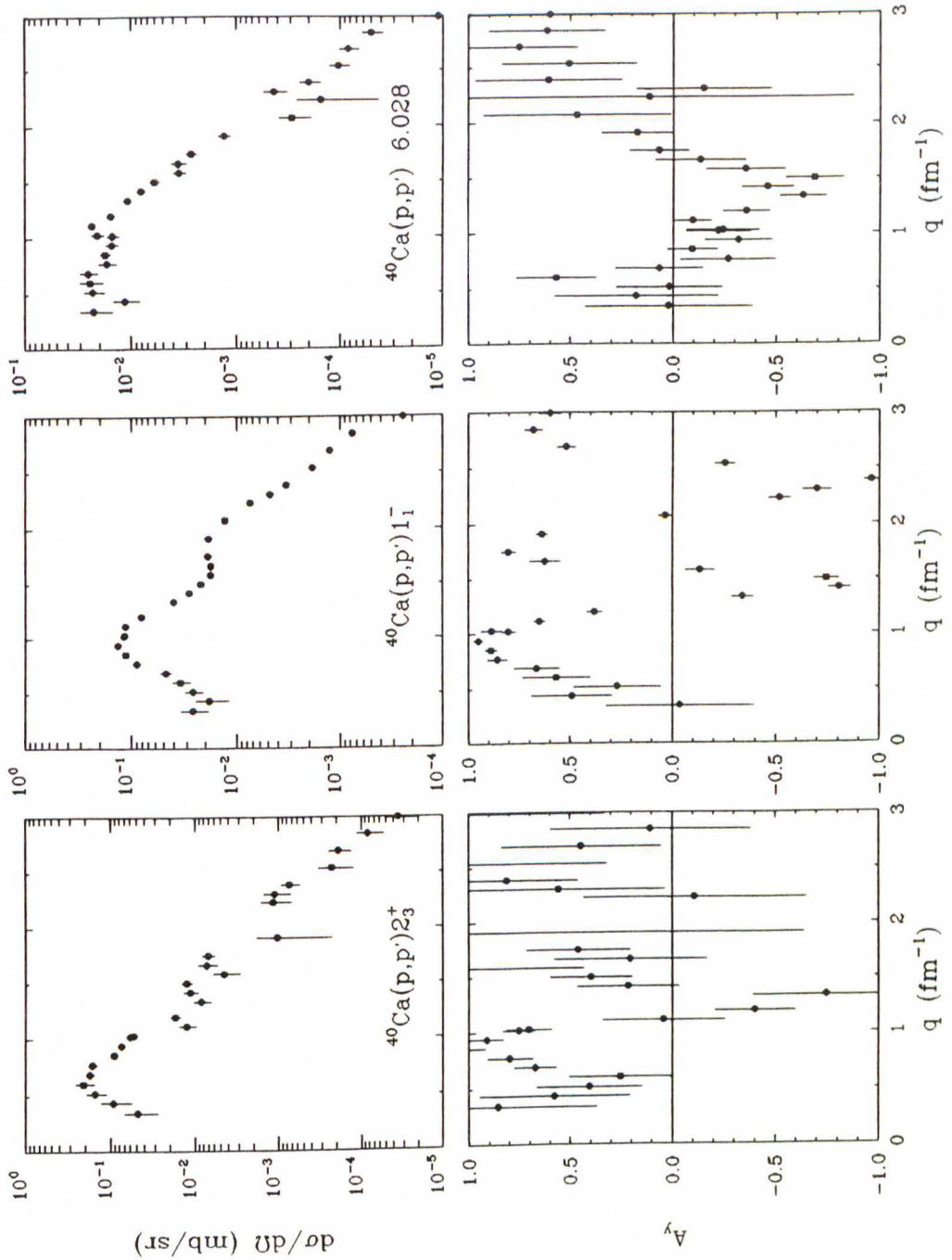

Figure 6.40: ^{40}Ca$(\vec{p},p')$ at E_P = 200 MeV: 2^+_3 (5.6301 MeV), 1^-_1 (5.9033 MeV), and 6.028 (6.028 MeV).

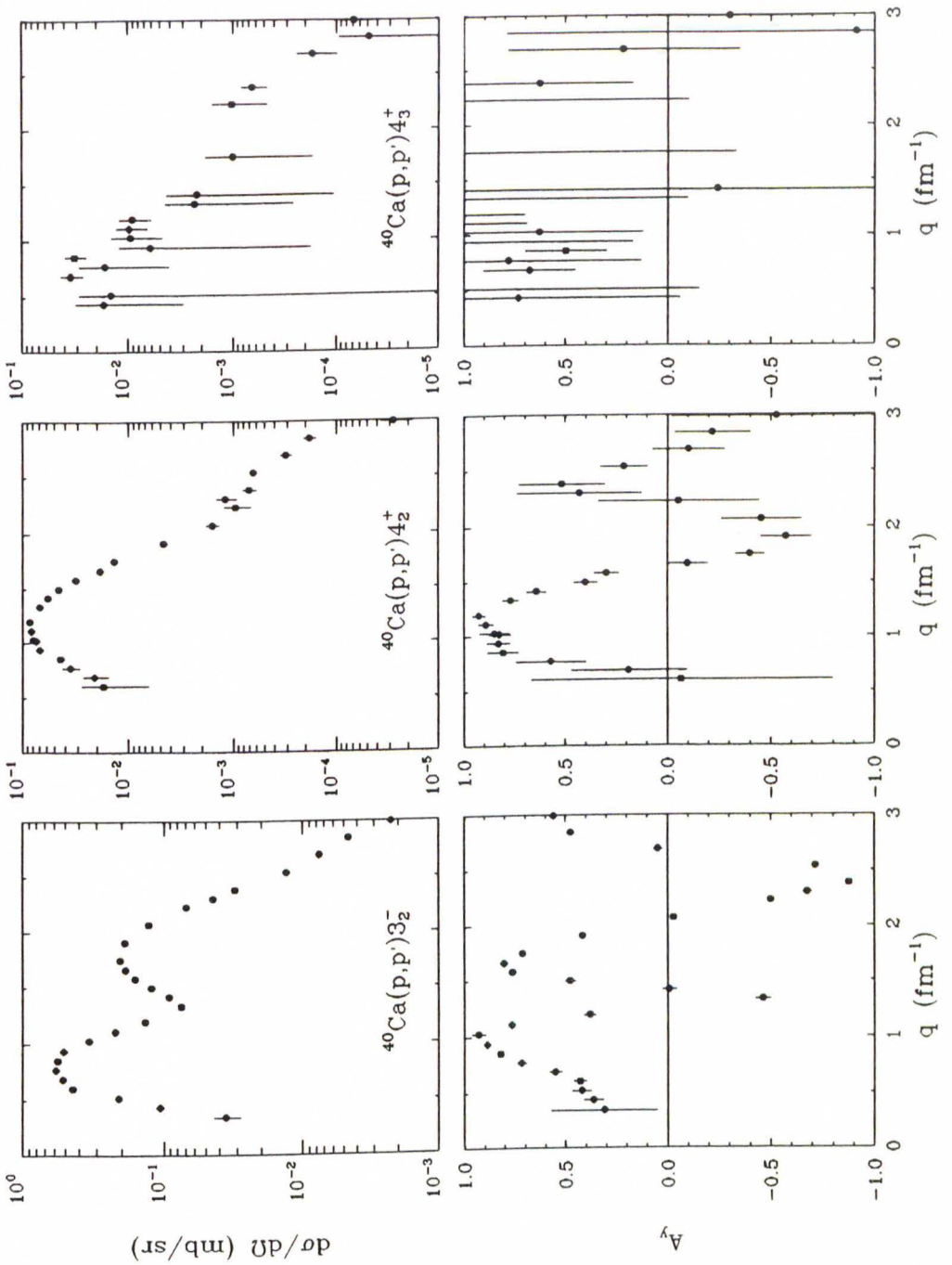

Figure 6.41: ^{40}Ca$(\vec{p},p')$ at E_P = 200 MeV: 3_2^- (6.2858 MeV), 4_2^+ (6.5084 MeV), and 4_3^+ (6.5436 MeV).

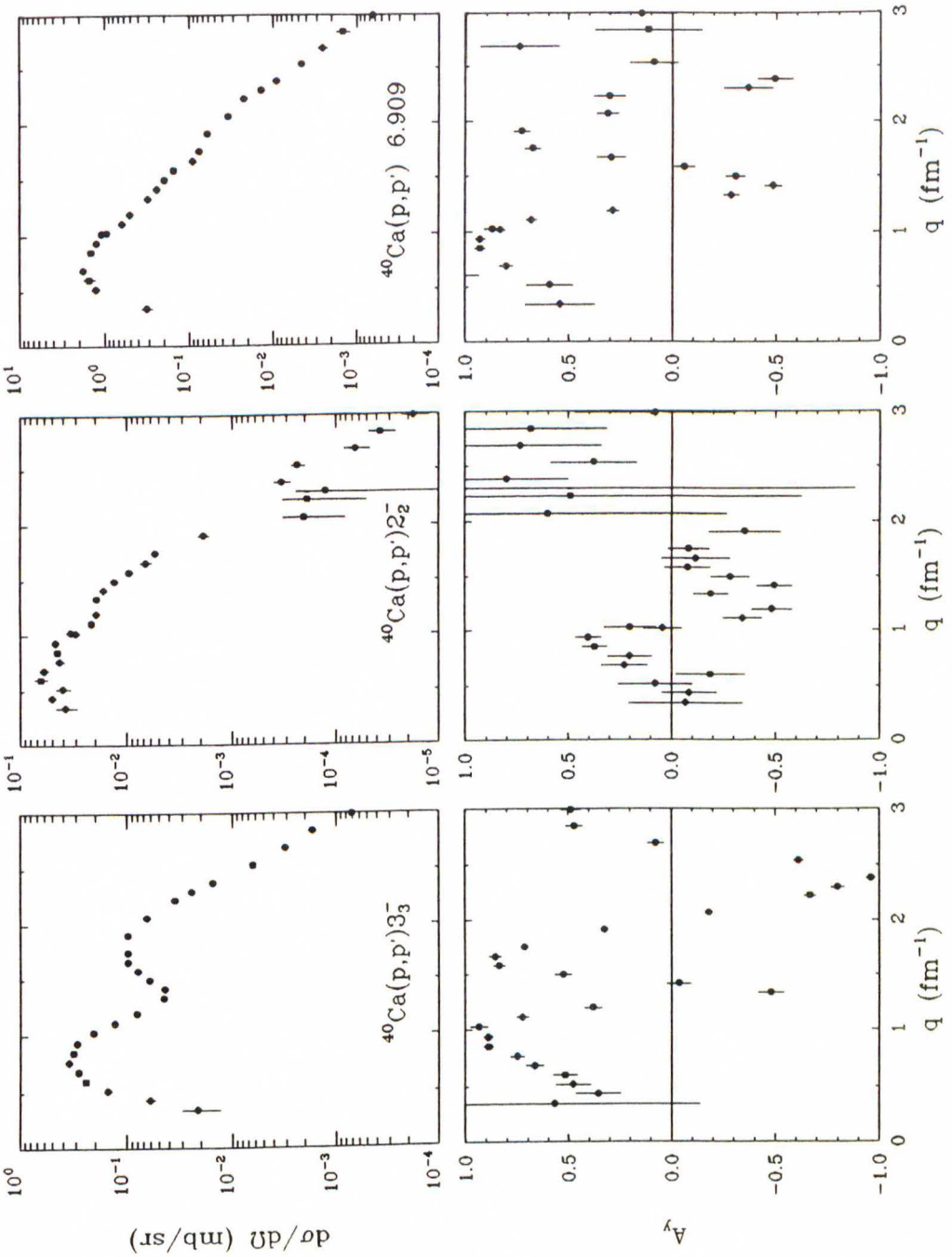

Figure 6.42: ^{40}Ca$(\vec{p},p')$ at E_P = 200 MeV: 3_3^- (6.5833 MeV), 2_2^- (6.7509 MeV), and 6.909 (6.909 MeV).

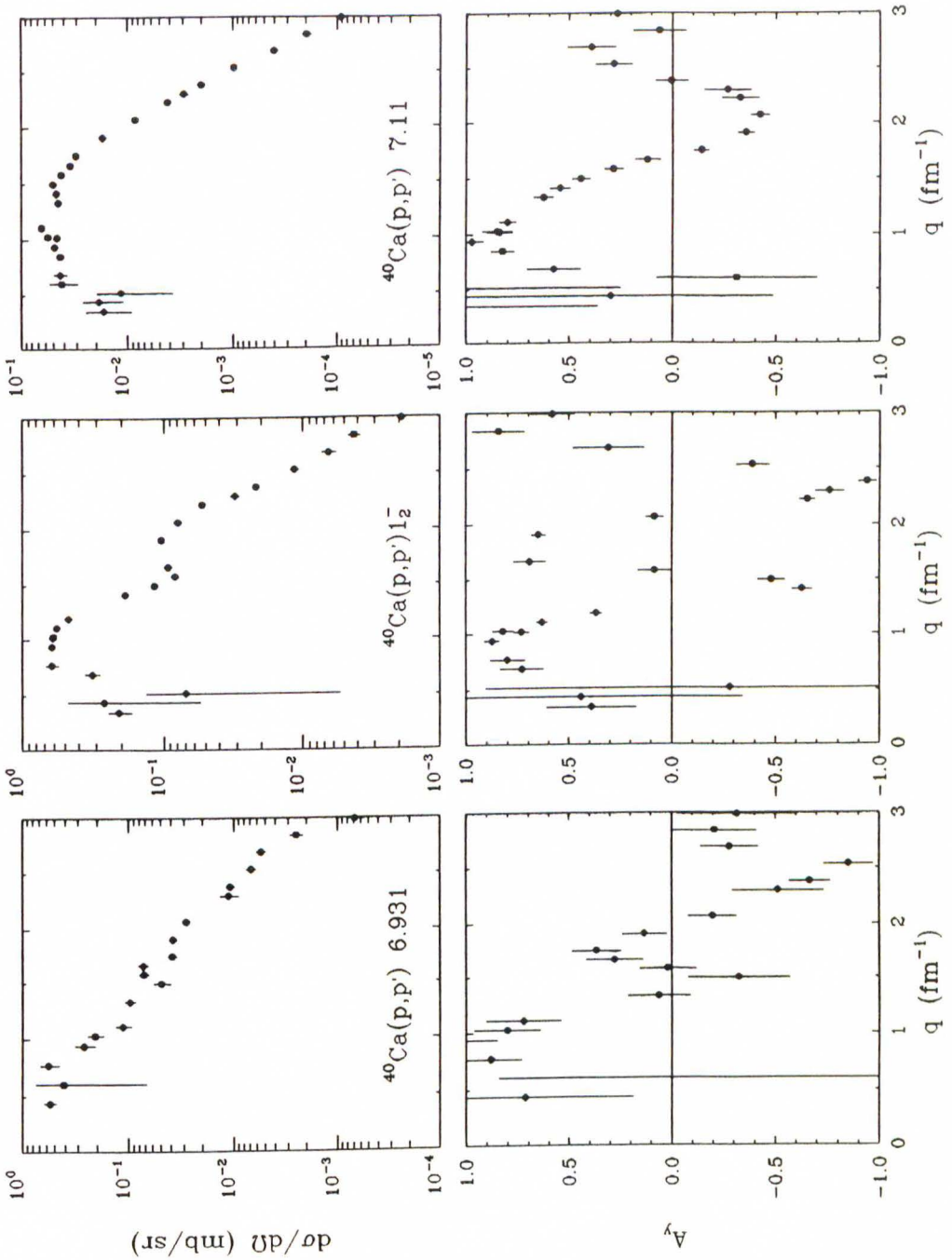

Figure 6.43: ^{40}Ca$(\vec{p},p')$ at E_P = 200 MeV: 6.931 (6.931 MeV), 1_2^- (6.951 MeV), and 7.11 (7.11 MeV).

7 Results and Discussion

7.1 Data Selection and Iteration Procedure

The ^{16}O and ^{40}Ca nuclei provide an excellent laboratory for the study of medium modifications to the effective interaction. Inelastic transitions whose amplitude is concentrated in the nuclear surface are sensitive to the low density properties of the effective interaction, while amplitudes concentrated in the interior are sensitive to the high density properties of the interaction. Intermediate cases determine the rate at which the effects depend upon density. Inelastic monopole and isoscalar electric dipole transitions tend to be good interior states. Inelastic transition densities involving large orbital angular momentum transfers, on the other hand, tend to peak at the surface.

States with various multipolarities and with both interior and surface character can be easily resolved for the two targets, even if only modest resolution is available. For our interaction analysis we choose the 3_1^- state at 6.130 MeV, the 2_1^+ state at 6.917 MeV, the 1_1^- state at 7.117 MeV, the 4_1^+ state at 10.356 MeV, and the 2_3^+ state at 11.520 MeV from ^{16}O (see Tables 6.2 and 6.3 in Chapter 6). The data for the 4_2^+ are omitted because of contamination by an unresolved 3^+ state; the 2_2^+ is also omitted because it is very weakly excited and because of evidence of multistep contributions [Kel 89a]. Finally, the 0_2^+ state at 6.049 MeV is small and is difficult to resolve from the neighboring 3_1^- state. The 0_3^+ state is special and was omitted because of the possible spin-convection density contributions near $q = 1.5$ fm^{-1}, where the electroexcitation form factor passes through a minimum [Pet 85]. The

bulge in the cross section is prominent at 100 MeV, becomes less noticeable at 200 MeV , and has essentially vanished at 318 MeV. Kelly *et al.* performed at 135 MeV fits both with and without this state and found essentially no differences in their fitting results. None of the fits can reproduce the cross section for momentum transfers in the region between 1.2 and 2.0 fm^{-1}. However, the analyzing power data and the remainder of the cross section data are fitted well either way. Furthermore, they find that the other data are not affected in any noticeable way by the presence or absence of this state in the fit [Kel 89b]. Therefore, although we show calculations for the 0_3^+ state in the subsequent sections, the effective interactions were obtained without it.

For ^{40}Ca we choose, with the exception of the 0_2^+ state at 3.352 MeV, which is very weak and which possibly may also have multistep contributions, all the states for which transition densities from (e, e') are available [Mis 83]. Those states are the 3_1^- state at 3.736 MeV, the 2_1^+ state at 3.904 MeV, the 5_1^- state at 4.492 MeV, the 3_2^- state at 6.286 MeV, and the 3_3^- state at 6.583 MeV. Both the 3_2^- and the 3_3^- states have strong interior lobes and should, therefore, probe the high density aspects of the effective interaction. Finally, we also included the elastic scattering data in some of the fits. The results which include elastic data are discussed in Section 7.4.

For all the energies we performed separate fits to the states of each of the two targets, and also a simultaneous fit to all the states of both targets. This should help us to detect an A dependence, if present. For the analysis, we folded additional uncertainties into the fitted data. This assures that all states have a similar influence upon the analysis and that the data are equally

weighted for all momentum transfers. Furthermore, we achieve smaller values for χ^2_ν in this fashion, and also equalize the quality of the cross section and analyzing power data, as measured by χ^2_ν per datum. Because most of the electron scattering data is limited to $q \leq 2.7$ fm^{-1}, and because of uncertainties in our reaction model at large momentum transfers (e.g. coupled channels effects become important), our analysis includes only momentum transfers up to 2.7 fm^{-1}.

All our fits employed a self-consistency cycle. The first iteration usually utilized distorted waves based either upon the PH interaction (in the case of ^{16}O), or a previously fitted empirical interaction (interaction fitted to ^{16}O for ^{40}Ca). After removal of the $(1 + \rho\partial/\partial\rho)$ contribution (see Section 2.8.3) the fitted interaction is then used to compute a new optical potential and distorted waves. The fit is repeated and the distortion iterated until convergence is achieved. We usually observe that good convergence is obtained within about seven iterations. The results in the following sections represent the endpoint of the self-consistency cycle. One reason that we generally excluded elastic scattering from the fit is that it serves as an independent check for this self-consistency procedure.

We found that the final fitting results are stable and independent from the starting parameters. This was verified by gridding each of the six parameters of the empirical effective interaction from Chapter 2, Eqs. (2.114)–(2.116), while letting all the other parameters vary. Each parameter grid consisted generally of four or five more or less widely spaced values for the parameter. The range of parameter values was chosen to allow interpolation

of the parameter with the minimum χ^2_ν. Grids were done at 200 MeV for both ^{16}O and ^{40}Ca, and for ^{16}O at 318 and 500 MeV. The grids demonstrate that there is a unique solution in the space of χ^2_ν for each target at 200 and 318 MeV. At 500 MeV, on the other hand, we found two true solutions (see also [Fla 90]). The results for the interaction grids are compiled in the tables of Appendix D.

7.2 Fit to Inelastic Data

7.2.1 100 MeV

The parameters for the empirical effective interaction resulting from the fits to inelastic data of ^{16}O and ^{40}Ca at 100 MeV are collected in Table 7.1. The data for the interaction fit are from this work. For the results shown here, the interactions were modeled upon the PH free interaction which gave results superior to fits using the FL t-matrix at this energy. For all the fits it was necessary to constrain the b_3 parameter which, as a grid search proves, is not strongly determined by the data. Unless elastic scattering is included, for ^{16}O we additionally had to constrain d_2 to prevent that parameter from getting unreasonably large. For both parameters we chose the PH values, a choice which is later justified by the combined fit to both elastic and inelastic data. In the case of ^{40}Ca and also the combined fit we found that no reasonable and stable fit could be obtained unless both b_1 and b_3 were constrained. If we constrain d_2 and b_3, as in the case of ^{16}O, b_1 cannot be determined and the fit does not converge. With b_1 and b_3 constrained, the free d_2 parameter

assumes a rather large value in the final result which yields opposite signs of $(S_2 - d_2)$ at saturation density for elastic and inelastic scattering (we saw in Section 2.7.3 that for inelastic scattering the d_2 parameter is to multiplied by a factor of 5/3 to account for the rearrangement contribution). Our self-consistency procedure may be affected by this effect.

In Figure 7.1 we compare the effective interaction (EMP) from the fit to ^{16}O with the PH interaction. The $\mathrm{Re}t_{00}^{C}$ and $\mathrm{Re}t_{0}^{LS}$ components both appear to have less density dependence, quite in contrast to the $\mathrm{Im}t_{00}^{C}$ component. At large momentum transfers or for large density, the real central part resembles very closely the nuclear matter interaction. However, we also see that the strength is reduced at low density. In accordance with previous analyses ([Kel 89b, Kel 90a]) it was found, that in order to obtain a good fit to the surface peaked inelastic states, the scale factors S_i cannot be constrained to unity . However, after having reduced the strength at low density to fit the surface states, the subsequent density dependence has to be reduced as well to fit the interior states. The fact that the effective interaction does not heal to the free interaction at low densities, and the fact that the interaction is less effective in the interior relative to the nuclear matter interaction, has been interpreted as nonlocal density dependence of the effective interaction beyond the local density approximation. In a finite nucleus, nuclear orbits at the surface sense, due to their finite spread, some of the high-density nuclear interior; by the same token, interior orbits extend to less dense regions.

In Figures 7.2–7.6 we show our fits to the various states of ^{16}O and ^{40}Ca. In these figures we compare calculations based on our empirical effec-

tive interactions (EMP) for ^{16}O and ^{40}Ca with LDA and NRIA calculations based on the PH interaction. For the NRIA we used the PH g-matrix to generate distorted waves and the PH t-matrix for the inelastic transition. Although none of the analyzing powers are described particularly well, we see improvements in the cross section for almost all the states. The effects are most dramatic for the ^{16}O states: for the surface-type states like the 3_1^- and the 4_1^+ states, the forward cross section is lowered by the reduced strength of the interaction at low densities. For the 1_1^- interior state, on the other hand, we see that the reduced density dependence of our empirical interaction increases the cross section relative to the LDA. In the case of the 2_3^+ state the reduction of the interaction strength proves to be slightly too severe. Finally, although the 0_3^+ state was not included in the fit, our interaction provides a description of this state which is about equal to the one by the LDA. The 1_1^-, 0_3^+, and the 2^+ analyzing powers are still significantly improved by the EMP. The major improvements provided by the empirical interaction for ^{40}Ca are in the cross section of the 5_1^- state and the second cross section maxima of the 3_2^- and 3_3^- states. The effect of the density dependence is, however, more clearly seen in the 3_1^- and 2_1^+ analyzing powers where the NRIA prediction is too high. Although these states peak at the surface, significant medium modifications to the NRIA are necessary to adequately describe the analyzing powers.

Elastic scattering was not explicitly included in the fits of this section and was simply predicted from inelastic scattering using the $(1 + \rho\partial/\partial\rho)$ prescription from Sections 2.7.3 and 2.8.3. For elastic scattering at this energy,

it appears that the LDA based on the PH interaction provides the best description of both the cross section and analyzing power data. The fact that the PH interaction gives better results for elastic scattering suggests that there might be a problem in the self-consistency procedure which may be related to the opposite signs of $(S_2 - d_2)$ for elastic and inelastic scattering at saturation density. It might be that second order terms in the $(1 + \rho\partial/\partial\rho)$ prescription are needed at this energy to restore the consistency between elastic and inelastic scattering. The empirical interaction is still quite successful for ^{16}O at 135 MeV [Kel 89b], but seems to deteriorate rapidly between 135 and 100 MeV.

Figures 7.7 and 7.8 show the optical potentials for elastic scattering. While for ^{16}O only the imaginary central potentials vary significantly, for ^{40}Ca also the real central potentials vary in the center by about 17% (the empirical potential being more attractive). For the imaginary central part, the empirical potential is less absorptive than either the LDA or NRIA potentials. Finally, the empirical and LDA spin-orbit interactions are virtually identical.

	$\mathrm{Re}t_{00}^{C}$		$\mathrm{Im}t_{00}^{C}$		$\mathrm{Re}\tau_{0}^{LS}$			$\left[\mathrm{Im}\tau_{0}^{LS}\right]$	
Data set	S_1	b_1	S_2	d_2	S_3	b_3	$t^{(f)}$	d_4	a_{41}
^{16}O	0.86	41.8	0.69	[0.55]	0.82	[3.7]	PH	0.60	-4.61
^{40}Ca	0.95	[41.8]	1.10	0.89	0.89	[3.7]	PH	$\mu_4 = 3.0$ fm^{-1}	
^{16}O+^{40}Ca	0.92	[41.8]	0.97	0.82	0.82	[3.7]	PH	$[\alpha\gamma\beta\delta] = [3220]$	
Theory[a]	[1.0]	72.7	[1.0]	0.55	[1.0]	3.7	PH	ref.: Table 2.1	

Table 7.1: Empirical effective interactions for 100 MeV protons. We use the following exponents $[\alpha\gamma\beta\delta]$ and masses μ: [3310], $\mu_1 = 1.5$ fm^{-1} ($\mathrm{Re}t_{00}^{C}$); [2210] ($\mathrm{Im}t_{00}^{C}$); [3320], $\mu_3 = 6.0$ fm^{-1} ($\mathrm{Re}\tau_{0}^{LS}$). Units: S_i and d_i (1), b_1 (MeV fm^3), b_3 and a_{41} (MeV fm^5). Square brackets indicate that the parameter or component is fixed.
[a]Values from Table 2.5.

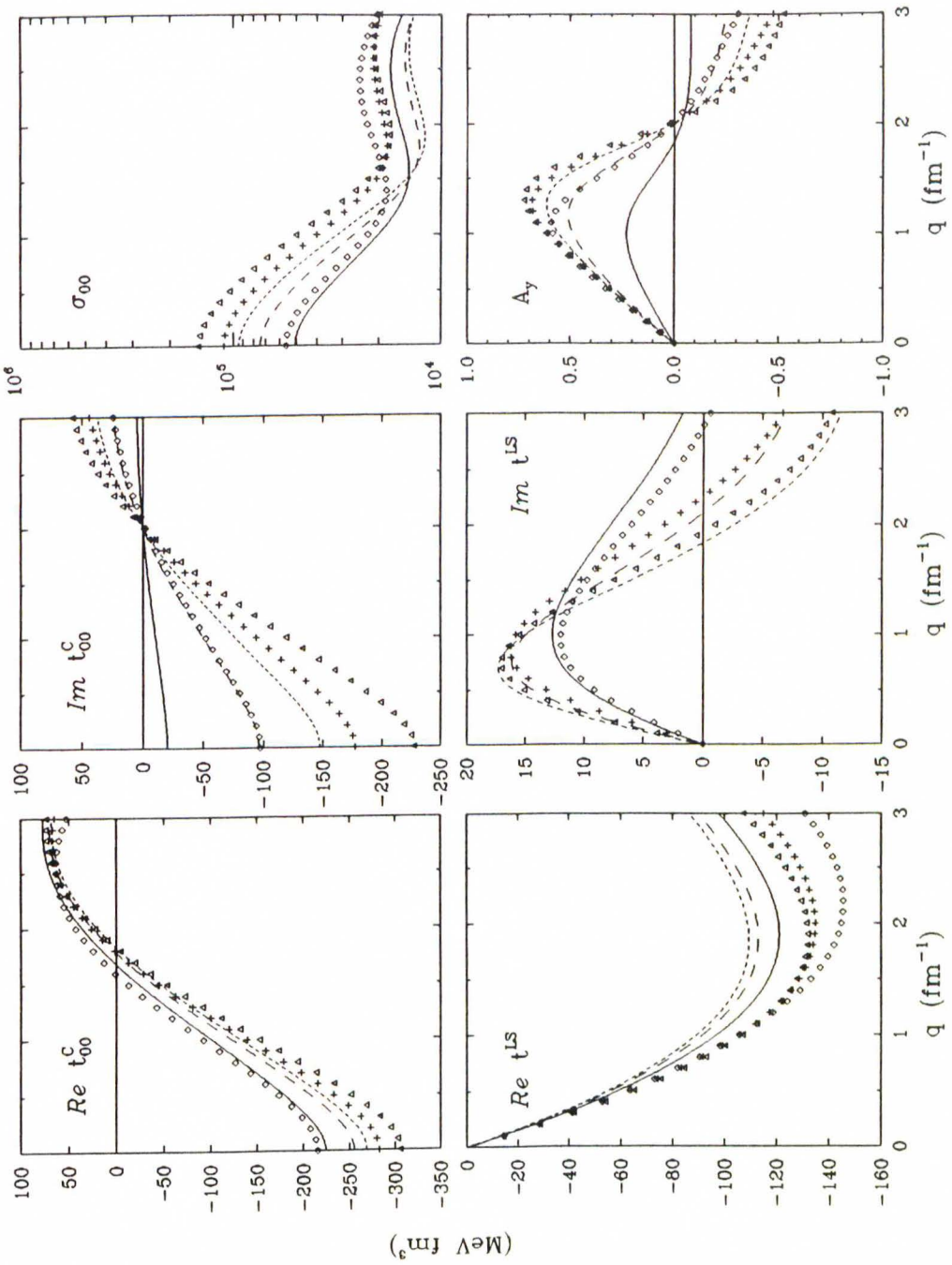

Figure 7.1: Comparison of the EMP(^{16}O) and PH interactions at 100 MeV for $k_F = 0.6$ fm^{-1} (triangles, short dashes), $k_F = 1.0$ fm^{-1} (crosses, dashes), and $k_F = 1.4$ fm^{-1} (diamonds, solid).

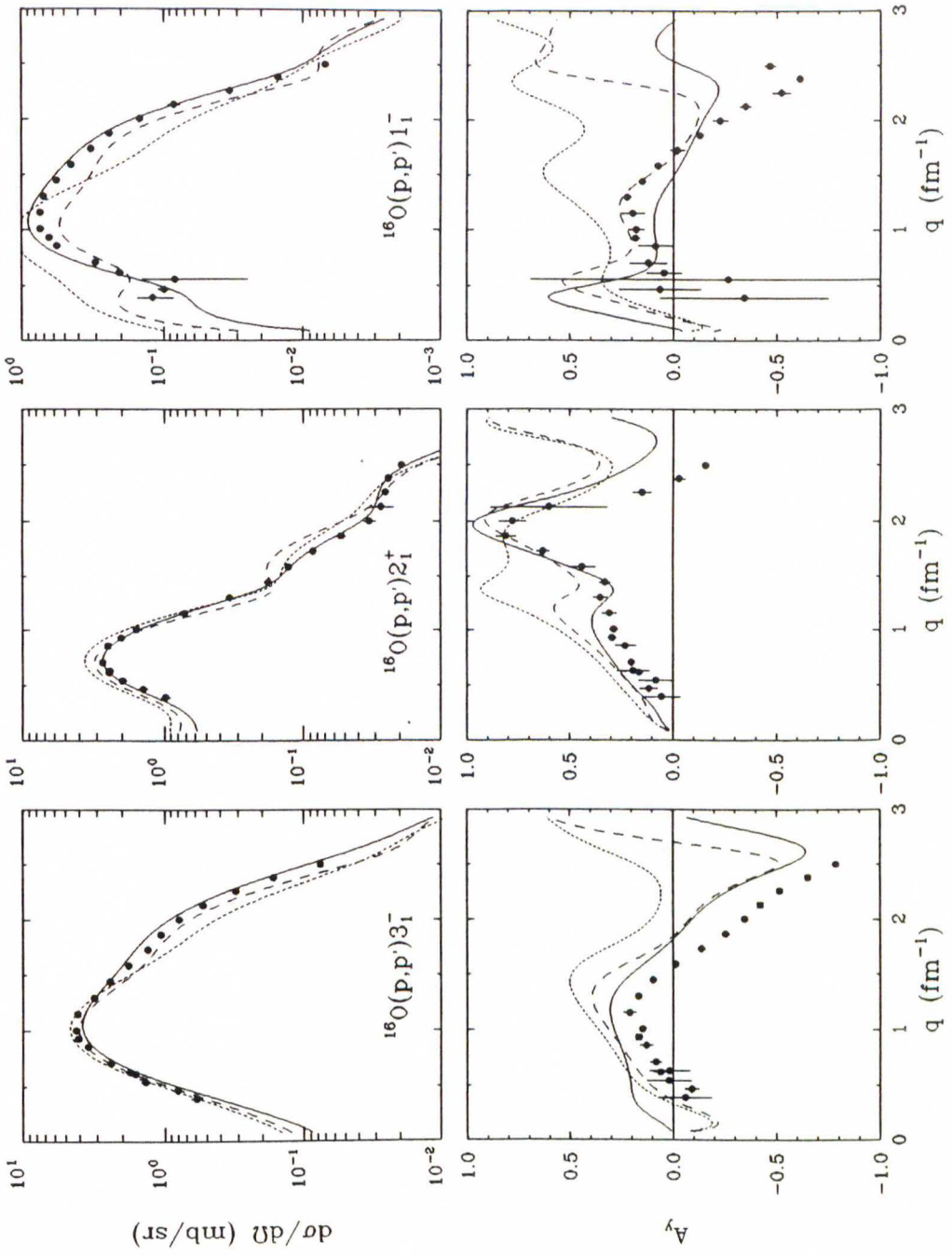

Figure 7.2: Comparison of EMP (solid), LDA (dashes), and NRIA (short dashes) calculations for the 3^-_1, 2^+_1, and 1^-_1 inelastic states of ^{16}O at 100 MeV. The data are from this work. EMP based on PH t-matrix, LDA on PH g-matrix, and NRIA on PH t-matrix (the distorted waves are generated with the PH g-matrix).

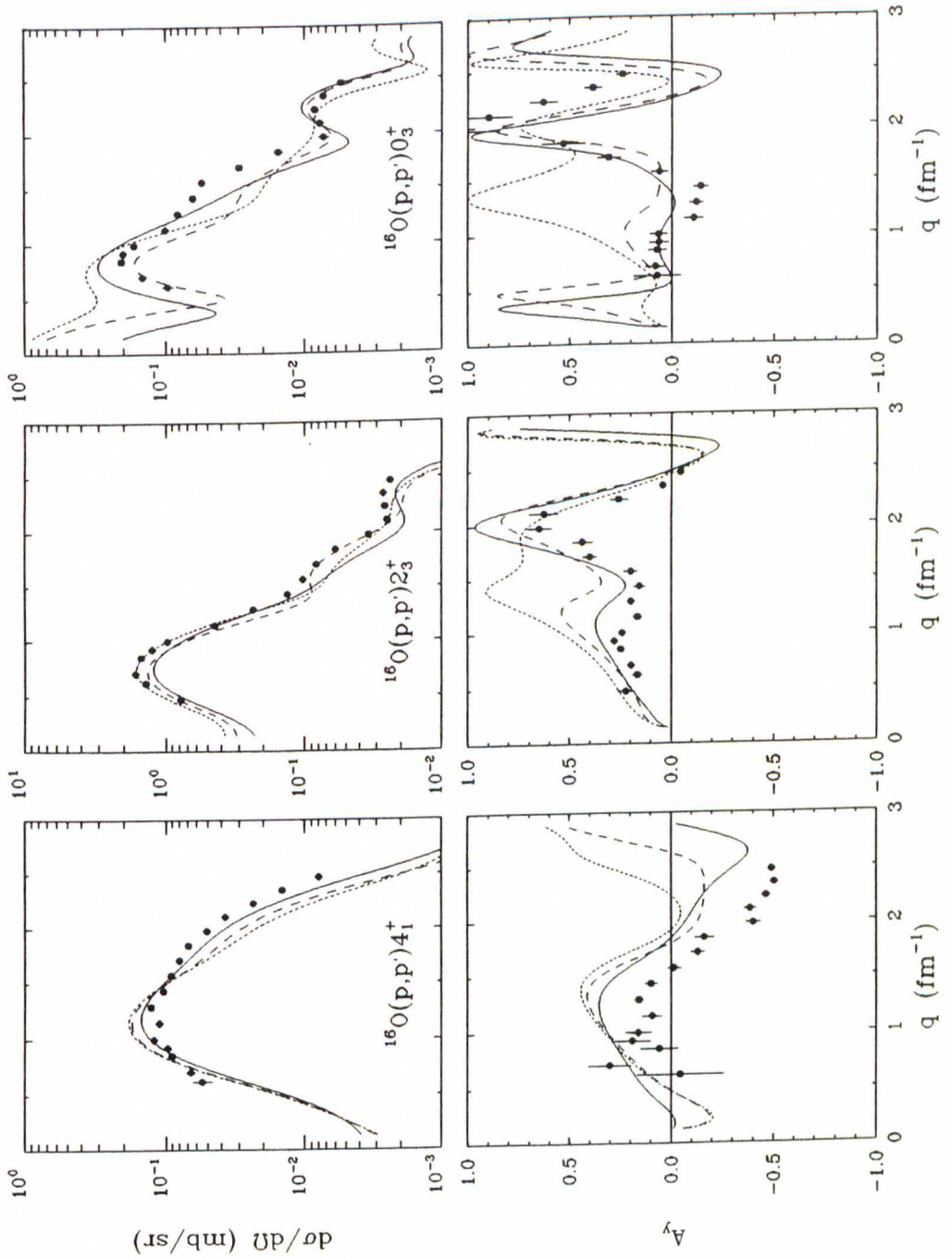

Figure 7.3: Comparison of EMP (solid), LDA (dashes), and NRIA (short dashes) calculations for the 4^+_1, 2^+_3, and 0^+_3 inelastic states of ^{16}O at 100 MeV. The data are from this work. EMP based on PH t-matrix, LDA on PH g-matrix, and NRIA on PH t-matrix (the distorted waves are generated with the PH g-matrix).

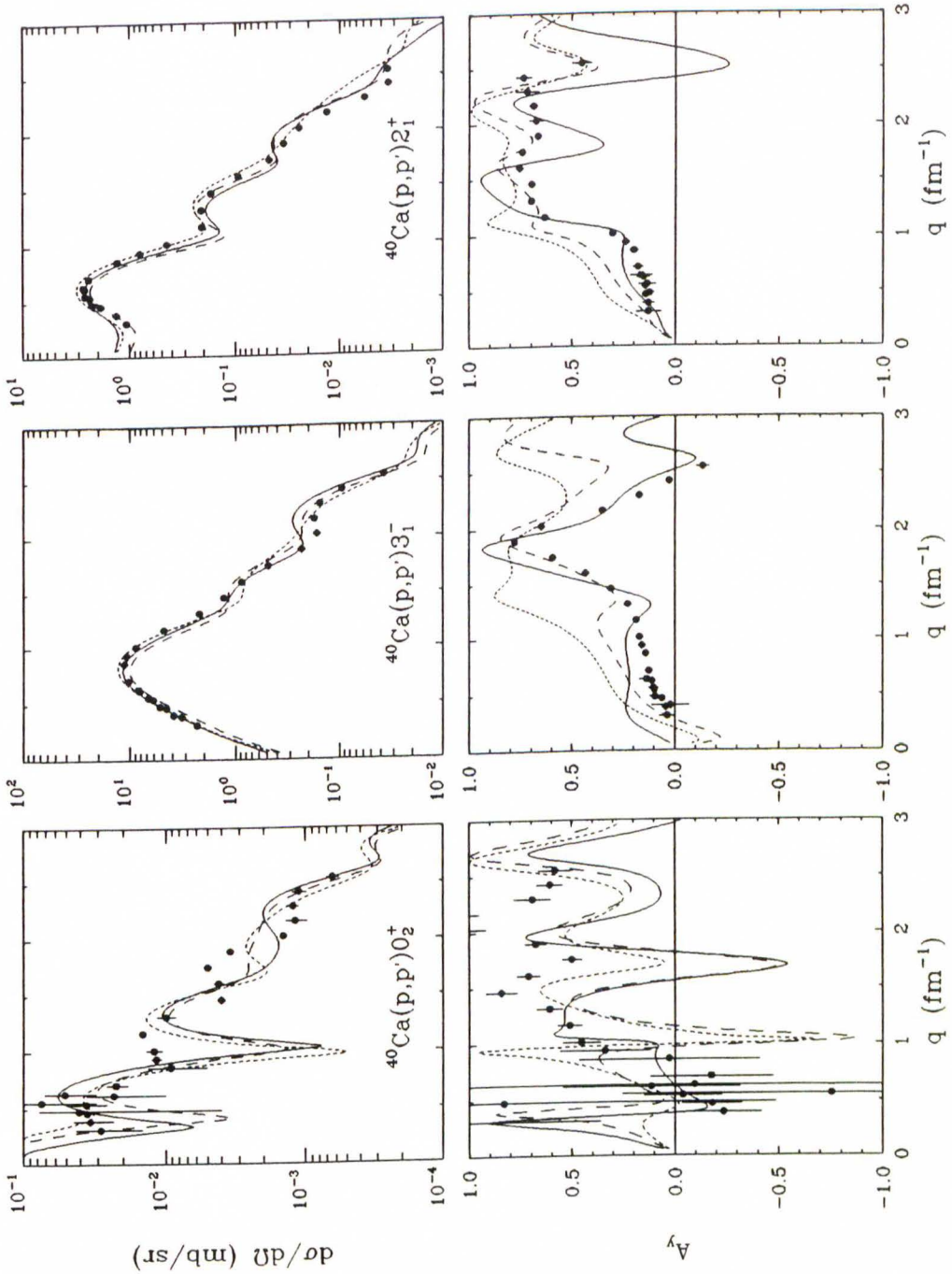

Figure 7.4: Comparison of EMP (solid), LDA (dashes), and NRIA (short dashes) calculations for the 0^+_2, 3^-_1, and 2^+_1 inelastic states of ^{40}Ca at 100 MeV. The data are from this work. EMP based on PH t-matrix, LDA on PH g-matrix, and NRIA on PH t-matrix (the distorted waves are generated with the PH g-matrix).

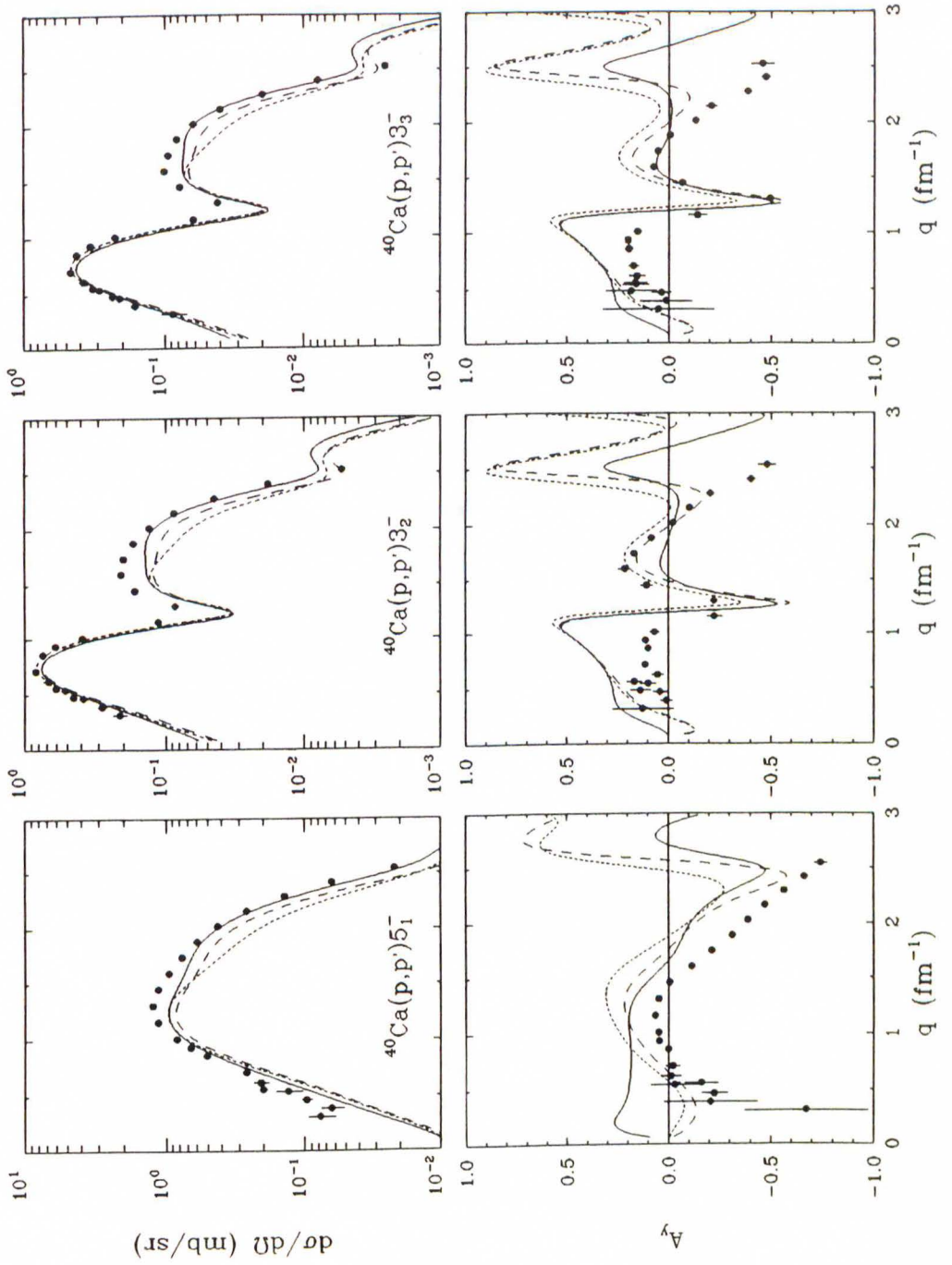

Figure 7.5: Comparison of EMP (solid), LDA (dashes), and NRIA (short dashes) calculations for the 5^-_1, 3^-_2, and 3^-_3 inelastic states of ^{40}Ca at 100 MeV. The data are from this work. EMP based on PH t-matrix, LDA on PH g-matrix, and NRIA on PH t-matrix (the distorted waves are generated with the PH g-matrix).

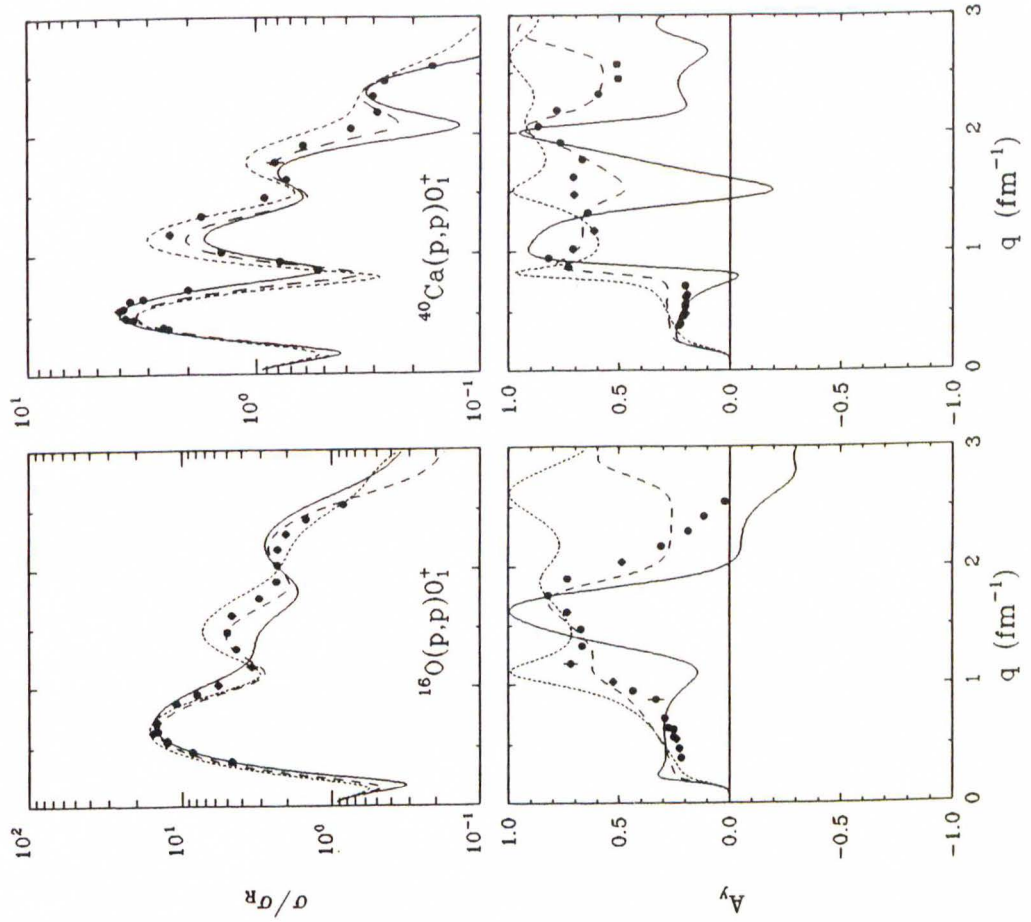

Figure 7.6: Comparison of EMP (solid), LDA (dashes), and NRIA (short dashes) elastic calculations for ^{16}O and ^{40}Ca at 100 MeV. The data are from this work. EMP based on PH t-matrix, LDA on PH g-matrix, and NRIA on PH t-matrix.

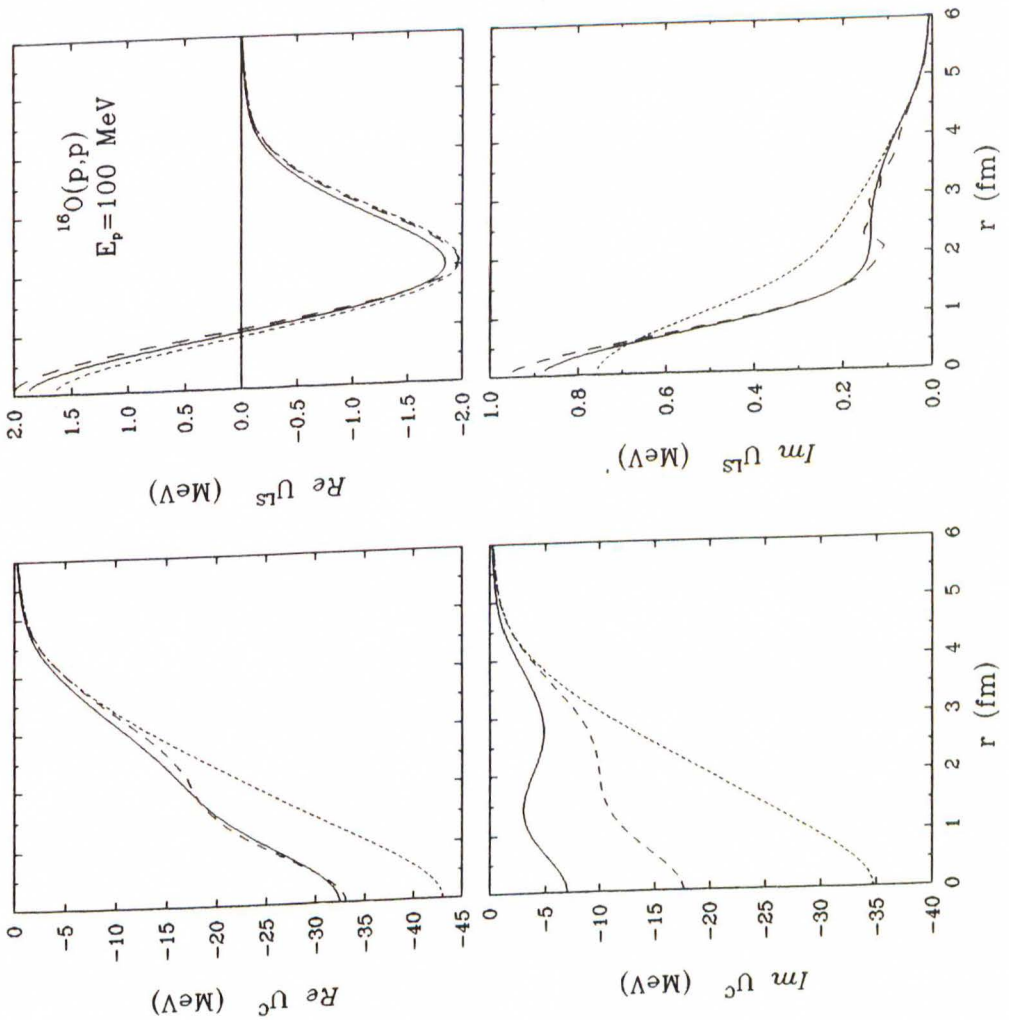

Figure 7.7: Optical potentials for elastic scattering of 100 MeV protons by ^{16}O for the EMP (solid), LDA (dashes), and NRIA (short dashes) interactions. EMP based on PH t-matrix, LDA on PH g-matrix, and NRIA on PH t-matrix.

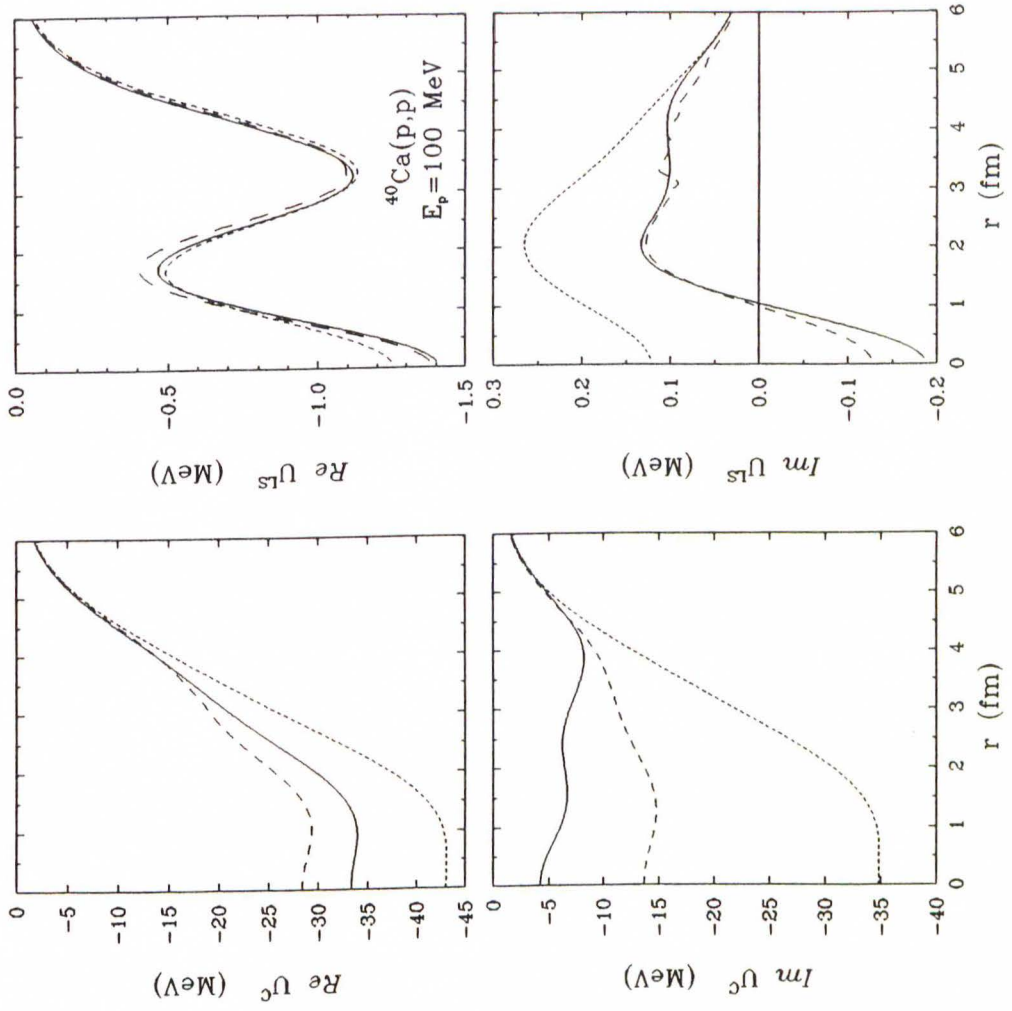

Figure 7.8: Optical potentials for elastic scattering of 100 MeV protons by ^{40}Ca for EMP (solid), LDA (dashes), and NRIA (short dashes) interactions. EMP based on PH t-matrix, LDA on PH g-matrix, and NRIA on PH t-matrix.

7.2.2 200 MeV

In Table 7.2 we show the results for 200 MeV protons. As in the case for 100 MeV, the data for this interaction fit are from this work. The fit was very stable and none of the parameters had to be constrained. Again the PH free interaction proved superior to the FL t-matrix as a model for the free interaction. In Figure 7.9 we compare the interaction for ^{16}O with the PH interaction. Very noticeable at this energy, and especially in the Ret_{00}^{C} component, is now the overall reduction in strength of the empirical interaction. Figure 7.10 compares our empirical interaction with the LR interaction. The real central component seems to be shifted upward and has about the same density dependence as the LR interaction. The imaginary central component of the empirical interaction, however, displays much less density dependence than the corresponding LR component. Figures 7.11–7.15 shows the fits to ^{16}O, and ^{40}Ca and Figures 7.16 and 7.17 show the optical potentials for elastic scattering. With the exception of the forward angle cross section of the 2_3^+ state of ^{16}O which is still too low, and some of the analyzing powers below about 1.0 fm^{-1} which are slightly too high, the empirical interaction at this energy provides a description of all the data which is much superior to either LDA or NRIA calculations. In particular, the empirical model follows the deep excursions of the analyzing power data above 1.0 fm^{-1} much more closely than the other calculations. Again, although neither the 0_3^+ state of ^{16}O nor the 0_2^+ state of ^{40}Ca were included in the fit, most of the cross section data and essentially all of the analyzing power data are described very well. We see that for the 0_3^+ cross section data, the minimum predicted

	$\mathrm{Re}t_{00}^{C}$		$\mathrm{Im}t_{00}^{C}$		$\mathrm{Re}\tau_{0}^{LS}$			$\left[\mathrm{Im}\tau_{0}^{LS}\right]$	
Data set	S_1	b_1	S_2	d_2	S_3	b_3	$t^{(f)}$	d_4	a_{41}
^{16}O	0.70	65.5	0.77	0.14	0.84	2.03	PH	0.38	-3.36
^{40}Ca	0.61	60.5	0.84	0.15	0.85	5.73	PH	$\mu_4 = 4.0$ fm^{-1}	
^{16}O+^{40}Ca	0.66	59.8	0.80	0.16	0.85	3.27	PH	$[\alpha\gamma\beta\delta] = [3220]$	
Theory[a]	[1.0]	84.0	[1.0]	0.23	[1.0]	2.10	PH	ref.: Table 2.1	

Table 7.2: Empirical effective interactions for 200 MeV protons. We use the following exponents $[\alpha\gamma\beta\delta]$ and masses μ: [3310], $\mu_1 = 1.5$ fm^{-1} ($\mathrm{Re}t_{00}^{C}$); [2210] ($\mathrm{Im}t_{00}^{C}$); [3320], $\mu_3 = 6.0$ fm^{-1} ($\mathrm{Re}\tau_{0}^{LS}$). Units: S_i and d_i (1), b_1 (MeV fm^3), b_3 and a_{41} (MeV fm^5). Square brackets indicate that the parameter or component is fixed.
[a]Values from Table 2.5.

between about 1.2 and 2.0 fm^{-1} is filled up; for the 0_2^+ state, this region is around 1.0 fm^{-1}. The elastic state of ^{16}O features an enhancement of its cross section in just about the same region as the 0_3^+ state. At 200 MeV the empirical interaction is clearly superior in its description of all the scattering observables. It should be pointed out again, that the elastic data were not included in the fits and that the (truly impressive) Figure 7.15 shows predictions based on the effective interaction determined solely from inelastic scattering. Most notably, the spin rotation functions at small momentum transfers, which are underestimated by both the LDA and the NRIA, are correctly reproduced by the empirical effective interaction. As in the case of 100 MeV, the spin-orbit potentials are not very different for EMP and LDA. At 200 MeV the EMP and LDA real central potentials are more distinct than for 100 MeV, the EMP potential being slightly more repulsive.

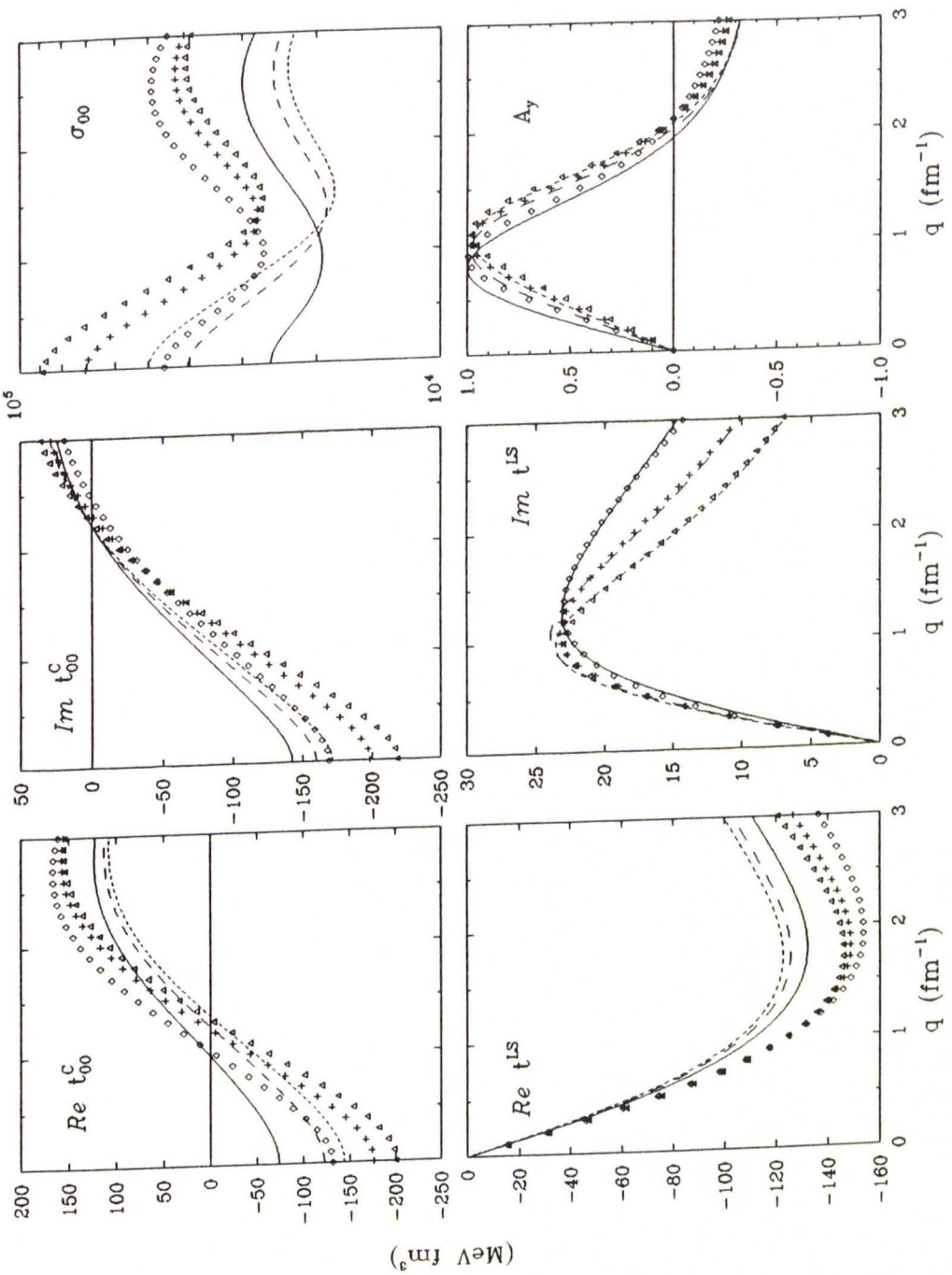

Figure 7.9: Comparison of the EMP(^{16}O) and PH interactions at 200 MeV for $k_F = 0.6$ fm^{-1} (triangles, short dashes), $k_F = 1.0$ fm^{-1} (crosses, dashes), and $k_F = 1.4$ fm^{-1} (diamonds, solid).

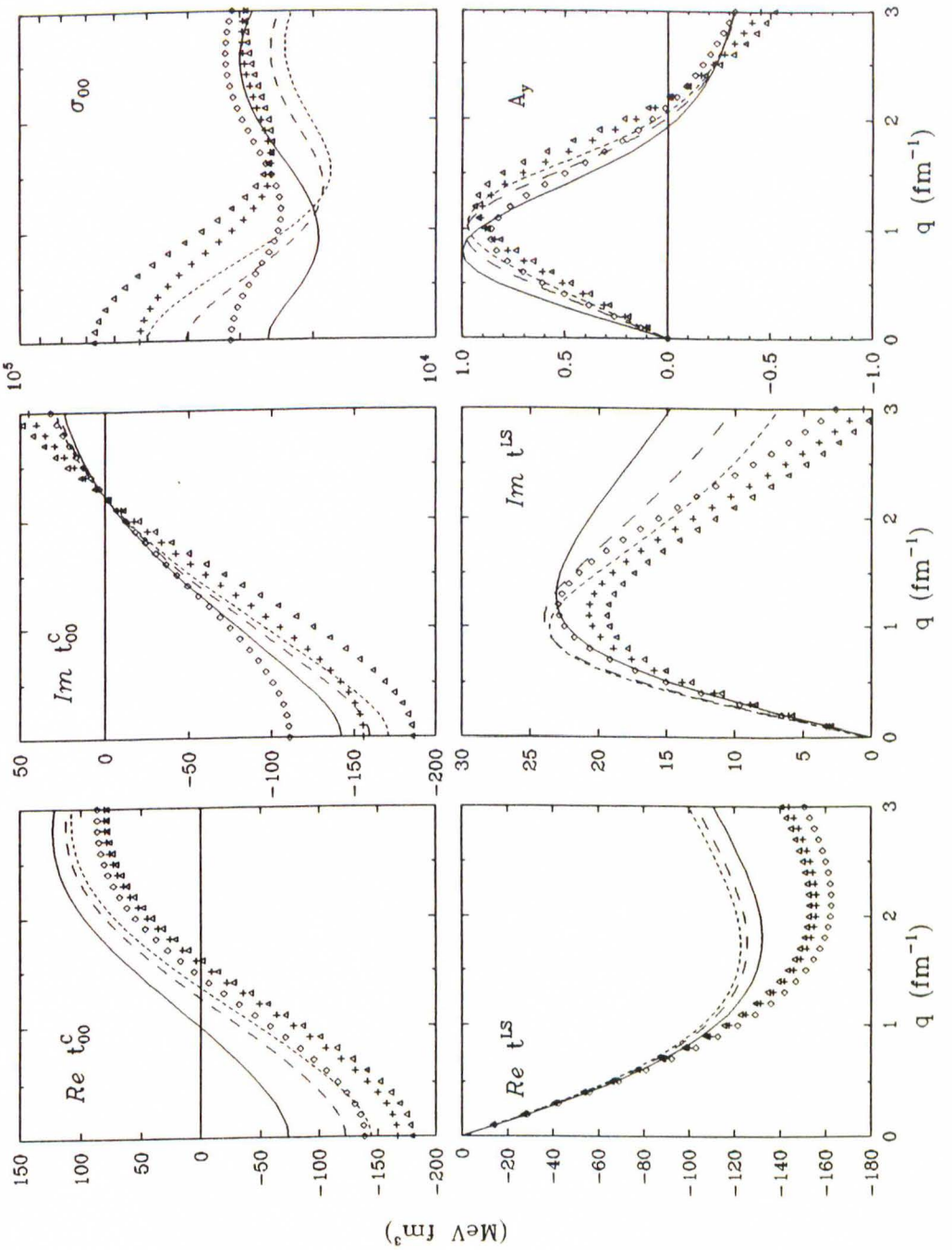

Figure 7.10: Comparison of the EMP(^{16}O) and LR interactions at 200 MeV for $k_F = 0.6$ fm^{-1} (triangles, short dashes), $k_F = 1.0$ fm^{-1} (crosses, dashes), and $k_F = 1.4$ fm^{-1} (diamonds, solid). LR medium modifications are modeled upon the FL t-matrix

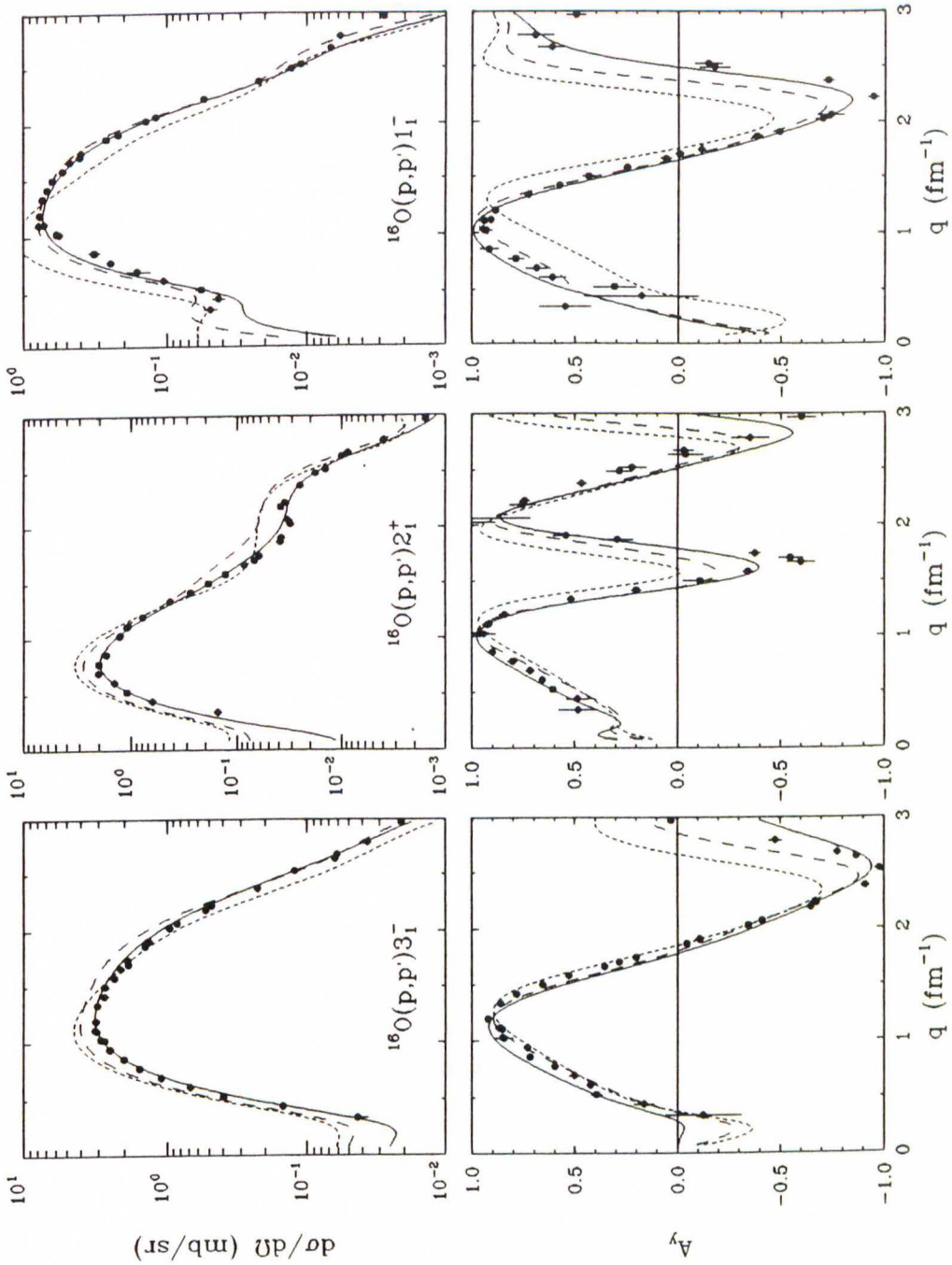

Figure 7.11: Comparison of EMP (solid), LDA (dashes), and NRIA (short dashes) calculations for the 3^-_1, 2^+_1, and 1^-_1 inelastic states of ^{16}O at 200 MeV. The data are from this work. EMP based on PH t-matrix, LDA on PH g-matrix, and NRIA on PH t-matrix (the distorted waves are generated with the PH g-matrix).

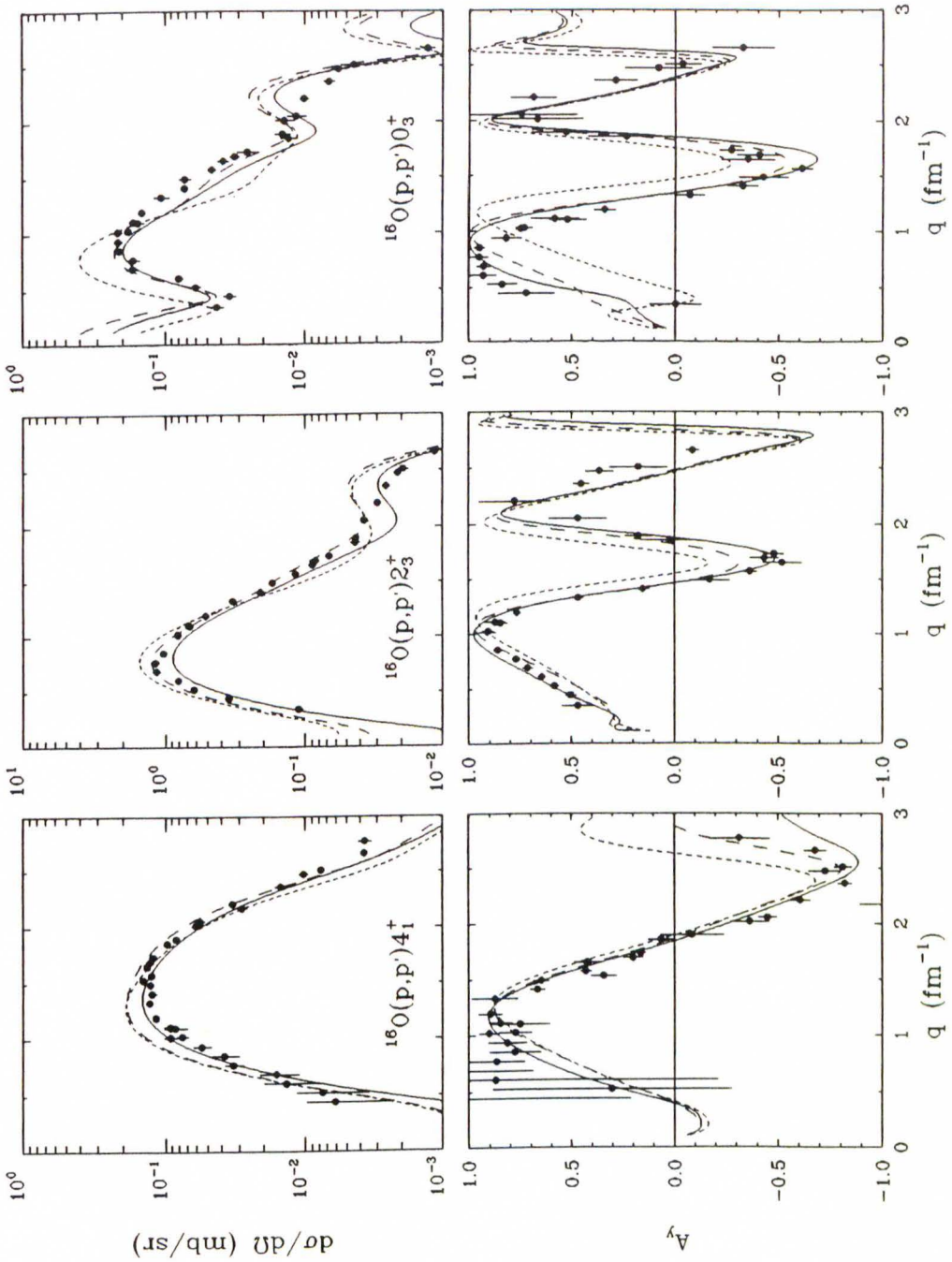

Figure 7.12: Comparison of EMP (solid), LDA (dashes), and NRIA (short dashes) calculations for the 4_1^+, 2_3^+, and 0_3^+ inelastic states of ^{16}O at 200 MeV. The data are from this work. EMP based on PH t-matrix, LDA on PH g-matrix, and NRIA on PH t-matrix (the distorted waves are generated with the PH g-matrix).

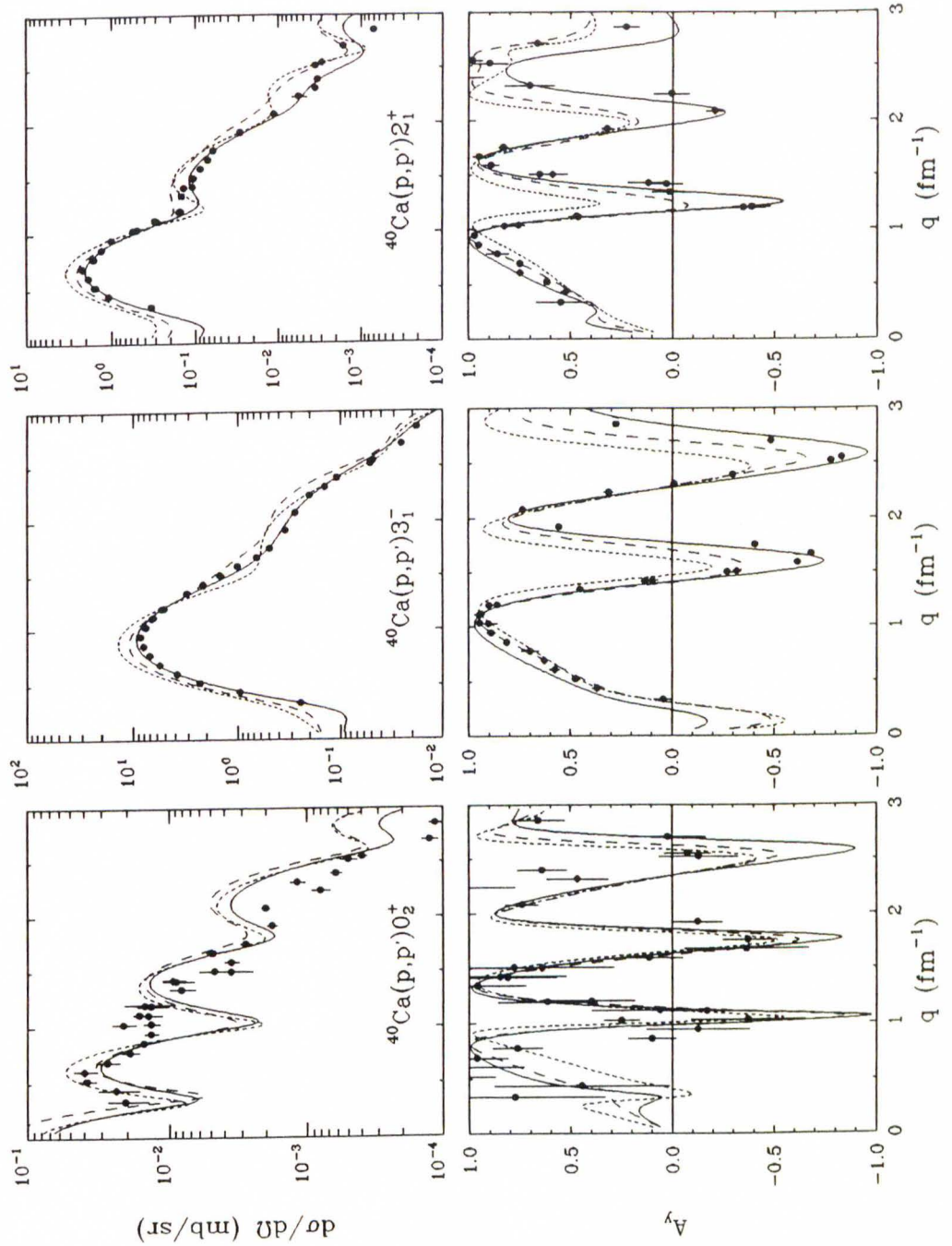

Figure 7.13: Comparison of EMP (solid), LDA (dashes), and NRIA (short dashes) calculations for the 0_2^+, 3_1^-, and 2_1^+ inelastic states of ^{40}Ca at 200 MeV. The data are from this work. EMP based on PH t-matrix, LDA on PH g-matrix, and NRIA on PH t-matrix (the distorted waves are generated with the PH g-matrix).

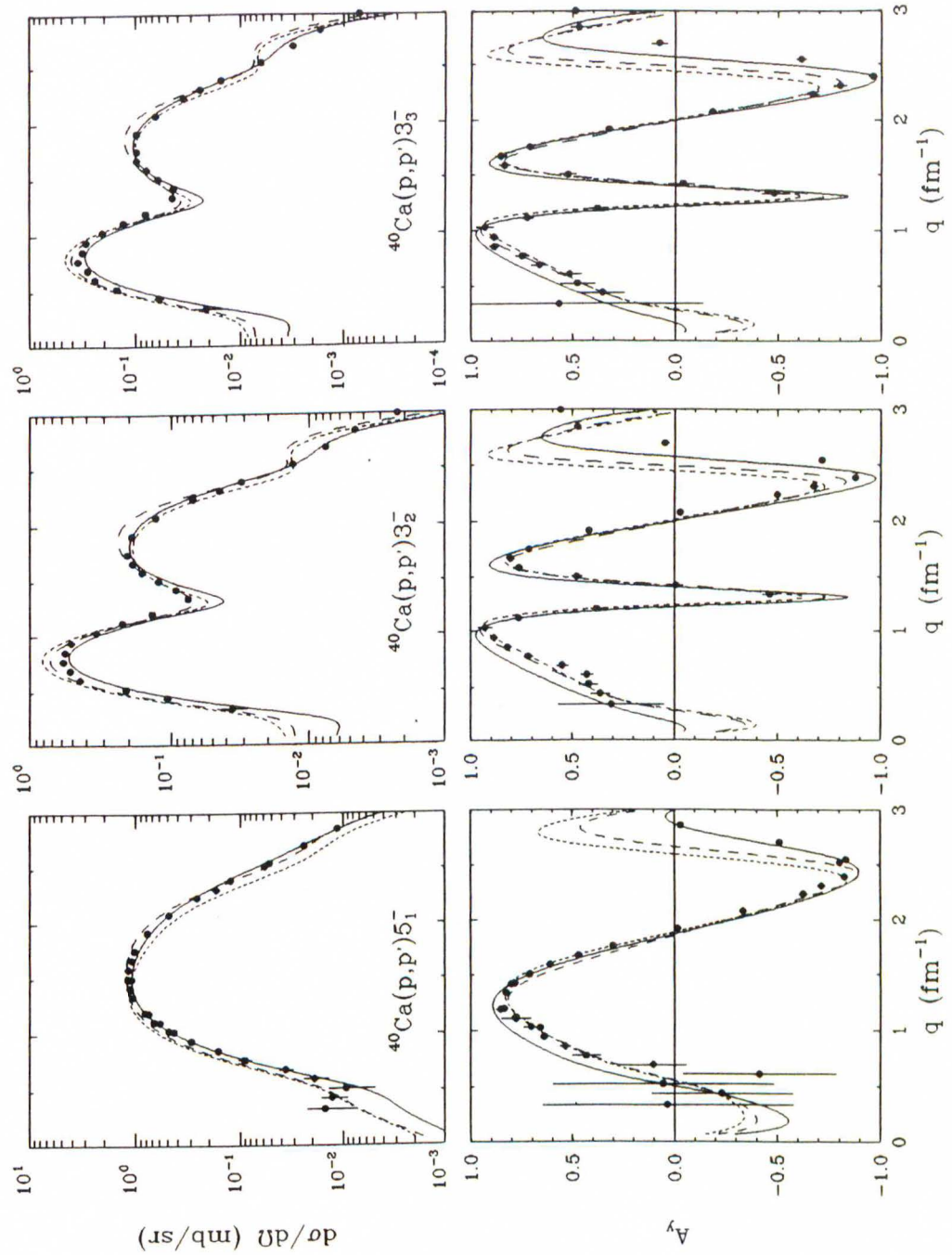

Figure 7.14: Comparison of EMP (solid), LDA (dashes), and NRIA (short dashes) calculations for the 5^-_1, 3^-_2, and 3^-_3 inelastic states of ^{40}Ca at 200 MeV. The data are from this work. EMP based on PH t-matrix, LDA on PH g-matrix, and NRIA on PH t-matrix (the distorted waves are generated with the PH g-matrix).

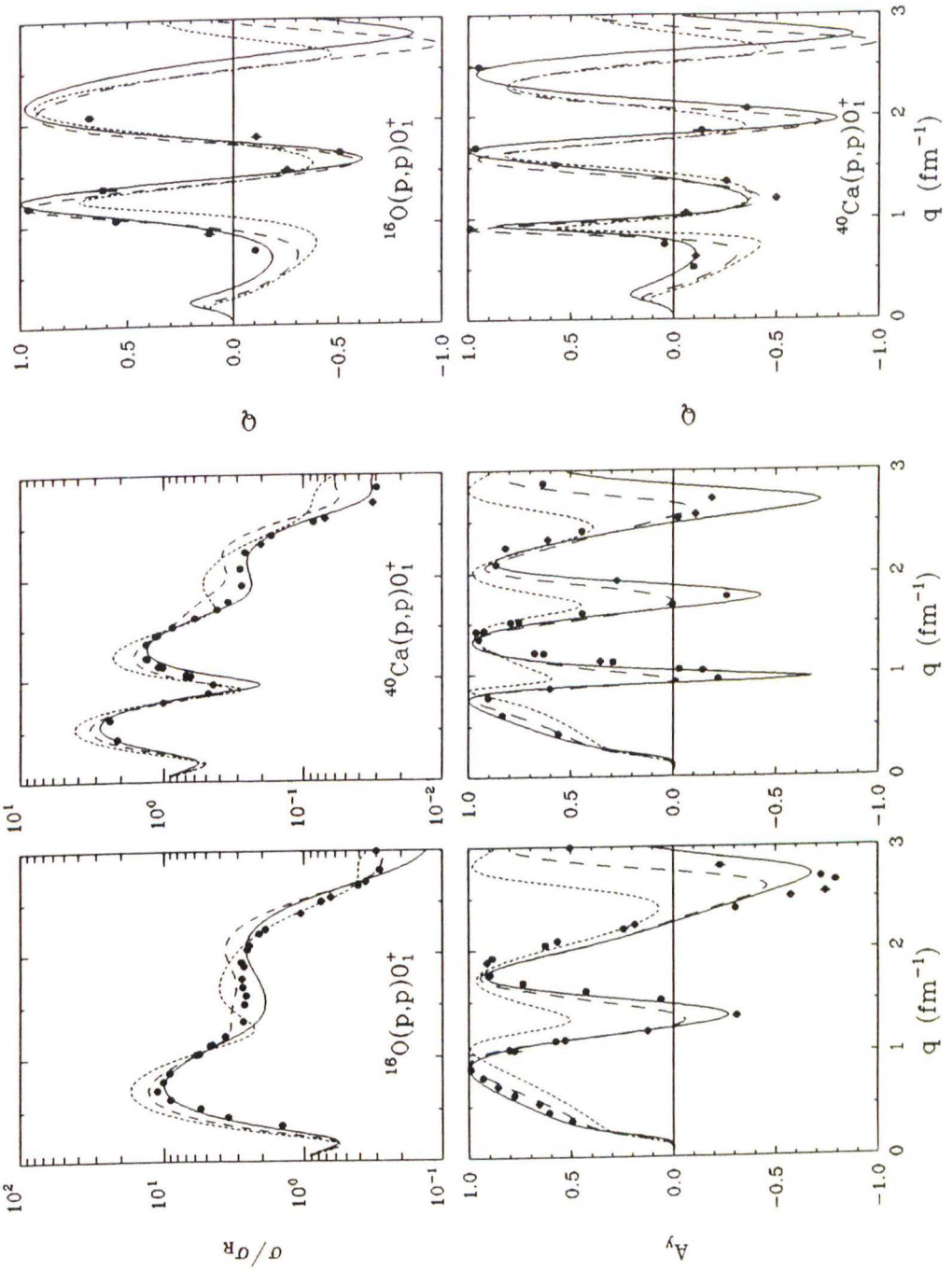

Figure 7.15: Comparison of EMP (solid), LDA (dashes), and NRIA (short dashes) elastic calculations for ^{16}O and ^{40}Ca at 200 MeV. The data for σ and A_y are from this work, the data for Q are from [Ste 85] and P. Schwandt, private communication. EMP based on PH t-matrix, LDA on PH g-matrix, and NRIA on PH t-matrix.

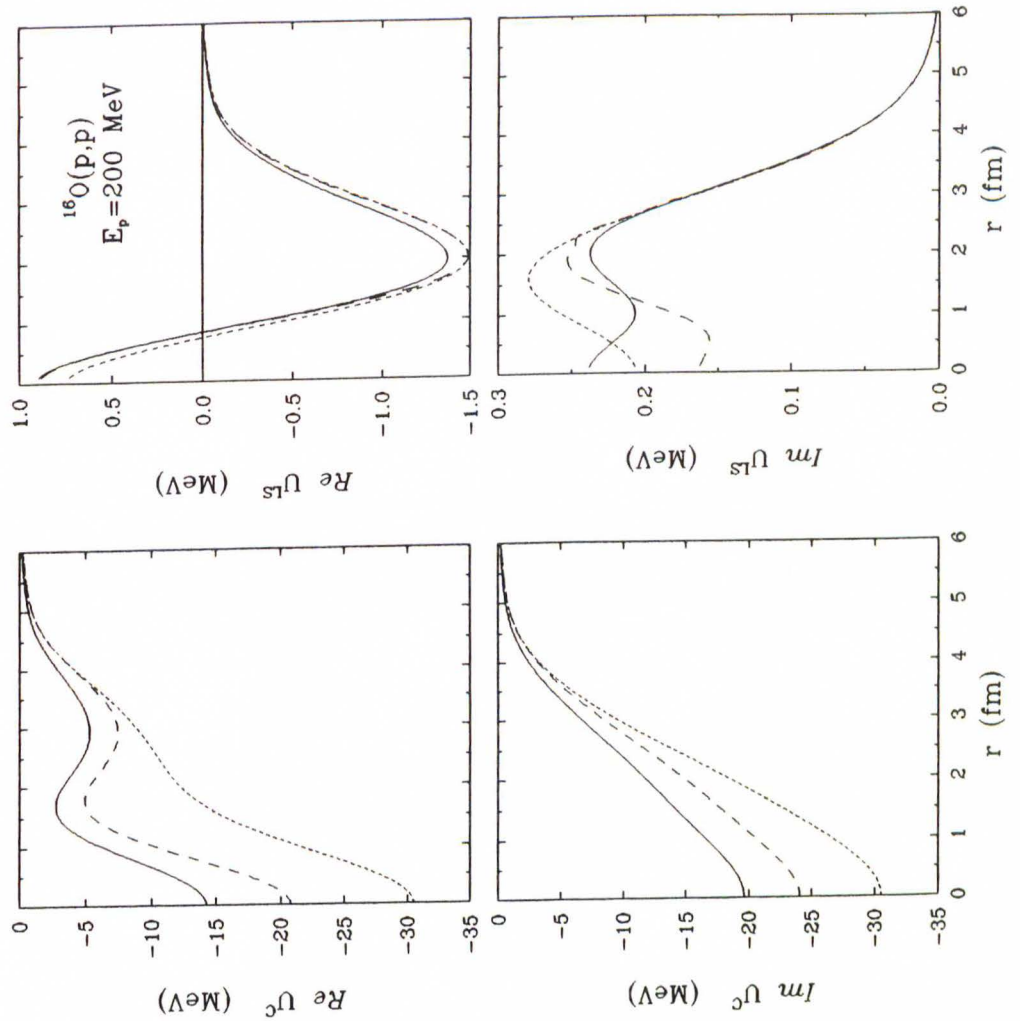

Figure 7.16: Optical potentials for elastic scattering of 200 MeV protons by ^{16}O for the EMP (solid), LDA (dashes), and NRIA (short dashes) interactions. EMP based on PH t-matrix, LDA on PH g-matrix, and NRIA on PH t-matrix.

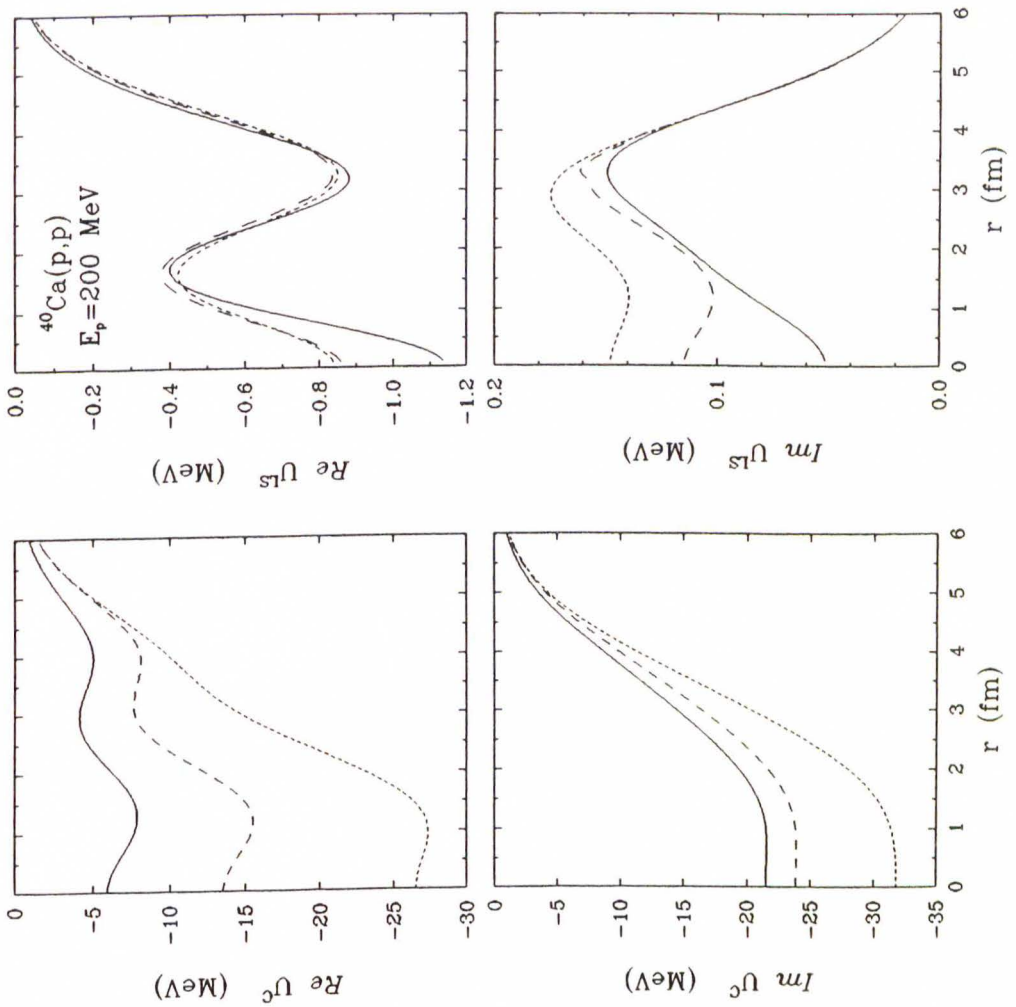

Figure 7.17: Optical potentials for elastic scattering of 200 MeV protons by ^{40}Ca for EMP (solid), LDA (dashes), and NRIA (short dashes) interactions. EMP based on PH t-matrix, LDA on PH g-matrix, and NRIA on PH t-matrix (the distorted waves are generated with the PH g-matrix).

7.2.3 318 MeV

Below 300 MeV the PH free interaction was used for the effective interaction analysis since it provided somewhat better fits, as measured by χ^2_ν, than the FL t-matrix (e.g. [Kel 89b]). At 318 MeV, however, due to the very large amplitude of the Ret^C_{00} component at large momentum transfer, the fits based upon the PH t-matrix yield unstable results which oscillate between two or three solutions (J. J. Kelly, private communication) unless some of the parameters are constrained. The FL free interaction, on the other hand has been shown to give stable fits at 318 MeV [Kel 90b], and is also used in this work.

Above 300 MeV the most natural thing is to compare the effective interaction to the LR interaction which is specifically designed for energies above the pion threshold and which, for energies above 400 MeV, is indeed the only available interaction. However, for the sake of consistency with the analyses at 100 and 200 MeV, we will compare the empirical interaction for 318 MeV also with the corresponding PH theoretical interaction. Finally, elastic and inelastic scattering calculations with the empirical interaction are compared to LDA and NRIA calculations which, like for 100 and 200 MeV, are based on the PH interaction. In the paper of Kelly *et al.* [Kel 90b] scattering calculations with the empirical interaction are compared to LDA calculations based on the LR interaction, and to NRIA calculations based on the FL free interaction.

The fitted parameters for the 318 MeV interactions are listed in Table 7.3. The ^{16}O data for this fit are from [Kel 90b], while the data for ^{40}Ca

are from [Fel 90]. We see in the table that the scale factors of the central components become equal to unity or even slightly larger than unity, while S_3 retains approximately the same value as for the lower energies. Figure 7.18 shows a comparison of our empirical interaction with the LR medium modifications modeled upon the FL t-matrix, while Figure 7.19 shows a comparison with the PH interaction at 318 MeV. In contrast to the lower energies, it appears that the real parts of both the EMP central and the EMP spin-orbit interaction show more density dependence than either the corresponding PH or LR components. In the table this stronger density dependence is reflected by the larger values for b_1 and b_3. For the spin-orbit interaction, this result should be taken with a grain of salt since, as the effective interaction grid for 318 MeV in Appendix D shows, the b_3 parameter is not very well determined by the data at this energy. For the imaginary central component it seems that the density dependence is reversed compared to the theoretical interactions. This is also reflected in the parameters where $d_2 < 0$ and $S_2 - d_2 > 1$. The magnitude of the density dependence of the imaginary central component for our empirical interaction is comparable to the PH interaction, but is much less than that of the LR interaction and is of opposite sign. While at low densities the empirical interaction is very similar to the LR interaction, at high densities it is much larger. On the other hand, compared to the PH interaction, the empirical interaction is larger at small momentum transfers and smaller at large momentum transfers.

In Figures 7.20–7.24 we compare calculations based on the empirical interactions EMP from the fits to ^{16}O and ^{40}Ca to LDA and NRIA calculations

which are both based on the PH interaction. Distorted waves for the NRIA calculations were generated with the PH g-matrix. The EMP description of the data is superior for all the states and all the observables. In particular, we want to point out the analyzing powers at small momentum transfers which are overestimated by both the LDA and the NRIA. For the ^{16}O elastic cross sections we observe that although the first maximum is described well by the empirical interaction, for momentum transfers above about 1.5 fm^{-1} the cross section calculation appears to be shifted outward a little bit too much. For ^{40}Ca this shift does not occur until about 2.2 fm^{-1}. Finally, in Figures 7.25 and 7.26 we show the optical potentials for elastic scattering at this energy. The EMP potentials are based on the interactions fitted to ^{16}O and ^{40}Ca, repectively. The LDA and NRIA potentials are based on the PH g-matrix and PH t-matrix, respectively. The EMP real central potentials are much more repulsive in the nuclear center than either the LDA or the NRIA potentials. For ^{40}Ca the EMP potential assumes a positive value of about +11 MeV. In comparison, the NRIA potential has a strength of about −13 MeV in the center, while the LDA potential almost vanishes. The EMP imaginary central potentials are less damped than the corresponding LDA potentials.

	$\mathrm{Re}t_{00}^{C}$		$\mathrm{Im}t_{00}^{C}$		$\mathrm{Re}\tau_{0}^{LS}$			$\left[\mathrm{Im}\tau_{0}^{LS}\right]$	
Data set	S_1	b_1	S_2	d_2	S_3	b_3	$t^{(f)}$	d_4	a_{41}
^{16}O	1.07	144.7	1.02	-0.07	0.83	7.14	FL	0.0	-1.58
^{40}Ca	1.04	140.0	1.00	-0.01	0.78	5.25	FL	$\mu_4 = 1.0$ fm^{-1}	
^{16}O+^{40}Ca	1.07	142.2	1.00	-0.04	0.78	5.88	FL	$[\alpha\gamma\beta\delta] = [3320]$	
PH-Theory[a]	[1.0]	80.5	[1.0]	0.04	[1.0]	1.03	PH	ref.: [Kel 90b]	
LR-Theory[a]	[1.0]	61.2	[1.0]	0.27	[1.0]	1.90	FL		

Table 7.3: Empirical effective interactions for 318 MeV protons ([Kel 90b], and J. J. Kelly, private communication). We use the following exponents $[\alpha\gamma\beta\delta]$ and masses μ: [3310], $\mu_1 = 2.0$ fm^{-1} ($\mathrm{Re}t_{00}^{C}$); [2210] ($\mathrm{Im}t_{00}^{C}$); [3320], $\mu_3 = 6.0$ fm^{-1} ($\mathrm{Re}\tau_{0}^{LS}$). Units: S_i and d_i (1), b_1 (MeV fm^3), b_3 and a_{41} (MeV fm^5). Square brackets indicate that the parameter or component is fixed.
[a]Values from Table 2.5.

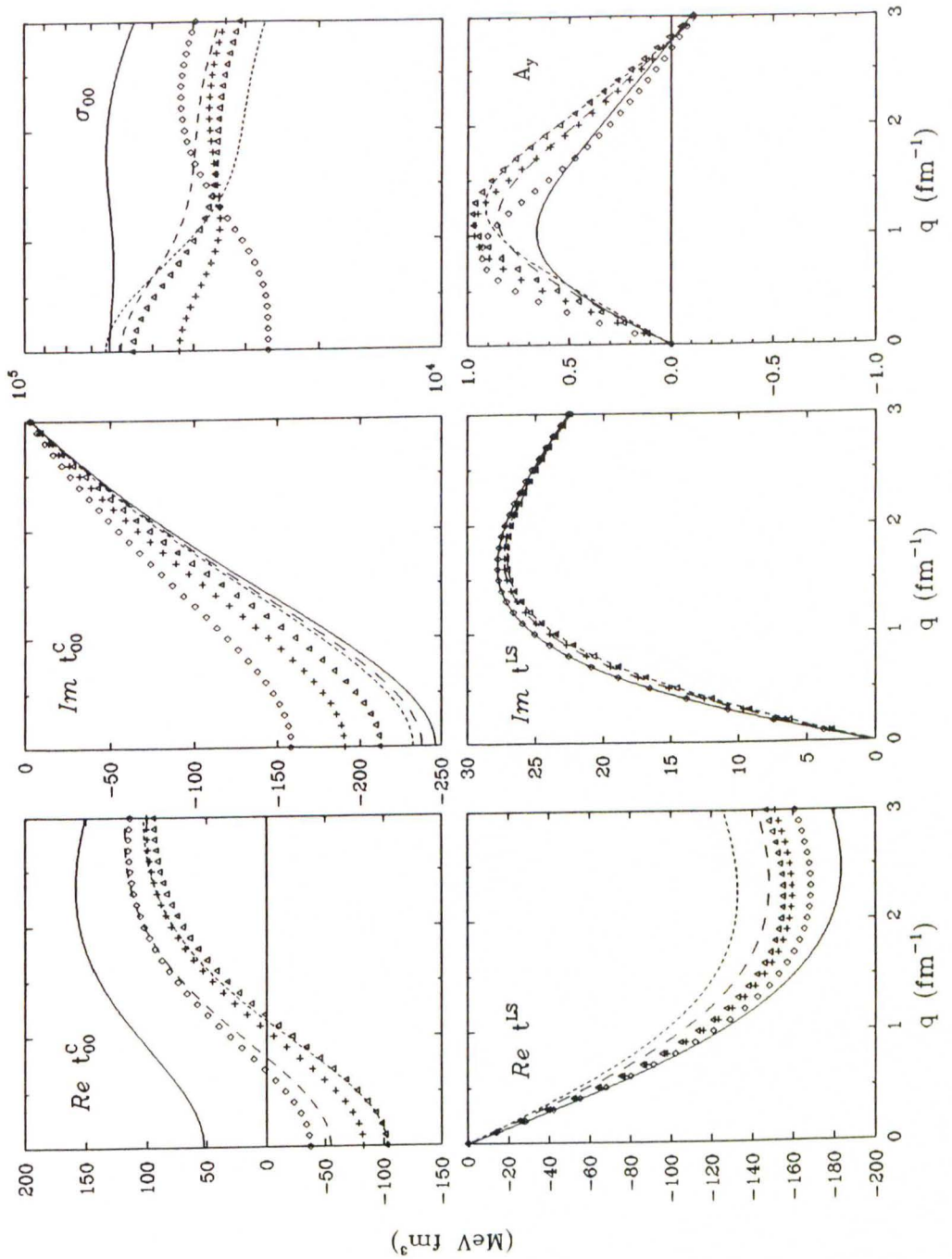

Figure 7.18: Comparison of the EMP(^{16}O) and LR interactions at 318 MeV for $k_F = 0.6$ fm^{-1} (triangles, short dashes), $k_F = 1.0$ fm^{-1} (crosses, dashes), and $k_F = 1.4$ fm^{-1} (diamonds, solid). LR medium modifications are modeled upon the FL t-matrix.

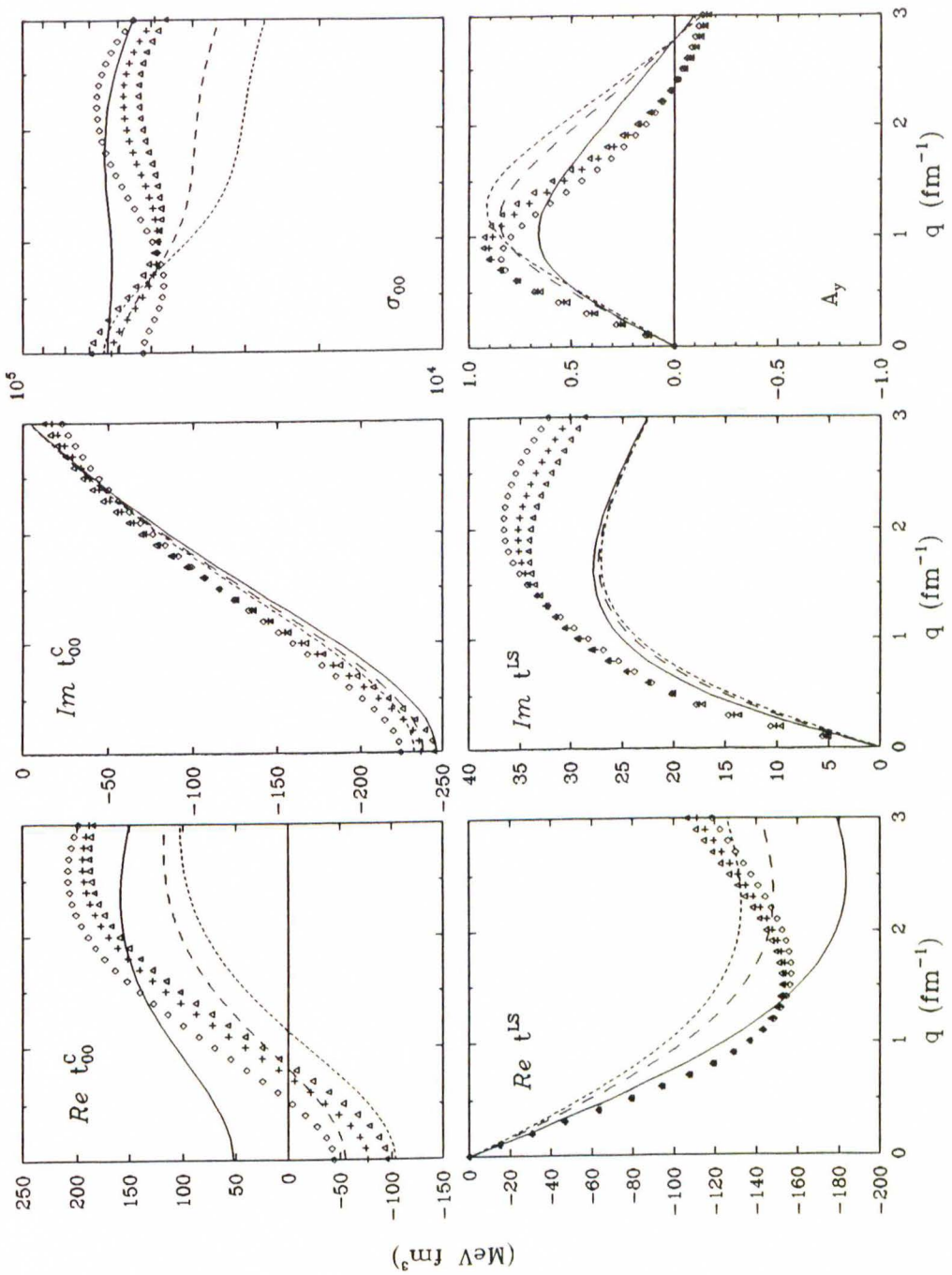

Figure 7.19: Comparison of the EMP(^{16}O) and PH interactions at 318 MeV for $k_F = 0.6$ fm^{-1} (triangles, short dashes), $k_F = 1.0$ fm^{-1} (crosses, dashes), and $k_F = 1.4$ fm^{-1} (diamonds, solid).

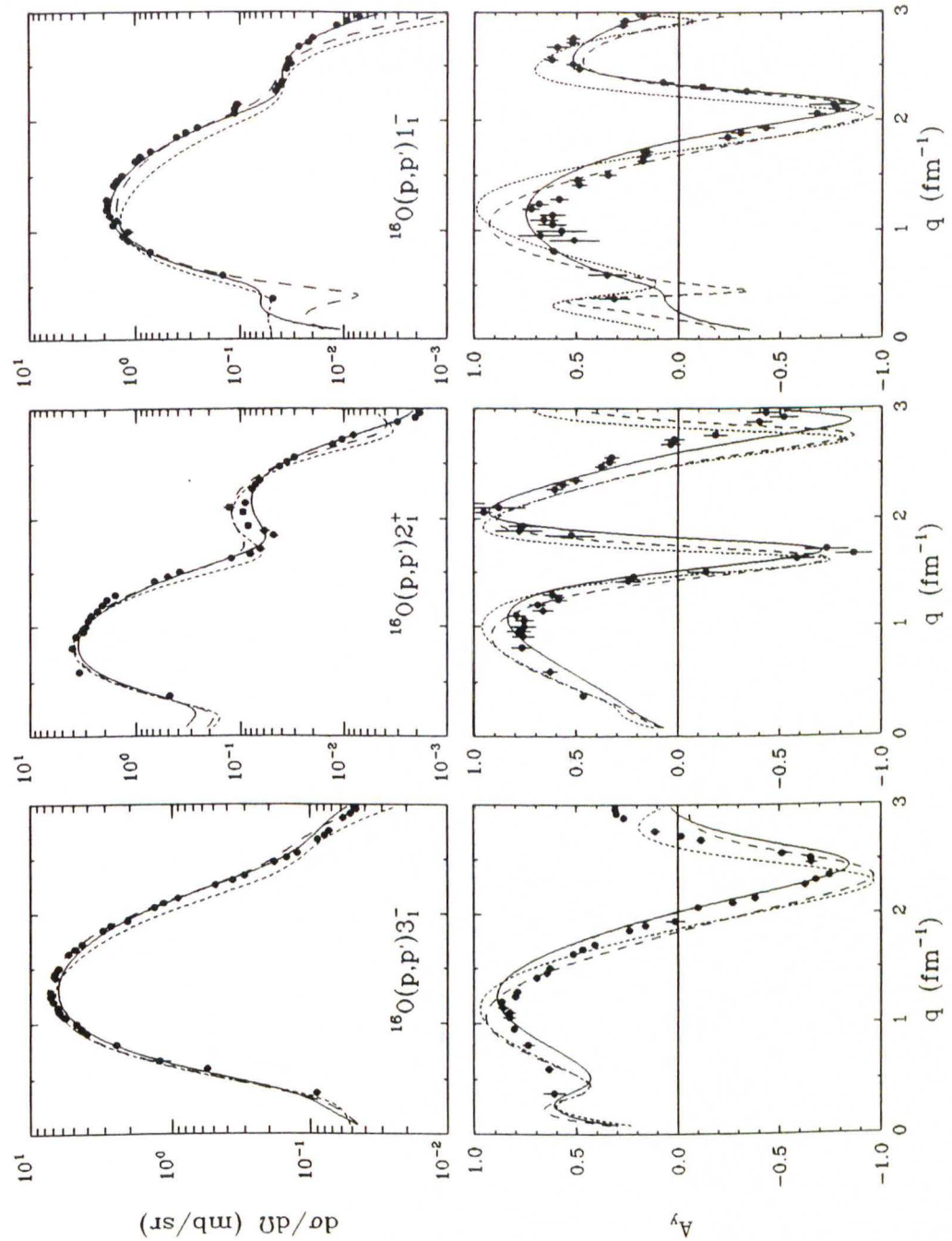

Figure 7.20: Comparison of EMP (solid), LDA (dashes), and NRIA (short dashes) calculations for the 3^-_1, 2^+_1, and 1^-_1 inelastic states of ^{16}O at 318 MeV. The data are from [Kel 90b]. EMP based on FL t-matrix, LDA on PH g-matrix, and NRIA on PH t-matrix (the distorted waves are generated with the PH g-matrix).

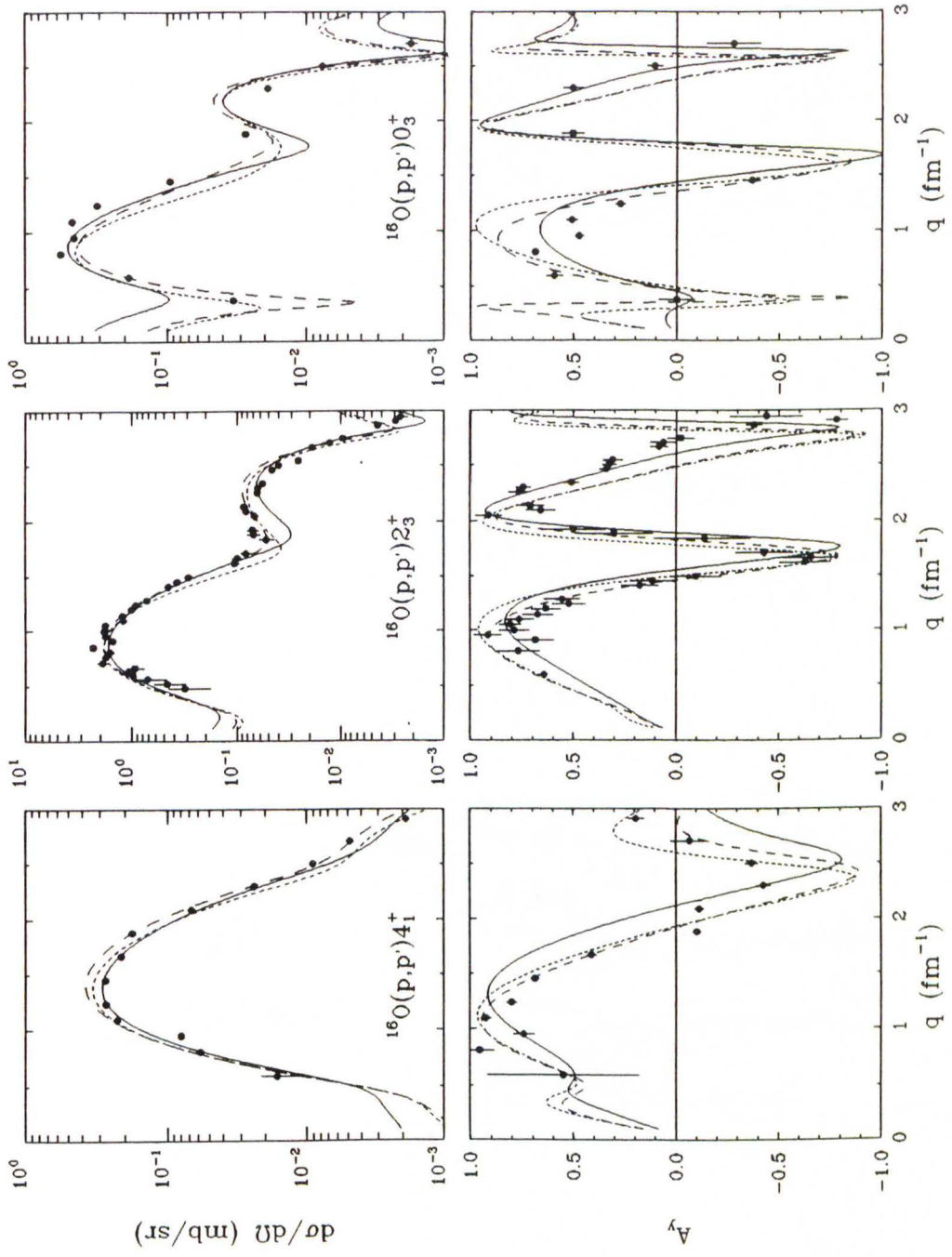

Figure 7.21: Comparison of EMP (solid), LDA (dashes), and NRIA (short dashes) calculations for the 4_1^+, 2_3^+, and 0_3^+ inelastic states of ^{16}O at 318 MeV. The data are from [Kel 90b]. EMP based on FL t-matrix, LDA on PH g-matrix, and NRIA on PH t-matrix (the distorted waves are generated with the PH g-matrix).

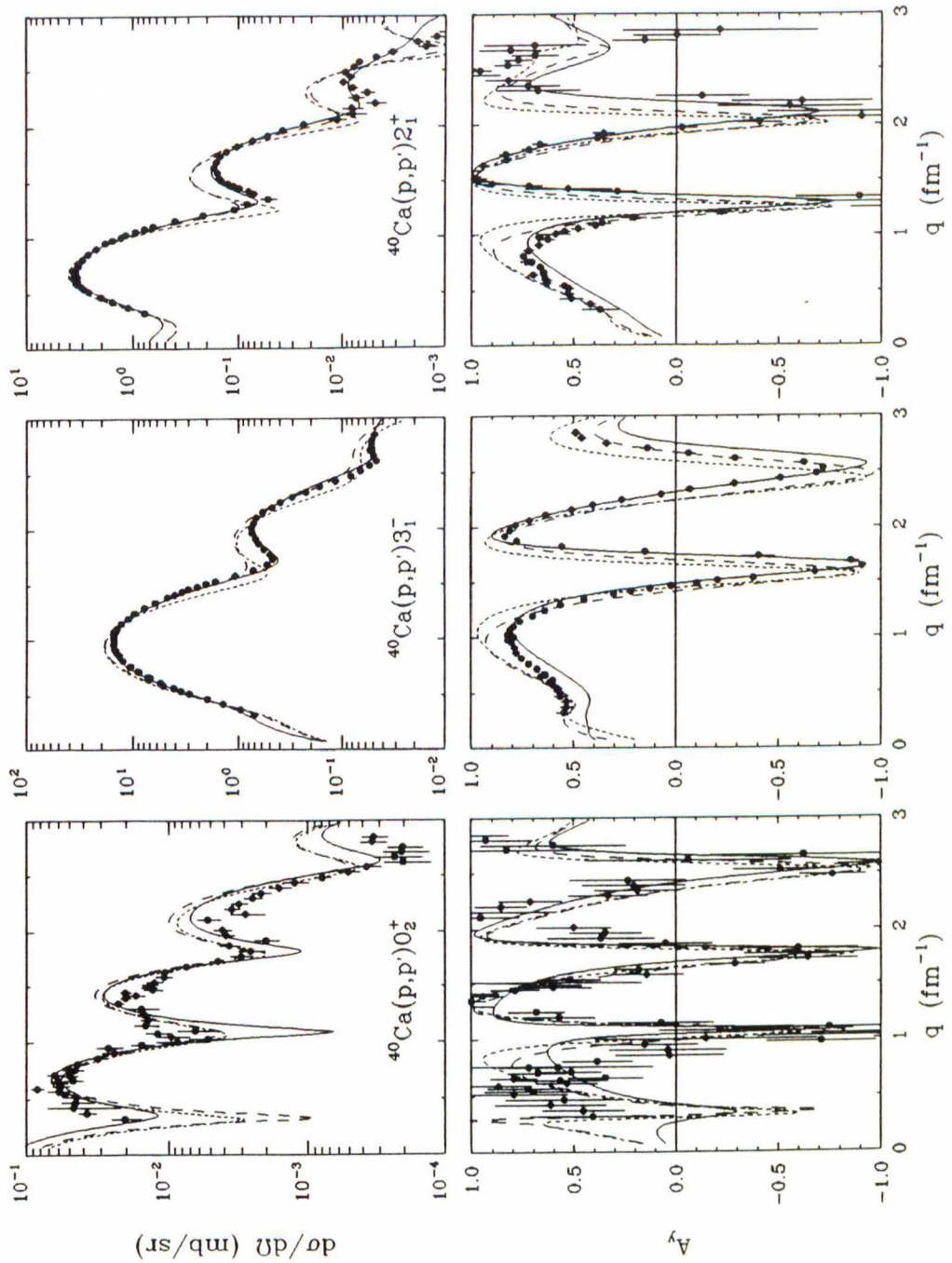

Figure 7.22: Comparison of EMP (solid), LDA (dashes), and NRIA (short dashes) calculations for the 0^+_2, 3^-_1, and 2^+_1 inelastic states of ^{40}Ca at 318 MeV. The data are from [Fel 90]. EMP based on FL t-matrix, LDA on PH g-matrix, and NRIA on PH t-matrix (the distorted waves are generated with the PH g-matrix).

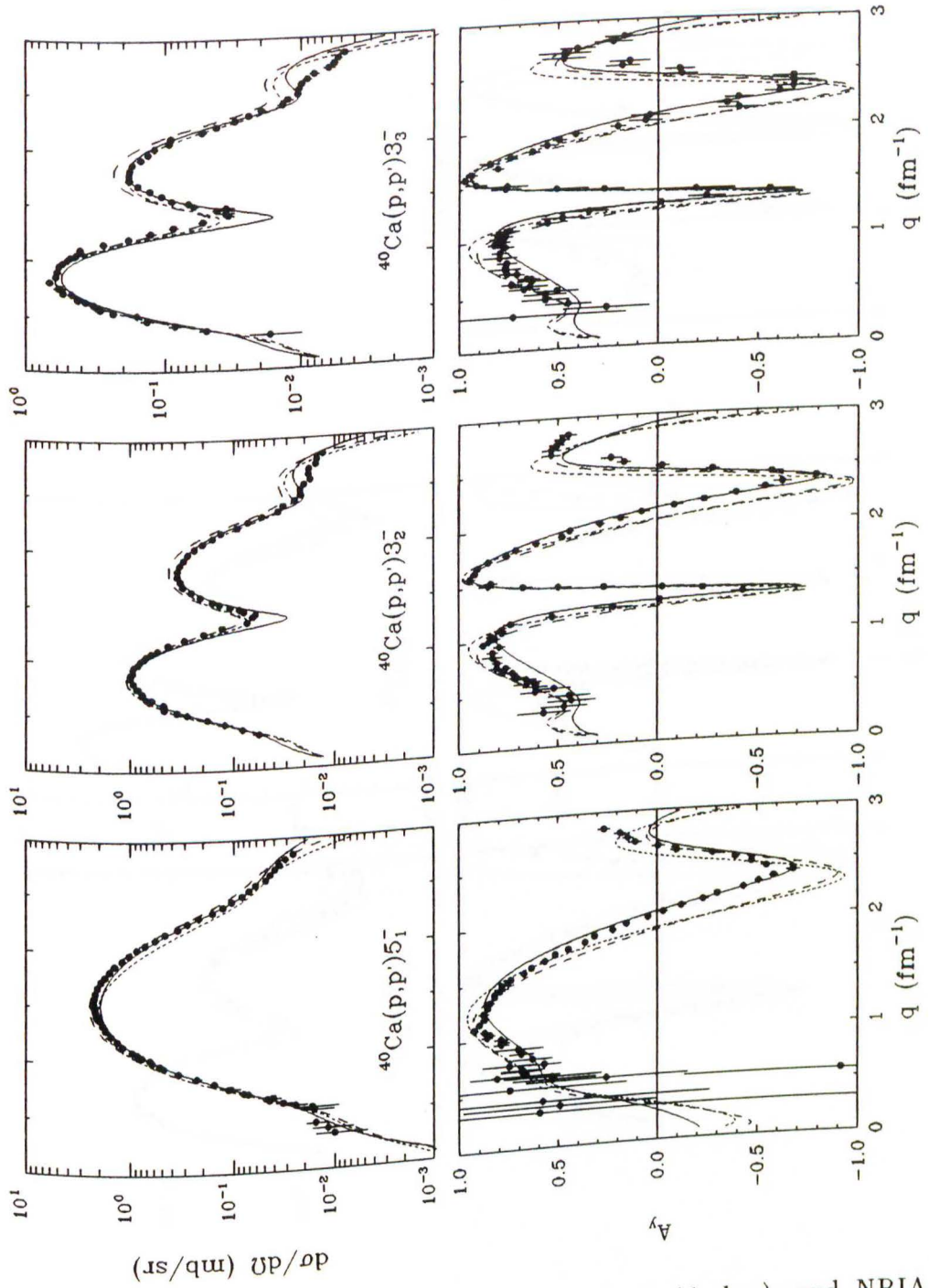

Figure 7.23: Comparison of EMP (solid), LDA (dashes), and NRIA (short dashes) calculations for the 5_1^-, 3_2^-, and 3_3^- inelastic states of ^{40}Ca at 318 MeV. The data are from [Fel 90]. EMP based on FL t-matrix, LDA on PH g-matrix, and NRIA on PH t-matrix (the distorted waves are generated with the PH g-matrix).

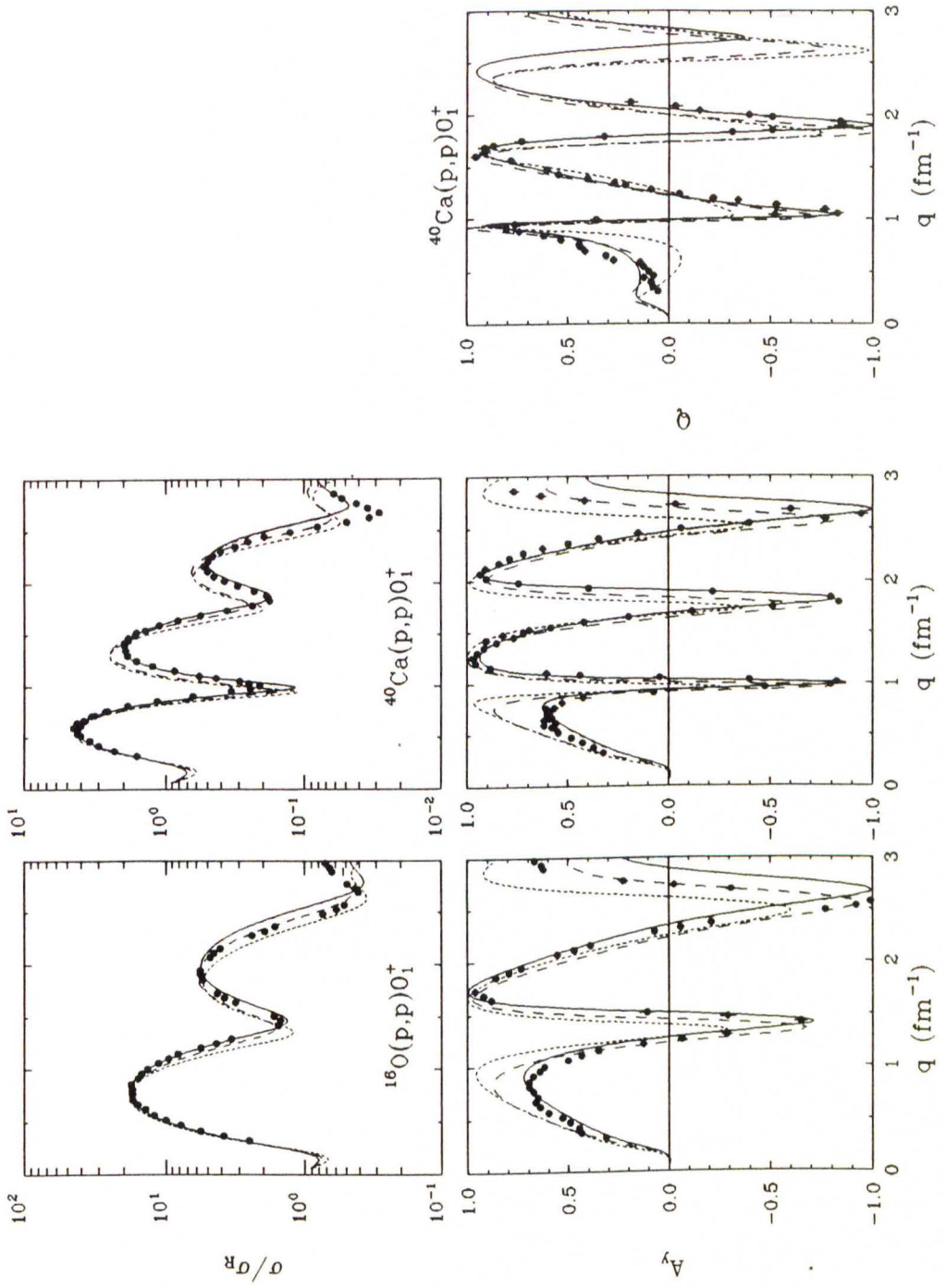

Figure 7.24: Comparison of EMP (solid), LDA (dashes), and NRIA (short dashes) elastic calculations for ^{16}O and ^{40}Ca at 318 MeV. The data for σ and A_y are from [Kel 90b] (^{16}O) and from [Fel 90] (^{40}Ca); the data for Q are from [Ble 88]. EMP based on FL t-matrix, LDA on PH g-matrix, and NRIA on PH t-matrix.

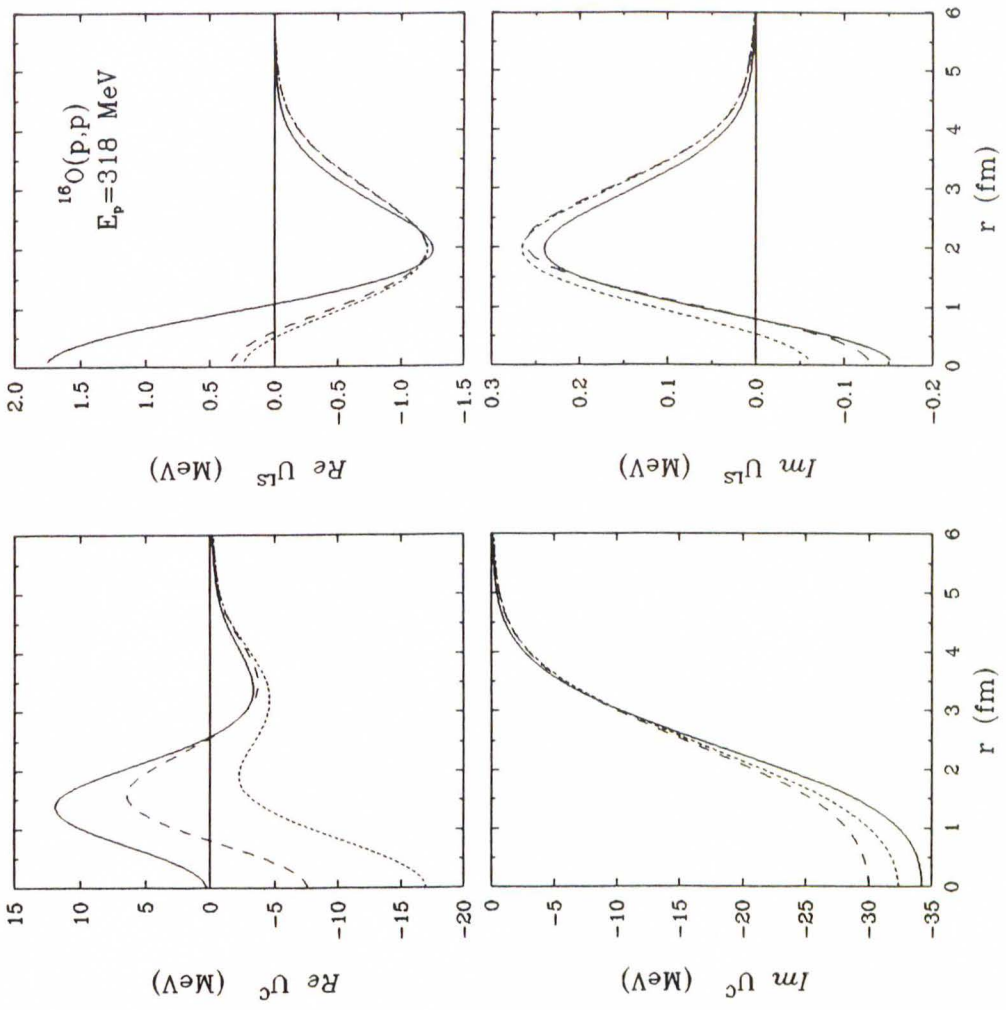

Figure 7.25: Optical potentials for elastic scattering of 318 MeV protons by ^{16}O for the EMP (solid), LDA (dashes), and NRIA (short dashes) interactions. EMP based on FL t-matrix, LDA on PH g-matrix, and NRIA on PH t-matrix.

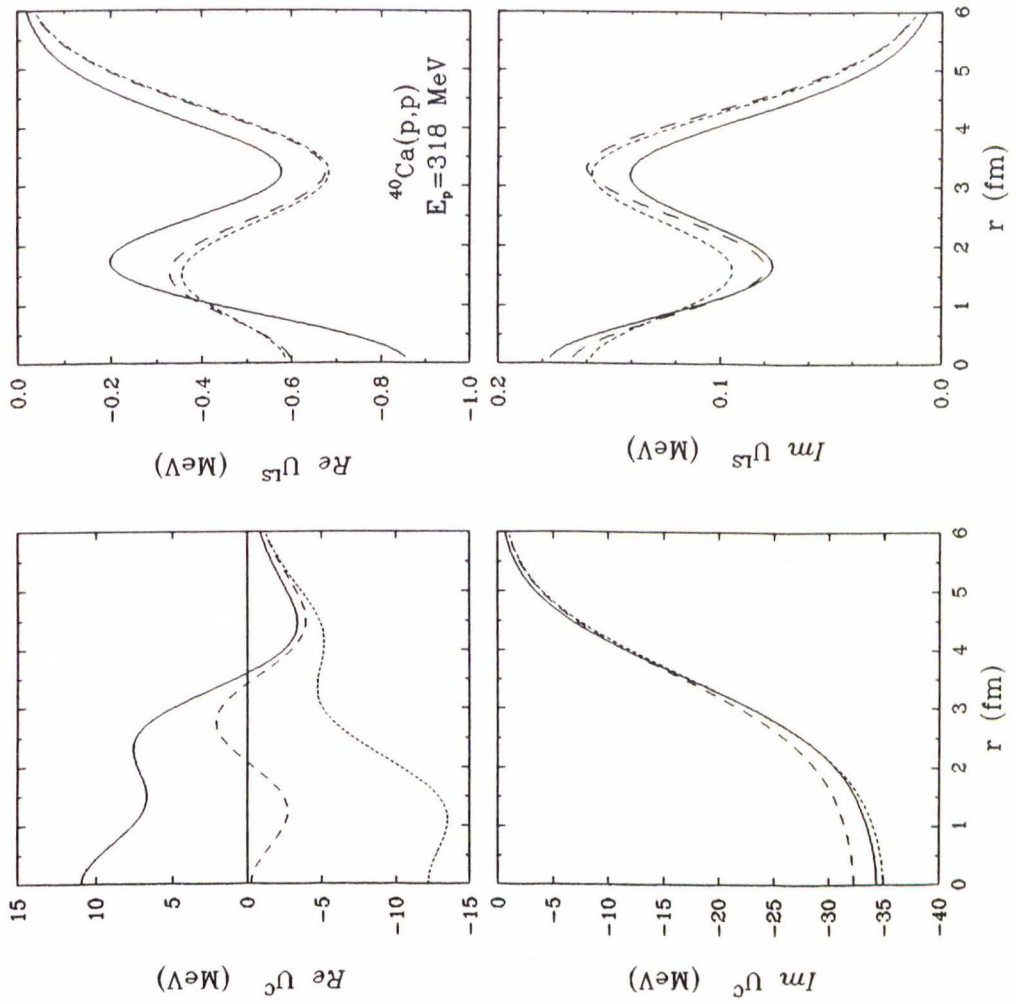

Figure 7.26: Optical potentials for elastic scattering of 318 MeV protons by ^{40}Ca for EMP (solid), LDA (dashes), and NRIA (short dashes) interactions. EMP based on FL t-matrix, LDA on PH g-matrix, and NRIA on PH t-matrix.

7.2.4 500 MeV

In this work we only want to discuss elastic scattering at 500 MeV. Inelastic scattering is discussed in detail in the paper by Flanders *et al.* [Fla 90]. Like in the case of 318 MeV, the empirical interaction is based upon the FL t-matrix. The data for ^{16}O are from [Fla 90], the ^{40}Ca data from [Set 85, Lis 89].

The parameters for the various fits to inelastic ^{16}O and ^{40}Ca data are collected in Table 7.4. We show calculations for elastic scattering for the first effective interaction from Table 7.4 (called "EI-1" in [Fla 90]) in Figure 7.27 (solid curves). In this figure we also show for comparison an LDA calculation based on the reparametrized LR interaction from Table 2.3 (dashed curves), and an NRIA calculation based on the FL t-matrix (short dashes). The improvements of the EMP predictions over the LDA and NRIA predictions are remarkable, especially for the spin-observables at low-q. These observables were in the past only correctly described by the relativistic models. In Figures 7.28 and 7.29 we display the EMP(EI-1) (solid), LDA (dashes), and NRIA (short dashes) potentials, and additionally the IA2 potentials (long dashes). The EMP and IA2 central potentials are indeed very similar over the whole region of the nucleus. The imaginary central potentials are more absorptive than either the LDA or the NRIA potentials. This trend was already observed in the previous section for 318 MeV, albeit much less pronounced.

We want to point out that the EMP elastic scattering calculations for ^{40}Ca, which are shown in Figure 7.27, were done with an interaction from

a fit to inelastic ^{16}O data. The excellent result confirms both the consistency between elastic and inelastic scattering, and the A independence of the effective interaction.

In Table 7.4 both the b_1 and the b_3 parameter are again larger than the corresponding LR parameter but, as in the case of 318 MeV, b_3 also is not strongly determined by the data. Like for 318 MeV, d_2 is larger than the theoretical parameter and has the opposite sign. We find that $S_2 - d_2 > 1$ which leads to a reverse density dependence of the imaginary central component of the interaction. This result confirms the corresponding findings at 318 MeV.

Finally, we want to mention that for the case of ^{16}O we used a grid on the interaction parameters and found a second solution in the space of χ^2_ν. The grid is shown in Appendix D. We find that if S_1 is restricted to the vicinity of 0.88, a slightly better value of χ^2_ν is obtained with a larger value of b_1, and values for the other parameters which are similar to the first solution. For a more detailed discussion of this, we refer to the paper of Flanders *et al.* [Fla 90].

	$\mathrm{Re}t_{00}^{C}$		$\mathrm{Im}t_{00}^{C}$		$\mathrm{Re}\tau_{0}^{LS}$			$\left[\mathrm{Im}\tau_{0}^{LS}\right]$	
Data set	S_1	b_1	S_2	d_2	S_3	b_3	$t^{(f)}$	d_4	a_{41}
^{16}O	1.26	121.1	0.84	-0.28	0.72	4.65	FL	0.0	-1.92
^{16}O^{b}	0.88	152.2	0.80	-0.30	0.73	5.14	FL	$\mu_4 = 1.0$ fm^{-1}	
^{40}Ca	0.82	236.1	0.93	-0.18	0.71	6.95	FL	$[\alpha\gamma\beta\delta] = [3320]$	
^{16}O+^{40}Ca	0.87	199.5	0.88	-0.25	0.73	5.80	FL	ref.: [Fla 90]	
Theory^{a}	[1.0]	76.0	[1.0]	0.15	[1.0]	1.34	FL		

Table 7.4: Empirical effective interactions for 500 MeV protons [Fla 90]. We use the following exponents $[\alpha\gamma\beta\delta]$ and masses μ: [3310], $\mu_1 = 2.0$ fm^{-1} ($\mathrm{Re}t_{00}^{C}$); [2210] ($\mathrm{Im}t_{00}^{C}$); [3320], $\mu_3 = 6.0$ fm^{-1} ($\mathrm{Re}\tau_{0}^{LS}$). Units: S_i and d_i (1), b_1 (MeV fm^3), b_3 and a_{41} (MeV fm^5). Square brackets indicate that the parameter or component is fixed.
[a] Values from Table 2.5; [b] Second solution.

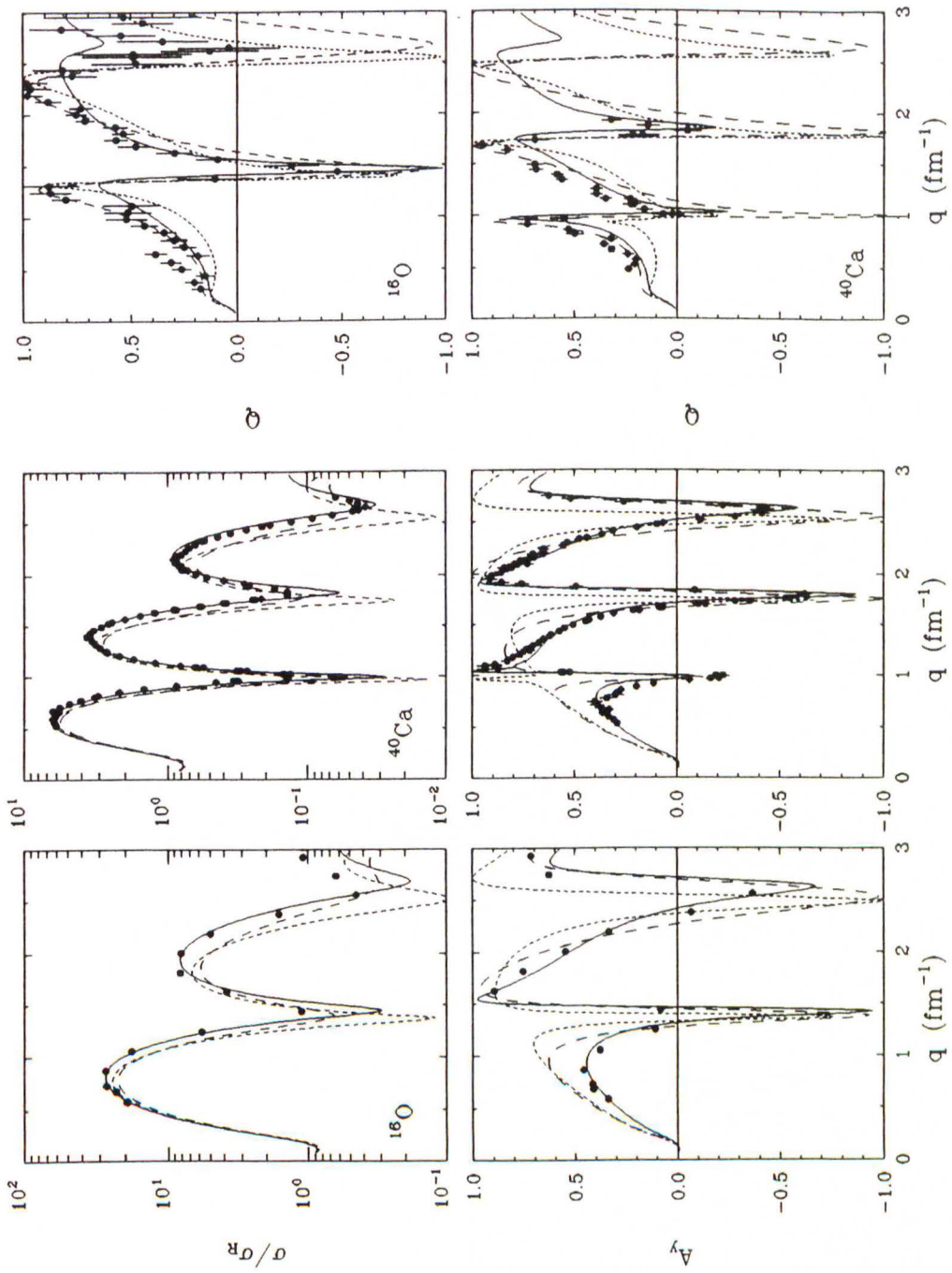

Figure 7.27: Comparison of EMP(^{16}O) (solid), LDA (dashes), and NRIA (short dashes) elastic calculations for ^{16}O and ^{40}Ca at 500 MeV. The data for ^{16}O are from [Fla 90], the data for ^{40}Ca are from [Set 85, Lis 89]. EMP based on FL t-matrix, LDA on LR interraction, and NRIA on FL t-matrix.

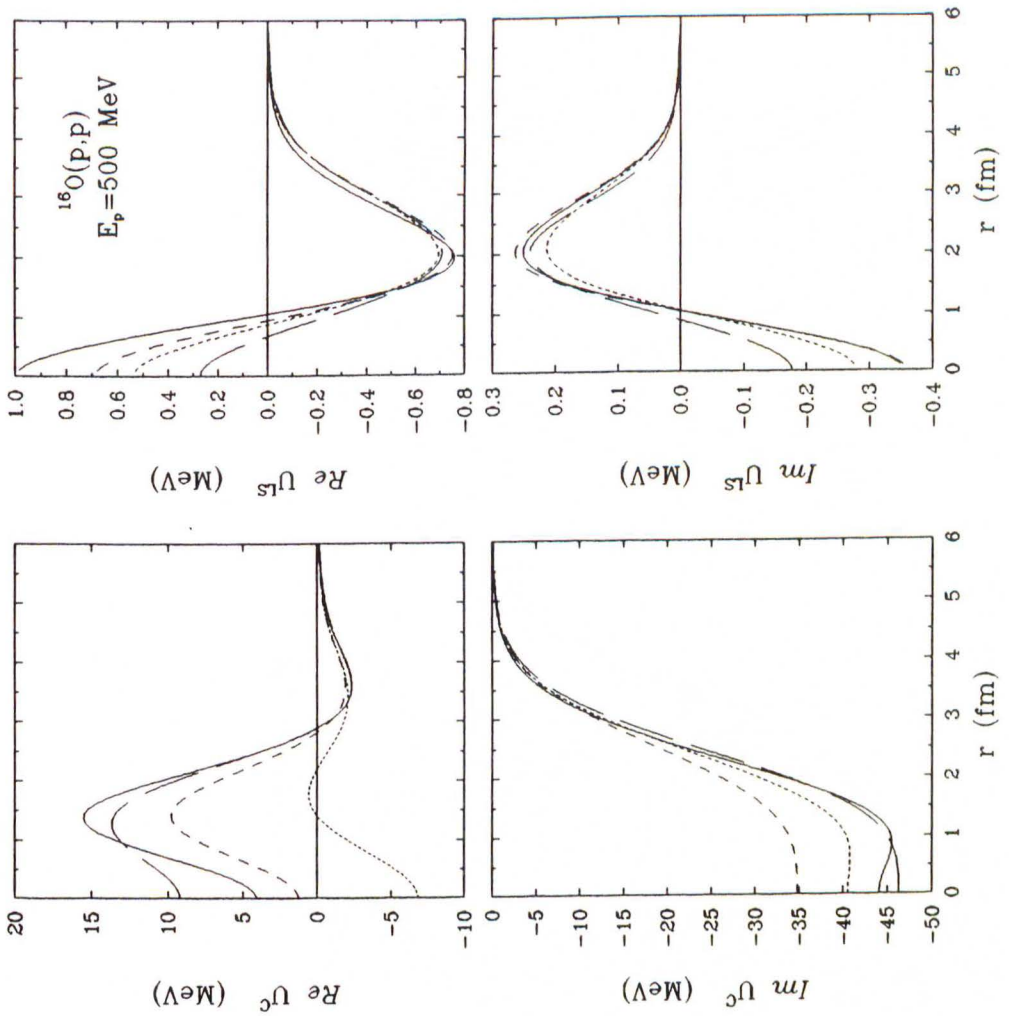

Figure 7.28: Optical potentials for elastic scattering of 500 MeV protons by ^{16}O for the EMP(^{16}O) (solid), IA2 (long dashes), LDA (dashes), and NRIA (short dashes) interactions. EMP based on FL t-matrix, LDA on LR interaction, and NRIA on FL t-matrix.

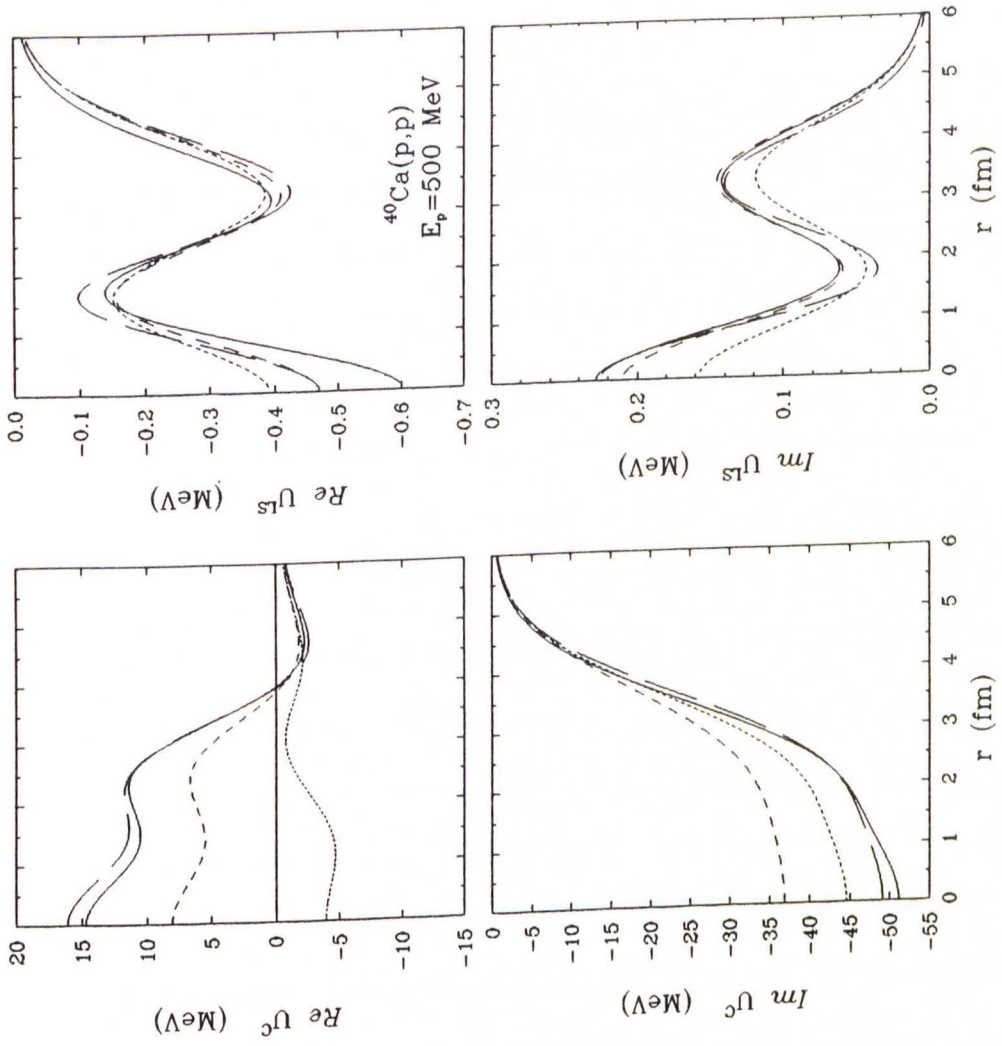

Figure 7.29: Optical potentials for elastic scattering of 500 MeV protons by ^{40}Ca for the EMP(^{16}O) (solid), IA2 (long dashes), LDA (dashes), and NRIA (short dashes) interactions. EMP based on FL t-matrix, LDA on LR interaction, and NRIA on FL t-matrix.

7.2.5 Interior Sensitivity

We investigated to a certain extent the energy dependence of the interior sensitivity to the effective interaction. The results of this analysis confirm and complement the ones from Figure 1.1 of Chapter 1. The computer code LEA [Kel LEA] has the capability to eliminate the effect of the scattering potential within a certain radius r. This "notch" test calculates on a grid of values for the "notch" radius r the scattering observables for an arbitrary inelastic state. Then it measures the difference between the calculation and the data in terms of χ^2_ν. We have done this test for the 3^-_1 surface state (Figure 7.30) and the 1^-_1 interior state (Figure 7.31) of ^{16}O. In these figures a small value of χ^2_ν signifies small sensitivity to the effective interaction. The 3^-_1 state, as expected, is sensitive to the effective interaction only at the surface and shows essentially no sensitivity at all inside about 1.5 fm. At large radii we can discern the energy dependence of the interior sensitivity from the spread of the three calculations for 100 (dashes), 200 (dot-dashes), and 318 MeV (solid). The increase in χ^2_ν with increasing energy and the associated increasing sensitivity to the effective interaction is due to the increasing transparency of the nucleus as we go from 100 to 200 MeV. This "window of visibility" is open up to about 500 MeV where the sensitivity decreases again due to the growing absorption. For the interior-peaked 1^-_1 state we see sensitivity at smaller radii for all the energies. Therefore, the 1^-_1 data are sensitive to the high density properties of the effective interaction.

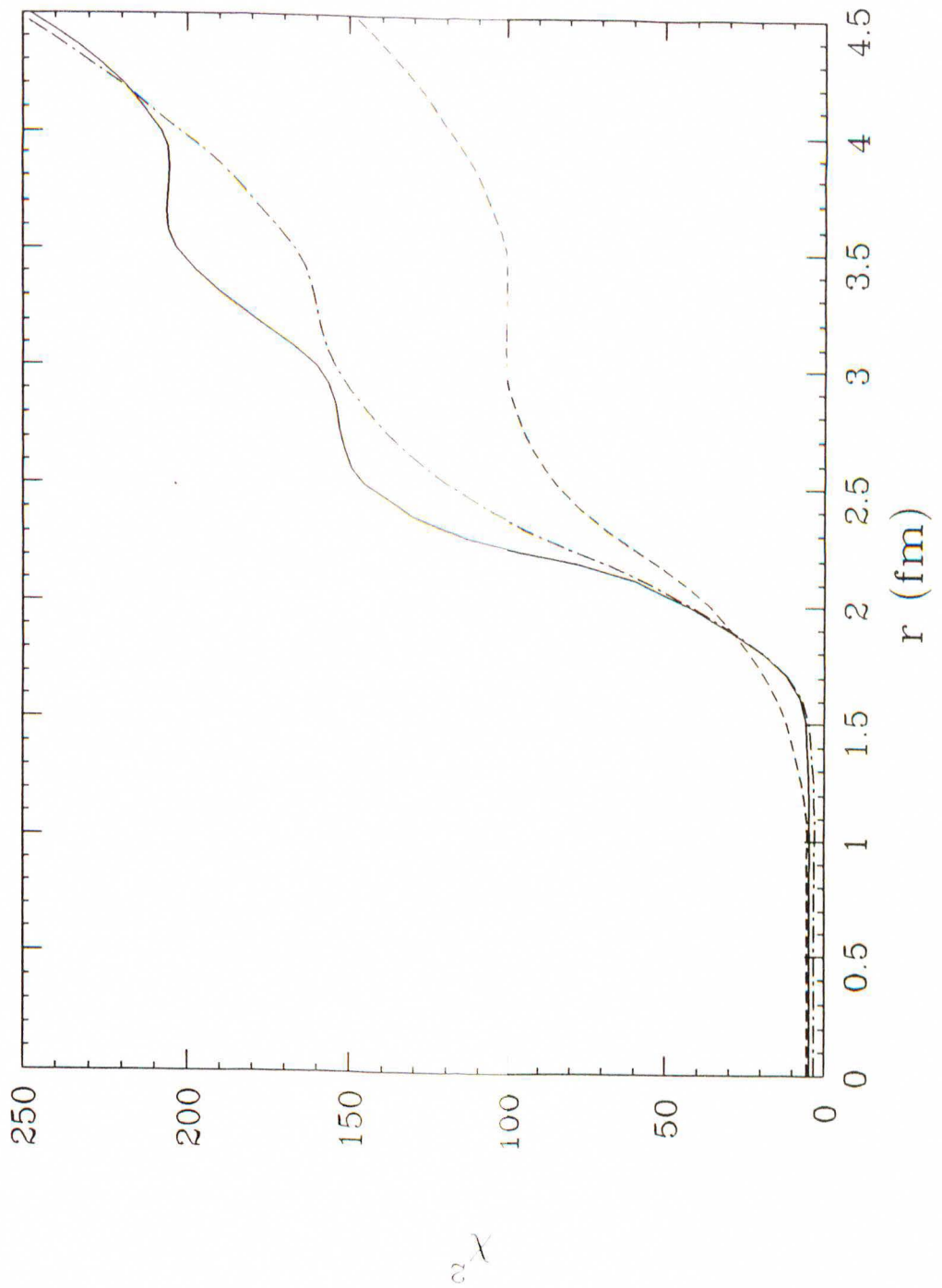

Figure 7.30: Energy dependence of the interior sensitivity to the effective interaction for the 3_1^- state of ^{16}O: 100 MeV (dashes), 200 MeV (dot-dashes), 318 MeV (solid).

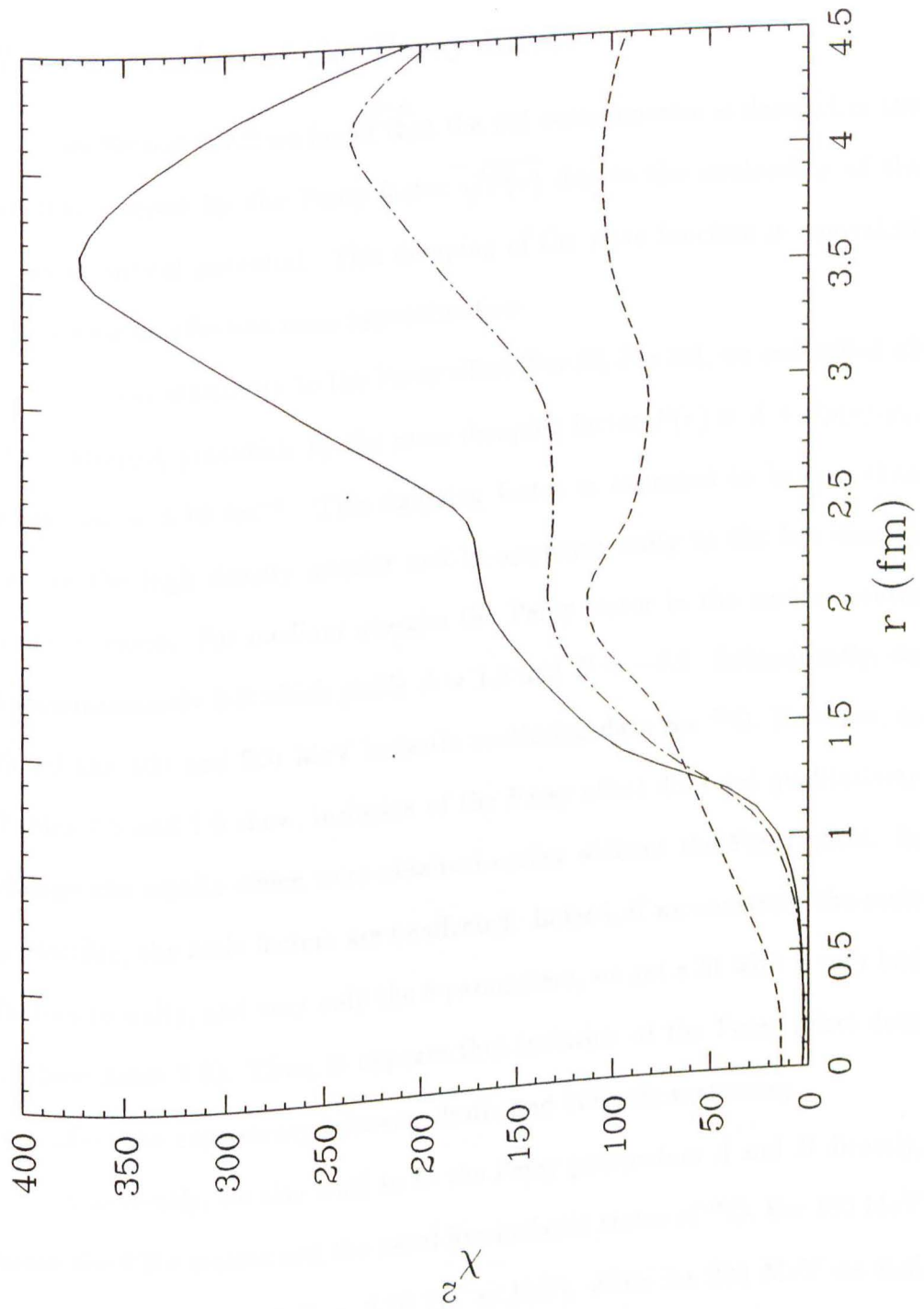

Figure 7.31: Energy dependence of the interior sensitivity to the effective interaction for the 1_1^- state of ^{16}O: 100 MeV (dashes), 200 MeV (dot-dashes), 318 MeV (solid).

7.3 Inclusion of the Perey Effect

In Section 2.7.2 we found that the NA wave function is damped in the nuclear interior by the Perey factor $\sqrt{P(\boldsymbol{r})}$ due to the nonlocality of the original optical potential. This damping of the wave function is equivalent to making an effective mass approximation.

To test sensitivity to the Perey effect [Per 62, Per 63], we multiplied all the scattering potentials by the same damping factor $P(r) = A + B\rho(r)/\rho_0$, where $\rho_0 = 0.16$ fm^{-1}. This damping factor is expected to be less than one in the high density interior and to approach unity in the low density surface region. For medium energies the Perey factor in the nuclear center is approximately 0.8 which yields $A = 1.0$ and $B \approx -0.2$. Subsequently, we fitted the 100 and 200 MeV inelastic scattering data for ^{16}O. However, as Tables 7.5 and 7.6 show, inclusion of the Perey effect does not qualitatively change the results which were obtained earlier without the Perey effect. In particular, the scale factors are unaffected. Indeed, if we constrain the scale factors to unity, and vary only the b-parameters, we get a fit with a very bad χ^2_ν (see Table 7.6). Thus, it appears that inclusion of the Perey effect does not affect the consistency between elastic and inelastic scattering.

Conversely, we also tried to fit the Perey parameters A and B directly, using the PH t-matrix and the usual five inelastic states of ^{16}O. For 100 MeV we find $A = 0.88$ and $B = 0.59$ ($\chi^2_\nu = 11.7$), while for 200 MeV we find $A = 0.76$ and $B = 0.28$ ($\chi^2_\nu = 7.3$). These parameters correspond to an interaction which is enhanced in the interior and suppressed in the surface relative to the LDA. This is in good qualitative agreement with our more

sophisticated empirical interaction analysis, but is in complete disagreement with the conventional Perey effect.

	$\mathrm{Re}t_{00}^{C}$		$\mathrm{Im}t_{00}^{C}$		$\mathrm{Re}\tau_{0}^{LS}$			
Fit	S_1	b_1	S_2	d_2	S_3	b_3	$t^{(f)}$	χ^2_ν
No Perey[a]	0.86	41.8	0.69	[0.55]	0.82	[3.7]	PH	10.2
Perey	0.85	39.2	0.68	[0.54]	0.84	6.6	PH	10.2
Theory[b]	[1.0]	72.7	[1.0]	0.55	[1.0]	3.7	PH	-

Table 7.5: Empirical effective interaction with Perey effect for ^{16}O and 100 MeV protons ($A = 1.0$, $B = -0.15$). We use the following exponents $[\alpha\gamma\beta\delta]$ and masses μ: [3310], $\mu_1 = 1.5$ fm^{-1} ($\mathrm{Re}t_{00}^{C}$); [2210] ($\mathrm{Im}t_{00}^{C}$). Units: S_i and d_2 (1), b_1 (MeV fm^3), b_3 (MeV fm^5). Square brackets indicate that the parameter or component is fixed.
[a]Values from Table 7.1; [b]Values from Table 2.5.

	$\mathrm{Re}t_{00}^{C}$		$\mathrm{Im}t_{00}^{C}$		$\mathrm{Re}\tau_{0}^{LS}$			
Fit	S_1	b_1	S_2	d_2	S_3	b_3	$t^{(f)}$	χ^2_ν
No Perey[a]	0.70	65.5	0.77	0.14	0.84	2.03	PH	4.3
Perey	0.68	84.5	0.79	0.13	0.86	6.64	PH	4.4
Perey	[1.0]	31.4	[1.0]	0.52	[1.0]	1.88	PH	25.9
Theory[b]	[1.0]	84.0	[1.0]	0.23	[1.0]	2.10	PH	-

Table 7.6: Empirical effective interaction with Perey effect for ^{16}O and 200 MeV protons ($A = 1.0$, $B = -0.20$). We use the following exponents $[\alpha\gamma\beta\delta]$ and masses μ: [3310], $\mu_1 = 1.5$ fm^{-1} ($\mathrm{Re}t_{00}^{C}$); [2210] ($\mathrm{Im}t_{00}^{C}$). Units: S_i and d_2 (1), b_1 (MeV fm^3), b_3 (MeV fm^5). Square brackets indicate that the parameter or component is fixed.
[a]Values from Table 7.2; [b]Values from Table 2.5.

7.4 Inclusion of Elastic Data

We tested the effect of including elastic data explicitly in the fit of the effective interaction. Some results of this analysis for 100 and 200 MeV are shown in the following tables and figures. In Tables 7.7 and 7.8 we compare the parameters from fits to inelastic data only, from combined fits to elastic and inelastic data, and from fits to elastic data only. We also include the PH parameters for reference and convenience.

First we consider the 100 MeV fits. In the case of ^{16}O the inclusion of elastic scattering data renders constraining d_2 unnecessary. The damping factor $S_2 - d_2$ increases by a factor of about 2.2. The main effect on the other parameters is an increase in the scale factors and in b_1. We did also fits to elastic data alone and found that, relative to the fit to inelastic data, the damping factor is three times larger while b_1 is smaller than for the inelastic fit. The damping factor for the elastic fit is 0.42 and is therefore very close to the PH value of 0.45. We gridded the b_3 parameter and found it to be not very well determined by the data. The grid finds the minimum in χ^2_ν to be around 6.0 for elastic scattering alone; a similar grid for inelastic scattering alone yields a value close to the PH value of 3.7. Therefore, we tried combined elastic and inelastic fits with both values for b_3. We see in the table that the values of the other parameters are indeed relatively insensitive to the choice of b_3. Inclusion of elastic data does not help the fit to ^{40}Ca or the combined fit to ^{16}O and ^{40}Ca: we still get unstable fits for these cases, unless we constrain b_1. Figures 7.32–7.34 show inelastic and elastic scattering for the various interactions which exclude (solid) and include (dashes, long dashes) elastic

data. For the inelastic data no improvement of either interaction over the others can be discerned from inspection of the figures. For the elastic state, the combined fit to elastic and inelastic data tries to fill in some strength around 1.5 fm^{-1}. Thus, although the parameters are slightly different for the various fits, the predictions for elastic and inelastic scattering are essentially indistinguishable.

The differences between the various interactions are very small for the case for 200 MeV, as Table 7.8 and Figures 7.35–7.37 show. For the fit to elastic data only, the best result is obtained when b_1 is fixed to the inelastic value. The elastic fit yields a slight improvement in the cross section and gives the same analyzing power as the combined fit to elastic and inelastic data.

The results for the fits including elastic scattering at 100 MeV, and the fact that the PH interaction describes elastic scattering better suggest that the self-consistency procedure might have problems at this energy. The damping factor $(S_2 - d_2)$ changes from 0.14 for the inelastic fit to 0.31 for the combined fit, and to 0.42 for the elastic fit. The PH value is 0.45. It has been speculated that at 100 MeV second order terms in the $(1 + \rho\partial/\partial\rho)$ prescription might be necessary for the consistency between elastic and inelastic scattering. At 200 MeV, on the other hand, self-consistency works well with the $(1 + \rho\partial/\partial\rho)$ prescription. In the following, the empirical interactions which are used in calculations are always those from the fits to the inelastic data.

	$\mathrm{Re}t_{00}^{C}$		$\mathrm{Im}t_{00}^{C}$		$\mathrm{Re}\tau_{0}^{LS}$			
Data set	S_1	b_1	S_2	d_2	S_3	b_3	$t^{(f)}$	$S_2 - d_2$
in	0.86	41.8	0.69	[0.55]	0.82	[3.7]	PH	0.14
el+in	0.90	53.6	0.87	0.56	0.98	[3.7]	PH	0.31
el+in[b]	0.91	51.9	0.91	0.59	0.96	[6.0]	PH	0.32
el	0.90	40.2	0.82	0.39	0.92	[3.7]	PH	0.43
el	0.90	34.3	0.81	0.39	0.86	[6.0]	PH	0.42
Theory[a]	[1.0]	72.7	[1.0]	0.55	[1.0]	3.7	PH	0.45

Table 7.7: Empirical effective interactions for 100 MeV protons from fits to elastic and inelastic ^{16}O data. We use the following exponents $[\alpha\gamma\beta\delta]$ and masses μ: [3310], $\mu_1 = 1.5$ fm^{-1} ($\mathrm{Re}t_{00}^{C}$); [2210] ($\mathrm{Im}t_{00}^{C}$); [3320], $\mu_3 = 6.0$ fm^{-1} ($\mathrm{Re}\tau_{0}^{LS}$). For $\mathrm{Im}\tau_{0}^{LS}$ see Table 7.1. Units: S_i and d_i (1), b_1 (MeV fm^3), b_3 and a_{41} (MeV fm^5). Square brackets indicate that the parameter or component is fixed.
[a]Values from Table 2.5; [b]Fit with b_3 from grid on elastic data.

	$\mathrm{Re}t_{00}^{C}$		$\mathrm{Im}t_{00}^{C}$		$\mathrm{Re}\tau_{0}^{LS}$			
Data set	S_1	b_1	S_2	d_2	S_3	b_3	$t^{(f)}$	$S_2 - d_2$
in	0.70	65.5	0.77	0.14	0.84	2.03	PH	0.63
in+el	0.63	69.0	0.77	0.12	0.86	2.27	PH	0.65
el	0.57	[65.5]	0.73	0.11	0.90	1.55	PH	0.62
Theory[a]	[1.0]	84.0	[1.0]	0.23	[1.0]	2.10	PH	0.77

Table 7.8: Empirical effective interactions for 200 MeV protons from fits to elastic and inelastic ^{16}O data. We use the following exponents $[\alpha\gamma\beta\delta]$ and masses μ: [3310], $\mu_1 = 1.5$ fm^{-1} ($\mathrm{Re}t_{00}^{C}$); [2210] ($\mathrm{Im}t_{00}^{C}$); [3320], $\mu_3 = 6.0$ fm^{-1} ($\mathrm{Re}\tau_{0}^{LS}$). For $\mathrm{Im}\tau_{0}^{LS}$ see Table 7.2. Units: S_i and d_i (1), b_1 (MeV fm^3), b_3 and a_{41} (MeV fm^5). Square brackets indicate that the parameter or component is fixed.
[a]Values from Table 2.5.

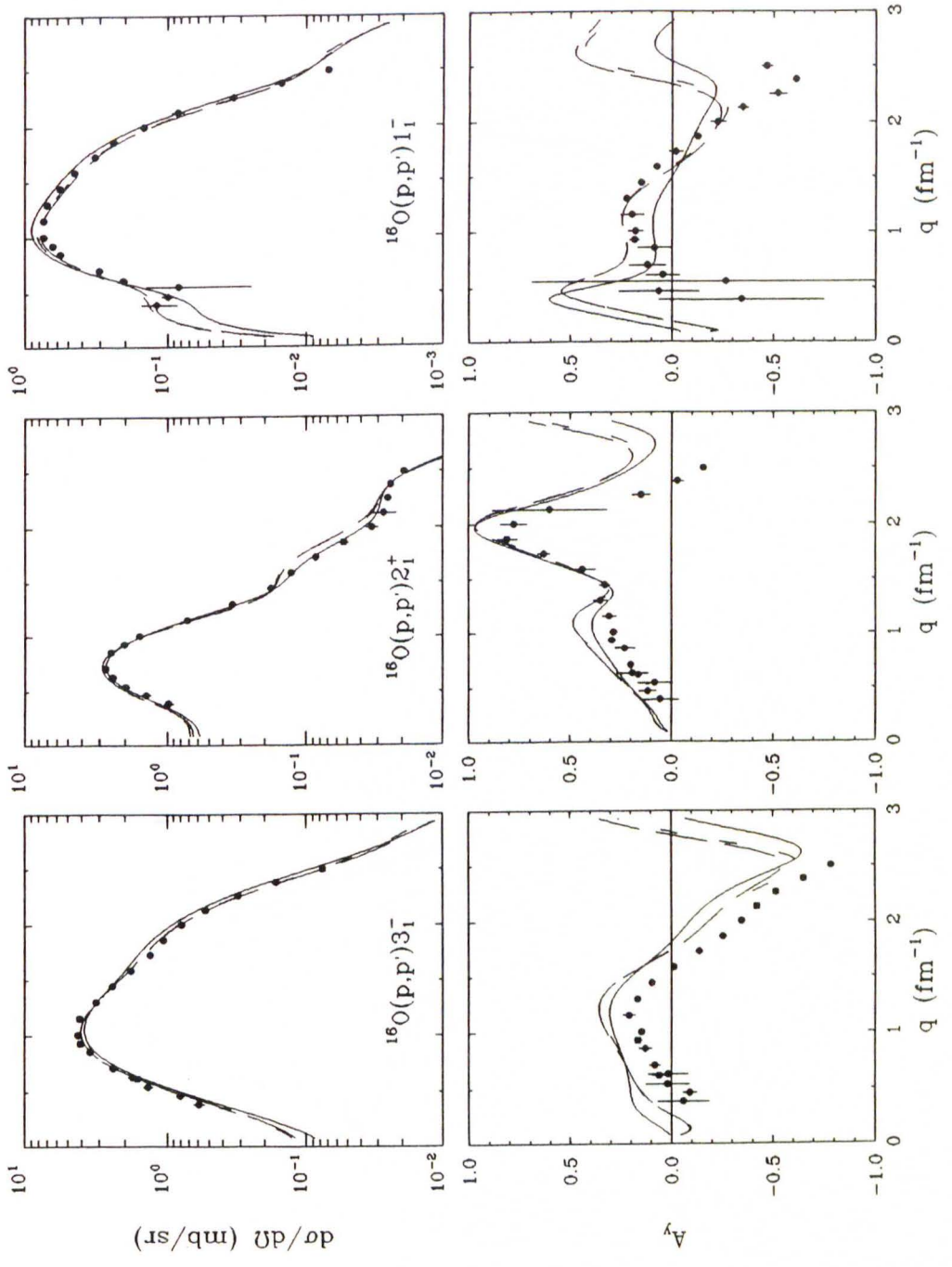

Figure 7.32: Comparison of EMPs from fit to inelastic data only (solid), and from combined fits to both elastic and inelastic data: $b_3 = 6.0$ (dashes), and $b_3 = 3.7$ (long dashes). Shown are the 3^-_1, 2^+_1, and 1^-_1 inelastic states of ^{16}O at 100 MeV. The data are from this work.

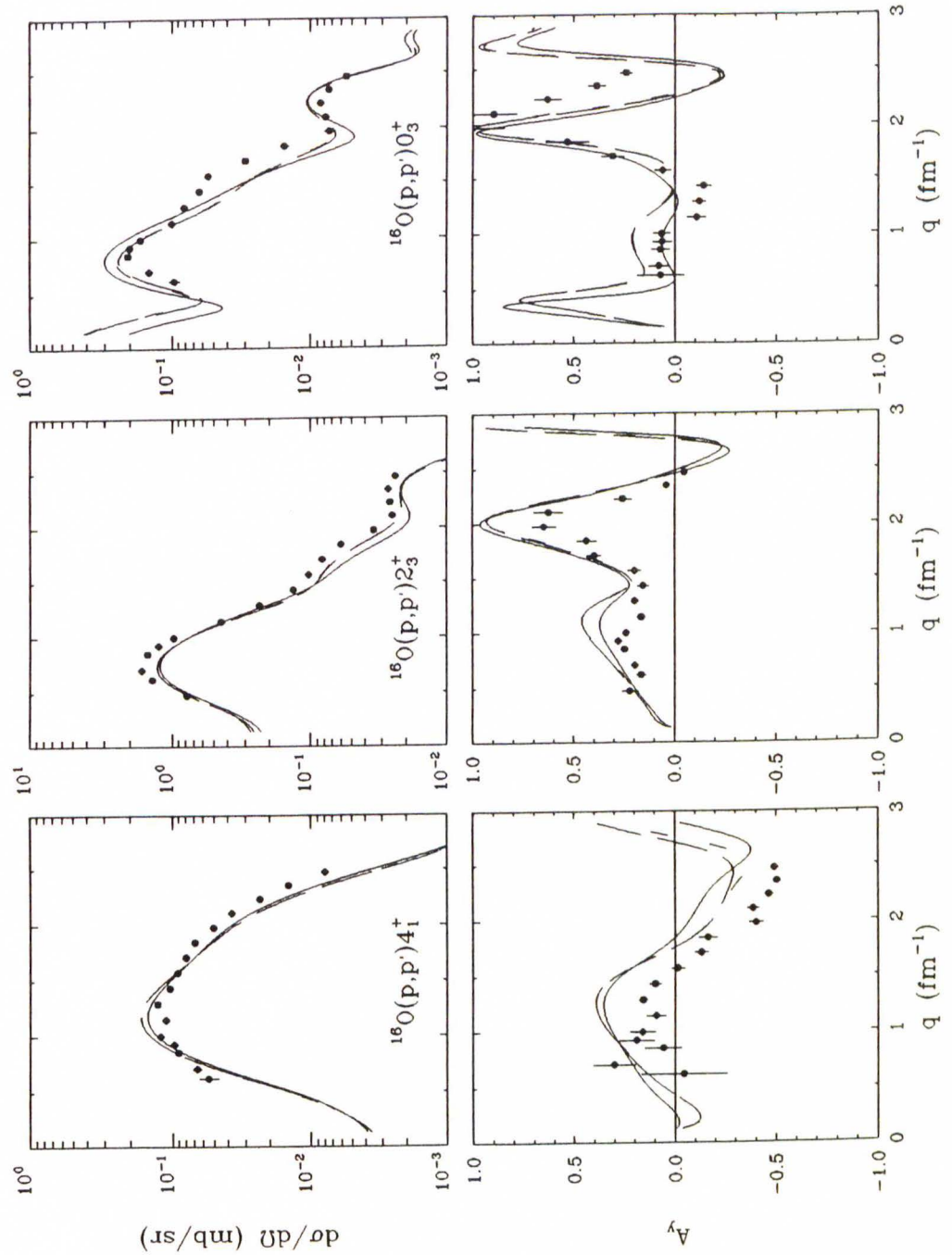

Figure 7.33: Comparison of EMPs from fit to inelastic data only (solid), and from combined fits to both elastic and inelastic data: $b_3 = 6.0$ (dashes), and $b_3 = 3.7$ (long dashes). Shown are the 4^+_1, 2^+_3, and 0^+_3 inelastic states of ^{16}O at 100 MeV. The data are from this work.

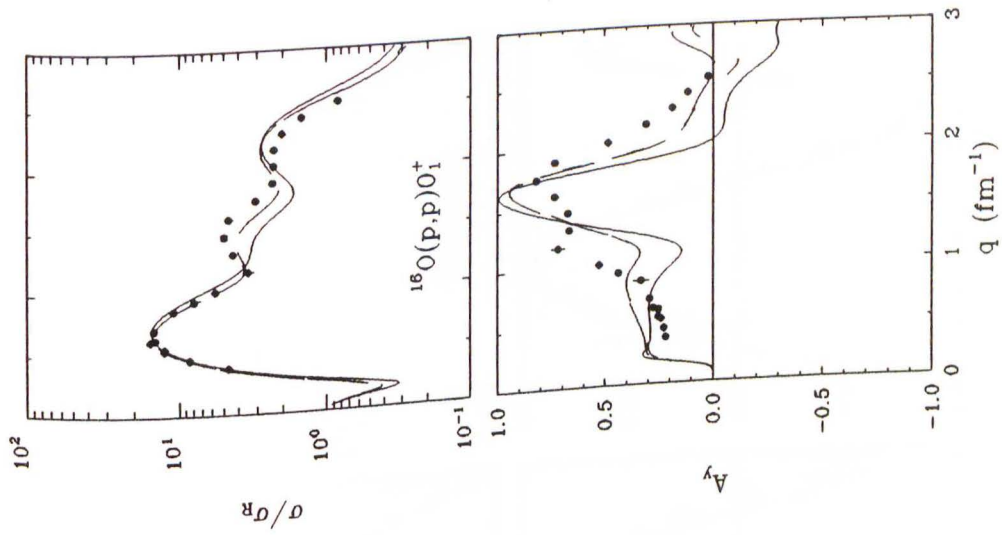

Figure 7.34: Comparison of EMPs from fit to inelastic data only (solid), and from combined fits to both elastic and inelastic data: $b_3 = 6.0$ (dashes), and $b_3 = 3.7$ (long dashes). Shown are calculations for the ground state of ^{16}O at 100 MeV. The data are from this work.

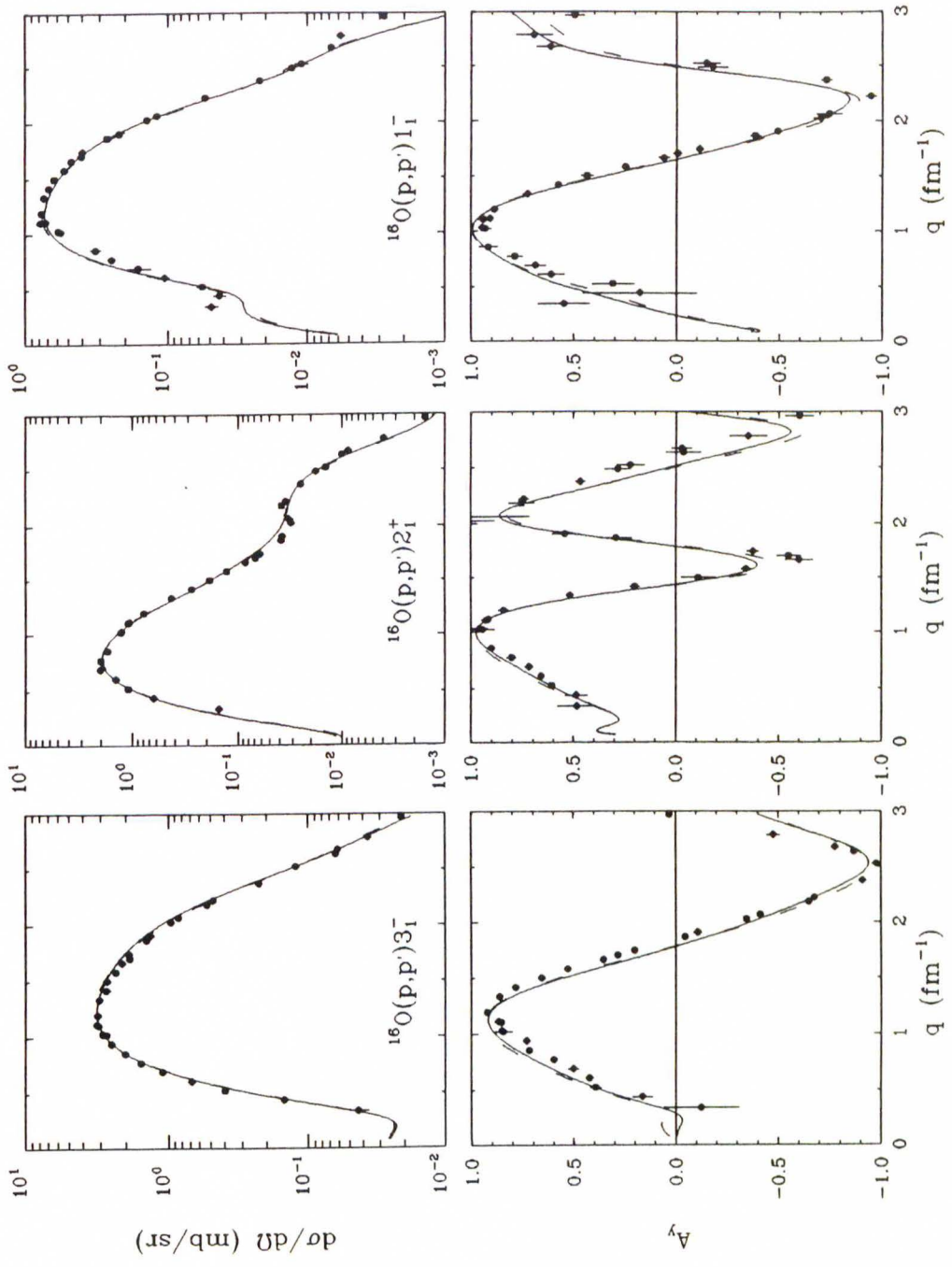

Figure 7.35: Comparison of EMPs from fit to inelastic data only (solid), and from a combined fit to both elastic and inelastic data (dashes). Shown are the 3^-_1, 2^+_1, and 1^-_1 inelastic states of ^{16}O at 200 MeV. The data are from this work.

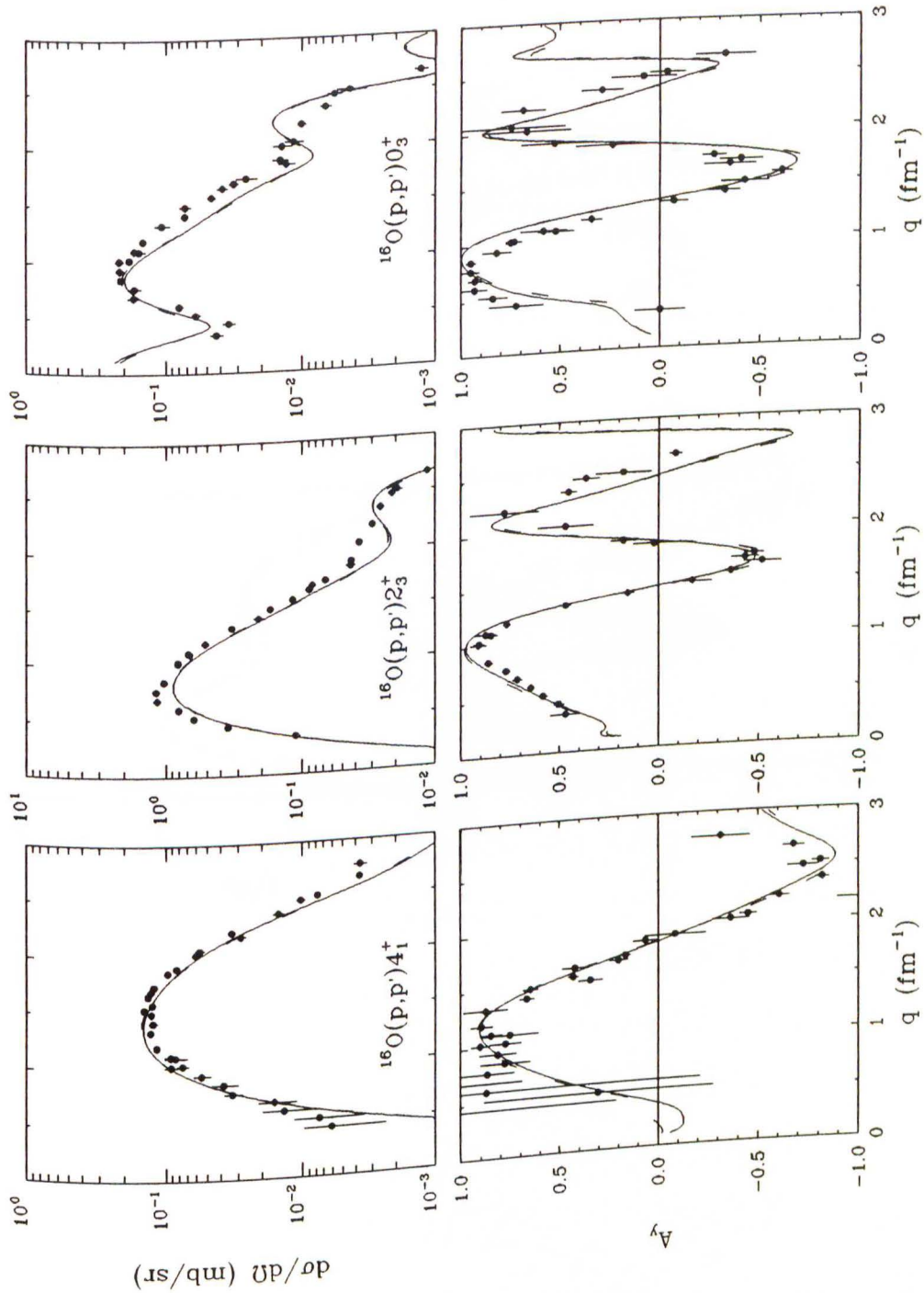

Figure 7.36: Comparison of EMPs from fit to inelastic data only (solid), and from a combined fit to both elastic and inelastic data (dashes). Shown are the 4^+_1, 2^+_3, and 0^+_3 inelastic states of ^{16}O at 200 MeV. The data are from this work.

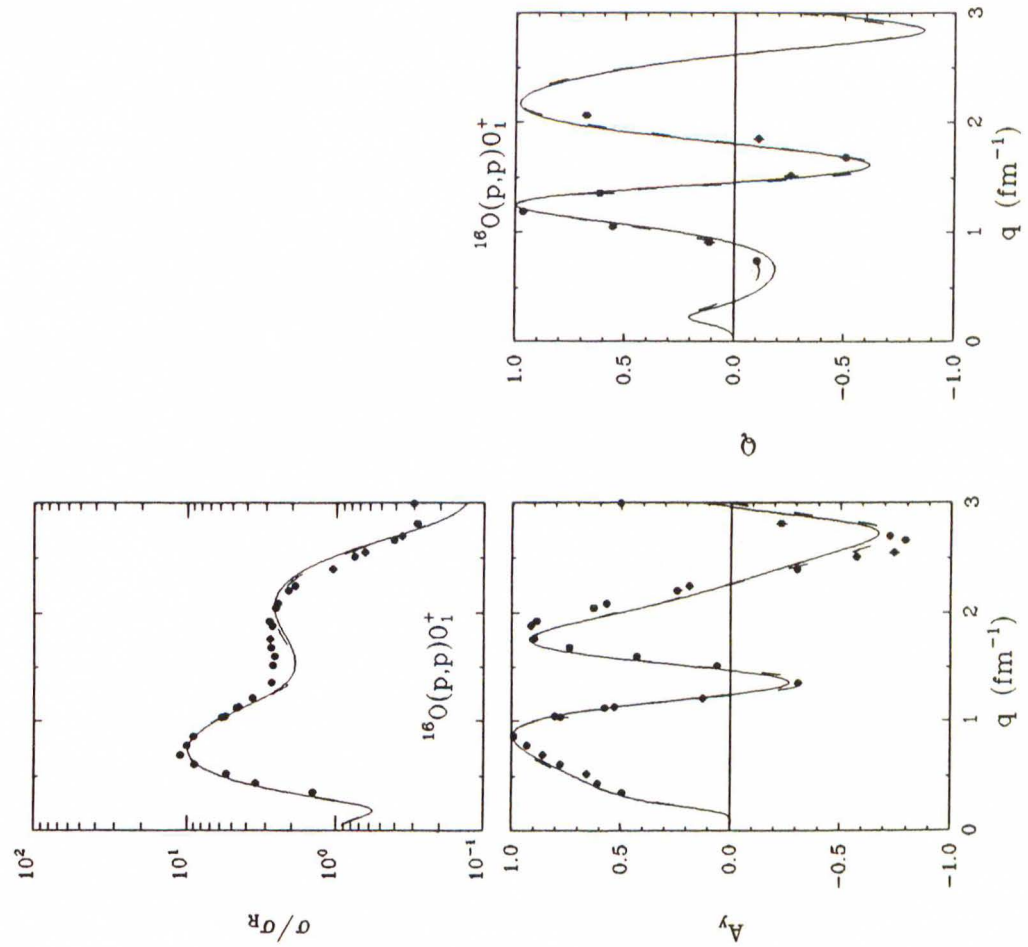

Figure 7.37: Comparison of EMPs from fit to inelastic data only (solid), and from a combined fit to both elastic and inelastic data (dashes). Shown are calculations for the ground state of ^{16}O at 200 MeV. The data are from this work.

7.5 A Dependence of the Effective Interaction

If the LDA prescription is to be considered sound, the empirical interaction must satisfy the following three conditions. The first condition is that the effective interaction must be capable of describing all the relevant data for a given target at a given energy. We have demonstrated in the previous sections, in accordance with other work [Kel 89b, Kel 90a, Kel 90b, Fla 90], that we can indeed find interactions which describe all the states for particular nuclei at particular energies. As a second and more stringent condition, the effective interaction should be independent of the target nucleus in which the reaction occurs. In Figures 7.38–7.52 we show for each energy and for each target calculations based on the interactions fitted to ^{16}O (solid) and to ^{40}Ca (dashes). The interactions from the combined fits produce scattering results intermediate between the two single-target fits and are omitted to reduce clutter. We see in these figures that, although we extract numerically different values[1] for the interaction parameters from the two targets, the differences in the description of data are minute, especially for 200 and 318 MeV. The minor differences at 100 MeV are probably related to our difficulty in extraction of a stable interaction for this energy. Our analysis extends the A independence of the effective interaction, previously shown for the case of ^{16}O and ^{28}Si at 180 MeV [Kel 90a], to energies between 100 and 318 MeV and to a larger range of A.

[1] In general we found that ^{16}O constrained the parameters of the empirical interaction better than ^{40}Ca which is a larger nucleus and is overall less transparent than oxygen.

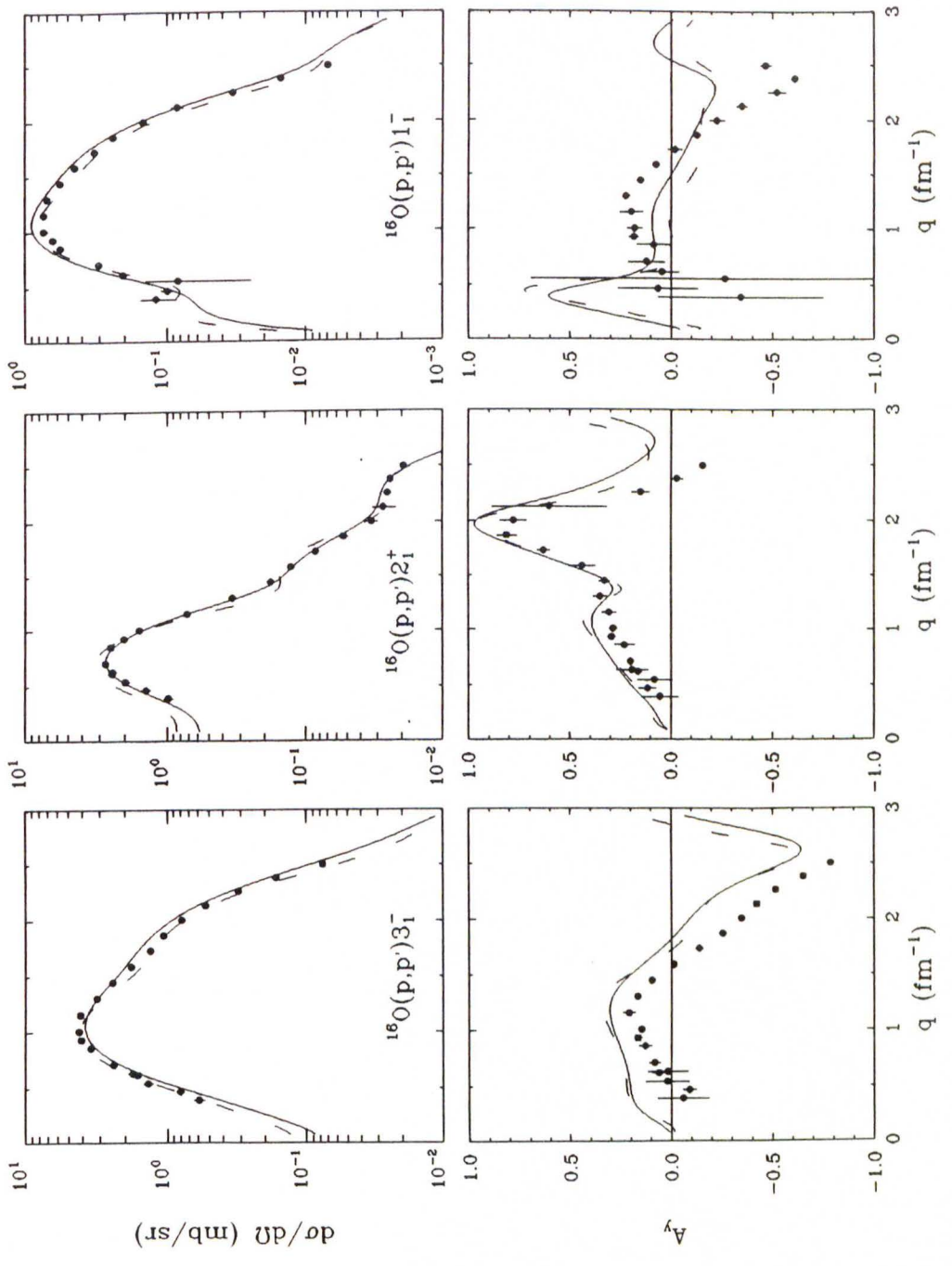

Figure 7.38: Comparison of EMP(^{16}O) (solid) and EMP(^{40}Ca) (dashes). We show calculations for the 3^-_1, 2^+_1, and 1^-_1 inelastic states of ^{16}O at 100 MeV. The data are from this work.

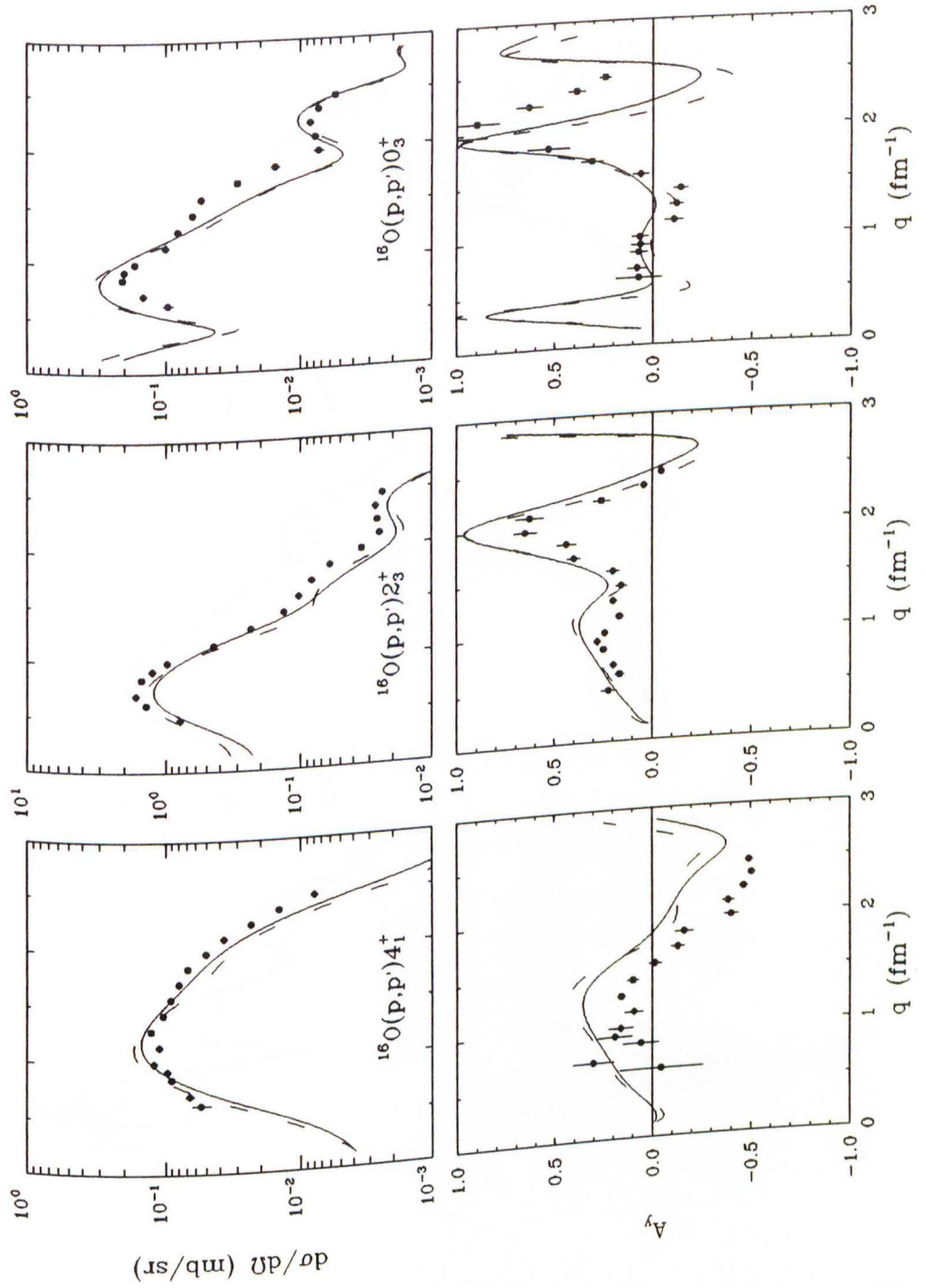

Figure 7.39: Comparison of EMP(^{16}O) (solid) and EMP(^{40}Ca) (dashes). We show calculations for the 4^+_1, 2^+_3, and 0^+_3 inelastic states of ^{16}O at 100 MeV. The data are from this work.

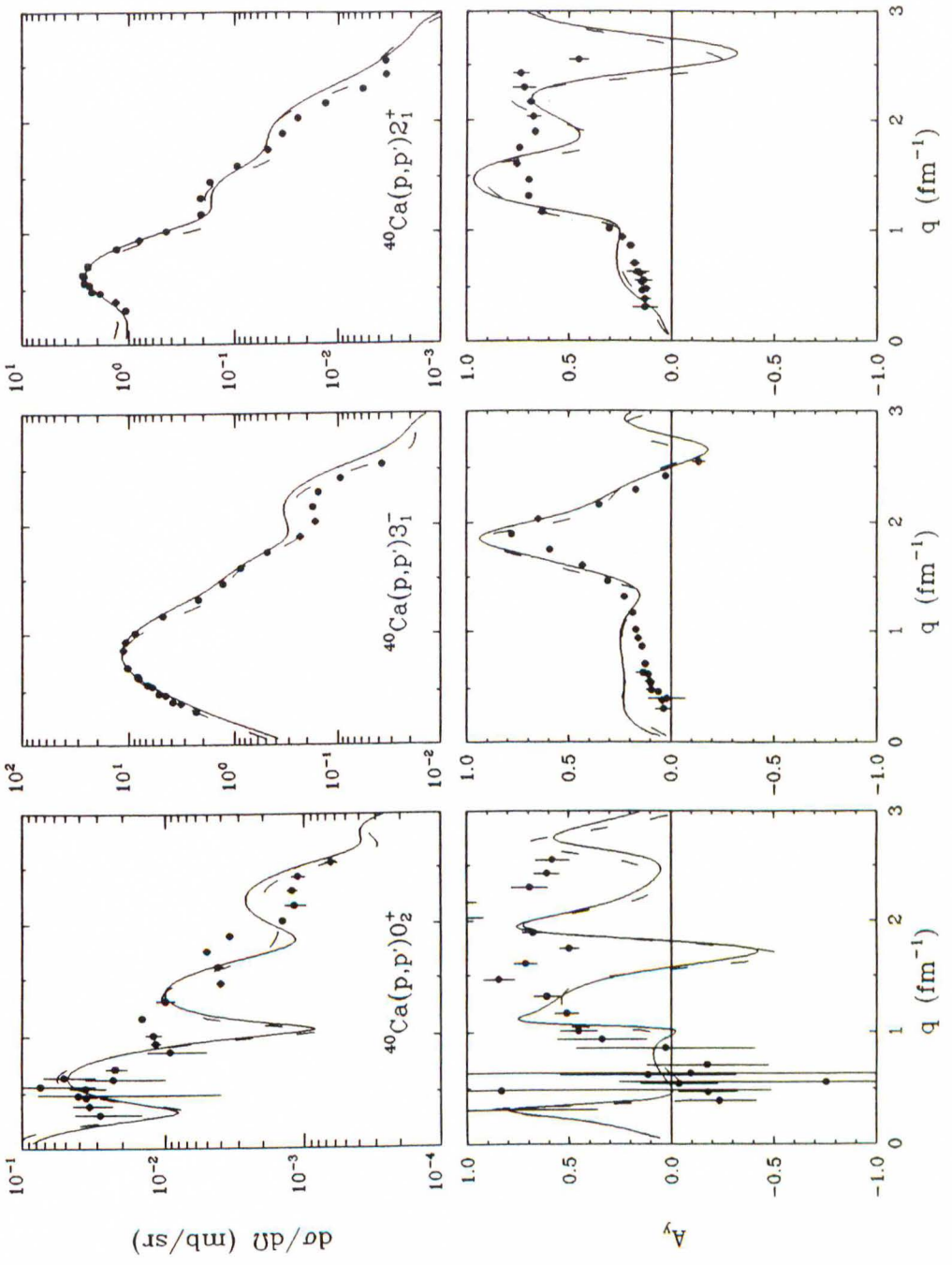

Figure 7.40: Comparison of EMP(^{16}O) (solid) and EMP(^{40}Ca) (dashes). We show calculations for the 0_2^+, 3_1^-, and 2_1^+ inelastic states of ^{40}Ca at 100 MeV. The data are from this work.

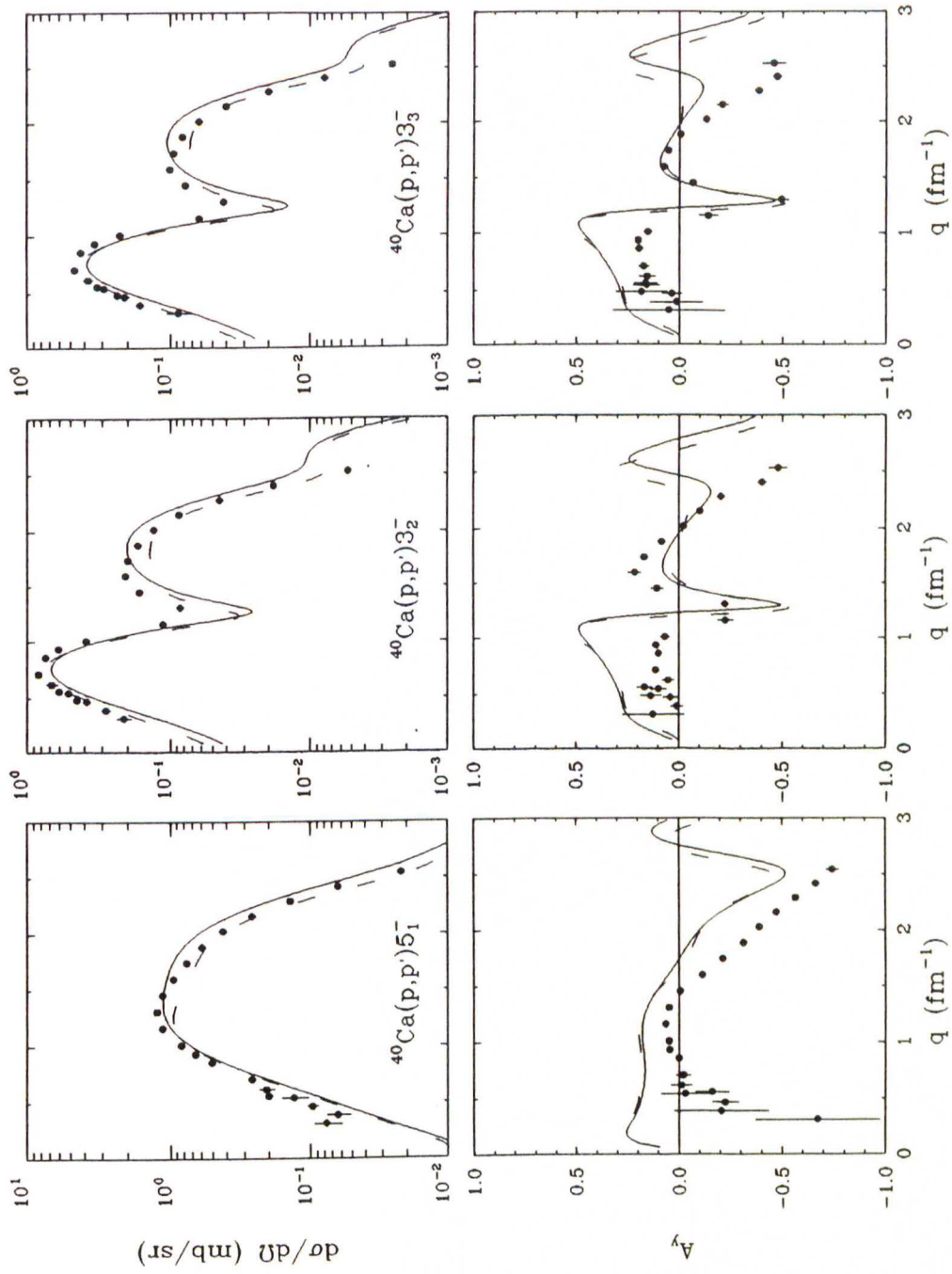

Figure 7.41: Comparison of EMP(^{16}O) (solid) and EMP(^{40}Ca) (dashes). We show calculations for the 5^-_1, 3^-_2, and 3^-_3 inelastic states of ^{40}Ca at 100 MeV. The data are from this work.

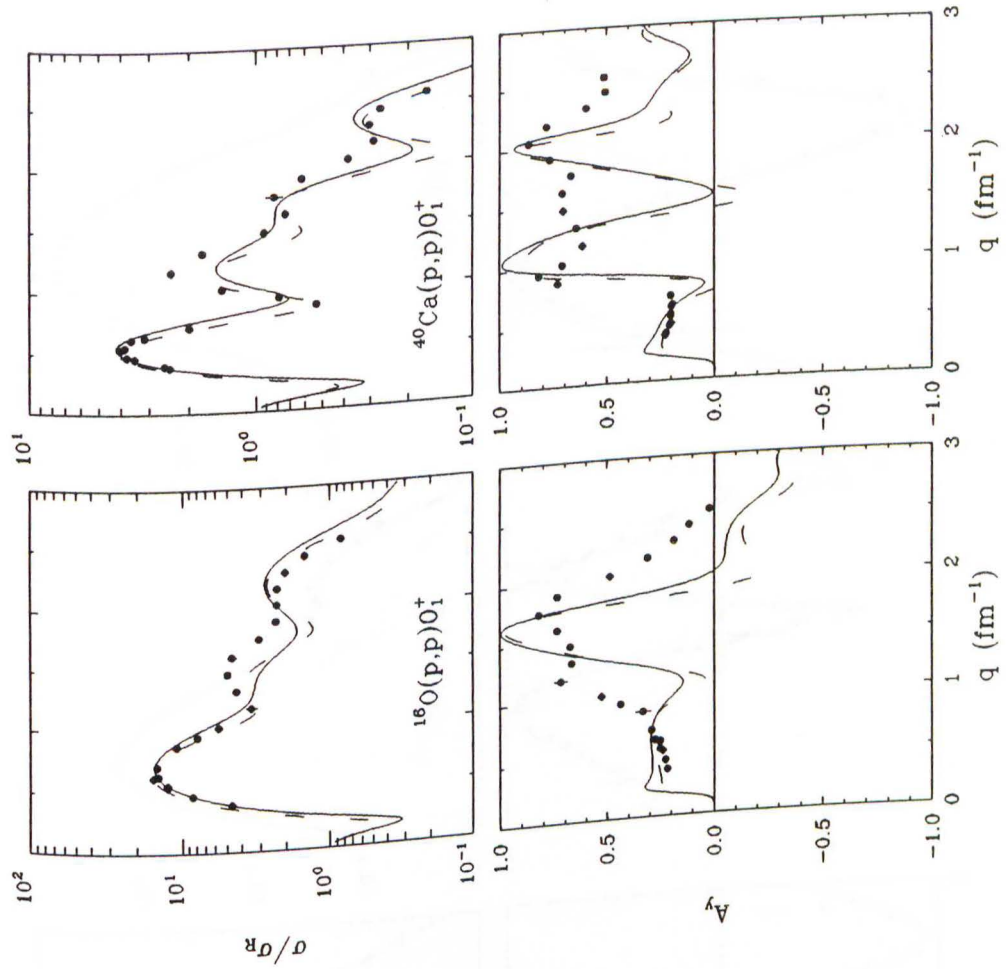

Figure 7.42: Comparison of EMP(^{16}O) (solid) and EMP(^{40}Ca) (dashes). We show calculations for the ground states of ^{16}O and ^{40}Ca at 100 MeV. The data are from this work.

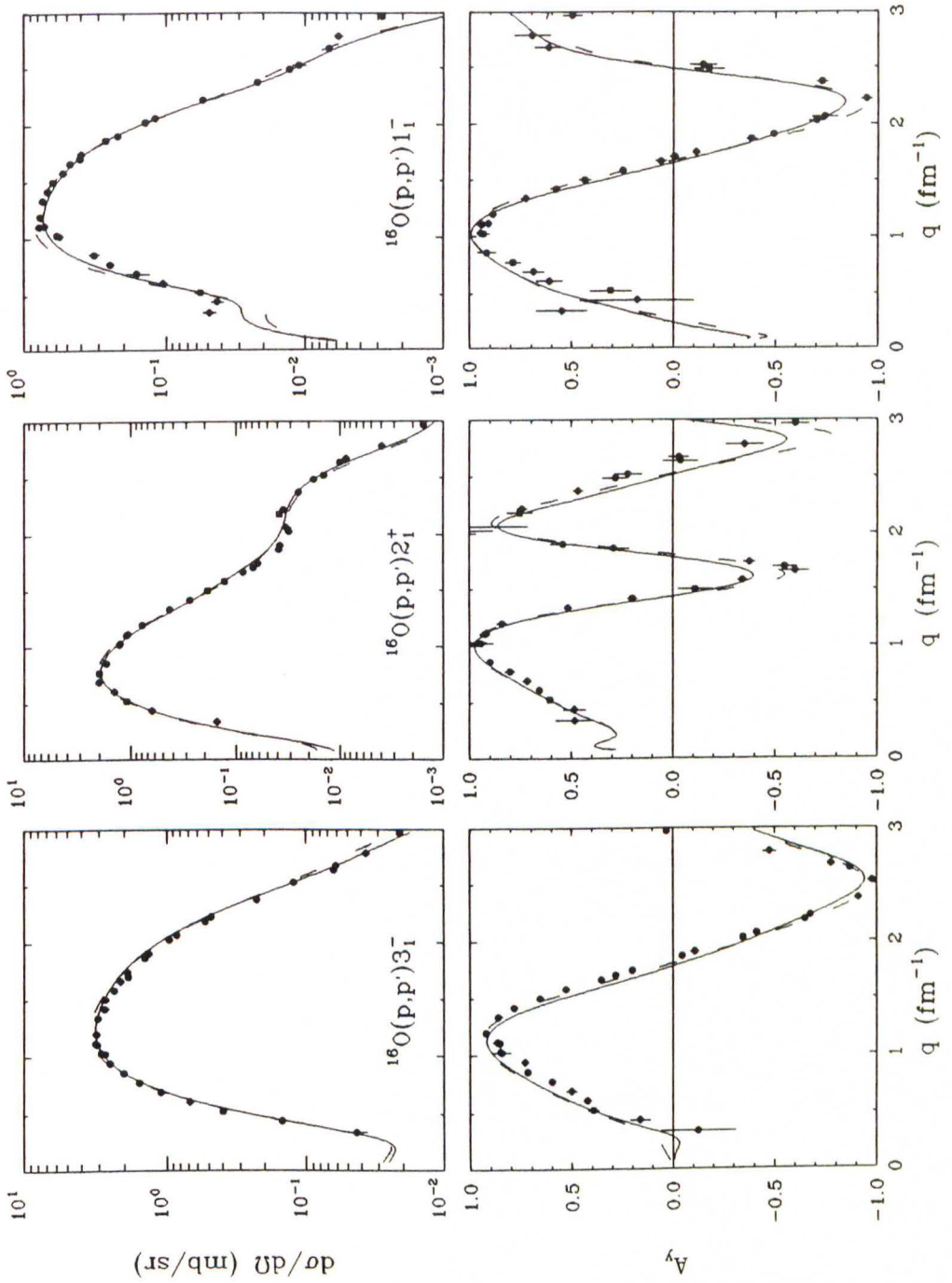

Figure 7.43: Comparison of EMP(^{16}O) (solid) and EMP(^{40}Ca) (dashes). We show calculations for the 3^-_1, 2^+_1, and 1^-_1 inelastic states of ^{16}O at 200 MeV. The data are from this work.

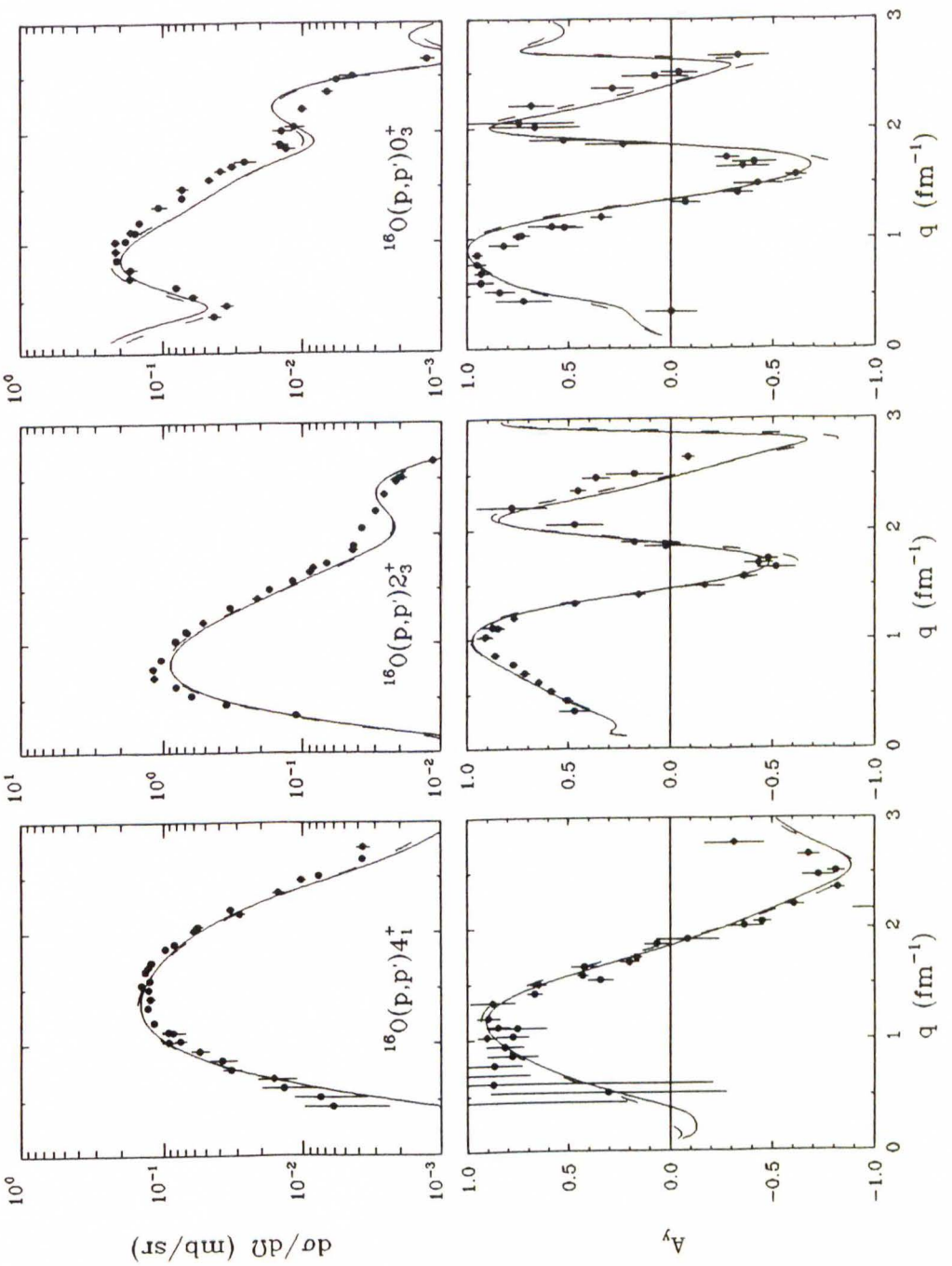

Figure 7.44: Comparison of EMP(^{16}O) (solid) and EMP(^{40}Ca) (dashes). We show calculations for the 4^+_1, 2^+_3, and 0^+_3 inelastic states of ^{16}O at 200 MeV. The data are from this work.

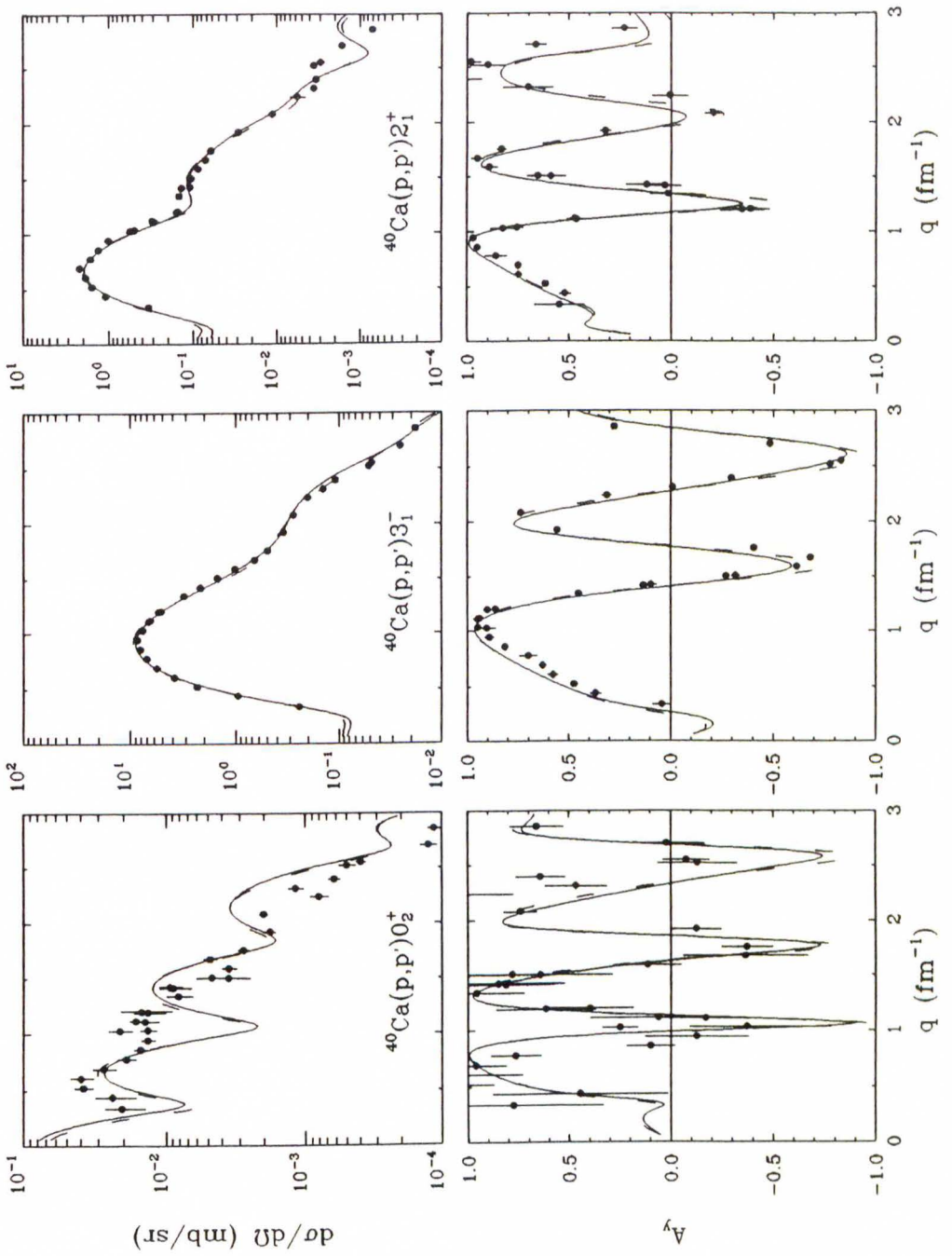

Figure 7.45: Comparison of EMP(^{16}O) (solid) and EMP(^{40}Ca) (dashes). We show calculations for the 0^+_2, 3^-_1, and 2^+_1 inelastic states of ^{40}Ca at 200 MeV. The data are from this work.

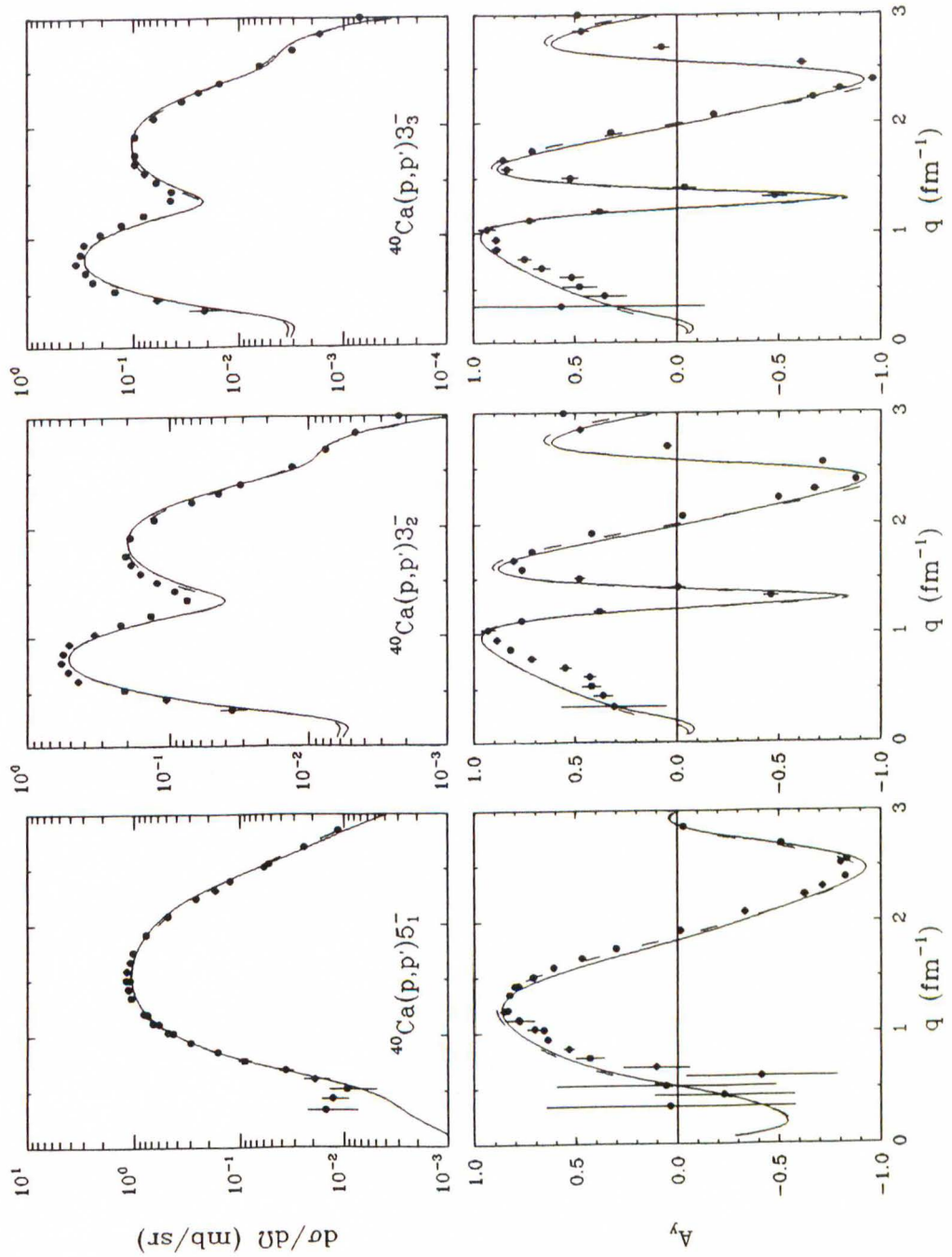

Figure 7.46: Comparison of EMP(^{16}O) (solid) and EMP(^{40}Ca) (dashes). We show calculations for the 5^-_1, 3^-_2, and 3^-_3 inelastic states of ^{40}Ca at 200 MeV. The data are from this work.

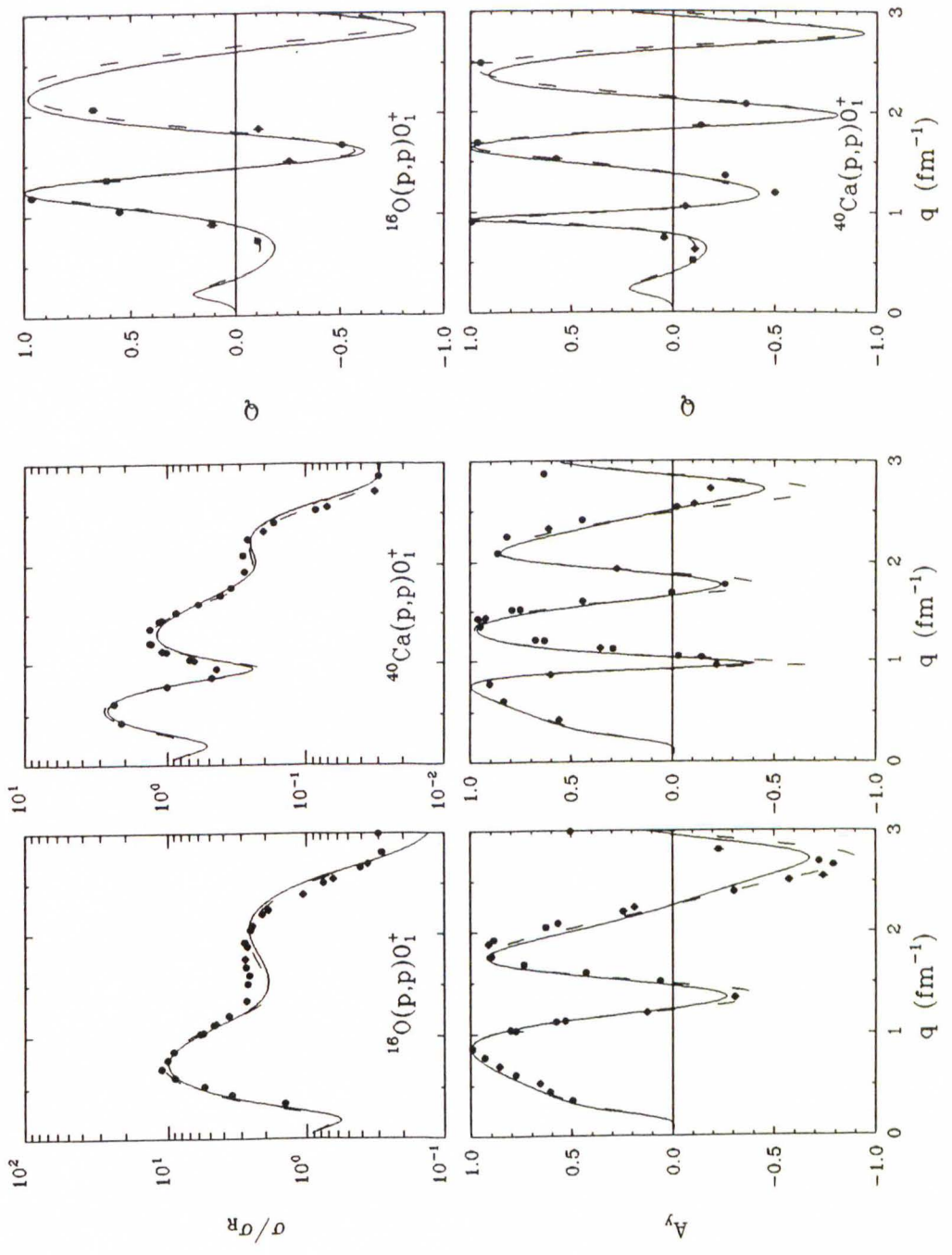

Figure 7.47: Comparison of EMP(^{16}O) (solid) and EMP(^{40}Ca) (dashes). We show calculations for the ground states of ^{16}O and ^{40}Ca at 200 MeV. The data for σ and A_y are from this work, the data for Q are from [Ste 85] and P. Schwandt, private communication.

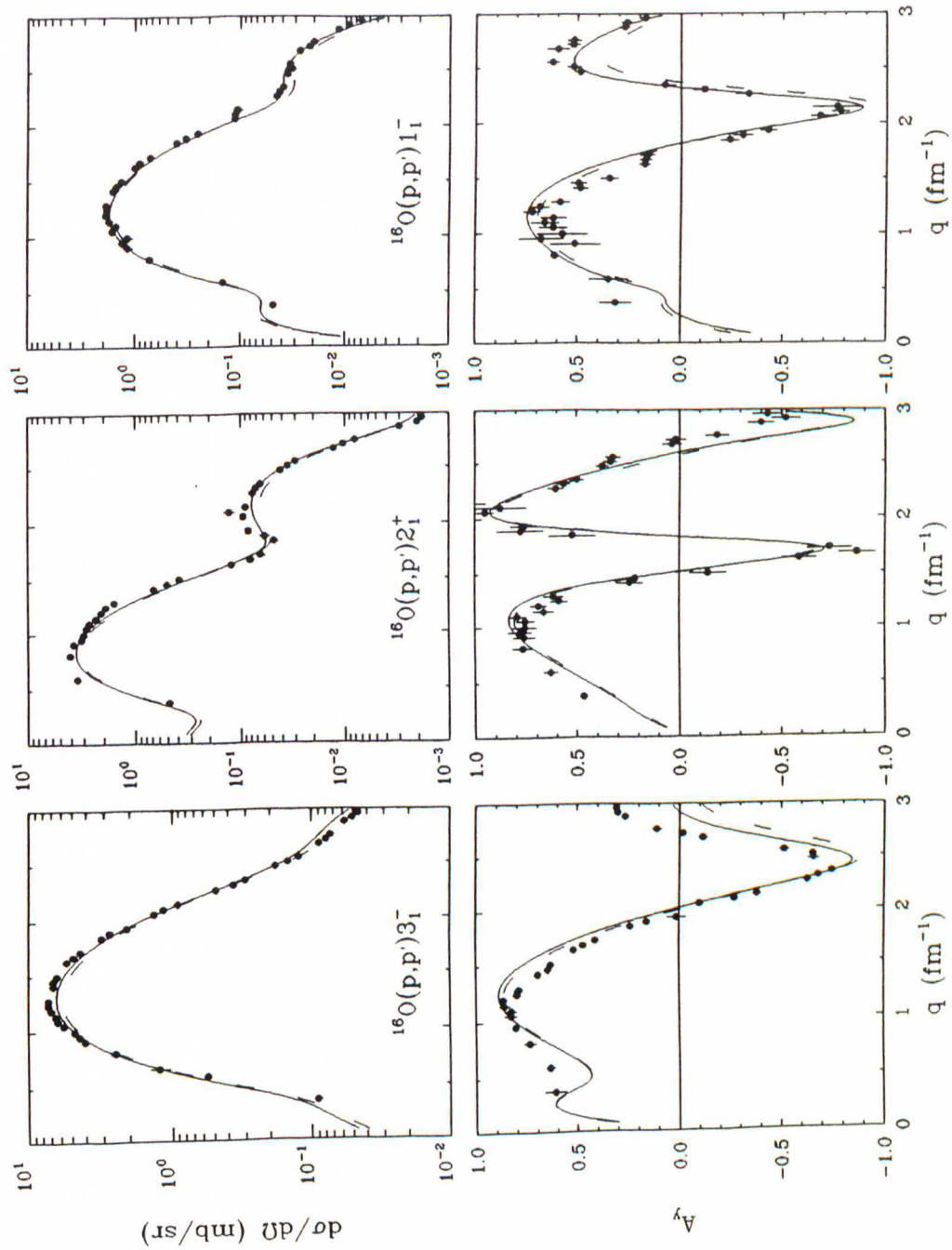

Figure 7.48: Comparison of EMP(^{16}O) (solid) and EMP(^{40}Ca) (dashes). We show calculations for the 3^-_1, 2^+_1, and 1^-_1 inelastic states of ^{16}O at 318 MeV. The data are from [Kel 90b].

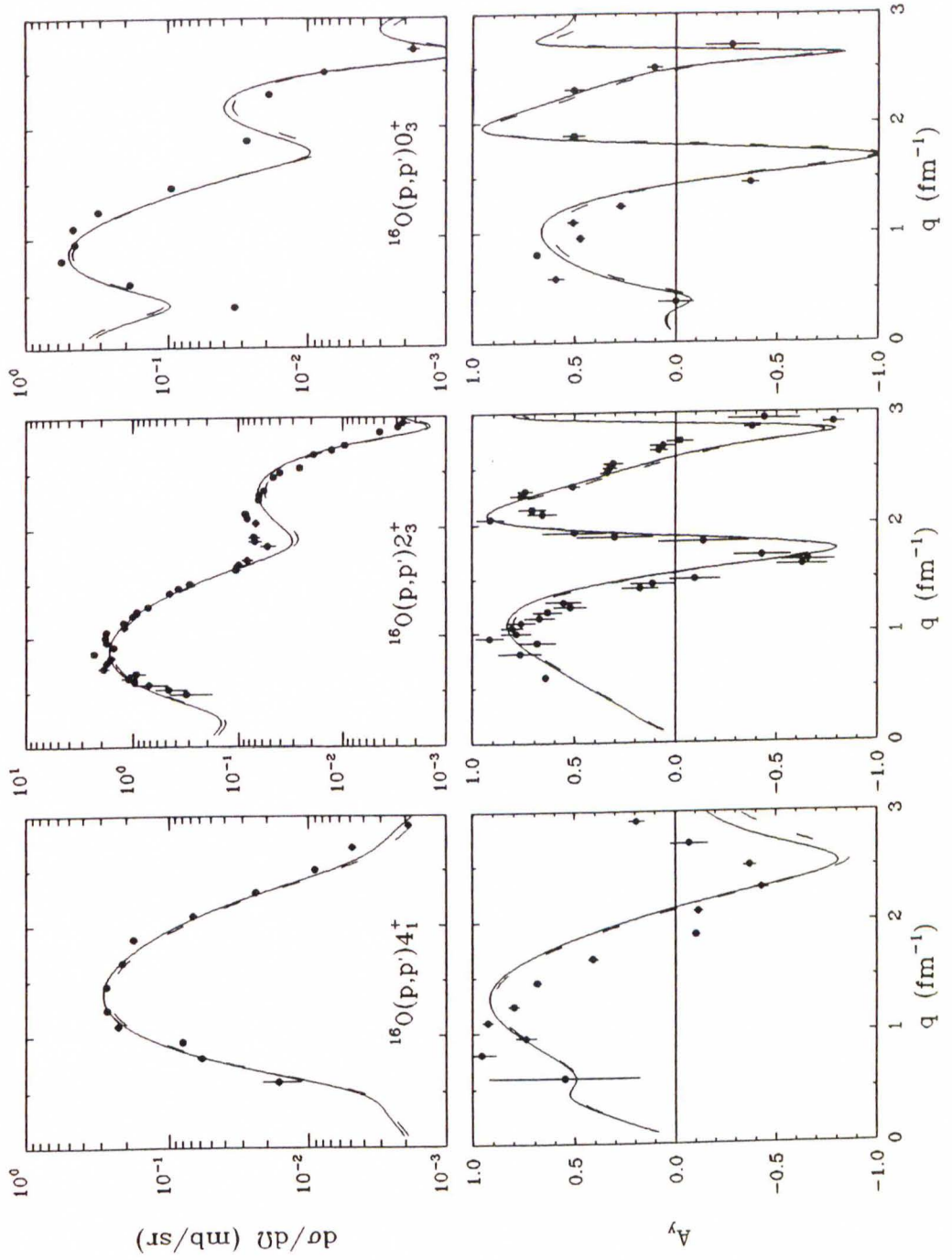

Figure 7.49: Comparison of EMP(^{16}O) (solid) and EMP(^{40}Ca) (dashes). We show calculations for the 4^+_1, 2^+_3, and 0^+_3 inelastic states of ^{16}O at 318 MeV. The data are from [Kel 90b].

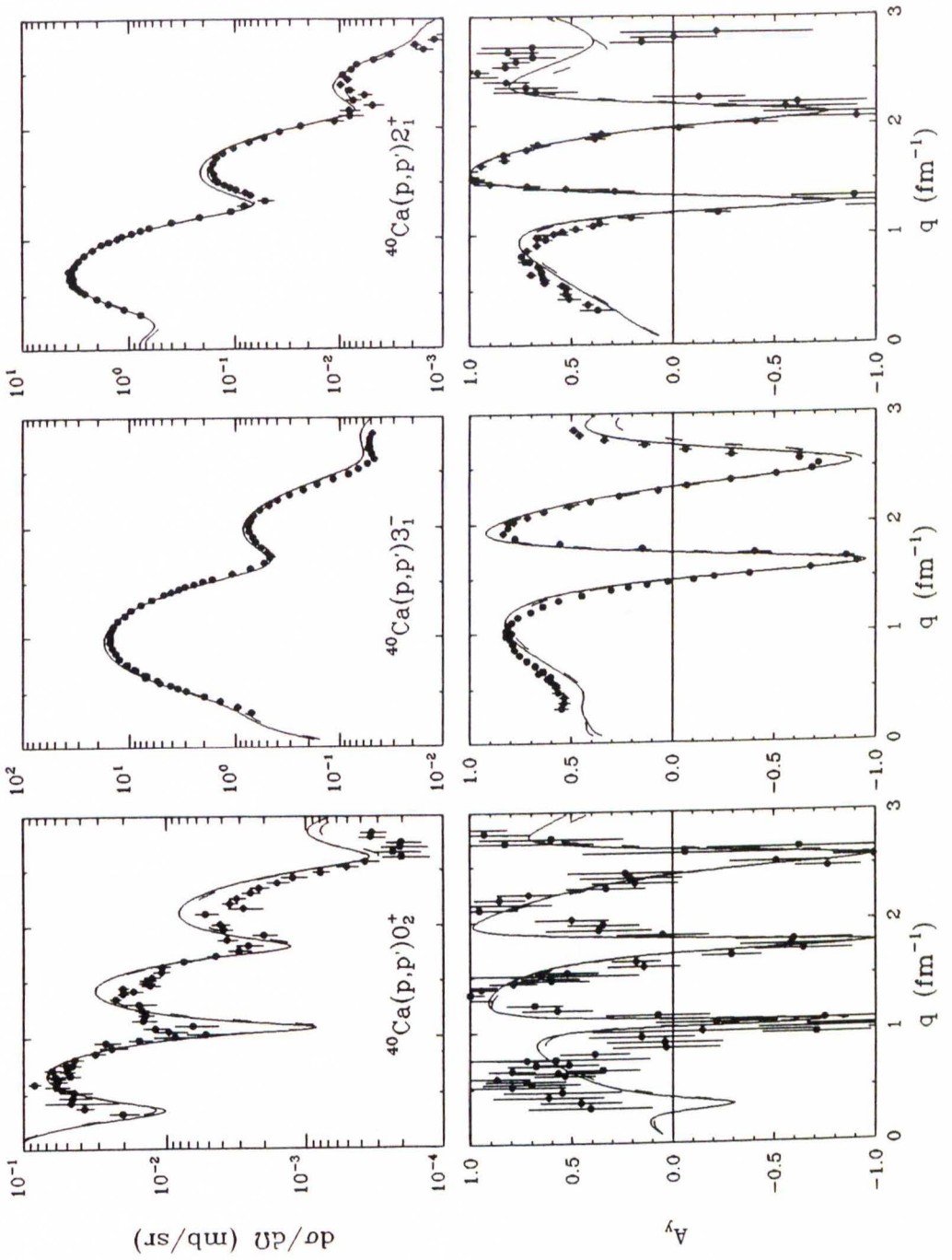

Figure 7.50: Comparison of EMP(^{16}O) (solid) and EMP(^{40}Ca) (dashes). We show calculations for the 0^+_2, 3^-_1, and 2^+_1 inelastic states of ^{40}Ca at 318 MeV. The data are from [Fel 90].

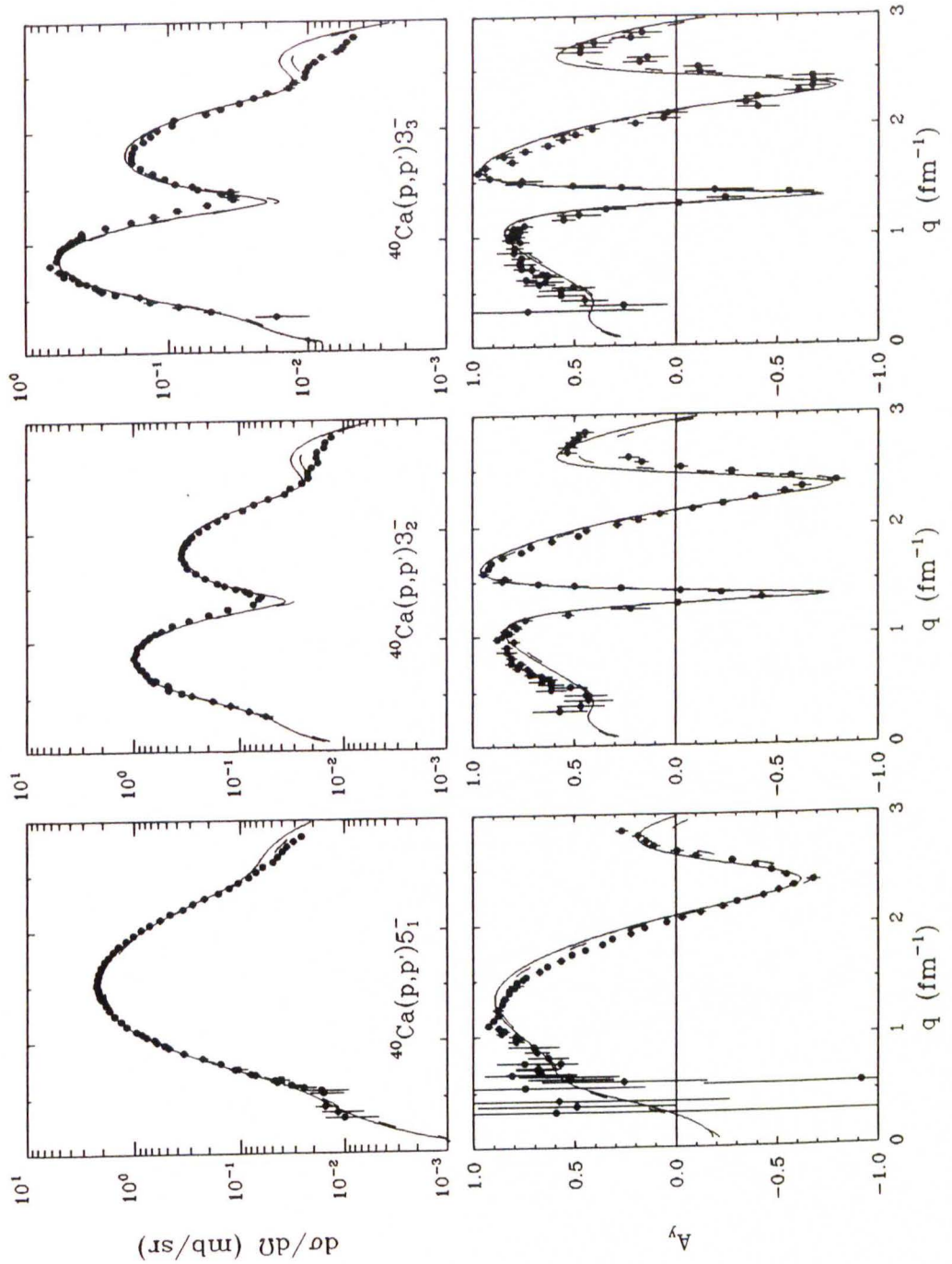

Figure 7.51: Comparison of EMP(^{16}O) (solid) and EMP(^{40}Ca) (dashes). We show calculations for the 5^-_1, 3^-_2, and 3^-_3 inelastic states of ^{40}Ca at 318 MeV. The data are from [Fel 90].

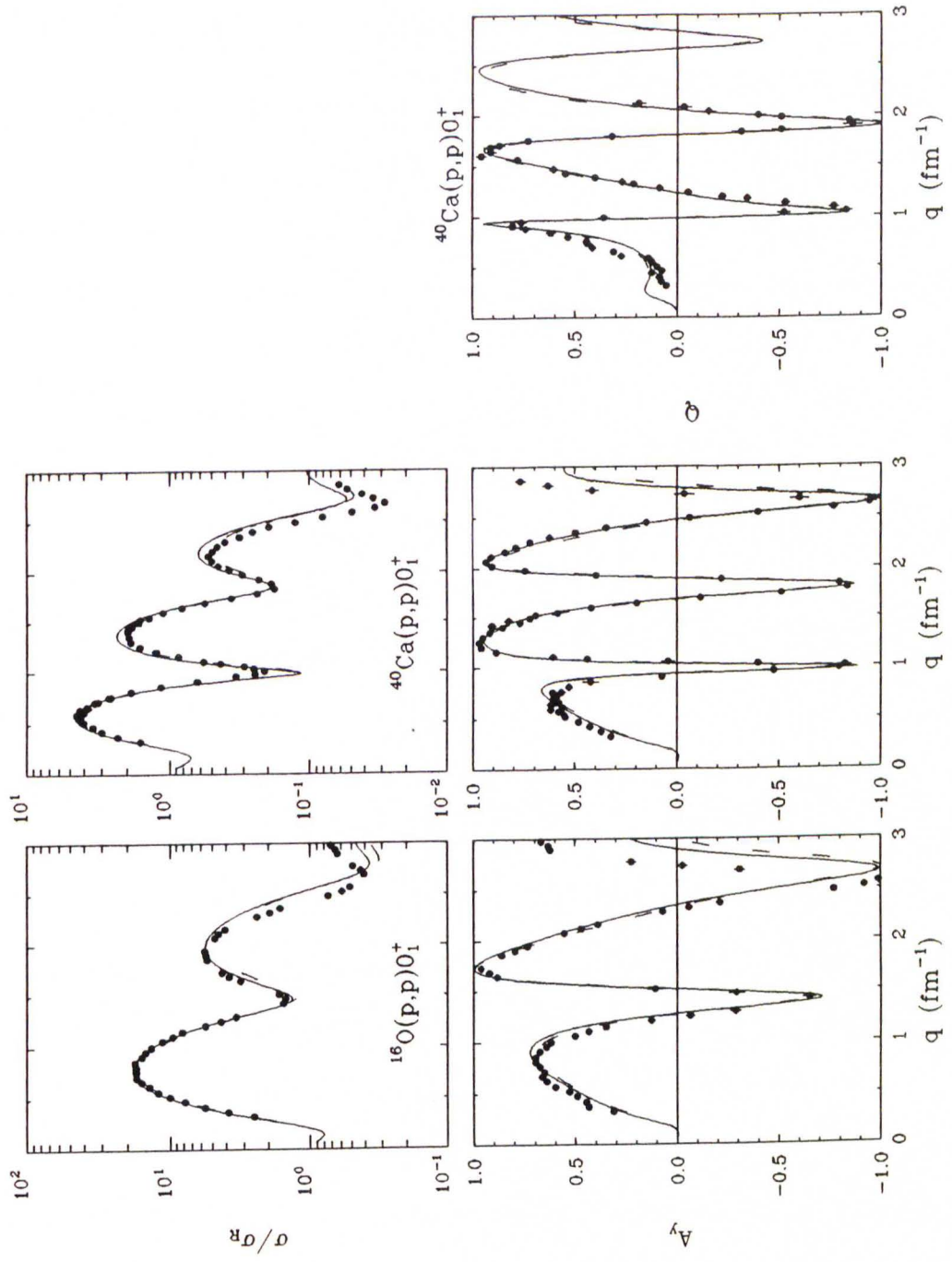

Figure 7.52: Comparison of EMP(^{16}O) (solid) and EMP(^{40}Ca) (dashes). We show calculations for the ground states of ^{16}O and ^{40}Ca at 318 MeV. The data for σ and A_y are from [Kel 90b] (^{16}O), and from [Fel 90] (^{40}Ca); the data for Q are from [Ble 88].

7.6 Comparison with IA2 and Dirac Phenomenology

In Figures 7.53 and 7.54 we compare the empirical interaction EMP from fits to ^{16}O (solid) with the full IA2 (long dashes), the relativistic NP (dashes), and the NRIA (short dashes) models for elastic scattering of 200 and 318 MeV protons from ^{16}O and ^{40}Ca. The corresponding optical potentials are displayed in Figures 7.55–7.58. The EMP for 200 MeV is based on the PH t-matrix, while for 318 MeV the FL t-matrix was used. The NRIA calculations for both 200 and 318 MeV are based on the PH t-matrix.

At 200 MeV the empirical interaction is superior in its description of the data. In particular, the IA2 produces cross sections which are too large. The reason for this can be seen in the figures for the 200 MeV optical potentials. If we compare the central optical potentials we notice that although the real parts of the EMP and IA2 compare quite well (both show the same repulsive behaviour), the EMP imaginary central potential is damped relative to the corresponding IA2 potential due to Pauli blocking which is still important at this energy. Thus, the deficiencies in the IA2 can be reduced by applying *ad hoc* Pauli blocking to the imaginary central potential. This was done by Murdock and Horowitz for a related RIA model [Mur 87].

At 318 MeV, this Pauli blocking effect should be less important due to its E^{-1} dependence. Indeed, the empirical and IA2 imaginary central potentials are almost identical at this energy. Nevertheless, the empirical model still provides a slightly better description of the data. Although the ^{16}O calculation is shifted outward a little bit too much at large momentum transfers, the empirical description of the second and the third cross section

maximum of ^{40}Ca is much improved over the IA2, for which predictions are too high. Also, the low-q analyzing powers are slightly better for the empirical interaction.

The principal difference between the relativistic and nonrelativistic approaches to elastic scattering is the contribution of virtual $N\overline{N}$ pairs in the nuclear medium (see Chapter 2). In a Schrödinger equivalent formulation, this contribution manifests itself as an effective density dependence which can be described as primarily a short-ranged repulsive interaction. The figures show that the the pair contributions to the spin-orbit and the imaginary central potential are small (the differences between the NP and IA2 are small). By contrast, the repulsive pair contribution has a strong impact on the real central potential, a behaviour which is also exhibited by our effective interaction.

Finally, we compare elastic scattering calculations with our effective interaction to calculations based on a recent phenomenological global Dirac optical model by Hama *et al.* [Ham 90]. A phenomenological Lorentz-scalar–Lorentz-vector model is fitted to a large set of elastic scattering data for a wide variety of targets and energies, and the resulting fitted Dirac optical potential parameters bear both energy (E) and mass number (A) dependence. The targets which are used for this analysis are ^{40}Ca, ^{48}Ca, ^{56}Fe, ^{60}Ni, ^{90}Zr, and ^{208}Pb, i.e. the mass number ranges between $40 \leq A \leq 208$. The energy range covered by the data set is between 65 and 1044 MeV. The authors show that their global optical potential interpolates quite well in E and A. An extrapolation is not recommended, however. Since the data set did not

include data for $q > 3$ fm^{-1}, the authors do not expect their model to perform well for higher momentum transfers.

Figures 7.59 and 7.60 show calculations for elastic scattering from ^{40}Ca for 100, 200, and 318 MeV based on the empirical interactions EMP (solid) which were fitted to ^{40}Ca and the global Dirac optical potential model DP (dashes). Considering that both 100 and 318 MeV are interpolated energies, the excellent performance of the Dirac phenomenology is extremely remarkable at all the energies and for all the observables. The only exception is the cross section at 200 MeV, an energy for which ^{40}Ca data [Ste 85] were available and included the fit.

In Figures 7.61–7.63 we compare the empirical optical potentials which are based on interactions fitted to inelastic ^{40}Ca (solid) and ^{16}O (dashes) data with the global optical potential (short dashes) for the three energies. The parameters for the empirical interactions are those from Tables 7.1, 7.2, and 7.3. Since the spin-orbit potentials are small, we want to concentrate on the central potentials. At 318 MeV, where our empirical description of the data is most similar to the DP prediction, also the potentials are most similar. The DP imaginary central potential is about 17–20% less absorptive than the empirical potentials, and the DP real central potential does not display the dip in the interior which is present for the empirical potentials. At 200 MeV where the quality of the data description by the empirical interactions is still comparable to the Dirac phenomenology, we find that the (large) imaginary central potentials are almost identical, while the real central potentials display differences whose impact on the scattering data are difficult

to judge. The surface depression of the DP potential is more pronounced than for our empirical potentials. These, however, have a depression deeper in the interior which is absent for the DP potential. Since elastic scattering in some fashion samples an average of the whole nucleus, it is conceivable that on the average the different real central potentials have the same effect. Comparing our empirical potentials to the DP potential is most interesting for 100 MeV, the energy where our model does very poorly and the DP does very well. We notice that our real central potentials are between about 11 and 22% more attractive than the DP potential, but the main difference is undoubtedly to be found in the imaginary central potentials. The DP potential is much more absorptive within a radius of about 4 fm than the empirical potentials. For $r < 4$ fm the absorptive potential for the empirical interaction is only -3 to -4 MeV, whereas the DP potential assumes a depth of about -11 MeV at the nuclear center. However, as we recall from Section 7.4, at 100 MeV the damping factor $S_2 - d_2$ for the interactions from inelastic fits is much smaller than the corresponding damping factor for interactions which include elastic scattering (Table 7.7). Potentials based on the interactions from the combined fit to elastic and inelastic data, or to elastic data alone, would be much more absorptive in the center.

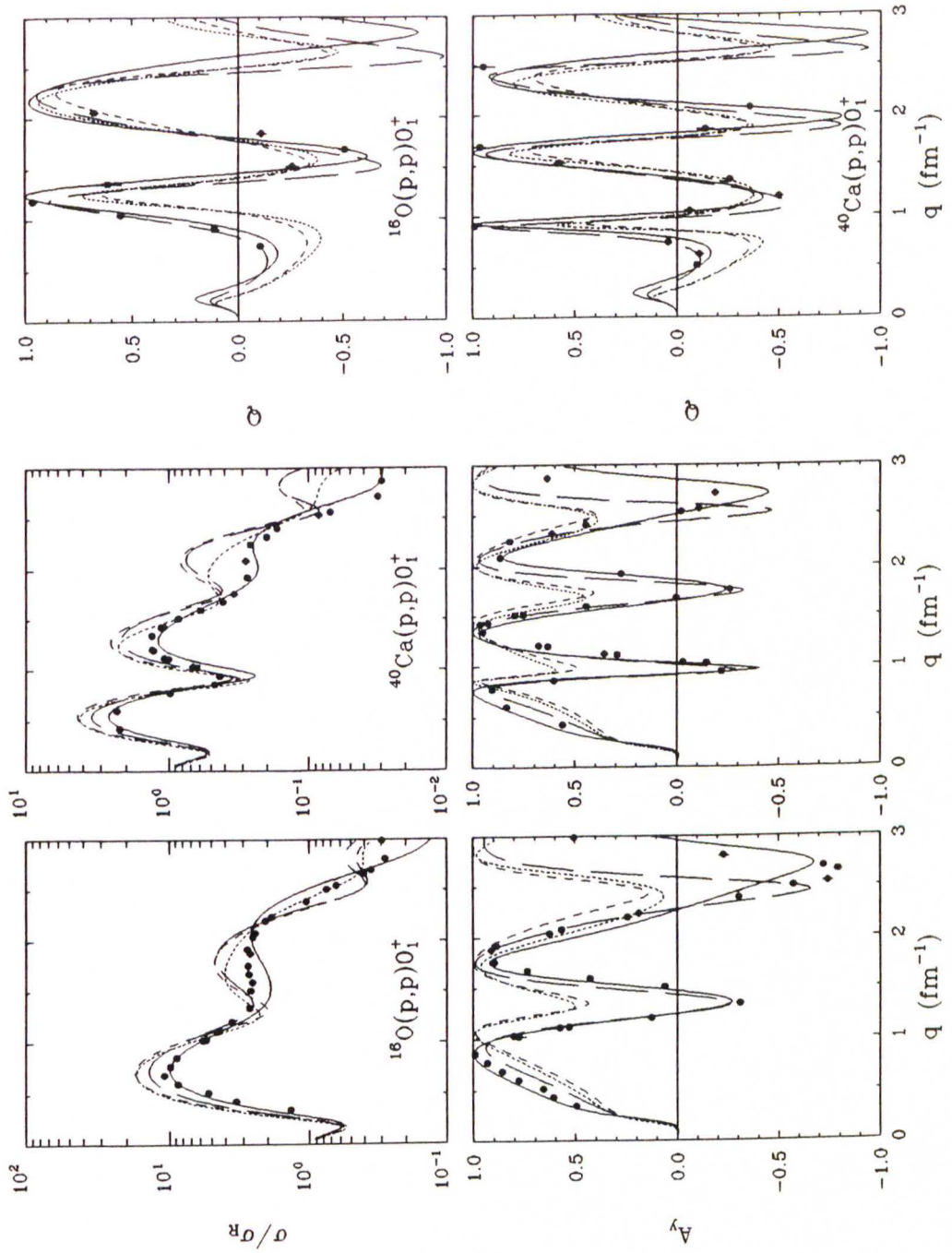

Figure 7.53: Comparison of calculations for elastic scattering at 200 MeV based on the empirical interaction EMP(^{16}O) (solid), IA2 (long dashes), NP (dashes), and NRIA (short dashes). Both EMP and NRIA are based on the PH t-matrix. The data for σ and A_y are from this work, the data for Q are from [Ste 85] and P. Schwandt, private communication.

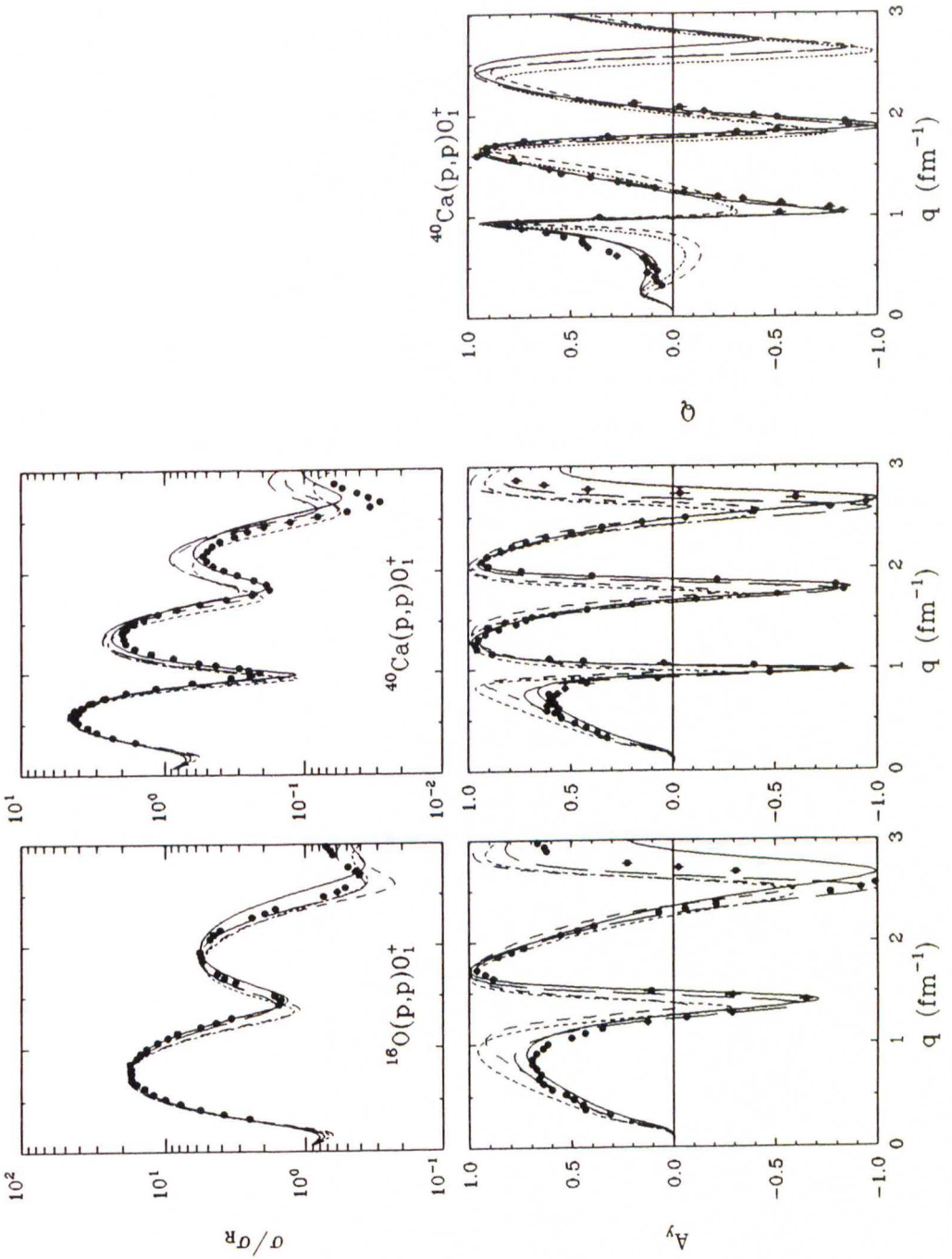

Figure 7.54: Comparison of calculations for elastic scattering at 318 MeV based on the empirical interaction EMP(^{16}O) (solid), IA2 (long dashes), NP (dashes), and NRIA (short dashes). EMP is based on the FL, NRIA on the PH t-matrix. The data for σ and A_y are from [Fel 90, Kel 90b]; the data for Q are from [Ble 88].

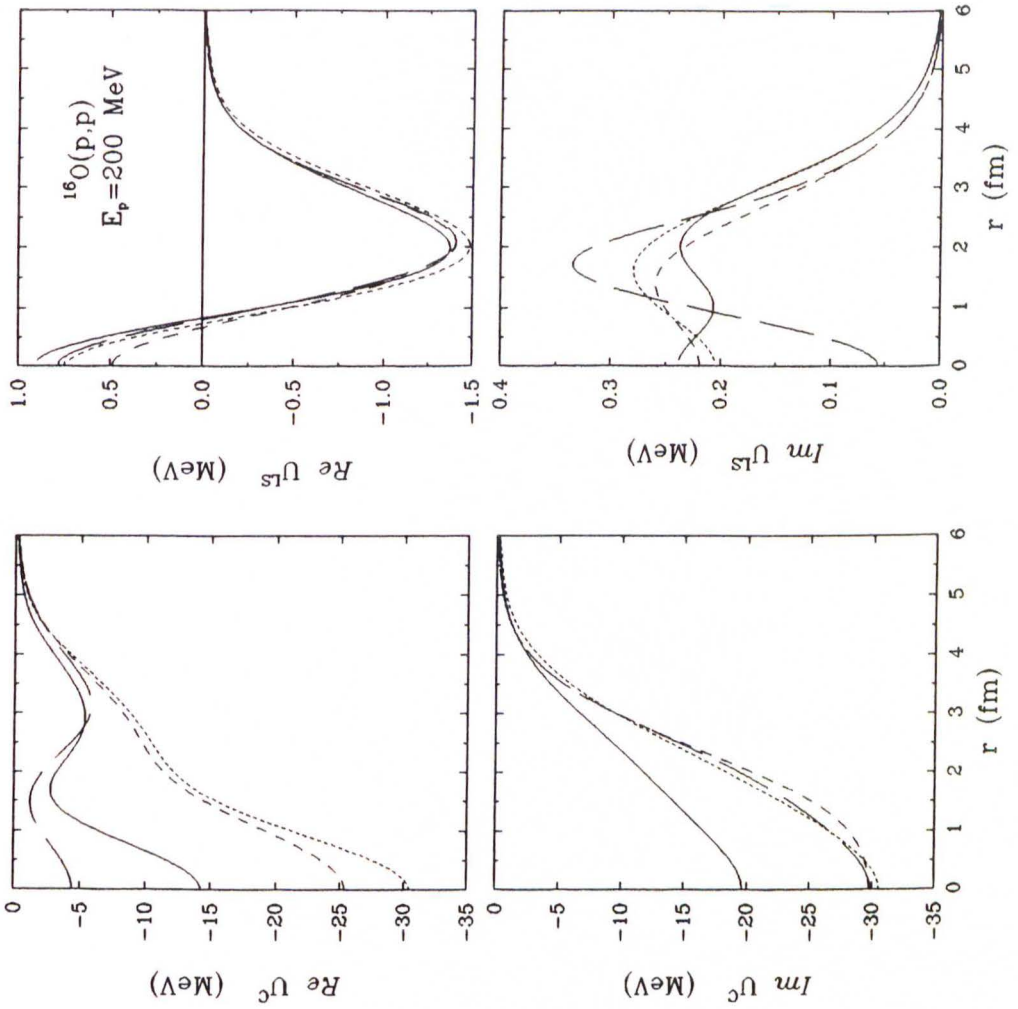

Figure 7.55: Comparison of the EMP(^{16}O) (solid), full IA2 (long dashes), NP (dashes), and NRIA (short dashes) optical potentials for 200 MeV elastic scattering by ^{16}O. Both EMP and NRIA are based on the PH interaction.

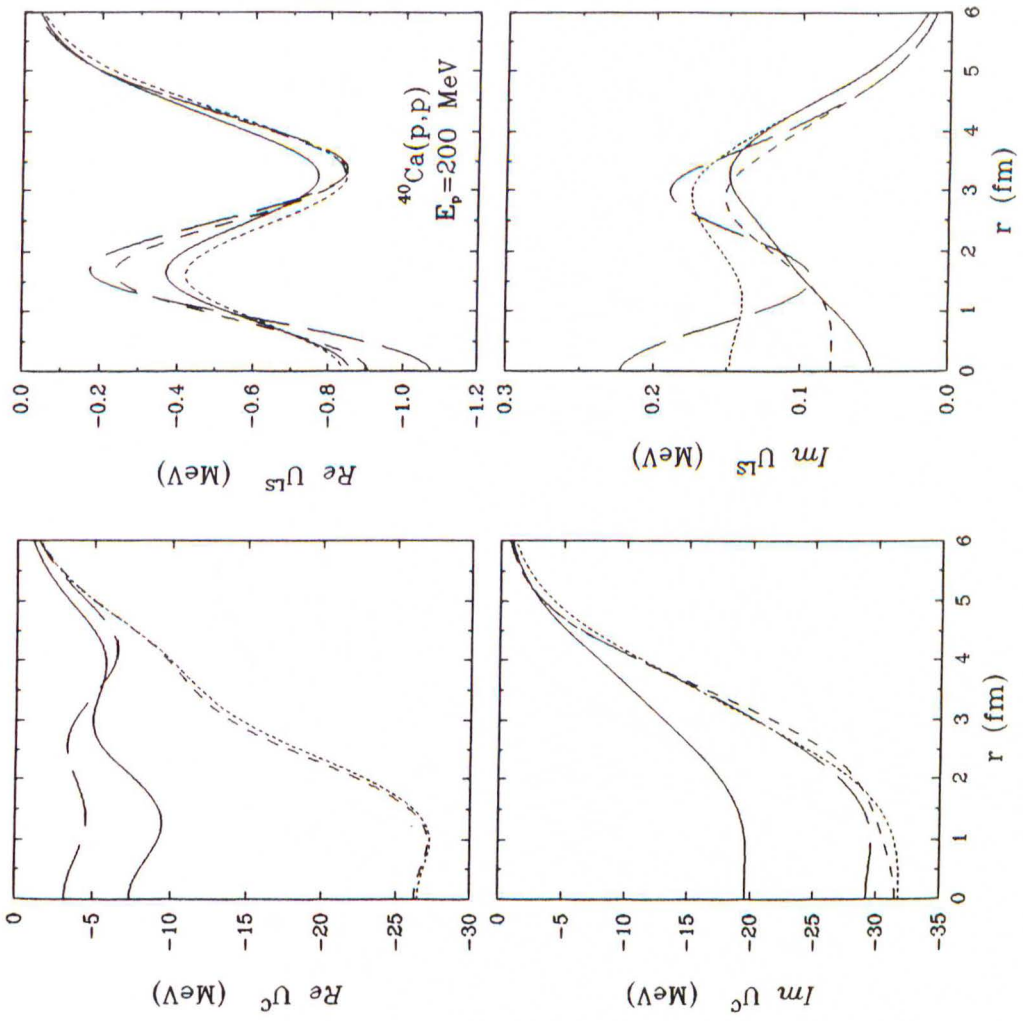

Figure 7.56: Comparison of the EMP(^{16}O) (solid), full IA2 (long dashes), NP (dashes), and NRIA (short dashes) optical potentials for 200 MeV elastic scattering by ^{40}Ca. Both EMP and NRIA are based on the PH interaction.

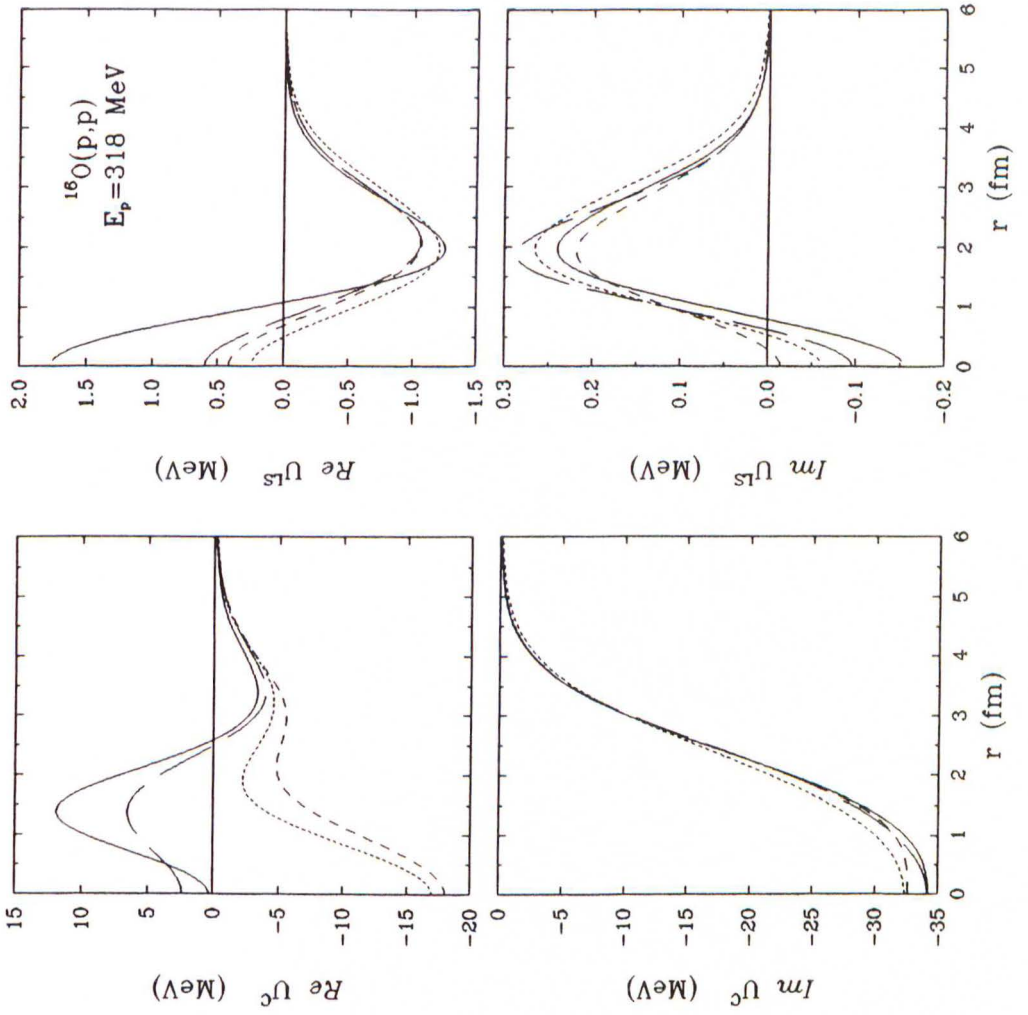

Figure 7.57: Comparison of the EMP(^{16}O) (solid), full IA2 (long dashes), NP (dashes), and NRIA (short dashes) optical potentials for 318 MeV elastic scattering by ^{16}O. EMP is based on the FL, NRIA on the PH interaction.

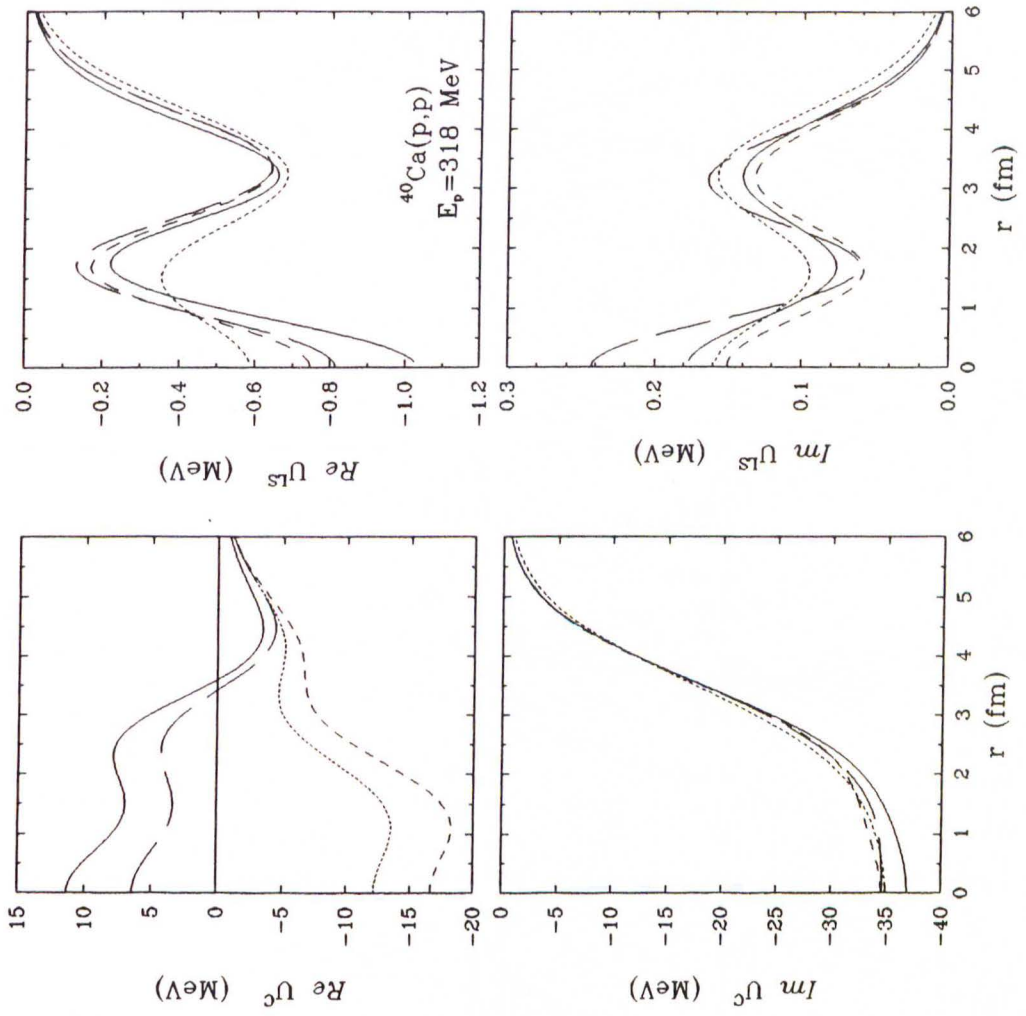

Figure 7.58: Comparison of the EMP(^{16}O) (solid), full IA2 (long dashes), NP (dashes), and NRIA (short dashes) optical potentials for 318 MeV elastic scattering by ^{40}Ca. EMP is based on the FL, NRIA on the PH interaction.

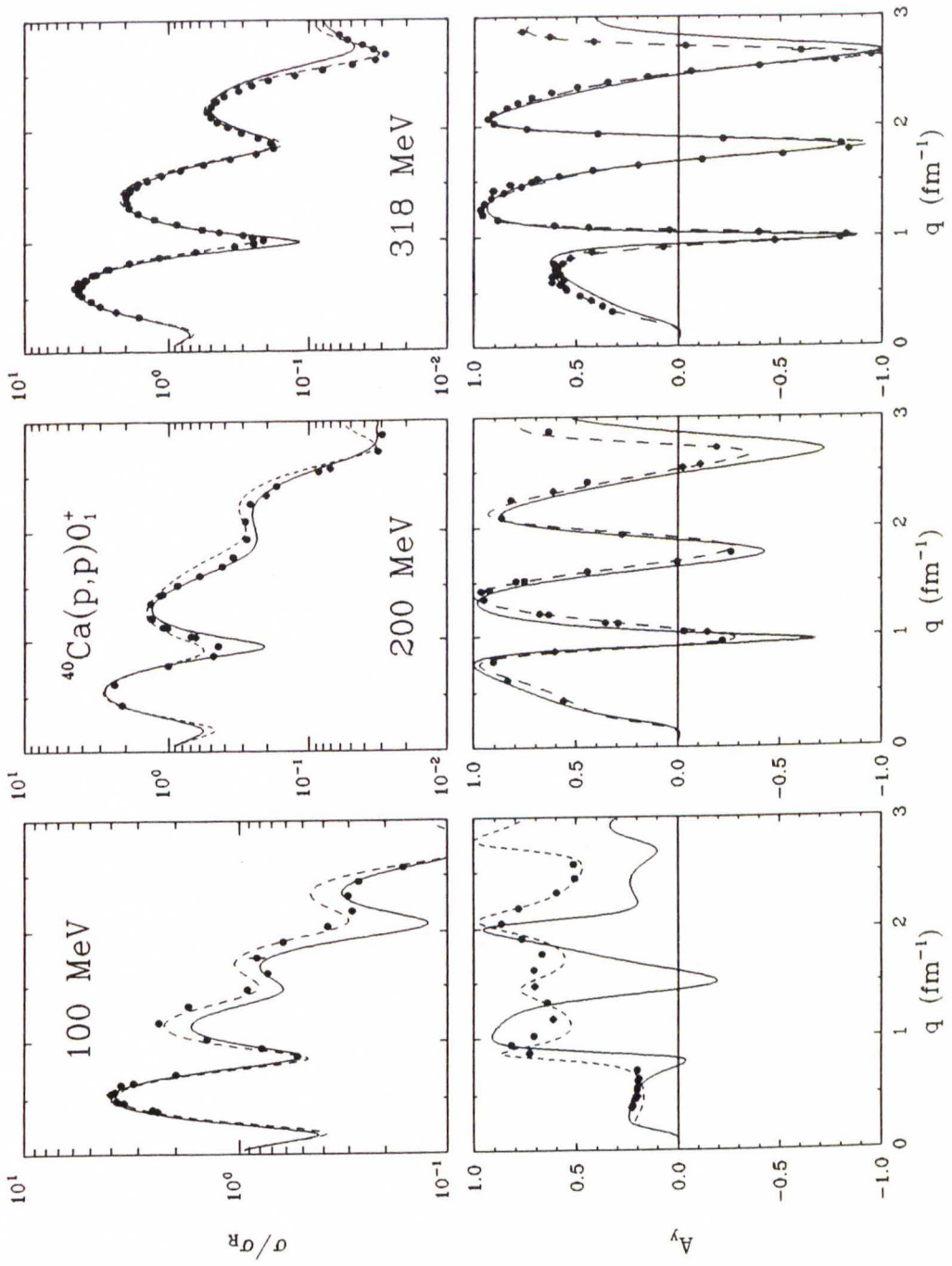

Figure 7.59: Comparison of EMP(^{40}Ca) (solid) and Dirac phenomenology DP (dashes) calculations for σ/σ_R and A_y). The data for 100 and 200 MeV are from this work, the data for 318 MeV are from [Fel 90].

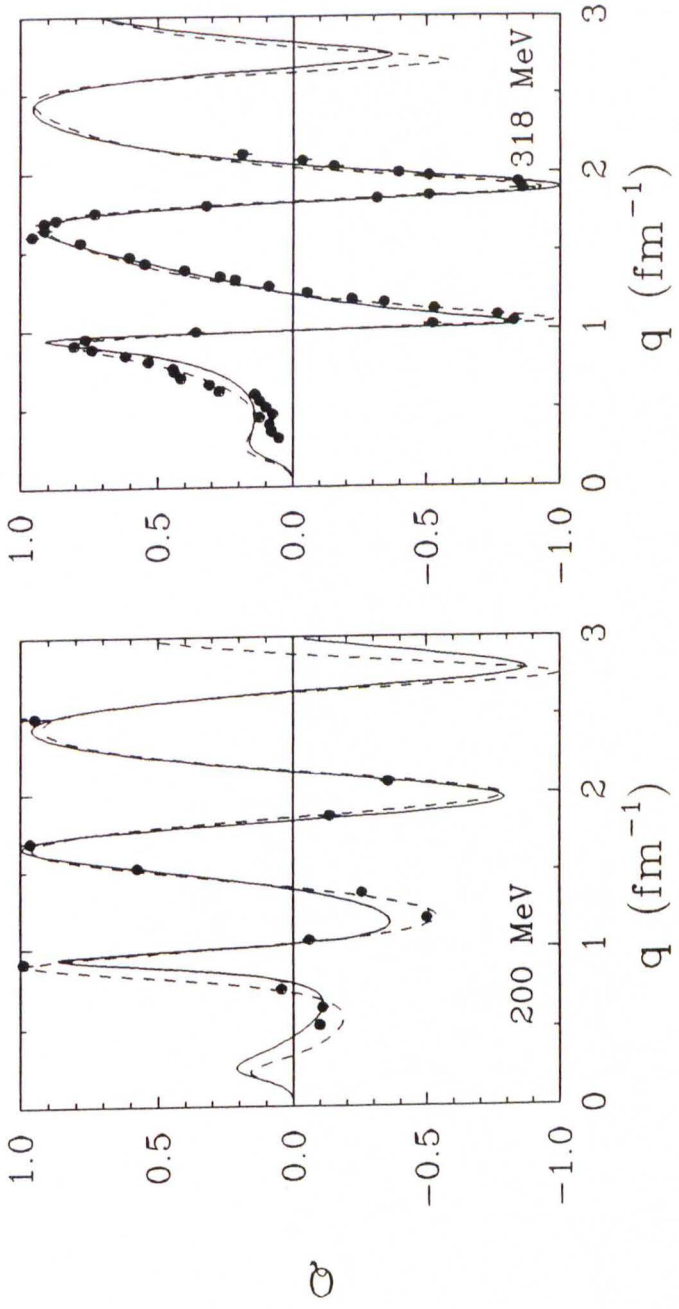

Figure 7.60: Comparison of EMP(^{40}Ca) (solid) and Dirac phenomenology DP (dashes) calculations for Q. The 200 MeV data for Q are from [Ste 85] and P. Schwandt, private communication; the 318 MeV Q data are from [Ble 88].

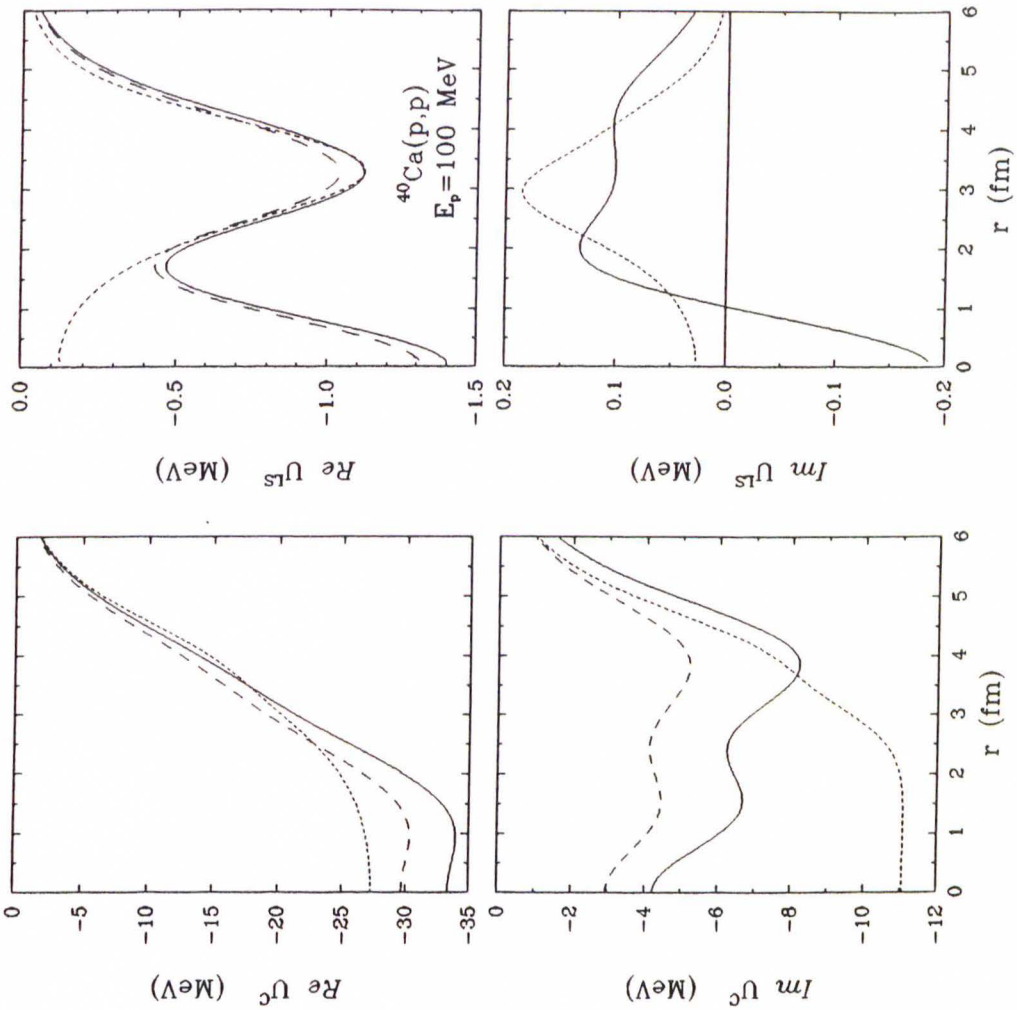

Figure 7.61: Comparison of the EMP(^{40}Ca) (solid), EMP(^{16}O) (dashes), and DP (short dashes) optical potentials for ^{40}Ca at 100 MeV.

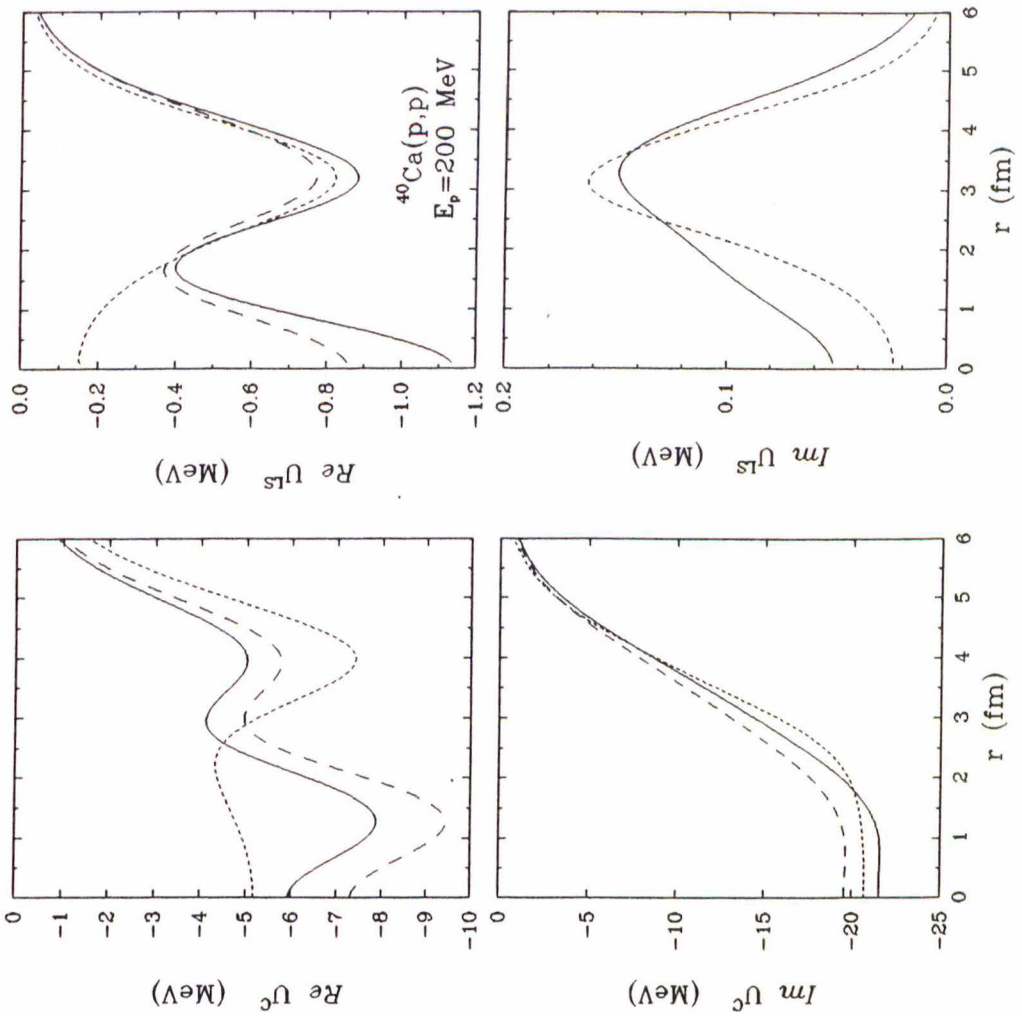

Figure 7.62: Comparison of the EMP(^{40}Ca) (solid), EMP(^{16}O) (dashes), and DP (short dashes) optical potentials for ^{40}Ca at 200 MeV.

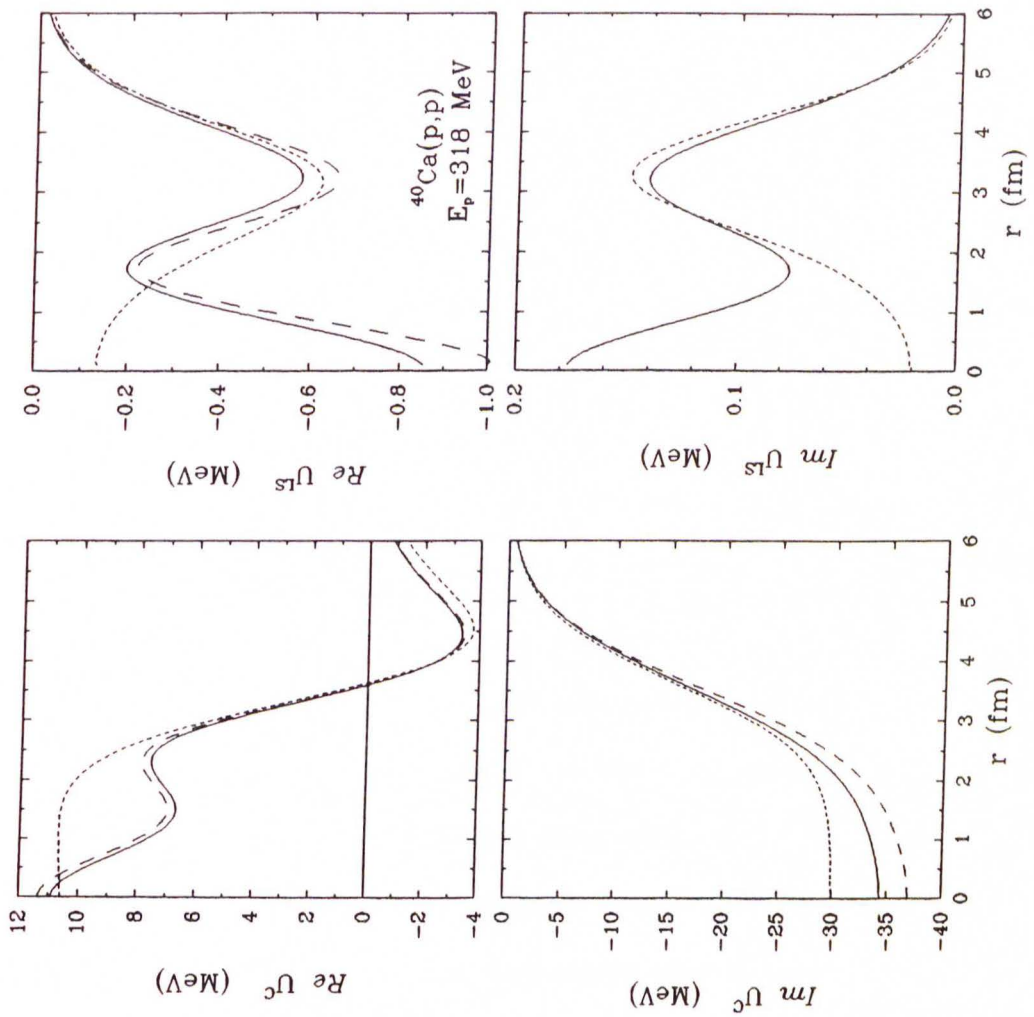

Figure 7.63: Comparison of the EMP(^{40}Ca) (solid), EMP(^{16}O) (dashes), and DP (short dashes) optical potentials for ^{40}Ca at 318 MeV.

7.7 Energy Dependence of the Effective Interaction

Finally, we want to address the last topic of this work, the energy dependence of the effective interaction. The interaction parameters for energies between 100 and 500 MeV are collected in Table 7.9. In Figures 7.64–7.66 we compare our empirical interactions for 100, 200, and 318 MeV with both the density dependent PH and LR interactions. The figures show that the overall density dependence of the real central component for 100 and 200 MeV is smaller than the PH interaction and that the interaction is suppressed for low densities. Relative to the LR interaction at 200 MeV, we find that our EMP is still suppressed at low density, but retains similar density dependence. At 318 MeV, the real central component is more density dependent than either interaction. With the exception of 100 MeV, the imaginary central EMP component is less density dependent than either the PH or LR interactions. For 100 and 200 MeV we see again the suppression at low densities. At 318 MeV, however, the density dependence appears to flip around and is opposite to that from theory. This behaviour makes the imaginary central component more absorptive with increasing density which is in contrast to the lower energies. The effect is even larger at 500 MeV [Fla 90]. These results may be associated with a new absorption mechanism, such as the opening of the pion channel. Finally, for the real spin-orbit component we observe suppression at low density for all the energies. However, although the overall density dependence is also reduced for 100 and 200 MeV, at 318 and 500 MeV we observe an enhanced density dependence which is much larger than that of either the PH or LR interactions.

In Figures 7.67 and 7.68 we graphically display the energy dependence of the parameters. The PH (solid) and LR (dashes) parameters are also given for comparison. One problem is that below 318 MeV we used the PH free interaction for the fit, while for 318 MeV and above we used the FL t-matrix. Figure 7.68 shows the difference between the two free interactions at the various energies. For 318 MeV the $\mathrm{Re}t_{00}^{C}$ component of the PH interaction is much stronger at $q = 2.0$ fm^{-1} than the corresponding FL component, thus making the b_1 parameter modeled upon FL larger than it would be with the PH free interaction. Therefore, the apparent discontinuity in the energy dependence of this parameter at 318 MeV might be to a certain extent artificial. A fit with the PH free interaction at this energy had proved to be difficult and unstable in the past. Fits with the FL free interaction at all energies are planned or in progress. The real and imaginary central scale factors are multiplied with their respective free interaction at zero momentum transfer to remove the impact of the different t-matrices. For the d_2 parameter we see the smooth E^{-1} behaviour which has been predicted from theory, but also the change of sign around 300 MeV which is not predicted by the theory. An interpretation of the real spin-orbit results is more difficult and will need more work. It is possible, however, that large correlations between b_3 and other parameters confuse the results. For example, it is striking that at 180 MeV the scale factor appears to be too high while at the same time the b-parameter is too small. It was also found that b_3 for 100 MeV and for energies $\geq$ 300 MeV is not a very strongly determined parameter, and that for instance at 100 MeV both a value of 6.0 and 3.7 satisfies the data.

T_L	$\mathrm{Re}t_{00}^C$		$\mathrm{Im}t_{00}^C$		$\mathrm{Re}\tau_0^{LS}$		(elas.)	(inel.)
(MeV)	S_1	b_1	S_2	d_2	S_3	b_3	$S_2 - d_2$	$S_2 - \frac{5}{3}d_2$
100	0.86	41.8	0.69	0.55	0.82	3.79	0.14	-0.23
135[a]	0.84	56.8	0.81	0.44	0.84	3.14	0.37	0.08
180[b]	0.75	62.9	0.76	0.23	0.88	0.51	0.53	0.38
200	0.70	65.5	0.77	0.14	0.84	2.03	0.63	0.54
318[c]	1.07	144.7	1.02	-0.07	0.83	7.14	1.09	1.14
500[d]	1.26	121.1	0.84	-0.28	0.72	4.65	1.12	1.31
500[d,e]	0.88	152.2	0.80	-0.30	0.73	5.14	1.10	1.30

Table 7.9: Interactions parameters for ^{16}O at various energies. Both the interactions at 318 and 500 MeV are based on the FL t-matrix, while the interactions at the lower energies employ the free PH interaction. Mass parameters $\mu_1 = 1.5$ fm^{-1} (2.0 fm^{-1}) were used for energies up to (above) 200 MeV. Units: S_i and d_i (1), b_1 (MeV fm^3), b_3 (MeV fm^5).
[a]Ref. [Kel 89b]; [b]Ref. [Kel 90a]; [c]Ref. [Kel 90b]; [d]Ref. [Fla 90]; [e]Second solution.

If it can be shown that the discontinuity in b_1 is indeed due to the different free interactions and that the energy variation of b_3 can be explained by correlations and/or insensitivity of the data to this parameter, the effective interaction could then be said to display a reasonably smooth energy dependence.

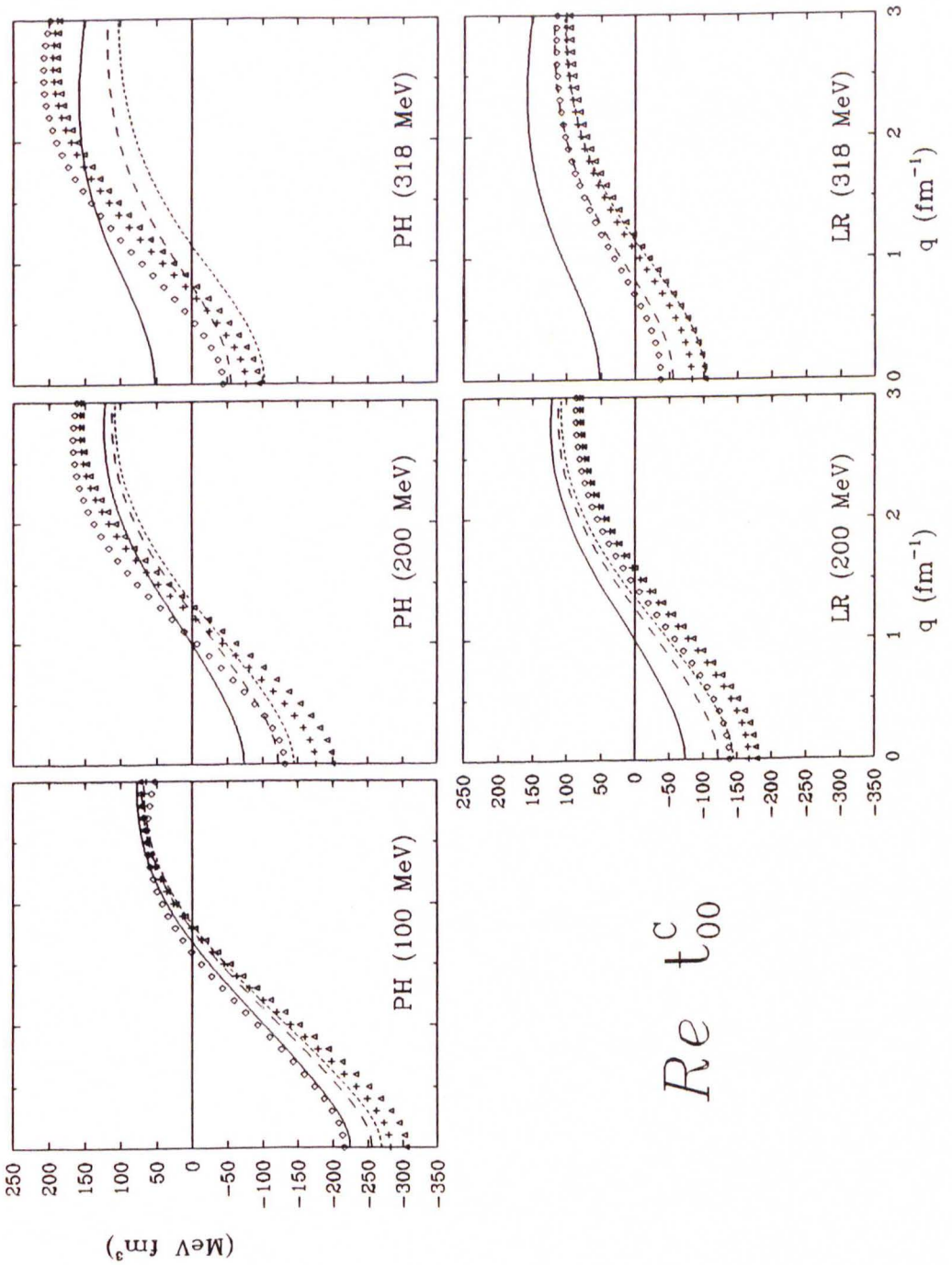

Figure 7.64: Comparison of the EMP(^{16}O), PH, and LR interactions for the Ret_{00}^C component; $k_F = 0.6$ fm^{-1} (triangles, short dashes), $k_F = 1.0$ fm^{-1} (crosses, dashes), and $k_F = 1.4$ fm^{-1} (diamonds, solid).

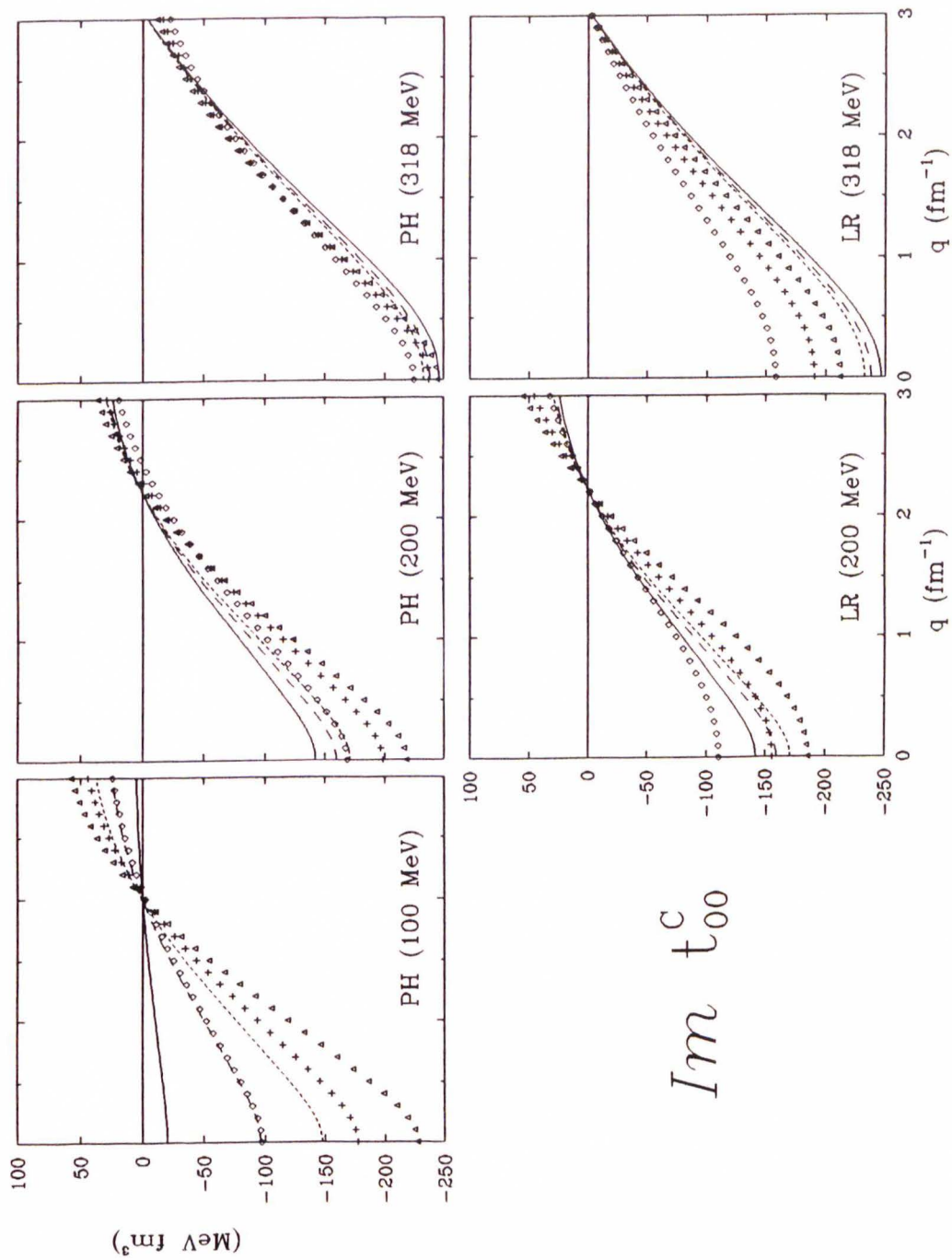

Figure 7.65: Comparison of the EMP(^{16}O), PH, and LR interactions for the Imt_{00}^{C} component; $k_F = 0.6$ fm^{-1} (triangles, short dashes), $k_F = 1.0$ fm^{-1} (crosses, dashes), and $k_F = 1.4$ fm^{-1} (diamonds, solid).

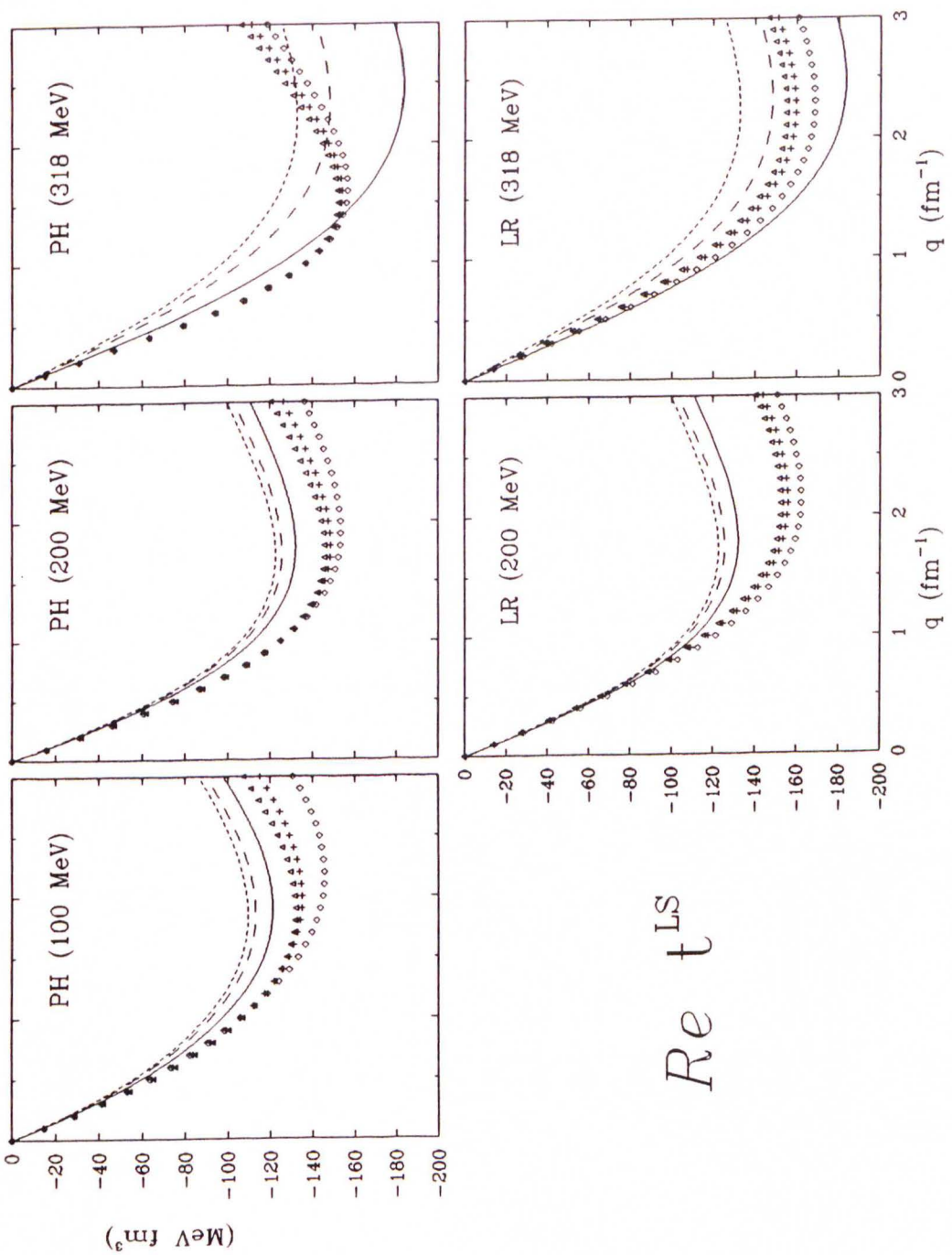

Figure 7.66: Comparison of the EMP(^{16}O), PH, and LR interactions for the Ret_0^{LS} component; $k_F = 0.6$ fm^{-1} (triangles, short dashes), $k_F = 1.0$ fm^{-1} (crosses, dashes), and $k_F = 1.4$ fm^{-1} (diamonds, solid).

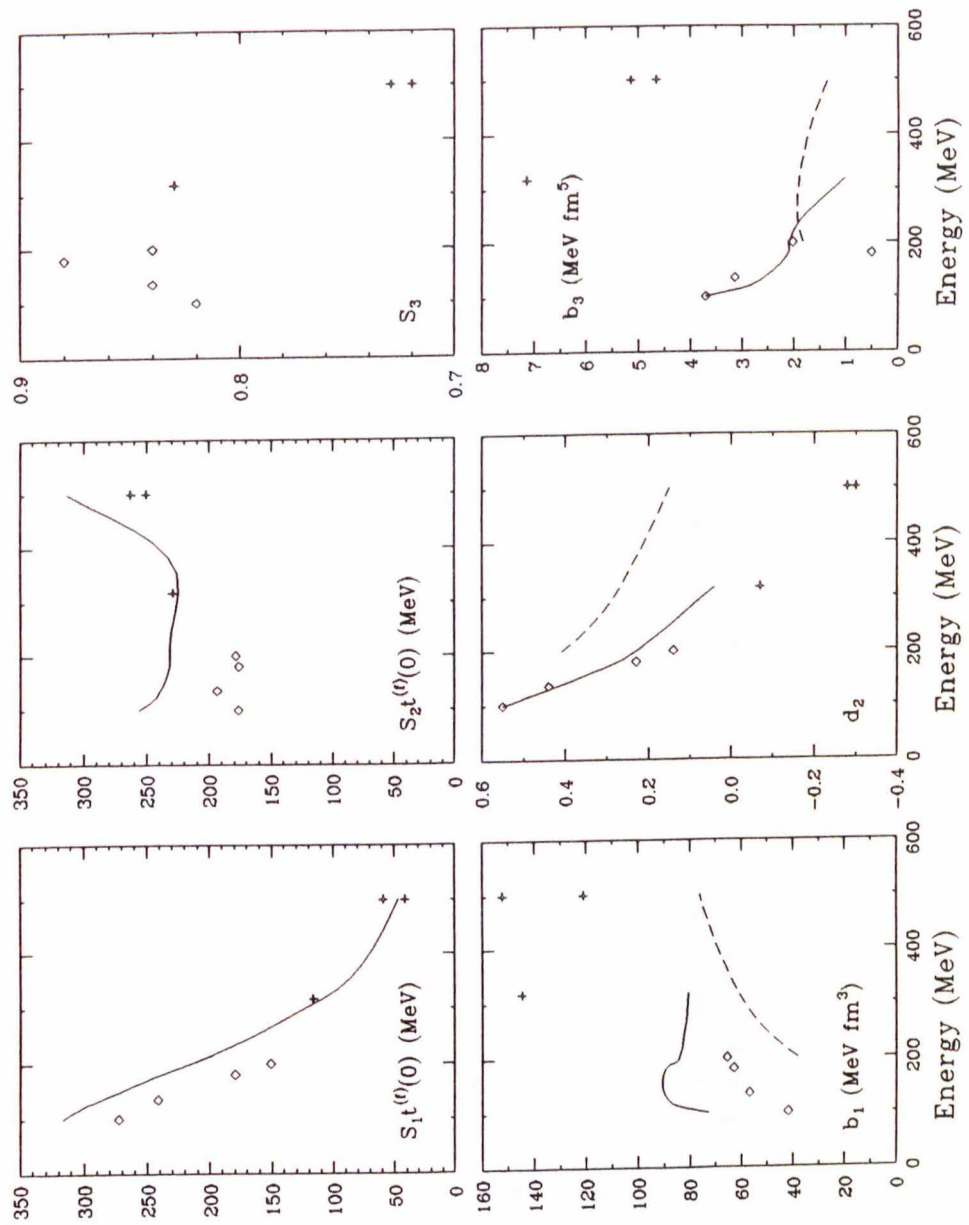

Figure 7.67: Energy dependence of the interaction parameters for ^{16}O. 100–200 MeV (diamonds) with PH free interaction, 318 and 500 MeV (crosses) with FL free interaction. For comparison, the energy dependence of the PH (solid) and LR (dashes) interaction are also given.

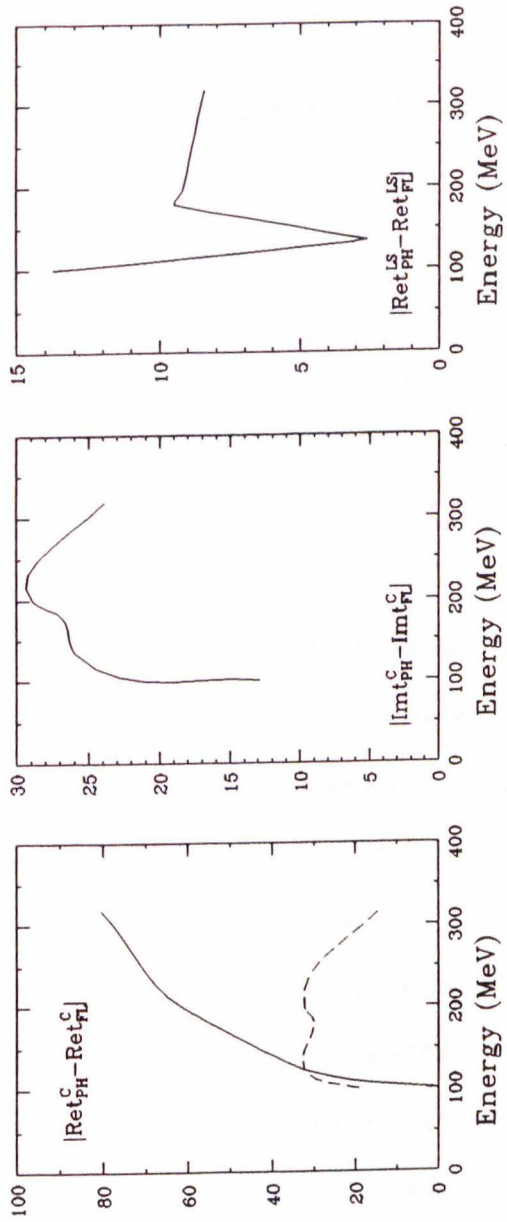

Figure 7.68: Difference of the PH and FL t-Matrices. Plotted is the absolute value of the difference. In the first panel, dashes denote $q = 0.0$ fm^{-1}, solid $q = 2.0$ fm^{-1}. In the second panel the difference is plotted for $q = 0.0$ fm^{-1}, in the third panel for $q = 2.0$ fm^{-1}.

7.8 Outlook

In order to resolve the question whether there is indeed a discontinuity in the energy dependence of our model near 300 MeV, it would be helpful to complement our data for 200 and 318 MeV by measurements at an intermediate energy, say 260 MeV. Also, the empirical interaction analysis should be done with the FL t-matrix for all the energies. An independent check for the absorption mechanism above 300 MeV would be for example $(e, e'p)$ measurements where the proton is generated deep inside the high-density interior of the nucleus.

Measurements which would be useful to extend the empirical effective interaction to higher energies include inelastic measurements above 500 MeV where data for the low-lying collective states are so far sparse. Measurements of the inelastic $D_{\alpha\beta}$ observables for energies below 300 MeV would provide a challenging test for our present interactions.

To extend the momentum transfer range of the effective interaction, the corresponding range for electroexcitation measurements and analyses should be extended. It should be interesting to see whether or not coupled channels effects become important at large momentum transfers. The present analysis of the ^{40}Ca(e, e') data should be improved and extended to strong states such as the 1^-_1 state at 5.903 MeV. This also holds for the analysis of available electroexcitation data of other targets such as ^{28}Si.

Systematic fits to the elastic scattering data, which are abundant for many of the interesting targets at many energies, should help to illuminate further the A and E dependence of the effective interaction. On the theoret-

ical side, the density dependence of the IA2 should be clarified. To achieve a clear separation of all the different contributions to the density dependence, relativistic full-folding calculations which include medium modifications due to Pauli blocking, dispersion, isobars, etc., are necessary.

The nonlocal effects which where found for the empirical effective interaction should stimulate the development of a theory of the finite nucleus which predicts the necessary corrections to the LDA. The $(1 + \rho\partial/\partial\rho)$ prescription should be extended to low energies. In particular, the role of second order terms should be explored. Finally, a theory which explains both the increasing short-range repulsion and increasing absorption above 300 MeV should be developed.

8 Summary and Conclusions

We have measured the cross sections and analyzing powers for many states of ^{16}O and of the calcium isotopes ^{40,42,44,48}Ca at 100 and 200 MeV. We also made measurements at 318 MeV for ^{32,34}S and the calcium isotopes. The data for ^{16}O and ^{40}Ca are the ones which are discussed in this work and are used for the study of effective interactions. Data for ^{16}O at 318 MeV for these studies were taken from [Kel 90b]; the 500 MeV data for ^{16}O are from [Fla 90], the ones for ^{40}Ca from [Set 85, Lis 89]. We study effective interactions for natural-parity isoscalar transitions in self-conjugate nuclei within a local $t\rho$ folding model. We assume that for this type of transition we have full and accurate knowledge of both the reaction mechanism and the nuclear structure. We believe that direct one-step processes which can be treated within the single-scattering approximation are the dominant reaction process and that channel coupling effects are negligible. All the nuclear structure information which is relevant for the extraction of an effective interaction is assumed to be accurately known from complementary electron scattering measurements. Charge symmetry ensures that for our self-conjugate targets neutron and proton densities are very nearly equal.

If proton scattering is to be used for nuclear structure studies as a probe complementary to electron scattering, we must assure ourselves of the accuracy of the effective interaction for proton-nucleus scattering. It has been found that even at high energies medium modifications to the effective interaction still remain important. Several theoretical models are available

which try to estimate these medium modifications. However, although these models all contain the basic ingredients of Pauli blocking and binding energy corrections and predict qualitatively similar medium effects, their quantitative predictions differ substantially when implemented via the local density approximation (LDA) for nucleon-nucleus scattering. Since all of the models are based on different NN potentials and employ different approximations and numerical procedures to arrive at a local effective interaction, an estimate of their accuracy and a comparison of the individual models is very difficult. The accuracy of these theoretical models is inadequate for the use in nuclear structure studies where we want to minimize the residual uncertainties in the transition densities due to uncertainties in the reaction mechanism and the effective interaction.

We have, therefore, developed a phenomenology which is guided by theory and which can be used to fit various theoretical models, as well as data. With a physically motivated analytical form which involves only six free parameters, this empirical effective interaction not only facilitates the task of comparing theories to each other, but also allows a quantitative comparison of the effective interaction parameters fitted to data with those from theory. Finally, the empirical interaction proves to be much superior in its description of the data, making it an accurate tool for nuclear structure studies. The phenomenology also permits study of the validity of the LDA prescription in a manner which is largely independent of the accuracy of nuclear matter calculations. If the LDA is to be considered sound, the empirical interaction will satisfy three criteria. First, a unique interaction must be capable of

describing all relevant data for a given target and energy. Second, a more stringent condition is that the effective interaction be independent of target. Third, the parameters should vary smoothly with energy and hopefully be comparable with the parameters from theory.

In this work, we have demonstrated for the case of both surface and interior states of ^{16}O and ^{40}Ca that we can indeed find a unique interaction which describes all the states of a particular target at a given energy. Elastic scattering can be either explicitly included in the fit or just predicted based on the effective interaction from inelastic scattering. Either way, we find no significant differences in the quality of the description of elastic scattering for energies above 100 MeV. Our work shows, therefore, that proper treatment of the rearrangement contribution ensures consistency between elastic and inelastic scattering. We furthermore established the A independence of the empirical effective interaction by demonstrating that, although the numerical values of the parameters from fits to different targets might vary slightly, fits to different data sets nevertheless represent the same interaction. Data for ^{16}O are described nearly as well by the interaction fitted to ^{40}Ca data, and data for ^{40}Ca are described well by the interaction from ^{16}O. Thus, we find that the effective interaction, although it is strongly dependent on the local density, is largely insensitive to the target. The LDA appears to provide a reasonable and accurate model for the density dependence of the effective interaction in nuclei.

As we go from 135 to 100 MeV, the ability of the empirical effective interaction to accurately describe the data, deteriorates rapidly. This applies

especially to analyzing power data at 100 MeV which look dramatically different from the ones above 135 MeV. While the analyzing powers above 135 MeV have essentially the same features, albeit sharper and more pronounced for the higher energies, most of the structure in the 100 MeV analyzing powers has vanished or is very suppressed. The fact that at 100 MeV the PH interaction is superior to our empirical effective interaction in the description of elastic scattering, and is nearly as good for inelastic scattering, suggests that the consistency requirement between elastic and inelastic scattering might have broken down. One possible source that could cause such a breakdown is the rearrangement contribution which might require second order terms at this energy in order to describe the density dependence adequately. Another possibility is that coupled channel effects might become significant at this energy. Finally, interior contributions might be stronger than at higher energies. To clarify all these problems, further investigations at lower energies are needed.

Our empirical effective interaction differs from theoretical interactions in several important ways. Between 100 and 200 MeV we find that the interaction at low densities is suppressed relative to the free interaction—the effective interaction for finite nuclei never heals to the free interaction, even at the surface. Second, the subsequent density dependence of the empirical interaction is substantially smaller than predicted by nuclear matter calculations. This means that modifications of the interaction are less effective in the high-density interior of a finite nucleus than expected for infinite nuclear matter of the same density. These results have been interpreted as a nonlocal

density dependence beyond the LDA which is characteristic of finite nuclei. Evidently, the nonlocal effect is due to the finite spread of the nucleon wave functions. Nevertheless, the consistency of the empirical interaction suggests that a local approximation to the effective interaction for finite nuclei is still possible and reasonable.

For 318 MeV we find that the nature of the medium modifications to the effective interaction appear to change. At this energy the damping factor applied to the imaginary central component of the interaction is smaller in magnitude and of opposite sign than predicted by theory. In contrast to the behaviour at lower energies, where Pauli blocking is responsible for the damping of the absorption, the phenomenology suggests that for energies near 318 MeV absorption is enhanced. A similar effect with greater magnitude has been reported for 500 MeV [Fla 90]. Therefore, a new absorption mechanism may be important for energies above 300 MeV which is not present in the existing theories. This new mechanism may be associated with the pion threshold. The second observation is that the density dependence of the real central interaction is much stronger than theoretical predictions. This is also in contrast to the case at lower energies. Finally, although the density dependence of the spin-orbit interaction is much more difficult to determine above 200 MeV, the fits suggest enhanced density dependence above 300 MeV.

For all the energies that we have examined, the energy dependence of the Pauli blocking parameter appears to be consistent with the E^{-1} behaviour which is predicted by a simple phase space argument and which is also supported by more sophisticated nuclear matter calculations. Since we

interpret the slight discontinuities in the energy dependence of some of the other parameters to be mainly due to the use of very different free interactions in the fit, we believe that the effective interaction varies reasonably smoothly with energy.

Finally, we have compared our results with the relativistic IA2 model for elastic scattering, as well as with a recent global optical potential from Dirac phenomenology (DP). We found that the Dirac phenomenology provides an exceptionally good description for our elastic data and that, therefore, we almost can consider it as a benchmark for optical potentials generated by our empirical interactions. At 200 and 318 MeV, where our empirical results are of nearly the same quality as the DP results, we also find that our empirical potentials are very similar to the ones from Dirac phenomenology. At 100 MeV, where our empirical interaction performs poorly, we find significant differences in the imaginary central potentials and slight differences in the real central potentials. This comparison will give new impetus to reexamine the 100 MeV interaction.

We find that the optical potentials which emerge from our phenomenological analysis are very similar to the Schrödinger equivalent potentials from the relativistic IA2. The contribution of virtual $N\overline{N}$ pairs, which distinguishes the relativistic approach from the nonrelativistic impulse approximation, is evidently simulated by an effective density dependence which is comparable to that of our phenomenology. It would probably be very profitable and instructive, therefore, to cast relativistic calculations into a form similar to our phenomenology so that theoretical predictions of the density

dependent parameters could be quantitatively compared to their fitted values. New relativistic calculations probably should also try to elucidate the role of full-folding and additionally incorporate medium effects such as Pauli blocking and binding energy corrections.

A Nuclear Densities

The nuclear structure information needed for the extraction of an effective interaction from proton scattering data within a $t\rho$ folding model comes from electron scattering. In the plane-wave Born approximation (PWBA) the unpolarized cross section for the electroexcitation of a nucleus from a state of angular momentum J_i to a state of angular momentum J_f can be written in terms of longitudinal and transverse contributions as [DeF 66]

$$\begin{aligned}\sigma_{\mathrm{PWBA}}(q) &= \eta\sigma_{\mathrm{Mott}}Z^2\left[\frac{q_\mu^4}{q^4}|F^L(q)|^2\right. \\ &\quad \left.+\left[\frac{1}{2}\frac{|q_\mu^2|}{q^2}+\tan^2\frac{\theta}{2}\right]|F^T(q)|^2\right], \qquad \text{(A.1)}\end{aligned}$$

where q^2 and q_μ^2 are the squares of the three- and four-momentum transfers, respectively, Z is the atomic number of the target nucleus, and θ is the scattering angle. The cross section for a point-charge, σ_{Mott}, is given by

$$\sigma_{\mathrm{Mott}} = \left[\frac{\alpha}{2E_P}\right]^2\frac{\cos^2(\theta/2)}{\sin^4(\theta/2)}, \qquad \text{(A.2)}$$

where E_P is the incident energy and α is the fine structure constant. The density of final states factor is

$$\eta = \left[1+\frac{k_f - k_i\cos\theta}{E_T}\right]^{-1}, \qquad \text{(A.3)}$$

where k_f (k_i) is the exit (incident) electron momentum and E_T is the total energy, including the rest mass, of the recoil nucleus. Factors of $\hbar$ and c have been suppressed. All the structure information is contained in the longitudinal and transverse form factors $F^L(q)$ and $F^T(q)$, respectively. The simplest

class of transitions for which the relevant structure information can be completely determined from electron scattering consists of those natural-parity isoscalar transitions of self-conjugate nuclei whose transverse form factors are negligible. In the PWIA the Jth multipole $F_J^L(q)$ of the longitudinal form factor is related to the Fourier-Bessel transform of the transition charge density $\rho_J(r)$ by

$$F_J^L(q) = \frac{\sqrt{4\pi}}{Z} \frac{\hat{J}_f}{\hat{J}_i} \int dr\, r^2 j_J(qr) \rho_J(r), \tag{A.4}$$

where $\hat{x} = \sqrt{2x+1}$. The results of electromagnetic structure analyses are often presented in terms of multipole moments of the transition density. The transition amplitude for a CJ transition is directly proportional to the matrix element

$$M_{\lambda J} = \int dr\, r^{\lambda+2+k} \rho_J(r), \tag{A.5}$$

where $k = 0$ ($k = 2$) for $J > 0$ ($J = 0$). For the ground state one recovers with $4\pi M_{\lambda=0} = Z$ the nuclear charge. Finally, the transition radius is the rms radius for a specific excitation

$$R_{\rm tr}^2 = M_{J+2,J}/M_{JJ}. \tag{A.6}$$

The plane-wave approximation, Eq. (A.1), does not account for the distotion of the incoming and outgoing waves by the Coulomb field of the target nucleus. For the actual analysis of the data, the distortions due to the spherical component of the ground-state charge distribution are included in the distorted-wave Born approximation (DWBA) [But 86].

Ground state as well as transition charge densities are usually expressed

as a linear series of the form

$$\rho_l(r) = \sum_{n=1}^{N} a_n f_{nl}(r), \tag{A.7}$$

where the radial basis functions $f_{nl}(r)$ in principle can be drawn from any convenient complete set. Most often used in the analysis of electron scattering data, however, are certain variations of the Fourier-Bessel expansion, e.g.

$$\begin{aligned} f_{nl}(r) &= j_l(q_n r), \quad \text{where } j_l(q_n R) = 0 \quad \text{(FBE)} \\ f_{nl}(r) &= q_n j_l(q_n r), \quad \text{where } j_{l-1}(q_n R) = 0 \quad \text{(MHFBE).} \end{aligned} \tag{A.8}$$

These basis functions are all defined to vanish for $r > R$, the cutoff radius. An alternative expansion, used for the ^{16}O 1_1^- state, is the Laguerre-Gaussian expansion (LGE)

$$f_{nl}(r) = x^l e^{-x^2} L_n^{l+1/2}(2x^2), \tag{A.9}$$

where $x = r/b$ and $L_n^a(z)$ is a generalized Laguerre polynomial of the form

$$L_n^a(z) = \sum_{m=0}^{n} (-)^m \frac{\Gamma(a+n+1)}{\Gamma(n-m+1)\Gamma(a+m+1)} \frac{z^m}{m!}. \tag{A.10}$$

The expansion is complete for any value for the harmonic oscillator parameter b. For a thorough discussion of the properties and the application of the various available expansions we refer to [Kel 88].

In the following we tabulate (Tables A.1 and A.2) and graphically display (Figures A.1–A.3) the ground state and transition charge densities used in our analysis. Point-nucleon densities were obtained from the charge densities by numerically unfolding the nucleon form factor $f(q) = [1 + (q/\Lambda)^2]^{-2}$, where $\Lambda = 4.33$ fm^{-1}. Source for the ground state density of ^{16}O is [Lah 82], for ^{40}Ca it is [Emr 83]. Source for the transition charge densities of ^{16}O

is [But 86]. Reference for the transition charge densities of the 0_2^+ state of ^{40}Ca is [Har 84], for all the other states [Mis 83]. It should be pointed out that the electron scattering analysis of the ^{40}Ca data is considered to be still preliminary (J. J. Kelly, private communication).

J_n^π	0_1^+	3_1^-	2_1^+	1_1^-	4_1^+	2_3^+	0_3^+
R,b	8.0	8.0	8.0	1.8	8.0	8.0	8.0
exp	FBE	FBE	FBE	LGE	FBE	FBE	FBE
a_1	202.38	99.542	73.808	619.386	26.944	50.471	-8.974
a_2	447.93	303.073	158.471	136.488	69.711	119.461	-82.744
a_3	335.33	402.446	108.520	-57.730	75.343	95.774	-147.279
a_4	35.030	293.928	-0.544	2.520	43.729	7.200	-100.967
a_5	-122.93	125.227	-55.323	2.033	13.465	-58.751	21.704
a_6	-103.29	32.413	-34.005	1.693	3.114	-35.584	83.182
a_7	-34.036	4.905	-5.508	-1.839	-1.504	13.435	-9.535
a_8	-4.1627	-0.450	1.143	0.582	0.620	-4.283	-0.713
a_9	-9.4435	-0.229	-0.181		-0.254	1.488	0.376
a_{10}	-2.5771	0.210	0.021		0.107	-0.556	0.248
a_{11}	2.3759	-0.125	-0.023		-0.047	0.221	-0.952
a_{12}	-1.0603	0.067	0.019		0.021	-0.092	3.769
a_{13}	0.41480						
M_{JJ}	0.6367	14.20	2.791	-0.0195	20.5	1.843	1.062
$R_{\rm tr}$	2.737	4.049	4.026	16.48	4.48	3.98	

Table A.1: Expansion coefficients (without uncertainties) for ground state and transition charge densities of ^{16}O [Lah 82, But 86]. The coefficients are in units of 10^{-4} fm^{-3}. R, b and $R_{\rm tr}$ are in units of fm; M_{JJ} is in units of e·fm^{J+k}, see Eq. (A.5).

J_n^π	0_1^+	0_2^+	3_1^-	2_1^+	5_1^-	3_2^-	3_3^-
R,b	8.0	10.0	8.0	8.0	8.0	8.0	8.0
exp	FBE	FBE	MHFBE	MHFBE	MHFBE	MHFBE	MHFBE
a_1	448.46	-2.2476	179.482	81.665	56.553	44.985	33.781
a_2	613.26	-17.616	351.656	128.609	137.879	50.232	37.595
a_3	-16.818	-21.914	192.042	32.624	141.606	-33.921	-25.548
a_4	-262.17	15.940	-27.665	-31.568	73.720	-80.067	-57.362
a_5	-29.725	40.341	-67.746	-14.666	15.049	-39.761	-27.150
a_6	85.534	-2.7266	-21.607	-4.262			
a_7	35.322	-36.432	2.272	-5.767			
a_8	-4.8258	-25.479					
a_9	-3.9346						
a_{10}	2.0338						
a_{11}	0.25461						
a_{12}	-0.17794						
a_{13}	0.067394						
a_{14}	-0.021033						
M_{JJ}	1.5917	0.700	50.55	4.493	542.1	15.87	11.86
R_{tr}	3.450		4.817	4.812	5.344	5.496	5.473

Table A.2: *Expansion coefficients (without uncertainties) for ground state and transition charge densities of ^{40}Ca [Emr 83, Mis 83, Har 84]. The coefficients are in units of 10^{-4} fm^{-3}. R, b and R_{tr} are in units of fm; M_{JJ} is in units of e·fm^{J+k}, see Eq. (A.5).*

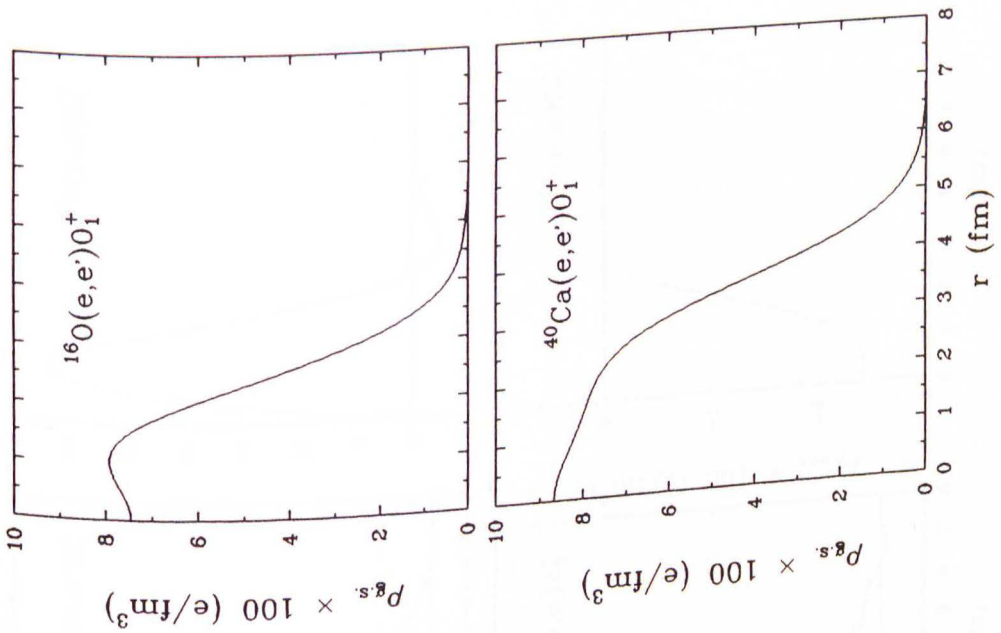

Figure A.1: Ground state charge densities for ^{16}O [Lah 82] and ^{40}Ca [Emr 83].

Figure A.2: Transition charge densities for ^{16}O [But 86].

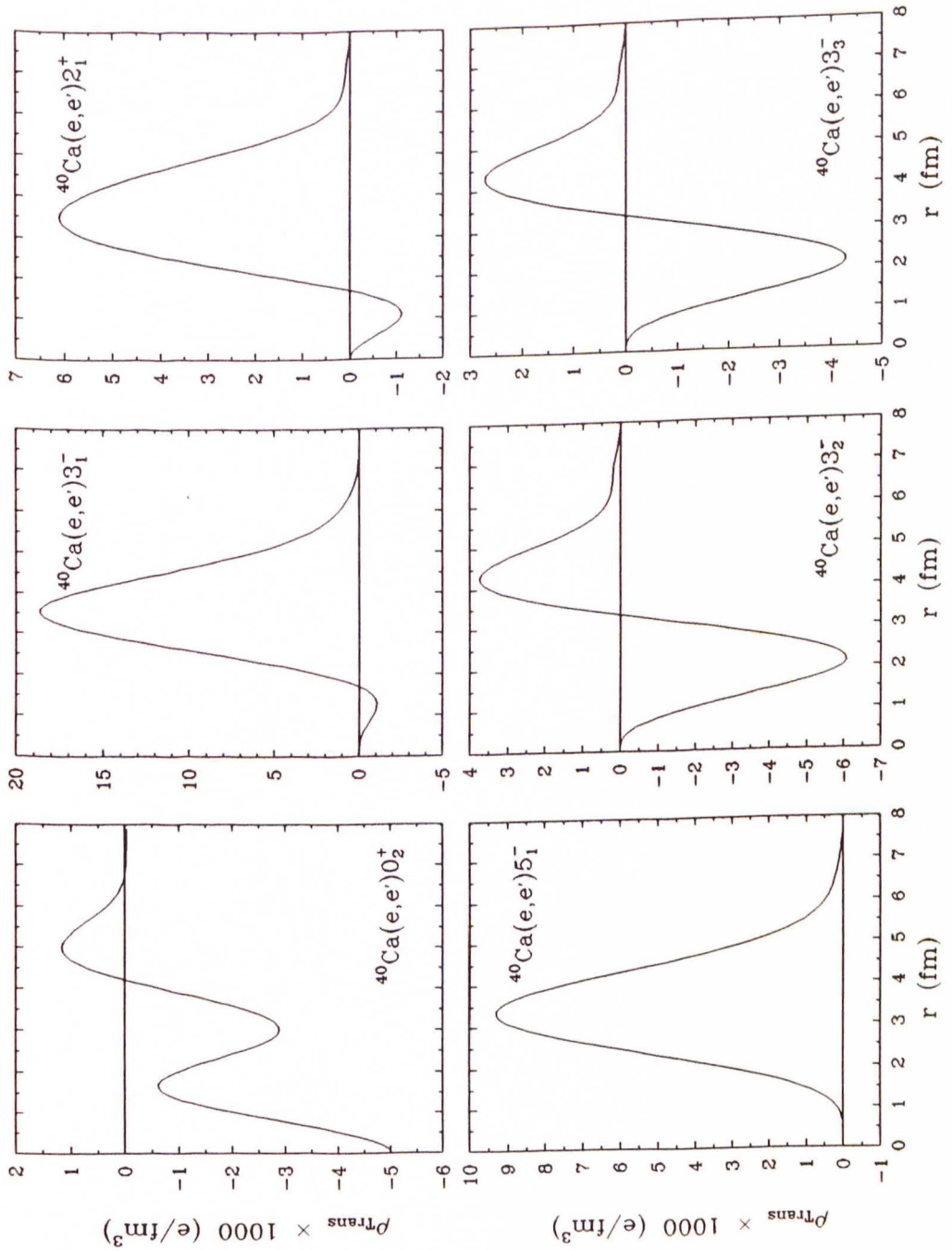

Figure A.3: Transition charge densities for ^{40}Ca [Mis 83, Har 84].

B Differential Recoil Diagrams

Consider inelastic scattering in the laboratory frame as shown in Figure B.1. Four-vector conservation requires that

$$P_1 + P_2 = P_3 + P_4. \tag{B.1}$$

Using Lorentz invariance one can eliminate the unknown momentum of the recoiling (excited) target nucleus by

$$P_4^2 = (M + X)^2 = (P_1 + P_2 - P_3)^2, \tag{B.2}$$

where M is the target nucleon mass and X the excitation energy. After some algebraic manipulations one obtains with the auxiliary quantity $A = E_1 + M$ (the total energy of the system)

$$AE_3 = m^2 + E_1 M - MX - \frac{X^2}{2} + p_1 p_3 \cos\theta. \tag{B.3}$$

In this equation m, p_1 and E_1 are the mass, three-momentum and (total) energy of the incoming projectile, p_3 and E_3 the corresponding quantities of the scattered (i.e. outgoing) projectile, and θ is the scattering angle in the laboratory frame. Expressing E_3 in terms of m and p_3 and introducing $B = m^2 + E_1 M - MX - \frac{X^2}{2}$, yields a quadratic equation for p_3

$$\underbrace{(A^2 - p_1^2 \cos^2\theta)}_{a} p_3^2 + \underbrace{(-2Bp_1 \cos\theta)}_{b} p_3 + \underbrace{(A^2 m^2 - B^2)}_{c} = 0. \tag{B.4}$$

The solution of this equation is

$$p_3 = \frac{-b + \sqrt{b^2 - 4ac}}{2a}, \tag{B.5}$$

which yields the energy of the scattered projectile

$$E_3 = \sqrt{p_3^2 + m^2}. \tag{B.6}$$

If E_{a3} denotes the energy of any reference state and E_{b3} the one of any other state (e.g. a different excited state of the same nucleus or any excited state of any other nucleus), we can calculate the differential recoil, defined as

$$\Delta = E_{a3} - E_{b3}. \tag{B.7}$$

Figure B.2 shows the differential recoil (here expressed as Q value, $Q = -\Delta$) at 100 and 200 MeV, with the gound state of ^{16}O as reference state, for the measured excited states of oxygen and beryllium. Since at some angles we also observed the lowest two states of carbon, they have been included as well.

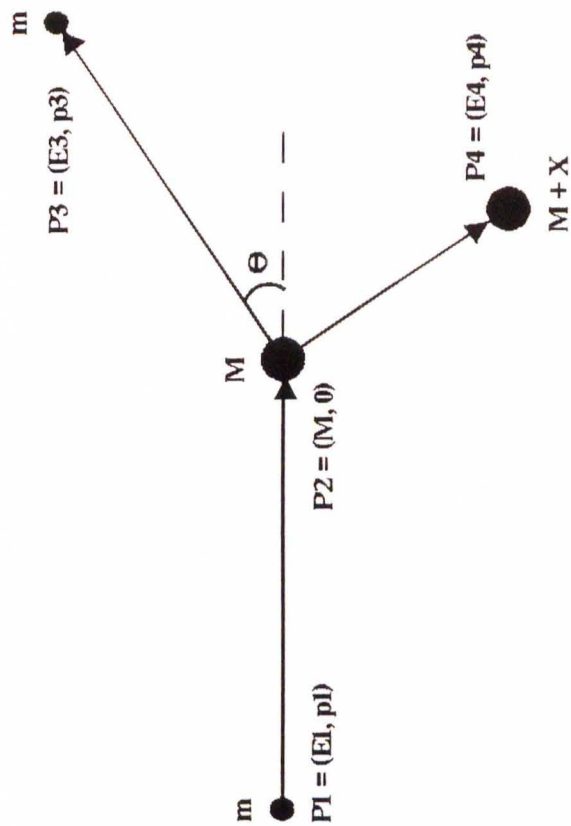

Figure B.1: Kinematics of an inelastic binary reaction.

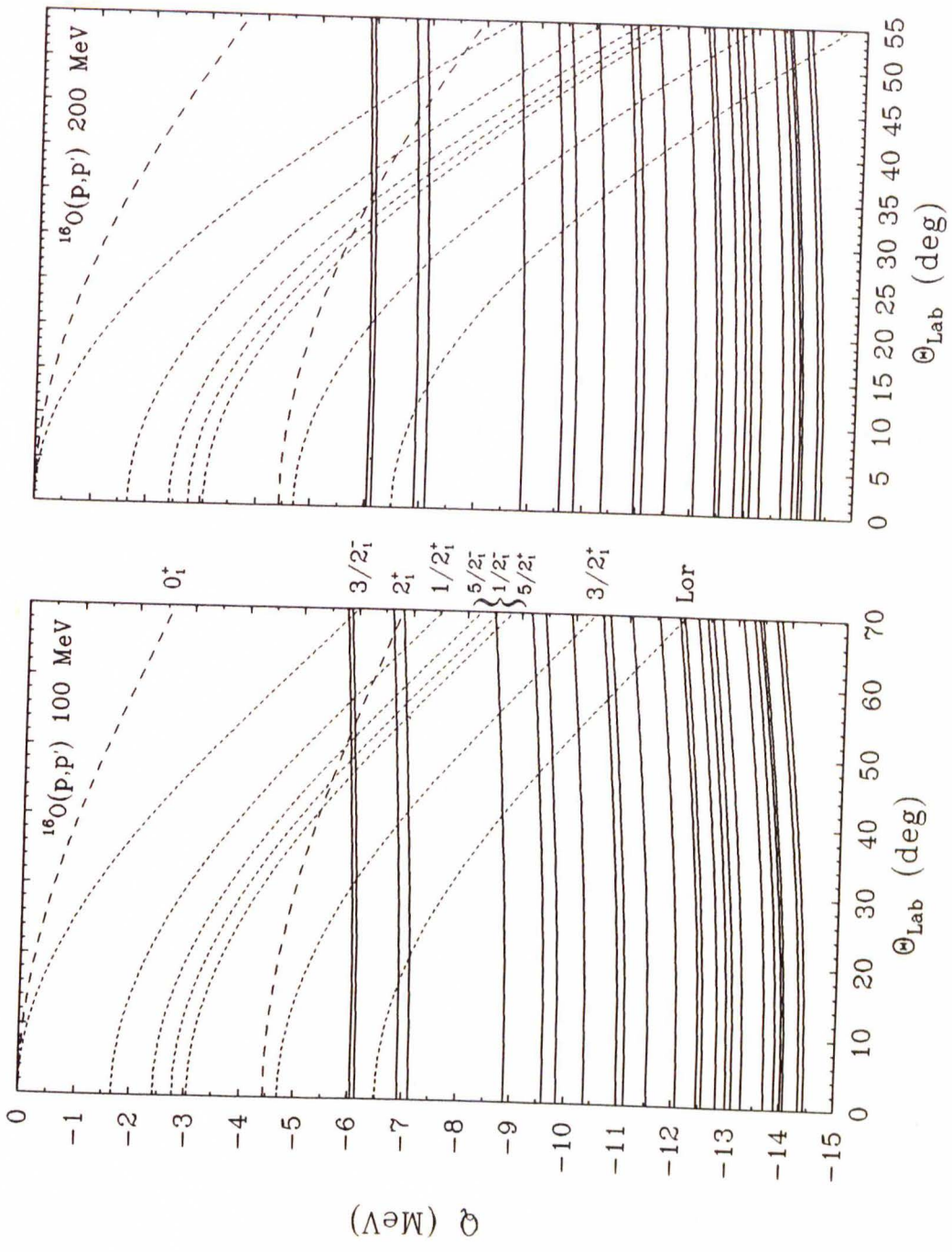

Figure B.2: Differential recoil for 100 and 200 MeV kinematics. Reference state is the ground state of ^{16}O. The dashed curves denote ^{12}C, the dotted curves ^{9}Be.

C RAYTRACE Simulations of the K600

We investigated the impact of the H- and K-coils on the Θ_{tgt} calibration. The kinematic coils are used to compensate for the k appropriate to a particular reaction and to compensate for aberrations (important for large acceptances). The polynomial for Θ_{tgt} which was given in Chapter 4 is based on a reaction with a specific value of k and corresponds to one specific set of H- and K-coil settings. For these studies we used an improved IUCF version of the RAYTRACE code originally developed by Spencer and Enge, and by Enge and Kowalski [Spe 67, Eng 70]. The output was transformed, where necessary, to the focal plane coordinates (x_f, θ_f). Figure C.1 shows the variation of rays with different δ's across the focal plane; the locations of the wire plane and the VDC windows are based on design values. Note that the D-coordinate system is a *lefthanded* system. In the following figures we show the effect of the kinematic coils on both the focal plane and on nuclear lines ($k = 0$) as observed in $x_f\theta_f$; we used the angles which are defined by the multislit in Chapter 4 as input for the angles at the target. Calculations were done for seven values of δ between $\pm 4.65\%$ (c.f. Figure C.1). The strength of the kinematic coils is here represented as the ratio of the K-coil and dipole 2, $r_K = B_K(0)/B_D(0)$, and the ratio of the H-coil and dipole 1, $r_H = B_H(0)/B_D(0)$, respectively. The $B(0)$ are the field strengths experi-

enced by the center ray[1]. The K-coil both shifts and, since r_k is usually a few percents only, slightly deforms the focal plane; the effect in $x_f\theta_f$ is a shift and a tilt of a nuclear line. Conversely, the K-coil can therefore be used to correct the shift of the focal plane and the associated tilt in $x_f\theta_f$ caused by a reaction with $k \neq 0$. The magnitude of the tilt is focal plane position dependent. The main effect of the H-coil is a slight rotation of the focal plane and a shift and bend of nuclear lines in $x_f\theta_f$. The H-coil can therefore be used to correct the focal plane rotation due to $(x \mid \theta\delta) \neq 0$ and to straighten out aberrations due to $(x \mid \theta^2) \neq 0$.

To estimate the effect of the kinematic coils on our calibration polynomial for Θ_{tgt}, we consider the central ray ($\delta = 0$) with $x_f = 670.13$ mm and $\theta_f = 641.31$ mrad (from RAYTRACE). For this ray an H-coil variation of $\Delta r_H = 0.01$ causes variations of $\Delta x_f = 5.38$ mm and $\Delta\theta_f = 0.40$ mrad, respectively. A K-coil variation of $\Delta r_K = 0.01$ causes variations of $\Delta x_f = 6.44$ mm and $\Delta\theta_f = 1.45$ mrad, respectively. In Chapter 4, the measurements for the gold target and the BeO target were taken with kinematic coil

[1] For the K-coil, we have with the effective length $L(0) = 47.5$ cm, the nominal field at the center $B(0) = 5.66$ GA^{-1}, and the ratio $Q/D = -0.013$ (ratio of the quadrupole and dipole components of the K-coil)

$$\int B(x,z)dz = B(0)L(0)[1 + (Q/D)x]; \tag{C.1}$$

for the H-coil, with $L(0) = 24.5$ cm, $B(0) = 4.70$ GA^{-1}, and $H/D = -3.6 \cdot 10^{-4}$ (ratio of the haxapole and dipole components of the H-coil) we have

$$\int B(x,z)dz = B(0)L(0)[1 + (H/D)x^2] \tag{C.2}$$

(P. Schwandt, IUCF, private communication).

setting that differed by $\Delta r_H = 0.01$ and $\Delta r_K = 0.02$. We found that the reproducibility of Θ_{tgt} for gold was worse by about 2.4 mrad than for BeO when the polynomial based on the BeO data was used. The effect on the angle at the target is evaluated for the central ray with

$$\Delta\Theta_{tgt} = \sqrt{\left(\frac{\partial\Theta_{tgt}}{\partial x_f}\right)^2 (\Delta x_f)^2 + \left(\frac{\partial\Theta_{tgt}}{\partial\theta_f}\right)^2 (\Delta\theta_f)^2} \qquad \text{(C.3)}$$

and the coefficients from Eq. (4.11). For our case of gold and BeO we find that the H-coil makes a contribution of 0.39 mrad and the K-coil a contribution of 1.65 mrad to the value of Θ_{tgt}; both together change Θ_{tgt} by 2.03 mrad. Considering that the H-coil does not vary much during a run period and that the K-coil setting depends strongly on k, this calculation shows that the angle inaccuracies for targets with different k are caused mainly by variations in the kinematic coil settings.

Finally, we want to present calibration polynomials for Θ_{tgt} and for δ (used for missing mass spectra) which we found for rays generated with RAYTRACE. The computed rays sample a grid in $r_K r_H$ where r_H and r_K vary betweeen ± 0.25, include eight (with the central ray) angles at the target, and sample seven values of δ between $\pm 4.65\%$ (we fit a total of 1524 rays). For Θ_{tgt} and δ we find

$$\begin{aligned}\Theta_{tgt} \;=\; & a + bx_f + c\theta_f + dr_K + er_H \\ & + fx_f^2 + g\theta_f^2 + hx_f\theta_f + ir_K x_f + jr_H x_f + kr_K\theta_f + lr_H\theta_f \\ & + mr_K x_f^2 + nr_H\theta_f^2, \end{aligned} \qquad \text{(C.4)}$$

and

$$
\begin{aligned}
\delta \;=\;& a + bx_f + c\theta_f + dr_K + er_H \\
& + fx_f^2 + g\theta_f^2 + hx_f\theta_f + ir_K x_f + jr_H x_f + kr_K\theta_f + lr_H\theta_f \\
& + mr_H r_K + nr_K x_f^2 + or_K\theta_f^2 + pr_K x_f\theta_f \\
& + qr_H x_f^2 + sr_H\theta_f^2 + tr_H x_f\theta_f,
\end{aligned}
\tag{C.5}
$$

respectively. The values of the parameters are listed in Table C.1. The uncertainties are estimated from the error matrix and reflect the large correlations among some of the coefficients. The $\Theta_{\rm tgt}$ polynomial reproduces the angle at the target for the input rays to better than 0.17 mrad. In the case of the δ polynomial, in the final fit some of the coefficients were held fixed to values from a previous fit. We find that this polynomial reproduces δ for the input rays to about 0.03% (absolute value—δ has the units %).

Polyn.	Θ_{tgt}		δ	
Coeff.	Value	$\pm\Delta$ (%)	Value	$\pm\Delta$ (%)
a	-3.04985E+02	1.1	7.33331E+00	3.7
b	-5.41538E−03	34.4	-1.09068E−02	6.8
c	4.99095E−01	2.3	1.63160E−03	-
d	-1.30807E+02	1.9	4.86517E+01	-
e	-5.79378E+01	26.3	-3.88741E+01	-
f	-9.38733E−06	7.3	-1.05095E−06	52.8
g	5.70454E−05	17.7	-1.84326E−06	22.4
h	-7.12595E−05	4.6	3.99000E−07	-
i	-2.61264E−02	16.2	1.88963E−03	-
j	-4.38560E−03	20.0	-2.52274E−02	35.1
k	1.90439E−01	1.8	-9.05960E−02	3.3
l	1.96344E−01	24.7	1.68374E−01	5.8
m	-1.92327E−05	16.7	-6.77000E−01	-
n	-1.27212E−04	30.2	-3.18000E−07	-
o	-	-	2.60058E−05	19.4
p	-	-	1.26675E−05	10.8
q	-	-	-3.82000E−06	-
s	-	-	-1.56582E−04	9.9
t	-	-	4.74701E−05	29.6

Table C.1: Coefficients for the Θ_{tgt} and δ polynomials from RAYTRACE simulations. The quoted uncertainties for the coefficients are relative errors in units of %. Coefficients without listed error were held fixed to values from another fit.

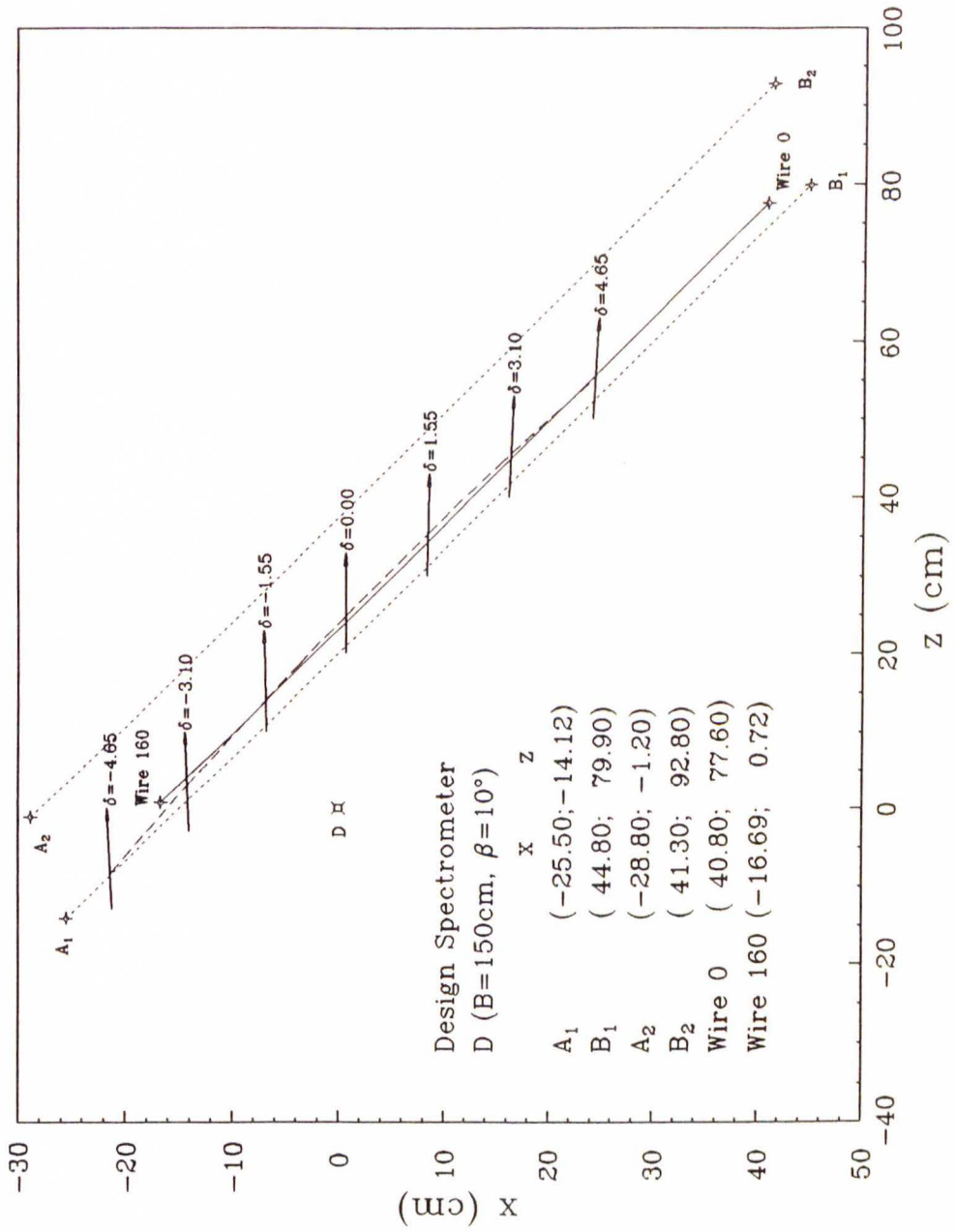

Figure C.1: Design K600 medium dispersion focal plane from RAYTRACE calculations in the D-coordinate system of dipole 2. The dotted lines are the front and rear window of the front VDC, the dashed line is the focal plane, and the solid line denotes the wire plane. The rays represent trajectories of specific δ with respect to the central ray.

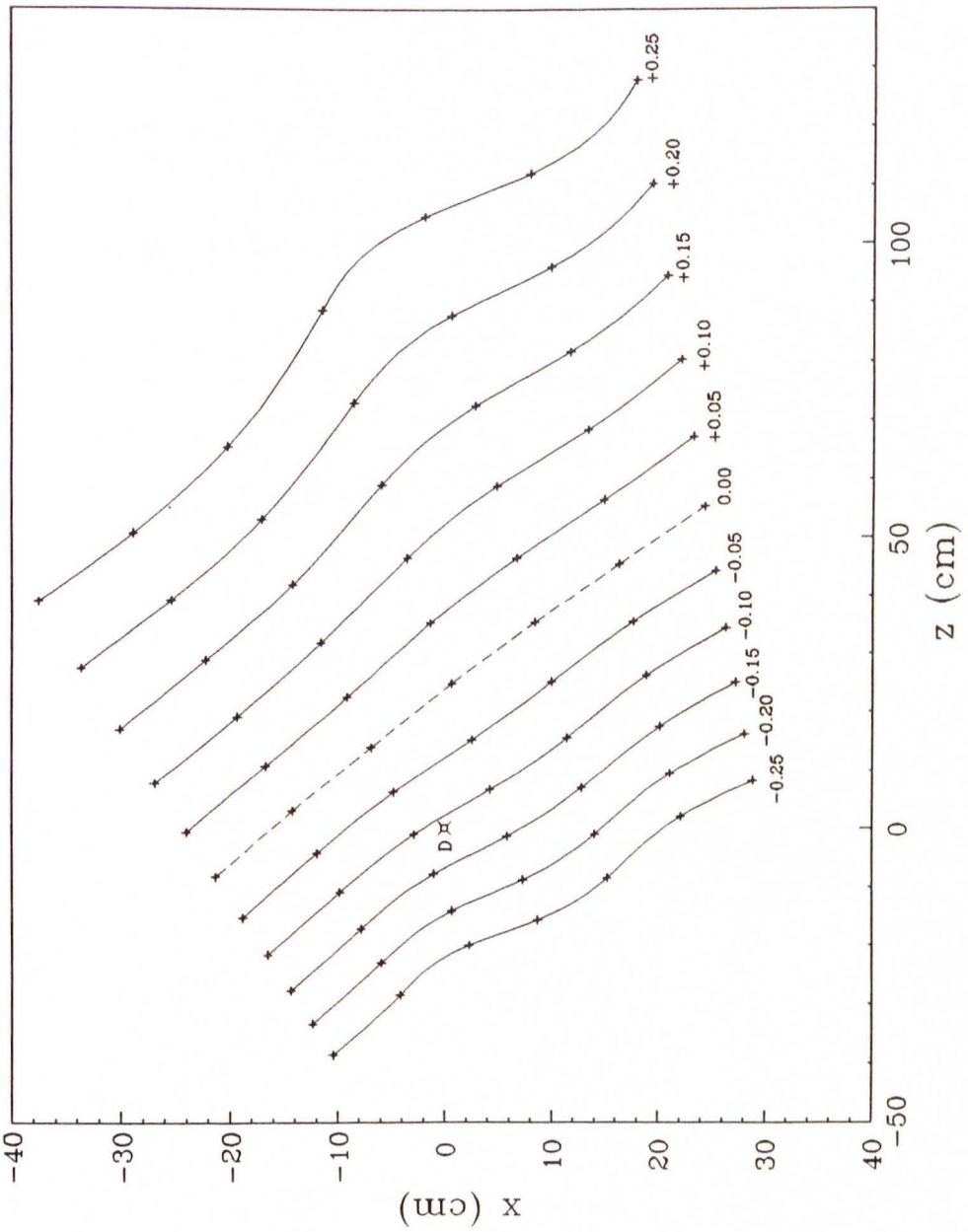

Figure C.2: Effect of the K-coil on the focal plane from RAYTRACE calculations in the D-coordinate system of dipole 2; the numbers represent the strength of the K-coil field in the center as fraction of the corresponding dipole 2 field. The K-coil both shifts and deforms the focal plane.

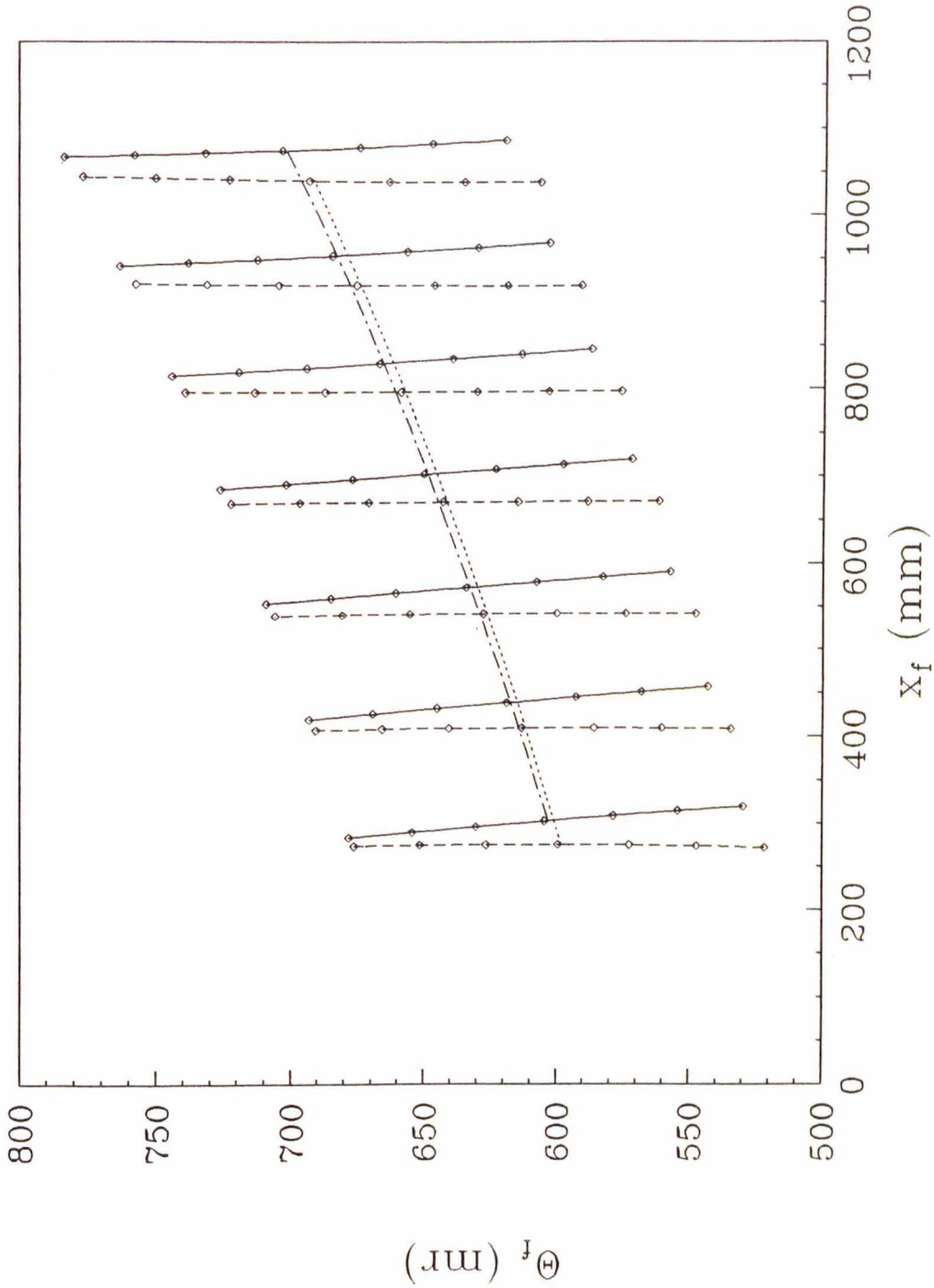

Figure C.3: Effect of the K-coil on nuclear lines in $x_f\theta_f$ (front) from RAYTRACE calculations. The dashed lines are without K-coil; for the solid lines the K-coil strength is 5% of the dipole 2 strength. The diamond symbols represent the seven Θ_{tgt} angles defined by the multislit from Chapter 4. The K-coil shifts and tilts lines; the strength of the tilt varies with x_f.

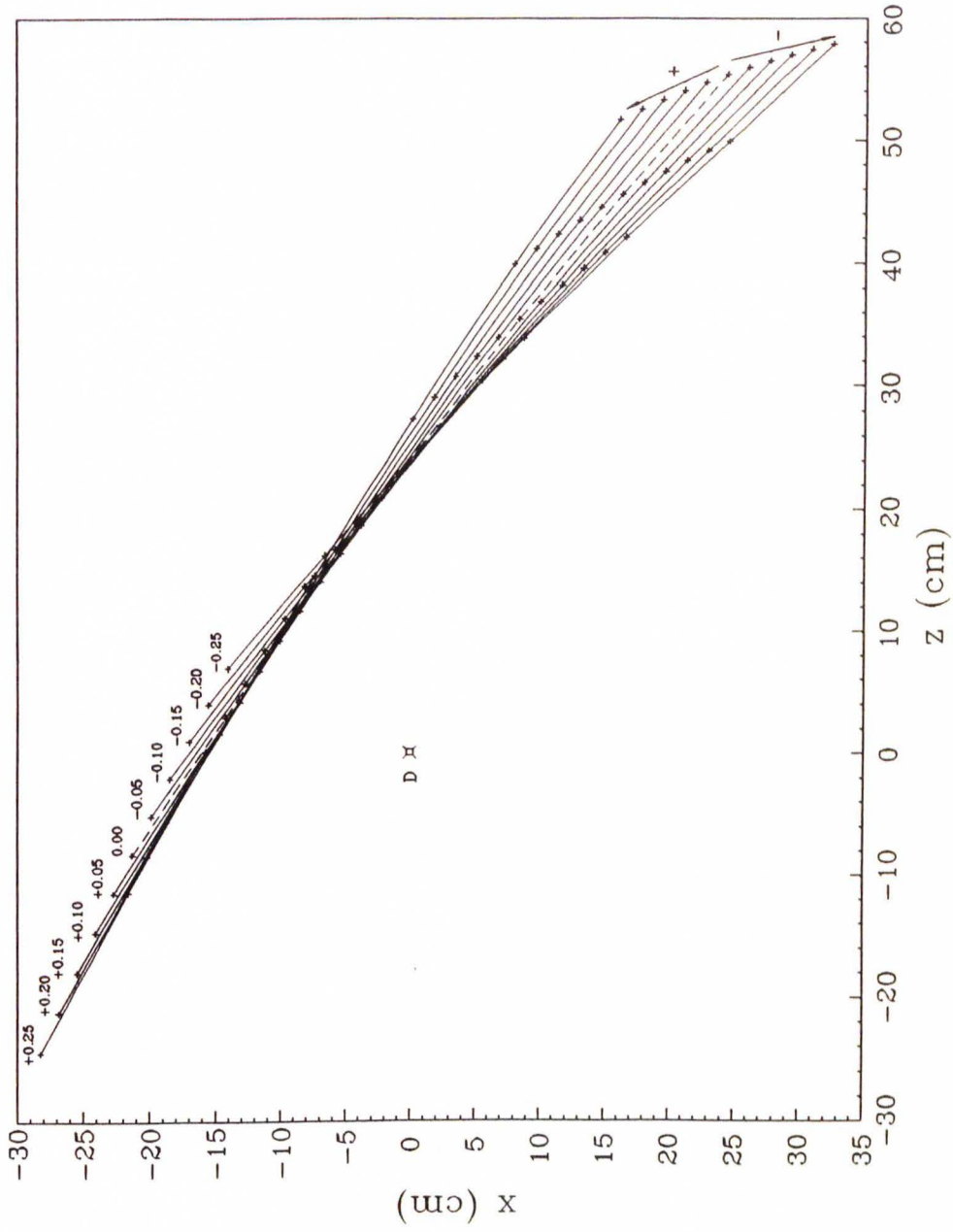

Figure C.4: Effect of the H-coil on the focal plane from RAYTRACE calculations in the D-coordinate system of dipole 2; the numbers represent the strength of the H-coil field in the center as fraction of the corresponding dipole 1 field. The main effect of the H-coil is a (slight) rotation of the focal plane.

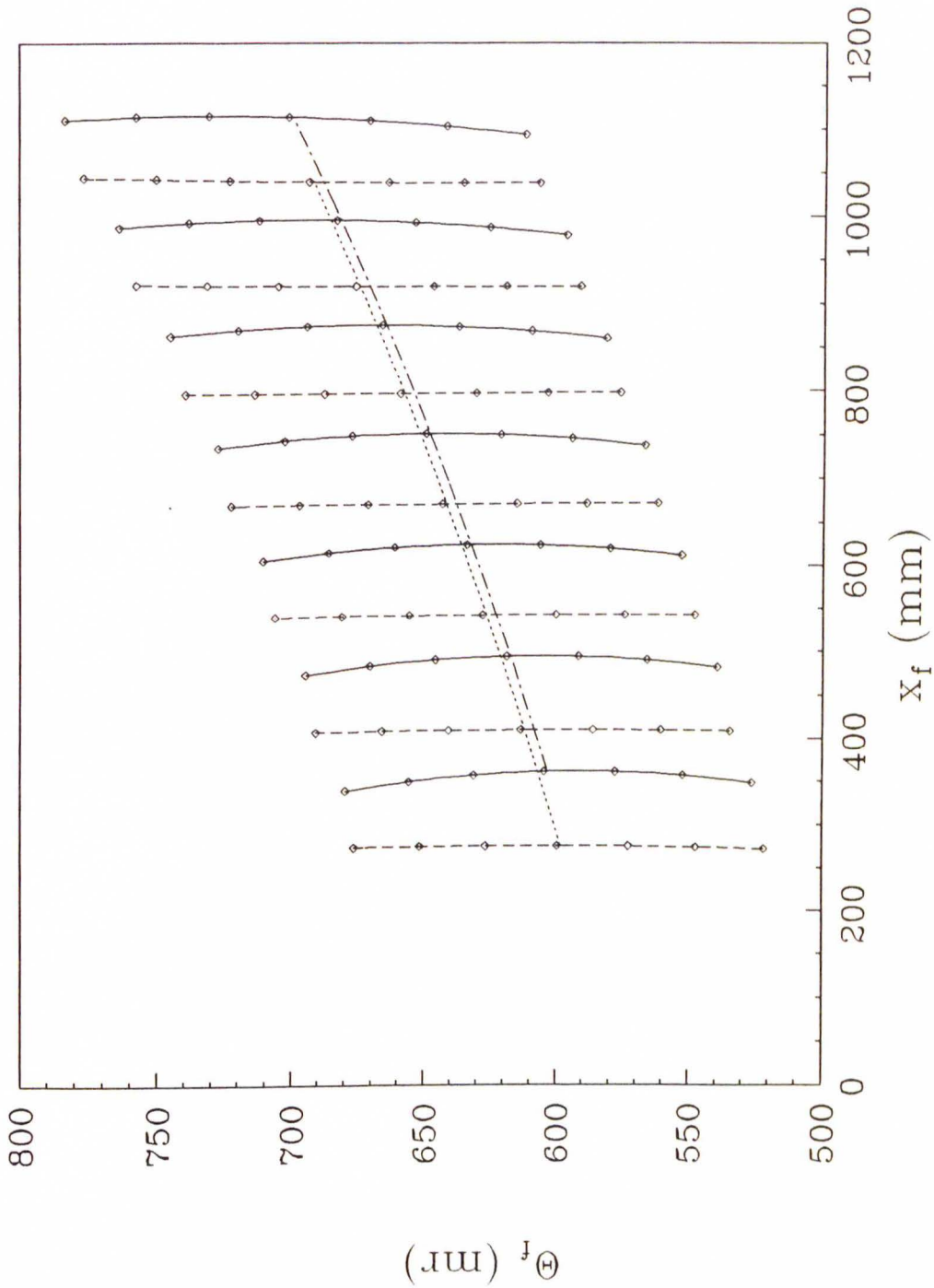

Figure C.5: Effect of the H-coil on nuclear lines in $x_f\theta_f$ (front) from RAYTRACE calculations. The dashed lines are without H-coil; for the solid lines the H-coil strength is 15% of the dipole 1 strength. The diamond symbols represent the seven Θ_{tgt} angles defined by the multislit from Chapter 4. The H-coil shifts and bends lines; the strength of the bend varies with x_f.

D Effective Interaction Grids

s1	b1	s2	d2	s3	b3	it	chir	chig/std	parg
0.680(11)	65.1(1.9)	0.769(9)	0.165(10)	0.844(7)	1.67(24)		4.28	4.28	
0.500	83.2(1.8)	0.803(8)	0.180(10)	0.885(7)	2.08(24)	9	5.95		
0.600	79.5(1.7)	0.795(9)	0.164(10)	0.871(7)	1.95(25)	6	4.53	4.15	0.644
0.700	64.4(1.8)	0.770(9)	0.169(10)	0.846(7)	1.96(24)	3	4.22	3.E-1	(6)
0.800	33.6(1.5)	0.751(8)	0.257(10)	0.785(6)	2.50(17)	10	6.43		
0.690(10)	60.0	0.767(9)	0.181(10)	0.846(6)	2.19(20)	3	4.27		
0.689(10)	63.0	0.770(9)	0.174(10)	0.848(7)	2.07(21)	3	4.22	4.11	78.4
0.688(10)	66.0	0.773(9)	0.168(10)	0.850(7)	1.95(22)	3	4.18	3.E-4	(2.6)
0.687(10)	69.0	0.776(9)	0.162(10)	0.852(7)	1.83(22)	3	4.15		
0.697(9)	49.2(1.7)	0.600	0.100(8)	0.839(6)	0.21(20)	7	5.59		
0.694(9)	59.3(1.8)	0.700	0.137(8)	0.848(6)	1.10(22)	6	4.50	4.14	0.801
0.684(10)	70.0(1.9)	0.800	0.177(8)	0.850(6)	2.23(24)	4	4.14	1.E-2	(10)
0.667(11)	80.2(2.0)	0.900	0.221(9)	0.846(7)	4.26(25)	2	4.48		
0.706(10)	75.5(1.8)	0.718(7)	0.050	0.845(7)	1.62(24)	6	4.58		
0.693(10)	70.6(1.9)	0.755(7)	0.125	0.849(7)	1.83(23)	6	4.19	4.17	0.155
0.684(11)	63.7(1.9)	0.788(7)	0.200	0.851(7)	1.86(22)	3	4.25	1.E-2	(9)
0.682(11)	50.7(1.8)	0.805(7)	0.275	0.846(6)	2.12(20)	7	4.70		
0.712(12)	87.9(2.0)	0.923(9)	0.180(11)	0.700	7.17(21)	7	5.74		
0.697(11)	72.2(2.0)	0.825(9)	0.176(10)	0.800	3.82(21)	6	4.32	4.08	0.827
0.674(10)	62.7(1.8)	0.720(9)	0.152(10)	0.900	0.02(18)	6	4.48	2.E-1	(6)
0.625(10)	53.1(1.6)	0.610(8)	0.125(9)	1.000	-3.37(14)	8	7.29		
0.702(10)	75.2(1.6)	0.756(9)	0.132(10)	0.881(6)	0.00	4	4.32		
0.695(10)	71.5(1.7)	0.766(9)	0.149(10)	0.865(5)	1.00	4	4.19	4.16	1.60
0.687(11)	66.7(1.7)	0.774(9)	0.167(10)	0.849(5)	2.00	4	4.17	3.E-3	(23)
0.679(11)	60.2(1.8)	0.781(9)	0.188(10)	0.831(5)	3.00	4	4.28		

Table D.1: Interaction grid: ^{16}O (200 MeV).

s1	b1	s2	d2	s3	b3	it	chir	chig/std	parg
0.582(13)	72.5(2.8)	0.895(8)	0.198(13)	0.842(7)	5.63(26)		9.11	9.11	
0.400	80.2(2.6)	0.880(8)	0.146(13)	0.843(6)	5.80(21)	6	9.96		
0.500	71.7(2.9)	0.897(8)	0.198(13)	0.852(6)	6.19(24)	2	9.74	8.90	0.501
0.600	71.5(2.6)	0.893(8)	0.200(13)	0.839(6)	5.65(25)	3	9.06	1.E+0	(5)
0.700	-19.7(1.7)	0.833(7)	0.386(10)	0.759(5)	5.06(12)	10	13.51		
0.582(12)	69.0	0.893(3)	0.204(12)	0.842(6)	5.87(23)	3	9.10		
0.581(12)	71.0	0.895(8)	0.201(12)	0.842(6)	5.85(24)	3	9.11	9.10	68.3
0.581(12)	73.0	0.897(8)	0.197(12)	0.841(6)	5.84(24)	3	9.14	2.E-3	(1.3)
0.579(12)	75.0	0.899(8)	0.194(12)	0.841(6)	5.87(24)	4	9.18		
0.607(10)	45.5(2.2)	0.700	0.140(10)	0.857(5)	1.35(20)	5	10.84		
0.597(11)	58.5(2.5)	0.800	0.170(10)	0.850(6)	3.72(23)	8	9.43	9.13	0.865
0.579(12)	74.1(2.8)	0.900	0.196(11)	0.841(6)	5.93(26)	5	9.17	5.E-2	(7)
0.555(14)	87.7(3.0)	1.000	0.236(11)	0.832(6)	7.83(27)	9	10.29		
0.575(13)	78.7(2.6)	0.898(7)	0.170	0.836(7)	6.32(26)	6	9.36		
0.579(13)	74.9(2.5)	0.898(7)	0.190	0.840(7)	5.98(25)	5	9.19	9.06	0.228
0.580(13)	70.9(2.5)	0.897(7)	0.210	0.843(6)	5.57(25)	2	9.08	5.E-3	(6)
0.580(12)	67.3(2.5)	0.898(7)	0.230	0.844(6)	5.26(24)	3	9.06		
0.547(15)	121.5(3.0)	1.066(8)	0.143(15)	0.700	12.07(29)	10	14.94		
0.605(12)	70.4(2.7)	0.930(8)	0.215(13)	0.800	5.64(23)	3	9.24	8.89	0.852
0.579(12)	54.3(2.3)	0.802(8)	0.211(12)	0.900	1.95(19)	5	9.83	5.E-1	(3)
0.532(11)	32.2(2.0)	0.634(7)	0.190(11)	1.000	-3.22(12)	6	14.45		
0.611(11)	79.7(2.4)	0.878(8)	0.176(13)	0.860(6)	4.00	7	9.25		
0.595(12)	77.0(2.5)	0.889(8)	0.186(13)	0.850(6)	5.00	5	9.17	9.14	5.56
0.577(12)	72.2(2.5)	0.898(8)	0.199(13)	0.839(6)	6.00	3	9.14	3.E-2	(26)
0.555(12)	66.7(2.7)	0.905(8)	0.210(12)	0.826(6)	7.00	2	9.24		

Table D.2: Interaction grid: ^{40}Ca (200 MeV).

s1	b1	s2	d2	s3	b3	it	chir	chig/std	parg
1.000	144.7(1.6)	1.000	-0.071(10)	0.849(10)	6.81(23)		5.65	5.65	
0.750	143.4(1.7)	0.989(10)	-0.033(13)	0.900(11)	6.43(24)	6	6.61		
0.900	146.8(1.7)	1.009(10)	-0.050(13)	0.862(11)	6.88(24)	5	5.98	5.63	1.102
1.050	145.6(1.7)	1.022(10)	-0.064(13)	0.835(11)	7.14(25)	4	5.62	4.E-2	(21)
1.200	142.8(1.7)	1.034(10)	-0.074(14)	0.810(11)	7.42(26)	7	5.71		
1.079(33)	120.0	0.993(10)	-0.038(13)	0.903(14)	6.86(25)	8	5.65		
1.080(32)	135.0	1.013(10)	-0.056(13)	0.858(13)	7.12(25)	4	5.52	5.49	133.3
1.062(30)	150.0	1.028(10)	-0.069(14)	0.819(13)	7.22(25)	5	5.72	5.E-2	(2.0)
1.034(28)	165.0	1.043(9)	-0.073(15)	0.793(13)	7.02(25)	3	6.46		
-0.583(27)	45.3(1.5)	0.750	-0.308(6)	1.275(6)	-1.81(13)	10	7.54		
0.980(36)	129.9(1.6)	0.900	-0.111(12)	0.915(13)	5.02(25)	6	5.82	5.57	0.982
1.080(31)	148.6(1.8)	1.050	-0.051(11)	0.817(13)	7.65(24)	8	5.73	1.E-2	(10)
1.153(30)	156.3(2.1)	1.200	0.037(10)	0.764(13)	10.26(24)	9	7.32		
1.115(26)	174.0(1.7)	0.946(7)	-0.300	0.745(12)	5.80(22)	5	8.43		
1.108(27)	164.3(1.7)	0.983(7)	-0.200	0.770(12)	6.77(22)	6	6.78	5.63	-0.028
1.081(29)	151.6(1.7)	1.016(7)	-0.100	0.810(13)	7.24(23)	8	5.79	4.E-2	(10)
1.022(32)	134.1(1.8)	1.032(8)	0.000	0.882(13)	6.84(24)	4	5.67		
1.297(23)	161.8(1.8)	1.103(9)	-0.090(13)	0.600	10.43(22)	8	7.99		
1.154(25)	153.6(1.8)	1.056(9)	-0.076(14)	0.750	8.40(24)	6	6.02	5.57	0.873
0.982(28)	137.6(1.7)	0.991(9)	-0.054(14)	0.900	6.20(26)	8	5.63	1.E-2	(11)
0.737(35)	111.7(1.7)	0.887(9)	-0.021(13)	1.050	3.73(25)	10	6.58		
1.111(30)	147.6(1.6)	1.002(9)	-0.102(13)	0.867(13)	5.00	2	5.84		
1.088(30)	146.4(1.7)	1.011(9)	-0.083(13)	0.849(13)	6.00	2	5.68	5.63	7.04
1.069(31)	146.3(1.7)	1.021(9)	-0.069(13)	0.835(13)	7.00	5	5.63	3.E-3	(27)
1.058(31)	144.5(1.8)	1.034(9)	-0.054(12)	0.813(13)	8.00	5	5.67		

Table D.3: Interaction grid: ^{16}O (318 MeV).

s1	b1	s2	d2	s3	b3	it	chir	chig/std	parg
1.000	190.3(2.4)	1.000	−0.069(9)	0.701(15)	7.12(24)		4.90	4.90	
0.750	173.7(3.1)	0.810(9)	−0.274(13)	0.736(14)	5.05(25)	9	4.50		
0.900	158.6(3.1)	0.803(9)	−0.287(13)	0.733(14)	5.16(24)	9	4.47	4.46	0.856
1.050	141.9(3.0)	0.794(9)	−0.302(12)	0.731(14)	5.21(24)	9	4.58	4.E-4	(33)
1.200	123.7(2.9)	0.785(9)	−0.317(12)	0.730(14)	5.20(23)	9	4.84		
0.860(25)	180.0	0.848(9)	−0.193(13)	0.713(14)	5.74(23)	8	4.35		
0.819(25)	186.0	0.856(9)	−0.178(13)	0.711(14)	5.77(23)	8	4.40	4.34	173.4
0.775(24)	192.0	0.864(9)	−0.162(13)	0.709(14)	5.79(24)	9	4.46	2.E-4	(3.1)
0.731(24)	198.0	0.872(9)	−0.146(13)	0.707(14)	5.81(24)	9	4.56		
1.217(37)	114.4(4.0)	0.750	−0.350(9)	0.729(14)	4.97(21)	10	5.08		
1.157(37)	156.9(3.9)	0.900	−0.189(9)	0.717(14)	6.33(23)	10	4.53	4.59	0.880
1.203(35)	179.1(3.7)	1.050	−0.018(9)	0.690(15)	7.77(24)	10	5.47	1.E-1	(11)
1.239(35)	200.5(3.6)	1.200	0.155(9)	0.649(16)	9.10(25)	10	7.41		
1.176(36)	123.9(4.1)	0.768(7)	−0.350	0.734(14)	5.02(20)	10	4.89		
1.221(36)	122.3(4.0)	0.793(7)	−0.300	0.727(14)	5.29(20)	9	4.84	4.84	−0.308
1.278(35)	118.6(3.9)	0.820(7)	−0.250	0.721(14)	5.56(20)	7	4.93	1.E-3	(11)
1.348(35)	113.0(3.8)	0.848(7)	−0.200	0.714(14)	5.84(20)	10	5.16		
1.113(36)	154.1(3.5)	0.862(9)	−0.185(12)	0.450	7.67(14)	9	6.21		
1.186(36)	131.5(3.9)	0.803(9)	−0.282(12)	0.650	5.94(17)	10	4.87	4.87	0.722
1.218(38)	111.7(4.2)	0.762(9)	−0.358(12)	0.850	4.03(19)	10	5.25	1.E-1	(14)
1.137(39)	107.9(4.5)	0.738(9)	−0.384(12)	1.050	1.99(20)	10	6.75		
1.207(37)	122.0(3.8)	0.783(9)	−0.321(11)	0.734(11)	5.10	10	4.86		
1.204(37)	128.4(3.7)	0.801(9)	−0.280(11)	0.695(11)	6.00	10	4.77	4.77	6.07
1.202(36)	133.7(3.7)	0.821(9)	−0.240(11)	0.656(11)	6.90	10	4.84	6.E-5	(19)
1.202(36)	137.9(3.7)	0.843(9)	−0.201(11)	0.617(11)	7.80	9	5.05		

Table D.4: Interaction grid: ^{16}O (500 MeV).

E List of Runs

The notation in the following list of runs is as follows: the first of added runs is denoted by ">", each subsequent run is denoted by "+"; excluded states following a "^" belong to the previous line. An "*" denotes a run with encoder problem and the quoted angle is the corrected angle. An "!" denotes a run with a scaler problem; the necessary scale factor f for the affected polarized cross section (u for spin-up, d for spin-down) is given in the last column. March 1988 runs show an "all" in the column for excluded states since they were not used at all in the present work, and are just listed here for completeness.

	Run	Angle	By	Evts	Tangle	Tgt	Ap	Ifs	Cup	Polup	Poldn	Energy	Excluded States
	348	-16.00	el	145	-8.00	new	B1	20	I87	0.748	0.748	100.70	16O:1m1
	349	-16.00	in	100	-8.00	new	B1	20	I87	0.749	0.749	100.70	
	358	-14.00	el	116	-7.00	new	B2	20	I87	0.757	0.761	100.70	
	363	-12.00	el	186	-7.00	new	B2	20	I87	0.757	0.761	100.70	
	364	-12.00	in	57	-7.00	new	B2	20	I87	0.757	0.761	100.70	16O:4p1
	397	-12.00	el	93	-6.00	new	B2	6	S87	0.757	0.761	100.70	
	365!	-10.00	el	185	-5.00	new	B2	6	I87	0.757	0.761	100.70	fu=6216.195
	390	-10.00	el	154	-5.00	new	B2	6	S87	0.757	0.761	100.70	
	404	14.00	el	87	7.00	new	A1	20	S87	0.757	0.761	100.70	16O:3m1,2p1
	408	16.00	el	72	8.00	new	B1	20	S87	0.757	0.761	100.70	16O:1m1
	137	18.00	el	283	9.00	old	A1	60	E87	0.727	0.750	100.50	
	138	18.00	in	245	9.00	old	A1	60	E87	0.727	0.750	100.50	16O:3m1
	224	18.00	el	208	9.00	new	A1	60	I87	0.736	0.748	100.70	
>	228	18.00	el	11	9.00	new	A1	20	I87	0.736	0.748	100.70	
+	229	18.00	el	168	9.00	new	A1	20	I87	0.736	0.748	100.70	
	230	18.00	el	83	9.00	new	A1	20	E87	0.736	0.748	100.70	
>	262	18.00	el	61	9.00	new	B1	60	I87	0.733	0.753	100.70	
+	263	18.00	el	68	9.00	new	B1	60	I87	0.734	0.753	100.70	
>	5	22.00	el	93	11.00	old	A1	20	E87	0.756	0.774	100.50	16O:3m1,2m1;
+	6	22.00	el	215	11.00	old	A1	20	E87	0.756	0.774	100.50	9Be:1p1,3p1
	7	22.00	in	202	11.00	old	A1	20	E87	0.756	0.774	100.50	9Be:Lor
	212!	22.00	el	111	11.00	new	B2	60	E87	0.736	0.748	100.70	fd=10380.102
	220	22.00	el	75	11.00	new	A1	60	E87	0.736	0.748	100.70	
>	222	22.00	el	87	11.00	new	A1	60	I87	0.736	0.748	100.70	
+	223	22.00	el	95	11.00	new	A1	60	I87	0.736	0.748	100.70	9Be:5p1
	139	24.00	el	132	12.00	old	A1	60	E87	0.727	0.750	100.50	
	140	24.00	in	174	12.00	old	A1	60	E87	0.727	0.750	100.50	16O:3m1;9Be:Lor
	18	26.00	el	183	13.00	old	A1	60	E87	0.756	0.774	100.50	
	19	26.00	in	232	13.00	old	A1	60	E87	0.756	0.774	100.50	16O:3m1;9Be:Lor
	160	26.00	el	104	13.00	new	A1	60	E87	0.736	0.748	100.70	
	161	26.00	in	51	13.00	new	A1	60	E87	0.736	0.748	100.70	16O:2p2,2m1,0m1;9Be:3p1
	28!	30.00	el	85	15.00	old	A1	6	E87	0.756	0.774	100.50	fu=69.313
	30!	30.00	in	258	15.00	old	A1	20	E87	0.756	0.774	100.50	16O:3m1; fd=41.878
	162	30.00	el	109	15.00	new	A1	60	E87	0.736	0.748	100.70	
	38	34.00	el	127	17.00	old	B2	20	E87	0.756	0.774	100.50	
>	39	34.00	in	22	17.00	old	A1	60	E87	0.756	0.774	100.50	
+	40	34.00	in	438	17.00	old	A1	60	E87	0.756	0.774	100.50	16O:0p2,3m1

Table E.1: a) BeO runs at $E_P = 100$ MeV. Notation: the first of added runs is denoted by ">", each subsequent run by "+"; excluded states following a "^" belong to the previous line. An "!" denotes a run with a scaler problem; the scale factor f for spin-up (u) or spin-down (d) is given in the last column.

	Run	Angle	By	Evts	Tangle	Tgt	Ap	Ifs	Cup	Polup	Poldn	Energy	Excluded States
	155	34.00	el	228	17.00	new	B2	60	E87	0.736	0.748	100.70	
	156	34.00	in	178	17.00	new	B2	60	E87	0.736	0.748	100.70	
	47	38.00	el	114	19.00	old	A1	60	E87	0.756	0.774	100.50	
	48	38.00	in	376	19.00	old	A1	60	E87	0.756	0.774	100.50	
	168	38.00	el	65	19.00	new	A1	60	E87	0.736	0.748	100.70	9Be:3p1
	56	42.00	el	107	21.00	old	A1	60	E87	0.750	0.766	100.50	9Be:1m1
	57	42.00	in	258	21.00	old	A1	60	E87	0.749	0.765	100.50	
	174	42.00	el	82	21.00	new	B2	60	E87	0.736	0.748	100.70	
	58	46.00	in	212	23.00	old	A1	60	E87	0.748	0.764	100.50	
	59	46.00	el	133	23.00	old	A1	60	E87	0.748	0.763	100.50	9Be:1m1
	179	46.00	el	99	23.00	new	B2	20	E87	0.736	0.748	100.70	
	80	50.00	el	77	25.00	old	B2	200	E87	0.727	0.750	100.50	
	81	50.00	in	133	25.00	old	B2	200	E87	0.727	0.750	100.50	16O:3m4;9Be:3m1,5p1
	186	50.00	el	100	25.00	new	B2	60	E87	0.736	0.748	100.70	
	82	54.00	in	204	27.00	old	B2	200	E87	0.727	0.750	100.50	16O:0m1;9Be:5p1
	83	54.00	el	83	27.00	old	B2	200	E87	0.727	0.750	100.50	
	190	54.00	el	125	17.00	new	B2	60	E87	0.736	0.748	100.70	
	91	58.00	el	58	29.00	old	B2	200	E87	0.727	0.750	100.50	16O:2p1
	92	58.00	el	55	29.00	old	B3	200	E87	0.727	0.750	100.50	16O:2p1;9Be:1p1
	93	58.00	el	55	29.00	old	A7	200	E87	0.727	0.750	100.50	16O:2p1;9Be:1p1
>	94	58.00	in	111	29.00	old	B3	200	E87	0.727	0.750	100.50	16O:0p2,2p1;9Be:3m1,5m1
+	95	58.00	in	103	29.00	old	B3	200	E87	0.727	0.750	100.50	
	194	58.00	el	100	19.00	new	B2	60	E87	0.736	0.748	100.70	9Be:1p1
	124	62.00	el	90	31.00	old	A7	60	E87	0.727	0.750	100.50	
	125	62.00	in	315	31.00	old	A7	60	E87	0.727	0.750	100.50	9Be:3m1,1p1
	201	62.00	el	72	31.00	new	A7	60	E87	0.736	0.748	100.70	
	114	66.00	el	100	33.00	old	A7	60	E87	0.727	0.750	100.50	16O:0p2
	116	66.00	el	140	33.00	old	A7	60	E87	0.727	0.750	100.50	16O:0p2
>	117	66.00	in	338	33.00	old	A7	60	E87	0.727	0.750	100.50	
+	118	66.00	in	209	33.00	old	A7	60	E87	0.727	0.750	100.50	
	206	66.00	el	81	33.00	new	A7	60	E87	0.736	0.748	100.70	16O:0p2;9Be:5m1
	111	70.00	el	94	35.00	old	A7	60	E87	0.727	0.750	100.50	
	112	70.00	in	539	35.00	old	A7	60	E87	0.727	0.750	100.50	
	209	70.00	el	70	35.00	new	A7	60	E87	0.736	0.748	100.70	

Table E.1: b) BeO runs at $E_P = 100$ MeV (cont.) Notation: the first of added runs is denoted by ">", each subsequent run by "+"; excluded states following a "^" belong to the previous line. An "!" denotes a run with a scaler problem; the scale factor f for spin-up (u) or spin-down (d) is given in the last column.

Run	Angle	By	Evts	Tangle	Tgt	Ap	Ifs	Cup	Polup	Poldn	Energy	Excluded States
303	-16.00	el	52	-8.00	thn	B1	6	I87	0.740	0.744	100.70	
304	-16.00	el	56	-8.00	thn	B1	6	I87	0.740	0.744	100.70	
305	-16.00	el	12	-8.00	thn	B1	6	I87	0.740	0.744	100.70	
306	-16.00	el	59	-8.00	thn	B1	20	I87	0.740	0.744	100.70	
307	-16.00	el	49	-8.00	thk	B1	6	I87	0.740	0.744	100.70	
308	-16.00	el	70	-8.00	thk	B1	6	I87	0.740	0.744	100.70	
344	-16.00	el	53	-8.00	thk	B1	20	I87	0.744	0.741	100.70	
345!	-16.00	in	18	-8.00	thk	B1	20	I87	0.744	0.742	100.70	fu=382.577
346	-16.00	in	226	-8.00	thk	B1	20	I87	0.745	0.744	100.70	
347	-16.00	in	66	-8.00	thn	B1	20	I87	0.747	0.747	100.70	
>2289	-16.00	el	60	0.00	thk	A1	2	S88	0.728	0.748	100.50	all
+2290	-16.00	el	86	0.00	thk	A1	2	S88	0.728	0.748	100.50	all
311	-14.00	el	38	-7.00	thn	B1	6	I87	0.740	0.744	100.70	
312	-14.00	el	43	-7.00	thn	B1	6	I87	0.740	0.744	100.70	
313	-14.00	el	51	-7.00	thn	B1	6	I87	0.740	0.744	100.70	
314	-14.00	el	41	-7.00	thn	B1	6	I87	0.740	0.744	100.70	
315	-14.00	el	56	-7.00	thk	B1	6	I87	0.740	0.744	100.70	
316	-14.00	el	50	-7.00	thk	B1	6	I87	0.740	0.744	100.70	
350	-14.00	el	255	-7.00	thk	B1	20	I87	0.751	0.752	100.70	0p2
> 351	-14.00	in	202	-7.00	thk	B1	20	I87	0.752	0.754	100.70	
+ 352	-14.00	in	136	-7.00	thk	B1	20	I87	0.753	0.756	100.70	
353	-14.00	in	102	-7.00	thk	A1	20	I87	0.754	0.757	100.70	
> 355	-14.00	in	49	-7.00	thn	B2	20	I87	0.756	0.759	100.70	
+ 356	-14.00	in	266	-7.00	thn	B2	20	I87	0.757	0.761	100.70	
357	-14.00	in	182	-7.00	thn	B4	20	I87	0.757	0.761	100.70	
2286	-14.00	el	84	0.00	thk	A1	2	S88	0.728	0.748	100.50	all
317	-12.00	el	51	-6.00	thn	B1	6	I87	0.740	0.744	100.70	
318	-12.00	el	49	-6.00	thn	B1	6	I87	0.740	0.744	100.70	
319	-12.00	el	61	-6.00	thn	B1	6	I87	0.740	0.744	100.70	
320	-12.00	el	64	-6.00	thn	B1	6	I87	0.740	0.744	100.70	
361	-12.00	in	67	-7.00	thk	B4	20	I87	0.757	0.761	100.70	
362	-12.00	in	254	-7.00	thk	B4	20	I87	0.757	0.761	100.70	
2282	-12.00	el	93	0.00	thk	A1	2	S88	0.728	0.748	100.50	all
321	-10.00	el	54	-5.00	thn	B1	6	I87	0.740	0.744	100.70	
322!	-10.00	el	58	-5.00	thn	B1	6	I87	0.740	0.744	100.70	fu=507.527
323	-10.00	el	47	-5.00	thn	B1	6	I87	0.740	0.744	100.70	
324	-10.00	el	45	-5.00	thk	B1	6	I87	0.740	0.744	100.70	
325	-10.00	el	51	-5.00	thk	B1	6	I87	0.740	0.744	100.70	
366	-10.00	el	106	-5.00	thn	B2	6	I87	0.757	0.761	100.70	
367	-10.00	in	129	-5.00	thn	B2	6	I87	0.757	0.761	100.70	
368	-10.00	in	151	-5.00	thn	B4	6	I87	0.757	0.761	100.70	
378	-10.00	el	211	-5.00	thk	A1	6	S87	0.757	0.761	100.70	
379	-10.00	in	98	-5.00	thk	A1	6	S87	0.757	0.761	100.70	
380	-10.00	in	264	-5.00	thk	B4	6	S87	0.757	0.761	100.70	
381	-10.00	in	156	-5.00	thk	B2	6	S87	0.757	0.761	100.70	

Table E.2: a) ^{40}Ca runs at $E_P = 100$ MeV. Notation: the first of added runs is denoted by "$>$", each subsequent run by "$+$"; excluded states following a "$\wedge$" belong to the previous line. An "!" denotes a run with a scaler problem; the scale factor f for spin-up (u) or spin-down (d) is given in the last column.

Run	Angle	By	Evts	Tangle	Tgt	Ap	Ifs	Cup	Polup	Poldn	Energy	Excluded States
2279	-10.00	el	148	0.00	thk	A1	2	S88	0.728	0.748	100.50	all
384	-8.00	in	53	-4.00	thn	B2	6	S87	0.757	0.761	100.70	
300	10.00	el	61	6.00	thn	B1	6	I87	0.740	0.745	100.70	
301	10.00	el	70	6.00	thn	B1	6	I87	0.740	0.745	100.70	
302	10.00	el	57	6.00	thn	B1	6	I87	0.740	0.745	100.70	
329	10.00	el	164	5.00	thn	B1	6	I87	0.740	0.744	100.70	
332	10.00	el	108	5.00	thk	B1	6	I87	0.740	0.744	100.70	
333	10.00	in	25	5.00	thk	B1	6	I87	0.740	0.744	100.70	2p1,5m1,2p2,1m1,2m2,6.91
2267	10.00	el	111	5.00	thk	A1	20	S88	0.728	0.748	100.50	all
>2293	10.00	el	87	0.00	thk	A1	2	S88	0.728	0.748	100.50	all
+2294	10.00	el	80	0.00	thk	A1	2	S88	0.728	0.748	100.50	all
294	12.00	el	43	6.00	thn	B1	6	I87	0.740	0.746	100.70	
295	12.00	el	57	6.00	thn	B1	6	I87	0.740	0.746	100.70	
296	12.00	el	54	6.00	thk	B1	6	I87	0.740	0.746	100.70	
297	12.00	el	51	6.00	thk	B1	6	I87	0.740	0.746	100.70	
299	12.00	el	53	6.00	thk	B1	6	I87	0.740	0.746	100.70	
334	12.00	el	97	6.00	thk	B1	6	I87	0.740	0.741	100.70	
335	12.00	in	152	6.00	thk	B1	6	I87	0.740	0.741	100.70	5m1,4p1
336	12.00	in	173	6.00	thk	B1	6	I87	0.740	0.741	100.70	5m1,6.028,7.11
>2297	12.00	el	76	0.00	thk	A1	2	S88	0.728	0.748	100.50	all
+2298	12.00	el	267	0.00	thk	A1	2	S88	0.728	0.748	100.50	all
>2323	12.00	in	277	6.00	thk	B2	20	S88	0.728	0.748	100.50	all
+2324	12.00	in	212	6.00	thk	B2	20	S88	0.728	0.748	100.50	all
288	14.00	el	32	7.00	thn	B1	6	I87	0.740	0.747	100.70	
289	14.00	el	32	7.00	thn	B1	6	I87	0.740	0.747	100.70	0p2
290	14.00	el	45	7.00	thn	B1	6	I87	0.740	0.747	100.70	0p2
291	14.00	el	178	7.00	thn	B1	6	I87	0.740	0.747	100.70	
292	14.00	el	56	7.00	thk	B1	6	I87	0.740	0.747	100.70	
293	14.00	el	53	7.00	thk	B1	6	I87	0.740	0.746	100.70	
337	14.00	el	102	7.00	thk	B1	20	I87	0.740	0.740	100.70	
> 339	14.00	in	32	7.00	thk	B1	20	I87	0.740	0.740	100.70	
+ 340	14.00	in	154	7.00	thk	B1	20	I87	0.740	0.739	100.70	1m1,1m2
2301	14.00	el	79	0.00	thk	A1	2	S88	0.728	0.748	100.50	all
2317	14.00	in	420	7.00	thk	B2	20	S88	0.728	0.748	100.50	all
280	16.00	el	75	8.00	thn	B1	20	I87	0.740	0.750	100.70	
281	16.00	el	56	8.00	thn	B1	6	I87	0.740	0.749	100.70	
282	16.00	el	58	8.00	thn	B1	6	I87	0.740	0.749	100.70	
283	16.00	el	67	8.00	thn	B1	6	I87	0.740	0.749	100.70	
284	16.00	el	63	8.00	thk	B1	6	I87	0.740	0.749	100.70	
285	16.00	el	31	8.00	thn	B1	6	I87	0.740	0.748	100.70	
286	16.00	el	46	8.00	thn	B1	6	I87	0.740	0.748	100.70	
287	16.00	el	39	8.00	thk	B1	6	I87	0.740	0.748	100.70	
2304	16.00	el	79	0.00	thk	A1	2	S88	0.728	0.748	100.50	all

Table E.2: b) ^{40}Ca runs at $E_P = 100$ MeV (cont.) Notation: the first of added runs is denoted by ">", each subsequent run by "+"; excluded states following a "^" belong to the previous line. An "!" denotes a run with a scaler problem; the scale factor f for spin-up (u) or spin-down (d) is given in the last column.

Run	Angle	By	Evts	Tangle	Tgt	Ap	Ifs	Cup	Polup	Poldn	Energy	Excluded States
2311	16.00	in	216	0.00	thk	B2	20	S88	0.728	0.748	100.50	all
132	18.00	el	123	9.00	thk	A1	60	E87	0.727	0.750	100.50	
136	18.00	in	357	9.00	thk	A1	60	E87	0.727	0.750	100.50	
266	18.00	el	5	9.00	thn	B1	60	I87	0.740	0.757	100.70	
267	18.00	el	26	9.00	thn	B1	60	I87	0.740	0.756	100.70	
268	18.00	el	26	9.00	thn	B1	60	I87	0.740	0.756	100.70	
269	18.00	el	17	9.00	thk	B1	60	I87	0.740	0.756	100.70	
270	18.00	el	52	9.00	thk	B1	60	I87	0.740	0.756	100.70	
271	18.00	el	62	9.00	thk	B1	60	I87	0.740	0.756	100.70	
272	18.00	el	58	9.00	thk	B1	6	I87	0.740	0.753	100.70	
273	18.00	el	35	9.00	thn	B1	6	I87	0.740	0.752	100.70	
274	18.00	el	34	9.00	thn	B1	6	I87	0.740	0.752	100.70	
275	18.00	el	20	9.00	thn	B1	6	I87	0.740	0.752	100.70	
276	18.00	el	34	9.00	thn	B1	20	I87	0.740	0.751	100.70	
277	18.00	el	29	9.00	thn	B1	20	I87	0.740	0.750	100.70	
278	18.00	el	31	9.00	thk	B1	20	I87	0.740	0.750	100.70	
279	18.00	el	31	9.00	thk	B1	20	I87	0.740	0.750	100.70	
341	18.00	el	79	9.00	thk	B1	20	I87	0.740	0.737	100.70	
> 342	18.00	in	215	9.00	thk	B1	20	I87	0.740	0.737	100.70	
+ 343	18.00	in	52	9.00	thk	B1	20	I87	0.740	0.736	100.70	
2335	18.00	in	902	9.00	thk	B2	20	S88	0.728	0.748	100.50	all
2221	20.00	el	484	10.00	thk	B4	60	E88	0.728	0.748	100.50	all
2228	20.00	in	612	10.00	thk	A1	60	E88	0.728	0.748	100.50	all
2229	20.00	el	41	10.00	thk	A1	60	E88	0.728	0.748	100.50	all
2264	20.00	el	169	10.00	thk	A1	60	S88	0.728	0.748	100.50	all
1	22.00	el	329	11.00	thk	A1	6	E87	0.756	0.774	100.50	
2	22.00	el	263	11.00	thk	A1	20	E87	0.756	0.774	100.50	
8	22.00	in	150	11.00	thk	A1	20	E87	0.756	0.774	100.50	
2235	22.00	el	36	11.00	thk	A1	60	E88	0.728	0.748	100.50	all
2241	22.00	in	209	11.00	thk	A1	60	E88	0.728	0.748	100.50	all
141	24.00	el	104	12.00	thk	A1	60	E87	0.727	0.750	100.50	
> 144	24.00	in	224	12.00	thk	A1	60	E87	0.727	0.750	100.50	
+ 145	24.00	in	546	12.00	thk	A1	60	E87	0.727	0.750	100.50	
2244	24.00	el	70	11.00	thk	A1	60	E88	0.728	0.748	100.50	all
2247	24.00	in	934	11.00	thk	A1	60	E88	0.728	0.748	100.50	all
2248	24.00	in	1209	11.00	thk	B4	60	E88	0.728	0.748	100.50	all
11	26.00	el	120	11.00	thk	A1	20	E87	0.756	0.774	100.50	
> 12	26.00	el	363	11.00	thk	A1	20	E87	0.756	0.774	100.50	
+ 13	26.00	el	589	11.00	thk	A1	20	E87	0.756	0.774	100.50	
21	26.00	in	100	13.00	thk	A1	60	E87	0.756	0.774	100.50	
22	26.00	in	103	13.00	thk	A1	60	E87	0.756	0.774	100.50	
> 23	30.00	el	259	15.00	thk	A1	60	E87	0.756	0.774	100.50	

Table E.2: c) ^{40}Ca runs at $E_P = 100$ MeV (cont.) Notation: the first of added runs is denoted by ">", each subsequent run by "+"; excluded states following a "^" belong to the previous line. An "!" denotes a run with a scaler problem; the scale factor f for spin-up (u) or spin-down (d) is given in the last column.

	Run	Angle	By	Evts	Tangle	Tgt	Ap	Ifs	Cup	Polup	Poldn	Energy	Excluded States
+	24	30.00	el	320	15.00	thk	A1	60	E87	0.756	0.774	100.50	
	27	30.00	in	251	15.00	thk	A1	60	E87	0.756	0.774	100.50	
	32	30.00	in	204	15.00	thk	B2	60	E87	0.756	0.774	100.50	
	33	34.00	el	147	17.00	thk	A1	20	E87	0.756	0.774	100.50	
>	36	34.00	in	262	17.00	thk	B2	60	E87	0.756	0.774	100.50	
+	37	34.00	in	356	17.00	thk	B2	60	E87	0.756	0.774	100.50	
>	41	38.00	el	92	19.00	thk	A1	60	E87	0.756	0.774	100.50	
+	42	38.00	el	95	19.00	thk	A1	60	E87	0.756	0.774	100.50	
	45	38.00	in	246	19.00	thk	B2	60	E87	0.756	0.774	100.50	
	46	38.00	in	198	19.00	thk	B2	60	E87	0.756	0.774	100.50	
	49	38.00	in	189	19.00	thk	B2	60	E87	0.756	0.774	100.50	
	52	42.00	el	187	21.00	thk	B2	60	E87	0.753	0.771	100.50	
>	53	42.00	in	277	21.00	thk	B2	60	E87	0.752	0.769	100.50	
+	54	42.00	in	205	21.00	thk	B2	60	E87	0.752	0.769	100.50	4m1
	60	46.00	el	82	23.00	thk	B2	60	E87	0.743	0.757	100.50	
>	66	46.00	in	45	23.00	thk	B3	60	E87	0.737	0.750	100.50	
+	67	46.00	in	536	23.00	thk	B3	60	E87	0.729	0.750	100.50	
	68	46.00	in	61	23.00	thk	B2	60	E87	0.728	0.750	100.50	
	72	50.00	el	119	25.00	thk	B2	60	E87	0.727	0.750	100.50	
	73	50.00	in	27	25.00	thk	B2	60	E87	0.727	0.750	100.50	
	74	50.00	in	57	25.00	thk	B3	60	E87	0.727	0.750	100.50	
>	75	50.00	in	155	25.00	thk	B3	200	E87	0.727	0.750	100.50	
+	76	50.00	in	5	25.00	thk	B3	200	E87	0.727	0.750	100.50	
+	77	50.00	in	403	25.00	thk	B3	200	E87	0.727	0.750	100.50	
	85	54.00	el	42	27.00	thk	B2	200	E87	0.727	0.750	100.50	
>	89	54.00	in	218	27.00	thk	B3	200	E87	0.727	0.750	100.50	
+	90	54.00	in	301	27.00	thk	B3	200	E87	0.727	0.750	100.50	
>	96	58.00	el	19	29.00	thk	B3	200	E87	0.727	0.750	100.50	
+	97	58.00	el	69	29.00	thk	B3	200	E87	0.727	0.750	100.50	
>	101	58.00	in	383	29.00	thk	A7	200	E87	0.727	0.750	100.50	
+	102	58.00	in	184	29.00	thk	A7	200	E87	0.727	0.750	100.50	
	127	62.00	el	99	31.00	thk	A7	60	E87	0.727	0.750	100.50	
>	128	62.00	in	53	31.00	thk	A7	60	E87	0.727	0.750	100.50	
+	129	62.00	in	410	31.00	thk	A7	60	E87	0.727	0.750	100.50	
	119	66.00	el	82	33.00	thk	A7	60	E87	0.727	0.750	100.50	
>	122	66.00	in	267	33.00	thk	A7	60	E87	0.727	0.750	100.50	
+	123	66.00	in	203	33.00	thk	A7	60	E87	0.727	0.750	100.50	
	103	70.00	el	75	35.00	thk	A7	200	E87	0.727	0.750	100.50	

Table E.2: d) ^{40}Ca runs at $E_p = 100$ MeV (cont.) Notation: the first of added runs is denoted by "$>$", each subsequent run by "$+$"; excluded states following a "^" belong to the previous line. An "!" denotes a run with a scaler problem; the scale factor f for spin-up (u) or spin-down (d) is given in the last column.

	Run	Angle	By	Evts	Tangle	Tgt	Ap	Ifs	Cup	Polup	Poldn	Energy	Excluded States	
	107	70.00	in	179	35.00	thk	A7	200	E87	0.727	0.750	100.50		
>	108	70.00	in	65	35.00	thk	A7	60	E87	0.727	0.750	100.50		
+	109	70.00	in	148	35.00	thk	A7	60	E87	0.727	0.750	100.50		
+	110	70.00	in	67	35.00	thk	A7	60	E87	0.727	0.750	100.50		

Table E.2: e) ^{40}Ca runs at E_P = 100 MeV (cont.) Notation: the first of added runs is denoted by ">", each subsequent run by "+"; excluded states following a "^" belong to the previous line. An "!" denotes a run with a scaler problem; the scale factor f for spin-up (u) or spin-down (d) is given in the last column.

Run	Angle	By	Evts	Tangle	Tgt	Ap	Ifs	Cup	Polup	Poldn	Energy	Excluded States
867	-6.00	in	546	0.00	new	B2	6	I88	0.717	0.733	201.24	
853	6.00	el	118	6.50	new	B1	20	I88	0.717	0.733	201.24	
840	7.50	el	152	6.50	new	B1	20	I88	0.750	0.766	201.24	
846	7.50	in	42	6.50	new	B2	20	I88	0.735	0.751	201.24	
847	7.50	in	546	6.50	new	B2	6	I88	0.733	0.749	201.24	
834	9.00	el	125	6.50	new	B1	20	I88	0.768	0.784	201.24	
839!	9.00	in	511	6.50	new	B2	20	I88	0.755	0.771	201.24	16O:2m2,2m3; fd=1003.315
821	10.50	el	108	6.50	new	B1	20	I88	0.770	0.786	201.24	
831	10.50	in	316	6.50	new	B2	20	I88	0.770	0.786	201.24	16O:2m2,2m3
832	10.50	in	201	6.50	new	B2	20	I88	0.770	0.786	201.24	16O:2m2,2m3
767	12.00	el	308	5.00	new	B2	20	I88	0.766	0.784	201.24	
915	12.00	in	60	0.00	new	B2	20	I88	0.765	0.788	201.24	
916	12.00	in	489	0.00	new	B2	20	I88	0.765	0.789	201.24	
773	13.50	el	233	6.50	new	B2	20	I88	0.770	0.786	201.24	
907	13.50	in	478	0.00	new	B2	20	I88	0.764	0.785	201.24	9Be:Lor
780	15.00	el	279	6.50	new	B2	20	I88	0.770	0.786	201.24	
786	15.00	in	266	6.50	new	B2	20	I88	0.770	0.786	201.24	
787	15.00	el	138	6.50	new	B2	20	I88	0.770	0.786	201.24	
> 788	15.00	el	224	6.50	new	B2	20	I88	0.770	0.786	201.24	
+ 789	15.00	el	91	6.50	new	B2	20	I88	0.770	0.786	201.24	
790	15.00	in	181	6.50	new	B2	20	I88	0.770	0.786	201.24	
> 792	15.00	in	435	6.50	new	B2	20	I88	0.770	0.786	201.24	
+ 793	15.00	in	300	6.50	new	B2	20	I88	0.770	0.786	201.24	
801	16.50	in	97	6.50	new	B2	20	I88	0.770	0.786	201.24	16O:2p1,1m1,2p2,2p3;9Be:
802	16.50	in	359	6.50	new	B2	20	I88	0.770	0.786	201.24	16O:2p1,1m1,2p3. ^5m1
803	16.50	el	150	6.50	new	B2	20	I88	0.770	0.786	201.24	16O:0p1,3m1,2p1,1m1,2p3; ^9Be:3m1,5m1
604	18.00	el	72	9.00	new	B2	60	E87	0.732	0.754	201.53	
605	18.00	in	203	9.00	new	B2	60	E87	0.732	0.754	201.53	
809	18.00	el	167	6.50	new	B2	20	I88	0.770	0.786	201.24	9Be:3m1
815	18.00	el	23	6.50	new	B2	20	I88	0.770	0.786	201.24	9Be:3m1
816	18.00	in	152	6.50	new	B2	20	I88	0.770	0.786	201.24	
818	18.00	in	497	6.50	new	B2	20	I88	0.770	0.786	201.24	
597	19.50	el	92	9.75	new	B2	60	E87	0.732	0.754	201.53	
598	19.50	in	245	9.75	new	B2	60	E87	0.732	0.754	201.53	
610	19.50	el	66	9.75	new	B2	60	E87	0.732	0.754	201.53	
819	19.50	el	100	6.50	new	B2	20	I88	0.770	0.786	201.24	16O:2m1,0m1,2m3,4p3
590	21.00	el	106	10.50	new	B2	60	E87	0.732	0.754	201.53	

Table E.3: a) BeO runs at $E_P = 200$ MeV. Notation: the first of added runs is denoted by ">", each subsequent run by "+"; excluded states following a "^" belong to the previous line. An "*" denotes a run with encoder problem, an "!" a run with a scaler problem; the scale factor f for spin-up (u) or spin-down (d) is given in the last column.

Run	Angle	By	Evts	Tangle	Tgt	Ap	Ifs	Cup	Polup	Poldn	Energy	Excluded States
591	21.00	in	233	10.50	new	B2	60	E87	0.732	0.754	201.53	
613	21.00	el	103	10.50	new	B2	60	E87	0.732	0.754	201.53	
584	23.50	el	65	11.75	new	B2	60	E87	0.732	0.754	201.53	
585	23.50	in	550	11.75	new	B2	60	E87	0.732	0.754	201.53	
617	23.50	el	51	11.75	new	B2	60	E87	0.732	0.754	201.53	
501	25.00	in	210	12.50	new	B2	20	E87	0.732	0.754	201.53	
507	25.00	in	156	12.50	new	B2	60	E87	0.732	0.754	201.53	
577	26.50	el	104	13.25	new	B2	60	E87	0.732	0.754	201.53	
578	26.50	in	230	13.25	new	B2	60	E87	0.732	0.754	201.53	
627	27.25	el	130	13.63	new	B5	60	E87	0.732	0.754	201.53	all
508	28.00	el	159	14.00	new	B2	60	E87	0.732	0.754	201.53	
515	28.00	in	552	14.00	new	B2	60	E87	0.732	0.754	201.53	
571	29.50	el	78	14.75	new	B2	60	E87	0.732	0.754	201.53	
633	30.25	in	156	15.13	new	B5	60	E87	0.732	0.754	201.53	16O:4p3;9Be:1m1
516	31.00	in	541	15.50	new	B2	60	E87	0.732	0.754	201.53	
517	31.00	el	250	15.50	new	B2	60	E87	0.732	0.754	201.53	
634!	33.25	el	124	16.63	new	B2	60	E87	0.732	0.754	201.53	fd=5182.256
526	34.00	el	121	17.00	new	B2	60	E87	0.732	0.754	201.53	16O:2m3;9Be:1p1
528	34.00	in	546	17.00	new	B2	60	E87	0.732	0.754	201.53	16O:3m4,4p3;9Be:1p1
637	36.25	el	68	18.13	new	B2	60	E87	0.732	0.754	201.53	16O:2p3
532	37.00	el	294	18.50	new	B2	60	E87	0.732	0.754	201.53	
534	37.00	in	287	18.50	new	B2	60	E87	0.732	0.754	201.53	
639	39.25	el	55	19.63	new	B2	60	E87	0.732	0.754	201.53	16O:1m1,0m1,4p2,2p3,0p3, ^3m4,4p3,4m1;9Be:3m1
540	40.00	el	111	20.00	new	B2	60	E87	0.732	0.754	201.53	
541	40.00	in	353	20.00	new	B2	60	E87	0.732	0.754	201.53	
546	43.00	in	326	21.50	new	B2	60	E87	0.732	0.754	201.53	
547	43.00	el	172	21.50	new	B2	60	E87	0.732	0.754	201.53	
645	45.25	el	84	22.60	new	B5	60	E87	0.732	0.754	201.53	16O:3m1;9Be:3m1
552	46.00	el	107	23.00	new	B5	60	E87	0.732	0.754	201.53	
553	46.00	el	454	23.00	new	B5	60	E87	0.732	0.754	201.53	

Table E.3: b) BeO runs at $E_P = 200$ MeV (cont.) Notation: the first of added runs is denoted by "$>$", each subsequent run by "$+$"; excluded states following a "^" belong to the previous line. An "$*$" denotes a run with encoder problem, an "!" a run with a scaler problem; the scale factor f for spin-up (u) or spin-down (d) is given in the last column.

Run	Angle	By	Evts	Tangle	Tgt	Ap	Ifs	Cup	Polup	Poldn	Energy	Excluded States
647	48.25	e1	94	24.00	new	B5	60	E87	0.732	0.754	201.53	16O:1m1
557	49.00	e1	555	24.50	new	B5	60	E87	0.732	0.754	201.53	
650!	51.25	e1	103	22.60	new	B5	60	E87	0.732	0.754	201.53	16O:2p2; fd=218.717
566	55.00	e1	496	27.50	new	B5	60	E87	0.732	0.754	201.53	

Table E.3: c) BeO runs at E_P = 200 MeV (cont.) Notation: the first of added runs is denoted by ">", each subsequent run by "+"; excluded states following a "^" belong to the previous line. An "*" denotes a run with encoder problem, an "!" a run with a scaler problem; the scale factor f for spin-up (u) or spin-down (d) is given in the last column.

Run	Angle	By	Evts	Tangle	Tgt	Ap	Ifs	Cup	Polup	Poldn	Energy	Excluded States
> 868	-7.50	el	38	0.00	thk	B1	6	I88	0.717	0.733	201.24	
+ 869	-7.50	el	34	0.00	thk	B1	6	I88	0.717	0.733	201.24	
862	-6.00	in	427	6.50	thk	B2	6	I88	0.717	0.733	201.24	2m2
863	-6.00	in	708	0.00	thk	B2	6	I88	0.717	0.733	201.24	
841	7.50	el	42	6.50	thk	B1	20	I88	0.749	0.765	201.24	0p1
842	7.50	el	244	6.50	thk	B1	20	I88	0.747	0.763	201.24	
845	7.50	in	454	6.50	thk	B2	20	I88	0.739	0.755	201.24	
> 848	7.50	in	263	6.50	thk	B2	6	I88	0.729	0.745	201.24	
+ 849	7.50	in	233	6.50	thk	B2	6	I88	0.727	0.743	201.24	6.91
850	7.50	in	500	6.50	thk	B2	20	I88	0.725	0.741	201.24	6.91
835	9.00	el	306	6.50	thk	B1	20	I88	0.767	0.783	201.24	0p1
838	9.00	in	449	6.50	thk	B2	20	I88	0.759	0.775	201.24	
822	10.50	el	94	6.50	thk	B1	20	I88	0.770	0.786	201.24	
828	10.50	in	327	6.50	thk	B1	20	I88	0.770	0.786	201.24	4m1,1m1,6.03,4p2,6.91,
829	10.50	in	189	6.50	thk	B2	20	I88	0.770	0.786	201.24	^1m2,7.11
766	12.00	in	352	5.00	thk	B2	20	I88	0.765	0.782	201.24	6.93
774	13.50	el	147	6.50	thk	B2	20	I88	0.770	0.786	201.24	
> 775	13.50	in	62	6.50	thk	B2	20	I88	0.770	0.786	201.24	
+ 776	13.50	in	241	6.50	thk	B2	20	I88	0.770	0.786	201.24	
+ 777	13.50	in	202	6.50	thk	B2	20	I88	0.770	0.786	201.24	6.91,7.11
781	15.00	el	243	6.50	thk	B1	20	I88	0.770	0.786	201.24	
> 785	15.00	in	278	6.50	thk	B2	20	I88	0.770	0.786	201.24	
+ 794	15.00	in	334	6.50	thk	B2	20	I88	0.770	0.786	201.24	
+ 795	15.00	in	346	6.50	thk	B2	20	I88	0.770	0.786	201.24	1m2
> 797	16.50	in	537	6.50	thk	B2	20	I88	0.770	0.786	201.24	
+ 798	16.50	in	326	6.50	thk	B2	20	I88	0.770	0.786	201.24	
> 804	16.50	el	53	6.50	thk	B2	20	I88	0.770	0.786	201.24	
+ 805	16.50	el	78	6.50	thk	B2	20	I88	0.770	0.786	201.24	
603	18.00	el	71	9.00	thk	B2	60	E87	0.732	0.754	201.53	
607	18.00	in	208	9.00	thk	B2	60	E87	0.732	0.754	201.53	
810	18.00	el	157	6.50	thk	B2	20	I88	0.770	0.786	201.24	
811	18.00	in	675	6.50	thk	B2	20	I88	0.770	0.786	201.24	2p2,4p1,3m2,3m3
1012	18.00	el	69	9.00	thk	B2	20	E88	0.743	0.763	201.40	
595	19.50	el	99	9.75	thk	B2	60	E87	0.732	0.754	201.53	
> 600	19.50	in	152	9.75	thk	B7	60	E87	0.732	0.754	201.53	
+ 601	19.50	in	404	9.75	thk	B7	60	E87	0.732	0.754	201.53	2p2,4p1
820	19.50	el	99	6.50	thk	B2	20	I88	0.770	0.786	201.24	
1007	19.50	el	83	9.75	thk	B2	60	E88	0.744	0.764	201.40	

Table E.4: a) ^{40}Ca runs at $E_P = 200$ MeV. Notation: the first of added runs is denoted by "$>$", each subsequent run by "$+$"; excluded states following a "$\wedge$" belong to the previous line. An "$*$" denotes a run with encoder problem, an "$!$" a run with a scaler problem; the scale factor f for spin-up (u) or spin-down (d) is given in the last column.

Run	Angle	By	Evts	Tangle	Tgt	Ap	Ifs	Cup	Polup	Poldn	Energy	Excluded States
589	21.00	el	112	10.50	thk	B2	60	E87	0.732	0.754	201.53	
593	21.00	in	540	10.50	thk	B7	60	E87	0.732	0.754	201.53	6.93,7.11
1004	21.00	el	82	10.50	thk	B2	60	E88	0.744	0.765	201.40	
583	23.50	el	101	11.75	thk	B2	60	E87	0.732	0.754	201.53	
587	23.50	in	566	11.75	thk	B2	60	E87	0.732	0.754	201.53	1m2
> 503	25.00	el	13	12.50	thk	B2	20	E87	0.732	0.754	201.53	
+ 504	25.00	el	70	12.50	thk	B2	20	E87	0.732	0.754	201.53	
505	25.00	in	481	12.50	thk	B2	20	E87	0.732	0.754	201.53	6.93
999	25.00	el	62	12.50	thk	B2	60	E88	0.745	0.766	201.40	
574	26.50	el	69	13.25	thk	B2	60	E87	0.732	0.754	201.53	
> 580	26.50	in	213	13.25	thk	B2	60	E87	0.732	0.754	201.53	
+ 581	26.50	in	301	13.25	thk	B2	60	E87	0.732	0.754	201.53	
946*	26.60	el	115	9.00	thk	B2	60	E88	0.760	0.783	201.24	
512	28.00	el	60	14.00	thk	B2	60	E87	0.732	0.754	201.53	
513	28.00	in	498	14.00	thk	B2	60	E87	0.732	0.754	201.53	
568	29.50	el	151	14.75	thk	B2	60	E87	0.732	0.754	201.53	
569	29.50	in	334	14.75	thk	B2	60	E87	0.732	0.754	201.53	
> 520	31.00	el	240	15.50	thk	B2	60	E87	0.732	0.754	201.53	
+ 521	31.00	el	567	15.50	thk	B2	60	E87	0.732	0.754	201.53	1m2
> 524	34.00	el	569	17.00	thk	B5	60	E87	0.732	0.754	201.53	
+ 525	34.00	el	437	17.00	thk	B5	60	E87	0.732	0.754	201.53	
> 530	37.00	el	577	18.50	thk	B5	60	E87	0.732	0.754	201.53	
+ 531	37.00	el	480	18.50	thk	B5	60	E87	0.732	0.754	201.53	
538	40.00	el	535	20.00	thk	B5	60	E87	0.732	0.754	201.53	
539	40.00	el	97	20.00	thk	B2	60	E87	0.732	0.754	201.53	
> 967*	41.60	el	155	22.50	thk	B4	60	E88	0.757	0.780	201.24	
+ 968*	41.60	el	112	22.50	thk	B4	60	E88	0.757	0.780	201.24	
> 544	43.00	el	548	21.50	thk	B5	60	E87	0.732	0.754	201.53	
+ 548	43.00	el	551	21.50	thk	B5	60	E87	0.732	0.754	201.53	
972*	45.60	el	298	24.50	thk	B4	60	E88	0.757	0.779	201.24	
> 550	46.00	in	562	23.00	thk	B5	60	E87	0.732	0.754	201.53	
+ 551	46.00	el	566	23.00	thk	B5	60	E87	0.732	0.754	201.53	

Table E.4: b) ^{40}Ca runs at $E_P = 200$ MeV (cont.) Notation: the first of added runs is denoted by "$>$", each subsequent run by "$+$"; excluded states following a "$\wedge$" belong to the previous line. An "$*$" denotes a run with encoder problem, an "!" a run with a scaler problem; the scale factor f for spin-up (u) or spin-down (d) is given in the last column.

	Run	Angle	By	Evts	Tangle	Tgt	Ap	Ifs	Cup	Polup	Poldn	Energy	Excluded States
>	555	49.00	e1	547	24.50	thk	B5	60	E87	0.732	0.754	201.53	
+	556	49.00	e1	559	24.50	thk	B5	60	E87	0.732	0.754	201.53	
>	559	52.00	e1	555	26.00	thk	B5	60	E87	0.732	0.754	201.53	
+	560	52.00	e1	558	26.00	thk	B5	60	E87	0.732	0.754	201.53	
>	564	55.00	e1	576	27.50	thk	B5	60	E87	0.732	0.754	201.53	
+	565	55.00	e1	567	27.50	thk	B5	60	E87	0.732	0.754	201.53	
+	567	55.00	e1	569	27.50	thk	B5	60	E87	0.732	0.754	201.53	

Table E.4: c) ^{40}Ca runs at E_P = 200 MeV (cont.) Notation: the first of added runs is denoted by ">", each subsequent run by "+"; excluded states following a "^" belong to the previous line. An "*" denotes a run with encoder problem, an "!" a run with a scaler problem; the scale factor f for spin-up (u) or spin-down (d) is given in the last column.

F Data Tables

The notation for these tables is as follows: angles are listed in degrees. Center-of-mass momentum transfers $q_{c.m.}$ are listed in units of fm^{-1}. Center-of-mass differential cross sections $\sigma_{c.m.}(q)$ are quoted in mb/sr and their uncertainties $\Delta\sigma$ in percent; the uncertainties in the analyzing powers are absolute quantities. The tabulated uncertainties include statistical errors, fitting errors and uncertainties from the polarization. In the case of multiple measurements a weighted average is given, with the uncertainty being the larger of the uncertainty of the mean or the standard deviation about the mean. The uncertainty in the laboratory angle may be as large as 0.2°. The overall reproducibility of the data is estimated to be within 3%, the uncertainty in overall normalization is estimated to be about 5%.

F.1 ^{9}Be$(\vec{p},p')$ and ^{16}O$(\vec{p},p')$ at E_P = 100 MeV

θ_L	$\theta_{c.m.}$	$q_{c.m.}$	$\sigma_{c.m.}(q)$	$\Delta\sigma(\%)$	A_y	ΔA_y
-15.80	17.71	0.620	1.654E+02	0.5	0.260	0.007
-13.80	15.47	0.542	2.181E+02	0.6	0.222	0.007
-11.80	13.24	0.464	2.756E+02	0.8	0.220	0.005
-9.80	10.99	0.386	3.170E+02	1.0	0.201	0.005
14.20	15.92	0.558	1.963E+02	0.6	0.253	0.008
16.20	18.16	0.636	1.467E+02	0.7	0.261	0.009
18.20	20.39	0.713	9.974E+01	1.3	0.296	0.005
22.20	24.85	0.867	4.314E+01	3.1	0.307	0.037
24.20	27.08	0.942	2.566E+01	0.5	0.383	0.007
26.20	29.30	1.019	1.555E+01	3.2	0.414	0.010
30.20	33.73	1.169	5.214E+00	3.7	0.489	0.048
34.20	38.14	1.316	2.185E+00	2.3	0.476	0.019
38.20	42.53	1.461	1.436E+00	5.4	0.441	0.017
42.20	46.91	1.604	1.056E+00	5.1	0.424	0.024
46.20	51.26	1.743	6.917E−01	2.8	0.384	0.030
50.20	55.58	1.878	4.689E−01	4.9	0.288	0.026
54.20	59.88	2.011	3.093E−01	1.2	0.186	0.025
58.20	64.15	2.139	1.935E−01	0.6	0.018	0.010
62.20	68.39	2.264	1.180E−01	2.8	-0.117	0.012
66.20	72.59	2.385	7.587E−02	2.5	-0.230	0.008
70.20	76.77	2.502	5.359E−02	5.0	-0.273	0.028

Table F.1: a) ^{9}Be$(\vec{p},p)3/2_1^-$; E_P = 100 MeV

θ_L	$\theta_{c.m.}$	$q_{c.m.}$	$\sigma_{c.m.}(q)$	$\Delta\sigma(\%)$	A_y	ΔA_y
18.20	20.41	0.711	4.105E−02	94.2	0.765	1.159
22.20	24.87	0.864	7.244E−02	16.5	0.165	0.406
24.20	27.10	0.939	1.030E−01	12.7	-0.087	0.190
26.20	29.32	1.015	1.129E−01	6.7	0.243	0.137
30.20	33.76	1.164	9.965E−02	15.3	0.385	0.066
34.20	38.17	1.311	5.806E−02	12.8	0.390	0.037
38.20	42.57	1.456	3.175E−02	20.6	0.208	0.086
42.20	46.95	1.597	2.267E−02	7.7	0.210	0.082
46.20	51.30	1.736	1.449E−02	15.5	0.041	0.056
50.20	55.62	1.871	1.045E−02	12.4	0.085	0.076
54.20	59.92	2.002	1.205E−02	8.2	-0.188	0.046
58.20	64.19	2.128	1.244E−02	6.5	-0.099	0.095
62.20	68.44	2.255	1.093E−02	10.9	0.009	0.868
66.20	72.65	2.375	2.335E−03	17.1	-0.174	0.119
70.20	76.83	2.489	1.552E−03	5.0	-0.216	0.072

Table F.1: b) ^{9}Be$(\vec{p},p')1/2_1^+$ (1.680 MeV); E_P = 100 MeV

θ_L	$\theta_{c.m.}$	$q_{c.m.}$	$\sigma_{c.m.}(q)$	$\Delta\sigma(\%)$	A_y	ΔA_y
-15.80	17.73	0.617	4.119E+00	3.2	0.101	0.042
-13.80	15.49	0.540	3.479E+00	4.4	0.131	0.057
-11.80	13.25	0.463	2.409E+00	3.9	0.048	0.051
-9.80	11.01	0.385	1.658E+00	4.8	0.196	0.068
14.20	15.94	0.555	3.596E+00	4.7	0.144	0.063
16.20	18.18	0.633	4.837E+00	3.9	0.076	0.051
18.20	20.42	0.710	5.488E+00	4.1	0.189	0.032
22.20	24.88	0.862	6.361E+00	8.4	0.199	0.038
24.20	27.11	0.937	5.961E+00	1.0	0.258	0.014
26.20	29.33	1.013	5.143E+00	6.1	0.289	0.007
30.20	33.77	1.162	3.835E+00	1.8	0.345	0.035
34.20	38.19	1.309	2.334E+00	4.2	0.282	0.008
38.20	42.59	1.453	1.538E+00	4.9	0.176	0.009
42.20	46.96	1.594	1.051E+00	2.7	0.024	0.011
46.20	51.32	1.732	7.419E−01	2.2	-0.104	0.023
50.20	55.64	1.867	5.617E−01	2.9	-0.188	0.010
54.20	59.94	1.999	4.123E−01	1.9	-0.270	0.016
58.20	64.22	2.127	2.470E−01	3.6	-0.325	0.040
62.20	68.46	2.251	1.442E−01	3.0	-0.390	0.017
66.20	72.67	2.368	7.922E−02	1.7	-0.435	0.017
70.20	76.85	2.484	3.911E−02	0.8	-0.488	0.010

Table F.1: c) ^{9}Be$(\vec{p},p')5/2_1^-$ (2.429 MeV); E_P = 100 MeV

θ_L	$\theta_{c.m.}$	$q_{c.m.}$	$\sigma_{c.m.}(q)$	$\Delta\sigma(\%)$	A_y	ΔA_y
24.20	27.11	0.936	1.622E−01	71.4	-1.358	1.658
26.20	29.34	1.013	1.313E−01	73.3	0.371	0.931
30.20	33.78	1.161	1.158E−01	39.1	0.148	0.526
34.20	38.20	1.308	5.268E−02	34.9	0.138	0.630
38.20	42.59	1.450	4.729E−02	62.7	0.545	0.864
42.20	46.97	1.591	7.669E−02	13.4	0.104	0.191
46.20	51.32	1.729	5.917E−02	17.4	0.280	0.256
50.20	55.65	1.866	5.749E−02	38.9	0.183	0.202
58.20	64.23	2.123	2.082E−02	15.4	-0.561	0.217
70.20	76.86	2.482	8.412E−03	7.0	-0.262	0.103

Table F.1: d) ^{9}Be$(\vec{p},p')1/2_1^-$ (2.78 MeV); E_P = 100 MeV

θ_L	$\theta_{c.m.}$	$q_{c.m.}$	$\sigma_{c.m.}(q)$	$\Delta\sigma(\%)$	A_y	ΔA_y
18.20	20.42	0.709	1.732E−01	25.6	0.347	0.566
22.20	24.89	0.861	2.274E−01	14.0	0.550	0.216
24.20	27.12	0.936	1.545E−01	22.8	0.659	0.334
26.20	29.34	1.012	1.698E−01	17.3	0.419	0.168
30.20	33.78	1.161	1.131E−01	11.1	0.663	0.142
34.20	38.20	1.307	9.732E−02	6.9	0.319	0.146
38.20	42.60	1.451	7.706E−02	12.2	0.307	0.113
42.20	46.98	1.592	4.813E−02	19.1	0.467	0.073
46.20	51.33	1.730	3.200E−02	41.9	0.189	0.383
50.20	55.66	1.865	1.540E−02	20.3	-0.106	0.378
54.20	59.96	1.996	2.031E−02	17.4	-0.442	0.255
58.20	64.24	2.121	6.535E−03	15.3	0.189	0.236
62.20	68.48	2.245	5.755E−03	7.3	0.036	0.109
66.20	72.69	2.364	5.300E−03	14.4	-0.095	0.213
70.20	76.87	2.480	1.357E−03	59.6	-0.263	0.810

Table F.1: e) ^{9}Be$(\vec{p},p')5/2_1^+$ (3.049 MeV); E_P = 100 MeV

θ_L	$\theta_{c.m.}$	$q_{c.m.}$	$\sigma_{c.m.}(q)$	$\Delta\sigma(\%)$	A_y	ΔA_y
18.20	20.44	0.707	6.190E−01	22.1	0.479	0.366
22.20	24.91	0.859	2.982E−01	21.6	0.557	0.272
24.20	27.14	0.933	1.697E−01	44.2	-0.268	0.688
26.20	29.37	1.008	1.358E−01	33.6	-0.214	0.510
34.20	38.23	1.302	1.059E−01	15.8	0.631	0.200
42.20	47.02	1.584	3.006E−02	23.3	0.643	0.356
46.20	51.38	1.721	8.871E−03	54.7	-0.463	0.847
50.20	55.71	1.855	6.220E−03	50.6	-0.288	0.765
54.20	60.01	1.986	1.052E−02	19.8	0.394	0.313
58.20	64.29	2.113	1.142E−02	16.0	-0.292	0.229
70.20	76.93	2.470	1.154E−02	7.2	-0.391	0.103

Table F.1: f) ^{9}Be$(\vec{p},p')3/2^{+}_{1}$ (4.704 MeV); E_P = 100 MeV

θ_L	$\theta_{c.m.}$	$q_{c.m.}$	$\sigma_{c.m.}(q)$	$\Delta\sigma(\%)$	A_y	ΔA_y
-15.80	17.77	0.615	5.733E+00	35.7	0.190	0.474
-11.80	13.28	0.463	3.021E+00	16.9	0.120	0.222
18.20	20.46	0.705	4.101E+00	4.6	0.250	0.062
22.20	24.94	0.856	4.229E+00	5.1	0.037	0.073
26.20	29.40	1.006	3.572E+00	5.2	0.336	0.067
30.20	33.84	1.152	2.101E+00	2.8	0.305	0.036
34.20	38.27	1.298	1.792E+00	12.1	0.274	0.023
38.20	42.68	1.439	1.159E+00	2.8	0.187	0.040
42.20	47.06	1.578	7.190E−01	4.2	0.171	0.060
46.20	51.42	1.714	5.531E−01	3.8	-0.068	0.056
50.20	55.76	1.848	4.810E−01	5.2	-0.100	0.076
54.20	60.07	1.977	4.253E−01	4.8	-0.108	0.072
58.20	64.34	2.103	3.179E−01	3.8	-0.319	0.054
62.20	68.59	2.226	1.864E−01	3.1	-0.299	0.045
66.20	72.81	2.344	1.853E−01	11.4	-0.457	0.165
70.20	76.99	2.458	1.037E−01	10.7	-0.799	0.083

Table F.1: g) ^{9}Be$(\vec{p}, p')$ Lor (6.5 MeV); E_P = 100 MeV

θ_L	$\theta_{c.m.}$	$q_{c.m.}$	$\sigma_{c.m.}(q)$	$\Delta\sigma(\%)$	A_y	ΔA_y
-15.80	16.88	0.621	3.369E+02	0.4	0.251	0.005
-13.80	14.75	0.543	4.672E+02	0.4	0.240	0.005
-11.80	12.61	0.465	5.914E+02	0.3	0.227	0.005
-9.80	10.48	0.386	6.770E+02	0.3	0.219	0.014
14.20	15.17	0.558	4.156E+02	0.5	0.252	0.006
16.20	17.31	0.636	2.847E+02	0.6	0.276	0.007
18.20	19.44	0.714	1.829E+02	1.0	0.293	0.002
22.20	23.70	0.869	6.185E+01	1.1	0.332	0.037
24.20	25.83	0.944	3.234E+01	0.5	0.437	0.006
26.20	27.95	1.021	1.698E+01	4.0	0.527	0.005
30.20	32.20	1.173	5.860E+00	8.8	0.717	0.031
34.20	36.43	1.322	4.595E+00	2.4	0.666	0.016
38.20	40.65	1.469	3.459E+00	1.3	0.673	0.012
42.20	44.86	1.614	2.212E+00	6.9	0.734	0.018
46.20	49.06	1.756	1.041E+00	2.1	0.820	0.012
50.20	53.25	1.895	5.870E−01	4.2	0.733	0.015
54.20	57.41	2.032	4.377E−01	1.1	0.486	0.018
58.20	61.57	2.165	3.370E−01	2.0	0.309	0.014
62.20	65.70	2.294	2.363E−01	1.9	0.187	0.018
66.20	69.82	2.421	1.402E−01	3.0	0.117	0.016
70.20	73.92	2.543	6.473E−02	4.4	0.023	0.011

Table F.2: a) $^{16}O(\vec{p},p)0_1^+$; E_P = 100 MeV

θ_L	$\theta_{c.m.}$	$q_{c.m.}$	$\sigma_{c.m.}(q)$	$\Delta\sigma(\%)$	A_y	ΔA_y
-15.80	16.91	0.616	1.275E−01	10.2	0.309	0.134
-13.80	14.77	0.539	7.844E−02	68.1	-1.300	1.257
-11.80	12.64	0.463	7.987E−02	19.3	0.438	0.326
14.20	15.20	0.555	1.744E−01	43.5	0.018	0.577
16.20	17.34	0.631	1.062E−01	66.6	1.296	1.074
18.20	19.48	0.707	1.346E−01	13.3	0.179	0.203
22.20	23.74	0.858	1.657E−01	11.6	0.242	0.160
24.20	25.87	0.933	8.654E−02	8.6	0.106	0.190
26.20	28.00	1.008	8.378E−02	10.1	0.212	0.136
30.20	32.25	1.157	6.275E−02	11.9	0.163	0.093
34.20	36.50	1.304	5.913E−02	15.3	0.164	0.074
38.20	40.73	1.448	3.909E−02	13.2	0.268	0.162
42.20	44.94	1.591	3.819E−02	15.3	0.393	0.092
46.20	49.15	1.730	2.370E−02	15.8	0.600	0.142
54.20	57.51	2.001	1.478E−02	22.0	0.191	0.094
58.20	61.67	2.132	1.388E−02	7.8	0.208	0.057
62.20	65.81	2.259	1.122E−02	12.5	0.016	0.064
66.20	69.93	2.381	9.047E−03	5.5	-0.013	0.081

Table F.2: b) $^{16}O(\vec{p},p')0_2^+$ (6.0494 MeV); E_P = 100 MeV

θ_L	$\theta_{c.m.}$	$q_{c.m.}$	$\sigma_{c.m.}(q)$	$\Delta\sigma(\%)$	A_y	ΔA_y
-15.80	16.91	0.616	1.628E+00	1.7	0.061	0.036
-13.80	14.78	0.539	1.368E+00	8.2	0.019	0.107
-11.80	12.64	0.463	8.053E−01	3.0	-0.090	0.035
-9.80	10.50	0.387	5.922E−01	9.6	-0.060	0.127
16.20	17.34	0.631	1.763E+00	7.5	0.017	0.099
18.20	19.48	0.707	2.408E+00	4.6	0.083	0.028
22.20	23.74	0.858	3.492E+00	1.0	0.129	0.033
24.20	25.88	0.932	4.077E+00	1.3	0.166	0.019
26.20	28.00	1.008	4.231E+00	3.2	0.147	0.012
30.20	32.26	1.157	4.140E+00	0.6	0.210	0.031
34.20	36.50	1.303	3.161E+00	3.3	0.168	0.007
38.20	40.73	1.448	2.455E+00	1.7	0.097	0.005
42.20	44.94	1.590	1.809E+00	2.8	-0.013	0.005
46.20	49.15	1.730	1.323E+00	2.4	-0.138	0.019
50.20	53.34	1.867	1.069E+00	2.5	-0.255	0.019
54.20	57.51	2.001	7.913E−01	3.0	-0.347	0.008
58.20	61.67	2.132	5.339E−01	1.2	-0.421	0.004
62.20	65.81	2.259	3.093E−01	2.3	-0.515	0.007
66.20	69.93	2.383	1.662E−01	3.5	-0.651	0.013
70.20	74.03	2.503	7.605E−02	5.0	-0.785	0.009

Table F.2: c) $^{16}O(\vec{p},p')3^-_1$ (6.1299 MeV); E_P = 100 MeV

θ_L	$\theta_{c.m.}$	$q_{c.m.}$	$\sigma_{c.m.}(q)$	$\Delta\sigma(\%)$	A_y	ΔA_y
-15.80	16.92	0.615	2.462E+00	1.3	0.164	0.018
-13.80	14.78	0.540	1.986E+00	6.6	0.082	0.086
-11.80	12.64	0.464	1.416E+00	7.7	0.117	0.043
-9.80	10.50	0.388	9.810E−01	7.9	0.055	0.092
16.20	17.35	0.631	2.450E+00	6.3	0.193	0.079
18.20	19.48	0.706	2.743E+00	1.1	0.202	0.011
22.20	23.75	0.857	2.510E+00	1.4	0.230	0.052
24.20	25.88	0.931	2.022E+00	1.7	0.295	0.019
26.20	28.01	1.007	1.581E+00	2.7	0.286	0.020
30.20	32.26	1.155	7.207E−01	4.5	0.308	0.035
34.20	36.51	1.301	3.414E−01	4.5	0.351	0.034
38.20	40.74	1.446	1.803E−01	2.0	0.330	0.027
42.20	44.95	1.587	1.285E−01	5.9	0.440	0.067
46.20	49.16	1.727	8.527E−02	2.2	0.630	0.031
50.20	53.35	1.863	5.318E−02	7.7	0.810	0.049
54.20	57.52	1.997	3.329E−02	10.3	0.778	0.068
58.20	61.68	2.127	2.723E−02	19.1	0.601	0.283
62.20	65.82	2.254	2.527E−02	2.4	0.150	0.045
66.20	69.94	2.378	2.418E−02	1.5	-0.028	0.031
70.20	74.05	2.498	1.937E−02	2.8	-0.155	0.015

Table F.2: d) $^{16}O(\vec{p},p')2_1^+$ (6.9171 MeV); E_P = 100 MeV

θ_L	$\theta_{c.m.}$	$q_{c.m.}$	$\sigma_{c.m.}(q)$	$\Delta\sigma(\%)$	A_y	ΔA_y
-15.80	16.92	0.615	2.048E−01	6.5	0.046	0.086
-11.80	12.64	0.464	9.898E−02	11.2	0.065	0.198
-9.80	10.50	0.388	1.191E−01	28.6	-0.343	0.408
14.20	15.21	0.555	8.307E−02	69.8	-0.266	0.958
18.20	19.48	0.706	3.039E−01	5.8	0.122	0.091
22.20	23.75	0.857	5.658E−01	4.5	0.087	0.085
24.20	25.88	0.931	6.406E−01	3.4	0.185	0.025
26.20	28.01	1.007	7.404E−01	6.7	0.180	0.037
30.20	32.27	1.155	7.420E−01	5.2	0.196	0.058
34.20	36.51	1.301	7.024E−01	4.7	0.224	0.018
38.20	40.74	1.445	5.695E−01	1.3	0.152	0.008
42.20	44.96	1.587	4.498E−01	2.3	0.075	0.015
46.20	49.16	1.726	3.262E−01	2.8	-0.018	0.036
50.20	53.35	1.862	2.415E−01	4.1	-0.126	0.015
54.20	57.53	1.996	1.476E−01	5.1	-0.225	0.039
58.20	61.68	2.126	8.423E−02	9.8	-0.348	0.027
62.20	65.83	2.253	3.360E−02	4.7	-0.520	0.045
66.20	69.95	2.377	1.515E−02	2.1	-0.609	0.014
70.20	74.05	2.497	6.951E−03	4.0	-0.465	0.027

Table F.2: e) $^{16}O(\vec{p},p')1_1^-$ (7.1169 MeV); E_P = 100 MeV

θ_L	$\theta_{c.m.}$	$q_{c.m.}$	$\sigma_{c.m.}(q)$	$\Delta\sigma(\%)$	A_y	ΔA_y
-15.80	16.93	0.616	1.271E−01	7.2	0.394	0.095
-11.80	12.65	0.466	1.330E−01	7.6	0.423	0.097
18.20	19.49	0.705	1.469E−01	3.4	0.332	0.048
22.20	23.77	0.854	1.227E−01	4.6	0.019	0.065
24.20	25.90	0.929	1.256E−01	4.4	-0.029	0.066
26.20	28.03	1.003	1.244E−01	3.7	-0.111	0.053
30.20	32.28	1.150	9.404E−02	3.5	-0.390	0.053
34.20	36.53	1.296	1.062E−01	5.4	-0.388	0.041
38.20	40.76	1.438	9.793E−02	2.3	-0.393	0.034
42.20	44.98	1.579	8.192E−02	2.7	-0.393	0.039
46.20	49.19	1.717	6.474E−02	2.5	-0.333	0.036
50.20	53.38	1.853	4.918E−02	2.9	-0.352	0.043
54.20	57.56	1.985	3.109E−02	2.5	-0.372	0.036
58.20	61.72	2.115	2.045E−02	2.4	-0.384	0.034
62.20	65.86	2.241	1.074E−02	2.2	-0.222	0.032
66.20	69.98	2.364	6.612E−03	2.1	-0.168	0.031
70.20	74.09	2.483	2.725E−03	4.6	0.160	0.073

Table F.2: f) $^{16}O(\vec{p},p')2_1^-$ (8.8719 MeV); E_P = 100 MeV

θ_L	$\theta_{c.m.}$	$q_{c.m.}$	$\sigma_{c.m.}(q)$	$\Delta\sigma(\%)$	A_y	ΔA_y
-15.80	16.93	0.616	5.511E−02	49.6	0.027	0.657
18.20	19.50	0.705	4.812E−02	31.2	1.125	0.513
42.20	44.99	1.576	3.892E−02	24.1	-0.083	0.350
50.20	53.39	1.849	1.606E−02	49.3	-1.297	0.921
54.20	57.57	1.982	8.294E−03	28.0	-1.039	0.506
58.20	61.73	2.111	1.047E−02	11.8	-0.676	0.172
62.20	65.87	2.237	1.449E−02	10.1	-0.360	0.143
66.20	70.00	2.359	8.679E−03	6.2	-0.562	0.087
70.20	74.10	2.478	1.885E−03	51.1	-1.374	0.735

Table F.2: g) $^{16}O(\vec{p},p')1_2^-$ (9.585 MeV); E_P = 100 MeV

θ_L	$\theta_{c.m.}$	$q_{c.m.}$	$\sigma_{c.m.}(q)$	$\Delta\sigma(\%)$	A_y	ΔA_y
-15.80	16.93	0.617	9.041E−02	9.2	0.104	0.121
-11.80	12.65	0.468	6.465E−02	12.6	-0.225	0.166
18.20	19.50	0.705	1.152E−01	4.0	-0.033	0.060
22.20	23.77	0.854	1.321E−01	4.3	-0.052	0.061
24.20	25.91	0.928	1.365E−01	4.0	-0.027	0.060
26.20	28.04	1.002	1.418E−01	3.3	0.077	0.046
30.20	32.29	1.148	1.039E−01	3.2	0.013	0.045
34.20	36.54	1.294	8.546E−02	6.6	0.126	0.077
38.20	40.77	1.435	6.333E−02	2.6	0.173	0.036
42.20	45.00	1.575	4.390E−02	3.6	0.105	0.051
46.20	49.20	1.713	3.541E−02	4.3	0.077	0.062
50.20	53.40	1.848	3.046E−02	5.2	-0.052	0.077
54.20	57.57	1.981	1.718E−02	4.3	-0.189	0.063
58.20	61.73	2.110	1.268E−02	3.6	-0.329	0.051
62.20	65.88	2.235	7.215E−03	3.7	-0.491	0.050
66.20	70.00	2.358	3.995E−03	2.7	-0.578	0.037
70.20	74.11	2.477	1.654E−03	3.6	-0.860	0.049

Table F.2: h) $^{16}O(\vec{p},p')2_2^+$ (9.8445 MeV); E_P = 100 MeV

θ_L	$\theta_{c.m.}$	$q_{c.m.}$	$\sigma_{c.m.}(q)$	$\Delta\sigma(\%)$	A_y	ΔA_y
-15.80	16.94	0.617	5.510E−02	16.1	-0.045	0.213
18.20	19.50	0.705	6.634E−02	7.3	0.301	0.104
22.20	23.78	0.854	9.031E−02	6.6	0.057	0.093
24.20	25.91	0.927	9.684E−02	6.1	0.189	0.088
26.20	28.04	1.002	1.217E−01	3.8	0.161	0.064
30.20	32.30	1.147	1.114E−01	3.4	0.093	0.048
34.20	36.55	1.293	1.278E−01	3.1	0.157	0.022
38.20	40.78	1.434	1.043E−01	2.0	0.098	0.029
42.20	45.00	1.574	9.185E−02	2.3	-0.015	0.032
46.20	49.21	1.711	8.038E−02	2.4	-0.131	0.034
50.20	53.40	1.846	6.937E−02	3.2	-0.162	0.047
54.20	57.58	1.978	5.075E−02	2.5	-0.400	0.037
58.20	61.74	2.107	3.766E−02	2.1	-0.386	0.029
62.20	65.89	2.233	2.356E−02	1.6	-0.464	0.022
66.20	70.01	2.355	1.454E−02	1.3	-0.504	0.018
70.20	74.12	2.473	7.915E−03	1.3	-0.491	0.018

Table F.2: i) $^{16}O(\vec{p},p')4_1^+$ (10.356 MeV); $E_P = 100$ MeV

θ_L	$\theta_{c.m.}$	$q_{c.m.}$	$\sigma_{c.m.}(q)$	$\Delta\sigma(\%)$	A_y	ΔA_y
-15.80	16.94	0.617	6.730E−02	11.4	-0.113	0.152
-11.80	12.66	0.470	5.482E−02	15.2	-0.254	0.204
18.20	19.51	0.706	6.384E−02	6.3	-0.302	0.097
22.20	23.78	0.853	5.043E−02	8.8	-0.351	0.134
24.20	25.92	0.927	3.060E−02	13.0	-0.264	0.201
26.20	28.05	1.000	2.579E−02	12.0	-0.559	0.191
30.20	32.31	1.146	1.790E−02	12.2	-0.042	0.175
34.20	36.55	1.291	2.074E−02	5.6	0.169	0.076
38.20	40.79	1.432	1.809E−02	6.4	0.388	0.088
42.20	45.01	1.572	1.708E−02	6.5	0.544	0.093
46.20	49.22	1.709	1.513E−02	6.6	0.140	0.095
50.20	53.41	1.844	1.118E−02	10.2	0.478	0.156
58.20	61.75	2.104	4.139E−03	14.2	0.408	0.232
62.20	65.90	2.229	3.578E−03	7.9	-0.026	0.116
66.20	70.02	2.351	1.037E−03	11.7	0.056	0.176
70.20	74.13	2.470	3.666E−04	18.9	0.050	0.283

Table F.2: j) $^{16}\mathrm{O}(\vec{p},p')0_1^-$ (10.957 MeV); $\mathrm{E_P}$ = 100 MeV

θ_L	$\theta_{c.m.}$	$q_{c.m.}$	$\sigma_{c.m.}(q)$	$\Delta\sigma(\%)$	A_y	ΔA_y
-15.80	16.94	0.618	3.823E−02	74.0	1.076	1.060
18.20	19.51	0.706	3.008E−02	61.8	-0.296	1.036
22.20	23.78	0.853	4.484E−02	77.6	-0.344	1.353
24.20	25.92	0.927	3.924E−02	66.8	0.677	1.214
26.20	28.05	1.001	6.959E−02	16.6	0.067	0.234
30.20	32.31	1.146	8.522E−02	11.6	0.161	0.164
34.20	36.56	1.291	7.401E−02	15.9	0.007	0.218
38.20	40.79	1.431	8.887E−02	7.7	0.121	0.109
42.20	45.01	1.571	5.446E−02	28.8	0.316	0.501
46.20	49.22	1.708	5.742E−02	17.9	-0.280	0.283
50.20	53.42	1.843	3.867E−02	31.1	-1.228	0.546
58.20	61.76	2.103	3.357E−02	29.2	-0.248	0.392
62.20	65.90	2.228	2.671E−02	17.3	-0.266	0.238
66.20	70.03	2.350	2.108E−02	18.6	-0.260	0.264
70.20	74.13	2.469	1.196E−02	18.3	-0.318	0.285

Table F.2: k) $^{16}O(\vec{p},p')4_2^+$ (11.097 MeV); E_P = 100 MeV

θ_L	$\theta_{c.m.}$	$q_{c.m.}$	$\sigma_{c.m.}(q)$	$\Delta\sigma(\%)$	A_y	ΔA_y
-15.80	16.94	0.618	1.392E+00	1.9	0.166	0.025
-11.80	12.66	0.472	7.839E−01	3.0	0.222	0.039
18.20	19.51	0.706	1.644E+00	0.9	0.197	0.013
22.20	23.79	0.853	1.503E+00	1.1	0.248	0.015
24.20	25.92	0.926	1.254E+00	1.2	0.280	0.017
26.20	28.05	1.000	9.787E−01	1.2	0.241	0.016
30.20	32.31	1.145	4.468E−01	1.5	0.166	0.021
34.20	36.56	1.289	2.356E−01	1.4	0.198	0.019
38.20	40.80	1.430	1.336E−01	1.9	0.156	0.027
42.20	45.02	1.570	1.032E−01	2.3	0.200	0.033
46.20	49.23	1.707	8.197E−02	2.5	0.399	0.035
50.20	53.42	1.841	5.964E−02	3.4	0.437	0.050
54.20	57.60	1.973	3.438E−02	3.8	0.648	0.060
58.20	61.76	2.101	2.518E−02	4.3	0.625	0.072
62.20	65.91	2.226	2.612E−02	2.8	0.258	0.044
66.20	70.03	2.348	2.688E−02	1.2	0.042	0.018
70.20	74.14	2.466	2.386E−02	0.9	-0.044	0.013

Table F.2: 1) $^{16}O(\vec{p},p')2_3^+$ (11.520 MeV); E_P = 100 MeV

θ_L	$\theta_{c.m.}$	$q_{c.m.}$	$\sigma_{c.m.}(q)$	$\Delta\sigma(\%)$	A_y	ΔA_y
-15.80	16.95	0.619	9.621E−02	8.8	0.071	0.117
18.20	19.52	0.706	1.456E−01	3.4	0.080	0.050
22.20	23.79	0.853	2.051E−01	3.2	0.070	0.045
24.20	25.93	0.926	2.000E−01	3.2	0.062	0.047
26.20	28.06	0.999	1.672E−01	3.0	0.065	0.043
30.20	32.32	1.144	9.963E−02	3.2	-0.107	0.047
34.20	36.57	1.287	8.134E−02	2.3	-0.120	0.033
38.20	40.80	1.429	6.320E−02	2.5	-0.142	0.036
42.20	45.03	1.568	5.463E−02	2.8	0.061	0.040
46.20	49.24	1.705	2.958E−02	4.0	0.309	0.057
50.20	53.43	1.839	1.551E−02	7.2	0.533	0.108
54.20	57.61	1.970	7.318E−03	8.4	1.193	0.154
58.20	61.77	2.098	7.772E−03	6.5	0.898	0.115
62.20	65.92	2.223	8.438E−03	4.1	0.631	0.069
66.20	70.05	2.345	7.362E−03	2.7	0.387	0.044
70.20	74.15	2.463	5.484E−03	2.0	0.242	0.030

Table F.2: m) $^{16}O(\vec{p},p')0_3^+$ (12.049 MeV); E_P = 100 MeV

θ_L	$\theta_{c.m.}$	$q_{c.m.}$	$\sigma_{c.m.}(q)$	$\Delta\sigma(\%)$	A_y	ΔA_y
18.20	19.52	0.706	9.331E−03	82.6	-1.376	1.982
24.20	25.93	0.926	1.645E−02	51.5	0.467	0.753
26.20	28.06	0.999	6.207E−02	12.1	0.060	0.170
30.20	32.32	1.143	1.331E−01	4.8	0.020	0.068
34.20	36.57	1.287	7.560E−02	4.6	0.316	0.062
38.20	40.81	1.428	5.644E−02	5.1	0.269	0.071
42.20	45.03	1.567	5.640E−02	4.6	0.111	0.066
46.20	49.24	1.703	4.126E−02	5.7	0.026	0.082
50.20	53.44	1.837	2.616E−02	9.2	0.136	0.137
54.20	57.62	1.968	1.600E−02	9.4	-0.268	0.136
58.20	61.78	2.096	1.122E−02	9.7	-0.433	0.135
62.20	65.93	2.221	1.040E−02	6.9	-0.450	0.095
66.20	70.05	2.342	2.983E−03	19.0	-0.463	0.251
70.20	74.16	2.460	2.076E−03	18.2	-1.331	0.258

Table F.2: n) $^{16}O(\vec{p},p')1_3^-$ (12.440 MeV); E_P = 100 MeV

θ_L	$\theta_{c.m.}$	$q_{c.m.}$	$\sigma_{c.m.}(q)$	$\Delta\sigma(\%)$	A_y	ΔA_y
-15.80	16.95	0.619	2.445E−01	4.8	0.012	0.064
-11.80	12.66	0.474	2.143E−01	5.8	-0.107	0.076
18.20	19.52	0.706	2.147E−01	2.7	0.052	0.040
22.20	23.80	0.853	1.536E−01	3.8	-0.173	0.056
24.20	25.93	0.926	1.302E−01	4.4	-0.124	0.065
26.20	28.06	0.999	1.052E−01	4.3	-0.204	0.063
30.20	32.32	1.143	6.679E−02	5.2	-0.328	0.077
34.20	36.57	1.286	4.374E−02	4.5	-0.366	0.069
38.20	40.81	1.428	2.806E−02	5.7	-0.339	0.086
42.20	45.04	1.566	2.419E−02	6.2	0.109	0.088
46.20	49.25	1.703	1.991E−02	7.0	0.461	0.104
50.20	53.44	1.837	1.869E−02	7.9	0.285	0.118
54.20	57.62	1.968	1.343E−02	7.0	0.594	0.120
58.20	61.78	2.096	1.061E−02	6.3	0.390	0.104
62.20	65.93	2.220	5.759E−03	7.7	0.377	0.133
66.20	70.06	2.342	3.790E−03	6.9	0.158	0.109
70.20	74.16	2.459	1.647E−03	12.0	0.303	0.209

Table F.2: o) $^{16}O(\vec{p},p')2_2^-$ (12.530 MeV); E_P = 100 MeV

θ_L	$\theta_{c.m.}$	$q_{c.m.}$	$\sigma_{c.m.}(q)$	$\Delta\sigma(\%)$	A_y	ΔA_y
18.20	19.52	0.707	7.847E−03	75.6	1.325	1.254
22.20	23.80	0.853	1.501E−02	42.6	0.781	0.637
30.20	32.33	1.143	4.017E−02	10.0	0.024	0.142
34.20	36.58	1.286	4.682E−02	5.4	0.016	0.077
38.20	40.81	1.427	2.035E−02	9.4	-0.021	0.135
42.20	45.04	1.566	1.503E−02	10.9	-0.254	0.162
46.20	49.25	1.702	1.360E−02	10.4	-0.134	0.151
50.20	53.45	1.836	8.895E−03	15.9	-0.121	0.235
54.20	57.63	1.967	6.313E−03	13.7	-0.247	0.203
58.20	61.79	2.094	4.948E−03	12.4	-0.517	0.180
62.20	65.93	2.219	3.652E−03	9.5	-0.128	0.137
66.20	70.06	2.340	6.387E−04	46.1	0.065	0.696
70.20	74.17	2.458	8.651E−04	28.3	0.424	0.474

Table F.2: p) $^{16}O(\vec{p},p')0_2^-$ (12.796 MeV); E_P = 100 MeV

θ_L	$\theta_{c.m.}$	$q_{c.m.}$	$\sigma_{c.m.}(q)$	$\Delta\sigma(\%)$	A_y	ΔA_y
-15.80	16.95	0.620	7.014E−01	3.5	0.332	0.047
18.20	19.52	0.707	6.420E−01	1.7	0.303	0.025
22.20	23.80	0.853	4.283E−01	2.6	0.363	0.037
24.20	25.94	0.926	3.277E−01	3.3	0.360	0.049
26.20	28.07	0.998	2.590E−01	2.9	0.298	0.039
30.20	32.33	1.143	1.161E−01	4.2	0.165	0.059
34.20	36.58	1.285	7.590E−02	3.6	0.065	0.051
38.20	40.82	1.426	4.557E−02	4.5	-0.038	0.064
42.20	45.04	1.565	2.994E−02	6.1	-0.282	0.091
46.20	49.25	1.701	2.703E−02	5.8	0.011	0.084
50.20	53.45	1.835	2.284E−02	8.2	-0.121	0.123
54.20	57.63	1.966	1.312E−02	8.1	-0.204	0.123
58.20	61.79	2.094	9.296E−03	8.1	-0.222	0.121
62.20	65.94	2.218	6.604E−03	6.0	-0.167	0.087
66.20	70.07	2.339	3.730E−03	7.6	-0.043	0.112
70.20	74.17	2.457	2.221E−03	10.1	0.084	0.155

Table F.2: q) $^{16}O(\vec{p},p')2_3^-$ (12.969 MeV); E_P = 100 MeV

θ_L	$\theta_{c.m.}$	$q_{c.m.}$	$\sigma_{c.m.}(q)$	$\Delta\sigma(\%)$	A_y	ΔA_y
-15.80	16.95	0.620	5.627E−01	6.8	0.192	0.092
18.20	19.52	0.707	5.574E−01	3.2	0.032	0.047
22.20	23.80	0.853	5.658E−01	3.3	0.101	0.047
24.20	25.94	0.926	5.199E−01	3.6	0.120	0.053
26.20	28.07	0.998	4.339E−01	3.2	0.154	0.044
30.20	32.33	1.142	3.656E−01	2.7	0.124	0.038
34.20	36.58	1.285	3.389E−01	1.7	0.185	0.024
38.20	40.82	1.426	2.389E−01	2.0	0.101	0.028
42.20	45.04	1.565	1.586E−01	2.5	0.068	0.036
46.20	49.25	1.701	1.050E−01	3.0	0.005	0.044
50.20	53.45	1.835	6.925E−02	4.8	-0.001	0.071
54.20	57.63	1.965	4.527E−02	4.3	0.002	0.063
58.20	61.79	2.093	3.005E−02	4.4	-0.186	0.065
62.20	65.94	2.217	1.917E−02	3.6	-0.219	0.052
66.20	70.07	2.338	1.038E−02	5.3	-0.274	0.075
70.20	74.18	2.456	6.604E−03	9.7	0.185	0.157

Table F.2: r) $^{16}O(\vec{p},p')13.08$ (13.08 MeV); E_P = 100 MeV

θ_L	$\theta_{c.m.}$	$q_{c.m.}$	$\sigma_{c.m.}(q)$	$\Delta\sigma(\%)$	A_y	ΔA_y
-15.80	16.95	0.620	8.633E−02	15.6	-0.165	0.209
18.20	19.52	0.707	1.312E−01	5.6	0.077	0.082
22.20	23.80	0.853	1.726E−01	4.9	0.062	0.069
24.20	25.94	0.926	1.676E−01	4.9	0.113	0.071
26.20	28.07	0.998	1.585E−01	4.3	0.105	0.061
30.20	32.33	1.142	1.522E−01	3.2	0.041	0.046
34.20	36.58	1.285	1.384E−01	2.2	0.163	0.031
38.20	40.82	1.426	1.010E−01	2.6	0.163	0.037
42.20	45.05	1.564	6.143E−02	3.5	0.307	0.051
46.20	49.26	1.700	3.125E−02	5.2	0.193	0.075
54.20	57.63	1.964	1.082E−02	8.8	0.035	0.131
58.20	61.80	2.092	8.559E−03	7.7	-0.224	0.111
62.20	65.94	2.216	6.320E−03	6.1	-0.287	0.088
66.20	70.07	2.337	3.296E−03	10.5	-0.368	0.150
70.20	74.18	2.455	2.931E−03	11.2	-0.113	0.158

Table F.2: s) $^{16}\mathrm{O}(\vec{p},p')3^-_4$ (13.259 MeV); $\mathrm{E_P}$ = 100 MeV

F.2 $^{40}Ca(\vec{p}, p')$ at $E_P = 100$ MeV

θ_L	$\theta_{c.m.}$	$q_{c.m.}$	$\sigma_{c.m.}(q)$	$\Delta\sigma(\%)$	A_y	ΔA_y
-15.80	16.23	0.621	5.352E+02	1.4	0.199	0.011
-13.80	14.18	0.543	1.015E+03	5.3	0.200	0.014
-11.80	12.13	0.465	1.648E+03	2.9	0.207	0.010
-9.80	10.07	0.386	2.414E+03	2.7	0.226	0.019
10.20	10.48	0.402	2.171E+03	2.6	0.224	0.003
12.20	12.54	0.480	1.562E+03	6.8	0.201	0.018
14.20	14.59	0.559	8.720E+02	1.2	0.200	0.008
16.20	16.64	0.637	4.229E+02	0.7	0.193	0.004
18.20	18.70	0.715	1.687E+02	3.3	0.201	0.007
22.20	22.80	0.869	2.055E+01	0.5	0.730	0.006
24.20	24.85	0.946	2.168E+01	0.5	0.821	0.006
26.20	26.90	1.023	2.879E+01	2.5	0.710	0.003
30.20	31.00	1.175	2.782E+01	0.3	0.614	0.004
34.20	35.10	1.325	1.250E+01	0.4	0.643	0.005
38.20	39.19	1.474	4.301E+00	0.4	0.705	0.005
42.20	43.27	1.621	2.362E+00	0.6	0.709	0.007
46.20	47.35	1.765	1.883E+00	8.7	0.668	0.009
50.20	51.42	1.907	1.040E+00	0.6	0.770	0.007
54.20	55.49	2.046	4.803E−01	1.1	0.868	0.011
58.20	59.55	2.183	2.830E−01	0.8	0.784	0.009
62.20	63.61	2.317	2.326E−01	0.6	0.596	0.008
66.20	67.66	2.447	1.665E−01	0.6	0.509	0.008
70.20	71.70	2.574	8.274E−02	0.7	0.512	0.008

Table F.3: a) $^{40}\mathrm{Ca}(\vec{p},p)0_1^+$; $\mathrm{E_P}$ = 100 MeV

θ_L	$\theta_{c.m.}$	$q_{c.m.}$	$\sigma_{c.m.}(q)$	$\Delta\sigma(\%)$	A_y	ΔA_y
-15.80	16.24	0.617	2.323E−02	56.9	0.114	0.431
-13.80	14.19	0.540	3.630E−02	28.4	-0.038	0.188
-11.80	12.13	0.462	3.590E−02	16.6	-0.179	0.143
-9.80	10.08	0.385	3.404E−02	31.8	-0.235	0.184
-7.80	8.02	0.307	2.868E−02	49.5	1.302	0.639
12.20	12.54	0.478	4.076E−02	90.2	0.830	1.319
14.20	14.60	0.555	7.497E−02	58.8	-0.755	1.008
16.20	16.65	0.633	5.140E−02	39.7	-0.095	1.119
18.20	18.71	0.710	2.237E−02	17.2	-0.176	0.297
22.20	22.81	0.862	9.176E−03	45.1	0.028	0.437
24.20	24.86	0.939	1.161E−02	8.3	0.340	0.220
26.20	26.91	1.014	1.208E−02	13.0	0.453	0.093
30.20	31.01	1.165	1.458E−02	5.2	0.511	0.061
34.20	35.11	1.314	9.959E−03	14.9	0.608	0.066
38.20	39.20	1.462	4.023E−03	6.6	0.844	0.077
42.20	43.29	1.607	4.195E−03	8.4	0.713	0.056
46.20	47.37	1.750	5.050E−03	4.0	0.501	0.048
50.20	51.44	1.891	3.474E−03	5.4	0.677	0.053
54.20	55.51	2.029	1.449E−03	6.1	1.040	0.080
58.20	59.57	2.164	1.185E−03	17.6	1.117	0.048
62.20	63.63	2.297	1.229E−03	8.9	0.693	0.091
66.20	67.68	2.426	1.115E−03	11.7	0.608	0.064
70.20	71.72	2.552	6.384E−04	9.9	0.581	0.084

Table F.3: b) $^{40}\mathrm{Ca}(\vec{p},p')0_2^+$ (3.3521 MeV); $\mathrm{E_P}$ = 100 MeV

θ_L	$\theta_{c.m.}$	$q_{c.m.}$	$\sigma_{c.m.}(q)$	$\Delta\sigma(\%)$	A_y	ΔA_y
-15.80	16.24	0.617	8.216E+00	2.7	0.111	0.009
-13.80	14.19	0.540	6.085E+00	1.5	0.099	0.005
-11.80	12.13	0.462	4.556E+00	0.9	0.062	0.009
-9.80	10.08	0.385	3.257E+00	4.6	0.044	0.007
-7.80	8.02	0.308	2.345E+00	3.1	0.036	0.040
10.20	10.49	0.401	3.907E+00	6.7	0.023	0.091
12.20	12.54	0.478	5.232E+00	5.6	0.095	0.027
14.20	14.60	0.555	6.765E+00	1.4	0.103	0.023
16.20	16.65	0.632	8.415E+00	3.7	0.136	0.036
18.20	18.71	0.709	1.042E+01	1.7	0.127	0.016
22.20	22.81	0.862	1.142E+01	0.4	0.142	0.005
24.20	24.86	0.938	1.084E+01	0.4	0.161	0.006
26.20	26.92	1.014	8.858E+00	1.8	0.172	0.004
30.20	31.02	1.164	4.813E+00	1.2	0.187	0.007
34.20	35.11	1.313	2.226E+00	1.3	0.228	0.006
38.20	39.20	1.460	1.304E+00	0.6	0.309	0.013
42.20	43.29	1.605	8.805E−01	0.4	0.433	0.008
46.20	47.37	1.748	4.877E−01	0.4	0.594	0.016
50.20	51.45	1.889	2.333E−01	1.3	0.779	0.011
54.20	55.51	2.027	1.661E−01	1.0	0.648	0.008
58.20	59.58	2.162	1.759E−01	1.2	0.351	0.009
62.20	63.63	2.294	1.554E−01	0.9	0.173	0.008
66.20	67.68	2.423	9.515E−02	0.5	0.027	0.004
70.20	71.72	2.549	3.750E−02	0.8	-0.134	0.030

Table F.3: c) $^{40}\mathrm{Ca}(\vec{p},p')3_1^-$ (3.7364 MeV); $\mathrm{E_P}$ = 100 MeV

θ_L	$\theta_{c.m.}$	$q_{c.m.}$	$\sigma_{c.m.}(q)$	$\Delta\sigma(\%)$	A_y	ΔA_y
-15.80	16.24	0.617	2.673E+00	1.9	0.155	0.031
-13.80	14.19	0.540	2.383E+00	2.3	0.146	0.018
-11.80	12.13	0.462	1.885E+00	0.9	0.144	0.011
-9.80	10.08	0.385	1.333E+00	3.5	0.130	0.028
-7.80	8.02	0.308	1.075E+00	4.7	0.130	0.060
12.20	12.54	0.478	2.235E+00	4.8	0.124	0.020
14.20	14.60	0.555	2.635E+00	3.1	0.136	0.041
16.20	16.65	0.632	2.715E+00	8.7	0.165	0.053
18.20	18.71	0.709	2.436E+00	2.6	0.180	0.023
22.20	22.81	0.861	1.311E+00	0.9	0.200	0.020
24.20	24.87	0.937	8.020E−01	0.8	0.239	0.011
26.20	26.92	1.013	4.471E−01	1.4	0.303	0.017
30.20	31.02	1.164	2.083E−01	5.7	0.632	0.023
34.20	35.11	1.313	2.106E−01	1.5	0.698	0.011
38.20	39.20	1.460	1.709E−01	3.9	0.697	0.011
42.20	43.29	1.605	9.425E−02	1.1	0.757	0.013
46.20	47.37	1.748	4.784E−02	1.4	0.743	0.015
50.20	51.45	1.888	3.472E−02	3.8	0.668	0.014
54.20	55.52	2.026	2.469E−02	1.4	0.675	0.035
58.20	59.58	2.161	1.341E−02	1.7	0.689	0.020
62.20	63.63	2.293	5.785E−03	2.7	0.720	0.057
66.20	67.68	2.422	3.434E−03	7.6	0.737	0.039
70.20	71.72	2.548	3.489E−03	4.7	0.454	0.049

Table F.3: d) $^{40}\mathrm{Ca}(\vec{p},p')2_1^+$ (3.9041 MeV); $\mathrm{E_P}$ = 100 MeV

θ_L	$\theta_{c.m.}$	$q_{c.m.}$	$\sigma_{c.m.}(q)$	$\Delta\sigma(\%)$	A_y	ΔA_y
-15.80	16.24	0.616	2.075E−01	12.4	-0.012	0.050
-13.80	14.19	0.539	1.314E−01	21.7	-0.031	0.120
-11.80	12.13	0.462	9.633E−02	8.7	-0.225	0.065
-9.80	10.08	0.385	6.335E−02	19.4	-0.205	0.229
-7.80	8.02	0.309	7.670E−02	22.6	-0.673	0.300
14.20	14.60	0.555	1.996E−01	6.0	-0.162	0.082
18.20	18.71	0.708	2.638E−01	4.2	-0.021	0.036
22.20	22.81	0.860	5.092E−01	2.8	0.000	0.013
24.20	24.87	0.936	6.664E−01	0.7	0.045	0.009
26.20	26.92	1.012	8.367E−01	2.3	0.048	0.014
30.20	31.02	1.162	1.142E+00	0.5	0.065	0.012
34.20	35.11	1.311	1.248E+00	0.6	0.049	0.004
38.20	39.21	1.458	1.142E+00	0.6	-0.006	0.017
42.20	43.29	1.602	9.599E−01	1.9	-0.113	0.004
46.20	47.37	1.745	7.743E−01	0.5	-0.212	0.006
50.20	51.45	1.885	6.007E−01	0.9	-0.311	0.005
54.20	55.52	2.023	4.269E−01	0.6	-0.388	0.005
58.20	59.58	2.158	2.646E−01	0.5	-0.472	0.004
62.20	63.64	2.290	1.405E−01	0.4	-0.564	0.010
66.20	67.69	2.419	6.329E−02	0.8	-0.663	0.007
70.20	71.73	2.544	2.193E−02	1.7	-0.742	0.031

Table F.3: e) $^{40}\mathrm{Ca}(\vec{p},p')5_1^-$ (4.4915 MeV); $\mathrm{E_P}$ = 100 MeV

θ_L	$\theta_{c.m.}$	$q_{c.m.}$	$\sigma_{c.m.}(q)$	$\Delta\sigma(\%)$	A_y	ΔA_y
-15.80	16.24	0.616	1.036E−01	35.8	1.133	0.589
26.20	26.92	1.011	3.995E−03	66.3	-0.388	0.789
30.20	31.02	1.160	1.636E−03	43.5	0.481	0.577
34.20	35.12	1.309	3.071E−04	81.7	0.335	0.974
42.20	43.30	1.600	4.187E−04	64.8	-0.408	0.903
50.20	51.45	1.882	1.568E−04	229.9	0.003	1.015
62.20	63.64	2.286	1.204E−04	74.5	1.240	0.967
66.20	67.69	2.414	6.051E−05	101.7	0.589	1.130
70.20	71.73	2.540	1.165E−04	30.9	0.727	0.437

Table F.3: f) $^{40}\mathrm{Ca}(\vec{p},p')0_3^+$ (5.213 MeV); $\mathrm{E_P}$ = 100 MeV

θ_L	$\theta_{c.m.}$	$q_{c.m.}$	$\sigma_{c.m.}(q)$	$\Delta\sigma(\%)$	A_y	ΔA_y
-15.80	16.24	0.616	1.663E−01	9.0	0.086	0.191
-13.80	14.19	0.539	1.654E−01	7.1	-0.013	0.039
-11.80	12.13	0.463	1.444E−01	7.4	0.073	0.096
-9.80	10.08	0.386	1.165E−01	11.3	0.108	0.104
-7.80	8.02	0.310	8.680E−02	21.7	0.083	0.278
12.20	12.55	0.478	1.220E−01	15.7	0.471	0.208
14.20	14.60	0.555	1.679E−01	9.2	0.018	0.124
18.20	18.71	0.708	1.802E−01	3.0	0.055	0.040
22.20	22.82	0.859	1.192E−01	14.0	-0.015	0.242
24.20	24.87	0.935	9.600E−02	3.4	0.053	0.046
26.20	26.92	1.010	5.969E−02	24.5	0.052	0.211
30.20	31.02	1.160	1.948E−02	32.3	0.485	0.112
34.20	35.12	1.309	1.768E−02	23.2	0.690	0.076
38.20	39.21	1.455	1.669E−02	15.5	0.403	0.093
42.20	43.30	1.600	1.315E−02	17.9	0.391	0.097
46.20	47.38	1.742	5.476E−03	19.6	0.716	0.223
50.20	51.45	1.882	3.846E−03	22.9	0.804	0.120
54.20	55.52	2.019	4.352E−03	8.9	0.489	0.098
58.20	59.59	2.154	3.252E−03	13.4	0.186	0.224
62.20	63.64	2.285	2.880E−03	31.5	0.474	0.153
66.20	67.69	2.414	1.575E−03	35.6	0.118	0.235
70.20	71.73	2.539	5.338E−04	10.3	1.037	0.192

Table F.3: g) $^{40}\mathrm{Ca}(\vec{p},p')2_2^+$ (5.249 MeV); $\mathrm{E_P}$ = 100 MeV

θ_L	$\theta_{c.m.}$	$q_{c.m.}$	$\sigma_{c.m.}(q)$	$\Delta\sigma(\%)$	A_y	ΔA_y
-15.80	16.24	0.616	3.704E−02	30.0	0.183	0.404
-13.80	14.19	0.539	1.955E−02	20.7	0.221	0.268
-9.80	10.08	0.386	2.187E−02	93.8	0.084	0.524
-7.80	8.02	0.310	3.204E−02	50.7	-0.248	0.674
18.20	18.71	0.708	3.835E−02	34.8	0.331	0.168
22.20	22.82	0.859	6.807E−02	29.7	0.289	0.336
24.20	24.87	0.935	6.908E−02	9.4	0.223	0.062
26.20	26.92	1.010	7.302E−02	17.1	0.282	0.183
30.20	31.02	1.160	4.991E−02	11.5	0.137	0.052
34.20	35.12	1.309	2.639E−02	20.0	0.059	0.102
38.20	39.21	1.455	1.738E−02	18.5	0.384	0.095
42.20	43.30	1.599	1.081E−02	20.8	0.546	0.118
46.20	47.38	1.742	7.319E−03	20.2	0.486	0.162
50.20	51.45	1.882	3.905E−03	24.1	0.930	0.449
54.20	55.52	2.019	2.355E−03	19.5	0.911	0.184
58.20	59.59	2.154	3.147E−03	14.8	0.445	0.192
62.20	63.64	2.285	1.908E−03	51.0	-0.248	0.272
66.20	67.69	2.414	1.420E−03	17.1	-0.263	0.246
70.20	71.73	2.539	5.717E−04	13.5	-1.178	0.204

Table F.3: h) ^{40}Ca$(\vec{p},p')4_1^+$ (5.279 MeV); E_P = 100 MeV

θ_L	$\theta_{c.m.}$	$q_{c.m.}$	$\sigma_{c.m.}(q)$	$\Delta\sigma(\%)$	A_y	ΔA_y
-15.80	16.25	0.616	1.369E−01	19.1	-0.256	1.280
-13.80	14.19	0.539	4.339E−02	26.7	0.278	0.330
-11.80	12.13	0.463	2.123E−01	36.0	0.372	0.458
-7.80	8.02	0.310	7.682E−02	45.1	-0.698	0.692
18.20	18.71	0.707	2.337E−01	11.1	0.293	0.146
22.20	22.82	0.859	1.181E−01	25.6	0.019	0.135
24.20	24.87	0.934	4.418E−02	25.4	0.210	0.223
26.20	26.92	1.010	4.120E−02	25.7	0.268	0.277
30.20	31.02	1.159	5.479E−02	24.6	0.207	0.100
34.20	35.12	1.308	4.488E−02	13.0	-0.060	0.201
38.20	39.21	1.454	2.559E−02	33.8	-0.598	0.536
42.20	43.30	1.598	2.394E−02	28.5	0.125	0.388
46.20	47.38	1.740	2.457E−02	26.9	-0.124	0.306
50.20	51.46	1.880	2.181E−02	9.0	-0.323	0.199
54.20	55.53	2.017	1.489E−02	30.6	0.071	0.160
58.20	59.59	2.152	5.689E−03	33.3	-0.934	0.635
62.20	63.65	2.283	2.440E−03	65.3	-1.375	0.920
66.20	67.69	2.412	1.406E−03	87.9	-0.244	1.186
70.20	71.74	2.537	8.217E−04	32.3	-0.094	0.452

Table F.3: i) $^{40}\mathrm{Ca}(\vec{p},p')4_1^-$ (5.6143 MeV); $\mathrm{E_P}$ = 100 MeV

θ_L	$\theta_{c.m.}$	$q_{c.m.}$	$\sigma_{c.m.}(q)$	$\Delta\sigma(\%)$	A_y	ΔA_y
-15.80	16.25	0.616	1.325E−01	22.5	0.684	1.090
-13.80	14.19	0.539	2.197E−01	10.8	0.152	0.106
-11.80	12.13	0.463	1.741E−01	15.9	0.188	0.214
-9.80	10.08	0.386	1.204E−01	15.1	0.104	0.337
-7.80	8.02	0.310	4.018E−02	97.1	1.093	1.502
12.20	12.55	0.478	1.965E−01	18.3	0.087	0.459
14.20	14.60	0.555	2.598E−01	11.8	0.084	0.161
18.20	18.71	0.707	2.334E−01	4.0	0.068	0.053
22.20	22.82	0.859	4.884E−02	39.5	0.412	0.488
24.20	24.87	0.934	6.184E−02	12.1	0.139	0.162
26.20	26.92	1.010	4.878E−02	18.7	0.061	0.249
30.20	31.02	1.159	8.233E−03	89.7	-1.268	1.318
34.20	35.12	1.307	1.248E−02	32.1	1.116	0.355
38.20	39.21	1.454	4.709E−02	17.4	-0.076	0.116
42.20	43.30	1.598	3.631E−02	31.7	-0.428	0.113
46.20	47.38	1.740	1.437E−02	28.0	-0.196	0.521
50.20	51.46	1.880	6.498E−03	98.3	0.058	0.642
54.20	55.53	2.017	5.008E−03	37.5	-0.967	0.418
58.20	59.59	2.152	5.811E−03	29.5	0.417	0.675
62.20	63.65	2.283	4.737E−03	18.6	-0.024	0.129
66.20	67.69	2.412	2.419E−03	11.7	0.120	0.158
70.20	71.74	2.537	9.154E−04	49.2	0.263	0.734

Table F.3: j) $^{40}\mathrm{Ca}(\vec{p},p')2_3^+$ (5.6301 MeV); $\mathrm{E_P}$ = 100 MeV

θ_L	$\theta_{c.m.}$	$q_{c.m.}$	$\sigma_{c.m.}(q)$	$\Delta\sigma(\%)$	A_y	ΔA_y
-15.80	16.25	0.616	3.345E−02	12.6	0.119	0.300
-13.80	14.19	0.539	4.101E−02	30.1	0.072	0.202
-11.80	12.14	0.463	4.891E−02	8.5	0.043	0.312
-9.80	10.08	0.387	5.828E−02	13.4	0.149	0.192
-7.80	8.02	0.311	5.248E−02	29.5	0.387	0.369
18.20	18.71	0.707	8.193E−02	10.6	0.063	0.039
22.20	22.82	0.858	1.373E−01	3.6	0.062	0.042
24.20	24.87	0.934	1.338E−01	1.5	0.081	0.070
26.20	26.92	1.009	1.101E−01	2.1	0.063	0.036
30.20	31.02	1.159	5.936E−02	3.0	0.056	0.024
34.20	35.12	1.307	3.361E−02	2.9	-0.001	0.026
38.20	39.21	1.453	2.140E−02	9.0	0.214	0.028
42.20	43.30	1.597	1.944E−02	2.2	0.479	0.026
46.20	47.38	1.739	1.363E−02	6.4	0.649	0.073
50.20	51.46	1.879	1.232E−02	4.6	0.537	0.047
54.20	55.53	2.016	1.200E−02	1.9	0.318	0.048
58.20	59.59	2.150	9.521E−03	1.6	0.156	0.028
62.20	63.65	2.282	4.925E−03	4.6	0.016	0.026
66.20	67.70	2.410	2.040E−03	4.8	-0.176	0.043
70.20	71.74	2.535	6.366E−04	5.0	-0.120	0.081

Table F.3: k) $^{40}\mathrm{Ca}(\vec{p},p')1_1^-$ (5.9033 MeV); $\mathrm{E_P}$ = 100 MeV

θ_L	$\theta_{c.m.}$	$q_{c.m.}$	$\sigma_{c.m.}(q)$	$\Delta\sigma(\%)$	A_y	ΔA_y
-15.80	16.25	0.616	4.896E−02	17.6	0.347	0.118
-13.80	14.19	0.539	6.319E−02	27.2	0.293	0.056
-11.80	12.14	0.463	5.403E−02	8.3	0.204	0.112
-9.80	10.08	0.387	6.791E−02	9.4	0.185	0.123
-7.80	8.02	0.311	9.548E−02	19.7	0.569	0.236
14.20	14.60	0.555	5.580E−02	15.7	0.125	0.213
18.20	18.71	0.707	4.293E−02	11.1	-0.016	0.069
22.20	22.82	0.858	3.800E−02	4.3	-0.272	0.114
24.20	24.87	0.934	3.690E−02	3.2	-0.432	0.044
26.20	26.92	1.009	3.115E−02	9.8	-0.557	0.090
30.20	31.02	1.158	3.734E−02	4.9	-0.373	0.032
34.20	35.12	1.306	2.319E−02	2.5	-0.566	0.033
38.20	39.21	1.452	1.571E−02	4.4	-0.403	0.053
42.20	43.30	1.597	8.944E−03	3.4	-0.358	0.047
46.20	47.38	1.739	4.645E−03	8.0	-0.253	0.132
50.20	51.46	1.878	2.382E−03	6.4	0.108	0.131
54.20	55.53	2.015	1.421E−03	7.4	0.544	0.096
58.20	59.59	2.149	1.222E−03	5.8	0.577	0.163
62.20	63.65	2.281	9.562E−04	14.2	0.346	0.173
66.20	67.70	2.409	5.017E−04	5.7	0.407	0.100
70.20	71.74	2.534	3.346E−04	7.3	0.383	0.073

Table F.3: 1) ^{40}Ca$(\vec{p},p')$6.028 (6.028 MeV); E_P = 100 MeV

θ_L	$\theta_{c.m.}$	$q_{c.m.}$	$\sigma_{c.m.}(q)$	$\Delta\sigma(\%)$	A_y	ΔA_y
-15.80	16.25	0.616	6.799E−01	9.2	0.053	0.030
-13.80	14.19	0.539	5.190E−01	1.3	0.099	0.040
-11.80	12.14	0.463	3.853E−01	2.5	0.042	0.036
-9.80	10.08	0.387	2.844E−01	7.3	0.010	0.030
-7.80	8.02	0.312	2.124E−01	11.8	0.126	0.150
12.20	12.55	0.478	4.542E−01	3.9	0.137	0.052
14.20	14.60	0.555	6.021E−01	2.7	0.168	0.037
18.20	18.71	0.707	8.383E−01	5.6	0.113	0.011
22.20	22.82	0.858	7.473E−01	2.3	0.099	0.011
24.20	24.87	0.933	6.075E−01	1.5	0.111	0.013
26.20	26.92	1.008	3.909E−01	4.6	0.068	0.023
30.20	31.03	1.158	1.133E−01	2.3	-0.224	0.038
34.20	35.12	1.306	8.566E−02	1.2	-0.223	0.016
38.20	39.21	1.452	1.652E−01	2.2	0.107	0.028
42.20	43.30	1.596	2.074E−01	1.5	0.214	0.031
46.20	47.38	1.737	1.991E−01	1.1	0.169	0.009
50.20	51.46	1.877	1.697E−01	1.5	0.084	0.009
54.20	55.53	2.014	1.309E−01	0.8	-0.024	0.007
58.20	59.59	2.148	8.677E−02	0.5	-0.102	0.007
62.20	63.65	2.279	4.473E−02	0.9	-0.203	0.017
66.20	67.70	2.407	1.834E−02	0.7	-0.402	0.022
70.20	71.74	2.532	5.334E−03	2.7	-0.479	0.043

Table F.3: m) $^{40}\mathrm{Ca}(\vec{p},p')3_2^-$ (6.2858 MeV); $\mathrm{E_P}$ = 100 MeV

θ_L	$\theta_{c.m.}$	$q_{c.m.}$	$\sigma_{c.m.}(q)$	$\Delta\sigma(\%)$	A_y	ΔA_y
-15.80	16.25	0.616	2.511E−02	35.5	0.278	0.269
-13.80	14.19	0.539	1.379E−02	46.0	0.198	0.480
-11.80	12.14	0.463	1.528E−02	39.2	-0.414	0.769
-9.80	10.08	0.388	1.543E−02	22.0	-0.017	0.375
12.20	12.55	0.479	1.299E−02	94.2	-0.078	1.293
14.20	14.60	0.555	2.908E−02	32.0	0.274	0.438
18.20	18.71	0.706	5.236E−02	28.1	-0.346	0.395
22.20	22.82	0.858	9.873E−02	11.8	0.063	0.139
24.20	24.87	0.933	1.047E−01	2.2	0.081	0.074
26.20	26.93	1.008	1.065E−01	4.8	0.124	0.066
30.20	31.03	1.157	9.744E−02	4.7	0.152	0.055
34.20	35.12	1.305	6.393E−02	1.9	0.138	0.025
38.20	39.22	1.451	3.986E−02	2.6	0.068	0.087
42.20	43.30	1.595	2.186E−02	2.8	-0.077	0.037
46.20	47.39	1.737	1.199E−02	3.6	0.056	0.049
50.20	51.46	1.876	5.707E−03	4.7	0.162	0.072
54.20	55.53	2.013	2.172E−03	10.8	0.422	0.117
58.20	59.59	2.147	1.084E−03	28.1	0.406	0.197
62.20	63.65	2.278	1.029E−03	9.6	-0.182	0.128
66.20	67.70	2.406	9.672E−04	6.7	-0.194	0.089
70.20	71.74	2.531	7.596E−04	4.6	-0.196	0.076

Table F.3: n) $^{40}\mathrm{Ca}(\vec{p},p')4_2^+$ (6.5084 MeV); $\mathrm{E_P}$ = 100 MeV

θ_L	$\theta_{c.m.}$	$q_{c.m.}$	$\sigma_{c.m.}(q)$	$\Delta\sigma(\%)$	A_y	ΔA_y
-13.80	14.19	0.539	1.754E−02	41.9	-0.687	0.594
18.20	18.71	0.706	6.602E−03	59.6	-1.352	1.150
24.20	24.87	0.933	3.452E−03	78.0	0.352	0.803
26.20	26.93	1.008	1.940E−02	33.1	0.068	0.525
34.20	35.12	1.305	7.752E−03	18.6	0.104	0.198
54.20	55.53	2.013	3.548E−04	97.1	1.332	1.787
58.20	59.60	2.147	7.170E−04	103.1	-0.234	0.434
62.20	63.65	2.278	5.744E−04	110.3	-0.188	0.855
66.20	67.70	2.406	3.304E−04	37.6	-0.994	0.503
70.20	71.74	2.531	1.539E−04	80.5	0.625	0.692

Table F.3: o) $^{40}\mathrm{Ca}(\vec{p},p')4_3^+$ (6.5436 MeV); $\mathrm{E_P}$ = 100 MeV

θ_L	$\theta_{c.m.}$	$q_{c.m.}$	$\sigma_{c.m.}(q)$	$\Delta\sigma(\%)$	A_y	ΔA_y
-15.80	16.25	0.616	3.766E−01	7.6	0.157	0.040
-13.80	14.19	0.540	2.926E−01	1.7	0.161	0.065
-11.80	12.14	0.463	2.100E−01	8.0	0.037	0.049
-9.80	10.08	0.388	1.630E−01	4.3	0.014	0.128
-7.80	8.02	0.312	8.768E−02	21.2	0.051	0.272
12.20	12.55	0.479	2.353E−01	6.6	0.185	0.125
14.20	14.60	0.555	3.258E−01	4.3	0.165	0.058
18.20	18.71	0.707	4.693E−01	1.4	0.173	0.026
22.20	22.82	0.858	4.240E−01	1.3	0.196	0.021
24.20	24.87	0.933	3.375E−01	1.9	0.200	0.014
26.20	26.93	1.008	2.255E−01	5.1	0.153	0.019
30.20	31.03	1.157	6.218E−02	5.6	-0.141	0.045
34.20	35.12	1.305	4.170E−02	2.3	-0.493	0.032
38.20	39.22	1.451	7.782E−02	3.2	-0.066	0.017
42.20	43.30	1.594	1.002E−01	1.5	0.076	0.013
46.20	47.39	1.736	9.417E−02	1.8	0.054	0.013
50.20	51.46	1.876	8.187E−02	1.5	-0.005	0.011
54.20	55.53	2.012	6.228E−02	1.4	-0.131	0.013
58.20	59.60	2.146	4.001E−02	0.9	-0.207	0.029
62.20	63.65	2.278	1.980E−02	3.2	-0.383	0.017
66.20	67.70	2.406	7.908E−03	1.7	-0.472	0.021
70.20	71.74	2.530	2.561E−03	2.0	-0.458	0.056

Table F.3: p) $^{40}\mathrm{Ca}(\vec{p},p')3_3^-$ (6.5833 MeV); $\mathrm{E_P}$ = 100 MeV

θ_L	$\theta_{c.m.}$	$q_{c.m.}$	$\sigma_{c.m.}(q)$	$\Delta\sigma(\%)$	A_y	ΔA_y
-15.80	16.25	0.616	8.261E−02	13.5	0.115	0.103
-13.80	14.19	0.540	9.151E−02	20.9	0.180	0.105
-11.80	12.14	0.464	1.051E−01	9.6	0.282	0.066
-9.80	10.08	0.388	1.367E−01	7.9	0.139	0.081
-7.80	8.02	0.313	1.286E−01	15.7	0.279	0.198
12.20	12.55	0.479	1.659E−01	8.2	0.181	0.168
14.20	14.60	0.555	9.967E−02	9.7	0.141	0.131
18.20	18.71	0.707	6.894E−02	7.8	0.037	0.115
22.20	22.82	0.857	6.752E−02	5.5	-0.250	0.132
24.20	24.87	0.933	4.611E−02	8.1	-0.337	0.047
26.20	26.93	1.008	4.385E−02	6.0	-0.479	0.039
30.20	31.03	1.157	4.221E−02	4.7	-0.381	0.029
34.20	35.12	1.304	3.635E−02	4.8	-0.261	0.025
38.20	39.22	1.450	2.846E−02	6.4	-0.169	0.058
42.20	43.30	1.594	1.697E−02	2.5	-0.109	0.033
46.20	47.39	1.735	8.613E−03	7.0	-0.107	0.043
50.20	51.46	1.875	4.432E−03	7.7	-0.056	0.108
54.20	55.53	2.011	2.711E−03	10.9	0.240	0.073
58.20	59.60	2.145	1.951E−03	4.7	0.351	0.064
62.20	63.65	2.277	1.320E−03	4.8	0.308	0.067
66.20	67.70	2.405	9.289E−04	4.1	0.227	0.057
70.20	71.75	2.529	4.429E−04	7.0	0.328	0.114

Table F.3: q) $^{40}\mathrm{Ca}(\vec{p},p')2_2^-$ (6.7509 MeV); $\mathrm{E_P}$ = 100 MeV

θ_L	$\theta_{c.m.}$	$q_{c.m.}$	$\sigma_{c.m.}(q)$	$\Delta\sigma(\%)$	A_y	ΔA_y
-15.80	16.25	0.616	2.245E+00	4.2	0.138	0.052
-13.80	14.19	0.540	1.924E+00	9.3	0.149	0.020
-11.80	12.14	0.464	1.367E+00	4.8	0.081	0.048
-9.80	10.08	0.388	1.039E+00	7.9	0.122	0.046
-7.80	8.02	0.313	7.589E−01	6.9	0.181	0.088
12.20	12.55	0.479	1.896E+00	9.0	0.064	0.113
14.20	14.60	0.555	2.357E+00	2.7	0.107	0.036
18.20	18.71	0.707	2.240E+00	3.3	0.134	0.039
22.20	22.82	0.857	1.612E+00	1.4	0.127	0.057
24.20	24.87	0.932	1.241E+00	1.0	0.143	0.020
26.20	26.93	1.007	8.407E−01	4.2	0.179	0.018
30.20	31.03	1.156	3.976E−01	3.1	0.352	0.067
34.20	35.12	1.304	2.607E−01	1.9	0.571	0.021
38.20	39.22	1.450	2.400E−01	7.9	0.580	0.048
42.20	43.31	1.593	1.452E−01	2.2	0.673	0.043
46.20	47.39	1.735	6.455E−02	6.5	0.846	0.140
50.20	51.46	1.874	4.531E−02	5.1	0.857	0.115
54.20	55.53	2.011	4.853E−02	2.9	0.683	0.070
58.20	59.60	2.145	3.738E−02	3.3	0.493	0.047
62.20	63.65	2.276	2.272E−02	6.8	0.368	0.064
66.20	67.70	2.404	9.022E−03	8.8	0.056	0.121
70.20	71.75	2.528	3.767E−03	35.7	0.258	0.354

Table F.3: r) ^{40}Ca$(\vec{p},p')$6.909 (6.909 MeV); E_P = 100 MeV

θ_L	$\theta_{c.m.}$	$q_{c.m.}$	$\sigma_{c.m.}(q)$	$\Delta\sigma(\%)$	A_y	ΔA_y
-15.80	16.25	0.616	1.598E−01	37.0	1.039	0.508
-13.80	14.19	0.540	1.267E−01	15.7	0.211	0.197
-11.80	12.14	0.464	7.265E−02	98.9	1.316	1.657
-9.80	10.08	0.388	6.145E−02	47.1	0.029	0.805
-7.80	8.02	0.313	1.102E−01	42.8	-0.713	0.659
18.20	18.71	0.707	2.157E−01	39.5	0.282	0.190
22.20	22.82	0.857	1.179E−01	139.2	-0.176	0.627
24.20	24.87	0.932	1.471E−01	10.2	0.068	0.137
26.20	26.93	1.007	1.673E−01	48.4	0.137	0.272
30.20	31.03	1.156	1.063E−01	29.6	0.430	0.143
34.20	35.13	1.304	1.009E−01	9.1	0.131	0.071
38.20	39.22	1.449	4.415E−02	19.0	0.010	0.412
42.20	43.31	1.593	3.631E−02	17.6	-0.199	0.549
46.20	47.39	1.735	3.745E−02	14.0	0.022	0.106
50.20	51.46	1.874	3.570E−02	22.6	-0.178	0.137
54.20	55.53	2.011	2.505E−02	10.9	-0.448	0.131
58.20	59.60	2.144	2.060E−02	11.4	-0.440	0.106
62.20	63.65	2.275	1.334E−02	24.7	-0.573	0.149
66.20	67.70	2.403	9.062E−03	13.6	-0.470	0.095
70.20	71.75	2.528	4.222E−03	22.4	-0.722	0.181

Table F.3: s) ^{40}Ca$(\vec{p}, p')$6.931 (6.931 MeV); E_P = 100 MeV

θ_L	$\theta_{c.m.}$	$q_{c.m.}$	$\sigma_{c.m.}(q)$	$\Delta\sigma(\%)$	A_y	ΔA_y
-15.80	16.25	0.616	3.177E−01	39.2	0.103	0.257
-13.80	14.19	0.540	2.349E−01	37.0	0.156	0.089
-11.80	12.14	0.464	4.550E−01	6.7	0.068	0.148
-9.80	10.08	0.388	4.432E−01	12.3	0.172	0.106
-7.80	8.02	0.313	3.512E−01	12.0	0.118	0.153
12.20	12.55	0.479	4.052E−01	23.9	0.073	0.132
18.20	18.71	0.707	4.306E−01	13.2	-0.035	0.097
22.20	22.82	0.857	7.075E−01	16.4	0.015	0.029
24.20	24.87	0.932	7.125E−01	4.6	0.057	0.019
26.20	26.93	1.007	5.539E−01	11.2	-0.008	0.058
30.20	31.03	1.156	2.898E−01	13.4	-0.170	0.118
34.20	35.13	1.304	1.643E−01	8.4	-0.127	0.104
38.20	39.22	1.449	1.404E−01	6.6	0.142	0.071
42.20	43.31	1.593	1.185E−01	7.8	0.453	0.106
46.20	47.39	1.735	9.490E−02	8.8	0.596	0.084
50.20	51.46	1.874	7.772E−02	13.2	0.587	0.171
54.20	55.53	2.010	6.911E−02	6.4	0.424	0.144
58.20	59.60	2.144	5.072E−02	3.8	0.294	0.045
62.20	63.65	2.275	2.629E−02	4.2	0.145	0.059
66.20	67.70	2.403	9.284E−03	8.1	-0.019	0.109
70.20	71.75	2.528	3.116E−03	31.5	0.027	0.425

Table F.3: t) $^{40}\mathrm{Ca}(\vec{p},p')1_2^-$ (6.951 MeV); $\mathrm{E_P}$ = 100 MeV

θ_L	$\theta_{c.m.}$	$q_{c.m.}$	$\sigma_{c.m.}(q)$	$\Delta\sigma(\%)$	A_y	ΔA_y
-15.80	16.25	0.616	5.340E−02	26.9	0.553	0.135
-13.80	14.19	0.540	5.420E−02	35.4	0.139	0.187
-11.80	12.14	0.464	4.124E−02	12.2	0.244	0.157
-9.80	10.08	0.388	3.039E−02	42.2	0.095	0.252
-7.80	8.02	0.314	2.947E−02	45.8	0.281	0.573
14.20	14.60	0.555	6.427E−02	15.1	0.045	0.205
18.20	18.71	0.707	5.299E−02	7.6	0.213	0.120
22.20	22.82	0.857	5.605E−02	23.7	0.286	0.147
24.20	24.88	0.932	6.428E−02	2.9	0.172	0.069
26.20	26.93	1.007	6.787E−02	3.8	0.201	0.042
30.20	31.03	1.156	8.567E−02	2.0	0.235	0.032
34.20	35.13	1.303	6.461E−02	3.1	0.174	0.020
38.20	39.22	1.449	6.266E−02	3.7	0.104	0.041
42.20	43.31	1.592	5.179E−02	2.3	0.001	0.018
46.20	47.39	1.734	3.703E−02	3.9	-0.069	0.034
50.20	51.46	1.873	2.501E−02	2.3	-0.171	0.044
54.20	55.54	2.010	1.519E−02	3.6	-0.215	0.026
58.20	59.60	2.143	7.495E−03	4.3	-0.303	0.029
62.20	63.66	2.274	3.329E−03	3.0	-0.447	0.046
66.20	67.71	2.402	1.638E−03	4.2	-0.437	0.046
70.20	71.75	2.527	8.634E−04	7.3	-0.232	0.041

Table F.3: u) ^{40}Ca$(\vec{p},p')$7.11 (7.11 MeV); E_P = 100 MeV

F.3 $^{9}\mathrm{Be}(\vec{p},p')$ and $^{16}\mathrm{O}(\vec{p},p')$ at $E_P = 200$ MeV

θ_L	$\theta_{c.m.}$	$q_{c.m.}$	$\sigma_{c.m.}(q)$	$\Delta\sigma(\%)$	A_y	ΔA_y
6.14	6.96	0.351	1.794E+02	1.7	0.542	0.016
7.64	8.65	0.436	1.667E+02	1.0	0.555	0.011
9.14	10.35	0.522	1.219E+02	1.0	0.594	0.011
10.64	12.05	0.607	1.122E+02	0.9	0.711	0.008
12.14	13.74	0.692	8.704E+01	0.8	0.782	0.009
13.64	15.44	0.777	5.227E+01	0.7	0.854	0.007
15.14	17.13	0.861	3.376E+01	1.2	0.931	0.007
18.27	20.66	1.038	1.251E+01	1.0	0.951	0.008
19.64	22.20	1.114	8.676E+00	1.1	0.894	0.010
19.77	22.35	1.122	8.438E+00	2.0	0.901	0.034
21.27	24.03	1.205	5.244E+00	0.6	0.817	0.005
23.77	26.84	1.343	2.631E+00	0.6	0.542	0.018
25.27	28.52	1.426	1.837E+00	3.0	0.367	0.007
26.77	30.20	1.508	1.366E+00	2.8	0.223	0.009
28.27	31.88	1.589	1.019E+00	3.5	0.140	0.007
29.77	33.55	1.671	8.209E−01	1.4	0.109	0.019
30.52	34.39	1.711	7.187E−01	1.1	0.114	0.014
31.27	35.22	1.751	6.605E−01	1.2	0.111	0.016
33.52	37.72	1.871	4.584E−01	1.3	0.087	0.018
34.27	38.55	1.911	4.116E−01	3.1	0.089	0.010
36.52	41.05	2.029	3.038E−01	1.9	0.036	0.025
37.27	41.87	2.068	2.636E−01	1.6	0.049	0.011
40.27	45.18	2.224	1.595E−01	1.2	0.010	0.013
43.27	48.48	2.376	8.513E−02	1.0	-0.014	0.023
46.27	51.75	2.526	5.272E−02	4.6	0.019	0.041
48.52	54.20	2.637	3.234E−02	3.2	-0.003	0.043
49.27	55.02	2.674	2.651E−02	1.9	-0.010	0.026
51.52	57.46	2.782	1.372E−02	3.9	0.057	0.051

Table F.4: a) $^{9}\mathrm{Be}(\vec{p},p)3/2_1^-$; $\mathrm{E_P}$ = 200 MeV

θ_L	$\theta_{c.m.}$	$q_{c.m.}$	$\sigma_{c.m.}(q)$	$\Delta\sigma(\%)$	A_y	ΔA_y
12.14	13.75	0.691	7.197E−02	49.9	0.625	0.364
13.64	15.44	0.775	1.648E−01	18.2	1.035	0.095
15.14	17.14	0.860	1.297E−01	39.8	0.934	0.123
16.64	18.83	0.944	1.052E−01	22.3	0.867	0.088
18.14	20.52	1.028	8.879E−02	12.8	0.662	0.097
18.27	20.67	1.036	9.987E−02	14.2	0.969	0.099
19.64	22.21	1.111	9.295E−02	14.2	0.910	0.103
19.77	22.36	1.119	1.242E−01	14.4	0.829	0.198
21.27	24.04	1.203	8.821E−02	9.7	0.805	0.119
23.77	26.85	1.341	6.003E−02	9.3	0.678	0.115
25.27	28.53	1.423	3.980E−02	12.1	0.652	0.063
26.77	30.21	1.505	3.592E−02	13.6	0.325	0.100
27.52	31.05	1.546	3.915E−02	12.9	0.636	0.167
28.27	31.89	1.586	2.546E−02	8.9	0.260	0.255
29.77	33.56	1.667	2.634E−02	11.4	0.391	0.148
30.52	34.40	1.707	2.910E−02	11.0	0.095	0.141
31.27	35.23	1.748	2.048E−02	4.6	0.042	0.064
33.52	37.74	1.867	1.734E−02	10.0	-0.380	0.132
36.52	41.06	2.025	1.399E−02	14.6	-0.654	0.180
37.27	41.89	2.064	1.249E−02	24.9	-0.482	0.432
39.52	44.37	2.180	8.680E−03	25.5	-0.841	0.267
40.27	45.20	2.219	4.710E−03	11.7	-0.358	0.145
43.27	48.49	2.371	2.651E−03	9.6	-0.773	0.211
45.52	50.96	2.484	3.870E−03	25.4	-0.310	0.331

Table F.4: b) ^{9}Be$(\vec{p},p')1/2^{+}_{1}$ (1.680 MeV); E_P = 200 MeV

θ_L	$\theta_{c.m.}$	$q_{c.m.}$	$\sigma_{c.m.}(q)$	$\Delta\sigma(\%)$	A_y	ΔA_y
12.14	13.75	0.690	3.271E+00	2.4	0.674	0.019
13.64	15.45	0.775	3.518E+00	2.2	0.768	0.016
15.14	17.14	0.859	3.886E+00	2.0	0.845	0.007
18.14	20.53	1.027	3.953E+00	1.4	0.891	0.012
18.27	20.67	1.035	3.964E+00	1.8	0.969	0.013
19.64	22.21	1.110	3.667E+00	1.7	0.942	0.013
19.77	22.36	1.119	3.817E+00	1.6	0.950	0.019
21.27	24.05	1.202	3.365E+00	3.5	0.939	0.007
23.77	26.86	1.340	2.670E+00	1.5	0.829	0.010
25.27	28.54	1.422	2.231E+00	5.4	0.710	0.008
26.77	30.22	1.503	2.014E+00	0.7	0.582	0.014
28.27	31.90	1.585	1.546E+00	4.4	0.420	0.006
29.77	33.57	1.666	1.368E+00	1.3	0.253	0.016
30.52	34.41	1.706	1.118E+00	1.3	0.180	0.016
31.27	35.24	1.746	1.136E+00	1.2	0.102	0.006
33.52	37.74	1.866	8.134E−01	1.5	-0.084	0.020
34.27	38.58	1.905	6.958E−01	4.2	-0.198	0.021
36.52	41.07	2.023	4.677E−01	1.7	-0.427	0.022
37.27	41.90	2.062	4.142E−01	0.8	-0.437	0.014
39.52	44.38	2.178	2.696E−01	3.8	-0.688	0.044
40.27	45.21	2.217	2.122E−01	2.2	-0.652	0.017
43.27	48.50	2.369	9.734E−02	1.0	-0.813	0.012
45.52	50.97	2.481	5.589E−02	7.3	-0.849	0.074
46.27	51.78	2.519	5.167E−02	3.6	-0.846	0.016
49.27	55.05	2.665	2.650E−02	4.7	-0.740	0.055
51.52	57.49	2.773	1.356E−02	12.3	-0.574	0.135

Table F.4: c) ^{9}Be$(\vec{p},p')5/2_1^-$ (2.429 MeV); E_P = 200 MeV

θ_L	$\theta_{c.m.}$	$q_{c.m.}$	$\sigma_{c.m.}(q)$	$\Delta\sigma(\%)$	A_y	ΔA_y
12.14	13.75	0.690	7.095E−01	28.6	0.529	0.229
13.64	15.45	0.775	1.451E+00	13.8	0.808	0.090
15.14	17.14	0.859	6.281E−01	21.8	0.893	0.076
16.64	18.84	0.943	6.978E−01	13.7	0.770	0.253
18.14	20.53	1.027	3.704E−01	23.5	0.691	0.183
18.27	20.67	1.035	3.226E−01	33.5	0.768	0.266
19.64	22.22	1.110	2.924E−01	41.5	0.454	0.357
19.77	22.36	1.118	3.562E−01	19.3	0.629	0.101
21.27	24.05	1.201	2.294E−01	28.8	0.610	0.211
23.77	26.86	1.339	1.168E−01	19.0	0.566	0.324
25.27	28.54	1.421	1.272E−01	30.0	0.706	0.179
26.77	30.22	1.503	6.230E−02	46.9	1.202	0.608
28.27	31.90	1.584	8.692E−02	15.7	0.197	0.198
29.77	33.57	1.665	9.329E−02	45.2	0.835	0.631
31.27	35.24	1.745	1.306E−01	51.1	0.103	0.148
33.52	37.75	1.865	1.404E−01	24.0	-0.320	0.313
34.27	38.58	1.904	1.258E−01	50.5	-0.092	0.260
36.52	41.07	2.022	7.220E−02	25.2	0.153	0.342
37.27	41.90	2.061	1.803E−02	92.1	-1.366	1.639
40.27	45.21	2.216	6.290E−03	99.5	1.032	2.030
43.27	48.51	2.368	4.749E−03	75.4	-1.366	1.116

Table F.4: d) ^{9}Be$(\vec{p},p')1/2^{-}_{1}$ (2.78 MeV); E_P = 200 MeV

θ_L	$\theta_{c.m.}$	$q_{c.m.}$	$\sigma_{c.m.}(q)$	$\Delta\sigma(\%)$	A_y	ΔA_y
12.14	13.75	0.690	7.752E−02	91.3	0.763	0.682
15.14	17.14	0.859	1.014E−01	31.1	0.270	0.288
16.64	18.84	0.943	8.317E−02	54.7	0.680	0.488
18.14	20.53	1.026	7.050E−02	61.2	0.395	0.359
18.27	20.68	1.034	7.868E−02	51.2	0.675	0.436
19.64	22.22	1.110	1.107E−01	38.3	0.955	0.277
19.77	22.37	1.118	8.759E−02	18.8	0.732	0.611
21.27	24.05	1.201	6.844E−02	22.1	0.635	0.543
23.77	26.86	1.339	8.721E−02	18.7	0.608	0.153
25.27	28.54	1.421	4.629E−02	33.7	0.298	0.176
26.77	30.22	1.502	7.223E−02	30.7	0.306	0.144
28.27	31.90	1.584	3.459E−02	14.5	0.502	0.180
29.77	33.57	1.664	3.316E−02	36.0	0.075	0.473
31.27	35.25	1.745	2.500E−02	45.9	0.309	0.613
33.52	37.75	1.864	2.000E−02	44.3	-0.020	0.589
37.27	41.91	2.061	1.479E−02	45.5	-0.161	0.412
40.27	45.21	2.215	7.356E−03	30.8	-0.120	0.413
43.27	48.51	2.367	3.728E−03	20.8	-0.186	0.271

Table F.4: e) ^{9}Be$(\vec{p},p')5/2_1^+$ (3.049 MeV); E_P = 200 MeV

θ_L	$\theta_{c.m.}$	$q_{c.m.}$	$\sigma_{c.m.}(q)$	$\Delta\sigma(\%)$	A_y	ΔA_y
12.14	13.76	0.689	9.662E−01	13.0	0.671	0.090
13.64	15.46	0.773	1.002E+00	9.9	0.887	0.066
15.14	17.15	0.857	1.035E+00	7.2	0.889	0.041
16.64	18.85	0.941	8.215E−01	7.5	0.799	0.069
18.14	20.54	1.025	6.657E−01	16.3	0.726	0.060
18.27	20.68	1.033	5.708E−01	11.6	0.913	0.083
19.64	22.23	1.108	6.492E−01	10.8	0.986	0.076
19.77	22.37	1.116	6.321E−01	5.0	0.905	0.058
21.27	24.06	1.199	5.808E−01	13.7	0.850	0.087
23.77	26.87	1.336	3.126E−01	4.2	0.821	0.071
25.27	28.56	1.418	2.261E−01	10.0	0.829	0.145
26.77	30.24	1.500	1.875E−01	22.9	0.461	0.096
27.52	31.07	1.540	2.026E−01	14.2	0.255	0.187
28.27	31.91	1.581	7.942E−02	20.5	0.301	0.164
29.77	33.59	1.661	4.029E−02	41.9	0.459	0.560
30.52	34.43	1.701	3.177E−02	44.1	-0.547	0.684
31.27	35.26	1.741	5.441E−02	15.9	-0.270	0.130
33.52	37.76	1.860	2.811E−02	32.2	-0.366	0.439
34.27	38.60	1.900	2.964E−02	40.4	-0.237	0.186
36.52	41.09	2.018	2.398E−02	42.0	0.186	0.572
37.27	41.92	2.056	1.720E−02	63.1	-0.061	0.456
39.52	44.41	2.172	1.731E−02	71.9	-1.366	1.391
43.27	48.53	2.362	4.371E−03	54.5	-1.366	0.775

Table F.4: f) ^{9}Be$(\vec{p},p')3/2^{+}_{1}$ (4.704 MeV); E_P = 200 MeV

θ_L	$\theta_{c.m.}$	$q_{c.m.}$	$\sigma_{c.m.}(q)$	$\Delta\sigma(\%)$	A_y	ΔA_y
-5.86	6.65	0.337	2.661E+00	21.0	1.075	0.447
7.64	8.67	0.436	1.456E+00	63.8	0.546	0.705
9.14	10.37	0.521	2.090E+00	40.4	0.820	0.297
10.64	12.07	0.605	3.860E+00	24.5	0.650	0.226
12.14	13.77	0.689	3.466E+00	3.2	0.813	0.023
13.64	15.46	0.773	3.338E+00	11.8	0.739	0.096
15.14	17.16	0.856	3.325E+00	9.7	0.920	0.051
16.64	18.85	0.940	3.641E+00	3.2	0.885	0.040
18.14	20.55	1.023	3.627E+00	11.8	0.922	0.070
18.27	20.69	1.031	2.802E+00	10.4	0.936	0.068
19.64	22.24	1.106	2.812E+00	8.2	0.937	0.061
19.77	22.38	1.114	3.053E+00	6.8	0.977	0.111
21.27	24.07	1.197	2.562E+00	8.2	0.908	0.022
23.77	26.88	1.334	2.157E+00	2.9	0.817	0.092
25.27	28.57	1.415	1.697E+00	3.1	0.715	0.049
26.77	30.25	1.497	1.454E+00	3.9	0.624	0.057
28.27	31.93	1.577	1.023E+00	3.8	0.445	0.126
29.77	33.60	1.658	9.167E−01	8.7	0.411	0.111
30.52	34.44	1.698	8.758E−01	7.3	0.088	0.096
31.27	35.28	1.738	8.954E−01	5.8	0.081	0.039
33.52	37.78	1.857	7.449E−01	8.2	-0.172	0.109
34.27	38.62	1.896	6.969E−01	5.2	-0.119	0.132
36.52	41.11	2.013	5.283E−01	10.0	-0.078	0.135
37.27	41.94	2.052	3.718E−01	5.3	-0.339	0.092
39.52	44.43	2.168	2.384E−01	10.6	-0.602	0.113
40.27	45.25	2.206	2.138E−01	5.1	-0.522	0.138
43.27	48.55	2.357	1.191E−01	14.9	-0.718	0.137

Table F.4: g) ^{9}Be$(\vec{p}, p')$ Lor (6.5 MeV); E_P = 200 MeV

θ_L	$\theta_{c.m.}$	$q_{c.m.}$	$\sigma_{c.m.}(q)$	$\Delta\sigma(\%)$	A_y	ΔA_y
6.14	6.60	0.351	3.551E+02	1.1	0.494	0.011
7.64	8.22	0.436	3.607E+02	0.9	0.607	0.010
9.14	9.83	0.522	2.766E+02	0.9	0.656	0.011
10.64	11.44	0.607	2.466E+02	0.7	0.778	0.007
12.14	13.05	0.692	1.817E+02	0.8	0.859	0.010
13.64	14.66	0.777	1.033E+02	0.7	0.931	0.008
15.14	16.27	0.862	6.155E+01	1.3	0.991	0.007
18.14	19.49	1.031	1.948E+01	1.7	0.777	0.035
18.27	19.63	1.039	1.793E+01	0.9	0.803	0.008
19.64	21.10	1.115	1.136E+01	0.9	0.577	0.009
19.77	21.23	1.124	1.064E+01	3.4	0.532	0.009
21.27	22.84	1.207	6.475E+00	0.9	0.126	0.007
23.77	25.51	1.347	3.121E+00	0.9	-0.309	0.021
26.77	28.72	1.512	1.926E+00	1.0	0.060	0.014
28.27	30.32	1.595	1.511E+00	0.9	0.428	0.011
29.77	31.92	1.677	1.311E+00	1.3	0.736	0.014
31.27	33.52	1.758	1.099E+00	0.8	0.897	0.009
33.52	35.91	1.880	8.115E−01	1.1	0.912	0.011
34.27	36.71	1.920	7.812E−01	1.1	0.886	0.011
36.52	39.09	2.040	5.569E−01	1.5	0.627	0.017
37.27	39.89	2.080	4.952E−01	0.9	0.567	0.010
39.52	42.27	2.199	3.378E−01	1.7	0.244	0.022
40.27	43.06	2.238	2.839E−01	1.3	0.189	0.017
43.27	46.23	2.394	1.214E−01	1.2	-0.303	0.016
45.52	48.60	2.509	7.179E−02	1.6	-0.573	0.020
46.27	49.39	2.548	5.752E−02	1.9	-0.741	0.024
48.52	51.75	2.661	3.046E−02	1.9	-0.792	0.021
49.27	52.54	2.699	2.550E−02	1.1	-0.721	0.013
51.52	54.90	2.811	1.712E−02	2.0	-0.228	0.026
55.27	58.81	2.994	1.408E−02	1.1	0.505	0.013

Table F.5: a) $^{16}O(\vec{p},p)0_1^+$; E_P = 200 MeV

θ_L	$\theta_{c.m.}$	$q_{c.m.}$	$\sigma_{c.m.}(q)$	$\Delta\sigma(\%)$	A_y	ΔA_y
-5.86	6.31	0.337	5.491E−03	76.2	0.787	1.027
7.64	8.22	0.436	4.892E−02	16.8	0.795	0.320
9.14	9.84	0.521	9.247E−02	8.3	0.833	0.081
10.64	11.45	0.605	7.694E−02	23.7	0.907	0.233
12.14	13.06	0.689	1.723E−01	5.2	0.870	0.047
13.64	14.67	0.773	1.578E−01	5.5	0.897	0.124
15.14	16.29	0.857	1.635E−01	18.0	0.967	0.026
16.64	17.90	0.941	1.568E−01	9.3	0.922	0.089
18.14	19.50	1.024	1.191E−01	22.5	0.724	0.064
18.27	19.64	1.033	1.101E−01	8.0	0.763	0.265
19.64	21.11	1.108	6.102E−02	46.3	0.248	0.448
19.77	21.25	1.116	6.808E−02	21.0	0.440	0.241
21.27	22.86	1.199	6.987E−02	20.8	0.253	0.336
23.77	25.54	1.337	6.241E−02	13.4	-0.024	0.059
25.27	27.14	1.419	4.789E−02	49.9	0.074	0.447
26.77	28.74	1.501	3.386E−02	16.1	-0.006	0.220
27.52	29.54	1.542	4.473E−02	14.4	-0.609	0.197
28.27	30.35	1.583	3.277E−02	12.6	0.101	0.064
29.77	31.95	1.664	3.136E−02	12.2	0.383	0.156
30.52	32.74	1.705	3.029E−02	13.9	0.167	0.177
31.27	33.54	1.745	2.532E−02	8.6	0.643	0.134
36.52	39.13	2.025	2.302E−02	12.3	0.395	0.161
37.27	39.92	2.064	1.522E−02	7.0	0.594	0.094
39.52	42.31	2.182	1.180E−02	16.0	0.306	0.217
40.27	43.10	2.221	1.664E−02	5.0	-0.098	0.119
43.27	46.27	2.375	8.072E−03	5.8	-0.357	0.134

Table F.5: b) $^{16}O(\vec{p},p')0_2^+$ (6.0494 MeV); E_P = 200 MeV

θ_L	$\theta_{c.m.}$	$q_{c.m.}$	$\sigma_{c.m.}(q)$	$\Delta\sigma(\%)$	A_y	ΔA_y
-5.86	6.31	0.337	4.315E−02	16.1	-0.125	0.184
7.64	8.22	0.436	1.487E−01	4.3	0.162	0.049
9.14	9.84	0.521	3.965E−01	2.5	0.393	0.027
10.64	11.45	0.605	6.817E−01	3.2	0.423	0.020
12.14	13.06	0.689	1.096E+00	3.1	0.501	0.027
13.64	14.67	0.773	1.558E+00	2.5	0.597	0.015
15.14	16.29	0.857	2.013E+00	1.9	0.717	0.013
16.64	17.90	0.941	2.519E+00	3.1	0.731	0.009
18.14	19.51	1.024	2.724E+00	3.3	0.844	0.043
18.27	19.64	1.032	2.909E+00	1.8	0.851	0.009
19.64	21.11	1.108	3.127E+00	2.0	0.854	0.015
19.77	21.25	1.116	3.190E+00	1.6	0.867	0.022
21.27	22.86	1.199	3.136E+00	2.5	0.922	0.007
23.77	25.54	1.337	3.066E+00	1.0	0.862	0.010
25.27	27.14	1.419	2.748E+00	6.8	0.784	0.009
26.77	28.74	1.501	2.719E+00	0.9	0.657	0.008
28.27	30.35	1.583	2.365E+00	1.2	0.529	0.009
29.77	31.95	1.664	2.133E+00	1.0	0.355	0.012
30.52	32.75	1.704	1.880E+00	0.7	0.284	0.009
31.27	33.54	1.745	1.911E+00	1.8	0.201	0.006
33.52	35.94	1.865	1.432E+00	1.0	-0.045	0.013
34.27	36.74	1.905	1.342E+00	1.9	-0.107	0.022
36.52	39.13	2.024	9.635E−01	1.2	-0.345	0.015
37.27	39.92	2.064	8.506E−01	0.6	-0.411	0.007
39.52	42.31	2.182	5.298E−01	1.4	-0.647	0.017
40.27	43.10	2.221	4.818E−01	0.8	-0.675	0.009
43.27	46.27	2.375	2.267E−01	0.6	-0.910	0.009
46.27	49.43	2.528	1.229E−01	1.2	-0.977	0.023
48.52	51.80	2.640	6.301E−02	1.4	-0.868	0.016
49.27	52.58	2.678	6.099E−02	0.8	-0.776	0.009
51.52	54.94	2.788	3.682E−02	2.1	-0.475	0.032
55.27	58.86	2.970	2.088E−02	0.9	0.031	0.011

Table F.5: c) $^{16}O(\vec{p},p')3_1^-$ (6.1299 MeV); E_P = 200 MeV

θ_L	$\theta_{c.m.}$	$q_{c.m.}$	$\sigma_{c.m.}(q)$	$\Delta\sigma(\%)$	A_y	ΔA_y
-5.86	6.31	0.337	1.528E−01	6.7	0.484	0.095
7.64	8.22	0.437	6.361E−01	1.6	0.487	0.055
9.14	9.84	0.521	1.105E+00	1.4	0.606	0.015
10.64	11.45	0.605	1.449E+00	1.1	0.659	0.011
12.14	13.06	0.689	2.022E+00	6.4	0.718	0.020
13.64	14.68	0.773	2.005E+00	6.3	0.804	0.025
15.14	16.29	0.857	1.725E+00	4.1	0.902	0.015
18.14	19.51	1.024	1.299E+00	3.5	0.944	0.060
18.27	19.65	1.032	1.277E+00	3.5	0.961	0.041
19.64	21.12	1.107	1.108E+00	3.4	0.926	0.023
19.77	21.26	1.115	1.076E+00	5.3	0.916	0.015
21.27	22.86	1.198	7.891E−01	4.2	0.842	0.027
23.77	25.54	1.336	4.340E−01	2.8	0.517	0.018
25.27	27.14	1.418	2.772E−01	2.0	0.200	0.024
26.77	28.75	1.500	1.870E−01	4.7	-0.110	0.086
28.27	30.35	1.581	1.289E−01	4.7	-0.342	0.025
29.77	31.95	1.663	8.542E−02	5.3	-0.599	0.068
30.52	32.75	1.703	6.835E−02	4.2	-0.548	0.058
31.27	33.55	1.743	6.179E−02	2.2	-0.375	0.029
33.52	35.94	1.864	3.897E−02	5.8	0.292	0.077
34.27	36.74	1.903	3.760E−02	6.0	0.541	0.062
36.52	39.13	2.022	3.107E−02	9.0	1.023	0.116
37.27	39.93	2.062	3.312E−02	10.6	1.096	0.283
39.52	42.31	2.179	3.824E−02	5.9	0.753	0.064
40.27	43.10	2.218	3.486E−02	2.2	0.742	0.024
43.27	46.27	2.373	2.509E−02	7.1	0.467	0.023
45.52	48.65	2.487	1.797E−02	4.9	0.285	0.065
46.27	49.44	2.525	1.436E−02	8.3	0.222	0.069
48.52	51.80	2.638	1.008E−02	6.5	-0.037	0.087
49.27	52.59	2.675	8.738E−03	3.7	-0.028	0.050
51.52	54.95	2.786	3.949E−03	6.5	-0.350	0.092
55.27	58.87	2.967	1.569E−03	5.4	-0.598	0.069

Table F.5: d) $^{16}O(\vec{p},p')2_1^+$ (6.9171 MeV); E_P = 200 MeV

θ_L	$\theta_{c.m.}$	$q_{c.m.}$	$\sigma_{c.m.}(q)$	$\Delta\sigma(\%)$	A_y	ΔA_y
-5.86	6.31	0.338	4.897E−02	10.4	0.549	0.127
7.64	8.22	0.437	4.281E−02	10.1	0.178	0.278
9.14	9.84	0.521	5.670E−02	9.7	0.309	0.103
10.64	11.45	0.605	1.053E−01	6.9	0.610	0.066
12.14	13.06	0.689	1.615E−01	18.7	0.687	0.052
13.64	14.68	0.773	2.480E−01	4.0	0.787	0.039
15.14	16.29	0.857	3.228E−01	8.5	0.916	0.044
18.14	19.51	1.024	5.652E−01	4.1	0.932	0.031
18.27	19.65	1.032	5.889E−01	2.8	0.946	0.020
19.64	21.12	1.107	7.823E−01	4.5	0.940	0.030
19.77	21.26	1.115	7.228E−01	2.5	0.907	0.015
21.27	22.86	1.198	7.690E−01	2.6	0.886	0.019
23.77	25.54	1.335	7.412E−01	2.7	0.724	0.025
25.27	27.15	1.418	6.866E−01	1.1	0.576	0.013
26.77	28.75	1.500	6.264E−01	1.6	0.435	0.029
28.27	30.35	1.581	5.337E−01	1.9	0.248	0.012
29.77	31.95	1.662	4.767E−01	2.1	0.060	0.028
30.52	32.75	1.703	4.067E−01	1.5	-0.005	0.020
31.27	33.55	1.743	3.980E−01	0.8	-0.112	0.011
33.52	35.94	1.863	2.674E−01	1.9	-0.382	0.025
34.27	36.74	1.903	2.202E−01	1.1	-0.491	0.013
36.52	39.13	2.022	1.398E−01	3.3	-0.702	0.040
37.27	39.93	2.061	1.189E−01	1.7	-0.740	0.063
40.27	43.11	2.218	5.411E−02	6.5	-0.944	0.027
43.27	46.28	2.372	2.199E−02	3.5	-0.727	0.026
45.52	48.65	2.487	1.295E−02	5.5	-0.177	0.073
46.27	49.44	2.524	1.108E−02	10.8	-0.145	0.065
49.27	52.59	2.674	6.758E−03	5.2	0.613	0.071
51.52	54.95	2.785	5.761E−03	6.8	0.695	0.090
55.27	58.87	2.966	2.798E−03	3.4	0.496	0.048

Table F.5: e) $^{16}O(\vec{p},p')1_1^-$ (7.1169 MeV); E_P = 200 MeV

θ_L	$\theta_{c.m.}$	$q_{c.m.}$	$\sigma_{c.m.}(q)$	$\Delta\sigma(\%)$	A_y	ΔA_y
-5.86	6.31	0.340	2.399E−02	16.8	-0.075	0.203
7.64	8.23	0.438	2.815E−02	12.4	-0.273	0.154
9.14	9.84	0.522	2.421E−02	15.4	0.020	0.174
10.64	11.45	0.605	2.542E−02	16.8	-0.040	0.190
12.14	13.07	0.689	3.545E−02	16.1	-0.019	0.181
13.64	14.68	0.772	2.886E−02	17.9	-0.053	0.204
15.14	16.29	0.856	2.073E−02	23.1	-0.406	0.238
16.64	17.90	0.939	3.017E−02	15.3	-0.464	0.206
18.14	19.51	1.022	3.088E−02	29.3	-0.204	0.648
18.27	19.65	1.030	3.579E−02	15.3	-0.606	0.269
19.77	21.26	1.113	5.114E−02	16.0	-0.190	0.430
21.27	22.87	1.196	5.672E−02	7.6	-0.147	0.217
23.77	25.55	1.333	5.752E−02	5.4	-0.177	0.076
25.27	27.15	1.415	6.501E−02	6.0	-0.104	0.081
26.77	28.76	1.497	5.362E−02	9.8	-0.263	0.106
28.27	30.36	1.578	4.400E−02	5.2	-0.268	0.072
29.77	31.96	1.659	5.040E−02	9.3	0.183	0.122
30.52	32.76	1.699	3.775E−02	8.2	0.146	0.106
31.27	33.56	1.739	3.844E−02	3.6	-0.240	0.049
33.52	35.95	1.859	2.273E−02	9.0	-0.340	0.118
34.27	36.75	1.899	2.384E−02	4.4	-0.323	0.068
36.52	39.14	2.018	1.342E−02	14.8	-0.336	0.197
37.27	39.94	2.057	1.246E−02	9.5	-0.501	0.073
39.52	42.32	2.174	6.107E−03	19.4	-1.366	0.287
40.27	43.12	2.213	7.076E−03	5.8	-0.274	0.075
43.27	46.29	2.367	3.305E−03	9.1	-0.236	0.087
46.27	49.45	2.519	3.225E−03	11.8	-0.143	0.149
49.27	52.60	2.668	9.877E−04	11.4	1.165	0.217
51.52	54.96	2.779	1.111E−03	9.9	0.528	0.140

Table F.5: f) $^{16}O(\vec{p},p')2_1^-$ (8.8719 MeV); E_P = 200 MeV

θ_L	$\theta_{c.m.}$	$q_{c.m.}$	$\sigma_{c.m.}(q)$	$\Delta\sigma(\%)$	A_y	ΔA_y
7.64	8.23	0.439	1.453E−02	83.5	0.282	1.230
10.64	11.46	0.606	2.953E−02	82.3	0.240	0.855
12.14	13.07	0.689	7.998E−02	75.2	0.535	0.683
26.77	28.76	1.496	3.433E−02	70.1	0.869	0.874
27.52	29.56	1.536	3.828E−02	69.3	-0.488	1.052
28.27	30.36	1.577	7.003E−02	18.3	0.423	0.361
31.27	33.56	1.738	7.571E−02	30.8	0.334	0.390
36.52	39.14	2.016	2.357E−02	29.7	-0.346	0.400
37.27	39.94	2.055	1.429E−02	15.8	-0.288	0.206
39.52	42.33	2.172	9.546E−03	78.0	0.588	1.124
40.27	43.12	2.211	1.544E−02	32.4	-0.822	0.421
43.27	46.29	2.365	8.508E−03	11.2	-0.839	0.138
45.52	48.66	2.479	5.835E−03	39.5	-0.663	0.428
46.27	49.45	2.517	1.889E−03	75.3	-0.341	0.879

Table F.5: g) $^{16}O(\vec{p},p')1_2^-$ (9.585 MeV); E_P = 200 MeV

θ_L	$\theta_{c.m.}$	$q_{c.m.}$	$\sigma_{c.m.}(q)$	$\Delta\sigma(\%)$	A_y	ΔA_y
-5.86	6.31	0.342	4.525E−03	74.2	0.364	0.916
7.64	8.23	0.440	9.675E−03	31.0	-0.410	0.403
9.14	9.84	0.522	2.507E−02	14.8	0.095	0.165
10.64	11.46	0.606	3.569E−02	44.1	0.146	0.327
12.14	13.07	0.689	5.399E−02	21.0	0.318	0.108
13.64	14.68	0.772	5.920E−02	8.2	0.357	0.105
15.14	16.29	0.856	6.986E−02	8.1	0.419	0.059
16.64	17.91	0.939	6.881E−02	9.3	0.573	0.192
18.14	19.52	1.022	8.876E−02	7.2	0.795	0.167
18.27	19.66	1.030	9.234E−02	7.7	0.810	0.080
19.64	21.13	1.104	7.146E−02	19.2	0.883	0.137
19.77	21.26	1.112	8.512E−02	8.2	0.671	0.062
21.27	22.87	1.195	8.235E−02	11.8	0.807	0.046
23.77	25.55	1.332	7.605E−02	8.7	0.847	0.035
25.27	27.16	1.414	6.702E−02	4.8	0.911	0.053
26.77	28.76	1.495	6.735E−02	4.9	0.710	0.139
27.52	29.56	1.536	6.904E−02	7.9	0.393	0.101
28.27	30.36	1.576	5.497E−02	6.7	0.583	0.047
29.77	31.96	1.657	6.228E−02	8.4	0.451	0.107
30.52	32.76	1.697	5.943E−02	6.5	0.090	0.084
31.27	33.56	1.737	5.687E−02	5.6	0.228	0.071
33.52	35.96	1.857	3.604E−02	8.2	-0.075	0.109
34.27	36.76	1.897	3.309E−02	4.8	-0.126	0.064
36.52	39.15	2.015	2.378E−02	10.6	-0.211	0.141
37.27	39.94	2.055	2.308E−02	4.0	-0.495	0.065
39.52	42.33	2.172	1.128E−02	13.7	-1.296	0.190
40.27	43.12	2.210	1.250E−02	12.4	-0.697	0.055
43.27	46.29	2.364	6.695E−03	7.4	-0.842	0.069
45.52	48.67	2.478	3.123E−03	16.5	-1.042	0.192
46.27	49.46	2.516	3.019E−03	6.4	-1.033	0.101
49.27	52.61	2.665	1.160E−03	21.1	-1.347	0.297

Table F.5: h) $^{16}O(\vec{p},p')2_2^+$ (9.8445 MeV); E_P = 200 MeV

θ_L	$\theta_{c.m.}$	$q_{c.m.}$	$\sigma_{c.m.}(q)$	$\Delta\sigma(\%)$	A_y	ΔA_y
7.64	8.23	0.440	6.062E−03	60.9	1.312	0.789
9.14	9.84	0.523	7.495E−03	54.1	0.304	0.580
10.64	11.46	0.606	1.368E−02	43.8	0.871	1.080
12.14	13.07	0.689	1.614E−02	31.1	1.154	0.309
13.64	14.68	0.772	3.290E−02	15.4	0.867	0.139
15.14	16.30	0.855	3.823E−02	22.6	0.777	0.127
16.64	17.91	0.938	5.526E−02	14.4	0.814	0.094
18.14	19.52	1.021	9.228E−02	10.6	0.903	0.047
18.27	19.66	1.029	7.611E−02	9.8	0.775	0.081
19.64	21.13	1.104	8.579E−02	18.8	0.753	0.145
19.77	21.27	1.112	9.240E−02	11.7	0.849	0.056
21.27	22.87	1.194	1.170E−01	5.3	0.897	0.057
23.77	25.55	1.331	1.297E−01	3.8	0.876	0.113
25.27	27.16	1.413	1.245E−01	7.6	0.667	0.036
26.77	28.76	1.494	1.284E−01	3.4	0.647	0.038
27.52	29.56	1.535	1.447E−01	4.8	0.343	0.062
28.27	30.36	1.576	1.258E−01	2.2	0.430	0.026
29.77	31.97	1.656	1.355E−01	5.2	0.422	0.066
30.52	32.77	1.696	1.288E−01	3.8	0.201	0.048
31.27	33.56	1.737	1.225E−01	2.0	0.165	0.025
33.52	35.96	1.856	9.726E−02	4.6	0.066	0.061
34.27	36.76	1.896	8.406E−02	2.8	-0.085	0.155
36.52	39.15	2.014	6.089E−02	7.1	-0.364	0.091
37.27	39.95	2.053	5.710E−02	7.7	-0.449	0.045
39.52	42.33	2.170	2.864E−02	8.3	-1.005	0.105
40.27	43.12	2.209	3.348E−02	5.4	-0.605	0.051
43.27	46.30	2.363	1.514E−02	9.9	-0.821	0.034
45.52	48.67	2.476	1.033E−02	7.0	-0.726	0.078
46.27	49.46	2.514	7.709E−03	3.6	-0.811	0.042
49.27	52.61	2.663	3.732E−03	4.4	-0.678	0.053
51.52	54.97	2.773	3.696E−03	11.0	-0.314	0.147

Table F.5: i) $^{16}O(\vec{p},p')4_1^+$ (10.356 MeV); E_P = 200 MeV

θ_L	$\theta_{c.m.}$	$q_{c.m.}$	$\sigma_{c.m.}(q)$	$\Delta\sigma(\%)$	A_y	ΔA_y
-5.86	6.31	0.344	3.361E−02	21.4	0.121	0.271
7.64	8.23	0.441	3.642E−02	9.6	0.207	0.394
9.14	9.84	0.523	4.439E−02	9.2	0.222	0.101
10.64	11.46	0.606	4.037E−02	11.3	0.456	0.256
12.14	13.07	0.689	5.826E−02	10.2	0.391	0.098
13.64	14.68	0.772	4.818E−02	10.6	0.398	0.101
15.14	16.30	0.855	3.194E−02	34.1	0.469	0.207
16.64	17.91	0.938	2.376E−02	22.0	0.569	0.307
18.14	19.52	1.021	1.626E−02	36.0	-0.193	0.335
18.27	19.66	1.029	1.363E−02	39.0	0.468	0.387
19.77	21.27	1.112	1.189E−02	35.8	-0.556	0.619
21.27	22.88	1.194	7.540E−03	88.8	-0.499	0.510
23.77	25.56	1.331	8.042E−03	23.0	-1.366	0.521
25.27	27.16	1.412	8.822E−03	27.3	-0.544	0.739
26.77	28.76	1.494	9.298E−03	22.7	-0.543	0.354
27.52	29.57	1.534	1.369E−02	26.0	-0.699	0.393
28.27	30.37	1.575	8.380E−03	14.5	-0.526	0.220
29.77	31.97	1.655	5.409E−03	49.4	-0.170	0.676
30.52	32.77	1.695	1.148E−02	18.7	-0.500	0.283
31.27	33.57	1.735	1.193E−02	11.7	-0.286	0.116
33.52	35.96	1.855	6.016E−03	31.3	-0.399	0.423
34.27	36.76	1.895	1.055E−02	19.8	-0.224	0.268
36.52	39.15	2.013	5.906E−03	48.6	-0.220	0.638
37.27	39.95	2.052	3.818E−03	27.2	-0.918	0.386
40.27	43.13	2.208	2.028E−03	45.9	-0.138	0.456
43.27	46.30	2.361	1.350E−03	21.5	-1.072	0.269
46.27	49.46	2.512	6.738E−04	56.0	-1.363	0.796
51.52	54.98	2.771	5.892E−04	47.9	-1.366	0.925

Table F.5: j) $^{16}O(\vec{p},p')0_1^-$ (10.957 MeV); E_P = 200 MeV

θ_L	$\theta_{c.m.}$	$q_{c.m.}$	$\sigma_{c.m.}(q)$	$\Delta\sigma(\%)$	A_y	ΔA_y
15.14	16.30	0.855	2.649E−02	108.3	0.665	0.649
18.27	19.66	1.029	5.545E−02	56.4	1.006	0.477
19.77	21.27	1.111	3.779E−02	37.0	0.909	0.212
21.27	22.88	1.194	5.230E−02	60.6	0.961	0.350
23.77	25.56	1.330	6.134E−02	21.7	0.803	0.465
25.27	27.16	1.412	7.876E−02	25.3	0.860	0.283
26.77	28.77	1.493	6.400E−02	32.5	0.958	0.649
27.52	29.57	1.534	8.406E−02	62.5	0.462	0.873
28.27	30.37	1.574	7.228E−02	9.6	0.525	0.108
29.77	31.97	1.655	7.712E−02	21.4	0.555	0.254
30.52	32.77	1.695	7.202E−02	42.6	0.504	0.598
31.27	33.57	1.735	6.063E−02	26.6	0.607	0.241
36.52	39.15	2.013	5.056E−02	52.3	0.363	0.784
37.27	39.95	2.052	3.318E−02	45.9	-0.305	0.804
40.27	43.13	2.207	2.693E−02	34.5	0.133	0.446
43.27	46.30	2.361	1.452E−02	31.2	-0.325	0.492
45.52	48.67	2.474	1.445E−02	57.1	0.124	0.728
46.27	49.46	2.512	1.296E−02	67.6	0.041	0.891
51.52	54.98	2.771	2.932E−03	8.9	0.555	0.124

Table F.5: k) ^{16}O$(\vec{p},p')4_2^+$ (11.097 MeV); E_P = 200 MeV

θ_L	$\theta_{c.m.}$	$q_{c.m.}$	$\sigma_{c.m.}(q)$	$\Delta\sigma(\%)$	A_y	ΔA_y
-5.86	6.31	0.345	1.115E−01	6.7	0.469	0.079
7.64	8.23	0.442	3.551E−01	2.4	0.505	0.026
9.14	9.84	0.524	6.260E−01	2.0	0.583	0.021
10.64	11.46	0.607	8.098E−01	2.9	0.646	0.016
12.14	13.07	0.689	1.155E+00	4.4	0.715	0.026
13.64	14.69	0.772	1.181E+00	6.4	0.772	0.021
15.14	16.30	0.855	1.037E+00	2.1	0.861	0.021
18.14	19.52	1.021	8.172E−01	3.6	0.912	0.041
18.27	19.66	1.029	8.207E−01	2.2	0.908	0.027
19.64	21.13	1.103	6.761E−01	4.6	0.847	0.034
19.77	21.27	1.111	6.885E−01	5.4	0.875	0.051
21.27	22.88	1.193	5.191E−01	2.8	0.767	0.017
23.77	25.56	1.330	3.325E−01	4.4	0.468	0.025
25.27	27.16	1.412	2.101E−01	9.1	0.154	0.032
26.77	28.77	1.493	1.718E−01	3.0	-0.170	0.098
28.27	30.37	1.574	1.178E−01	2.4	-0.363	0.034
29.77	31.97	1.654	8.878E−02	7.0	-0.519	0.095
30.52	32.77	1.694	8.397E−02	4.9	-0.433	0.070
31.27	33.57	1.734	6.700E−02	3.3	-0.480	0.044
33.52	35.97	1.854	4.324E−02	7.9	0.021	0.105
34.27	36.76	1.893	4.288E−02	4.3	0.175	0.066
37.27	39.95	2.051	3.745E−02	4.7	0.469	0.140
40.27	43.13	2.206	2.981E−02	5.3	0.779	0.175
43.27	46.30	2.359	2.594E−02	2.8	0.453	0.040
45.52	48.68	2.473	2.120E−02	4.8	0.366	0.069
46.27	49.47	2.510	1.944E−02	8.2	0.177	0.140
49.27	52.62	2.659	1.148E−02	2.3	-0.085	0.031

Table F.5: 1) $^{16}O(\vec{p},p')2_3^+$ (11.520 MeV); E_P = 200 MeV

θ_L	$\theta_{c.m.}$	$q_{c.m.}$	$\sigma_{c.m.}(q)$	$\Delta\sigma(\%)$	A_y	ΔA_y
-5.86	6.31	0.346	4.274E−02	10.4	-0.002	0.126
7.64	8.23	0.443	3.475E−02	10.4	0.723	0.138
9.14	9.85	0.525	6.045E−02	7.4	0.840	0.074
10.64	11.46	0.607	7.976E−02	6.6	0.932	0.062
12.14	13.07	0.690	1.701E−01	10.4	0.930	0.035
13.64	14.69	0.772	1.686E−01	11.4	0.952	0.046
15.14	16.30	0.855	2.104E−01	6.1	0.950	0.026
16.64	17.91	0.938	2.142E−01	6.9	0.820	0.074
18.14	19.52	1.020	2.162E−01	6.5	0.749	0.026
18.27	19.66	1.028	1.832E−01	4.6	0.732	0.041
19.64	21.13	1.103	1.565E−01	10.2	0.522	0.092
19.77	21.27	1.111	1.687E−01	6.1	0.584	0.116
21.27	22.88	1.193	1.458E−01	6.3	0.341	0.053
23.77	25.56	1.329	1.065E−01	13.0	-0.071	0.070
25.27	27.17	1.411	7.250E−02	4.0	-0.326	0.075
26.77	28.77	1.492	7.240E−02	10.0	-0.425	0.120
28.27	30.37	1.573	4.640E−02	6.8	-0.610	0.050
29.77	31.97	1.653	3.879E−02	9.6	-0.350	0.130
30.52	32.77	1.693	3.196E−02	7.6	-0.405	0.109
31.27	33.57	1.733	2.597E−02	17.6	-0.271	0.060
33.52	35.97	1.853	1.317E−02	13.9	0.236	0.187
34.27	36.77	1.892	1.460E−02	13.3	0.529	0.169
36.52	39.16	2.010	1.411E−02	15.8	0.670	0.222
37.27	39.96	2.049	1.159E−02	15.8	0.749	0.271
40.27	43.14	2.205	1.013E−02	7.2	0.688	0.112
43.27	46.31	2.358	6.709E−03	9.5	0.290	0.105
45.52	48.68	2.471	5.757E−03	12.0	0.081	0.163
46.27	49.47	2.509	4.430E−03	24.9	-0.038	0.089
49.27	52.63	2.658	1.293E−03	12.0	-0.326	0.148

Table F.5: m) $^{16}O(\vec{p},p')0_3^+$ (12.049 MeV); E_P = 200 MeV

θ_L	$\theta_{c.m.}$	$q_{c.m.}$	$\sigma_{c.m.}(q)$	$\Delta\sigma(\%)$	A_y	ΔA_y
-5.86	6.31	0.347	1.592E−02	45.8	-1.314	0.814
7.64	8.23	0.443	2.061E−02	32.7	-0.375	0.423
9.14	9.85	0.525	3.923E−02	20.2	-0.666	0.275
10.64	11.46	0.607	1.375E−02	67.5	-1.299	1.248
12.14	13.07	0.690	2.301E−02	34.7	-0.869	0.523
13.64	14.69	0.773	1.213E−02	68.1	-1.309	1.321
16.64	17.91	0.938	3.234E−02	27.4	0.565	0.261
18.14	19.52	1.020	8.256E−02	14.6	0.653	0.172
18.27	19.66	1.028	7.508E−02	22.8	0.616	0.131
19.64	21.13	1.103	1.059E−01	31.9	0.646	0.246
19.77	21.27	1.111	9.800E−02	9.9	0.752	0.146
21.27	22.88	1.193	7.072E−02	13.0	1.076	0.079
23.77	25.56	1.329	5.400E−02	16.2	0.696	0.129
25.27	27.17	1.410	6.315E−02	7.3	0.673	0.084
26.77	28.77	1.491	5.675E−02	8.2	0.573	0.098
28.27	30.37	1.572	4.305E−02	6.3	0.209	0.085
29.77	31.98	1.653	4.459E−02	14.5	0.443	0.190
30.52	32.78	1.693	4.717E−02	10.5	0.117	0.137
31.27	33.58	1.733	2.930E−02	9.3	-0.046	0.093
33.52	35.97	1.852	2.439E−02	15.5	-0.383	0.207
34.27	36.77	1.891	1.515E−02	21.9	-0.168	0.291
36.52	39.16	2.009	1.544E−02	35.8	-0.151	0.481
37.27	39.96	2.048	1.108E−02	13.8	-0.499	0.179
39.52	42.34	2.165	5.640E−03	52.3	-0.737	0.692
40.27	43.14	2.204	1.069E−02	15.4	-0.358	0.149
43.27	46.31	2.357	6.304E−03	34.8	-0.130	0.351
46.27	49.47	2.508	4.303E−03	47.0	-0.751	0.533

Table F.5: n) $^{16}O(\vec{p},p')1_3^-$ (12.440 MeV); E_P = 200 MeV

θ_L	$\theta_{c.m.}$	$q_{c.m.}$	$\sigma_{c.m.}(q)$	$\Delta\sigma(\%)$	A_y	ΔA_y
-5.86	6.31	0.348	1.044E−01	5.6	-0.074	0.067
7.64	8.23	0.443	1.785E−01	3.2	-0.108	0.051
12.14	13.08	0.690	2.857E−01	5.4	-0.063	0.096
13.64	14.69	0.773	2.465E−01	4.3	-0.052	0.045
15.14	16.30	0.855	1.974E−01	5.3	0.018	0.068
16.64	17.91	0.938	1.709E−01	5.9	-0.007	0.178
18.14	19.52	1.020	1.451E−01	14.4	0.099	0.147
18.27	19.66	1.028	1.301E−01	5.8	0.056	0.144
19.64	21.13	1.102	1.208E−01	19.2	0.028	0.210
19.77	21.27	1.110	1.107E−01	10.0	0.077	0.108
21.27	22.88	1.193	9.535E−02	10.3	0.113	0.090
23.77	25.56	1.329	4.915E−02	10.1	0.002	0.100
25.27	27.17	1.410	1.665E−02	29.7	-0.739	0.638
26.77	28.77	1.491	1.591E−02	17.6	-0.448	0.405
27.52	29.57	1.532	1.532E−02	62.0	-0.428	0.943
28.27	30.37	1.572	9.710E−03	58.1	-0.452	0.224
29.77	31.98	1.652	7.506E−03	48.5	-0.692	0.762
30.52	32.78	1.693	7.120E−03	46.3	-1.122	0.874
31.27	33.58	1.732	6.618E−03	35.7	-0.152	0.427
33.52	35.97	1.852	3.277E−03	71.8	-0.362	0.953
34.27	36.77	1.891	1.181E−02	17.8	-0.131	0.239
36.52	39.16	2.009	7.395E−03	52.5	0.839	0.871
37.27	39.96	2.048	5.679E−03	16.8	0.166	0.234
39.52	42.34	2.165	2.625E−03	69.0	-1.366	1.106
40.27	43.14	2.203	4.164E−03	34.5	0.279	0.302
43.27	46.31	2.356	3.207E−03	16.4	-0.227	0.247
46.27	49.47	2.507	1.924E−03	51.6	0.371	0.846
49.27	52.63	2.656	1.033E−03	29.6	-0.263	0.389

Table F.5: o) $^{16}O(\vec{p},p')2_2^-$ (12.530 MeV); E_P = 200 MeV

θ_L	$\theta_{c.m.}$	$q_{c.m.}$	$\sigma_{c.m.}(q)$	$\Delta\sigma(\%)$	A_y	ΔA_y
-5.86	6.31	0.348	3.928E−02	14.9	0.114	0.178
7.64	8.23	0.444	1.164E−02	38.1	-0.432	0.501
12.14	13.08	0.690	1.191E−02	122.6	0.528	0.562
13.64	14.69	0.773	5.890E−03	99.4	-1.309	1.945
15.14	16.30	0.855	2.796E−02	37.3	1.047	0.510
16.64	17.91	0.938	1.620E−02	36.4	0.111	0.764
18.14	19.52	1.020	1.508E−02	75.7	1.089	0.934
18.27	19.66	1.028	7.659E−03	96.3	-1.205	2.239
19.64	21.13	1.102	4.734E−02	70.0	-0.037	0.799
19.77	21.27	1.110	2.928E−02	49.8	0.972	0.279
21.27	22.88	1.192	5.129E−02	10.0	0.848	0.222
23.77	25.56	1.329	4.734E−02	7.2	0.793	0.104
25.27	27.17	1.410	2.627E−02	16.6	0.718	0.131
26.77	28.77	1.491	2.251E−02	30.8	0.699	0.244
27.52	29.57	1.531	2.444E−02	22.7	0.159	0.292
28.27	30.38	1.572	1.899E−02	10.3	0.403	0.221
29.77	31.98	1.652	2.329E−02	19.4	-0.194	0.264
30.52	32.78	1.692	2.708E−02	12.5	0.274	0.161
31.27	33.58	1.732	1.454E−02	10.0	0.010	0.234
33.52	35.97	1.851	1.104E−02	22.9	-0.295	0.306
34.27	36.77	1.891	8.049E−03	28.2	0.202	0.386
36.52	39.16	2.009	1.332E−02	21.4	0.128	0.290
37.27	39.96	2.048	4.768E−03	25.3	-0.202	0.416
39.52	42.35	2.164	6.993E−03	30.4	1.107	0.499
40.27	43.14	2.203	3.064E−03	23.6	-0.624	0.276
43.27	46.31	2.356	1.996E−03	66.0	-0.551	0.513
46.27	49.48	2.507	2.808E−03	31.6	-0.694	0.457

Table F.5: p) $^{16}O(\vec{p},p')0_2^-$ (12.796 MeV); E_P = 200 MeV

θ_L	$\theta_{c.m.}$	$q_{c.m.}$	$\sigma_{c.m.}(q)$	$\Delta\sigma(\%)$	A_y	ΔA_y
-5.86	6.31	0.349	5.019E−01	2.8	0.229	0.035
7.64	8.23	0.444	6.650E−01	2.4	0.253	0.026
12.14	13.08	0.690	7.501E−01	1.9	0.277	0.034
13.64	14.69	0.773	6.087E−01	2.7	0.266	0.060
15.14	16.30	0.855	3.988E−01	12.1	0.265	0.068
16.64	17.91	0.938	2.953E−01	3.8	0.204	0.078
18.14	19.53	1.020	2.151E−01	5.3	0.342	0.086
18.27	19.67	1.028	1.781E−01	5.6	0.248	0.065
19.77	21.28	1.110	1.387E−01	13.1	0.277	0.093
21.27	22.88	1.192	6.497E−02	18.2	0.119	0.121
23.77	25.56	1.328	3.997E−02	16.1	0.297	0.105
25.27	27.17	1.410	3.128E−02	11.3	0.209	0.203
26.77	28.77	1.491	2.521E−02	14.4	0.090	0.215
28.27	30.38	1.571	2.844E−02	23.6	0.120	0.116
29.77	31.98	1.652	3.398E−02	13.3	0.067	0.175
30.52	32.78	1.692	2.035E−02	20.8	0.037	0.275
31.27	33.58	1.732	2.253E−02	7.6	0.256	0.098
33.52	35.97	1.851	1.921E−02	13.7	0.361	0.196
34.27	36.77	1.890	2.102E−02	47.1	0.683	0.875
36.52	39.16	2.008	1.933E−02	26.0	0.442	0.427
37.27	39.96	2.047	8.771E−03	17.1	0.461	0.212
39.52	42.35	2.164	3.725E−03	54.7	-0.387	0.680
40.27	43.14	2.202	6.863E−03	49.2	0.182	0.381
43.27	46.31	2.355	2.267E−03	32.9	0.306	0.288
46.27	49.48	2.506	1.054E−03	89.0	-0.545	1.034
49.27	52.63	2.654	8.052E−04	43.1	-0.154	0.559

Table F.5: q) $^{16}O(\vec{p},p')2_3^-$ (12.969 MeV); E_P = 200 MeV

θ_L	$\theta_{c.m.}$	$q_{c.m.}$	$\sigma_{c.m.}(q)$	$\Delta\sigma(\%)$	A_y	ΔA_y
-5.86	6.31	0.349	2.525E−01	5.7	0.203	0.068
7.64	8.23	0.444	2.812E−01	5.1	0.300	0.059
9.14	9.85	0.526	3.627E−01	4.5	0.356	0.048
10.64	11.46	0.608	3.336E−01	7.9	0.344	0.065
12.14	13.08	0.690	4.879E−01	4.5	0.432	0.036
13.64	14.69	0.773	3.953E−01	11.1	0.555	0.098
15.14	16.30	0.855	3.717E−01	10.2	0.733	0.026
16.64	17.91	0.938	3.951E−01	4.2	0.741	0.071
18.14	19.53	1.020	3.598E−01	5.3	0.753	0.055
18.27	19.67	1.028	3.340E−01	6.3	0.789	0.069
19.64	21.14	1.102	4.294E−01	8.4	0.816	0.081
19.77	21.28	1.110	3.405E−01	9.2	0.692	0.112
21.27	22.88	1.192	3.441E−01	3.7	0.817	0.042
23.77	25.56	1.328	3.472E−01	2.5	0.625	0.046
25.27	27.17	1.410	2.761E−01	12.1	0.522	0.058
26.77	28.77	1.491	2.401E−01	3.3	0.421	0.041
28.27	30.38	1.571	1.775E−01	4.3	0.237	0.032
29.77	31.98	1.652	1.513E−01	6.6	0.237	0.085
30.52	32.78	1.692	1.376E−01	5.4	0.137	0.070
31.27	33.58	1.731	1.200E−01	7.6	-0.140	0.036
33.52	35.98	1.851	6.969E−02	7.5	-0.343	0.099
34.27	36.77	1.890	6.233E−02	14.3	-0.098	0.568
36.52	39.17	2.008	4.812E−02	16.1	-0.300	0.191
37.27	39.96	2.047	4.073E−02	5.3	-0.510	0.114
39.52	42.35	2.163	2.042E−02	19.1	-1.366	0.294
40.27	43.14	2.202	2.317E−02	7.4	-0.393	0.100
43.27	46.31	2.355	1.124E−02	7.8	-0.215	0.205
46.27	49.48	2.506	1.148E−02	11.5	-0.279	0.140
49.27	52.63	2.654	4.756E−03	11.9	-0.268	0.156

Table F.5: r) $^{16}O(\vec{p},p')13.08$ (13.08 MeV); E_P = 200 MeV

θ_L	$\theta_{c.m.}$	$q_{c.m.}$	$\sigma_{c.m.}(q)$	$\Delta\sigma(\%)$	A_y	ΔA_y
-5.86	6.31	0.349	3.046E−02	18.1	-0.168	0.222
7.64	8.23	0.445	2.989E−02	37.7	0.135	0.188
9.14	9.85	0.526	3.282E−02	18.6	0.147	0.203
10.64	11.46	0.608	5.311E−02	28.2	0.288	0.151
12.14	13.08	0.690	9.310E−02	8.3	0.268	0.086
13.64	14.69	0.773	9.156E−02	13.5	0.393	0.110
15.14	16.30	0.855	8.979E−02	19.9	0.443	0.063
16.64	17.92	0.938	1.090E−01	32.8	0.378	0.138
18.14	19.53	1.020	1.163E−01	22.6	0.245	0.110
18.27	19.67	1.028	1.477E−01	6.8	0.566	0.078
19.64	21.14	1.102	1.672E−01	17.6	0.666	0.212
19.77	21.28	1.110	1.350E−01	5.8	0.356	0.091
21.27	22.89	1.192	1.257E−01	11.1	0.276	0.081
23.77	25.56	1.328	1.158E−01	7.9	0.366	0.046
25.27	27.17	1.409	9.616E−02	4.3	0.437	0.052
26.77	28.77	1.490	7.891E−02	5.9	0.372	0.083
27.52	29.58	1.531	5.978E−02	14.0	0.107	0.184
28.27	30.38	1.571	4.823E−02	5.1	0.358	0.113
29.77	31.98	1.651	4.128E−02	13.6	0.411	0.181
30.52	32.78	1.691	3.509E−02	10.8	0.054	0.141
31.27	33.58	1.731	2.401E−02	10.9	0.109	0.126
33.52	35.98	1.850	1.498E−02	18.7	-0.423	0.241
36.52	39.17	2.008	7.920E−03	38.9	-0.244	0.517
37.27	39.96	2.047	7.656E−03	13.8	-0.434	0.188
40.27	43.14	2.202	6.404E−03	13.7	-0.665	0.182
43.27	46.32	2.354	3.905E−03	12.4	-0.562	0.420
46.27	49.48	2.505	4.196E−03	18.1	-0.455	0.220
49.27	52.63	2.653	2.001E−03	22.7	-0.799	0.323

Table F.5: s) $^{16}O(\vec{p},p')3^-_4$ (13.259 MeV); E_P = 200 MeV

θ_L	$\theta_{c.m.}$	$q_{c.m.}$	$\sigma_{c.m.}(q)$	$\Delta\sigma(\%)$	A_y	ΔA_y
-5.86	6.32	0.350	1.728E−02	38.4	0.046	0.461
7.64	8.23	0.445	1.119E−02	69.3	0.551	0.470
9.14	9.85	0.527	1.822E−02	33.3	-0.357	0.425
10.64	11.46	0.608	1.262E−02	57.1	1.195	0.609
12.14	13.08	0.691	3.270E−02	43.7	0.717	0.176
13.64	14.69	0.773	2.369E−02	29.7	0.808	0.287
15.14	16.30	0.855	3.369E−02	15.4	0.752	0.240
16.64	17.92	0.938	3.125E−02	35.9	0.823	0.278
18.14	19.53	1.020	2.025E−02	40.5	1.268	0.353
18.27	19.67	1.028	2.316E−02	35.4	0.971	0.268
19.64	21.14	1.102	1.964E−02	87.8	-0.160	1.063
19.77	21.28	1.110	1.493E−02	96.9	0.714	0.558
23.77	25.57	1.328	1.028E−02	33.6	-1.365	0.775
25.27	27.17	1.409	2.000E−02	17.2	-0.071	0.235
26.77	28.78	1.490	2.442E−02	19.1	-0.062	0.330
27.52	29.58	1.530	3.516E−02	18.6	-0.154	0.253
28.27	30.38	1.570	3.339E−02	9.7	0.283	0.095
29.77	31.98	1.651	2.771E−02	20.5	0.061	0.269
30.52	32.78	1.691	1.020E−02	34.4	-0.268	0.484
33.52	35.98	1.849	2.826E−03	99.1	0.477	1.389
36.52	39.17	2.007	4.032E−03	81.7	-0.164	1.086
39.52	42.35	2.162	2.135E−02	14.1	1.325	0.235
43.27	46.32	2.353	6.919E−04	92.6	1.326	2.090
49.27	52.64	2.652	7.655E−04	66.0	-0.422	0.771

Table F.5: t) $^{16}O(\vec{p},p')1_1^+$ (13.664 MeV); E_P = 200 MeV

θ_L	$\theta_{c.m.}$	$q_{c.m.}$	$\sigma_{c.m.}(q)$	$\Delta\sigma(\%)$	A_y	ΔA_y
-5.86	6.32	0.351	1.248E−02	79.5	-1.305	1.308
7.64	8.23	0.446	9.068E−03	73.4	-0.061	0.815
10.64	11.46	0.609	1.249E−02	103.7	1.272	1.252
12.14	13.08	0.691	3.384E−02	26.7	0.475	0.266
13.64	14.69	0.773	4.614E−02	64.9	1.237	0.468
15.14	16.30	0.855	5.573E−02	17.9	0.822	0.173
16.64	17.92	0.938	5.792E−02	37.1	0.843	0.158
18.14	19.53	1.020	7.058E−02	15.2	0.754	0.312
18.27	19.67	1.028	7.045E−02	24.7	0.981	0.115
19.77	21.28	1.110	5.115E−02	40.2	0.599	0.182
21.27	22.89	1.192	7.695E−02	11.2	0.717	0.090
23.77	25.57	1.327	6.371E−02	11.8	0.782	0.186
25.27	27.17	1.409	7.202E−02	7.1	0.539	0.131
26.77	28.78	1.490	9.415E−02	9.8	0.594	0.145
27.52	29.58	1.530	9.889E−02	9.0	0.406	0.118
28.27	30.38	1.570	1.102E−01	5.4	0.513	0.038
29.77	31.98	1.650	1.184E−01	7.0	0.154	0.092
31.27	33.58	1.730	9.823E−02	2.9	0.257	0.036
33.52	35.98	1.849	7.757E−02	6.1	0.153	0.081
34.27	36.78	1.889	9.388E−02	7.5	0.110	0.099
36.52	39.17	2.006	7.204E−02	7.7	-0.132	0.103
37.27	39.97	2.045	7.893E−02	2.6	-0.187	0.101
40.27	43.15	2.200	5.839E−02	6.7	-0.351	0.050
43.27	46.32	2.353	3.302E−02	5.3	-0.455	0.135
46.27	49.48	2.503	2.000E−02	7.4	-0.696	0.116
49.27	52.64	2.651	1.400E−02	5.7	-0.696	0.067

Table F.5: u) $^{16}O(\vec{p},p')4_3^+$ (13.869 MeV); E_P = 200 MeV

θ_L	$\theta_{c.m.}$	$q_{c.m.}$	$\sigma_{c.m.}(q)$	$\Delta\sigma(\%)$	A_y	ΔA_y
7.64	8.23	0.446	3.596E−02	61.2	0.198	0.733
13.64	14.69	0.773	1.245E−02	64.1	0.058	0.702
16.64	17.92	0.938	2.618E−02	102.0	1.254	0.936
18.14	19.53	1.020	3.217E−02	43.5	1.220	0.326
19.77	21.28	1.110	2.444E−02	34.7	0.309	0.413
21.27	22.89	1.191	2.787E−02	41.9	0.510	0.447
23.77	25.57	1.327	1.699E−02	68.4	-1.366	1.439
26.77	28.78	1.489	9.642E−03	70.1	0.397	0.856
27.52	29.58	1.530	1.644E−02	55.2	-0.356	0.772
28.27	30.38	1.570	4.210E−03	71.1	-1.366	1.540
30.52	32.78	1.690	1.896E−02	18.8	1.326	0.339
34.27	36.78	1.888	3.842E−02	13.2	0.116	0.178
43.27	46.32	2.352	4.898E−03	19.6	-0.974	0.242
46.27	49.48	2.503	2.054E−03	84.1	0.774	1.524

Table F.5: v) $^{16}O(\vec{p},p')2_5^-$ (13.98 MeV); E_P = 200 MeV

θ_L	$\theta_{c.m.}$	$q_{c.m.}$	$\sigma_{c.m.}(q)$	$\Delta\sigma(\%)$	A_y	ΔA_y
-5.86	6.32	0.351	1.136E−01	22.0	-0.327	0.274
7.64	8.23	0.446	4.789E−02	36.5	0.736	0.425
9.14	9.85	0.527	2.562E−02	71.5	-1.137	1.233
12.14	13.08	0.691	1.032E−01	18.4	0.429	0.179
13.64	14.69	0.773	4.704E−02	49.1	0.997	0.429
15.14	16.30	0.855	8.410E−02	38.6	1.041	0.211
16.64	17.92	0.938	1.288E−01	20.1	0.844	0.259
18.14	19.53	1.020	1.209E−01	29.3	0.844	0.220
18.27	19.67	1.028	8.484E−02	28.9	1.058	0.216
19.64	21.14	1.102	1.530E−01	41.1	0.705	0.340
19.77	21.28	1.110	5.875E−02	98.8	0.896	0.197
21.27	22.89	1.191	9.139E−02	20.9	1.012	0.212
23.77	25.57	1.327	5.379E−02	32.6	0.217	0.245
25.27	27.17	1.408	4.191E−02	39.2	-0.208	0.303
26.77	28.78	1.489	2.684E−02	45.6	-0.604	0.739
28.27	30.38	1.570	3.949E−02	108.1	0.047	0.165
31.27	33.58	1.730	3.533E−02	13.8	-0.445	0.197
36.52	39.17	2.006	1.345E−02	73.9	1.326	1.345

Table F.5: w) $^{16}O(\vec{p},\vec{p}')0_4^+$ (14.032 MeV); E_P = 200 MeV

θ_L	$\theta_{c.m.}$	$q_{c.m.}$	$\sigma_{c.m.}(q)$	$\Delta\sigma(\%)$	A_y	ΔA_y
7.64	8.23	0.447	2.095E−02	57.2	-0.321	0.713
12.14	13.08	0.691	2.148E−02	83.2	1.277	0.627
13.64	14.69	0.773	3.162E−02	53.8	1.263	0.484
18.27	19.67	1.028	1.200E−02	71.9	0.792	0.614
19.77	21.28	1.109	1.579E−02	56.0	0.516	0.559
23.77	25.57	1.327	8.073E−03	34.7	-0.138	0.321
25.27	27.17	1.408	9.165E−03	56.0	0.120	0.333
26.77	28.78	1.489	5.782E−03	41.3	-0.459	0.609
27.52	29.58	1.529	4.290E−03	94.9	-0.753	1.528
28.27	30.38	1.569	1.102E−02	21.7	0.059	0.157
31.27	33.58	1.729	1.674E−02	8.6	0.171	0.201
33.52	35.98	1.848	1.018E−02	19.9	0.279	0.268
34.27	36.78	1.888	5.571E−03	35.8	0.046	0.477
36.52	39.17	2.005	7.082E−03	33.7	-0.508	0.474
37.27	39.97	2.044	7.716E−03	11.0	-0.144	0.142
40.27	43.15	2.199	4.786E−03	12.2	-0.323	0.225
43.27	46.32	2.351	1.848E−03	17.6	0.042	0.445
49.27	52.64	2.650	3.751E−04	80.7	0.345	1.263

Table F.5: x) $^{16}O(\vec{p},p')4_1^-$ (14.302 MeV); E_P = 200 MeV

θ_L	$\theta_{c.m.}$	$q_{c.m.}$	$\sigma_{c.m.}(q)$	$\Delta\sigma(\%)$	A_y	ΔA_y
7.64	8.23	0.447	4.244E−03	89.0	0.721	1.040
12.14	13.08	0.691	4.478E−03	93.4	-1.307	1.626
15.14	16.31	0.855	1.999E−02	68.9	0.804	0.236
16.64	17.92	0.938	2.446E−02	56.1	0.324	0.542
18.14	19.53	1.020	5.542E−02	58.9	1.172	0.354
18.27	19.67	1.027	4.945E−03	100.2	1.326	0.950
19.64	21.14	1.101	2.236E−02	54.0	0.708	0.455
28.27	30.38	1.569	5.590E−03	27.6	0.436	0.339
31.27	33.59	1.729	1.009E−02	47.4	0.264	0.142
33.52	35.98	1.848	5.116E−03	37.5	-0.336	0.509
34.27	36.78	1.887	1.356E−02	13.2	-0.186	0.177
36.52	39.17	2.005	1.222E−02	21.2	0.375	0.296
37.27	39.97	2.044	5.950E−03	16.2	-0.463	0.277
39.52	42.36	2.160	4.119E−03	44.7	-0.585	0.620
40.27	43.15	2.199	4.200E−03	15.1	-0.631	0.204
43.27	46.32	2.351	2.410E−03	15.4	-0.287	0.366
49.27	52.64	2.650	1.283E−03	29.8	-1.046	0.344

Table F.5: y) $^{16}O(\vec{p},p')5_1^+$ (14.399 MeV); E_P = 200 MeV

F.4 $^{40}\mathrm{Ca}(\vec{p}, p')$ at $\mathrm{E_P} = 200$ MeV

θ_L	$\theta_{c.m.}$	$q_{c.m.}$	$\sigma_{c.m.}(q)$	$\Delta\sigma(\%)$	A_y	ΔA_y
-7.36	7.58	0.421	1.778E+03	0.6	0.561	0.007
10.64	10.96	0.608	4.613E+02	0.7	0.834	0.007
13.64	14.05	0.778	7.187E+01	0.7	0.905	0.008
15.14	15.60	0.863	2.278E+01	1.4	0.604	0.021
16.64	17.14	0.948	1.446E+01	0.7	-0.219	0.008
18.14	18.68	1.033	1.482E+01	0.5	-0.145	0.020
18.27	18.82	1.041	1.544E+01	0.7	-0.030	0.009
19.64	20.23	1.117	1.716E+01	0.5	0.293	0.006
19.77	20.36	1.125	1.787E+01	0.6	0.356	0.007
21.14	21.77	1.202	1.647E+01	0.7	0.633	0.007
21.27	21.90	1.209	1.638E+01	0.6	0.677	0.007
23.77	24.47	1.349	1.056E+01	0.7	0.950	0.008
25.14	25.88	1.425	7.244E+00	1.0	0.963	0.010
25.27	26.02	1.433	6.828E+00	0.7	0.924	0.008
26.74	27.53	1.513	4.337E+00	0.8	0.794	0.009
26.77	27.56	1.516	4.276E+00	0.9	0.753	0.010
28.27	29.10	1.599	2.418E+00	1.1	0.444	0.014
29.77	30.64	1.682	1.367E+00	0.9	0.002	0.012
31.27	32.18	1.764	9.446E−01	0.4	-0.261	0.006
34.27	35.25	1.927	5.306E−01	0.4	0.273	0.006
37.27	38.33	2.089	3.927E−01	0.5	0.866	0.006
40.27	41.40	2.250	2.698E−01	1.7	0.819	0.018
41.74	42.90	2.326	1.813E−01	1.0	0.611	0.011
43.27	44.47	2.408	1.330E−01	0.6	0.445	0.007
45.74	46.99	2.535	5.413E−02	1.4	-0.023	0.018
46.27	47.53	2.565	4.259E−02	0.7	-0.109	0.010
49.27	50.59	2.720	1.525E−02	1.0	-0.188	0.013
52.27	53.65	2.872	1.146E−02	1.0	0.635	0.011
55.27	56.70	3.023	1.014E−02	0.7	0.844	0.008

Table F.6: a) $^{40}\mathrm{Ca}(\vec{p},p)0_1^+$; $\mathrm{E_P}$ = 200 MeV

θ_L	$\theta_{c.m.}$	$q_{c.m.}$	$\sigma_{c.m.}(q)$	$\Delta\sigma(\%)$	A_y	ΔA_y
-5.86	6.04	0.335	2.060E−02	31.9	0.774	0.441
7.64	7.87	0.436	2.393E−02	32.1	0.445	0.431
9.14	9.42	0.521	3.833E−02	14.8	1.267	0.129
10.64	10.96	0.606	3.973E−02	18.3	1.160	0.271
12.14	12.51	0.690	2.758E−02	18.8	0.962	0.153
13.64	14.05	0.775	1.905E−02	14.7	0.763	0.122
15.14	15.60	0.860	1.518E−02	10.7	0.100	0.119
16.64	17.14	0.944	1.344E−02	12.2	-0.127	0.253
18.14	18.69	1.029	2.127E−02	19.2	0.249	0.088
18.27	18.82	1.036	1.350E−02	13.7	-0.371	0.281
19.64	20.23	1.113	1.413E−02	20.4	-0.170	0.244
19.77	20.36	1.120	1.640E−02	10.4	0.061	0.337
21.14	21.77	1.196	1.345E−02	25.3	0.614	0.244
21.27	21.91	1.204	1.500E−02	40.0	0.396	0.212
23.77	24.48	1.343	8.191E−03	20.7	0.959	0.239
25.14	25.89	1.419	8.945E−03	25.9	0.811	0.241
25.27	26.02	1.427	9.413E−03	19.4	0.849	0.327
26.74	27.53	1.507	3.591E−03	30.0	0.642	0.356
26.77	27.56	1.509	4.741E−03	29.0	0.779	0.231
28.27	29.10	1.592	3.565E−03	12.2	0.113	0.162
29.77	30.64	1.674	4.869E−03	11.3	-0.365	0.305
31.27	32.18	1.756	2.809E−03	9.4	-0.372	0.126
34.27	35.26	1.919	1.809E−03	9.1	-0.125	0.123
37.27	38.33	2.080	2.022E−03	7.0	0.740	0.082
40.27	41.40	2.240	8.050E−04	15.7	1.174	0.224
41.74	42.91	2.316	1.189E−03	12.5	0.467	0.150
43.27	44.47	2.398	6.190E−04	9.4	0.641	0.122
45.74	47.00	2.524	5.009E−04	15.0	-0.129	0.195
46.27	47.54	2.554	3.972E−04	8.6	-0.075	0.115
49.27	50.60	2.708	1.261E−04	13.8	0.023	0.187
52.27	53.66	2.859	1.143E−04	11.0	0.660	0.133
55.27	56.71	3.009	1.110E−04	7.2	0.842	0.077

Table F.6: b) ^{40}Ca$(\vec{p},p')0_2^+$ (3.3521 MeV); E_P = 200 MeV

θ_L	$\theta_{c.m.}$	$q_{c.m.}$	$\sigma_{c.m.}(q)$	$\Delta\sigma(\%)$	A_y	ΔA_y
-5.86	6.04	0.335	2.448E−01	10.0	0.043	0.047
7.64	7.87	0.436	9.541E−01	3.6	0.369	0.027
9.14	9.42	0.521	2.343E+00	3.7	0.475	0.013
10.64	10.96	0.605	3.845E+00	1.2	0.578	0.025
12.14	12.51	0.690	5.654E+00	1.0	0.629	0.010
13.64	14.05	0.775	7.073E+00	6.7	0.698	0.045
15.14	15.60	0.859	8.120E+00	2.5	0.814	0.015
16.64	17.14	0.944	8.623E+00	1.7	0.891	0.024
18.14	18.69	1.028	7.725E+00	0.9	0.904	0.046
18.27	18.82	1.036	7.735E+00	0.8	0.949	0.010
19.64	20.23	1.112	6.743E+00	3.7	0.948	0.025
19.77	20.36	1.120	6.547E+00	0.8	0.939	0.005
21.14	21.77	1.196	5.437E+00	1.2	0.901	0.011
21.27	21.91	1.204	5.172E+00	0.8	0.861	0.005
23.77	24.48	1.343	3.116E+00	1.3	0.452	0.006
25.14	25.89	1.418	2.157E+00	1.5	0.133	0.018
25.27	26.02	1.426	2.174E+00	2.3	0.096	0.028
26.74	27.53	1.506	1.469E+00	1.2	-0.270	0.015
26.77	27.56	1.509	1.501E+00	1.7	-0.316	0.022
28.27	29.10	1.591	1.010E+00	1.9	-0.614	0.009
29.77	30.64	1.673	6.599E−01	0.8	-0.681	0.011
31.27	32.18	1.755	4.939E−01	0.6	-0.406	0.008
34.27	35.26	1.918	3.469E−01	0.6	0.556	0.007
37.27	38.33	2.079	2.776E−01	0.6	0.735	0.007
40.27	41.41	2.239	2.012E−01	0.7	0.312	0.024
41.74	42.91	2.314	1.430E−01	1.1	-0.008	0.014
43.27	44.47	2.396	1.093E−01	0.6	-0.295	0.008
45.74	47.00	2.523	5.169E−02	1.5	-0.776	0.016
46.27	47.54	2.552	4.805E−02	0.8	-0.829	0.009
49.27	50.60	2.706	2.549E−02	0.8	-0.483	0.010
52.27	53.66	2.858	1.808E−02	0.7	0.278	0.010
55.27	56.71	3.007	1.225E−02	0.7	0.622	0.008

Table F.6: c) ^{40}Ca$(\vec{p},p')3_1^-$ (3.7364 MeV); E_P = 200 MeV

θ_L	$\theta_{c.m.}$	$q_{c.m.}$	$\sigma_{c.m.}(q)$	$\Delta\sigma(\%)$	A_y	ΔA_y
-5.86	6.04	0.335	3.409E−01	3.1	0.547	0.123
7.64	7.87	0.436	1.088E+00	2.1	0.520	0.028
9.14	9.42	0.521	1.588E+00	2.3	0.616	0.018
10.64	10.96	0.605	1.870E+00	1.5	0.748	0.014
12.14	12.51	0.690	2.206E+00	1.5	0.749	0.015
13.64	14.05	0.775	1.637E+00	5.7	0.859	0.056
15.14	15.60	0.859	1.325E+00	5.7	0.951	0.010
16.64	17.14	0.943	1.018E+00	1.3	0.970	0.015
18.14	18.69	1.028	5.566E−01	2.3	0.824	0.061
18.27	18.82	1.036	5.026E−01	11.1	0.755	0.033
19.64	20.23	1.112	2.934E−01	12.6	0.463	0.048
19.77	20.36	1.120	3.084E−01	8.8	0.472	0.022
21.14	21.77	1.196	1.580E−01	8.0	-0.346	0.108
21.27	21.91	1.203	1.528E−01	4.0	-0.387	0.092
23.77	24.48	1.342	1.481E−01	8.4	0.013	0.090
25.14	25.89	1.418	1.380E−01	6.5	0.032	0.079
25.27	26.02	1.426	1.090E−01	2.7	0.119	0.103
26.74	27.53	1.506	1.059E−01	5.7	0.589	0.073
26.77	27.56	1.508	1.105E−01	2.3	0.653	0.051
28.27	29.10	1.591	8.762E−02	3.8	0.892	0.039
29.77	30.64	1.673	7.171E−02	2.7	0.951	0.032
31.27	32.18	1.755	6.148E−02	1.9	0.832	0.023
34.27	35.26	1.918	2.929E−02	2.2	0.323	0.028
37.27	38.33	2.079	1.134E−02	3.2	-0.205	0.045
40.27	41.41	2.238	5.727E−03	20.9	0.006	0.088
41.74	42.91	2.314	3.611E−03	9.7	0.702	0.122
43.27	44.47	2.396	3.370E−03	5.0	1.088	0.071
45.74	47.00	2.522	3.621E−03	6.6	0.900	0.089
46.27	47.54	2.552	2.991E−03	3.5	0.983	0.049
49.27	50.60	2.706	1.647E−03	3.8	0.664	0.052
52.27	53.66	2.857	7.022E−04	4.7	0.229	0.063
55.27	56.71	3.007	2.031E−04	9.1	0.375	0.113

Table F.6: d) ^{40}Ca$(\vec{p},p')2^+_1$ (2.9041 MeV); E_P = 200 MeV

θ_L	$\theta_{c.m.}$	$q_{c.m.}$	$\sigma_{c.m.}(q)$	$\Delta\sigma(\%)$	A_y	ΔA_y
-5.86	6.04	0.335	1.500E−02	50.5	0.034	0.613
7.64	7.87	0.436	1.284E−02	29.4	-0.230	0.345
9.14	9.42	0.520	9.365E−03	48.2	0.055	0.540
10.64	10.97	0.605	1.915E−02	27.3	-0.414	0.372
12.14	12.51	0.690	3.646E−02	14.7	0.103	0.163
13.64	14.06	0.774	9.058E−02	14.2	0.432	0.072
15.14	15.60	0.859	1.634E−01	2.7	0.535	0.027
16.64	17.14	0.943	2.971E−01	2.0	0.640	0.019
18.14	18.69	1.027	4.350E−01	5.8	0.658	0.017
18.27	18.82	1.035	4.877E−01	2.3	0.704	0.036
19.64	20.23	1.111	5.897E−01	2.6	0.777	0.075
19.77	20.37	1.119	6.734E−01	4.3	0.782	0.011
21.14	21.77	1.195	7.566E−01	2.9	0.854	0.024
21.27	21.91	1.203	8.192E−01	1.0	0.836	0.011
23.77	24.48	1.342	1.080E+00	0.8	0.827	0.008
25.14	25.89	1.417	1.139E+00	2.1	0.801	0.019
25.27	26.02	1.425	1.157E+00	0.9	0.784	0.018
26.74	27.53	1.504	1.112E+00	1.4	0.711	0.015
26.77	27.56	1.507	1.204E+00	0.6	0.709	0.011
28.27	29.10	1.590	1.188E+00	0.6	0.610	0.007
29.77	30.64	1.672	1.101E+00	1.4	0.470	0.008
31.27	32.18	1.754	1.039E+00	0.4	0.301	0.006
34.27	35.26	1.916	7.838E−01	0.4	-0.016	0.005
37.27	38.34	2.077	4.871E−01	0.4	-0.333	0.005
40.27	41.41	2.236	2.622E−01	0.7	-0.626	0.022
41.74	42.91	2.312	1.728E−01	1.0	-0.714	0.012
43.27	44.48	2.394	1.246E−01	0.6	-0.825	0.008
45.74	47.00	2.520	5.835E−02	1.4	-0.804	0.015
46.27	47.54	2.550	5.293E−02	0.7	-0.833	0.008
49.27	50.60	2.703	2.430E−02	0.8	-0.511	0.010
52.27	53.66	2.855	1.147E−02	0.9	-0.030	0.012
55.27	56.71	3.004	5.621E−03	0.9	0.195	0.012

Table F.6: e) ^{40}Ca$(\vec{p},p')5_1^-$ (4.4915 MeV); E_P = 200 MeV

θ_L	$\theta_{c.m.}$	$q_{c.m.}$	$\sigma_{c.m.}(q)$	$\Delta\sigma(\%)$	A_y	ΔA_y
7.64	7.87	0.436	2.143E−02	102.9	1.313	1.265
10.64	10.97	0.605	1.146E−02	110.8	-0.780	1.802
13.64	14.06	0.774	1.004E−02	57.1	-0.620	0.813
19.77	20.37	1.118	1.324E−03	79.8	1.075	0.721
28.27	29.10	1.588	8.662E−04	48.6	-0.489	0.686
31.27	32.18	1.752	3.574E−04	71.4	0.430	0.911
46.27	47.54	2.547	7.559E−05	42.9	-0.615	0.535

Table F.6: f) ^{40}Ca$(\vec{p},p')0_3^+$ (5.213 MeV); E_P = 200 MeV

θ_L	$\theta_{c.m.}$	$q_{c.m.}$	$\sigma_{c.m.}(q)$	$\Delta\sigma(\%)$	A_y	ΔA_y
7.64	7.87	0.436	4.219E−02	27.6	0.521	0.333
9.14	9.42	0.521	1.173E−01	15.2	0.550	0.149
10.64	10.97	0.605	9.885E−02	77.3	0.848	0.308
12.14	12.51	0.689	1.333E−01	9.1	0.712	0.085
13.64	14.06	0.774	1.256E−01	11.1	0.898	0.094
15.14	15.60	0.858	1.190E−01	6.6	0.911	0.052
16.64	17.14	0.942	8.308E−02	8.1	0.932	0.063
18.27	18.82	1.034	5.597E−02	10.2	0.956	0.086
21.27	21.91	1.202	2.610E−02	9.4	0.412	0.107
23.77	24.48	1.340	1.666E−02	10.3	-0.393	0.147
25.27	26.02	1.423	1.531E−02	10.7	-0.177	0.147
26.77	27.56	1.506	1.426E−02	9.8	-0.191	0.132
28.27	29.10	1.588	1.066E−02	10.5	0.035	0.142
29.77	30.65	1.670	1.103E−02	13.7	0.458	0.205
31.27	32.18	1.752	9.883E−03	7.1	0.538	0.092
34.27	35.26	1.914	6.610E−03	7.4	0.695	0.087
37.27	38.34	2.075	4.776E−03	8.4	0.180	0.112
40.27	41.41	2.234	2.046E−03	19.7	0.065	0.267
41.74	42.91	2.310	1.152E−03	25.3	-0.615	0.335
43.27	44.48	2.392	1.006E−03	14.9	-0.749	0.184
46.27	47.54	2.547	5.001E−04	16.6	-0.240	0.212
49.27	50.60	2.701	4.971E−04	10.8	0.504	0.155
52.27	53.66	2.852	2.346E−04	18.2	0.998	0.227
55.27	56.72	3.001	1.297E−04	18.4	0.834	0.184

Table F.6: g) $^{40}\mathrm{Ca}(\vec{p},p')2_2^+$ (5.249 MeV); $\mathrm{E_P}$ = 200 MeV

θ_L	$\theta_{c.m.}$	$q_{c.m.}$	$\sigma_{c.m.}(q)$	$\Delta\sigma(\%)$	A_y	ΔA_y
7.64	7.87	0.436	1.126E−02	110.5	1.342	1.436
10.64	10.97	0.605	5.148E−02	45.1	-0.339	0.603
12.14	12.51	0.689	3.066E−02	34.2	0.184	0.363
13.64	14.06	0.774	3.564E−02	34.8	0.467	0.310
15.14	15.60	0.858	6.255E−02	11.1	0.799	0.088
16.64	17.14	0.942	6.495E−02	9.8	0.919	0.075
18.27	18.82	1.034	6.803E−02	8.8	0.967	0.075
21.27	21.91	1.202	6.323E−02	4.7	0.881	0.044
23.77	24.48	1.340	3.774E−02	5.3	0.475	0.068
25.27	26.02	1.423	2.991E−02	6.3	0.145	0.082
26.77	27.56	1.506	1.894E−02	7.5	-0.142	0.101
28.27	29.10	1.588	1.245E−02	8.9	-0.652	0.121
29.77	30.65	1.670	8.744E−03	13.7	-0.953	0.203
31.27	32.19	1.752	4.771E−03	12.4	-0.536	0.181
34.27	35.26	1.914	3.954E−03	10.7	0.650	0.126
37.27	38.34	2.075	4.338E−03	7.9	0.871	0.100
40.27	41.41	2.234	3.512E−03	11.0	0.023	0.148
41.74	42.91	2.310	2.885E−03	11.1	0.098	0.146
43.27	44.48	2.392	2.209E−03	6.9	-0.249	0.089
46.27	47.54	2.547	1.067E−03	7.8	-0.740	0.094
49.27	50.60	2.701	4.064E−04	12.9	-0.926	0.185
52.27	53.66	2.852	3.126E−04	11.7	0.130	0.152
55.27	56.72	3.001	2.126E−04	10.1	0.613	0.109

Table F.6: h) ^{40}Ca$(\vec{p},p')4_1^+$ (5.279 MeV); E_P = 200 MeV

θ_L	$\theta_{c.m.}$	$q_{c.m.}$	$\sigma_{c.m.}(q)$	$\Delta\sigma(\%)$	A_y	ΔA_y
-5.86	6.04	0.336	3.515E−02	81.6	0.440	0.892
7.64	7.87	0.436	3.904E−02	107.4	-1.363	1.950
12.14	12.51	0.689	1.840E−02	109.0	1.253	1.047
15.14	15.60	0.858	2.519E−02	34.6	0.147	0.362
16.64	17.15	0.942	1.660E−02	42.5	0.564	0.378
19.77	20.37	1.118	2.134E−02	13.7	0.366	0.171
21.27	21.91	1.201	1.176E−02	19.2	-0.032	0.259
23.77	24.48	1.340	1.626E−02	13.0	-0.286	0.177
25.27	26.02	1.423	1.377E−02	15.7	-0.467	0.228
26.77	27.56	1.505	1.105E−02	16.1	-0.751	0.228
28.27	29.11	1.588	1.692E−02	10.3	-0.201	0.140
29.77	30.65	1.670	1.339E−02	15.1	-0.222	0.201
31.27	32.19	1.751	1.058E−02	11.3	-0.424	0.146
34.27	35.26	1.913	1.098E−02	7.9	-0.466	0.098
37.27	38.34	2.074	8.420E−03	7.4	-0.388	0.095
40.27	41.41	2.233	1.809E−03	25.9	0.089	0.346
41.74	42.91	2.309	1.394E−03	29.1	-0.595	0.394
43.27	44.48	2.391	8.809E−04	21.2	-0.232	0.295
46.27	47.54	2.546	6.270E−04	17.2	0.187	0.223
49.27	50.61	2.699	2.285E−04	25.7	0.638	0.333
52.27	53.66	2.851	3.795E−05	79.6	-0.237	1.098
55.27	56.72	3.000	2.295E−05	63.1	-1.362	1.288

Table F.6: i) $^{40}\mathrm{Ca}(\vec{p},p')4_1^-$ (5.6143 MeV); $\mathrm{E_P}$ = 200 MeV

θ_L	$\theta_{c.m.}$	$q_{c.m.}$	$\sigma_{c.m.}(q)$	$\Delta\sigma(\%)$	A_y	ΔA_y
-5.86	6.04	0.336	4.833E−02	42.5	0.855	0.486
7.64	7.87	0.436	9.339E−02	39.7	0.577	0.370
9.14	9.42	0.521	1.536E−01	25.6	0.406	0.259
10.64	10.97	0.605	2.095E−01	25.4	0.252	0.254
12.14	12.51	0.689	1.766E−01	11.7	0.671	0.104
13.64	14.06	0.774	1.655E−01	12.4	0.796	0.112
15.14	15.60	0.858	9.147E−02	9.9	1.085	0.082
16.64	17.15	0.942	7.520E−02	10.0	0.912	0.084
18.14	18.69	1.026	5.925E−02	6.5	0.752	0.080
18.27	18.82	1.034	5.405E−02	10.0	0.702	0.112
19.77	20.37	1.118	1.265E−02	22.4	0.042	0.296
21.27	21.91	1.201	1.731E−02	13.5	-0.401	0.194
23.77	24.48	1.340	8.469E−03	23.8	-0.748	0.357
25.27	26.02	1.423	1.152E−02	18.6	0.217	0.248
26.77	27.56	1.505	1.275E−02	14.2	0.396	0.202
28.27	29.11	1.588	4.518E−03	35.0	1.023	0.565
29.77	30.65	1.670	7.325E−03	26.7	0.206	0.372
31.27	32.19	1.751	7.054E−03	16.7	0.461	0.255
34.27	35.26	1.913	1.046E−03	78.1	1.154	1.638
40.27	41.41	2.233	1.172E−03	39.8	-0.107	0.542
41.74	42.91	2.309	1.120E−03	36.3	0.558	0.520
43.27	44.48	2.391	7.465E−04	24.8	0.812	0.349
46.27	47.54	2.546	2.276E−04	45.6	1.299	0.681
49.27	50.61	2.699	1.908E−04	30.5	0.447	0.391
52.27	53.66	2.851	8.388E−05	36.3	0.107	0.487
55.27	56.72	3.000	3.559E−05	40.6	1.323	0.667

Table F.6: j) ^{40}Ca$(\vec{p},p')2^+_3$ (5.6301 MeV); E_P = 200 MeV

θ_L	$\theta_{c.m.}$	$q_{c.m.}$	$\sigma_{c.m.}(q)$	$\Delta\sigma(\%)$	A_y	ΔA_y
-5.86	6.04	0.336	2.640E−02	29.1	-0.034	0.358
7.64	7.87	0.436	1.837E−02	35.3	0.491	0.197
9.14	9.42	0.521	2.619E−02	20.0	0.269	0.212
10.64	10.97	0.605	3.454E−02	19.0	0.567	0.166
12.14	12.51	0.689	4.755E−02	12.0	0.664	0.109
13.64	14.06	0.774	8.926E−02	5.9	0.857	0.048
15.14	15.60	0.858	1.137E−01	3.4	0.888	0.027
16.64	17.15	0.942	1.345E−01	3.4	0.951	0.025
18.14	18.69	1.026	1.182E−01	3.8	0.802	0.032
18.27	18.82	1.034	1.171E−01	4.9	0.885	0.051
19.77	20.37	1.117	1.141E−01	2.7	0.649	0.029
21.27	21.91	1.201	8.077E−02	3.1	0.381	0.038
23.77	24.48	1.339	3.986E−02	3.9	-0.340	0.053
25.27	26.02	1.422	2.853E−02	4.5	-0.806	0.053
26.77	27.57	1.505	2.198E−02	4.9	-0.744	0.060
28.27	29.11	1.587	1.773E−02	5.3	-0.134	0.072
29.77	30.65	1.669	1.764E−02	6.2	0.622	0.074
31.27	32.19	1.751	1.880E−02	3.3	0.803	0.036
34.27	35.26	1.913	1.859E−02	2.4	0.637	0.028
37.27	38.34	2.073	1.290E−02	2.3	0.035	0.031
40.27	41.41	2.232	7.403E−03	4.3	-0.518	0.054
41.74	42.91	2.308	4.773E−03	6.0	-0.699	0.069
43.27	44.48	2.390	3.333E−03	3.7	-0.961	0.037
46.27	47.54	2.545	1.868E−03	3.6	-0.254	0.048
49.27	50.61	2.698	1.265E−03	3.7	0.519	0.046
52.27	53.66	2.850	7.625E−04	3.8	0.680	0.044
55.27	56.72	2.999	2.456E−04	4.7	0.597	0.056

Table F.6: k) $^{40}\mathrm{Ca}(\vec{p},p')1_1^-$ (5.9033 MeV); $\mathrm{E_P}$ = 200 MeV

θ_L	$\theta_{c.m.}$	$q_{c.m.}$	$\sigma_{c.m.}(q)$	$\Delta\sigma(\%)$	A_y	ΔA_y
-5.86	6.04	0.337	2.262E−02	33.4	0.022	0.407
7.64	7.87	0.436	1.147E−02	27.8	0.180	0.397
9.14	9.42	0.521	2.305E−02	22.5	0.018	0.257
10.64	10.97	0.605	2.458E−02	24.6	0.570	0.194
12.14	12.51	0.689	2.548E−02	19.0	0.068	0.211
13.64	14.06	0.773	1.707E−02	18.7	-0.266	0.231
15.14	15.60	0.858	1.769E−02	10.6	-0.093	0.122
16.64	17.15	0.942	1.539E−02	13.2	-0.316	0.164
18.14	18.69	1.025	1.513E−02	13.3	-0.218	0.157
18.27	18.82	1.033	2.102E−02	12.7	-0.240	0.175
19.77	20.37	1.117	2.359E−02	6.6	-0.094	0.090
21.27	21.91	1.201	1.560E−02	7.9	-0.355	0.114
23.77	24.48	1.339	1.090E−02	8.1	-0.628	0.113
25.27	26.02	1.422	8.098E−03	9.6	-0.456	0.126
26.77	27.57	1.505	6.029E−03	10.6	-0.683	0.138
28.27	29.11	1.587	3.522E−03	14.1	-0.349	0.191
29.77	30.65	1.669	3.579E−03	16.2	-0.130	0.218
31.27	32.19	1.750	2.700E−03	10.7	0.069	0.143
34.27	35.26	1.912	1.312E−03	13.2	0.175	0.173
37.27	38.34	2.073	2.915E−04	34.6	0.469	0.458
40.27	41.41	2.232	1.545E−04	72.3	0.116	0.987
41.74	42.91	2.307	4.359E−04	25.4	-0.147	0.327
43.27	44.48	2.389	2.019E−04	23.1	0.608	0.358
46.27	47.54	2.545	1.040E−04	21.9	0.508	0.329
49.27	50.61	2.698	8.403E−05	21.2	0.751	0.285
52.27	53.66	2.849	5.007E−05	22.3	0.616	0.286
55.27	56.72	2.998	1.118E−05	41.1	0.602	0.513

Table F.6: 1) ^{40}Ca$(\vec{p},p')$6.028 (6.028 MeV); E_P = 200 MeV

θ_L	$\theta_{c.m.}$	$q_{c.m.}$	$\sigma_{c.m.}(q)$	$\Delta\sigma(\%)$	A_y	ΔA_y
-5.86	6.04	0.337	3.589E−02	22.1	0.310	0.261
7.64	7.87	0.436	1.059E−01	6.0	0.364	0.048
9.14	9.42	0.521	2.100E−01	4.4	0.420	0.046
10.64	10.97	0.605	4.440E−01	4.9	0.429	0.032
12.14	12.51	0.689	5.199E−01	2.9	0.550	0.029
13.64	14.06	0.773	5.824E−01	2.4	0.716	0.022
15.14	15.60	0.857	5.652E−01	1.5	0.820	0.013
16.64	17.15	0.941	5.154E−01	1.7	0.886	0.014
18.27	18.82	1.033	3.401E−01	3.0	0.930	0.036
19.77	20.37	1.117	2.222E−01	1.9	0.765	0.019
21.27	21.91	1.200	1.360E−01	2.3	0.380	0.028
23.77	24.48	1.339	7.529E−02	2.8	-0.463	0.037
25.27	26.02	1.422	9.187E−02	2.4	-0.008	0.033
26.77	27.57	1.504	1.226E−01	2.0	0.478	0.025
28.27	29.11	1.586	1.612E−01	1.7	0.762	0.019
29.77	30.65	1.668	1.881E−01	1.8	0.804	0.019
31.27	32.19	1.750	2.057E−01	1.0	0.713	0.011
34.27	35.26	1.912	1.901E−01	0.7	0.417	0.009
37.27	38.34	2.072	1.281E−01	0.7	-0.029	0.009
40.27	41.41	2.231	6.945E−02	1.3	-0.499	0.017
41.74	42.92	2.307	4.471E−02	1.9	-0.676	0.022
43.27	44.48	2.388	3.099E−02	1.2	-0.877	0.013
46.27	47.55	2.544	1.313E−02	1.4	-0.715	0.016
49.27	50.61	2.697	7.565E−03	1.4	0.048	0.019
52.27	53.67	2.848	4.629E−03	1.5	0.476	0.018
55.27	56.72	2.997	2.249E−03	1.5	0.560	0.018

Table F.6: m) $^{40}\mathrm{Ca}(\vec{p},p')3^-_2$ (6.2858 MeV); $\mathrm{E_P}$ = 200 MeV

θ_L	$\theta_{c.m.}$	$q_{c.m.}$	$\sigma_{c.m.}(q)$	$\Delta\sigma(\%)$	A_y	ΔA_y
10.64	10.97	0.605	1.733E−02	62.8	-0.064	0.732
12.14	12.51	0.689	2.114E−02	26.5	0.190	0.282
13.64	14.06	0.773	3.562E−02	18.6	0.571	0.172
15.14	15.60	0.857	4.413E−02	8.6	0.806	0.076
16.64	17.15	0.941	6.903E−02	6.7	0.828	0.056
18.14	18.69	1.025	7.494E−02	5.7	0.824	0.054
18.27	18.82	1.033	7.932E−02	7.2	0.849	0.073
19.77	20.37	1.117	8.339E−02	4.1	0.891	0.036
21.27	21.91	1.200	8.562E−02	3.9	0.926	0.031
23.77	24.48	1.338	6.928E−02	3.8	0.769	0.040
25.27	26.02	1.421	5.835E−02	4.1	0.641	0.047
26.77	27.57	1.504	4.589E−02	4.5	0.401	0.056
28.27	29.11	1.586	3.158E−02	4.6	0.298	0.061
29.77	30.65	1.668	1.859E−02	7.3	-0.097	0.098
31.27	32.19	1.749	1.378E−02	5.2	-0.399	0.069
34.27	35.26	1.911	4.668E−03	8.5	-0.572	0.122
37.27	38.34	2.072	1.594E−03	14.3	-0.454	0.194
40.27	41.41	2.231	9.567E−04	29.0	-0.052	0.389
41.74	42.92	2.306	1.199E−03	21.5	0.431	0.305
43.27	44.48	2.388	7.056E−04	14.5	0.518	0.210
46.27	47.55	2.543	6.465E−04	8.4	0.214	0.115
49.27	50.61	2.696	3.128E−04	13.0	-0.101	0.175
52.27	53.67	2.847	1.845E−04	13.5	-0.216	0.184
55.27	56.72	2.996	2.781E−05	34.7	-0.526	0.511

Table F.6: n) $^{40}\mathrm{Ca}(\vec{p},p')4_2^+$ (6.5084 MeV); $\mathrm{E_P}$ = 200 MeV

θ_L	$\theta_{c.m.}$	$q_{c.m.}$	$\sigma_{c.m.}(q)$	$\Delta\sigma(\%)$	A_y	ΔA_y
7.64	7.88	0.437	1.711E−02	82.6	0.731	0.791
9.14	9.42	0.521	1.453E−02	101.5	1.287	1.154
12.14	12.51	0.689	3.478E−02	23.9	0.676	0.224
13.64	14.06	0.773	1.655E−02	75.3	0.779	0.648
15.14	15.60	0.857	3.206E−02	22.1	0.498	0.201
16.64	17.15	0.941	6.132E−03	97.1	1.272	0.831
18.27	18.82	1.033	9.492E−03	50.1	0.627	0.509
19.77	20.37	1.117	9.745E−03	33.0	1.284	0.310
21.27	21.91	1.200	9.061E−03	33.1	1.226	0.298
23.77	24.48	1.338	2.346E−03	88.8	1.112	1.097
25.27	26.02	1.421	2.211E−03	95.2	-0.241	1.386
31.27	32.19	1.749	1.005E−03	82.9	1.274	1.329
40.27	41.41	2.231	1.024E−03	53.9	1.307	1.103
43.27	44.48	2.388	6.571E−04	27.3	0.627	0.455
49.27	50.61	2.696	1.718E−04	42.6	0.217	0.568
52.27	53.67	2.847	4.871E−05	96.5	-0.912	1.701
55.27	56.72	2.996	6.821E−05	34.5	-0.300	0.493

Table F.6: o) $^{40}\mathrm{Ca}(\vec{p},p')4_3^+$ (6.5436 MeV); $\mathrm{E_P}$ = 200 MeV

θ_L	$\theta_{c.m.}$	$q_{c.m.}$	$\sigma_{c.m.}(q)$	$\Delta\sigma(\%)$	A_y	ΔA_y
-5.86	6.04	0.337	2.135E−02	39.6	0.568	0.703
7.64	7.88	0.437	6.047E−02	10.0	0.356	0.110
9.14	9.42	0.521	1.515E−01	8.2	0.477	0.084
10.64	10.97	0.605	2.440E−01	6.4	0.515	0.060
12.14	12.51	0.689	2.854E−01	4.3	0.664	0.041
13.64	14.06	0.773	3.526E−01	3.9	0.749	0.034
15.14	15.60	0.857	3.201E−01	2.6	0.886	0.022
16.64	17.15	0.941	2.942E−01	2.6	0.889	0.021
18.27	18.82	1.033	2.082E−01	3.9	0.933	0.042
19.77	20.37	1.117	1.307E−01	2.9	0.724	0.029
21.27	21.91	1.200	8.088E−02	3.6	0.379	0.042
23.77	24.48	1.338	4.492E−02	4.3	-0.479	0.061
25.27	26.02	1.421	4.413E−02	4.3	-0.037	0.058
26.77	27.57	1.504	6.163E−02	3.3	0.526	0.041
28.27	29.11	1.586	7.943E−02	2.6	0.838	0.028
29.77	30.65	1.668	9.875E−02	2.6	0.856	0.029
31.27	32.19	1.749	9.857E−02	1.5	0.714	0.017
34.27	35.27	1.911	9.808E−02	1.1	0.324	0.015
37.27	38.34	2.072	6.537E−02	1.1	-0.180	0.015
40.27	41.41	2.230	3.525E−02	2.2	-0.667	0.028
41.74	42.92	2.306	2.451E−02	3.0	-0.799	0.032
43.27	44.48	2.388	1.538E−02	1.9	-0.958	0.021
46.27	47.55	2.543	6.377E−03	2.0	-0.612	0.024
49.27	50.61	2.696	3.101E−03	2.9	0.077	0.039
52.27	53.67	2.847	1.700E−03	3.2	0.472	0.041
55.27	56.72	2.996	7.064E−04	3.7	0.488	0.048

Table F.6: p) ^{40}Ca$(\vec{p},p')3^-_3$ (6.5833 MeV); E_P = 200 MeV

θ_L	$\theta_{c.m.}$	$q_{c.m.}$	$\sigma_{c.m.}(q)$	$\Delta\sigma(\%)$	A_y	ΔA_y
-5.86	6.04	0.337	3.810E−02	22.2	-0.067	0.274
7.64	7.88	0.437	5.058E−02	8.1	-0.085	0.132
9.14	9.42	0.521	4.028E−02	15.9	0.080	0.179
10.64	10.97	0.605	6.466E−02	14.0	-0.187	0.165
12.14	12.51	0.689	6.025E−02	10.3	0.229	0.112
13.64	14.06	0.773	4.313E−02	9.8	0.203	0.106
15.14	15.60	0.857	4.524E−02	5.9	0.373	0.061
16.64	17.15	0.941	4.721E−02	6.4	0.404	0.065
18.14	18.69	1.025	3.049E−02	8.2	0.043	0.092
18.27	18.82	1.033	3.392E−02	9.7	0.201	0.126
19.77	20.37	1.116	2.171E−02	6.6	-0.342	0.093
21.27	21.91	1.200	1.960E−02	6.6	-0.482	0.095
23.77	24.48	1.338	1.935E−02	6.1	-0.188	0.083
25.27	26.02	1.421	1.674E−02	6.4	-0.494	0.085
26.77	27.57	1.503	1.320E−02	6.9	-0.282	0.094
28.27	29.11	1.585	9.564E−03	8.1	-0.077	0.110
29.77	30.65	1.667	6.676E−03	12.0	-0.116	0.163
31.27	32.19	1.749	5.423E−03	7.3	-0.083	0.099
34.27	35.27	1.911	1.884E−03	12.2	-0.352	0.172
37.27	38.34	2.071	2.044E−04	59.9	0.601	0.864
40.27	41.41	2.230	1.897E−04	73.1	0.492	1.117
41.74	42.92	2.305	1.266E−04	92.8	1.256	1.880
43.27	44.48	2.387	3.356E−04	18.2	0.801	0.298
46.27	47.55	2.542	2.369E−04	14.7	0.378	0.209
49.27	50.61	2.695	6.505E−05	27.7	0.735	0.396
52.27	53.67	2.847	3.745E−05	29.0	0.684	0.370
55.27	56.72	2.995	1.779E−05	29.4	0.082	0.389

Table F.6: q) ^{40}Ca$(\vec{p},p')2_2^-$ (6.7509 MeV); E_P = 200 MeV

θ_L	$\theta_{c.m.}$	$q_{c.m.}$	$\sigma_{c.m.}(q)$	$\Delta\sigma(\%)$	A_y	ΔA_y
-5.86	6.04	0.338	3.228E−01	15.1	0.544	0.168
9.14	9.42	0.521	1.294E+00	11.2	0.593	0.112
10.64	10.97	0.605	1.549E+00	15.3	1.272	0.063
12.14	12.51	0.689	1.821E+00	3.7	0.803	0.033
15.14	15.60	0.857	1.469E+00	3.3	0.931	0.026
16.64	17.15	0.941	1.261E+00	3.7	0.930	0.024
18.14	18.69	1.025	1.102E+00	2.2	0.832	0.023
18.27	18.82	1.033	9.604E−01	3.4	0.871	0.041
19.77	20.37	1.116	6.330E−01	2.4	0.682	0.026
21.27	21.91	1.200	5.130E−01	2.4	0.288	0.029
23.77	24.48	1.338	3.152E−01	2.8	-0.281	0.038
25.27	26.03	1.421	2.465E−01	3.1	-0.484	0.041
26.77	27.57	1.503	2.003E−01	3.5	-0.304	0.046
28.27	29.11	1.585	1.552E−01	3.7	-0.057	0.050
29.77	30.65	1.667	9.213E−02	5.4	0.296	0.071
31.27	32.19	1.748	7.683E−02	3.4	0.675	0.038
34.27	35.27	1.910	6.146E−02	3.5	0.730	0.040
37.27	38.34	2.071	3.485E−02	4.1	0.313	0.054
40.27	41.41	2.230	2.263E−02	5.4	0.303	0.077
41.74	42.92	2.305	1.409E−02	9.4	-0.365	0.117
43.27	44.48	2.387	9.209E−03	6.7	-0.493	0.085
46.27	47.55	2.542	4.627E−03	8.4	0.088	0.117
49.27	50.61	2.695	2.590E−03	12.5	0.739	0.191
52.27	53.67	2.846	1.472E−03	17.9	0.115	0.256
55.27	56.72	2.995	6.382E−04	11.9	0.147	0.169

Table F.6: r) ^{40}Ca$(\vec{p}, p')$6.909 (6.909 MeV); E_P = 200 MeV

θ_L	$\theta_{c.m.}$	$q_{c.m.}$	$\sigma_{c.m.}(q)$	$\Delta\sigma(\%)$	A_y	ΔA_y
7.64	7.88	0.437	5.538E−01	13.1	0.714	0.528
10.64	10.97	0.605	4.116E−01	83.3	-1.283	1.844
13.64	14.06	0.773	5.733E−01	21.0	0.880	0.148
16.64	17.15	0.941	2.652E−01	21.8	1.260	0.150
18.27	18.82	1.033	2.085E−01	17.3	0.800	0.159
19.77	20.37	1.116	1.145E−01	16.8	0.722	0.182
23.77	24.48	1.338	9.789E−02	11.2	0.062	0.151
26.77	27.57	1.503	4.915E−02	18.5	-0.324	0.245
28.27	29.11	1.585	7.211E−02	10.3	0.019	0.138
29.77	30.65	1.667	7.356E−02	10.7	0.279	0.139
31.27	32.19	1.748	3.881E−02	9.9	0.366	0.118
34.27	35.27	1.910	3.840E−02	8.3	0.135	0.107
37.27	38.34	2.071	2.864E−02	8.5	-0.196	0.116
41.74	42.92	2.305	1.124E−02	19.8	-0.512	0.219
43.27	44.48	2.387	1.085E−02	9.5	-0.665	0.099
46.27	47.55	2.542	6.863E−03	10.3	-0.851	0.119
49.27	50.61	2.695	5.496E−03	10.7	-0.277	0.138
52.27	53.67	2.846	2.532E−03	13.9	-0.206	0.203
55.27	56.72	2.995	6.818E−04	19.8	-0.315	0.293

Table F.6: s) ^{40}Ca$(\vec{p},p')$6.931 (6.931 MeV); E_P = 200 MeV

θ_L	$\theta_{c.m.}$	$q_{c.m.}$	$\sigma_{c.m.}(q)$	$\Delta\sigma(\%)$	A_y	ΔA_y
-5.86	6.04	0.338	2.087E−01	18.7	0.391	0.218
7.64	7.88	0.437	2.653E−01	79.4	0.442	0.781
9.14	9.42	0.521	6.983E−02	92.3	-0.281	1.185
12.14	12.51	0.689	3.215E−01	12.1	0.730	0.106
13.64	14.06	0.773	6.220E−01	10.3	0.802	0.085
16.64	17.15	0.941	6.207E−01	5.0	0.875	0.036
18.14	18.69	1.025	6.140E−01	3.6	0.732	0.037
18.27	18.82	1.033	6.066E−01	4.3	0.822	0.051
19.77	20.37	1.116	5.735E−01	2.5	0.631	0.028
21.27	21.91	1.199	4.735E−01	2.4	0.368	0.029
25.27	26.03	1.421	1.885E−01	3.6	-0.627	0.048
26.77	27.57	1.503	1.165E−01	5.1	-0.480	0.066
28.27	29.11	1.585	8.297E−02	6.0	0.084	0.080
29.77	30.65	1.667	9.303E−02	6.3	0.692	0.079
34.27	35.27	1.910	1.040E−01	2.8	0.649	0.034
37.27	38.34	2.071	7.896E−02	3.1	0.085	0.042
40.27	41.41	2.229	5.311E−02	3.4	-0.653	0.038
41.74	42.92	2.305	3.086E−02	7.2	-0.759	0.071
43.27	44.48	2.386	2.184E−02	5.0	-0.940	0.044
46.27	47.55	2.542	1.151E−02	7.0	-0.387	0.079
49.27	50.61	2.695	6.511E−03	11.3	0.309	0.173
52.27	53.67	2.846	4.255E−03	9.6	0.843	0.125
55.27	56.72	2.995	1.921E−03	7.7	0.582	0.108

Table F.6: t) $^{40}\mathrm{Ca}(\vec{p},p')1_2^-$ (6.951 MeV); $\mathrm{E_P}$ = 200 MeV

θ_L	$\theta_{c.m.}$	$q_{c.m.}$	$\sigma_{c.m.}(q)$	$\Delta\sigma(\%)$	A_y	ΔA_y
-5.86	6.04	0.338	1.692E−02	45.8	1.388	0.637
7.64	7.88	0.437	1.885E−02	41.0	0.299	0.785
9.14	9.42	0.521	1.170E−02	68.0	1.279	0.747
10.64	10.97	0.605	4.206E−02	29.4	-0.311	0.388
12.14	12.51	0.689	4.337E−02	13.9	0.577	0.132
15.14	15.60	0.857	4.327E−02	7.0	0.825	0.057
16.64	17.15	0.941	4.904E−02	7.1	0.971	0.052
18.14	18.69	1.024	4.656E−02	7.3	0.840	0.063
18.27	18.82	1.032	5.666E−02	7.5	0.852	0.074
19.77	20.37	1.116	6.501E−02	4.2	0.802	0.042
23.77	24.48	1.338	4.555E−02	4.0	0.626	0.049
25.27	26.03	1.420	4.724E−02	3.8	0.545	0.049
26.77	27.57	1.503	5.052E−02	3.4	0.445	0.043
28.27	29.11	1.585	4.263E−02	3.6	0.286	0.046
29.77	30.65	1.667	3.479E−02	4.6	0.122	0.061
31.27	32.19	1.748	3.085E−02	2.7	-0.140	0.036
34.27	35.27	1.910	1.737E−02	2.8	-0.355	0.039
37.27	38.34	2.070	8.560E−03	3.3	-0.422	0.044
40.27	41.41	2.229	4.201E−03	6.8	-0.327	0.090
41.74	42.92	2.304	2.946E−03	9.0	-0.266	0.113
43.27	44.48	2.386	2.013E−03	5.7	0.005	0.077
46.27	47.55	2.541	9.802E−04	6.5	0.285	0.089
49.27	50.61	2.694	4.058E−04	9.0	0.393	0.118
52.27	53.67	2.845	1.970E−04	9.5	0.063	0.127
55.27	56.72	2.994	9.229E−05	10.2	0.266	0.134

Table F.6: u) ^{40}Ca$(\vec{p},p')$7.11 (7.11 MeV); E_P = 200 MeV

References

[Ajz86/8] F. Ajzenberg-Selove, Nucl. Phys. **A460**, 1 (1986); **A490** 1 (1988).

[Amo 88] K. Amos, L. Berge, F. A. Brieva, A. Katsogiannis, L. Petris, and L. Rikus, Phys. Rev. C **37**, 934 (1988).

[Are 89] H. F. Arellano, F. A. Brieva, and W. G. Love, Phys. Rev. Lett. **63**, 605 (1989).

[Are 90a] H. F. Arellano, F. A. Brieva, and W. G. Love, Phys. Rev. C **41**, 2188 (1990).

[Are 90b] H. F. Arellano, F. A. Brieva, and W. G. Love, Phys. Rev. C **42**, 652 (1990).

[Arn 87] R. A. Arndt, L. D. Roper, R. A. Bryan, R. B. Clark, B. J. VerWest, and P. Signell, Phys. Rev. D **32**, 128 (1987); R. A. Arndt, J. S. Hyslop III, and L. D. Roper, *ibid.* **35**, 128 (1987); R. A. Arndt, and L. D. Roper, *Scattering Analysis Interactive Dial-in SAID* (Virginia Polytechnic Institute, Blacksburg, 1988).

[Bau 83] W. Bauhoff, H. V. von Geramb, and G. Pálla, Phys. Rev. C **27**, 2466 (1983).

[Ber 79] W. Bertozzi, M. V. Hynes, C. P. Sargent, W. Turchinetz, and C. Williamson, Nucl. Instr. and Meth. **162**, 211 (1979).

[Ber 86] G. P. A. Berg, L. C. Bland, B. M. Cox, D. DuPlantis, D. W. Miller, K. Murphy, P. Schwandt, K. A. Solberg, E. J. Stephenson,

B. S. Flanders, and H. Seifert, *The K600 Magnetic Spectrometer System*—IUCF Scientific and Technical Report, p. 152 (1986).

[Ber 88] G. P. A. Berg, L. C. Bland, D. DuPlantis, C. C. Foster, D. W. Miller, R. Sawafta, P. Schwandt, K. A. Solberg, and E. J. Stephenson, *The High Resolution K600 Spectrometer*—IUCF Scientific and Technical Report, p. 233 (1988).

[Ber 89] G. P. A. Berg, L. C. Bland, C. C. Foster, J. Lisantti, T. Rinckel, R. Sawafta, P. Schwandt, K. A. Solberg, and E. J. Stephenson, *The High Resolution K600 Spectrometer*—IUCF Scientific and Technical Report, p. 200 (1989).

[Bev 69] P. R. Bevington, *Data Reduction and Error Analysis for the Physical Sciences* (McGraw-Hill Book Company, Inc., New York, 1969).

[Ble 88] E. Bleszynski, B. Aas, D. Adams, M. Bleszynski, G. J. Igo, T. Jaroszewicz, A. Ling, D. Lopiano, F. Sperisen, M. G. Moshi, C. A. Whitten, Jr., K. Jones, and J. B. McClelland, Phys. Rev. C **37**, 1527 (1988).

[Bri77/8] F. A. Brieva, and J. R. Rook, Nucl. Phys. **A291**, 299 (1977); **A291**, 317 (1977); **A297**, 206 (1978); **A307**, 493 (1978).

[Bru 58] K. A. Brueckner, and J. L. Gammel, Phys. Rev. **109**, 102 (1958).

[But 86] T. N. Buti, J. J. Kelly, W. Bertozzi, J. M. Finn, F. W. Hersman, C. Hyde-Wright, M. V. Hynes, M. A. Kovash, S. Kowalski, R. W.

Lourie, B. Murdock, B. E. Norum, B. Pugh, C. P. Sargent, W. Turchinetz, and B. L. Berman, Phys. Rev. C **33**, 755 (1986).

[Cam 78] X. Campi, and A. Bouyssy, Phys. Lett. **73B**, 263 (1978).

[Car 84] J. A. Carr, F. Petrovich, and J. J. Kelly, in *Neutron-Nucleus Collisions—A Probe of Nuclear Structure (Burr Oak State Park, Glouster, Ohio, 1984)*, Proceedings of the Conference on Neutron-Nucleus Collisions—A Probe of Nuclear Structure, AIP Conf. Proc. No. 124, edited by J. Rapaport, R. W. Finlay, S. M. Grimes, and F. S. Dietrich (AIP, New York, 1985), p. 230.

[Che 85] T. Cheon, K. Takayanagi, and K. Yazaki, Nucl. Phys. **A437**, 301 (1985).

[Che 86] T. Cheon, K. Takayanagi, Nucl. Phys. **A455**, 653 (1986).

[Che 87] T. Cheon, Phys. Rev. C **35**, 2225 (1987).

[Cla 83] B. C. Clark, R. L. Mercer, and P. Schwandt, Phys. Lett. **122B**, 211 (1983); B. C. Clark, S. Hama, and R. L. Mercer, in *The Interaction Between Medium Energy Nucleons in Nuclei—1982*, AIP Conf. Proc. No. 97, edited by H. O. Meyer (AIP, New York, 1983), p. 260.

[Cle 55] E. Clementel, and C. Villi, Nuovo Cimento **2**, 176 (1955).

[Cok 90] W. R. Coker, and L. Ray, Phys. Rev. C **42**, 659 (1990).

[Cra 53] F. S. Crawford, Rev. Sci. Inst. **24**, 552 (1953).

[DeF 66] T. DeForest, and J. D. Walecka, Adv. Phys. **15**, 1 (1966).

[Dix 86] S. Dixit, Master's thesis, Massachusetts Institute of Technology, 1986.

[Dod 76] D. C. Dodder, G. M. Hale, N. Jarmie, and K. Witte, *Tables of Phase Shifts and Experimental Observables for p-^{4}He Elastic Scattering* (LA 6389-MS, UC 34d, Los Alamos Scientific Laboratory, 1976).

[Dod 77] D. C. Dodder, G. M. Hale, N. Jarmie, J. H. Jett, P. W. Keaton, Jr., R. A. Nisley, and K. Witte, Phys. Rev. C **15**, 518 (1977).

[Els 89] Ch. Elster, and P. C. Tandy, Phys. Rev. C **40**, 881 (1989).

[Els 90] Ch. Elster, T. Cheon, E. F. Redish, and P. C. Tandy, Phys. Rev. C **41**, 814 (1990).

[Emr 83] H. J. Emrich, Ph.D. thesis, University of Mainz, 1983.

[End 78] P. M. Endt, and C. van der Leun, Nucl. Phys. **A310**, 1 (1978).

[Eng 70] H. A. Enge, and S. B. Kowalski, 3rd Int. Conf. on *Magnet Technology* (1970).

[Fel 90] A. E. Feldman, Ph.D. thesis, University of Maryland, 1990.

[Fes 54] H. Feshbach, C. E. Porter, and W. F. Weisskopf, Phys. Rev. **96**, 448 (1954).

[Fla 90] B. S. Flanders, J. J. Kelly, H. Seifert, D. Lopiano, B. Aas, A. Azizi, G. Igo, G. Weston, C. Whitten, A. Wong, M. V. Hynes, J. McClelland, W. Bertozzi, J. M. Finn, C. E. Hyde-Wright, R. W. Lourie, B. E. Norum, P. E. Ulmer, and B. L. Berman, preprint (to be published).

[Fra 57] W. E. Frahn, and R. H. Lemmer, Nuove Cimento **5**, 1564 (1957); **6**, 664 (1957).

[Fra 85] M. A. Franey, and W. G. Love, Phys. Rev. C **31**, 488 (1985).

[Ger 79] H. V. von Geramb, F. A. Brieva, and J. R. Rook, in *Microscopic Optical Potentials*, edited by H. V. von Geramb (Springer-Verlag, Berlin, 1979), p. 104.

[Ger 83] H. V. von Geramb, in *The Interaction Between Medium Energy Nucleons in Nuclei—1982*, AIP Conf. Proc. No. 97, edited by H. O. Meyer (AIP, New York, 1983), p. 44.

[Ger 90] H. V. von Geramb, and K. A. Amos, Phys. Rev. C **41**, 1384 (1990).

[Gli 89] J. Glickman, Master's thesis, Massachusetts Institute of Technology, 1989.

[Glo 85] C. W. Glover, P. Schwandt, H. O. Meyer, W. W. Jacobs, J. R. Hall, M. D. Kaitchuck, and R. P. DeVito, Phys. Rev. C **31**, 1 (1985).

[Haf 70] M. I. Haftel, and F. Tabakin, Nucl. Phys. **A158**, 1 (1970).

[Ham 62] T. Hamada, and D. Johnston, Nucl. Phys. **34**, 382 (1962).

[Ham 90] S. Hama, B. C. Clark, E. D. Cooper, H. S. Sherif, and R. L. Mercer, Phys. Rev. C **41**, 2737 (1990).

[Har 84] P. Harihar, K. K. Seth, D. Barlow, S. Iversen, M. Kaletka, H. Nann, A. Saha, C. F. Williamson, J. W. Wong, M. Deady, W. J. Gerace, Phys. Rev. Lett. **53**, 152 (1984).

[Hüf 72] J. Hüfner, and C. Mahaux, Ann. Phys. **73**, 525 (1972).

[Hyn 81] M. V. Hynes, J. J. Kelly, B. W. Peterson, and B. E. Norum, (unpublished)

[IUCF 86] IUCF Scientific and Technical Report, p. 138 (1986).

[Jeu 74] J. P. Jeukenne, A. Lejeune, and C. Mahaux, Phys. Rev. C **10**, 1391 (1974).

[Jeu 76] J. P. Jeukenne, A. Lejeune, and C. Mahaux, Phys. Rep. **25**, 83 (1976); Phys. Rev. C **15**, 10 (1977); **16**, 80 (1977).

[K600 L] IUCF K600 Lectures.

[K600 P] A New Magnetic Spectrometer System for Intermediate Energy Physics at the Indiana University Cyclotron Facility—A Joint Proposal of the Indiana University Cyclotron Facility and the University of Maryland, 1980.

[Kel 81] J. J. Kelly, Ph.D. thesis, Massachusetts Institute of Technology, 1981.

[Kel 82] J. J. Kelly, *Proton Scattering to Collective States: what we learn about the Effective Interaction in the Nuclear Medium*—Invited talk presented at the 1982 IUCF Workshop on the Interaction between Medium Energy Nucleons in Nuclei, Bloomington, Indiana (October 28–30, 1982).

[Kel 85a] J. J. Kelly, in *Advanced Methods in the Evaluation of Nuclear Scattering Data*, Vol. 236 of *Lecture Notes in Physics*, edited by H. J. Krappe and R. Lipperheide (Springer-Verlag, Berlin, 1985), p. 335.

[Kel 85b] J. J. Kelly, *Effective Density-Dependent Interactions for Nucleon-Nucleus Scattering*—Lecture presented on June 12, 1985 at the National Summer School in Nuclear Physics, Georgetown University, Washington, D.C.

[Kel 86a] J. J. Kelly, in *Nuclear Structure at High Spin, Excitation, and Momentum Transfer (McCormick's Creek State Park, Bloomington, Indiana, 1985)*, Proceedings of the Workshop on Nuclear Structure at High Spin, Excitation, and Momentum Transfer, AIP Conf. Proc. No. 142, edited by Hermann Nann (AIP, New York, 1986), p. 27.

[Kel 86b] J. J. Kelly, W. Bertozzi, T. N. Buti, J. M. Finn, F. W. Hersman, C. Hyde-Wright, M. V. Hynes, B. E. Norum, A. D. Bacher, G. T. Emery, C. C. Foster, W. P. Jones, D. W. Miller, B. L. Berman, J. A. Carr, and F. Petrovich, Phys. Lett. **169B**, 157 (1986).

[Kel 86c] J. J. Kelly, in *Current Problems in Nuclear Physics*, edited by T. Paradellis, and S. Kossionides (Hellenic Physical Society Conference, Athens, 1986), Vol. 1, p. 325.

[Kel 87] J. J. Kelly, in *Relations Between Structure and Reactions in Nuclear Physics*, edited by D. H. Feng, M. Vallieres, and B. H. Wildenthal (World Scientific, Singapore, 1987), p. 222.

[Kel 88] J. J. Kelly, Phys. Rev. C **37**, 520 (1988).

[Kel 89a] J. J. Kelly, W. Bertozzi, T. N. Buti, J. M. Finn, F. W. Hersman, C. Hyde-Wright, M. V. Hynes, M. A. Kovash, B. Murdock, B. E. Norum, B. Pugh, F. N. Rad, A. D. Bacher, G. T. Emery, C. C. Foster, W. P. Jones, D. W. Miller, B. L. Berman, W. G. Love, J. A. Carr, and F. Petrovich, Phys. Rev. C **39**, 1222 (1989).

[Kel 89b] J. J. Kelly, Phys. Rev. C **39**, 2120 (1989).

[Kel 90a] J. J. Kelly, W. Bertozzi, T. N. Buti, J. M. Finn, F. W. Hersman, C. Hyde-Wright, M. V. Hynes, M. A. Kovash, B. Murdock, P. Ulmer, A. D. Bacher, G. T. Emery, C. C. Foster, W. P. Jones, D. W. Miller, and B. L. Berman, Phys. Rev. C **41** 2504 (1990); Q. Chen, J. J. Kelly, P. P. Singh, M. C. Radhakrishna, W. P. Jones,

and H. Nann, *ibid.* **41** 2514 (1990); J. J. Kelly, Q. Chen, P. P. Singh, M. C. Radhakrishna, W. P. Jones, and H. Nann, *ibid.* **41** 2525 (1990).

[Kel 90b] J. J. Kelly, A. E. Feldman, B. S. Flanders, H. Seifert, D. Lopiano, B. Aas, A. Azizi, G. Igo, G. Weston, C. Whitten, A. Wong, M. V. Hynes, J. McClelland, W. Bertozzi, J. M. Finn, C. E. Hyde-Wright, R. W. Lourie, P. E. Ulmer, B. E. Norum, and B. L. Berman, preprint (to be published).

[Kel ALL] J. J. Kelly, Computer Code ALLFIT.

[Kel LEA] J. J. Kelly, Computer Code LEA.

[Ker 59] A. K. Kerman, H. McManus, and R. M. Thaler, Ann. Phys. **8**, 551 (1959).

[Kha 89] M. A. Khandaker, A. E. Feldman, B. S. Flanders, J. J. Kelly, H. Seifert, P. Karen, B. E. Norum, and P. Welch, Bull. Am. Phys. Soc. **34**, 1233 (1989).

[Kir 89] Th. Kirst, K. Amos, L. Berge, M. Coz, and H. V. von Geramb, Phys. Rev. C **40**, 912 (1989).

[Lac 80] M. Lacombe, B. Loiseau, J. M. Richard, R. Vinh Mau, J. Cote, P. Pires, and R. de Tourreil, Phys. Rev. C **21**, 861 (1980).

[Lah 82] G. Lahm, Ph.D. thesis, University of Mainz, 1982.

[Lem 60] R. H. Lemmer, and A. E. S. Green, Phys. Rev. **119**, 1043 (1960).

[Lis 89] J. Lisantti, D. J. Horen, F. E. Bertrand, R. L. Auble, B. L. Burks, E. E. Gross, R. O. Sayer, D. K. McDaniels, K. W. Jones, J. B. McClelland, S. J. Seestrom-Morris, and L. W. Swenson, Phys. Rev. C **39**, 568 (1989).

[Lom 68] E. L. Lomon, and H. Feshbach, Ann. Phys. (N.Y.) **48**, 94 (1968).

[Lom 82] E. L. Lomon, Phys. Rev. D **26**, 576 (1982).

[Lov 78] W. G. Love, Nucl. Phys. **A312**, 160 (1978).

[Lov 81] W. G. Love, and M. A. Franey, Phys. Rev. C **24**, 1073 (1981).

[Lov 83] W. G. Love, in Proc. of the RCNP-Kikuchi Summer School on Nuclear Physics (Kyoto, Japan, 1983).

[Mac 87] R. Machleidt, K. Holinde, and Ch. Elster, Phys. Rep. **149**, 1 (1987).

[Mar 83] S. A. Martin *et al.*, Nucl. Instr. Meth. **214**, pp. 295 ff. (1983).

[May 84] T. Mayer-Kuckuk, *Kernphysik* (Teubner, Stuttgart, 1984).

[Mis 83] R. A. Miskimen, Ph.D. thesis, Massachusetts Institute of Technology, 1983.

[Møl 45] C. Møller, K. Dan. Vidensk. Selsk. Mat.-Fys. Medd. **23**, 1 (1945).

[Mur 87] D. P. Murdock, and C. J. Horowitz, Phys. Rev. C **35**, 1442 (1987).

[Nad 77] A. Nadasen, Ph.D. thesis, Indiana University, 1977 (available as IUCF Internal Report No. 77-5).

[Nak 84] K. Nakayama, S. Krewald, J. Speth, and W. G. Love, Nucl. Phys. **A431**, 419 (1984).

[Nak 88] K. Nakayama, and W. G. Love, Phys. Rev. C **38**, 51 (1988).

[Neg 72] J. W. Negele, and D. Vautherin, Phys. Rev. C **5**, 1472 (1972).

[McN 83] J. A. McNeil, J. R. Shepard, and S. J. Wallace, Phys. Rev. Lett. **50**, 1439 (1983).

[Ott 88] N. Ottenstein, S. J. Wallace, and J. A. Tjon, Phys. Rev. C **38**, 2272 (1988); **38**, 2289 (1988).

[Ott 90] N. Ottenstein, Ph.D. thesis, University of Maryland, 1990.

[Per 62] F. Perey, and B. Buck, Nucl. Phys. **32**, 353 (1962).

[Per 63] F. Perey, in *Proceedings of the Conference on Direct Interactions and Nuclear Reaction Mechanisms, Padova, 1963*, edited by E. Clementel and C. Villi (Gordon and Breach, New York, 1963).

[Pet 81] F. Petrovich, and W. G. Love, Nucl. Phys. **A354**, 499 (1981).

[Pet 85] F. Petrovich, J. A. Carr, R. J. Philpott, A. W. Carpenter, and J. J. Kelly, Phys. Lett. **165B**, 1 (1985).

[Pre 75] M. A. Preston, and R. K. Bhaduri, *Structure of the Nucleus* (Addison-Wesley Publishing Company, Inc., Reading, Massachusetts, 1975).

[McN 83] F. Petrovich, H. McManus, V. A. Madsen, and J. Atkinson, Phys. Rev. Lett. **22**, 895 (1969).

[Pic 84] A. Pickelsimer, P. C. Tandy, R. M. Thaler, and D. H. Wolfe, Phys. Rev. C **30**, 1861 (1984).

[Ray 85] L. Ray, and G. W. Hoffmann, Phys. Rev. C **31**, 538 (1985).

[Ray 87] L. Ray, Phys. Rev. C **35**, 1072 (1987).

[Ray 90] L. Ray, Phys. Rev. C **41**, 2816 (1990).

[Red 87] E. F. Redish, and K. Stricker-Bauer, Phys. Rev. C **35**, 1183 (1987).

[Rei 68] R. V. Reid, Ann. Phys. **50**, 411 (1968).

[Rik 84] L. Rikus, K. Nakano, and H. V. von Geramb, Nucl. Phys. **A414**, 413 (1984).

[Sat 83] G. R. Satchler, *Direct Nuclear Reactions* (Oxford University Press, New York, 1983).

[Sch 82] P. Schwandt, H. O. Meyer, W. W. Jacobs, A. D. Bacher, S. E. Vigdor, M. D. Kaitchuck, and T. R. Donoghue, Phys. Rev. C **26**, 55 (1982).

[Ser 86] B. D. Serot, and J. D. Walecka, *The Relativistic Nuclear Many-Body Problem*, Advances in Nuclear Physics, Vol. 16, edited by J. W. Negele, and E. Vogt (Plenum Press, New York, 1986).

[Set 85] K. K. Seth, D. Barlow, A. Saha, R. Soundranayagam, S. Iversen, M. Kaletka, M. Basko, D. Smith, G. W. Hoffman, M. L. Bartlett, R. Fergerson, J. McGill, and E. C. Milner, Phys. Lett. **158B**, 23 (1985).

[Sie 70] P. J. Siemens, Nucl. Phys. **A141**, 225 (1970).

[Sla 51] J. C. Slater, Phys. Rev. **81**, 385 (1951).

[Spe 67] J. E. Spencer, and H. A. Enge, Nucl. Instr. and Meth. **49**, 181 (1967).

[Ste 85] E. J. Stephenson, J. Phys. Soc. Jpn. (Suppl.) **55**, 316 (1985).

[Wal 85] S. J. Wallace, *Relativistic Description of Proton Nucleus Interactions*—Invited lecture presented at the 1985 RCNP-Kikuchi Summer School, Kyoto, Japan (August, 1985).

[Wal 87a] S. J. Wallace, *Relativistic Multiple Scattering*—Invited talk presented at the International Symposium on Medium Energy Physics, Beijing, China (June 23–27, 1987).

[Wal 87b] S. J. Wallace, Ann. Rev. Nucl. Part. Sci. **37**, 267 (1987).

[Wat 53] K. M. Watson, Phys. Rev. **89**, 575 (1953).

[Wya 60] P. J. Wyatt, J. G. Wills, and A. E. S. Green, Phys. Rev. **119**, 1031 (1960).

[Zei 71] B. Zeidman, *The HRS Spectrometer System, I. Concepts and Design* (LA 4773-MS, Part I, UC 28, Los Alamos Scientific Laboratory, 1971).